Irene Burghardt
Volkhard May
David A. Micha
Eric R. Bittner
Editors

SPRINGER SERIES IN CHEMICAL PHYSICS 93

Energy Transfer Dynamics in Biomaterial Systems

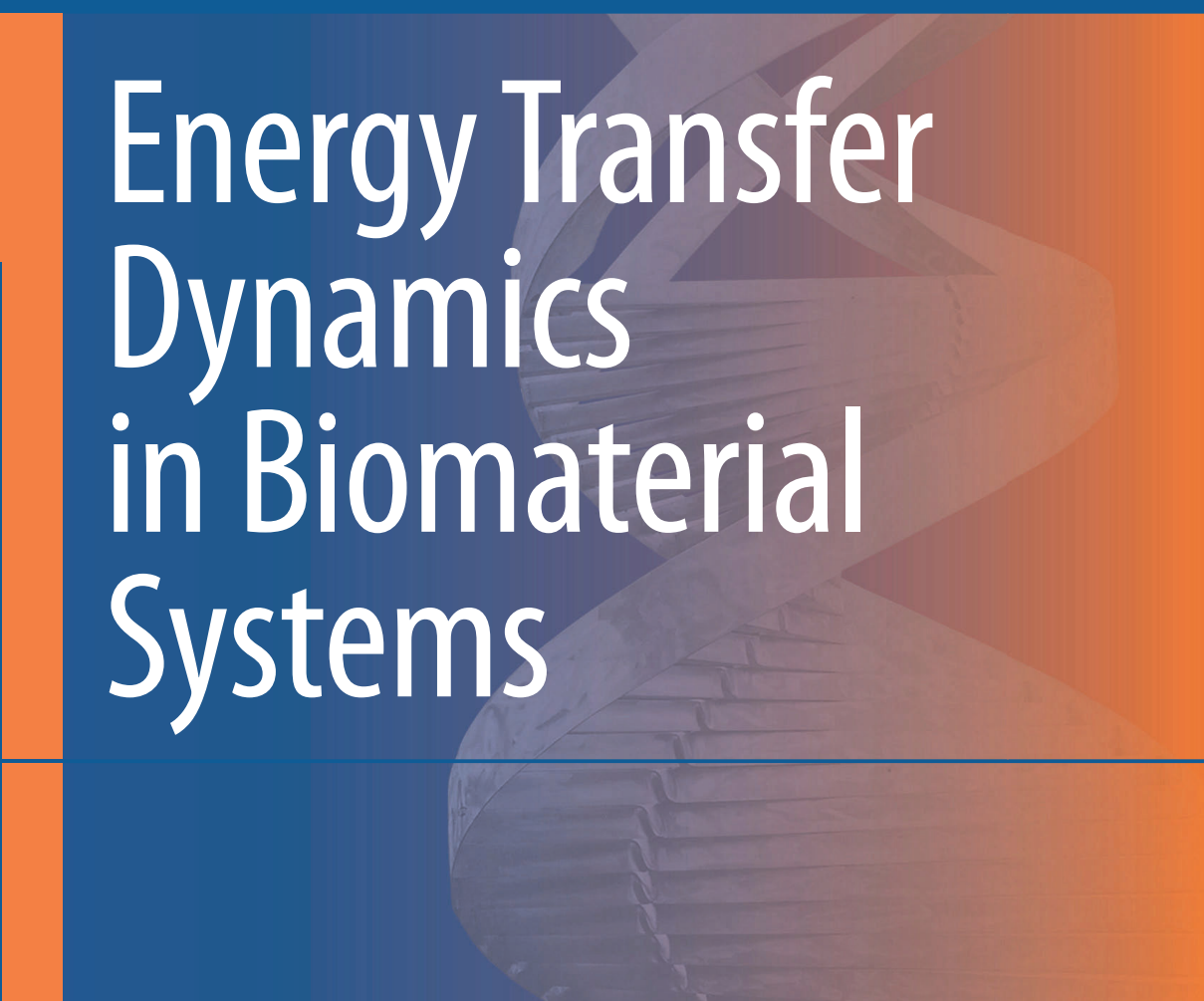

Springer

Springer Series in
CHEMICAL PHYSICS 93

Springer Series in

CHEMICAL PHYSICS

The purpose of this series is to provide comprehensive up-to-date monographs in both well established disciplines and emerging research areas within the broad fields of chemical physics and physical chemistry. The books deal with both fundamental science and applications, and may have either a theoretical or an experimental emphasis. They are aimed primarily at researchers and graduate students in chemical physics and related fields.

For further volumes
http://www.springer.com/series/676

Irene Burghardt
Volkhard May
David A. Micha
Eric R. Bittner
(Eds.)

Energy Transfer Dynamics in Biomaterial Systems

With 133 Figures

Springer

Irene Burghardt
Ecole Normale Supérieure
Département de Chimie
24 rue Lhomond
75231 Paris Cédex 05, France
E-Mail: irene.burghardt@ens.fr

David A. Micha
University of Florida
Departments of Chemistry and of Physics
2318 New Physics Building
P.O. Box 11843
Gainesville, FL 32606, USA
E-Mail: micha@qtp.ufl.edu

Volkhard May
Humboldt-Universität zu Berlin
Institut für Physik
AG Halbleitertheorie
Newtonstrasse 15
12489 Berlin, Germany
E-Mail: may@physik.hu-berlin.de

Eric R. Bittner
University of Houston
Department of Chemistry
136 Fleming Building
Houston, TX 77204, USA
E-Mail: bittner@uh.edu

ISSN 0172-6218
ISBN 978-3-642-02305-7 e-ISBN 978-3-642-02306-4
DOI 10.1007/978-3-642-02306-4
Springer Dordrecht Heidelberg London New York

Library of Congress Control Number: 2009934514

Cover motif: Clare College (Cambridge, England): DNA double helix sculpture (2007, photograph by Gisela Parker)

Cover design: eStudioCalamar Figueres/Berlin

Printed on acid-free paper

Springer is part of Springer Science+Business Media (www.springer.com)

Preface

The role of quantum coherence in promoting the efficiency of the initial stages of photosynthesis is an open and intriguing question.
Lee, Cheng, and Fleming, *Science* **316**, 1462 (2007)

The understanding and design of functional biomaterials is one of today's grand challenge areas that has sparked an intense exchange between biology, materials sciences, electronics, and various other disciplines. Many new developments are underway in organic photovoltaics, molecular electronics, and biomimetic research involving, e.g., artifical light-harvesting systems inspired by photosynthesis, along with a host of other concepts and device applications. In fact, materials scientists may well be advised to take advantage of Nature's 3.8 billion year head-start in designing new materials for light-harvesting and electro-optical applications.

Since many of these developments reach into the molecular domain, the understanding of nano-structured functional materials equally necessitates fundamental aspects of molecular physics, chemistry, and biology. The elementary energy and charge transfer processes bear much similarity to the molecular phenomena that have been revealed in unprecedented detail by ultrafast optical spectroscopies. Indeed, these spectroscopies, which were initially developed and applied for the study of small molecular species, have already evolved into an invaluable tool to monitor ultrafast dynamics in complex biological and materials systems. The molecular-level phenomena in question are often of intrinsically quantum mechanical character, and involve tunneling, non-Born-Oppenheimer effects, and quantum-mechanical phase coherence. Many of the advances that were made over recent years in the understanding of complex molecular systems can therefore be transposed and extended to the study of

biomaterials. As suggested by the above quotation, fundamental quantum effects like coherence and decoherence could eventually have a direct impact on biological and material function.

The present volume summarizes recent progress in this direction, focusing on the role of quantum dynamical phenomena in biological and nanostructured systems. The book grew out of a workshop that was held in October 2007 in Paris on the topic of "Energy flow dynamics in biomaterial systems". This workshop drew together researchers from several fields including the spectroscopy and theory of light-harvesting systems, DNA and organic materials, molecular electronics, quantum chemistry of excited states and nonadiabatically coupled systems, and mixed quantum-classical simulation methods for processes in condensed phases and in spatially extended systems. Similarly to the workshop, the scientific scope of this book is deliberately broad in terms of the physical systems studied and yet unified in the use of spectroscopic techniques, quantum dynamical methods, or a combination thereof to study transient and often ultrafast energy and charge transfer events in complex systems. The goal of this book is to illustrate the many aspects of today's theoretical picture of the fundamental electronic, vibronic, and transport phenomena in biological systems, molecular electronics materials, and biomimetic systems. At the same time, the book includes methodological parts which highlight that today's theoretical and simulation strategies still involve fundamental open questions, especially relating to the treatment of non-equilibrium transport, the mixing of quantum and classical descriptions and the coupling to environments of varying complexity.

The volume is structured into five parts, the first three of which are more focused on applications and systems, while the last two parts are mainly methodologically oriented. The first part addresses excitation energy transfer in photosynthetic reaction centers, polypeptides, and other multichromophoric systems. The second part gives a *tour d'horizon* of DNA research, involving photoexcitation and energy migration, anharmonic vibrational dynamics, as well as drug intercalation into DNA. In the third part, quantum transport at interfaces and junctions is addressed, with examples from organic photovoltaics and molecular electronics. The techniques used here range from explicit quantum simulations of high-dimensional interfacial electron-phonon dynamics to non-equilibrium Green's function techniques for studying charge transport along a molecular wire connected between two semi-infinite continua. Finally, the last two parts cover recent methodological developments in open system dynamics and hybrid quantum-classical methods, and highlight that the need for approximate but consistent quantum-statistical treatments is of paramount importance for all of the systems considered here.

Even though this volume can only cover certain aspects of a rapidly evolving field, we believe that it illustrates the many challenges ahead, and also the success of today's theoretical and spectroscopic methods in achieving a molecular-level understanding of nanostructured systems. As we learn more about the scientific foundations of the subject, we can hope to increase the

number of materials that would optimize functionality in both structure and properties. For example, lattices of nanostructured adsorbates could be good candidates for light harvesting, among many other types of novel materials. Therefore, theoretical insight and computational tools as provided in the following chapters might allow us to broaden the search for suitable light harvesting and conversion devices – a very timely quest as the world searches for renewable sources of energy.

We are grateful to the workshop participants who agreed to submit a chapter reviewing their work in a pedagogic style that would be accessible to someone who is not an expert in their particular discipline. Certainly without their enthusiasm and diligent efforts, this volume would never have got off the ground.

We also wish to thank Dr. Gayle Zachmann and the staff of the Paris Research Center (PRC) for providing a wonderful venue for this second "PRC workshop". Funding for the workshop came from various sources, including in particular the European Science Foundation's "Simulations of Bio-Materials" (SimBioMa) program, the French Centre National de la Recherche Scientifique (CNRS), and the US National Science Foundation (NSF) through the Materials Computation Center at the University of Illinois and the Texas Center for Superconductivity (TcSUH).

Finally, we are thankful to Dr. Marion Hertel, Ingrid Samide, and Dr. Christian Caron of the Springer office at Heidelberg for their cooperation and invaluable help with publishing this volume. We are also most grateful to Dr. Stephan Wefing for his help with the typesetting of the manuscript. Together with the preceding PRC workshop publication on "Quantum Dynamics of Complex Molecular Systems" (Springer Chemical Physics Series 83), we hope that this volume will foster new insights at the border between molecular sciences, biology, and materials research.

Paris, France — *Irene Burghardt*
Berlin, Germany — *Volkhard May*
Gainesville (Florida), USA — *David Micha*
Houston (Texas), USA, and Cambridge, Great Britain — *Eric Bittner*

March 2009

Contents

List of Contributors

Agostini, Federica
Dipartmento di Fisica
Università degli Studi di Roma "La Sapienza"
Piazzale Aldo Moro 2
00185 Roma
Italy
federica.agostini@roma1.infn.it

Bagchi, Biman
Solid State and Structural Chemistry Unit
Indian Institute of Science
Bangalore, 560012
India
bbagchi@sscu.iisc.ernet.in

Bittner, Eric R.
Department of Chemistry and the Texas Center for Superconductivity
University of Houston
Houston, TX 77204
USA
bittner@uh.edu

Bonella, Sara
Dipartmento di Fisica
Università "La Sapienza"
Piazzale Aldo Moro 2
00185 Roma
Italy
sara.bonella@roma1.infn.it

Burghardt, Irene
Ecole Normale Supérieure
Département de Chimie
24 Rue Lhomond
75231 Paris Cedex 05
France
irene.burghardt@ens.fr

Caprara, Sergio
Dipartmento di Fisica
Università degli Studi di Roma "La Sapienza"
Piazzale Aldo Moro 2
00185 Roma, Italy
sergio.caprara@roma1.infn.it

Ciccotti, Giovanni
CNISM Unità Roma 1
and Dipartmento di Fisica
Università degli Studi di Roma "La Sapienza"
Piazzale Aldo Moro 2
00185 Roma
Italy
giovanni.ciccotti@roma1.infn.it

Coker, David F.
Department of Chemistry
Boston University
590 Commonwealth Avenue
Boston, Massachusetts, 02215

U.S.A.
and
School of Physics
University College Dublin
Belfield
Dublin 4
Ireland
coker@bu.edu

Collini, Elisabetta
Department of Chemistry
80 St. George Street
Institute for Optical Sciences
and Centre for Quantum Information
and Quantum Control
University of Toronto
Toronto, Ontario M5S 3H6
Canada

Cuniberti, Gianaurelio
Institute for Material Science
and Max Bergmann Center of
Biomaterials
Dresden University of Technology
01062 Dresden
Germany
g.cuniberti@tu-dresden.de

Curutchet, Charles
Department of Chemistry
80 St. George Street
Institute for Optical Sciences
and Centre for Quantum Information
and Quantum Control
University of Toronto
Toronto, Ontario M5S 3H6
Canada

Czader, Arkadiusz
Department of Chemistry and the
Texas Center for
Superconductivity
University of Houston
Houston, TX 77204
USA
aczader@uh.edu

Došlić, N.
Department of Physical Chemistry
Rudjer Bošković Institute
10000 Zagreb
Croatia

Fidder, H.
Institut für Chemie und Biochemie
Freie Universität Berlin
Takustr. 3
14195 Berlin
Germany

Geva, Eitan
Chemistry Department
University of Michigan
930 N. University Ave.,
Ann Arbor MI, 48109-1055
USA
eitan@umich.edu

Grunwald, Robbie
Chemical Physics Theory Group
Department of Chemistry
University of Toronto
Toronto, Ontario, M5S 3H6 Canada
rgrunwal@chem.utoronto.ca

Gustavsson, Thomas
Laboratoire Francis Perrin
CEA/DSM/IRAMIS/SPAM - CNRS
URA 2453
CEA/Saclay, 91191 Gif-sur-Yvette
France
thomas.gustavsson@cea.fr

Gutiérrez, R.
Institute for Material Science
and Max Bergmann Center of
Biomaterials
Dresden University of Technology
01062 Dresden
Germany
rafael.gutierrez@tu-dresden.de

Heyne, K.
Institut für Physik
Freie Universität Berlin
Arnimallee
14195 Berlin
Germany
heyne@physik.fu-berlin.de

Hynes, James T.
Ecole Normale Supérieure
Department of Chemistry
CNRS, UMR 8640 PASTEUR
24 Rue Lhomond
75231 Paris Cedex 05
France
and
Department of Chemistry and Biochemistry
University of Colorado
Boulder CO 80309-0215
USA
hynes@chimie.ens.fr

Kapral, Raymond
Chemical Physics Theory Group
Department of Chemistry
University of Toronto
Toronto, Ontario, M5S 3H6 Canada
rkapral@chem.utoronto.ca

Kelly, Aaron
Chemical Physics Theory Group
Department of Chemistry
University of Toronto
Toronto, Ontario, M5S 3H6 Canada
akelly@chem.utoronto.ca

Kleinekathöfer, Ulrich
School of Engineering and Science
Jacobs University Bremen
Campusring 1
28759 Bremen
Germany
u.kleinekathoefer@jacobs-university.de

Kühn, Oliver
Institut für Physik
Universität Rostock
Universitätsplatz 3
18051 Rostock
Germany
oliver.kuehn@uni-rostock.de

Krishnan, G. M.
Institut für Chemie und Biochemie
Freie Universität Berlin
Takustr. 3
14195 Berlin
Germany

Lavery, Richard
Institut de Biologie et Chimie des Protéines
CNRS UMR 5086
Université de Lyon
7 passage du Vercors
Lyon 69367
France
richard.lavery@ibcp.fr

Leathers, Andrew
Departments of Chemistry and Physics
University of Florida
Gainesville, FL 32611-8435
USA
leathers@qtp.ufl.edu

Mac Kernan, Dónal
School of Physics
University College Dublin
Belfield
Dublin 4
Ireland
donal.mackernan@ucd.ie

Markovitsi, Dimitra
Laboratoire Francis Perrin
CEA/DSM/IRAMIS/SPAM - CNRS URA 2453
CEA/Saclay, 91191 Gif-sur-Yvette
France
dimitra.markovitsi@cea.fr

May, Volkhard
Institut für Physik, Humboldt-Universität zu Berlin
Newtonstraße 15
12489 Berlin
Germany
may@physik.hu-berlin.de

Micha, David A.
Departments of Chemistry and Physics
University of Florida
Gainesville, FL 32611-8435
USA
micha@qtp.ufl.edu

Mirkovic, Tihana
Department of Chemistry
80 St. George Street
Institute for Optical Sciences
and Centre for Quantum Information and Quantum Control
University of Toronto
Toronto, Ontario M5S 3H6
Canada

Mukherjee, Arnab
Ecole Normale Supérieure
Chemistry Department
24 Rue Lhomond
75231 Paris Cedex 05
France
Arnab.Mukherjee@colorado.edu

Pereverzev, Andrey
Department of Chemistry and Texas Center for
Superconductivity
University of Houston
Houston, Texas 77204
USA
andrey.pereverzev@mail.uh.edu

Ramon, John Glenn S.
Department of Chemistry and Texas Center for
Superconductivity
University of Houston
Houston, Texas 77204
USA

Ryndyk, D. A.
Institute for Theoretical Physics
University of Regensburg
D-93040 Regensburg
Germany
dmitry.ryndyk@physik.uni-regensburg.de

Scholes, Gregory D.
Department of Chemistry
80 St. George Street
Institute for Optical Sciences
and Centre for Quantum Information and Quantum Control
University of Toronto
Toronto, Ontario M5S 3H6
Canada
gscholes@chem.utoronto.ca

Shang, Jianyuan
Chemistry Department
University of Michigan
930 N. University Ave.
Ann Arbor MI, 48109-1055
USA

Song, Bo
Institute for Material Science
and Max Bergmann Center of Biomaterials
Dresden University of Technology
01062 Dresden
Germany
bo.song@tu-dresden.de

Tamura, Hiroyuki
Ecole Normale Supérieure
Département de Chimie

24 Rue Lhomond
75231 Paris Cedex 05
France
present address:
Advanced Institute for Material Research
Tohoku University
2-1-1 Katahira Aobaku Sendai
Japan
tamura.hiroyuki@orion.ocn.ne.jp

Zhu, Hui
Institut für Physik, Humboldt-Universität zu Berlin
Newtonstraße 15
12489 Berlin, Germany

Part I

Excitation Energy Transfer in Complex Molecular and Biological Systems

Electronic Energy Transfer in Photosynthetic Antenna Systems

Elisabetta Collini, Carles Curutchet, Tihana Mirkovic, and Gregory D. Scholes

Department of Chemistry, 80 St. George Street, Institute for Optical Sciences, and Centre for Quantum Information and Quantum Control, University of Toronto, Toronto, Ontario M5S 3H6 Canada gscholes@chem.utoronto.ca

Abstract. Electronic energy transfer is reviewed with a particular emphasis on its role in photosynthesis. The article describes the advances in theory that have been motivated by studies of photosynthetic light harvesting antenna proteins. Noting that most theoretical work presently focuses on just a few photosynthetic systems, the extraordinary scope and diversity of systems actually found in nature is described.

1 Introduction

Electronic energy transfer (EET) is a topic found in thousands of scientific papers each year. It is a process whereby the energy of absorbed light is transmitted between molecules. EET is used, for example, to harvest light in photosynthesis, measure distances in proteins, and it accelerates the photodegradation of polymers. [1] In recent years attention has turned to the study of EET in complex assemblies of molecules. An example of the importance of energy transfer involves the EET antenna-effect, which is essential to assist in the capture of light in photosynthesis. We now know that photosynthetic organisms, including higher plants, algae and bacteria, employ specialized antenna complexes that have evolved to optimize the spectral and spatial cross-section for light absorption. The light, once captured by an antenna protein, is efficiently distributed to specialized energy conversion machinery known as the reaction center. In the reaction center, the solar energy is converted to chemical energy. This chain of events is achieved, over a hierarchy of time scales and distances, with remarkable efficiency. Förster theory has enabled the efficiency of EET to be predicted and analyzed in numerous and diverse areas of study. Through studies of photosynthetic light harvesting antennas, recent work has contributed to learning how the nanoscale organization of molecules changes the way that EET happens. Theoretical work hints at interesting dynamical

I. Burghardt et al. (eds.), *Energy Transfer Dynamics in Biomaterial Systems*, Springer Series in Chemical Physics 93, DOI 10.1007/978-3-642-02306-4_1,

aspects of EET (coherence) that may be explored by learning precisely how the interplay between electronic couplings among molecules and their interaction with the random fluctuations of the environment dictate localization of excitation and dynamics of ensuing photo-processes. The current status and some future opportunities in the field will be described below.

Photosynthetic proteins have served as excellent model systems for studying EET and, in particular, for testing EET theory. This is because they are highly organized, photostable, and soluble multichromophoric systems. While many findings are not critically relevant to photosynthetic efficiency, they have had a considerable impact on our knowledge of the chemical physics of EET. The key feature of this body of work is bringing together detailed structural information with theory and photophysical measurements (including ultrafast laser spectroscopy). Questions previously addressed include whether wavefunction overlap contributes to electronic couplings between molecules, whether the point-dipole approximation realistically captures the Coulombic part of the interchromophore electronic coupling, and how excitonic effects change the dynamics. Questions of current interest include coherent contributions to dynamics, the nature of bath fluctuations (in particular the idea of correlated fluctuations), solvent screening in proteins, and extrapolation between the limits of weak versus strong electronic coupling.

2 Overview of photosynthetic organisms and their Light-Harvesting Antenna complexes

2.1 Introduction

According to the broadest definition of photosynthesis, any process in which some kind of cellular energy is derived from light can be defined as photosynthetic. Key processes in photosynthesis are the absorption of solar energy by antenna complexes and the efficient transfer of excitation energy to photochemical reaction centers (RCs), where the energy is trapped in the form of a stable charge separation, which eventually is converted to chemical energy through a series of dark reactions. There is a remarkable variety of organisms carrying out photosynthesis, from the well known green plants (trees, shrubs, grasses and other type of vegetation) to microscopic forms of life such as algae and photosynthetic bacteria. [2–4] In this section a brief overview of different types of photosynthetic organisms will be outlined, with particular attention to their antenna complexes. The vast majority of the pigments in a photosynthetic organism are not chemically active, but are bound in antenna complexes. The photosynthetic antenna system is organized to collect and deliver the energy of incident sunlight, by means of excitation transfer, to the reaction center complexes where photochemistry takes place. Their functions are to increase the effective cross section of photon absorption by

increasing the number of pigments associated with each photochemical complex and to optimize and regulate light absorption for various growth and habitat conditions. By incorporating many pigments into a single unit, the biosynthetically expensive reaction center and electron transport chain can be used to maximum efficiency. A remarkable variety of antenna complexes have been identified from various classes of photosynthetic organisms, showing no apparent correlations in their structural organization or in terms of the pigments they utilize. This seems to suggest different evolutionary patterns for different antennas, but also emphasizes the importance of the light-gathering process in general.

In section 2.2 an overview of the organisms capable of photosynthesis will be outlined, with particular attention to the evolutionary relationships between their antenna complexes. In section 2.3 some of the most representative antenna families will be described and discussed in more detail. Finally, a deeper look in the EET mechanism will be given in section 2.4, in which the dynamics of EET in a particular antenna complex will serve as an example.

2.2 Antenna complexes: evolutionary point of view

Among the many different ways to classify the light-harvesting complexes, one of the most informative for our purpose is to organize organisms according to their evolutionary relationship. This approach is also known as the phylogenetic approach [5] since the classification of organisms is based on comparison of the sequence of RNA molecules, believed to retain information about their evolutionary history. [6–8] The evolutionary tree of life drawn based on this method is shown in Fig. 1. Only the Eukarya and Bacteria domains are shown whereas the third domain (Archaea) is omitted here since no organisms belonging to this group show photosynthetic ability.

An overview of the main groups of prokaryotic and eukaryotic photosynthetic organisms is summarized in Table 1. The table illustrates the main groups in which prokaryotes and eukaryotes can be divided, together with their antenna complexes, reaction centers (RC), pigment types, photosynthetic reactions and ecology of significant organisms. Among the Bacteria domain, five different groups (or phyla) with photosynthetic ability can be distinguished. [9] Four of them (purple bacteria, green sulfur, green non-sulfur bacteria, and heliobacteria [10]) are anoxygenic, since they do not release oxygen as product of the photosynthetic reaction [11], whereas cyanobacteria are the only oxygenic group. [12]

According to the fossil records [13], the early photosensitizers were purple bacteria and green sulfur bacteria. Purple bacteria have been the subject of many structural [14] and spectroscopic studies. [15–17] Particular attention was focused on their antenna complexes (LH1, LH2), which represent the best understood system in terms of light collection and energy transfer. Recently, some interest has also been directed to green bacteria containing chlorosomes,

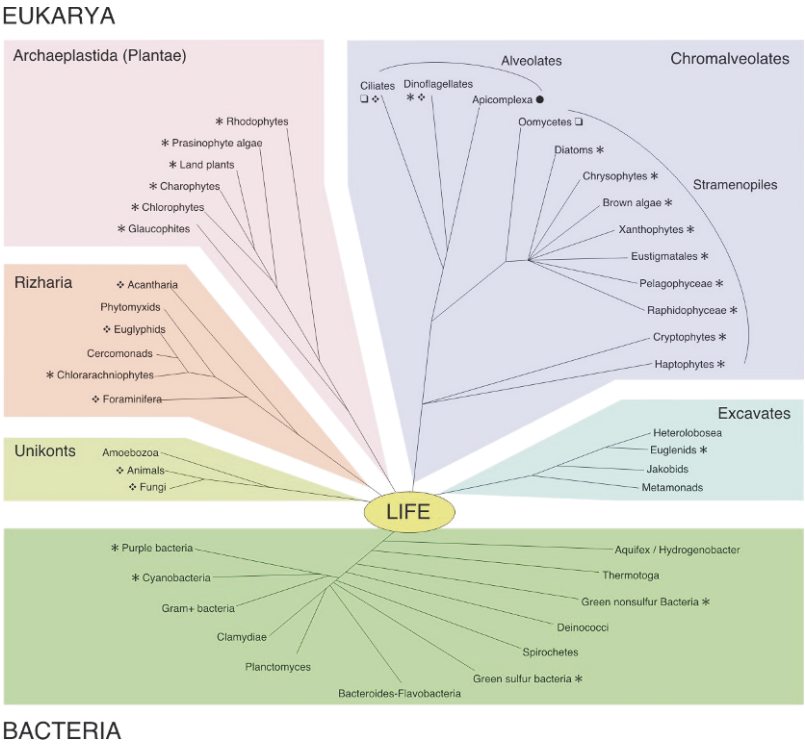

Fig. 1: Evolutionary tree of Eukarya and Bacteria domains. The third domain (Archaea) is omitted here since no organisms belonging to this group show photosynthetic ability. The tree is further annotated to indicate the distribution of photosynthesis among the major groups: ∗ photosynthetic organisms, • organisms with relict plastid but no photosynthetic genes, △ some species with algal symbionts or sequestered plastids, § organisms with no plastids but potentially photosynthetic genes in nucleus.

highly specialized antenna structures whose efficiency in light-harvesting allows these organisms to live in environments with the lowest light intensity of any known photosynthetic organism. [11,18] In green nonsulfur bacteria, each RC is accompanied by a membrane-intrinsic light-harvesting complex, generally denoted as B808-865, believed to be similar to LH1 of purple bacteria based on protein sequence similarities, although there is no direct evidence that it forms a ring around the RC.

The next step in the evolution of prokaryotic photosynthesis was the appearance of the first oxygenic organisms, the cyanobacteria. This group now encloses a large variety of organisms, living wherever light is available. [12] Cyanobacteria evolved a more sophisticated linear electron transfer involving two RCs instead of one as in anoxygenic bacteria. The two RC types can

be distinguished by their ability to reduce either quinones (type II) or FeS centers (type I) as terminal electron acceptors. Cyanobacteria (and all other oxygenic organisms) utilize both types of RCs in a two-step sequence known as the "Z-scheme" where H_2O is the reductant. [3] Anoxygenic photosynthetizers employ instead only one type of RC (purple bacteria: type II, green photosynthetic bacteria: type I) and different electron donors. [11] Structural models based on X-ray crystallographic data seem to confirm that the two RC types share a common evolutionary origin despite the substantial differences between the protein sequences. [19] The light-harvesting apparatus of cyanobacteria is characterized by large antenna complexes called phycobilisomes (PBS), elaborate multi-subunit structures containing chlorophylls (*Chl*) and bilins (*bil*, open-chain tetrapyrrole chromophores) associated with the cytoplasmic surface of the thylakoid membrane. [20]

In contrast to prokaryotes, which are single-cell organisms with simple cellular organization, eukaryotes are more sophisticated organisms. In many cases they are multi-cellular organisms with highly differentiated cells containing subcellular organelles, called chloroplasts [21], where photosynthesis is carried out. There is evidence that chloroplasts originated from a cyanobacteral-like cell initially incorporated from the host cell by an endosymbiosis process. [22] Photosynthetic eukaryotic organisms can be mainly divided in two groups: algae and plants. Algae can be further classified in many groups, based on different classification systems. The most commonly studied are green algae (chlorophytes), red algae (rhodophytes), chromophytes (including brown algae, diatoms and cryptophytes), and dinophytes. [23]

The red algal chloroplasts, like their cyanobacterial ancestors, use PBS as light-harvesting antennas as well as membrane-intrinsic antennas associated only to the photosystem (PS) I and binding *Chl* a. The green algal chloroplasts have membrane-intrinsic antenna proteins associated to both the photosystems, binding *Chl* b as well as *Chl* a, whereas the many groups of brown and yellow algae (dinoflagellates, cryptophytes, and chromophytes sensu lato) have related antenna proteins binding *Chl* c and *Chl* a. The antenna proteins of these two groups are members of a very large protein family, the light-harvesting complex (LHC) superfamily. Usually these complexes are referred as LHCI and LHCII, depending on their association with PS I or PS II, respectively.

Genetic analyses show that also the *Chl* a-binding proteins of red algae must be considered members of the LHC superfamily, even though they bind only *Chl* a and are associated only with PS I. [24] This shows that PBS (associated primarily with PS II) and membrane-intrinsic antennas of the LHC superfamily could coexist in the same chloroplast, and strongly supports a common evolutionary origin for all chloroplasts. [25]

Land plants are believed to originate from a single branch of the green algae. [26] This group is the most complex and heterogeneous: it includes bryophytes, which are the simplest ones, often resembling algae, and vascular

Table 1: Phototropic Organisms on Earth

taxon	group	antennae cmplx	RC	Photosynthesis reaction			representative organisms	pigments	Abs Max	ecology	ref
				e donor	C source	product					
Anoxygenic Bacteria											
Green Photosynthetic bacteria	Chloroflexaceae (Green non sulfur or filamentous bacteria)	Chlorosome (–25,000 BChls) B808-865 cmplx (32 or 24 BChls ?)	type II	sulfide	organic C, CO_2	S	chloroflexus auriantiacus	BChl a/c + car	740	Strict anaerobes, photoautotrophics, often found at the very lo west levels of the photic zone in lake or microbial mat environments	18
							candidatus chl. halophila	BChl a/c + car	760		28
	Chlorobiaceae (Green sulfur bacteria)	Chlorosome (–25,000 BChls) FMO protein cmplx (21 BChls)	type I	sulfide, reduced S, H_2,Fe	organic C, CO_2	sulfate	chlorobium tepidum	BChl a/c + car	750	Facultatively aerobics, often found in hot spring microbial mats either surface exposed or underlie a layer of cyanobacteria	18,29
							chlorobium vibrioforme	BChl a/d + car	725		18,29
							chlorobium phaeobateroides	BChl a/e + car	712		18
Purple bacteria	Chromatiaceae (Purple sulfur bacteria)	All species: LH1 (core antennae complx, 32 or 30 BChls)) Most species: LH2 (peripheric antennae cmplx, 18-16 + 9-8 BChls)	type II	organic and inorganic C, S, sulfate, sulfide, sulfite, H_2, Fe	organic C, CO_2	S, sulfate, CO_2	Thiocapsa pfennigii	BChl b+ car	850-1025	Extremely versatile metabolically: aerobic and anoxigenic heterotrophs and anoxigenic aoutotroph Widely distributed: fresh and marine waters, hot springs, anoxic aquatic sediments, sewage treatment ponds	30
							Chromatium purpuratum	BChl a+ car	800-830		15
							Chromatium vinosum	BChl a+ car	807 (888)		31
	Rhodospirillaceae (Purple non sulfur bacteria)						Rhodopseudomonas viridis	BChl b+ car	800-960		32,33
							Rhodopseudomonas palustris	BChl a+ car	800-850		15
							Rhodopseudomonas acidiophila	BChl a+ car	800-820		5,16,17
							Rhodobacter spaeroides	BChl a+ car	760-800-850		33
							Rhodospirillum rubrum (NO LH2)	BChl a+ car	800-875		33
Heliobacteria		no peripheral or accessory antennae	type I	sulfite, reduced S, sulfate	Pyruvate, ethanol, lactate, acetate and butyrate	?	heliobacillus mobilis	BChl g + car	791	Obligate anaerobes, photoheterotrophics, all known species can fix nitrogen, isolated from soil samples (typical habitat:rice paddy soil)	10
							heliobacterium chlorum	BChl g + car	787		
Oxygenic Bacteria											
Cyanobacteria		PBS (300 – 1000 bil depending upon species)	type I and II	H_2O, S	CO_2	O_2	Orders: 1. Gloeobacterales 2. Chroococcales 3. Pleurocapsales 4. Oscillatoriales 5. Nostocales 6. Stigonematales	Chl a/b/c/d + car + bil	from 400 to 700	found in almost every conceivable habitat, from oceans to fresh water to bare rock to soil. Most are found in fresh water, while others are marine, occur in damp soil, or even temporarily moistened rocks in deserts. A few are endosymbionts in lichens, plants, various protists, or sponges	12,34,35

Table 1: Phototropic Organisms on Earth (continued)

taxon	group	antennae cmplx	RC	Photosynthesis reaction			representative organisms	pigments	Abs Max	ecology	ref
Algae											
Rhodophytes (red algae)		LHCI (8 Chl a) PBS	type I and II	H_2O	CO_2	O_2	gigartina	Chl a/d + car + bil		fresh water, most common in tropical marine environments > 5,000 species known multicellular, filamentous, or unicellular	23,36,37
							porphyridium	Chl a + car +bil			
Chrlorophytes (green algae)		LCHI, LCHII (see higher plants)	type I and II	H_2O	CO_2	O_2	chlamydomonas	Chl a/b + car		mostly found in fresh water, but a fair number are marine or terrestrial (soil, tree bark) > 5,000 species known multicellular, unicellular, filamentous, colonial	23,36
							codium	Chl a/b + car			
							euglena	Chl a/b + car			
							Pisum (pea)	Chl a/b + car			
Chromophytes	Phaeo (brown algae)	FCP Chl a/c-LHC (number and nature of pigments depending upon species)	type I and II	H_2O	CO_2	O_2	Fucus, Laminaria	Chl a/c1,c2 + car		mostly marine; predominantly in temperate and cold oceans	23,36,38,39
	Bacillaria						Odontella, Phaeodactylum	Chl a/c1,c2 + car			
	Chryso						Giraudyopsis	Chl a/c1,c2 + car			
	Raphido						heterosigma	Chl a/c1,c2 + car			
	Xantho (yellow-green algae)						Pleurochloris	Chl a/c + car			
	Hapto						Pavlova,Isochrysis	Chl a/c1,c2 + car			
	Eustigma						Nannochloropsis	Chl a + car			
	Crypto	Chl a/c-LHC PBP (8 bil)					Chroomonas, cryptomonas	Chl a/c2 + car + bil			
Dynophytes		Chl a/c-LHC (11 Chls + 14 car) PCP (6 Chls + 12 car)					Amphidinium	Chl a/c2 + car		mostly found in warm, tropical oceans; mostly unicellular some are heterotrophic, living as parasites on fish and other protist some are bioluminescent	42
Plants											
Bryophytes Vascular plants		LHCI (~60 Chl a/b) LHCII (39-45 Chl a/b) CP29 (6Chla+2Chl b) CP26 (6Chla+3Chl b) CP24 (6Chla+4Chl b)	type I and II	H_2O	CO_2	O_2, VOCs		Chl a/b + car		moist land environments aquatic to desert	3,44,45,46

Chl = chlorophyll; *BChl* = bacteriochlorophyll; *car* = carotenoid; *bil* = bilin; FMO = Fenna-Matthews-Olson protein complex; LH1(2)=light-harvesting complex 1(2) in purple bacteria; PBS = phycobilisome; PBP = phycobiliprotein; LCHI(II) = light-harvesting *Chl* a/b-binding complex I(II) in higher plants; FCP = fucoxanthin-*Chl* a/c polypeptide; PCP = peridinin-chlorophyll-protein; *Chl* a/c-LHC= light-harvesting chlorophyll a/c-binding complex in chromophytes.

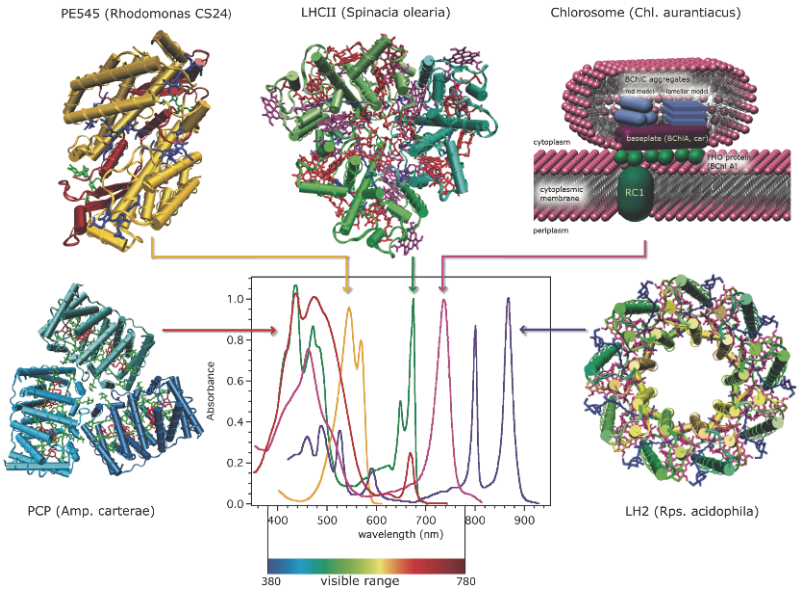

Fig. 2: Molecular structure and absorption spectra at 77K of some of the most representative light-harvesting antennas. The names of the corresponding organisms are given between brackets.

plants like ferns and seed plants. We direct the reader to the literature for a more comprehensive classification. [27]

2.3 Classes of Antenna: structure and function

As already pointed out, there are only two types of photosynthetic reaction centers showing a highly conserved molecular structure, despite the enormous diversity among photosynthetic organisms and their different habitats. [47] There are instead several classes of antenna complexes, which show no apparent correlations in the structural organization or in terms of the pigments they utilize. In the previous section a general overview of these complexes was given, with particular attention to the evolutionary relations between them. In this section some representative antenna systems will be considered in more detail.

Fig. 2 shows the absorption spectra and the structure of some of the most representative antenna complexes. The figure highlights how antenna complexes from different organisms can have extremely different protein structures and can differ widely in the nature, number and organization of the absorbing pigments. Photosynthetic organisms clearly must have evolved adapting their antenna complexes to the light quality in their habitats. In general, green

plants, largely based on land, have a limited repertoire of pigment types compared to algae living in aquatic environments where penetrating wavelengths of light may be variously attenuated by the water column and overlying organisms. A first broad classification of the antenna complexes can be made according to their position with respect to the photosynthetic membrane: integral membrane antennas, containing proteins that cross the lipid bilayer, and peripheral membrane antennas, which are linked to one side of the membrane, can thus be distinguished. In the second class lie, for example, phycobilisomes (PBSs) [20] of cyanobacteria and red algae, chlorosomes and FMO protein of green bacteria [16, 27–29] and peridinin-chlorophyll proteins (PCPs) of dinophytes. [42] Furthermore, integral membrane antennas can further be divided in core antennas, intimately associated with the RC, as CP43 and CP47 complexes of PS II or LH1 complex of purple bacteria, and accessory antennas, as LHCI / LCHII in PS I / II and LH2 complex of purple bacteria. In Fig. 3 a schematic model of the major light-harvesting complexes in different organisms is depicted, showing their relative positions with respect to the membrane and reaction centers.

LH1 and LH2 antenna complexes

The antenna system of purple bacteria is the best understood of all the light-harvesting antennas. It consists of two types of pigment-protein complexes known as light-harvesting 1 and 2 (LH1, LH2). The LH1 complex is an integral membrane core antenna, which is found in fixed proportion to the reaction centre and physically surrounding it. The LH2 complex is an integral accessory membrane antenna typically arranged more peripherally and not in contact with the reaction center, found in most but not all of the organisms. The exact ratio of LH2/LH1 complexes present in the photosynthetic membrane is controlled by growth conditions. [11, 18] LH1 complex consists of ca. 16 $\alpha-\beta$ subunits in the shape of a large ring of ca. 120Å diameter, surrounding the RC complex. LH2 is built up from subunits consisting of a heterodimer of α and β peptides along with three molecules of bacteriochlorophyll (*BChl*) a or b and one molecule of carotenoid. These subunits aggregate into larger complexes in which eight or nine subunits assemble into ring-shaped units of ca. 65Å diameter. [14]

The absorption spectrum of LH2 exhibits two bands, centered at 800 and approximately 850 nm (depending on the species). The structure of the complex provides a clear explanation for these two absorption features which arise from the same type of *BChl* a chromophore. The pigments contributing the 800 nm feature form a ring with the molecular plane of each *BChl* parallel to the membrane plane. These pigments are usually known as B800 pigments and owing to their large center-to-center distances they show photophysical features of monomeric *BChl* a. The pigments that contribute the 850 nm absorption feature (B850 pigments) are arranged with their molecular plane almost perpendicular to the membrane plane and their π-electron systems ap-

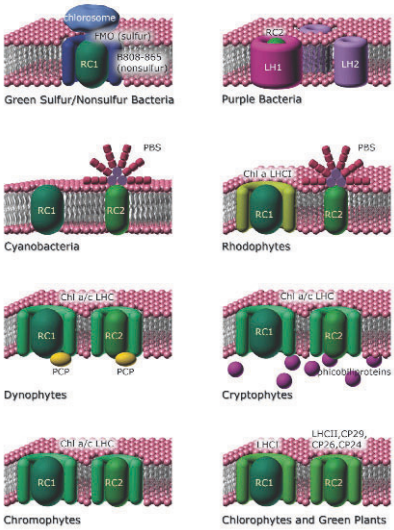

Fig. 3: Schematic model of light-harvesting compartments in photosynthetic organisms and their position with respect to the membrane and the reaction centers. RC1(2): Photosystem I(II) reaction centre. Peripheral membrane antennas: Chlorosome/FMO in green sulfur and nonsulfur bacteria, phycobilisome (PBS) in cyanobacteria and rhodophytes and peridinin-chlorophyll proteins (PCP) in dynophytes. Integral membrane accessory antennas: LH2 in purple bacteria, LHC family in all eukaryotes. Integral membrane core antennas: B808-867 complex in green nonsulfur bacteria, LH1 in purple bacteria, CP43/CP47 (not shown) in cyanobacteria and all eukaryotes.

proach closely (≈3.5 Å closest approach and ≈9 Å center-to-center). Their collective interaction with light leads to a band of exciton states, where the oscillator strength is concentrated into the states absorbing at ≈850 nm. This system is reviewed in refs [15,15,51]. The LH2 system has been deeply studied and a great deal has been learned by comparing experimental results and different theories proposed to explain EET mechanisms. A review covering other aspects of the light-harvesting proteins from purple bacteria can be found in ref. [48].

Chlorosomes and FMO protein

Chlorosomes are the characteristic light-harvesting complexes of green nonsulfur bacteria and green sulfur bacteria and constitute the most efficient low-light light-harvesting complexes found in nature. [52] The chlorosome is the only known photosynthetic system where the majority of pigments (*BChl* c, d, e) are not organized in pigment-protein complexes but instead are assembled

into aggregates filling the internal part of the chlorosome. No high-resolution structural information is available for this complex so researchers have developed models based on microscopy, NMR, small-angle X-ray diffraction and spectroscopic data. Rod-like [11, 53] and lamellar-like [54] models have been proposed, and it is not clear yet which model is more realistic. In addition to *BChl* c, d and e, all chlorosomes contain a small amount of *BChl* a. *BChl* a is associated with CsmA, a small protein in the so-called baseplate of the chlorosome. [11, 52] The chlorosomes from green filamentous bacteria are approximately 100 nm long, 20-40 nm wide and 10-20 nm high. Chlorosomes from green sulfur bacteria are considerably larger with lengths from 70 to 260 nm and widths from 30 to 100 nm. [18]

The Fenna-Matthews-Olson (FMO) protein is an unusual, water-soluble chlorophyll protein found only in green sulfur bacteria. [18] It is believed to be located between the chlorosome and the cytoplasmatic membrane and functions as an excitation transfer link between the chlorosome and the reaction center. Each subunit contains 7 *BChl* a molecules embedded in a primarily β sheet structured protein. The protein has a trimeric quaternary structure, with a three-fold axis of symmetry in the center of the complex. [55] The green nonsulfur bacteria do not contain the FMO protein. In these organisms the chlorosome transfers energy directly to the integral membrane core antenna B808-865, and then to the reaction center.

LHC family

The light-harvesting complexes (LHCs) are a superfamily of membrane-intrinsic chlorophyll-binding proteins present in all photosynthetic eukaryotes. LHCs of chlorophytes, chromophytes, dinophytes, and rhodophytes are similar in that they have three transmembrane α-helix regions and several highly conserved *Chl*-binding residues. All LHCs bind *Chl* a, but in specific taxa certain characteristic pigments accompany *Chl* a: *Chl* b and lutein in chlorophytes, *Chl* c and fucoxanthin in chromophytes, *Chl* c and peridinin in dinophytes, and zeaxanthin in rhodophytes. [25] The two major antennas belonging to this family are generally known as LHCI and LHCII since they are associated with PS I and PS II, respectively.

LHCI consists of four different membrane proteins with varying stoichiometry depending on light intensity and other environmental factors. These four proteins, binding in total ca. 80-100 *Chl*s and 55-60 carotenes, assemble into two dimers creating a half-moon-shaped belt on one side of the RC1 core. [43, 44, 56, 57] The LHCII complex is the most abundant membrane protein in the biosphere. It is organized into trimeric complexes consisting of various combinations of three very similar subunit proteins. The complex contains between 36 and 42 *Chl*s (a and b) and 10 to 12 xanthophyll molecules. [58, 59] Unlike LHCI, tightly bound to RC1, the LHCII complexes are usually found associated to PS II but under certain conditions they can dissociate from

it and migrate independently between stacked and unstacked regions of the thylakoid membrane. [60]

Beside the major trimeric peripheral antenna complexes LHCII, the outer antenna apparatus of PS II also contains the so-called minor peripheral antenna complexes CP24, CP26 and CP29. [59] These proteins show significant sequence homology with LHCII and are generally believed to adopt structure similar to that of LHCII, although these minor complexes are monomeric. They bind approximately 8-10 *Chl*s (a and b), besides several xanthophylls. In general, one copy of each protein is found per PS II RC. [46]

The PS II bind also two core antennas, CP43 and CP47, *Chl* a-binding proteins closely associated with RC2 in cyanobacteria and chloroplasts (there is always one CP43 and one CP47 per RC2). Both proteins bind approximately 14 *Chl* a and at least two β-carotene molecules. Since both CP47 and CP43 occupy the closer position to the RC, it is generally believed that they have an important role in transferring the energy absorbed by the major antennas to the RC. [36, 59] These core antenna proteins may play an important role in regulation of light-harvesting.

Phycobiliproteins and Phycobilisomes (PBS)

Cyanobacteria and red algae contain supramolecular light-harvesting complexes called phycobilisomes, that are attached to the stromal side of the photosynthetic membrane [3, 62]. Several types of PBS are found in various organisms, although the most studied type is know as hemidiscoidal PBS. This complex consists of two or three types of pigment-proteins known as phycobiliproteins. There are four major groups of phycobiliproteins, namely phycoerythrin (PE), phycoerythrocyanin (PEC), phycocyanin (PC), and allophycocyanin (APC), whose absorption is centered in the spectral region between 470 and 650 nm, the portion of the visible spectrum that is poorly utilized by chlorophyll. In cyanobacteria and red algae, phycobiliproteins are arranged into large protein complexes called phycobilisomes (PBSs) [20] composed of a core, which holds allophycocyanin, and several outwardly oriented rods that are made of stacked disks of phycocyanin and phycoerythrin. This antenna system is attached through the core allophycocyanin proteins to the stromal side of the thylakoid membrane, usually in close proximity to PS II. The overall architecture of the hemidiscoidal PBS is shown in Fig. 3.

Phycobiliproteins are found also in cryptophytes but, differently from cyanobacteria and red algae, they are not organized into a phycobilisome, but instead they are located in the thylakoid lumen. Unique for cryptophytes, their phycobiliproteins do not exhibit a trimeric aggregation state characteristic for cyanobacteria, but instead they are present as $\alpha_1\beta\,\alpha_2\beta$ heterodimers, with each α subunit having a distinct amino acid sequence. [40]

Peridinin-Chl* a-*protein (PCP)

The unique water-soluble peridinin-*Chl* a-protein (PCP) complexes are found in many dynoflagellates in addition to intrinsic membrane complexes. [64] It contains *Chl* a and the unusual carotenoid peridinin in stoichiometric ratio of 1:4. Unlike other families of antennas, the main light-harvesting pigments are carotenoids, not chlorophylls. The structure of the PCP consists of a protein that folds into four domains, each of which embeds four peridinin molecules and a single *Chl* a. The protein then forms trimers, suggested to be located in the lumen [64] in contact with both LHCI and LHCII [66], allowing efficient EET to occur.

2.4 Dynamics of EET: an example

In the previous sections we highlighted the enormous variety of structures and diversity of pigment cofactors used by photosynthetic organisms. Despite this variety, all antennas show high efficiency in the light-harvesting process, reaching almost 100% at low light levels. One of the key ways to attain this efficiency is to ensure that the EET processes for transport of excitation to the RC is ultrafast: excitation transfer must be fast enough to deliver excitations to RC and have them trapped in a time short compared to the excited state lifetime in the absence of trapping. Excited state lifetimes of isolated antenna complexes, where the reaction centers have been removed, are typically in the 1-5 ns range. Observed excited state lifetimes of systems where antennas are connected to reaction centers are generally on the order of a few tens of picoseconds, which is sufficiently fast so that under physiological conditions almost all the energy is trapped by photochemistry.

The photosynthetic cryptophyte, *Rhodomonas* CS24, is an interesting model organism for which the dynamics and the mechanism of light harvesting have recently been investigated. [67] The light harvesting apparatus of this algal species is located in the chloroplast which houses a complex system of flattened sacs of membranes, the thylakoids, which are embedded, or suspended, in a matrix, the stroma. The overall impression of the chloroplast structure, can be gathered from micrographs in Fig. 4. The localization of the chloroplast inside the unicellular organism is manifested from the confocal micrograph (Fig. 4 a), where the emission originates from chromophores active in light harvesting. In Fig. 4 b)-c) enough details are visible to portray the structural components of the chloroplast, where the interthylakoid space is seen as electron-transparent, whereas the intrathylakoid space is strongly electron-opaque. The intrathylakoid material has been identified as a densely packed matrix of phycobiliproteins, [63,68,69], phycoerythrin 545 (PE545) in the case of *Rhodomonas* CS24, which cryptophytes utilize as their primary light harvesting antenna. In addition to the phycobiliproteins located in the lumenal compartment of the thylakoids, the pigment composition of cryptophytes is completed with *Chl* a, *Chl* c2, and the carotenoid alloxanthin. [70,71]

The three main chlorophyll-protein complexes that have been isolated from the thylakoid membrane of *Rhodomonas* CS24 are PS I, PS II, and a *Chl* a/c2 carotenoid light-harvesting complex (LHC). A comprehensive organization model of cryptophyte thylakoid components based on the localization of PE in the intrathylakoid space has been proposed by Spear-Bernstein [63], suggesting that the reaction centres PS I and PS II in addition to the *Chl* a/c2 LHC are distributed throughout the thylakoids. More precisely, as depicted in Fig. 4 d), *Chl* a/c2 LHC may be predominantly located in the stacked regions of the thylakoid, whereas the unstacked regions accommodate a homogeneous distribution of both photosystems.

Studies [67] on electronic energy transfer *in vivo* on intact cells have shed light on how the major components of the photosynthetic apparatus work together in the processes of light absorption, energy transfer and trapping. The elucidation of this complex problem was possible due to the great advances that have been made in the understanding of the dynamics and mechanisms of light harvesting by isolated photosynthetic antenna complexes. [40, 72] *In vivo*, the primary function of these chromoproteins is to absorb light, and facilitate energy migration with great efficiency to a reaction centre of PS I or PS II. The initial energy hopping steps in the light harvesting process occur among the chromophores of the biliprotein and those fast, light-initiated processes have been studied extensively in proteins isolated from the photosynthetic organisms. [40,72] Isolated chromoproteins are ideal multichromophoric model systems for energy transfer studies, since their structural model can be elucidated on the basis of x-ray diffraction data, from which the positions, orientations and conformational differences of constituent bilins can exactly be determined. That information is fundamental for energy transfer studies, as it has become evident that subtle differences in the structural organization of light harvesting chromophores can lead to various adaptations and mechanisms of optimization for light capture and energy funneling.

Over the past years, progress in ultrafast spectroscopies and high-resolution techniques has allowed elucidation of detailed structural and dynamical information that has, in turn, prompted the development of improved methods for calculating molecular interactions and energy transfer mechanisms. Comparison between experimental measurements and theoretical models has recently revealed that the most rapid energy transfer events in photosynthetic proteins cannot be explained with the conventional Förster's theory. [1, 72] An introduction to Förster's theory and how to think about EET in multichromophoric systems will be outlined in the following section. Here we report, as an example, the study of light-harvesting dynamics in cryptophyte phycocyanin 645 by means of steady-state and time-resolved spectroscopy in combination with high-resolution structural analysis and quantum chemical calculations. [41,74]

Phycocyanin 645 (PC645) is a biliprotein antenna recently isolated from cryptophyte organism Chroomonas CCMP270. The crystal structure [Fig. 5, panel (a)] revealed that the protein consists of four polypeptide chains, α_1, α_2 plus two β subunits, arranged in a complex known by convention as a dimer of

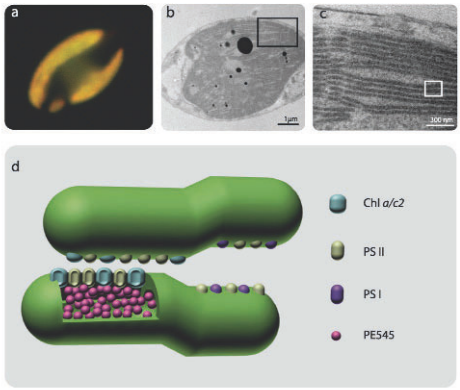

Fig. 4: (a) Confocal micrograph of Rhodomonas CS24, where the emission illustrates the location of the fluorescent chromophores of the light harvesting system housed inside the chloroplast of the unicellular organism. (b) Transmission electron micrograph of *Rhodomonas* CS24 displaying finer structural details, including the large network of thylakoid membranes within the chloroplast. (c) Magnified view of the thylakoids from (b), displaying the electron rich intrathylakoid region, filled with PE545. (d) A schematic diagram illustrating the possible organization of thylakoid components in cryptophyte algae based on the localization of the phycobiliprotein in the intrathylakoid space of Rhodomonas CS24.

$\alpha\beta$ monomers. [41] Three different types of bilins are employed as absorbing pigments: two 15,16-dihydrobiliverdins (DBVs), two mesobiliverdins (MBVs) and four phycocyanobilins (PCBs). The MBVs are located on both α-subunits at the α19 position, the DBVs on both β-subunits at the central doubly bound β50-61 position and the PCBs are located in both β-subunits at positions β82 and β158. The complexity of the bilin composition of cryptomonad biliproteins is suggested by the characteristic absorption spectrum that contains several absorption maxima [Fig. 5, panel (b)].

The timescales of population dynamics associated with the energy funnel were determined with pump-probe measurements with laser spectra centered at different wavelengths, so that different sets of pigments could be initially excited. From the pump-probe results analysis combined with quantum chemical calculations, the model of energy transfer depicted in panel (c) of Fig. 5 can be proposed.

Specifically, in the first step of the energy cascade, the light is captured by the DVB dimer located in the core of the complex. The energy is then transferred to peripherally located bilins (MBV, PCB 158) through a complex network of interactions that, owing to the very similar timescales and spectral features, are hard to separate. Probably, energy migration from DBV bilins to the MBV bilins occurs on a timescale ($T_1 \approx$0.6 ps) faster than the transfer

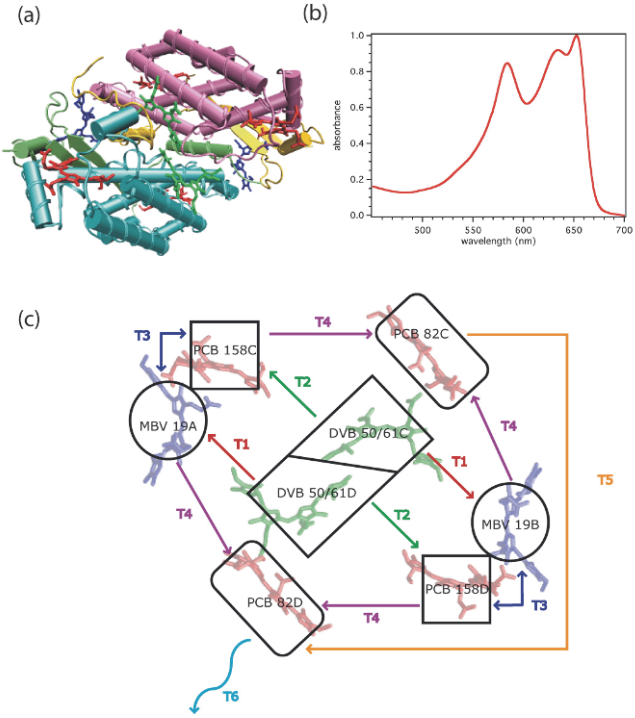

Fig. 5: (a) Crystal structure of PC645 at 1.4Å resolution showing the four subunits with different colors: α_1 (chain A) light green, α_2 (chain B) yellow, β (chain C) light blue, β (chain D) pink. The chromophores are also represented in different colors: central DVB dimer (green), PCBs (red) and MBVs (blue). (b) Absorption spectrum of PC645 at 77 K. (c) Model of energy transfer in PC645 based on ultrafast pump-probe measurements and quantum mechanical calculations. Bilins names are followed by a number and a letter identifying the amino acidic residue and the subunit chain to which the chromophores are linked, respectively.

to the PCB 158 bilins ($T_2 \approx 12$ ps), since the latter are slightly further apart from the central dimer and have a smaller spectral overlap with DBV bilins, compared to the MBV chromophores. The energy transfer processes between MBV and PCB 158 (T_3) and from them to the red-most PCB 82 bilins (T_4) cannot be resolved, due to their similar timescale, in the order of ten ps. The final energy transfer hop was specifically investigated and pump-probe anisotropy results confirmed that it occurs between the two red-most bilins PCB 82 with a timescale T_5 of approximately 15 ps. T_6 is the fluorescence lifetime of the emitting bilin, which have been found to be 1.44 ns. [75]

3 The mechanism of EET: Perspective from theory

3.1 Introduction

A key step in the understanding of the dynamics of EET was put forward by Förster more than 50 years ago, when he proposed an elegant theory relating experimental observables to the mechanisms of EET. [76] Förster's paper has had an enormous impact on many diverse areas of study, such us the understanding of the light-harvesting machinery in photosynthesis, [73] or the use of EET to achieve high internal quantum efficiencies in organic-based light emitting diodes. [77] A fascinating application of Förster theory is given by the fluorescence resonance energy transfer (FRET) technique, [78] in which EET is used as a spectroscopic ruler for the measurement of distances in biological systems, thus allowing to observe, for example, the dynamics of protein folding.

The great strength of Förster theory is that EET dynamics can be predicted from simple spectroscopic observables, such as the overlap between the donor emission and acceptor absortion line shapes. One important aspect of Förster theory, however, is the fact that it is formulated in the weak coupling limit, because it is based on the Golden Rule. This approximation assumes that the electronic interaction between donor and acceptor molecules is small compared to the coupling to the bath, so the bath equilibrates subsequent to donor excitation in a time scale considerably faster than that of EET. This ensures that the transfer is incoherent (Markovian). On the other hand, in the strong coupling limit the excitation is delocalized between the donor and the acceptor, giving rise to a so-called exciton state.

However, even when the weak coupling approximation holds, Förster theory predictions can be substantially affected by the approximations introduced in the ingredients needed to predict the rate: the electronic coupling between the donor and the acceptor, the solvent screening of this interaction, and the spectral overlap factor. In Förster theory, the shapes of the molecules are neglected, because the solvent-screened coupling promoting EET is approximated as an interaction between point transition dipoles immersed in a dielectric medium. On the other hand, the spectral overlap that ensures energy conservation in the EET process is obtained from donor and acceptor spectral lineshapes measured at the ensemble level. However, a more rigorous approach consists on estimating the overlap from the homogenously broadened single molecule spectra, and then performing the average over the ensemble static disorder. In addition, Förster theory has to be modified when one is dealing with multichromophoric systems, in which the incoherent hopping of excitation energy occurs between donor and acceptor states delocalized over several chromophores. [50]

In the last decade there has been an extraordinary progress towards accurate estimation of each one of the ingredients involved in the Förster rate equation, and comparison of these theories with available single-molecule EET

experiments has allowed researchers to better understand the intrinsic limitations of the Förster model. [80] In the following, we will introduce the Förster rate equation, then we will discuss recent advances achieved in the estimation of each one of these important quantities involved in the estimation of EET rates. Finally, we will comment on the special attributes of EET occurring in multichromophoric systems.

3.2 Förster theory for donor-acceptor pairs

The rate of EET between a pair of weakly coupled donor (D) and acceptor (A) molecules, according to Förster theory, [76] depends on the interchromophoric distance R, expressed in units of cm, their relative orientation (through the orientation factor k), and the spectral overlap I between donor emission and acceptor absorption spectra. The rate expression is:

$$k = \frac{1}{\tau_D} \frac{9000(\log 10)\kappa^2 \phi_D I}{128\pi^5 N_A n^4} \frac{1}{R^6} \tag{1}$$

where N_A is Avogadro's number (in units of mol^{-1}, n is the refractive index of the medium, ϕ_D is the fluorescence quantum yield and τ_D is the lifetime of the donor (in the same units as $1/k$).

The spectral overlap I is obtained from the overlap, on a wavenumber or wavelength scale, of the absortion spectrum of A, where intensity is in molar absorbance, with an area-normalized emission spectrum of D. I has units of $M^{-1}cm^3$

$$\begin{aligned} I &= \int_0^\infty \frac{a_A(\tilde{\nu}) f_D(\tilde{\nu})}{\tilde{\nu}^4} d\tilde{\nu} \\ &= \int_0^\infty a_A(\lambda) f_D(\lambda) \lambda^4 d\lambda \end{aligned} \tag{2}$$

Another way to express the rate introduces R_0, the Förster distance or critical transfer distance, at which the EET efficiency is 0.5:

$$k = \frac{1}{\tau_D} \left(\frac{R_0}{R} \right)^6 = \frac{1}{\tau_D} \left(\frac{8.785 \times 10^{-25} k^2 \phi_D I}{n^4 R^6} \right) \tag{3}$$

This latter expression is very useful, as R_0 is characteristic of each donor-acceptor pair, so it can be calibrated and then be used to predict distances from EET measurements. In Fig. 6 we show a schematic representation of the spectral overlap between donor emission and acceptor absorption given by Eq. 2 as well as a plot of the EET efficiency as a function of the donor-acceptor separation.

The great success of Förster theory lies on the simplicity of these expressions, which can be applied from purely spectroscopic data. However, the approximations underlying these equations are not evident at first sight. It is better to turn to the Golden Rule expression of the rate:

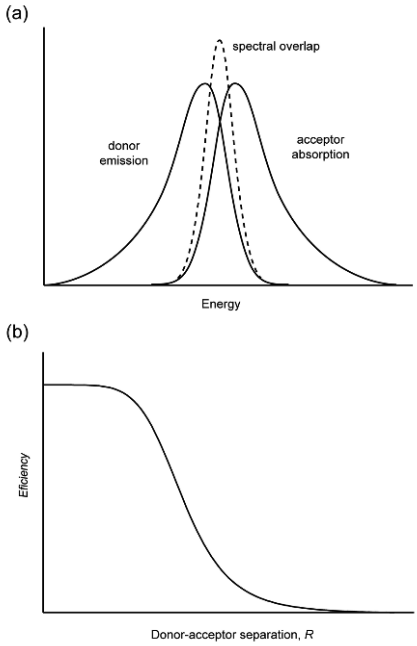

Fig. 6: Schematic representations of: (a) the spectral overlap between donor emission and acceptor absorption spectra promoting energy transfer; (b) energy transfer efficiency as a function of the donor acceptor distance.

$$k = \frac{2\pi}{\hbar}|sV_s|^2 \int_0^\infty d\epsilon J(\epsilon) \tag{4}$$

where V_s is the electronic coupling between the donor and the acceptor, s is the solvent screening factor, and $J(\epsilon)$ is the overlap between donor emission $f^{hom}(\epsilon)$ and acceptor absortion spectra $a^{hom}(\epsilon)$, both normalized to unit area on an energy scale, $J(\epsilon) = f^{hom}(\epsilon)a^{hom}(\epsilon)$.

In Eq. 4, one assumes that the electronic coupling $V = sV_s$ is independent of energy, and that there is no static disorder, the superscript *hom* indicating homogenously broadened spectra. However, the derivation of the Förster expression for the rate, Eq. 1, from the Golden Rule expression, Eq. 4, introduces two additional significant assumptions: i) that the electronic coupling can be appropriately described as a purely Coulombic interaction between point dipole transition moments of D and A, and ii) that the screening of this interaction by the surrounding medium can be described by the simple $s = 1/n^2$ factor. The characteristinc R^{-6} dependence of the Förster rate arises from the dipole approximation adopted in V_s. In addition, the orientation factor between the interacting dipoles is often assumed a value $\kappa^2 = 2/3$, which

is obtained as an average by considering that D and A are free to rotate independently in space. Obviously, if the rotational motion of the chromophores is significantly restricted, as is the case in many molecular systems, this latter assumption can lead to important discrepancies between theory and experiment (note that κ^2 can vary between 0 and 4). On the other hand, the dipole approximation and the screening factors assumed in Förster theory are a reasonable approximation if D and A are far apart, but more rigorous theoretical approaches demonstrate that they can severely fail to describe the coupling when D and A are in close proximity, as will be shown in next sections.

3.3 Electronic coupling

The electronic coupling is the driving force of EET processes, and accounts for the dependence of the rates on the interchromophoric separation and mutual orientation. In the last decade, there has been a lot of research effort aimed at the development of theoretical methods able to accurately estimate this quantity. [1] We shall start by noting that the electronic coupling can be partitioned into a long-range Coulombic contribution, V^{Coul}, and a short-range term which depends on the orbital overlap between D and A, V^{short}:

$$V_s = V^{Coul} + V^{short} \tag{5}$$

In Förster theory, [76] the short-range term V_{short} is neglected, and the Coulomb contribution is approximated as a dipole-dipole interaction between the transition dipole moments of D and A:

$$V_s \approx V^{Coul} \approx V^{dd} = \frac{\kappa \mu_D^T \mu_A^T}{R^3} \tag{6}$$

where the orientation factor is given by

$$\kappa = \hat{\mu}_D^T \cdot \hat{\mu}_A^T - 3(\hat{\mu}_D^T \cdot \hat{R})(\hat{\mu}_A^T \cdot \hat{R}) \tag{7}$$

and μ_D^T/μ_A^T are the transition dipole moments of D and A and R is their center-to-center separation ($\hat{\mu}_D^T$, $\hat{\mu}_A^T$, and $\hat{R}$ are the corresponding unit vectors).

As the transition dipole strength can be obtained from experimental spectra, Eq. 6 allows the derivation of the Förster rate expression, Eq. 1, which only depends on spectroscopic observables. However, for dipole-forbidden transitions, one must go beyond this expression and include higher order multipoles of the transition density in V^{Coul} or account for V^{short} terms. The short-range contribution accounts for overlap-induced interactions due to nonorthogonality of the D and A wavefunctions such as exchange, involving the two-electron term introduced by Dexter, or charge transfer. Here it is important to note that exchange interactions, however, are much weaker than charge transfer terms.

These short-range contributions to the coupling, however, are significant only when D and A are closely spaced (by $\approx$ 4 Å), [82] so in most cases it

is safe to neglect them as in Förster expression. The situation turns to be more delicate regarding an accurate calculation of the Coulomb term. There have been many studies pointing to the breakdown of the dipole approximation when the separation of the chromophores is similar to their molecular dimensions. [50] This happens because at close distances, the molecules begin to "feel" the shape of the others, so one cannot average the transition density onto a simple point dipole but has to take into account its distribution along the molecule. An efficient way of doing this is by computing transition charges displaced on the atomic sites, the transition monopole approximation (TMA), so that the V^{Coul} term is computed from the sum of pairwise interactions between these charges:

$$V^{Coul} = \sum_{ij} \frac{q^T_{D,i} q^T_{A,i}}{R_{ij}} \tag{8}$$

where $q^T_{D,i}$ and $q^T_{A,i}$ indicate transition charges located on sites i and j from D and A, respectively, and separated by a distance R_{ij}.

An accurate way of deriving these charges was proposed recently by Renger and co-workers based on fitting the electrostatic potential originated from quantum-mechanical (QM) derived transition densities, [83] the same way electrostatic charges are derived from ground state QM electrostatic potentials for use in molecular dynamics simulations.

A more rigorous approach, however, is to directly compute the interaction between the transition densities. This was first done numerically by discretizing the transition densities into finite volume elements of a 3D grid in the transition density cube (TDC) method: [84]

$$q^T_{X,i} = \int_{z_i}^{z_i+\delta_z} \int_{y_i}^{y_i+\delta_y} \int_{x_i}^{x_i+\delta_x} \rho^T_X(r) dx dy dz \tag{9}$$

where $q^T_{X,i}$ represent the charges distributed along the 3D grid representing the transition density $\rho^T_X(r)$ of molecule X. From these charges, the Coulomb coupling can be straightforwardly computed applying Eq. 8, but now the i and j indices indicate points in the 3D grids.

The TDC method takes into account the shape of the molecules in detail, and its accuracy in the calculation of the Coulomb coupling depends only on the size of the volume elements used in the grid (the "cube"). In this way, the TDC method has proven extremely useful in understanding the limitations of the point dipole approximation (PDA) in a variety of systems. In particular, how the PDA fails to describe the coupling when the interchromophoric center-to-center distance is comparable to the molecular dimensions, a situation found, for example, in many of the relevant interactions present in natural light-harvesting antennas. [50]

A further recent advance in the field has been the development of *ab initio* QM approaches able to compute analytically the Coulomb coupling between

transition densities, thus avoiding the discretization procedure used in the TDC method. [85–88] In this context, the most sophisticated method has been developed by Mennucci and co-workers, [85, 86] as in addition to the Coulomb term it solves for short-range contributions to the coupling, and more importantly, is able to coherently account for the effect of the environment both on the transition densities and on their interaction through the Polarizable Continuum Model (PCM). [89] We will discuss the importance of appropriately accounting for the effect of the surrounding environment in the next section, whereas here we will limit to the gas phase expressions. Such a method relies on a first-order perturbative expression of the coupling proposed by Hsu et al. [90] based on time-dependent density functional theory (TD-DFT). To first-order, the electronic coupling is given by:

$$V_s = \int dr \int dr' \rho_A^{T*}(r') \left(\frac{1}{|r - r'|} + g_{xc}(r', r) \right) \rho_D^T(r) - \omega_o \int dr \rho_A^{T*}(r) \rho_D^T(r) \tag{10}$$

where $g_{xc}(r', r)$ is the exchange plus correlation kernel, r is the electronic coordinate, and ω_o indicates the resonant transition energy.

In Eq. 10, V_s describes a chromophore-chromophore Coulomb and exchange-correlation (through the kernel g_{xc}) interaction corrected by an overlap contribution. The same expression can be applied to other methods different than TD-DFT to obtain the transition densities. In such cases, however, the exchange-correlation term reduces to an exchange contribution. We note also that short-range charge transfer contributions are not included in Eq. 10, as it relies on transition densities computed for the chromophores in the absence of their interaction. Obviously, the accuracy of the couplings obtained from either of the above mentioned approaches also strongly relies on the quality of the QM approach used to obtain the transition densities. Typically, semiempirical approaches or the configuration interaction of single excitations (CIS) methods have been widely used for such purpose, often along with empirical scaling procedures to correct for the overestimation of transition dipoles predicted by such methods. Of course, it would be desirable to avoid such scalings, and recently more accurate QM methods including electron correlation effects are starting to be used to obtain transition densities and compute EET couplings. These include time-dependent density functional theory (TD-DFT), [86] second-order approximate coupled cluster (CC2), [88] complete-active-space self-consistent-field (CASSCF) [91] and symmetry-adapted cluster/configuration interaction (SAC-CI). [91]

We have recently examined the applicability of Förster dipole-dipole approximation used in the calculation of the electronic coupling for a set of over 100 pairs of chromophores (chlorophylls, carotenoids, bilins) taken from structural models of photosystem II (PSII) from the cyanobacteria T. elongatus, the phycoerythrin 545 (PE545) and phycocyanin 645 (PC645) light-harvesting antenna from the cryptophyte algae *Rhodomonas* CS24 and Choomonas

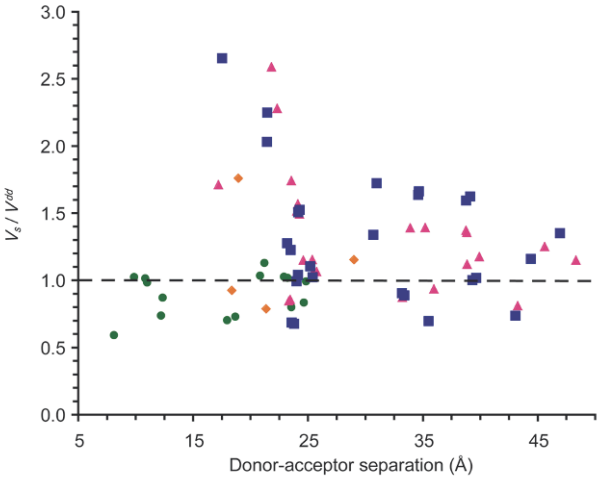

Fig. 7: Ratio between electronic couplings calculated from quantum-mechanically derived transition densities at the configuration interaction of single excitations (CIS) level, V_s, and the estimates of the dipole-dipole approximation used in Förster model, V^{dd}, as a function of the donor-acceptor center-to-center separation. Dipole-dipole values are obtained using the transition dipole moments given by the corresponding CIS calculations. Data points correspond to various chromophore pairs from the following structures: pink triangles = PE545, blue squares = PC645, green circles = PSII or LHCII, except orange diamonds = data involving the carotenoid in PSII. Reproduced with permission from J. Phys. Chem. B 2007, 111, 13253-13265. Copyright 2007 American Chemical Society.

CCMP270, and the peripheral light-harvesting complex (LHCII) from pea plant. In this study, [92] we evaluated the transition densities and transition dipoles from CIS quantum-mechanical calculations, and then compared the electronic couplings obtained by applying Eq. 10, the full V_s coupling, and the dipole-dipole coupling V^{dd} given by Eq. 6. Note here that at the CIS level the exchange-correlation term of Eq. 10 reduces to an exchange term. In Fig. 8 we plot the ratio V_s/V^{dd} as a function of the donor-acceptor separation for the various chromophore pairs. The results illustrate the strong errors that the dipole-dipole approximation can introduce in the estimation of the coupling. As expected, the dipole approximation improves at large donor-acceptor separations. However, even at separations much larger than the dimensions of the chromophores (≈15 Å for chlorophylls and bilins and ≈ 27 Å for the carotenoind in PS II) significant deviations are found, especially for bilin chromophores in PE545 and PC645, probably owing to their elongated and somewhat asymmetric structure.

3.4 Solvent screening

In the previous section, we have discussed the importance of taking into account the shape of the molecules in the calculation of electronic couplings, thus computing the interaction between transition densities not averaged over the molecular topology onto simple point dipoles. Similarly, taking into account the molecular shape has been recently demonstrated to be equally important in evaluating the screening of such interactions by the surrounding environment.

Let us start by considering the simple screening factor proposed by Förster, $s = 1/n^2$, where n is the refractive index of the medium. For a typical solvent, such as water, for example, this factor leads to strong reduction (by a factor of $\approx$4) in the predicted EET rate, such screening being independent of the relative position and orientation of the interacting chromophores. It is reasonable to think, however, that such screening would be different when two molecules are closely packed, so that the solvent (or surrounding medium) is excluded from the intermolecular region. Despite the importance of this issue, it has not been until recently that accurate studies on the screening of EET interactions have started to emerge due to the complexity of this problem. Hsu et al. [90] showed, for example, that when D and A share a common cavity inside the surrounding medium, the electronic coupling can be either enhanced or reduced, depending on the particular position and orientation of the molecules. However, in such a study the chromophores were assumed to be inserted in spherical cavities inside the dielectric representing the polarizable environment.

An important step towards the understanding of the screening of electronic couplings has been the development of a linear response model by Mennucci and co-workers, [85,86] which coherently couples the calculation of the transition densities, the excited-states calculation using a TD-DFT, CIS or ZINDO methods, and the interchromophore electronic coupling with the Polarizable Continuum Model (PCM) to account for the effect of the environment. [89] In the PCM model, the molecular system under scrutiny is fully described at a QM level, while the environment is represented as a structureless polarizable medium characterized by its macroscopic dielectric properties. Then, the response of the environment, obtained by solving the Laplace-Poisson equation, is represented as a set of apparent surface charges displaced on a properly molecular-shaped cavity. Such a method captures key features of the problem, such as accurate calculation of excited-states, the molecular shape, and the response of the surrounding medium to charge and, importantly, transition densities.

In the linear-response-PCM method, the electronic coupling is given by a sum of two terms:

$$V = V_s + V_{explicit} \tag{11}$$

$$V_{explicit} = \sum_k \left(\int dr \rho_A^{T*}(r) \frac{1}{|r-s|} \right) q(s_k; \varepsilon_{opt}, \rho_D^T) \tag{12}$$

where the k index runs over the apparent surface charges q displaced over the molecular-shaped cavity at position s_k that represent the solvent response. Here, such response to the transition densities is determined by the optical dielectric permittivity of the medium, ε_{opt}, i.e., approximately the square of the refractive index n.

The first term, V_s, accounts for the Coulomb-exchange direct interaction between D and A (see Eq.10), and the second, $V_{explicit}$, describes a solvent-mediated chromophore-chromophore contribution between the transition densities. In addition to this *explicit* medium effect ($V_{explicit}$), we note that another implicit effect of the environment is included in the V_s term, due to changes on the transition densities upon solvation. It is useful to define a screening factor s, conceptually equivalent to the $1/n^2$ term in the Förster equation, so that $V = sV_s$:

$$s = \frac{V_s + V_{explicit}}{V_s} \tag{13}$$

Recently, we have applied this methodology to examine the screening factor s for a set of over 100 pairs of chromophores (chlorophylls, carotenoids, bilins) taken from structural models of photosynthetic light-harvesting antenna systems discussed in the previous section. In that study, we found a striking exponential attenuation of s at separations less than about 20Å, thus interpolating between the limits of no apparent screening and a significant attenuation of the EET rate. Such observation reveals a previously unidentified contribution to the distance-dependence of Förster EET rate. We fitted our results to the following distance-dependent screening function, averaged over multiple chromophores, shapes and orientations:

$$s = A \exp(-\beta R) + s_o \tag{14}$$

where the pre-exponential factor is $A = 2.68$, the attenuation factor is $\beta = 0.27$, and $s_o = 0.54$ is the asymptotic value of s at large distances. We note that to simulate the protein environments we used values of static permittivity equal to $\varepsilon = 15$ and optical permittivity $n^2 \approx \varepsilon_{opt} = 2$. As realized by Förster, however, the screening is mainly affected only by the optical value. [92]

The asymptotic value of s, $s_0 = 0.54$, falls in between the predictions of Förster model, $s_o = 1/n^2 = 0.5$, which assumes infinitely thin point dipoles, and the Onsager value, $s_o = 3/(2n^2 + 1) = 0.6$, which considers point dipoles contained in spherical cavities. It is reasonable to think that real molecules fall in between these two limits. The solvent screening factors obtained for the data set, along with the fitted screening function, Eq. 14, and the Förster and Onsager values are plotted in Fig. 8.

On the other hand, in such studies we also focus on the implicit medium effects on the transition densities, and how these affect the estimation of the

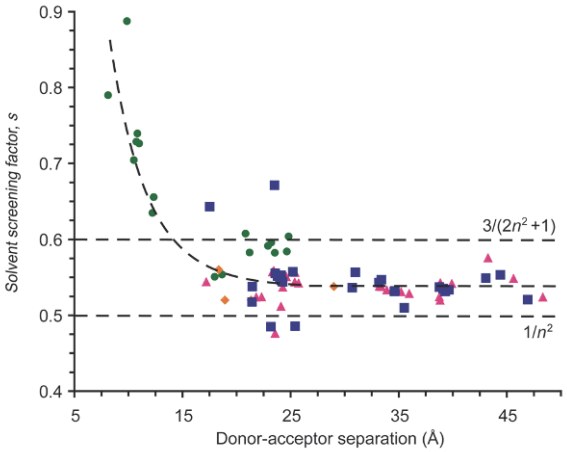

Fig. 8: Solvent screening of electronic couplings. The correspondence between data point and structure is pink triangles = PE545, blue squares = PC645, green circles = PSII or LHCII, except orange diamonds = data involving the carotenoid in PSII. The protein medium was modeled as a dielectric continuum with a relative static dielectric constant of $\epsilon = 15$ and optical dielectric constant of n^2=2. Calculated values for the solvent screening factor $s = (V_s + V_{explicit})/V_s$ for various chromophore pairs. The Förster value, $1/n^2$, is indicated by the lower horizontal line, and the Onsager value, $3/(2n^2 + 1)$, is the upper line. The dashed curve is a fit through the data points by Eq. 14. Reproduced with permission from J. Phys. Chem. B 2007, 111, 6978-6982. Copyright 2007 American Chemical Society.

coupling through the V_s term. [92] Unfortunately, such effects are significantly dependant on the particular system under consideration, so no general empirical rules can be drawn as done for the screening.

3.5 Spectral Overlap

As introduced in Section 3.1, Förster theory assumes that there is no inhomogeneous line broadening, i.e. static disorder, in the spectra of donor emission and acceptor absorption. However, if one considers an ensemble of inhomogeneously broadened spectra, the spectral overlap is given by:

$$J = \int_0^\infty d\omega \langle a_A^{hom}(\omega; \omega_a + \delta_a) f_D^{hom}(\omega; \omega_d + \delta_d) \rangle \tag{15}$$

where δ_a and δ_d are the static offsets for donor emission and acceptor absorption spectra, respectively, and the angle brackets mean ensemble averaging over these offsets, whereas $a_A^{hom}(\omega; \omega_a + \delta_a)$ and $f_D^{hom}(\omega; \omega_d + \delta_d)$ denote homogenous acceptor absorption and donor emission line shapes functions normalized to unit area on a frequency scale.

On the other hand, in the presence of static disorder the Förster expression assumes the following ensemble averaging:

$$J \approx \int_0^{\omega} d\omega \langle a_A^{hom}(\omega; \omega_a + \delta_a) \rangle \langle f_D^{hom}(\omega; \omega_d + \delta_d) \rangle \tag{16}$$

This expression is equivalent to Eq. 15 when there is a single donor-acceptor pair, or when there is no static disorder.

3.6 Special attributes of multichromophoric systems

Standard Förster theory describes incoherent hopping of the energy between weakly coupled molecules. However, in multichromophoric systems, there can be a mixture of weakly and strongly coupled chromophores. In such aggregate systems, different groups of molecules can show collective spectroscopic behaviour due to strong coupling, so that one can think of weakly coupled effective donor and acceptor states, each one contributed by a group of chromophores. In such a case, one can still express the EET rate between such effective donors and acceptors by using the Golden Rule expression, in the spirit of Förster theory. However, some modifications of Förster theory must be introduced. First, one has to consider electronic couplings and spectral overlaps between effective donor and acceptor states. [73] To this end, one has to include a correct ensemble averaging procedure to account for static disorder in the donor and acceptor transition energies. In contrast to standard Förster theory, however, such static disorder induces disorder also in the electronic couplings, given that the effective donor and acceptor states depend on the energies of the single units. This can be effectively done, for example, by considering electronic coupling-weighted spectral overlaps. [50] The subject has been the topic of several recent developments. [93]

4 Summary and conclusions

Photosynthetic organisms, including higher plants, algae and bacteria, have evolved specialized antenna complexes with the specific function of capturing solar energy then transferring it to the photochemical reaction centers where it is ultimately converted to chemical energy. This sequence of fine-tuned photophysical and photochemical reactions is achieved, over a hierarchy of time scales and distances, with remarkably efficiency. In the course of evolution, nature has produced an extraordinary variety of antenna systems showing no apparent correlations in terms of protein structure and in terms of types, number and organization of the absorbing pigments. The driving force of this evolutionary process was to adapt antenna complexes of different organisms to exploit with the greatest efficiency the solar light available in different habitats.

Investigations of various light-harvesting proteins, differing in the architectural arrangement of their chromophores, can help us understand strategies for optimizing light capture and funneling by EET in natural complexes. It is of particular interest to discover how the efficiency of light-harvesting relates to the structural organization of light-absorbing molecules on the nanometer length scale. Inspired by nature, optimization of EET is a fundamental key in the development of synthetic light-harvesting devices capable of mimicking the efficiency of the natural systems. Even though over the past years the development of ultrafast spectroscopies and high-resolution structural techniques have allowed us to elucidate the detailed operation of many of these complexes, especially components of purple bacteria, namely LH1 and LH2, and the major antenna complex of higher plants, LHCII, there are still several aspects in which our knowledge is limited.

Owing to the complex interplay of a variety of factors that affect the efficiency of EET, theory is expected to play a key role in relating structural and spectroscopic information. The challenge for attaining a fundamental understanding of EET in photosynthetic systems drives our deeper elucidation of theory. In recent years, there have been important advances in the application of sophisticated quantum-mechanical methods to the study of EET dynamics, as well as in the development of quantitative theories to describe EET in multichromophoric antenna systems. In this context, a big challenge is still represented by the need to develop strategies able to describe the effect of the complex protein environment in present models. That means exploring not only the effect of the structural arrangement of pigments in EET, but also learning how the protein tunes the pigments energies, and thus influences EET pathways. Another challenge for theory in the near future is to describe the coupling between the structural fluctuations of the protein host and the EET dynamics, which is a formidable challenge due to the different length and time scales involved. This will allow, for example, shedding light on the role of the protein in protecting electronic coherences, which have been suggested recently to play an important role in the nature of EET in photosynthetic proteins. [94]

Acknowledgements

The Natural Sciences and Engineering Research Council of Canada is gratefully acknowledged for support of this research. GDS acknowledges the support of an E. W. R. Steacie Memorial Fellowship.

References

1. G. D. Scholes, Annu. Rev. Phys. Chem., 54, 57, 2003.

2. R. van Grondelle, J. P. Dekker, T. Gillbro, V. Sundstrom, Biochim. Biophys. Acta, 1187, 1, 1994.
3. R. E. Blankenship, Molecular mechanisms of photosynthesis, Blackwell Science, Oxford, 2002.
4. N. Y. Kiang, J. Siefert, Govindjee, R. E. Blankenship, Astrobiology,7, 222, 2007.
5. W. F. Dolittle, Science, 284, 2124, 1999.
6. J. Fehling, D. Stoecker, S. L. Baldauf, in Evolution of Primary Producers in the Sea, Chap. 6, P. G. Falousky and A. H. Knoll eds., Elsevier, Boston, 2007, pp. 75-108 and references therein.
7. P. J. Keeling, Science, 317, 1875, 2007.
8. T. Cavalier-Smith, Int. J. Syst. Evol. Micobiol.,52, 7, 2002.
9. N. G. Carr, N. H. Mann (eds.), Photosynthetic Prokaryotes, Plenum Press, New York,1992.
10. (a) S. Neerken, J. Amesz, Biochim. Biophys. Acta, 1507, 278, 2001; (b) J. Amesz, J. Photochem. Photobiol. B, 30, 89, 1995.
11. R. E. Blankenship, M. T. Madigan, C.E. Bauer (eds.), Anoxygenic photosynthetic bacteria, Kluwer Academic Press, Dordrecht, 1995.
12. D. A. Bryant (ed.), The molecular Biology of Cyanobacteria, Kluwer Academic Press, Dordrecht, 1994.
13. J. M. Olson, Photosynthesis Res., 99, 109, 2006.
14. (a) G. McDermott, S. M. Prince, A. A. Freer, A. M. Hawthornthwaite-Lawless, M. Z. Papiz, R. J. Cogdell, N. W. Isaacs, Nature 374, 517, 2002; (b) G. McDermott, S. M. Prince, A. A. Freer, N. W. Isaacs, M. Z. Papiz, A. M. Hawthornthwaite-Lawless, R. J. Cogdell, Protein Eng., 8, 43, 1995; (c) J. Koepke, X. Hu, C. Muenke, K. Schulten, H. Michel1, Structure, 4, 581, 1996.
15. R. J. Cogdell, A. Gall, J. Köhler, Quart. Rev. Biophys., 39, 227, 2006.
16. R. J. Cogdell, N. W. Isaacs, T. D. Howard, K. McLuskey, N. J. Fraser, S. M. Prince, J. Bacteriol., 181, 3869, 1999.
17. R. van Grondelle, V. Novoderezhkin, Biochem., 40, 15057, 2001.
18. R. E. Blankenship, K. Matsuura, In Light-Harvesting Antennas in Photosynthesis, Chap. 6, B. R. Green and W. W. Parson (eds.), Kluwer Academic Publishers, Dordrecht, The Netherlands, 2003, pp. 195-217.
19. (a) W. D. Schubert, O. Klukas, W. Saenger, H. T. Witt, P. Fromme, N. Krauss, J. Mol. Biol., 280, 297, 1998; (b) Y. Zhang, M. Chen, B. B. Zhou, L. S. Jermiin, A. W. D. Larkum, J. Mol. Evol., 64, 321, 2007.
20. (a) R. MacColl, J. Struct. Biol., 124, 311, 1998; (b) A. R. Holzwarth, Physiol. Plant., 83, 518, 1991; (c) E. Gantt, Ann. Rev. Plant Physiol. 32, 327, 1981.
21. S. Govindjee, In Advances in Photosynthesis and Respiration, Vol. 20: Discoveries in Photosynthesis, J. T. Beatty, H. Gest, J. F. Allen (eds.), Kluwer Academic Publishers, Dordrecht, The Netherlands, 2005.
22. L. Margulis, Symbiosis in Cell Evolution : Microbial Communities in the Archean and Proterozoic Eons , Freeman, New York, 1993.
23. L. E. Graham, L. W. Wilcox, Algae, Prentice-Hall, Uppler Saddle River, NJ, 2000.
24. G. R. Wolfe, F. X. Cunningham Jr., D. Durnford, B. R. Green, E. Gantt, Nature, 367, 566, 1994.
25. D. G. Durnford, J. A. Deane, S. Tan, G. I. McFadden, E. Gantt, B. R. Green, J. Mol. Evol., 48, 59, 1999.

26. A. W. D. Larkum, M. Vesk, In Advances in Photosynthesis and Respiration, Vol. 14: Photosynthesis in Algae, A. W. D. Larkum, S. E. Douglas, J. A. Raven (eds.), Kluwer Academic Publishers, Dordrecht, The Netherlands, 2003.
27. L. Taiz, E. Zeiger, Plant Physiology, 4th ed., Sinauer Associates, Sunderland, MA, 2006.
28. (a) J. A. Klappenbach, B. K. Pierson, Arch. Microbiol., 181, 17, 2004; (b) T. L. Olson, A. M. L. van de Meene, J. N. Francis, B. K. Pierson, R. E. Blankenship, J. Bacteriology, 189, 4187, 2007.
29. M. F. Hohmann, R. E. Blankenship, Biochim. Biophys. Acta, 1767, 106, 2007.
30. K. E. Eimhjellen, H. Steensland, J. Traetteberg, Arc. Microbiol., 59, 82, 1967.
31. H. Kramer, J. Amesz, Photosyn. Res., 49, 237, 1996.
32. G. J. Hoogewerf, D. O. Jung, M. T. Madigan, FEMS Microbiol. Lett., 218, 359, 2003.
33. J. P. Thornber, R. J. Cogdell, B. K. Pierson, R. E. B. Seftor, J. Cell. Biochem., 23, 159, 1983.
34. W. Reuter, C. Muller, J. Photochem. Photobiol. B: Biol., 21, 3, 1993.
35. P. Jordan, P. Fromme, H. T. Witt, O. Klukas, W. Saenger, N. Krauss, Nature, 411, 909, 2001.
36. B. R. Green, D. G. Durnford, Annu. Rev. Plant Physiol. Plant Biol., 47, 685, 1996.
37. B. Grabowski, F. X. Cunningham, E. Gantt, PNAS, 98, 2911, 2001.
38. C. Passaquet, J. C. Thomas, L. Caron, N. Hauswirth, F. Puel, C. Berkaloff, FEBS, 280, 21, 1991.
39. E. Gantt, Photosyn. Res., 48, 47, 1996.
40. A. B. Doust, C. N. J. Marai, S. J. Harrop, K. E. Wilk, P. M. G. Gurmi, G. D. Scholes, J. Mol. Biol., 344, 135, 2004.
41. A. B. Doust, K. E. Wilk, P. M. G. Curmi, G. D. Scholes, J. Photochem. Photobiol. A: Chemistry, 184, 1, 2006.
42. (a) E. Hofmann, P. M. Wrench, F. P. Sharples, R. G. Hiller, W. Welte, K. Diederichs, Science, 272, 1788, 1996; (b) R. G. Hiller, P. M. Wrench, A. P. Gooley, G. Shoebridge, J. Breton, Photochem. Photobiol., 57, 125, 1992.
43. A. Ben-Shem, F. Frolow, N. Nelson, Nature, 426, 630, 2003.
44. Z. Liu, H. Yan, K. Wang, T. Kuang, L. Gui, X. An, W. Chang, Nature, 428, 287, 2004.
45. H. van Amerogen, R. van Grondelle, J. Phys. Chem. B, 105, 604, 2001.
46. R. Bassi, D. Sandon, R. Croce, Physiologia Plantarum, 100, 769, 1997.
47. W. D. Shubert, O. Klukas, W. Saenger, H. T. Witt, P. Fromme, N. Krauss, J. Mol. Biol., 280, 297, 1998.
48. B. Robert, R. J. Cogdell, R. van Grondelle, In Light-Harvesting Antennas in Photosynthesis, Chap. 6, B. R. Green and W. W. Parson (eds.), Kluwer Academic Publishers, Dordrecht, The Netherlands, 2003, pp. 169-194.
49. A. W. Roszak, T. D. Howard, J. Southall, A. T. Gardiner, C. J. Law, N. W. Isaacs, R. J. Cogdell, Science, 302, 1969, 2003.
50. G. D. Scholes, G. R. Fleming, Adv. Chem. Phys., 132, 57, 2005.
51. V. Sundstrom, T. Pullerits, R. van Grondelle, J. Phys. Chem. B, 103, 2327, 1999.
52. N. U. Frigaard, A. G. M. Chew, H. Li, J. A. Maresca, D. A. Bryant., Photosynth. Res., 78, 93, 2003.

53. (a) A. R. Holzwarth, K. Schaffner, Photosynth. Res., 41, 225, 1994; (b) G. T. Oostergetel, O. Reus, A.G.M. Chew, D. A. Bryant, E. J. Boekema, A.R. Holzwarth, FEBS Lett., 581, 5435, 2007.
54. J. Psenck, T. P. Ikonen, P. Laurinmki, M. C. Merckel, S. J. Butcher, R. E. Serimaa, R. Tuma, Biophys. J., 87,1165, 2004.
55. Y.-F. Li, W. Zhou, R. E. Blankenship, J. P. Allen, J. Mol. Biol., 272, 1, 1997.
56. A. N. Melkozernov, R. E. Blankenship, Photosyn. Res., 85, 33, 2005.
57. H. van Amerogen, J. P. Dekker, In Light-Harvesting Antennas in Photosynthesis, Chap. 7, B. R. Green and W. W. Parson (eds.), Kluwer Academic Publishers, Dordrecht, The Netherlands, 2003, pp. 219-251.
58. Z. Liu, H. Yan, K. Wang, T. Kuang, L. Gui, X. An, W. Chang, Nature, 428, 287, 2004.
59. P. Fromme, E. Scholodder, S. Jansson, In Light-Harvesting Antennas in Photosynthesis, Chap. 8, B.R. Green and W.W. Parson (eds.), Kluwer Academic Publishers, Dordrecht, The Netherlands, 2003, pp. 253-279.
60. B. R. Green, D. G. Durnford, Annu. Rev. Plant Physiol. Plant Mol. Biol., 47, 685, 1996.
61. T. K. Ahn, T. J. Avenson, M. Ballottari, Y.-C. Cheng, K. K. Niyogi, R. Bassi, G. R. Fleming, Science, 320, 794, 2008.
62. B. R. Green, In Light-Harvesting Antennas in Photosynthesis, Chap. 4, B. R. Green and W. W. Parson (eds.), Kluwer Academic Publishers, Dordrecht, The Netherlands, 2003, pp. 129-168.
63. (a) E. Gantt, M. R. Edwards, L. Provasoli, J. Cell. Biol., 48, 280, 1971; (b) L. Spear-Bernstein, K. R. Miller, J. Phycol., 25, 412, 1989.
64. A. N. Macpherson, R. G. Hiller, In Light-Harvesting Antennas in Photosynthesis, Chap. 11, B. R. Green and W. W. Parson (eds.), Kluwer Academic Publishers, Dordrecht, The Netherlands, 2003, pp. 323-352.
65. B. J. Norris, D. J. Miller, Mol.Biol., 24, 673, 1994.
66. M. Mimuro, N. Tamai, T. Ishimaru, I. Yamazaki, Biochim. Biophys. Acta, 1016, 280, 1990.
67. C. D. van der Weij-De Wit, A. B. Doust, I. H. M. van Stokkum, J. P. Dekker, K. E. Wilk, P. M. G. Curmi, G. D. Scholes, R.van Grondelle, J. Phys. Chem. B, 110, 25066, 2006.
68. L. Spear-Bernstein, and K. R. Miller, Protoplasma,129, 1, 1985.
69. M. Ludwig, and S. P. Gibbs, Journal of Cell Biology,108, 875, 1989.
70. E. Gantt, Phycobiliproteins of Cryptophyceae, In Biochem. Physiol. Protozoa (2nd Ed.), vol. 1, 121-137, Academic Press, New York, 1979.
71. D. Bruce, J. Biggins, T. Steiner, M. Thewalt, Photochem. Photobiol., 44, 519, 1986.
72. A. B. Doust, I. H. M. van Stokkum, D. S. Larsen, K. E. Wilk, P. M. G. Curmi, G. R. van Grondelle, G. D. Scholes, J. Phys. Chem. B , 109, 14219, 2005.
73. (a) G. R. Fleming, G. D. Scholes, Nature, 431, 256, 2004; (b) R. van Grondelle, V. I. Novoderezhkin, Phys. Chem. Chem. Phys., 8, 793, 2006; (c) G. D. Scholes, X. J. Jordanides, G. R. Fleming, J. Phys. Chem. B, 105, 1640, 2001.
74. T. Mirkovic, A. B. Doust, J. Kim, K. E. Wilk, C. Curutchet, B. Mennucci, R. Cammi, P. M. G. Curmi, G. D. Scholes, Photochem. Photobiol. Sci., 6, 964, 2007.
75. A. R. Holzwarth, J. Wendler, W. Wehrmeyer, Biochim. Biophys. Acta, 724, 388, 1983.

76. T. Förster, Ann. Phys., 437, 55, 1948.
77. J.-I. Lee, I.-N. Kang, D.-H. Hwang, H.-K. Shim, S. C. Jeoung, D. Kim, Chem. Mater., 8, 1925, 1996.
78. L. Stryer, R. P. Haugland, Proc. Natl. Acad. Sci. U.S.A., 58, 719, 1967.
79. S. Weiss, Nat. Struct. Biol., 7, 724, 2000.
80. C. Curutchet, B. Mennucci, G. D. Scholes, D. Beljonne, J. Phys. Chem. B, 112, 3759, 2008.
81. D. L. Dexter, J. Chem. Phys., 21, 836, 1953.
82. R. D. Harcourt, G. D. Scholes, K. P. Ghiggino, J. Chem. Phys., 101, 10521, 1994.
83. M. E. Madjet, A. Abdurahman, T. Renger, J. Phys. Chem. B, 110, 17268, 2006.
84. B. P. Krueger, G. D. Scholes, G. R. Fleming, J. Phys. Chem. B, 102, 5378, 1998.
85. M. F. Iozzi, B. Mennucci, J. Tomasi, R. Cammi, J. Chem. Phys., 120, 7029, 2004.
86. C. Curutchet, B. Mennucci, J. Am. Chem. Soc., 127, 16733, 2005.
87. C.-P. Hsu, Z.-Q. You, H.-C. Chen, J. Phys. Chem. C, 112, 1204, 2008.
88. B. Fückel, A. Köhn, M. E. Harding, G. Diezemann, H. Hinze, T. Basché, J. Gauss, J. Chem. Phys., 128, 74505, 2008.
89. J. Tomasi, B. Mennucci, R. Cammi, Chem. Rev., 105, 2999, 2005.
90. C.-P. Hsu, G. R. Fleming, M. Head-Gordon, T. Head-Gordon, J. Chem. Phys., 114, 3065, 2001.
91. A. Muoz-Losa, C. Curutchet, I. Fdez. Galvn, B. Mennuci, J. Chem. Phys., 129, 034104, 2008.
92. C. Curutchet, G. D. Scholes, B. Mennucci, R. Cammi, J. Phys. Chem. B, 111, 13253, 2007.
93. G. D. Scholes, C. Curutchet, B. Mennucci, R. Cammi, J. Tomasi, J. Phys. Chem. B, 111, 6978, 2007.
94. S. Jang, M. D. Newton, R. J. Silbey, Phys. Rev. Lett., 92, 218301, 2004.
95. (a) G. S. Engel, T. R. Calhoun, E. L. Read, T.-K. Ahn, T. Mancal, Y.-C. Cheng, R. E. Blankenship, G. R. Fleming, Nature, 446, 782, 2007. (b) H. Lee, Y.-C. Cheng, and G. R. Fleming, Science, 316, 1462 (2007).

Mixed Quantum Classical Simulations of Electronic Excitation Energy Transfer and Related Optical Spectra: Supramolecular Pheophorbide–a Complexes in Solution

Hui Zhu and Volkhard May

Institut für Physik, Humboldt-Universität zu Berlin, Newtonstraße 15, D-12489 Berlin, F. R. Germany
may@physik.hu-berlin.de

Abstract. Photoinduced electronic excitation energy transfer in chromophore complexes is studied by utilizing a mixed quantum classical methodology. In order to describe the electronic excitations a Frenkel–exciton model is used and treated quantum mechanically while all nuclear coordinates are described classically, finally by carrying out room-temperature MD simulations. The theory is applied to chromophore complexes dissolved in ethanol, with the single complex formed by a butanediamine dendrimer to which pheophorbide–a molecules are covalently linked. The improved exciton model introduced for the description of the chromophore complex accounts for charge distributions in the chromophores electronic ground and excited state. It also includes a correct description of the excitonic coupling among different chromophores by introducing atomic centered transition charges. Excitation energy transfer, linear absorbance, and time and frequency resolved luminescence are computed and a good agreement with measured data is found.

1 Introduction

It is of increasing interest to achieve a detailed understanding of photo absorption and excitation energy transfer (EET) dynamics in large chromophore complexes (CC). To mention a few examples we refer to EET studies in helical polyisocyanides with regularly arranged porphyrin pendants [1]. The properties of covalently linked multiporphyrin arrays have been reported in [2]. EET in dendrimeric structures was investigated either in using single molecule spectroscopy [3] or ensemble measurements [4]. Recent experiments uncover EET details in huge chromophore assemblies templated by the tobacco mosaic virus coat protein [5].

Of particular interest for the following are the different types of pheophorbide–a (Pheo) CC studied in [6, 7]. We focus here on those CC build up by butanediamine dendrimers to which Pheo molecules are covalently linked [6] (see

I. Burghardt et al. (eds.), *Energy Transfer Dynamics in Biomaterial Systems*, Springer Series in Chemical Physics 93, DOI 10.1007/978-3-642-02306-4_2,

also the Figs. 1, 2, and 3 as well as our own earlier work of Refs. [8–11]). Different generations of dendrimer Pheo complexes could be synthesized, so far extending from P_2 with two Pheo moieties, over P_4 with four up to P_{32} with 32 [6]. After photo excitation the P_n are capable to form Frenkel–exciton states and to generate singlet oxygen. Since the P_n posses a rather flexible structure they may realize conformations where some Pheo molecules are attached close together to form dimers, trimers etc.. It is a particular challenge to uncover signatures of different conformations and possible strong excitonic coupling. The latter results in a spatial delocalization of the CC excitation across some chromophores, it changes the spectrum of excitations and influences the type of EET dynamics. Spectra of linear absorbance and time and frequency resolved emission [6] should carry signatures of the excitonic coupling. Since it is observed up to the nanosecond region, the formation of delocalized states may interfere with numerous conformational transitions in the CC. Therefore, the related EET appears in a CC with pronounced structural changes.

Noting the structure of the dissolved CC P_{16} displayed in Fig. 1 it is obvious that only mixed quantum classical schemes may be ready to simulate the EET which proceeds on the highly flexible structure of the CC. The so–called QM/MM method (quantum mechanical/molecular mechanics method) represents a prominent example for such mixed methods. It has been applied to model, for example, surface reactivity and enzymatic activities by defining the quantum mechanical subsystem as that part which undergoes electronic changes associated with chemical activity. The rest of the system is described in using a molecular mechanics force field (see [12] as well as the recent publications [13–15], also for further references). While it is conceptually easy to account for the electrostatic and van der Waals interactions between the QM and MM regions a proper treatment of covalent bonds at this border is a subject of current studies. Interestingly, the majority of QM/MM method applications reported in literature does not concern the computation of (ultrafast) optical and infrared spectra of molecular systems. Such investigations are usually done under the headline of a mixed quantum classical description of molecular dynamics (see, for example, [16–18] and the nice general overview in [19]). In the mixed quantum classical scheme usually a quantum simulation of all electronic degrees of freedom is carried out while the nuclear degrees of freedom are put into a classical description [19–21]. *Ab initio* MD simulations represent an example for such mixed methods where the electronic structure problem is solved *on the fly*. Unfortunately, this approach is inappropriate for such huge systems which are of interest here (an exception might be the calculation schemes based on the DFT tight–binding method, see, e.g., [22]).

There are some recent application of a mixed quantum classical description to investigate quantum dynamics in large CC. The absorbance of a photosynthetic light harvesting complex caused by electronic Frenkel–exciton formation has been considered in Ref. [23], and Refs. [24,25] focused on excitation energy transfer in a DNA double helix strand. In both cases, however, the considerations have been restricted to an approximate description based on the use of

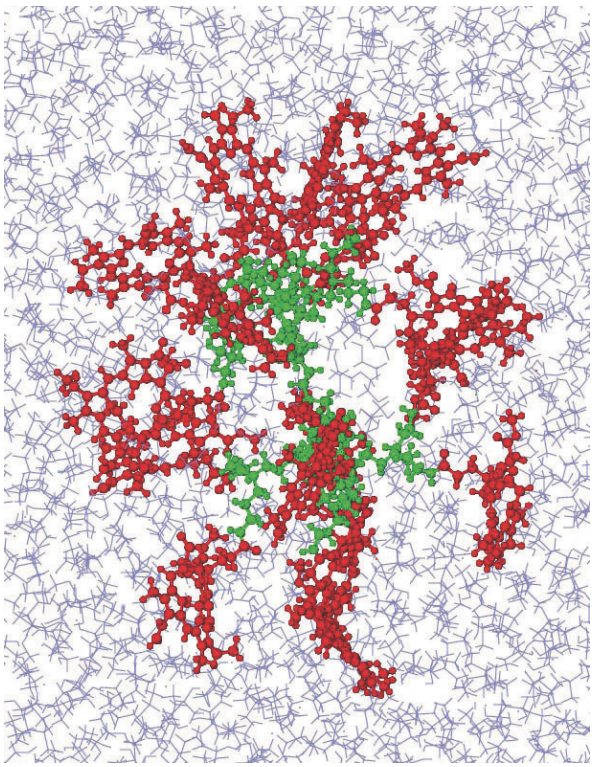

Fig. 1: The dendrimer Pheo complex P_{16} (with 16 chromophores) in a solvent box of ethanol molecules (the Pheo molecules are shown in red, the dendrimeric structure is displayed in green). Respective MD runs comprise 272613 atoms with 78 per Pheo, 310 of the dendrimeric structure and with 2895 ethanol molecules.

adiabatic exciton levels. Such a restriction had been overcome in Refs. [26–29] discussing infrared spectra of polypeptides within the amide I band. The only difference to the considerations here is the use of vibrational Frenkel–excitons (formed by the coupling of high frequency vibrational peptide group excitations) instead of electronic ones.

A specialty of our approach is the extension of the standard Frenkel exciton theory to the inclusion of permanent charge distributions in the electronic ground and excited state of the individual chromophores, what is indispensable when dealing with Pheo molecules. Resulting from the introduction of atomic partial charges the excited state of a Pheo molecule becomes strongly modulated, caused by its Coulomb coupling to the permanent charge distri-

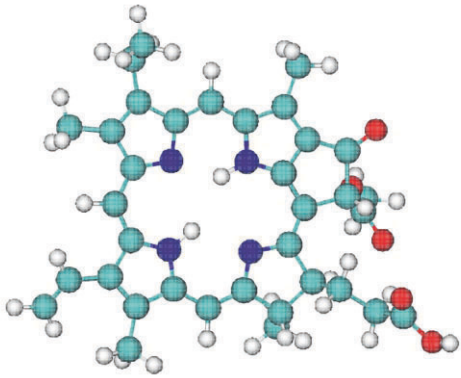

Fig. 2: The molecular structure of a single Pheo ($C_{35}H_{36}N_4O_5$, carbon in cyan, oxygen in red, nitrogen in blue, hydrogen in white).

bution of all other molecules (staying in the electronic ground state). Using the concept of atomic partial charges also for the excitonic coupling by introducing so–called *transition charges* [30] this coupling could be calculated nearly exactly (far beyond the approximation of coupled transition dipoles and much more efficient than the transition density cube method introduced in Ref. [31]).

The mixed quantum classical methodology which will be of interest for all subsequent consideration is known as *Ehrenfest dynamics* (see the recent review in [19]). It assumes the propagation of the time–dependent electronic wave function which depends on the actual nuclear configuration. The latter changes according to Newton's equation but in the mean field induced by the actual electronic state. Therefore, the approach accounts for a back reaction of the electron dynamics on that of the nuclei. As it is well–known, the mean–field approximation inherent to the Ehrenfest dynamics is overcome by the surface hopping method (see also [19]). According to the size of our CC this back reaction of the electron dynamics on the nuclear motion cannot be accounted for. Consequently, our MD simulations are done in the presence of the CC electronic ground–state force field. We simply arrive at a time dependent exciton Hamiltonian. Its ingredients, the single chromophore excitation energies E_m and the inter chromophore Coulomb couplings J_{mn} responsible for excitation energy transfer are considered as time–dependent quantities. Therefore, our approach can be related to the well known Haken–Strobl–Reineker model of electronic Frenkel excitons (see, for example, [32]), where the exciton vibrational coupling is replaced by time–dependent exciton parameters.

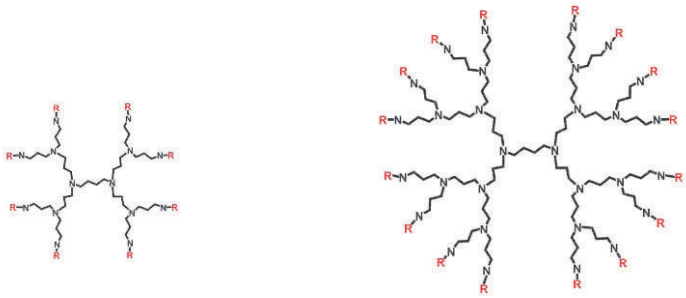

Fig. 3: Flat dendrimeric structure of P_8 (left) and of P_{16} (right, the red (light grey) R symbolize the covalently bound Pheo, Fig. 2).

In order to calculate ensemble averages the explicit time–dependence of the exciton Hamiltonian is replaced by stochastic processes. If drastic changes of J_{mn} appear due to CC conformational transitions it is hard to apply this approach (Refs. [33] and [34] introduced a dichotomically fluctuating transfer coupling to cover such large conformational transitions). Instead, as it will be demonstrated here, it is more appropriate to directly generate the time–dependence of the exciton parameters E_m and J_{mn} by MD simulations. Then, a microscopic account for solvent effects as well as a detailed description of solvent induced conformational transitions is possible.

The standard full quantum treatment of EET is either based on single chromophore populations (obeying rate equations with Förster–type rates) or on the excitonic density matrix following from a Redfield–like equation (see, for example, [35–38]). In any case one determines quantities which have been already averaged with respect to a CC ensemble and with respect to a thermal bath. Therefore, all descriptions are of such a type that thermal equilibrium is reached asymptotically due to energy relaxation and dephasing. This is in fundamental contrasts to mixed quantum classical approaches where a single quantum system moves in an environment (all nuclear coordinates) treated classically. In the most simple variant the solution of a time–dependent Schrödinger equation defined by an explicit time–dependent Hamiltonian has to be achieved. The resulting EET dynamics in this single CC is completely coherent. Dephasing appears if an ensemble average is carried out, i.e. if the results of different MD runs starting with different thermalized initial configurations have been averaged. This has some similarity to the Monte Carlo wave function method (see, for example, [39]) with the exception, however, that the environment does not cause quantum jumps but acts via a time–dependent Hamiltonian continuously on the excitation energy motion. We also note that the mixed quantum classical description of EET dynamics in CC is ready to describe any strength of electron (exciton) vibrational coupling. This is

in contrast to the full quantum description where it is usually necessary to distinguish between the weak and strong coupling case. When extended to a nanosecond time scale including an ensemble average of those quantities measured in the experiment the mixed quantum classical description of EET simultaneously accounts for what is often named dynamic as well as static disorder.

A mixed quantum classical description of EET does not represent a unique approach. On the one hand side, as already indicated, one may solve the time–dependent Schrödinger equation responsible for the electronic states of the system and couple it to the classical nuclear dynamics. Alternatively, one may also start from the full quantum theory and derive rate equations where, in a second step, the transfer rates are transformed in a mixed description (this is the standard procedure when considering linear or nonlinear optical response functions). Such alternative ways have been already studied in discussing the linear absorbance of a CC in [9] and the computation of the Förster–rate in [10].

The paper is organized as follows. The next section quotes details of the Frenkel exciton model necessary for the later discussion. Comments on a full quantum dynamical description of all those quantities which are of interest in the mixed description are shortly introduced in Section 3. The used mixed quantum classical methodology is introduced in Section 4. Its application to EET processes is given in 5, to the computation of linear absorbance in Section 3.2, and to the determination of emission spectra in Section 7. The paper ends with some concluding remarks in Section 8.

2 The Model for the Chromophore Complex in a Solvent

We first describe an appropriate model for the isolated CC (neglect of solute solvent coupling, see also Fig. 4). Afterwards, the electrostatic couplings within the CC and between the solvent and the CC are incorporated.

2.1 The Chromophore Complex Hamiltonian

For all the following considerations it is an important fact that within the CC of interest mutual chromophore wave function overlap and electron exchange effects among different chromophores do not take place (absence of the Dexter mechanism). Therefore, we may assume the orthogonality relation $\langle \varphi_{ma} | \varphi_{nb} \rangle = \delta_{m,n}\delta_{a,b}$ to be valid, where $\varphi_{ma}(r_m; R_m)$ denotes the electronic wave function of chromophore m in state a (electronic ground–state: $a = g$, first excited electronic state $a = e$). The electronic coordinates are abbreviated by r_m (related to the m'th chromophore center of mass). Moreover, the wave function parametrically depends on all nuclear coordinates R_m of chromophore m. The related single chromophore electronic Hamiltonian is denoted

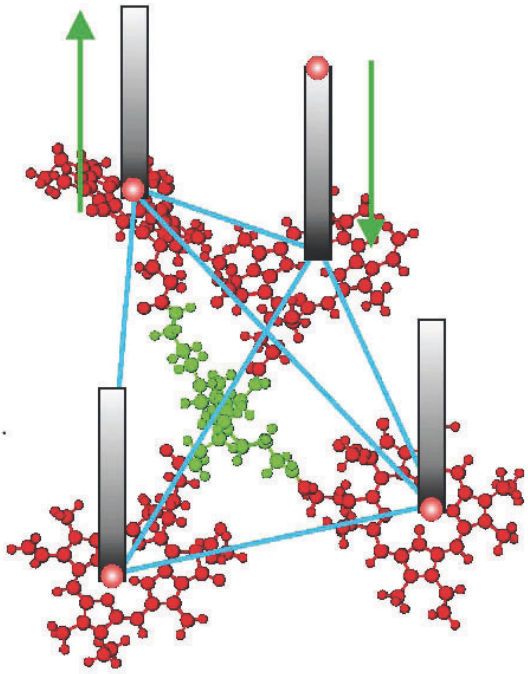

Fig. 4: Energy level scheme and interactions for the dendrimer Pheo complex P_4 (displayed in the background, solvent molecules are not shown). Every chromophore is characterized by an electronic ground–state and a single excited electronic state (the positioning of small red (light grey) spheres indicates that the chromophore right in the background has been excited while the others stay in their ground state). Full blue (light grey) lines indicate the inter chromophore Coulomb coupling affecting the CC ground state (Eq. (7)) as well as the excited CC state (Eqs. (10) and (11), the chromophore solvent coupling is not shown). The green (light grey, vertical) arrows symbolize the excitonic interaction responsible for EET (also Eq. (10)).

by $H_m^{(\mathrm{el})}$ and the eigenvalues are E_{ma}. Thus, the approach is based on isolated chromophore quantities with all additional couplings treated separately.

Accordingly, the total CC Hamiltonian takes the form (the presence of an external radiation field will be accounted for later)

$$H_{\mathrm{CC}} = T_{\mathrm{nuc}} + V_{\mathrm{CC}} \ , \tag{1}$$

where $T_{\mathrm{nuc}} = \sum_m T_m$ is the kinetic energy operator of all involved nuclear coordinates separated here into the contributions T_m of the various chromophores. The potential V_{CC} reads in more detail

$$V_{\mathrm{CC}} = \sum_m H_m^{(\mathrm{el})} + \frac{1}{2} \sum_{m,n} V_{mn} \ . \tag{2}$$

If electronic matrix elements have been taken the single chromophore electronic Hamiltonians $H_m^{(\mathrm{el})}$ will define the single chromophore potential energy surfaces (PES) U_{ma}. The V_{mn} cover the complete Coulomb interaction between chromophore m and n, including the interaction $V_{mn}^{(\mathrm{el-el})}$ among electrons, the interactions $V_{mn}^{(\mathrm{el-nuc})}$ as well as $V_{mn}^{(\mathrm{nuc-el})}$ among electrons and nuclei, and the interaction between nuclei $V_{mn}^{(\mathrm{nuc-nuc})}$.

Since inter chromophore electron exchange can be neglected the product of single chromophore electronic wave functions $\prod_m \varphi_{ma}(r_m; R_m)$ can be used as an expansion basis. To order the CC Hamiltonian with respect to the number of basic excitations we start with the electronic ground–state

$$\phi_0(r; R) = \prod_m \varphi_{mg}(r_m; R_m) \; . \tag{3}$$

Singly excited states (with the excitation of the single chromophore m into the state φ_{me}) are written as

$$\phi_m(r; R) = \varphi_{me}(r_m; R_m) \prod_{n \neq m} \varphi_{ng}(r_n; R_n) \; . \tag{4}$$

Doubly excited electronic CC states can be introduced in a similar way but are of no interest here. Possible ground–state excited–state couplings will be also neglected [10]. Therefore, the expansion simply reads (see also Fig. 4)

$$H_{\mathrm{CC}} \approx \langle \phi_0 | H_{\mathrm{CC}} | \phi_0 \rangle | \phi_0 \rangle \langle \phi_0 | + \sum_{m,n} \langle \phi_m | H_{\mathrm{CC}} | \phi_n \rangle | \phi_m \rangle \langle \phi_n | \; . \tag{5}$$

The overall electronic ground state matrix element follows as [9, 10]

$$\langle \phi_0 | H_{\mathrm{CC}} | \phi_0 \rangle \equiv \mathcal{H}_0 = T_{\mathrm{nuc}} + \mathcal{V}_0(R) \; , \tag{6}$$

with the ground–state vibrational Hamiltonian $\mathcal{H}_0$ and the respective PES

$$\mathcal{V}_0(R) = \sum_m U_{mg}(R_m) + \frac{1}{2} \sum_{m,n} J_{mn}(gg, gg; R_m, R_n) \; . \tag{7}$$

Besides the single chromophore PES U_{mg}, this expression includes inter chromophore couplings J_{mn} describing the Coulomb–interaction among the different unexcited chromophores. They are the electronic ground–state variant of the general expression

$$J_{mn}(ab, cd) = \int dr_m dr_n \; \varphi_{ma}^*(r_m) \varphi_{nb}^*(r_n) V_{mn} \varphi_{nc}(r_n) \varphi_{md}(r_m) \; , \tag{8}$$

which will be analyzed in more detail in Section 2.3.

The inter chromophore couplings are reduced here to a simple electrostatic coupling among the charge distribution of the electrons and nuclei in chromophore m and n. It appears if the electron charge and that of the nuclei are

locally unbalanced giving a local net charge within every chromophore. Since electron exchange is of no importance it might be sufficient to concentrate on the electrostatic coupling when determining the CC excitation energies (see next section), but $\mathcal{V}_0$ has to be extended by polarization forces if it is used to determine the MD force field.

The singly excited state matrix elements take the form [9,10] (see also Fig. 4)

$$\langle \phi_m | H_{\rm CC} | \phi_n \rangle \equiv \mathcal{H}_{mn} = \delta_{m,n} T_{\rm nuc} + \mathcal{V}_{mn}(R) \ , \tag{9}$$

with the PES matrix written as

$$\mathcal{V}_{mn}(R) = \delta_{m,n}(\mathcal{V}_0(R) + U_{meg}(R)) + (1 - \delta_{m,n}) J_{mn}(eg, eg; R_m, R_n) \ . \tag{10}$$

The $J_{mn}(eg, eg; R_m, R_n)$ define the so–called excitonic coupling responsible for EET and the formation of delocalized exciton states. The PES

$$\begin{aligned} U_{meg}(R) = U_{me}(R_m) + \sum_k J_{mk}(eg, ge; R_m, R_k) \\ -[U_{mg}(R_m) + \sum_k J_{mk}(gg, gg; R_m, R_k)] \ . \end{aligned} \tag{11}$$

characterizes the excitation of chromophore m and includes its electrostatic coupling (in the ground as well as in the excited state) with all other chromophores.

2.2 Standard Exciton Hamiltonian

The standard Hamiltonian for a CC (see, for example [40]) assumes that the single chromophore is locally neutral (the electron charge and that of the nuclei are completely balanced). Thus, it neglects inter–chromophore electrostatic couplings. The ground–state PES $\mathcal{V}_0$ is written in a form following from a vibrational normal–mode analysis:

$$\mathcal{H}_0 = \sum_j \hbar \omega_j c_j^+ c_j \ , \tag{12}$$

where the ω_j are the normal–mode frequencies, and the c_j^+ as well as c_j denote respective harmonic oscillator operators. Then, the singly excited state Hamiltonian matrix reduces to

$$\begin{aligned} \mathcal{H}_{mn} = \delta_{m,n}(E_m + \mathcal{H}_0) + (1 - \delta_{m,n}) J_{mn}(eg, eg) \\ + \sum_j \hbar \omega_j g_j(mn)(c_j + c_j^+) \ . \end{aligned} \tag{13}$$

The excitation energy of chromophore m, Eq. (11), but fixed at the Franck–Condon transition region is given by E_m (site energy). Excitation energy normal mode vibration coupling has been restricted to the lowest–order nuclear coordinate contribution and is characterized by the coupling matrix $g_j(mn)$. It may modulate the excitation energy (diagonal contribution) as well as the excitonic coupling (off–diagonal contribution). Standard exciton states

$$|\alpha\rangle = \sum_m C_\alpha(m)|\phi_m\rangle \tag{14}$$

follow by diagonalizing $\delta_{m,n}E_m + (1-\delta_{m,n})J_{mn}(eg,eg)$.

2.3 The Coulomb Interaction Matrix Element

To compute the Coulomb matrix element, Eq. (8), we first note that the multiple integration with respect to the coordinates of all electrons of chromophore m and n can be reduced to a two–fold coordinate integration. This becomes possible because of the antisymmetric character of the chromophore electronic wave functions. Therefore, we introduce single electron densities of chromophore m:

$$\varrho_{ab}^{(m)}(\mathbf{x}) = eN_m \int dr \delta(\mathbf{x}-\mathbf{r}_1)\varphi_{ma}^*(r)\varphi_{mb}(r)\ . \tag{15}$$

The integration covers all electronic coordinates of chromophore m (the respective electron number is given by N_m), and the δ–function guarantees that the electronic coordinate $\mathbf{r_1}$ is replaced by the new variable $\mathbf{x}$. If Eq. (15) is specified to $\varrho_{gg}^{(m)}(\mathbf{x})$ it gives the (permanent) electronic charge density in the electronic ground–state and $\varrho_{ee}^{(m)}(\mathbf{x})$ is that of the excited electronic state. If $a \neq b$ the so–called transition charge density is obtained.

A compact notation of Eq. (8) is achieved if we introduce the overall single chromophore charge density where electrons and nuclei contribute (the latter are positioned at $\mathbf{R}_\mu$ and have the charge number Z_μ)

$$n_{ab}^{(m)}(\mathbf{x}) = \varrho_{ab}^{(m)}(\mathbf{x}) - \delta_{a,b}\sum_{\mu\in m} eZ_\mu\delta(\mathbf{x}-\mathbf{R}_\mu)\ . \tag{16}$$

Now, Eq. (8) turns into the form [30]:

$$J_{mn}(ab,cd) = \int d^3\mathbf{x}d^3\mathbf{x}'\ \frac{n_{ad}^{(m)}(\mathbf{x})n_{bc}^{(n)}(\mathbf{x}')}{|\mathbf{x}-\mathbf{x}'|}\ . \tag{17}$$

The molecular density $n_{ab}^{(m)}$ reduces to the electronic transition density when $a \neq b$. It results in zero total charge when integrated ($\int d^3\mathbf{x}\, n_{ab}^{(m)}(\mathbf{x}) = 0$) indicating charge neutrality of the molecule.

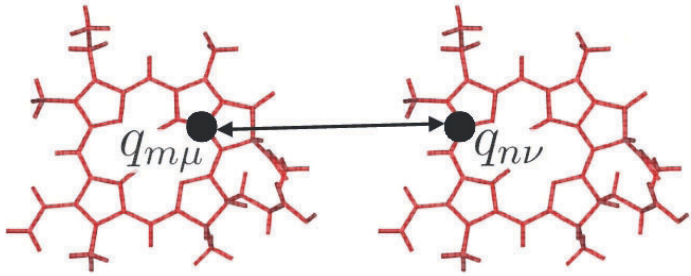

Fig. 5: Coulomb coupling between Pheo m and n formulated in terms of atomic centered partial charges (transition charges) $q_{m\mu}$ and $q_{n\nu}$, Eq. (18).

To carry out the computation of J_{mn} for a particular pair of chromophores the Coulomb matrix element can be translated with high accuracy into the following form (see Fig. 5 and [30]):

$$J_{mn}(ab, cd) = \sum_{\mu,\nu} \frac{q_{m\mu}(ad) q_{n\nu}(bc)}{|\mathbf{R}_{m\mu} - \mathbf{R}_{n\nu}|} \,. \tag{18}$$

The $q_{m\mu}(ad)$ and $q_{n\nu}(bc)$ are charges placed at the atoms of chromophore m positioned at $\mathbf{R}_{m\mu}$ and at the atoms of chromophore n positioned at $\mathbf{R}_{n\nu}$, respectively. If $a = d$ ($b = c$) the charges represent ordinary ones, but if $a \neq d$ ($b \neq c$) they are named *transition charges* (for more details see Section 4.2).

2.4 Inclusion of Solvent Molecules

The inclusion of non–balanced charge distributions in the chromophores ground and excited state suggests an account for respective solvent molecule contributions, resulting in a solvent solute Coulomb coupling. This is formally achieved by including all solvent molecules into the definition of the electronic CC states ϕ_0 and ϕ_m. Since solvent molecule excitation energies should be much larger than those of the chromophores, solvent solute EET does not appear. The respective coupling, however, is responsible for solute solvent polarization forces. Related contributions can be included on a microscopic basis, but this is postponed to future work. Here, we account for the related single chromophore excitation energy shift phenomenologically using experimental known values but neglect polarization effects on the excitonic coupling.

To include the electrostatic solvent solute coupling we multiply the ϕ_0 and ϕ_m by the solvent part $\phi_{\rm sol} = \prod_{m\in{\rm sol}} \tilde{\varphi}_{mg}$ with the single solvent molecule electronic ground–state wave functions $\tilde{\varphi}_{mg}$. As a result, the nuclear kinetic energy operator $T_{\rm nuc}$ has to include solvent contributions. Moreover, $\mathcal{V}_0$, Eq. (7), may include in its m and n summation solvent contributions. Concerning $\mathcal{V}_{mn}$, Eq. (10), besides $\mathcal{V}_0$ solvent contributions are restricted to the k–summations in $\mathcal{V}_{m\,eg}$, Eq. (11).

2.5 Adiabatic Exciton States

In contrast to Eq. (14) introducing ordinary exciton states, adiabatic exciton states are defined as the instantaneous eigenstates of the singly excited CC, i.e. they are obtained by diagonalizing $\mathcal{V}_{mn}$, Eq. (10). The states can be expanded according to

$$\Phi_\alpha(r;R) = \sum_m C_\alpha(m;R)\phi_m(r;R) \;, \tag{19}$$

forming an orthogonal basis at every set R of nuclear coordinates. We directly arrive at CC excitation energies when solving

$$\sum_n \Big(\mathcal{V}_{mn}(R) - \delta_{m,n}\mathcal{V}_0(R)\Big)C_\alpha(n;R) = \mathcal{E}_\alpha(R)C_\alpha(m;R) \;. \tag{20}$$

The $\mathcal{E}_\alpha$ and C_α can be used to describe excitation energy dynamics [10] but also to estimate the CC absorbance (see Section 6.3 and [8,9]).

2.6 Coupling to External Fields

The coupling to the classical radiation field reads

$$H_{\rm field}(t) = -\hat{\mu}\mathbf{E}(t) \;, \tag{21}$$

with the CC dipole operator

$$\hat{\mu} = \sum_m \mathbf{d}_m|\phi_m\rangle\langle\phi_0| + {\rm H.c.} \;, \tag{22}$$

where the $\mathbf{d}_m$ are the single chromophore transition dipole matrix elements. The quantized photon field enters via the standard Hamiltonian

$$H_{\rm phot} = \sum_{\lambda,\mathbf{k}} \hbar\omega_{\mathbf{k}}(a^+_{\lambda\mathbf{k}}a_{\lambda\mathbf{k}} + 1/2) \tag{23}$$

determined by creation and annihilation operators of photons $a^+_{\lambda\mathbf{k}}$ and $a_{\lambda\mathbf{k}}$, respectively (with polarization λ and wave vector $\mathbf{k}$) and by the photon energy $\hbar\omega_{\mathbf{k}}$. The coupling of photons to the CC takes the form

$$H_{\mathrm{CC-phot}} = \hbar \sum_{\lambda,\mathbf{k}} \hat{h}_{\lambda\mathbf{k}} (a_{\lambda\mathbf{k}} + a^{+}_{\lambda\mathbf{k}}) \ , \tag{24}$$

where we abbreviated

$$\hat{h}_{\lambda\mathbf{k}} = \sum_{m} g_{\lambda\mathbf{k}}(m) |\phi_m\rangle\langle\phi_0| + \mathrm{h.c.} \ . \tag{25}$$

The coupling constant follows as

$$g_{\lambda\mathbf{k}}(m) = -i \sqrt{\frac{2\pi\hbar}{V\omega_{\mathbf{k}}}} \omega_{meg} \mathbf{n}_{\lambda\mathbf{k}} \mathbf{d}_m \ . \tag{26}$$

V denotes the quantization volume, $\hbar\omega_{m\,eg}$ is the basic electronic transition energy in chromophore m, and $\mathbf{n}_{\lambda\mathbf{k}}$ the unit vector of transversal polarization.

3 Full Quantum Dynamical Description

We quote some central formulas valid for an exact quantum description of EET and related optical spectra. The formulas will serve as reference relations to change to a mixed quantum classical description. To present the full quantum formulas we need the so–called *site* representation of the overall statistical operator:

$$\hat{\rho}_{mn}(t) = \langle\phi_m|\hat{\rho}(t)|\phi_n\rangle \ , \tag{27}$$

which uses the singly excited CC states, Eq. (4). Obviously, this quantity remains an operator in the state space of all vibrational degrees of freedom.

3.1 Excitation Energy Transfer

The standard quantum statistical description of excitation energy motion in CC arrives at irreversible (dissipative) dynamics originated by energy relaxation and dephasing due to the coupling to vibrational degrees of freedom (see, for example, [40]). There are two basic approaches which have to be distinguished according to the interrelation between the excitonic coupling and the chromophore vibrational coupling (vibrational reorganization). If the latter dominates one can carry out a perturbation theory with respect to the excitonic coupling. EET may be described in terms of rate equations governing the single chromophore excited state populations

$$P_m(t) = \mathrm{tr}_{\mathrm{vib}}\{\hat{\rho}_{mm}(t)\} \ , \tag{28}$$

with the trace $\mathrm{tr}_{\mathrm{vib}}\{...\}$ accounting for all nuclear coordinates involved (intra chromophore, inter chromophore as well as solvent coordinates). Transition rates may be sufficient which are of second order with respect to the excitonic

coupling (often of the so–called Förster type, fourth–order rates of EET have been discussed recently in [41]):

$$k_{m\to n} = \frac{2}{\hbar^2}\mathrm{Re}\int\limits_0^\infty dt\ \mathrm{tr}_{\mathrm{vib}}\{\hat{R}_m U_m^+(t) J_{mn} U_n(t) J_{nm}\}\ . \tag{29}$$

The vibrational equilibrium statistical operators $\hat{R}_m$ and the time evolution operators $U_m(t)$ are defined by the Hamiltonians $H_m = \mathcal{V}_0 + T_m + U_{meg}$ (with the PES given in Eq. (11)).

Perturbation theory with respect to the chromophore vibrational coupling can be introduced if the excitonic coupling dominates. Now, it is advisable to change to an exciton representation and to introduce the (reduced) exciton density matrix

$$\rho_{\alpha\beta}(t) = \mathrm{tr}_{\mathrm{vib}}\{\langle\alpha|\hat{\rho}(t)|\beta\rangle\}\ , \tag{30}$$

where standard exciton levels, Eq. (14) (referring to the fixed CC ground state nuclear equilibrium configuration) have been used. Respective equations of motion with a second order account of exciton vibrational coupling have been widely used in literature (see, for example, [35–38], much less, however, has been published for the intermediate region where both couplings are comparable).

Both mentioned approaches are based on ensemble averages (quantum statistical averages with respect to a reservoir staying in thermal equilibrium). In the infinite time limit (ignoring radiative or non radiative decay) the $P_m(t)$ turn into respective equilibrium distributions f_m. In the case of the exciton density matrix the off–diagonal elements of $\rho_{\alpha\beta}(t)$ decay while the diagonal elements tend to an equilibrium distribution f_α. The mentioned theories are only applicable for small fluctuations around a single reference CC structure. Strong conformational changes cannot be accounted for.

3.2 Linear Absorption Spectra

Using the standard expression of the dipole–dipole correlation function the CC absorption cross section can be derived as [9, 42]:

$$\begin{aligned} I(\omega) = \mathrm{Re}\int\limits_0^\infty d\tau\ e^{i\omega\tau} \sum_{m,n} \\ \mathrm{tr}_{\mathrm{vib}}\{\hat{R}_0 d_m^{(0)*}(\tau) e^{i\mathcal{H}_0\tau/\hbar}\langle\phi_m|e^{-iH_{\mathrm{CC}}\tau/\hbar}|\phi_n\rangle d_n\}\ . \end{aligned} \tag{31}$$

Here, $\hat{R}_0$ denotes the respective statistical operator for the nuclear coordinate equilibrium motion in the electronic ground state of the CC. The d_n are scalar

single chromophore transition dipole matrix elements introduced in Eq. (22). They are obtained as the projection on the polarization direction of the incoming field (note that we disclaimed to introduce the Condon approximation). The time dependent transition dipole matrix elements $d_m^{(0)}(t)$ corresponds to a representation defined by the CC ground state vibrational Hamiltonian $\mathcal{H}_0$

$$d_m^{(0)}(\tau) = e^{i\mathcal{H}_0\tau/\hbar} d_m e^{-i\mathcal{H}_0\tau/\hbar} \,. \tag{32}$$

For comparison we present the absorption cross section for the case where inter–chromophore coupling can be neglected and where the use of the Condon–approximation becomes possible. We arrive at

$$I(\omega) = \sum_m |d_m|^2 \mathrm{Re} \int_0^\infty d\tau \; e^{i\omega\tau} \mathrm{tr}_{\mathrm{vib}}\{\hat{R}_{mg} e^{iH_{mg}\tau/\hbar} e^{-iH_{me}\tau/\hbar}\} \,. \tag{33}$$

The total absorption spectrum appears as the simple addition of the individual absorbance of all chromophores in the CC. The trace is reduced to the vibrational wave packet overlap in the electronic ground and excited state (averaged with respect to the chromophore electronic ground–state vibrational equilibrium, described by the density operator $\hat{R}_{mg}$; $H_{ma} = T_m + U_{ma}$).

3.3 Spectra of Time and Frequency Resolved Luminescence

Since exact formulas for time and frequency resolved emission spectra are less standard we shortly comment on the derivation of the full quantum expressions [43–45]. To characterize the emission we introduce the rate $R_{\lambda\mathbf{k}}(t)$ which follows as the number of photons emitted per time into the state with polarization λ and wave vector $\mathbf{k}$. Since emission appears into the photon vacuum we may set $R_{\lambda\mathbf{k}} = \partial N_{\lambda\mathbf{k}}/\partial t$, where

$$N_{\lambda\mathbf{k}} = \mathrm{tr}\{\hat{W}(t) a^+_{\lambda\mathbf{k}} a_{\lambda\mathbf{k}}\} \tag{34}$$

is the expectation value of the photon number at time t. The trace concerns the photon states as well as the CC and solvent contributions. The statistical operator $\hat{W}(t)$ also accounts for photon states and the presence of the exciting laser pulse. Therefore, the density operator of the CC solvent system introduced in Eq. (27) is obtained after a reduction which projects out photon contributions, i.e. we have to use

$$\hat{\rho}(t) = \mathrm{tr}_{\mathrm{phot}}\{\hat{W}(t)\} \,. \tag{35}$$

A trace which only accounts for CC and solvent states yields the reduced photon density operator

$$\hat{W}_{\mathrm{phot}}(t) = \mathrm{tr}_{\mathrm{CC+sol}}\{\hat{W}(t)\} \,. \tag{36}$$

The overall emission rate of photons with energy $\hbar\omega$ at time t reads (note the use of spherical coordinates for $\mathbf{k}$ and the abbreviation of the solid angle integration by $\int do$)

$$F(\omega;t) = \frac{V\omega^2}{(2\pi c)^3} \sum_{\lambda} \int do\, R_{\lambda\mathbf{k}}(t)\ . \tag{37}$$

It is sufficient to determine the quantity $R_{\lambda\mathbf{k}}$ in the second order with respect to the CC photon interaction. We further assume that the optical preparation of the excited state by the applied field $\mathbf{E}$ is short compared to the emission process and, finally, we neglect anti–resonant contributions. When calculating $F(\omega;t)$ we also have to perform a summation with respect to the transversal polarization and a solid angle integration. Introducing $\mathbf{d}_m = d_m\mathbf{e}_m$ where $\mathbf{e}_m$ is the unit vector pointing in the direction of the transition dipole moment one gets

$$\sum_{\lambda} \int do\, [\mathbf{n}_{\lambda\mathbf{k}}\mathbf{e}_m][\mathbf{n}_{\lambda\mathbf{k}}\mathbf{e}_n] = \frac{8\pi}{3}[\mathbf{e}_m\mathbf{e}_n]\ . \tag{38}$$

Consequently, $F(\omega;t)$ will contain the transition dipole matrix elements in forming a common scalar product. The full quantum expression for the emission rate (rate of ideal time and frequency resolved emission) takes the form

$$F(\omega;t) = \frac{4\omega^3}{3\pi c^3\hbar}\mathrm{Re}\int_{t_0}^{t} d\bar{t}\ e^{-i\omega(t-\bar{t})} \sum_{m,n,k}$$
$$\mathrm{tr}_{\mathrm{vib}}\{\hat{\rho}_{nk}(\bar{t})\langle\phi_k|e^{iH_{\mathrm{CC}}(t-\bar{t})/\hbar}|\phi_m\rangle e^{-i\mathcal{H}_0(t-t_0)/\hbar}[\mathbf{d}_m^{(0)}(t)\mathbf{d}_n^{(0)+}(\bar{t})]e^{i\mathcal{H}_0(\bar{t}-t_0)/\hbar}\}\ . \tag{39}$$

Again, we prevent to take the Condon approximation. The $\hat{\rho}_{nk}$ have been introduced in Eq. (27) and account for EET among the different chromophores (after optical excitation at t_0, note also the use of Eq. (32)). Many computations focus on emission spectra in the picosecond and sub–picosecond time–region where the influence of radiative and non–radiative decay can be neglected when determining the $\hat{\rho}_{nk}$ (see, for example, [44,45]). For the present nanosecond studies, however, it becomes essential to account for these processes when calculating $\hat{\rho}_{nk}(\bar{t})$ (see the subsequent section).

We consider an approximate expression for the emission spectrum. It neglects inter–chromophore coupling, assumes that the Condon–approximation can be carried out, and considers the case of fast vibrational relaxation in the excited electronic state of the individual chromophores:

$$F(\omega;t) = \frac{4\omega^3}{3\pi c^3\hbar} \sum_{m} |d_m|^2 P_m(t)\mathrm{Re}\int_{0}^{\infty} d\tau\ e^{-i\omega\tau}$$
$$\times\ \mathrm{tr}_{\mathrm{vib}}\{\hat{R}_{me}e^{iH_{me}\tau/\hbar}e^{-iH_{mg}\tau/\hbar}\}\ . \tag{40}$$

In this limiting case the time–dependence of the emission spectrum is determined by the overall probability P_m to find chromophore m in the excited state while the frequency distribution of the emitted photons is determined by the Fourier–transformed standard trace expression for the radiative decay of an excited molecular state (see, for example, [40]; $\hat{R}_{me}$ describes vibrational equilibrium in the excited electronic state).

As already indicated Eq. (39) (Eq. (40)) gives the rate of ideal time and frequency resolved emission. If compared with experimental data gained by single photon counting, $F(\omega;t)$ has to undergo a time averaging with the respective apparatus function which determines the possible time resolution of the measurement (for up conversion techniques see [44]).

Density Matrix Theory of Excitation Energy Motion Including Radiative Decay

To account for the radiative decay of CC excited states we consider the density operator $\hat{\rho}$, Eq. (35), reduced to the CC solvent states. It is a standard task of dissipative quantum dynamics to derive an equation of motion for $\hat{\rho}$ with a second order account for the CC–photon coupling, Eq. (24) (see, for example, [40]). Focusing on the excited CC–state contribution, in the most simple case (Markov and secular approximation) we expect the following equation of motion

$$\frac{\partial}{\partial t}\hat{\rho}_{mn}(t) = -\frac{i}{\hbar}\sum_k \left(\mathcal{H}_{mk}\hat{\rho}_{kn}(t) - \hat{\rho}_{mk}(t)\mathcal{H}_{kn}\right) - \frac{1}{2}(k_m + k_n)\hat{\rho}_{mn}(t)\ . \tag{41}$$

The rates k_m cover the $k_{m\to 0}$ accounting for the excited state decay of chromophore m (by radiative as well as non–radiative transitions) and the $k_m^{(\mathrm{ISC})}$ originated by inter–system crossing to triplet states (ISC rate). The simple k_m do not include the effect of excited state wave function delocalization and a possible decay out of exciton states [45]. Therefore, we shortly demonstrate the computation of the photon emission part of the k_m including such a delocalization effect (determination of excitonic augment rates). It will be important for the mixed quantum classical simulations discussed in the following (for more details see also [11]).

A dissipative quantum dynamics approach including spontaneous photon emission is based on a separation of the total Hamiltonian into a system part, here the CC Hamiltonian Eq. (1), the reservoir part given by the photon Hamiltonian and a system reservoir coupling $H_{\mathrm{S-R}}$ represented by the CC–photon coupling, Eq. (24). In most applications the latter Hamiltonian can be written as follows

$$H_{\mathrm{S-R}} = \sum K_u \Phi_u\ , \tag{42}$$

where the K_u are operators acting in the system state space and the Φ_u are operators defined with respect to the reservoir state space. To identify them with those entering the CC–photon coupling we have to set (see Eqs. (24), (25), and (26)) $K_u = \hat{h}_{\lambda\mathbf{k}}(R)$ and $\Phi_u = \hbar(a_{\lambda\mathbf{k}} + a^+_{\lambda\mathbf{k}})$, i.e. the index u equals $\lambda\mathbf{k}$.

The equation of motion for the reduced density operator (quantum master equation) takes the form [40]

$$\frac{\partial}{\partial t}\hat{\rho}(t) = -\frac{i}{\hbar}[H_{\mathrm{CC}}(t), \hat{\rho}(t)]_- - \hat{D}(t, t_0) \; , \tag{43}$$

According to Eq. (42) for $H_{\mathrm{S-R}}$ the part responsible for dissipation reads

$$\begin{aligned}\hat{D}(t, t_0) = &\sum_{u,v} \int_{t_0}^{t} d\bar{t} \\ &\Big(C_{uv}(t, \bar{t}) \Big[K_u(t), U_{\mathrm{CC}}(t, \bar{t}) K_v(\bar{t}) \hat{\rho}(\bar{t}) U^+_{\mathrm{CC}}(t, \bar{t}) \Big]_- \\ &- C^*_{uv}(t, \bar{t}) \Big[K_u(t), U_{\mathrm{CC}}(t, \bar{t}) \hat{\rho}(\bar{t}) K_v(\bar{t}) U^+_{\mathrm{CC}}(t, \bar{t}) \Big]_- \Big) \; .\end{aligned} \tag{44}$$

Be aware of the fact that we have to consider the non–Markovian version of the quantum master equation to stay at a level of description where the emission rate, Eq. (39), can be deduced. Moreover, to be ready for a translation to a mixed quantum classical description a variant has been presented where the time evolution operators might be defined by an explicitly time–dependent CC Hamiltonian, i.e. $\exp(-iH_{\mathrm{CC}}[t - \bar{t}]/\hbar)$ has been replaced by the more general expression $U_{\mathrm{CC}}(t, \bar{t})$.

Since the photon version of the reservoir correlation functions C_{uv} includes the photon statistical operator which is defined by the projector on the photon vacuum the correlation functions simply read

$$C_{\lambda\mathbf{k},\kappa\mathbf{q}}(t - \bar{t}) = \delta_{\lambda\mathbf{k},\kappa\mathbf{q}} e^{-i\omega_{\mathbf{k}}(t-\bar{t})} \; . \tag{45}$$

We change to CC excited state matrix elements of $\hat{\rho}$ as well as of Eq. (43) which are of only interest here. Using the same assumptions as to arrive at $F(\omega; t)$, Eq. (39), (matrix elements of the CC time evolution operator U_{CC} between the CC ground and a singly excited CC state do not contribute, anti–resonant contribution are neglected) we arrive at ($m \leftrightarrow n$ indicates the chromophore index interchange)

$$\begin{aligned}\hat{D}_{mn}(t, t_0) = &\sum_{k,l} \int_{t_0}^{t} d\bar{t} \, \frac{2}{3\pi c^3 \hbar} \int_0^{\infty} d\omega \omega^3 e^{-i\omega(t-\bar{t})} \\ &e^{-i\mathcal{H}_0(t-t_0)/\hbar} \mathbf{d}^{(0)}_m(t) \mathbf{d}^{(0)+}_k(\bar{t}) e^{i\mathcal{H}_0(\bar{t}-t_0)/\hbar} \hat{\rho}_{kl}(\bar{t}) \langle \phi_l | U^+_{\mathrm{CC}}(t, \bar{t}) | \phi_n \rangle \\ &+ \big(\text{c.c.} + (m \leftrightarrow n) \big) \; .\end{aligned} \tag{46}$$

e.g. [40]From this expression we, first, may deduce the time resolved spontaneous emission spectrum, Eq. (39). The total photon emission rate $F(t)$ is obtained from total rate of de–excitation of the CC which follows as the time derivative of the total probability $\sum_m \mathrm{tr}_{\mathrm{vib}}\{\hat{\rho}_{mm}(t)\}$ to have the CC in the singly excited state. We note

$$-\sum_m \frac{\partial \mathrm{tr}_{\mathrm{vib}}\{\hat{\rho}_{mm}(t)\}}{\partial t} = \sum_m \mathrm{tr}_{\mathrm{vib}}\{\hat{D}_{mm}(t,t_0)\} = \int_0^\infty d\omega\; F(\omega;t)\;, \qquad (47)$$

where $F(\omega;t)$ is identical with Eq. (39).

Second, Eq. (46) is ready to deduce excitonic augmented radiative decay rates since the matrix element $\langle\phi_l|U^+_{\mathrm{CC}}(t,\bar{t})|\phi_n\rangle$ fully account for the excitonic coupling among different chromophores (for details we refer to [46]).

4 Mixed Quantum Classical Description

A systematic route to achieve a mixed quantum classical description of EET may start with the partial Wigner representation $\hat{\rho}(R,P;t)$ of the total density operator referring to the CC solvent system. R and P represent the set of all involved nuclear coordinates and momenta, respectively. However, $\hat{\rho}(R,P;t)$ remains an operator in the space of electronic CC states (here ϕ_0 and the different ϕ_m). Setting up an equation of motion for $\hat{\rho}(R,P;t)$ up to the first order of the $\hbar$–expansion one can change to electronic matrix elements. Focusing on singly excited state dynamics we have to consider $\rho_{mn}(R,P;t) = \langle\phi_m|\hat{\rho}(R,P;t)|\phi_n\rangle$ which obeys the following equation

$$\begin{aligned}\frac{\partial}{\partial t}\rho_{mn}(R,P;t) &= -\frac{i}{\hbar}\sum_k \left(\mathcal{H}_{mk}\rho_{kn} - \rho_{mk}\mathcal{H}_{kn}\right)\\ &+\frac{1}{2}\sum_\nu \Big\{\sum_k \Big(\frac{\partial \mathcal{V}_{mk}}{\partial R_\nu}\frac{\partial \rho_{kn}}{\partial P_\nu} + \frac{\partial \rho_{mk}}{\partial P_\nu}\frac{\partial \mathcal{V}_{kn}}{\partial R_\nu}\Big) - 2\frac{\partial T_{\mathrm{nuc}}}{\partial P_\nu}\frac{\partial \rho_{mn}}{\partial R_\nu}\Big\}\,. \qquad (48)\end{aligned}$$

The first term on the right–hand side is identical with that of Eq. (41) (since the nuclear kinetic energy cancel the Hamiltonian matrix $\mathcal{H}_{mn}$ can be replaced by the PES matrix $\mathcal{V}_{mn}$, Eq. (10)). The derivatives in the second term on the right–hand side of Eq. (48) are responsible for the formation of a nuclear coordinate and momentum dependence of the density matrix. The multitude of involved coordinates and momenta, however, avoids any direct calculation of the $\rho_{mn}(R,P;t)$, and respective applications finally arrive at a computation of bundles of nuclear trajectories which try to sample the full density matrix.

Therefore, it is more appropriate to start from an approach which is known as *Ehrenfest* dynamics. In the present case it is based on the following time–dependent Schrödinger equation for the CC electronic wave function

$$i\hbar\frac{\partial}{\partial t}\Psi(r,R(t);t) = \left[H_{\mathrm{CC}}(R(t)) + H_{\mathrm{field}}(R(t);t)\right]\Psi(r,R(t);t)\,. \qquad (49)$$

The CC Hamiltonian has been introduced in Eq. (1) (again, the nuclear kinetic energy contribution may be removed), and the coupling to the radiation field follows from Eq. (21). The nuclear coordinates are time–dependent functions determined by Newton's equations

$$M_\nu \frac{\partial^2}{\partial t^2}\mathbf{R}_\nu(t) = -\nabla_\nu \langle \Psi(R(t);t)| \big[V_{\rm CC}(R(t)) + H_{\rm field}(R(t);t)\big] |\Psi(R(t);t)\rangle \ . \tag{50}$$

Here, the $\mathbf{R}_\nu$ denote the position of the ν'th nuclei and the M_ν are the related masses. Since the force the nuclei experience depends on the actual electronic state the latter reacts back on the nuclear dynamics. Noting, again, the huge amount of nuclear coordinates for the types of CC discussed in the following the mixed quantum classical approach should be of a type where this back reaction of the actual electronic state on the nuclear dynamics is neglected. Therefore, the potential $\langle \Psi | V_{\rm CC} + H_{\rm field} | \Psi \rangle$ appearing in Eq. (50) which is determined by the actual electronic excitation is replace by the one of the electronic ground–state (ground–state *classical path approximation* [16–18,21, 43], note also the additional neglect of the external field contribution). This is just the potential $\mathcal{V}_0$ introduced in Eq. (7). It defines the force field used in the MD simulations.

One may also introduce this approximation from a more qualitative point of view by stating that in a large CC the presence of only a single excitation should not change the nuclear dynamics considerably (the atomic partial charges changes by less than 5 % when moving from the ground to the excited state). Regardless of the concrete justification we will proceed in the spirit of ground–state *classical path approximation* in all what follows. In particular, this approximation avoids any difficulties related to electronic transitions induced by the external field. Next we present some details on the used MD approach and the used electrostatic couplings. Afterwards, EET dynamics as well as linear absorbance and photo emission spectra are discussed.

4.1 MD Simulations of the CC in a Solvent

MD simulations of the various P_n of interest (dissolved in ethanol) have been carried out with the NAMD program package [47] using the AMBER force field with the parm99 and GAFF parameter sets [48, 49] (details on how to handle the electrostatic interactions are given in the next section).

The assignment of the atom types and possibly missing bond and torsion angle parameters were done in analogy to existing atom types in the parameter set. To achieve the restrained electrostatic potential (RESP) fitting and to check the parameters we applied the Antechamber module [53] of the AMBER program. Afterwards, the RESP fitted atomic charges were used together with the GAFF parameter set.

The initial conformation of the P_n solvated in a box of ethanol molecules was built by the LEAP module of the AMBER program version 8.0 [54] with

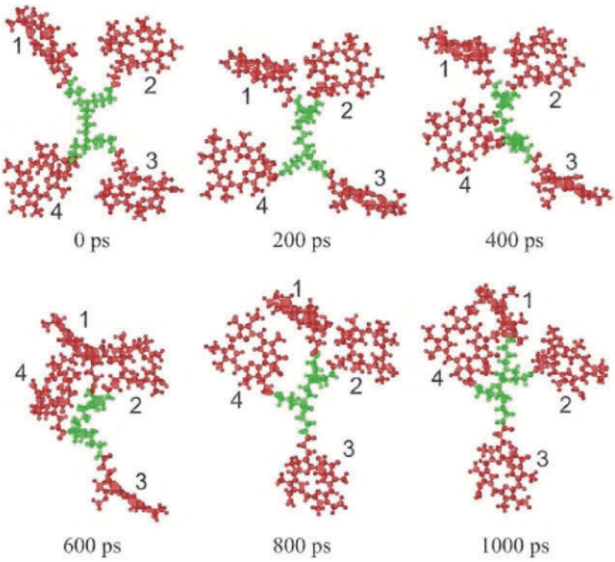

Fig. 6: Snapshots of P_4 in ethanol along a 1 ns room–temperature MD run (the chromophores have been labeled to identify their changed positions).

the GAFF [49] parameters for the CC. Parameters for the ethanol solvent model were obtained from Ref. [51], and have been made compatible with the AMBER force field [48]. Introducing periodic boundary conditions, the electrostatic interactions were computed by the particle mesh Ewald method [55]. The non–bonding potential cutoff distance has been fixed at 15 Å, which was sufficient to account for inter chromophore as well as chromophore solvent interactions and led to a reasonable computation time (an integration time step of 1 fs was used for the MD trajectories). The minimization procedure for the whole system, necessary to remove unfavorable conformations, has been carried out in two steps. First, P_n was kept fixed and only the spatial configurations of the ethanol molecules were minimized. In the second step, the entire system energy was minimized. Afterwards, the system was heated up from 0 to 300 K over a timescale of about 30 ps. All the simulations were performed at constant pressure and constant temperature. Bonds involving hydrogen atoms were constrained with the ShakeH algorithm [56].

We applied the Langevin temperature control [57] (temperature: 300 K, damping coefficient: 1/ps) and the Nosé-Hoover Langevin piston pressure control [58, 59] (target pressure: 1 atm, oscillation period: 100 fs, and oscillation decay time: 50 fs). To ensure stable temperature and pressure, an equilibra-

tion run of about 50 ps was performed. Then, a short simulation followed from which a number of initial configurations (coordinates and velocities) were sampled.

The coordinates of all atoms were recorded every 2 fs, and were used to construct the time–dependent CC Hamiltonian including the solvent–induced site energy shifts. A typical MD simulation time was 1 ns for each trajectory. Fig. 6 shows snapshots of P_4 along a 1 ns MD run with various positions of the single chromophores to each other. Compared with our earlier simulations reported in Ref. [8] the change from a methanol to an ethanol solvent reduced somewhat the conformational flexibility of P_4.

4.2 Coulomb Interactions

The electrostatic potentials related to Pheo and the dendrimeric part were calculated utilizing Gaussian03 [50] at the *ab initio* HF/6-31G* level and with fully optimized molecular geometries (the reliability of the Pheo data has been proven by TDDFT as well as HF–CIS calculations also used to determine the excited state electronic wave function). Afterwards, electrostatic potential based atom centered point charges were obtained in a two–step RESP fitting [51, 52] To be complete we note that the use of atomic centered charges is exact only for the nuclear equilibrium configuration at which they have been introduced. Using them within MD simulations probably my introduce small errors.

The excitonic coupling is determined according to Eq. (18) by introducing atomic centered transition charges $q_{m\mu}(eg)$ [30] (it has been also demonstrated in [30] that this approach reproduces exact data for the inter–chromophore coupling obtained by using the so–called density cube method [31], but with tremendously reduced computational efforts). In Ref. [8] we carried out TDDFT/B3LYP calculations to get charges for Pheo molecules. These atomic partial charges have been also used to calculate the single chromophore permanent and transition dipole moments. Carrying out structure minimization, the gas–phase value for the transition dipole moment is 4.6 D. The permanent dipole moment of the ground state amounts 5.8 D and that of the first excited state 4.9 D. Such calculations have been repeated for P_4 dissolved in ethanol. The values remain almost constant around 4.4 D with small fluctuations of about 0.2 D. To arrive at measured values for the transition dipole moment [60] transition charges are scaled by 0.81.

4.3 Influence of Intra Chromophore Vibrations

Intra chromophore vibrations, i.e. the relative motion of all atoms of a particular chromophore, of course, are included in the MD simulations. But, it is less easy to account for their influence on the EET dynamics. They enter via the single chromophore PES of the ground and the excited state $U_{mg}(R_m)$ and $U_{me}(R_m)$, respectively. If the nuclear coordinate dependence

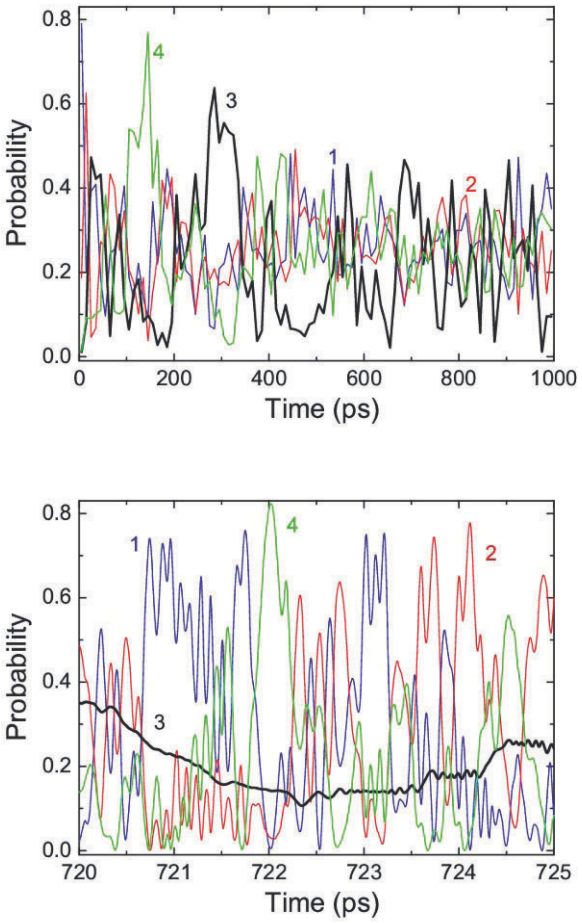

Fig. 7: EET in the CC P_4 including solvent induced modulations. Shown are the chromophore excited state populations, blue curve: $m = 1$, red curve: $m = 2$, black curve : $m = 3$, green curve : $m = 4$. Upper panel: averaged populations (across a time slice of 10 ps), lower panel: non–averaged populations in a 5 ps time window.

of both types of PES is known (possibly in a harmonic approximation) the single chromophore excitation energy fluctuation could be calculated from $U_{me}(R_m(t)) - U_{mg}(R_m(t))$. However, data for the two types of PES are not available at present and we have to carry out different versions of an approximate account of these vibrations (see below).

5 Mixed Description of Excitation Energy Transfer Dynamics

The mixed quantum classical description of EET can be achieved in using Eq. (49) together with the electronic ground–state classical path version of Eq. (50). As already indicated this approach is valid for any ratio between the excitonic coupling and the exciton vibrational interaction. If an ensemble average has been taken appropriately we may also expect the manifestation of electronic excitation energy dissipation and coherence decay, however, always in the limit of an infinite temperature approach.

To compute the overall CC electronic wave function $\Psi(r,t;R(t))$ introduced in Eq. (49) an expansion with respect to the CC electronic ground and the singly excited states is carried out

$$\Psi(r;R(t)) = A_0(t)\phi_0(r;R(t)) + \sum_m A_m(t)\phi_m(r;R(t)) \; . \tag{51}$$

If inserted into the time–dependent Schrödinger equation (49) an multiplication with ϕ_0^* and ϕ_m^* from the left results in equations of motion for the expansion coefficients. In doing so, one also produces overlap expressions like $\langle\phi_0|\partial/\partial t|\phi_0\rangle$, $\langle\phi_m|\partial/\partial t|\phi_0\rangle$, and $\langle\phi_m|\partial/\partial t|\phi_n\rangle$ (non–adiabatic couplings), which all can be neglected in line with the neglect of the mutual chromophore wave function overlap. Therefore, we obtain the expansion coefficient's equations of motion as

$$i\hbar\frac{\partial}{\partial t}A_0(t) = \mathcal{H}_0(t)A_0(t) - \sum_m \mathbf{d}_m^*(t)\mathbf{E}(t)A_m(t) \; , \tag{52}$$

and

$$i\hbar\frac{\partial}{\partial t}A_m(t) = \sum_n \mathcal{H}_{mn}(t)A_n(t) - \mathbf{d}_m(t)\mathbf{E}(t)A_0(t) \; . \tag{53}$$

Once MD simulations for the CC have been carried out the Eqs. (52) and (53) for the expansion coefficients can be easily solved (also in the presence of an external radiation field). Moreover, the coefficients are used to compute observables of interest. The excited state population follows as

$$P_m(t) = |A_m(t)|^2 \; . \tag{54}$$

Probably, an ensemble average $< P_m(t) >$ of the population would become of interest (it can be approximated by an appropriate time average [10]).

Fig. 7 displays the time averaged populations (upper panel) and non–averaged populations in a 5 ps time window (lower panel; the behavior is typical for all calculations). A remarkable excitation energy redistribution among the four chromophores becomes observable. The time window corresponds to the central snapshot (800 ps) of the lower part of Fig. 6. The

population of chromophore 3 stays rather constant while the close distance of the remaining chromophores to each other induces EET proceeding on a sub ps time scale (some further examples can be found in [10]). These fast oscillations are averaged out in an ensemble average [10]. In particular, Fig. 7 indicates the long–term survival of electronic coherences. If we compute, for example, $< A_m(t)A_n^*(t) >$ representing off–diagonal density matrix elements ρ_{mn} (if $m \neq n$) similar curves as in Fig. 7 are obtained (not shown). At best, they indicate intermediate dephasing which is compensated by something like rephasing, i.e. a later increase of $< A_m(t)A_n^*(t) >$. Excitation energy motion appears to be irregular since it is dominated by the equilibrium solvent dynamics inducing CC conformational changes.

6 Mixed Description of Linear Absorption Spectra

The standard translation of the full quantum formula of the absorbance, Eq. (31), to a mixed quantum classical description (see, e.g., [16–18]) is similar to what is the essence of the (electronic ground–state) classical path approximation introduced in the foregoing section. One assumes that all involved nuclear coordinates behave classically and their time–dependence is obtained by carrying out MD simulations in the systems electronic ground state. This approach when applied to the absorbance is known as the *dynamical classical limit* (DCL, see, for example, Res. [17]).

In Ref. [9] we demonstrated how one approaches the DCL for the CC absorption cross section, Eq. (31). In a first step, the overall time evolution operator $\exp(iH_{CC}t/\hbar)$ has to be replaced by the S–operator $S_1(t,0)$ which includes the difference Hamiltonian of the excited CC state and of the ground–state. Then, the vibrational Hamiltonian matrix appearing in the exponent of $S_1(t,0)$ is replace by an ordinary matrix the time-dependence of which follows from classical nuclear dynamics in the CC ground–state. The time–dependence of the dipole moment d_m^* follows from intra chromophore nuclear rearrangement and changes of the overall spatial orientation. At last, this translation procedure replaces the CC state matrix elements of the S–operator by complex time–dependent functions

$$\tilde{A}_m(t;n) = \langle \phi_m | S_1(t,0) | \phi_n \rangle \ . \tag{55}$$

The index n indicates that $|\phi_n\rangle$ is the initial state of the propagation, just resulting in $\tilde{A}_m(0;n) = \delta_{m,n}$. If the considerations are reduced to a complex with a single chromophore only $\tilde{A}(t)$ equals $\exp[-i/\hbar \int_0^t d\tau U_{eg}(R(\tau))]$, where U_{eg} has been introduced in Eq. (11) and is often named energy gap function [43].

Using $\tilde{A}_m(t;n)$ valid for the whole CC the absorbance is obtained as

$$I(\omega) = \mathrm{Re} \int_0^\infty dt\; e^{i\omega t} \sum_{m,n} < d_m^*(t) \tilde{A}_m(t;n) d_n > \,, \tag{56}$$

To distinguish this mixed quantum classical formula for the absorbance from the other introduced later we name it DCL absorbance. While in the full quantum formula, Eq. (31), it is guaranteed that $I(\omega)$ is always positive this is not the case here. Calculating the absorbance from a single MD run, negative values become possible. However, they are removed within the thermal averaging procedure via destructive interferences i.e. dephasing. The extend to which this becomes possible depends on the number of MD runs used to carry out the averaging. Often this number is restricted due to computational limitations and the incomplete destructive interferences are repaired by introducing an empirical dephasing term $\sim \exp(-t/\tau_{\mathrm{deph}})$. Now, however, the single MD run should only extend up to an upper time of some multiples of τ_{deph} ($t < 3...5\tau_{\mathrm{deph}}$).

The determination of the various coefficients $\tilde{A}_m(t;n)$ appearing in Eq. (56) is achieved via the following equations of motion

$$i\hbar \frac{\partial}{\partial t} \tilde{A}_m(t;n) = \sum_k \big(\mathcal{H}_{mk}(t) - \delta_{m,k} \mathcal{H}_0 \big) \tilde{A}_k(t;n) \,. \tag{57}$$

A similar translation scheme from the full quantum approach to a mixed quantum classical description has been used recently in Ref. [26–29] to calculate infrared absorption spectra of polypeptides within the amide I band (note that the translation scheme has been also used in the mentioned references to compute nonlinear response functions).

Since the translation scheme from the full quantum formula to a mixed quantum classical description is not unique we also refer to a slightly different way where the absorption coefficient is derived by linearizing the CC dipole moment $\mathbf{d}(t)$ with respect to the field–strength $\mathbf{E}$ [9].

6.1 Linear Response Theory Approach

In contrast to the computations of the preceding section we directly calculate the expectation value of the CC dipole operator (finally linearized with respect to the external field) applying the classical path approximation for nuclear dynamics. Such a direct calculation of the dipole operator expectation value becomes of particular interest when focusing on ultrafast nonlinear optical properties (transient absorption, photon echo signal, etc.).

Assuming the external field in the form $\mathbf{E}(t) = \mathbf{n} E(t) \exp(-i\omega t) + \mathrm{c.c.}$, with polarization unit vector $\mathbf{n}$, field envelope $E(t)$, and photon energy $\hbar\omega$, the absorption signal (the energy gain per sample volume the CC experiences at the presence of the field) can be written as $S_{\mathrm{abs}}(\omega) = 2\omega \mathrm{Im} \int dt\; E^*(t) P(t)$

(the integration has to cover the interval of the $E(t)$ action here from t_0 up to t_f). The polarization field $\mathbf{P}(t)$ with envelope $P(t)$ takes the same form as the electric field–strength. Since $\mathbf{P}$ is understood as the dipole moment per volume it can be calculated as $n_{\mathrm{CC}} < \mathbf{d}(t) >$ (n_{CC} is the volume density of CC in the sample). Thus, the polarization envelope follows as

$$P(t) \equiv e^{i\omega t}\mathbf{nP}(t) = n_{\mathrm{CC}} e^{i\omega t} < \mathbf{nd}(t) > \ . \tag{58}$$

If S_{abs} is divided by the intensity of the field, the absorption coefficient is obtained as $\alpha(\omega) = 2\pi S_{\mathrm{abs}}(\omega)/c \int dt\ |E(t)|^2$. According to Ref. [9] we arrive at:

$$S_{\mathrm{abs}}(\omega) = \frac{\omega n_{\mathrm{CC}}}{\hbar} \sum_m < |D(\omega; m)|^2 > , \tag{59}$$

where $D(\omega; m)$ is a total time–integrated function interpreted as the Fourier–transform with respect to the frequency ω of the external field (be aware of $t_0 \to -\infty$, $t_f \to \infty$). The related time–dependent D–function reads

$$D(t; m) = e^{i\omega t} E^*(t) \sum_n d_n^*(t) \tilde{A}_n(t; m) \ , \tag{60}$$

with the $\tilde{A}_n(t; m)$ introduced in Eq. (55).

To distinguish the absorbance calculated here from the DCL absorbance of Eq. (56) we will name it absorbance according to a direct use of linear response theory (LRT absorbance). For this type of absorbance it is guaranteed that it stays positive. The thermal averaging exclusively leads to a constructive interferences

6.2 Inclusion of Intra Chromophore Vibrations

As indicated in Section 4.3 there are no data available at present providing an intra chromophore coordinate dependence of the single chromophore electronic energies that could be included in the calculation of the absorbance. Therefore, we will suggest two approximations to include the effects induced by intra chromophore vibrations [9]. The first one introduces an additional random energy $\hbar\Delta\omega$ added to all chromophore excitation energies entering Eq. (11). When calculating $\tilde{A}_n(t; m)$, Eq. (57), $\hbar\Delta\omega$ can be easily included leading to a shift of the frequency argument by $\Delta\omega$ in the absorption signal, Eq. (59). An averaging with respect to the distribution of the $\hbar\Delta\omega$ results in an averaged LRT absorption cross section according to

$$\bar{I}(\omega) = \int d\Delta\omega\ g(\Delta\omega) I(\omega - \Delta\omega) \ . \tag{61}$$

The function $g(\Delta\omega)$ describes the distribution of the random energy shift around zero. We note that this approach is different from the standard way of

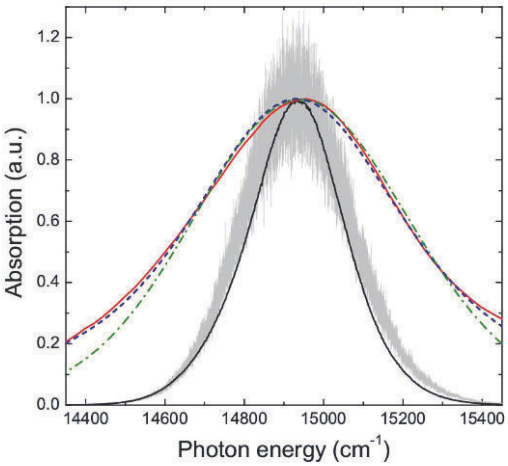

Fig. 8: Absorbance of the CC P_4 using different approximations (the red (full outer) line gives the measured spectrum). Black (full inner) curve: estimate according to Eq. (64) using adiabatic exciton levels (see also Fig. 10), gray area: LRT absorbance, Eq. (59), green (dash-dotted) curve: DCL absorbance including intra chromophore vibrations resulting in an additional broadening according to Eq. (62) (with vibrational reorganization energy of 110 cm^{-1}), blue (dashed) curve: the same as before but with the direct use of a dephasing time of 20 fs.

averaging by introducing an additional factor $\exp(-t/\tau_{\rm deph})$ in Eq. (56). Here, such a treatment is not possible since the LRT absorbance is determined by the square of a time integral.

Our more basic account for intra chromophore vibrations uses the DCL absorbance, Eq. (56). We stay at a quantum description of the intra chromophore vibrations and get the cross section as [9]

$$I(\omega) = \mathrm{Re} \int_0^\infty dt e^{i\omega t} \sum_{m,n} \vartheta_{mge}(t) < d_m^*(t) \tilde{A}_m(t;n) d_n > , \tag{62}$$

where we introduced the mth single chromophore trace expression

$$\vartheta_{mge}(t) = \mathrm{tr}_m\{\hat{R}_{mg} e^{ih_{mg}t/\hbar} e^{-ih_{me}t/\hbar}\} . \tag{63}$$

This is the standard quantum correlation function determining the absorbance of an isolated molecule, where the h_{ma} $(a = g, e)$ are the Hamiltonians of intra chromophore vibrations in chromophore m (defined with respect to the minimum of the actual PES) and $\hat{R}_{mg}$ denotes the respective electronic ground

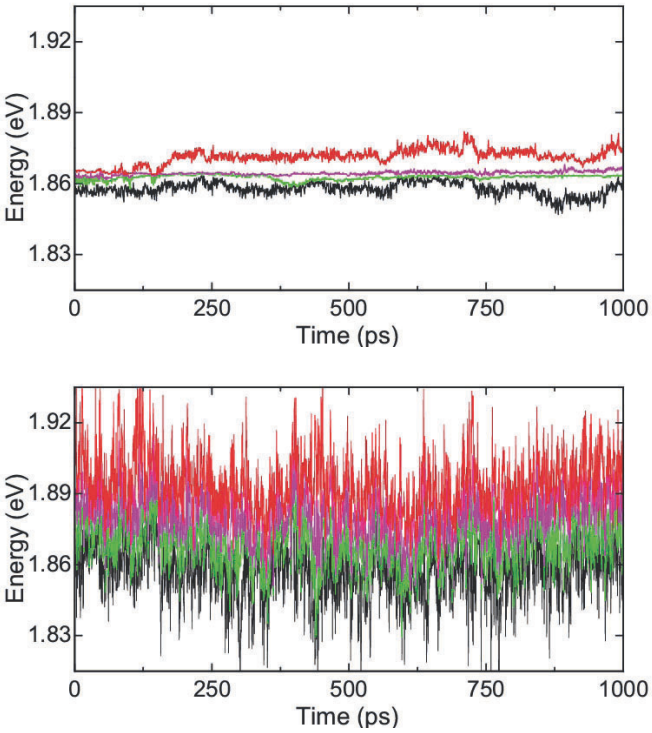

Fig. 9: Adiabatic exciton levels of P_4 (introduced in Section 2.5) versus time. Upper panel: neglect of the electrostatic CC solvent coupling, lower panel: inclusion of the electrostatic CC solvent coupling.

state vibrational equilibrium statistical operator. Note, that Eq. (62) neglects any vibrational overlap with respect to the inter–chromophore excitonic coupling [9].

Fig. 8 shows respective simulation results. The estimate using adiabatic exciton states (see the subsequent section) coincides with the LRT absorbance. Although the electrostatic coupling to solvent molecules has been included the achieved broadening is insufficient to meet the measured curve. An additional broadening due to the inclusion of intra chromophore vibrations removes this discrepancy.

6.3 Estimate of the Absorbance Using Adiabatic Exciton States

Adiabatic exciton states have been introduced in Section 2.5. They are used to arrive at the following approximate formula for the CC absorption cross section [9]:

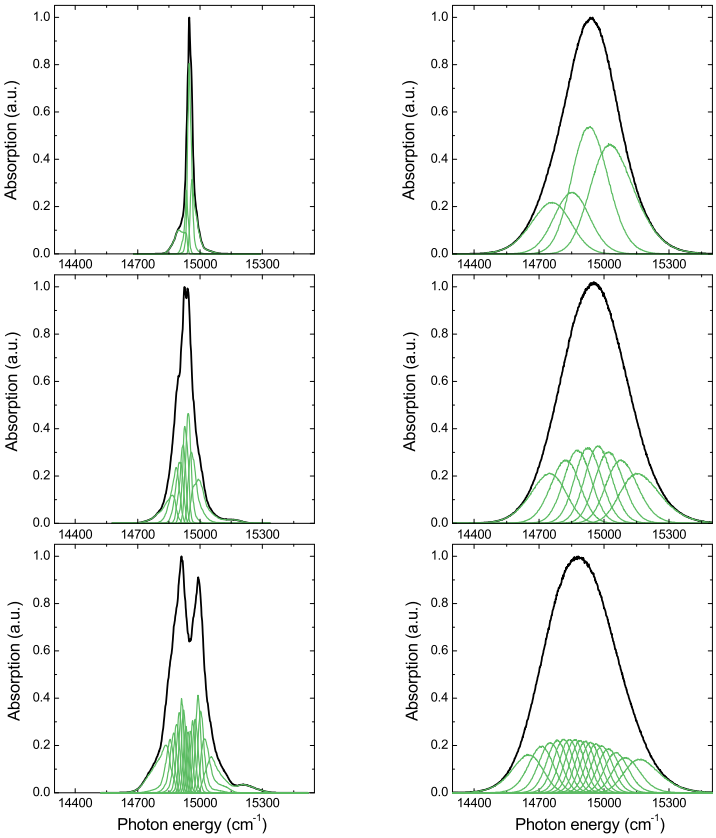

Fig. 10: Room temperature absorption spectra of P_4 (upper two panels), P_8 (two central panels), and P_{16} (bottom panels) estimated according to Eq. (66) and in using adiabatic exciton energies and oscillator strengths. The overall spectrum (thick line) follows as the sum of single exciton level contributions (thin lines). The left column of figures shows spectra without including the modulation of the chromophore excitation energy by a coupling to the solvent. The right column of figures shows spectra where this effect is included.

$$I(\omega) \sim \sum_{\alpha} \int dR\; R_0(R) O_\alpha(R) \delta(\omega - \mathcal{E}_\alpha(R)/\hbar)\;. \tag{64}$$

The oscillator strengths have been introduced according to

$$O_\alpha(R) = |\sum_n d_n(R) C^*_\alpha(n;R)|^2/d^2\;, \tag{65}$$

where d fixes a reference value of the dipole moment (absolute value of the molecular transition dipole). Moreover, $R_0(R)$ is the nuclear coordinate equilibrium distribution.

To evaluate the absorbance according to Eq. (64) we replace the nuclear coordinates by trajectories and $\int dR R_0(R)$ by an averaging with respect to different initial thermalized CC configurations. The frequency axis is divided into equidistant grid points ω_j with spacing $\Delta\omega$. Then, the oscillator strength weighted density of states of exciton level α can be computed in using d_α and $\mathcal{E}_\alpha$ at time steps t_k ($k = 1, ..., N$, θ denotes the unit–step function) [8]:

$$\mathcal{D}_\alpha(\omega_j) =< \frac{1}{N} \sum_k \theta(\omega_j + \Delta\omega/2 - \mathcal{E}_\alpha(t_k)/\hbar)$$
$$\theta(\mathcal{E}_\alpha(t_k)/\hbar - \omega_j + \Delta\omega/2)\, O_\alpha(t_k) > \ . \tag{66}$$

Consequently, the formula counts how often a fluctuating exciton level appears in a particular frequency interval. If the contributions of all four excitons levels are added up, the result becomes proportional to the absorbance. Fig. 8 shows the respective result for P_4. It coincides with the more involved computation according to the LRT scheme of Section 6.1. Respective adiabatic exciton levels are shown in Fig. 9 either for the neglect of the electrostatic solvent solute coupling as well as for its inclusion. In the latter case the spectra fluctuate rather strongly indicating that non–adiabatic couplings among exciton levels may become of some importance. However, the overall absorbance, Fig. 8, if compared with the LRT results does not give any hint on this particular effect.

Finally we indicate that the inclusion of intra chromophore vibrations according to Eq. (61) can be also translated to the present case yielding the averaged density of states as

$$\bar{\mathcal{D}}(\omega) = \int d\Delta\omega \; g(\Delta\omega) \sum_\alpha \mathcal{D}_\alpha(\omega - \Delta\omega) \ . \tag{67}$$

The function $g(\Delta\omega)$ has been already introduced in relation to Eq. (61).

Since the estimate of the absorbance using adiabatic exciton states leads to rather good results we use this approximation to compare in Fig. 10 the absorbance of P_4 with that of P_8 and P_{16}. While the neglect of an electrostatic solvent solute coupling (when calculating the chromophore excited states) gives structured absorption spectra with an increasing broadening at an increasing CC size the inclusion of the electrostatic solvent solute coupling leads to rather uniform spectra. The much stronger excited state energy fluctuations due to this coupling (cf. also Fig. (9)) results in a Gaussian like line shape.

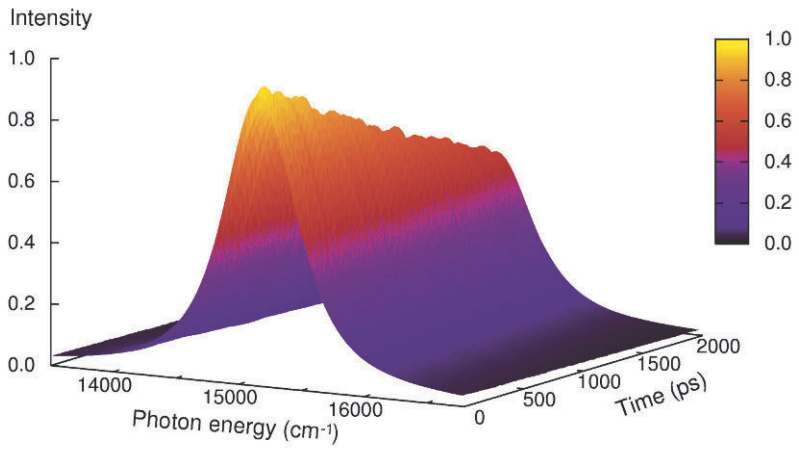

Fig. 11: Normalized time and frequency resolved emission spectrum of the CC P_4. A 6 ps time averaging has been carried out to mimic the apparatus function of the single photon detector. Radiative and non–radiative decay has been accounted for by a common chromophore excited–state life time of 5 ns.

7 Mixed Description of Time and Frequency Resolved Emission

A rather direct translation of $F(\omega;t)$, Eq. (39), to the mixed quantum classical case is obtained by, again, replacing the vibrational state trace by an averaging with respect to the initial CC equilibrium configuration. Such configurations are used for the MD run from t_0 to $\bar{t}$ and determine the respective density matrix propagation to arrive at $\rho_{nk}(\bar{t})$. Time evolution operators referring to the CC ground and first excited state are replaced by the quantity introduced in Eq. (55) and determined by Eq. (57). The magnitude and spatial orientation of the two transition dipole moments directly follows from the MD run. Thus, we arrive at

$$F(\omega;t) = \frac{4\omega^3}{3\pi c^3\hbar}\mathrm{Re}\int_{t_0}^{t} d\bar{t}\, e^{-i\omega(t-\bar{t})} \sum_{m,n,k} \\ < \rho_{nk}(\bar{t})\tilde{A}^*_m(t,\bar{t};k)[\mathbf{d}_m(t)\mathbf{d}^+_n(\bar{t})] > \ . \qquad (68)$$

A version of the reduced density operator to be used in the mixed quantum classical description may be obtained if we replace $\hat{\rho}(\bar{t})$ by the pure state

expression $|\Psi(\bar{t})\rangle\langle\Psi(\bar{t})|$, with the electronic CC wave function Ψ introduced in Eq. (49). Then, the $\hat{\rho}_{nk}(\bar{t})$ can be identified with $\langle\phi_m|\Psi(\bar{t})\rangle\langle\Psi(\bar{t})|\phi_m\rangle \equiv B_m(\bar{t})B_n^*(\bar{t})$. As already indicated in Section 3.3 such an approach, however, is unable to account for CC excited state decay just by photon emission. One has to achieve a mixed quantum classical translation of the complete reduced density operator. It should be reduced with respect to the photon states and may be computed in a way to include photon emission. This would be given by Eq. (41) if the quantities $\hat{\rho}_{mn}(\bar{t})$ introduced there are interpreted as density matrices $\rho_{mn}(\bar{t})$ and the $\mathcal{H}_{mn}$ as forming a time–dependent Hamiltonian matrix. Intra chromophore vibrations can be included as it already has been done in Eq. (62) for the absorbance, but now with $\vartheta_{mge}(t)$, Eq. (63), replaced by

$$\vartheta_{meg}(t) = \mathrm{tr}_m\{\hat{R}_{me}e^{ih_{me}t/\hbar}e^{-ih_{mg}t/\hbar}\} \; . \tag{69}$$

It describes single chromophore excited state decay where the statistical operator $\hat{R}_{me}$ defines intra chromophore vibrational equilibrium in the excited electronic state. The whole ϑ_{meg} has to be taken at time argument $t - \bar{t}$ and, then, to be multiplied to $\tilde{A}_m^*(t, \bar{t}; k)$ in Eq. (68).

Fig. 11 shows the time and frequency resolved emission spectrum of P_4 following from Eq. (68) by introducing a time averaging due to the finite time resolution of the single photon counting measurements. Predictably, the line shape is similar to that of the absorbance, Figs. 8 and 10 (for more details see [11]; concerning the inclusion of excitonic augmented decay rates as introduced at the end of Section 3.3 we refer to [46]).

8 Conclusions

A mixed quantum classical description of excitation energy transfer dynamics in huge pheophorbide–*a* complexes has been presented together with the computation of related spectra of the linear absorbance as well as of the time and frequency resolved spontaneous emission. Ground and excited electronic states of the whole set of chromophores forming the complex are defined according to the well known Frenkel exciton model (absence of charge transfer states between adjacent chromophores). Going beyond the standard formulation of the Frenkel exciton model electrostatic couplings among chromophores as well as chromophores and solvent molecules have been included. This extension became essential for pheophorbide–*a* molecules since their overall charge distribution in the ground and first excited state is noticeable unbalanced. Introducing atomic centered partial charges also for the transition charges entering the excitonic coupling among different chromophores, the latter could be described nearly exactly and for all possible nuclear configurations appearing in the MD runs.

According to the size of the system the MD runs have to be carried out in a way not to notice the actual CC excited state (electronic ground state classical path approximation). However, it seems rather reasonable that any back reaction of the actual excited electronic state should be of minor importance since even in the largest studies complexes only singly excited states (single exciton states) are incorporated.

While the mixed quantum classical description of CC linear absorbance has been already discussed at different places a formulation of time and frequency resolved spontaneous emission spectra is new in literature. Such spectra directly offer signatures of excitation energy transfer proceeding in a picosecond up to nanosecond time region. When trying to achieve a detailed explanation of the transfer processes, however, one should be always aware of the fact that the mixed quantum classical description corresponds to a high temperature limit, i.e it is only applicable if characteristic energy differences to be overcome in the excitation energy motion are comparable or less then the thermal energy $k_{\mathrm{B}}T$.

The whole approach offers a promising route to uncover the structure function relationships of huge supramolecular complexes either with biological or non–biological origin. Respective studies should proceed in a close collaboration of theory and experiment and with the focus on spectroscopic techniques.

Acknowledgments

Financial support by the Deutschen Forschungsgemeinschaft through project MA 1356–10/1 and 10/2 is gratefully acknowledged.

References

1. M. Fujitsuka, A. Okada, S. Tojo, F. Takei, K. Onitsuka, S. Takahashi, and T. Majima, J. Phys. Chem. B **108**, 11935 (2004).
2. E. Hindin, R. A. Forties, R. S. Loewe, A. Ambroise, C. Kirmaier, D. F. Bocian, J. S. Lindsey, D. Holten, and R. S. Knox, J. Phys. Chem. B **108**, 12821 (2004).
3. S. Masua, T. Vosch, M. Cotlet, P. Tinnefeld, S. Habuchi, T. D. M. Bell, I. Osterling, D. Beljonne, B. Champagne, K. Müllen, M. Sauer, J. Hofkens, and F. C. De Schryver, J. Phys. Chem. B **108**, 16686 (2004).
4. J. Larsen, B. Brüggemann, T. Khoury, J. Sly, M. J. Crossley, V. Sundström, and E. Åkesson, J. Phys. Chem. A **111**, 10589 (2007).
5. Y.–Z. Ma, R. A. MIller, G. R. Flemming, and M. B. Francis, J. Phys. Chem. B **112**, 6887 (2008).
6. S. Hackbarth, E. A. Ermilov, and B. Röder, Opt. Comm. **248**, 295 (2005).
7. M. Helmreich, E. A. Ermilov, M. Meyer, N. Jux, A. Hirsch, and B. Röder, J. Am. Chem. Soc. **127**, 8376 (2005).
8. H. Zhu, V. May, B. Röder, M. E. Madjet, and Th. Renger, Chem. Phys. Lett. **444**, 118 (2007).

9. H. Zhu, V. May, B. Röder, and Th. Renger, J. Chem. Phys. **128** (2008).
10. H. Zhu, V. May, and B. Röder, Chem. Phys. **351**, 117 (2008).
11. H. Zhu, B. Röder, and V. May, Chem. Phys. (in press).
12. G. Monard and K. M. Merz, Acc. Chem. Res. **32**, 904 (1999).
13. A. Altun, S. Shaik, and W. Thiel, J. Am. Chem. Soc. **129**, 8978 (2007).
14. G. Groenhof, L. V. Schäfer, M. Boggio–Pasqua, H. Grubmüller, and M. A. Robb, J. Am. Chem. Soc. **130**, 3250 (2008).
15. R. A. Mata, H.–J. Werner, S. Thiel, and W. Thiel, J. Chem. Phys. **128**, 025104 (2008).
16. O. V. Prezhdo and P. J. Rossky, J. Chem. Phys. **107**, 5863 (1997).
17. S. A. Egorov, E. Rabani, and B. J. Berne, J. Chem. Phys. **108**, 1407 (1997).
18. Q. Shi amd E. Geva, J. Chem. Phys. **122**, 064506 (2005).
19. D. Marx and J. Hutter, in J. Grotendorst (ed.), *Modern Methods and Algorithms of Quantum Chemistry* (J. von Neumann Institute for Computing, Jülich, 2000).
20. S. Hammes–Schiffer, J. Phys. Chem. A **102**, 10443 (1998).
21. N. L. Doltsini and D. Marx, J. Theor. Comp. Chem. **1**, 319 (2002).
22. G. de M. Seabra, R. C. Walker, M. Elstner, D. A. Case, and A. E. Roitberg, J. Phys. Chem. A **111**, 5655 (2007).
23. A. Damjanovic, I. Kosztin, U. Kleinekathöfer, and K. Schulten, Phys. Rev E **65**, 031919 (2002).
24. B. Bouvier, J.–P. Dognon, R. Lavery, D. Markovitsi, P. Millie, D. Onidas, and K. Zakrzewska, J. Phys. Chem. B **107**, 13512 (2003).
25. E. Emanuele, K. Zakrzewska, D. Markovitsi, R. Lavery, and P. Millie, J. Phys. Chem. B **109**, 16109 (2005).
26. S. Ham, S. Hahn, C. Lee, T.–K. Kim, K. Kwak, and M. Cho, J. Phys. Chem. B **108**, 9333 (2004).
27. T. la Cour Jansen, W. Zhuang, and S. Mukamel, J. Chem. Phys. **121**, 10577 (2004).
28. T. la Cour Jansen and J. Knoester, J. Phys. Chem. B **110**, 22910 (2006).
29. R. D. Gorbunov, P. H. Nguyen, M. Kobus, G. Stock, J. Chem. Phys. **126**, 054509 (2007).
30. M. E. Madjet, A. Abdrahman, and Th. Renger, J. Phys. Chem. B **110**, 17268 (2006).
31. B. P. Kruger, G. D. Scholes and G. D. Fleming, J. Phys. Chem. B **102**, 5378 (1998).
32. V. M. Kenkre and P. Reineker, in *Springer Tracts Mod. Phys.*, (Volume 94, Springer Verlag, 1982).
33. I. A. Goychuk, E. Petrov, and V. May, Phys. Rev. E 51, 5084 (1995).
34. I. A. Goychuk, E. Petrov, and V. May, J. Chem. Phys. 103, 4937 (1995).
35. H. van Amerongen, L. Valkunas, and R. van Grondelle, *Photosynthetic Excitons* (World Scientific, Singapore, 2000).
36. Th. Renger, V. May, and O. Kühn, Phys. Rep. **343**, 137 (2001).
37. Th. Renger and R. Marcus, J. Chem. Phys. **116**, 9997 (2002).
38. Th. Renger and R. A. Marcus, J. Phys. Chem. B **106**, 1809 (2002).
39. H.–P. Breuer, and F. Petruccione, *The Theory of Open Quantum Systems* (Oxford University Press, 2002).
40. V. May and O. Kühn, *Charge and Energy Transfer Dynamics in Molecular Systems* (Wiley-VCH, Berlin, 2000, second edition 2004).
41. V. May, J. Chem. Phys. **129**, 114109 (2008).

42. B. M. Auer and J. L. Skinner, J. Chem. Phys. **127**, 104105 (2007).
43. S. Mukamel, *Principles of Nonlinear Optical Spectroscopy*, (Oxford University Press, 1995).
44. M. F. Gelin, D. Egorova, and W. Domcke, Chem. Phys. **301**,129 (2004)
45. B. Brüggemann, K. Sznee, V. Novoderezhkin, R. van Grondelle, and V. May, J. Phys. Chem. B 108, 13536 (2004)
46. J. Megow and V. May, J. Chem. Phys. (in preparation).
47. J. C. Phillips, R. Braun, W. Wang, J. Gumbart, E. Tajkhorshid, E. Villa, C. Chipot, R. D. Skeel, L. Kale, and K. Schulten. Scalable molecular dynamics with NAMD. J. Comput. Chem. **26**, 1781 (2005) .
48. W. D. Cornell, P. Cieplak, C. I. Bayly, I. R. Gould, K. M. Merz, Jr.,D. M. Ferguson, D. C. Spellmeyer, T. Fox, J. W. Caldwell, and P. A. Kollman, J. Am. Chem. Soc. **117**, 5179 (1995).
49. J. Wang, R. M. Wolf, J. W. Caldwell and P. A. Kollman, J. Comput. Chem. **25**, 1157 (2004).
50. M. J. Frisch, G. W. Trucks, H. B. Schlegel, G. E. Scuseria, M. A. Robb, J. R. Cheeseman, J. A. Montgomery, Jr., T. Vreven, K. N. Kudin, J. C. Burant, J. M. Millam, S. S. Iyengar, J. Tomasi, V. Barone, B. Mennucci, M. Cossi, G. Scalmani, N. Rega, G. A. Petersson, H. Nakatsuji, M. Hada, M. Ehara, K. Toyota, R. Fukuda, J. Hasegawa, M. Ishida, T. Nakajima, Y. Honda, O. Kitao, H. Nakai, M. Klene, X. Li, J. E. Knox, H. P. Hratchian, J. B. Cross, V. Bakken, C. Adamo, J. Jaramillo, R. Gomperts, R. E. Stratmann, O. Yazyev, A. J. Austin, R. Cammi, C. Pomelli, J. W. Ochterski, P. Y. Ayala, K. Morokuma, G. A. Voth, P. Salvador, J. J. Dannenberg, V. G. Zakrzewski, S. Dapprich, A. D. Daniels, M. C. Strain, O. Farkas, D. K. Malick, A. D. Rabuck, K. Raghavachari, J. B. Foresman, J. V. Ortiz, Q. Cui, A. G. Baboul, S. Clifford, J. Cioslowski, B. B. Stefanov, G. Liu, A. Liashenko, P. Piskorz, I. Komaromi, R. L. Martin, D. J. Fox, T. Keith, M. A. Al-Laham, C. Y. Peng, A. Nanayakkara, M. Challacombe, P. M. W. Gill, B. Johnson, W. Chen, M. W. Wong, C. Gonzalez, and J. A. Pople, Gaussian 03, Revision D.01; Gaussian, Inc., Wallingford CT, 2004.
51. T. Fox and P. A. Kollman, J. Phys. Chem. B **102**, 8070 (1998).
52. C. I. Bayly, P. Cieplak, W. D. Cornell and P. A. Kollman, J. Phys. Chem. **97**, 10269 (1993).
53. J. Wang, W. Wang, P. A. Kollman and D. A. Case, J. Mol. Graphics and Model. **25**, 247 (2006).
54. D. A. Case, T. A. Darden, T. E. Cheatham, III, C. L. Simmerling, J. Wang, R. E. Duke, R. Luo, K. M. Merz, B. Wang, D. A. Pearlman, M. Crowley, S. Brozell, V. Tsui, H. Gohlke, J. Mongan, V. Hornak, G. Cui, P. Beroza, C. Schafmeister, J. W. Caldwell, W. S. Ross, and P.A. Kollman (2004), AMBER 8, University of California, San Francisco.
55. T. A. Darden, D. M. York, L. G. Pedersen, J. Chem. Phys. **98**, 10089 (1993).
56. J.-P. Ryckaert, G. Ciccotti, H. J. C. Berendsen, J. Comput. Phys. **23** 327 (1977).
57. M. G. Paterlini and D. M. Ferguson,Chemical Physics, **236**, 243 (1998).
58. G. J. Martyna, D. J. Tobias and M. L. Klein, J. Chem. Phys. **101**, 4177 (1994).
59. S. E. Feller, Y. Zhang, R. W. Pastor and B. R. Brooks, J. Chem. Phys. **103**, 4613 (1995).
60. I. Eichwurzel, H. Stiel and B. Röder, J. Photochem. Photobiol. B: Biol. **54**, 194 (2000).
61. A. R. Clapp, I. L. Medintz, and H. Mattoussi, ChemPhysChem **7**, 47 (2006).

62. J. Zhang, Y. Fu, and J. R. Lakowizc, J. Phys. Chem. C **111**, 50 (2007).
63. J. D. Weibel, C. F. Jackels and R. L. Swofford, J. Chem. Phys. **117**, 4245 (2002).

Conformational Structure and Dynamics from Single-Molecule FRET

Eitan Geva and Jianyuan Shang

Chemistry Department, University of Michigan, 930 N. University Ave., Ann Arbor MI, 48109-1055 eitan@umich.edu

Abstract. Various ways of extracting information on the conformational structure, dynamics and correlations between them from single-molecule measurements of florescence resonance energy transfer are surveyed. The information obtained via those various ways is then analyzed in detail in the case of an off-lattice model of a two-stranded coiled-coil polypeptide that follows Langevin dynamics. The analysis includes a consideration of the cases of a freely diffusing and surface-immobilized polypeptide as well as the effect of different types of surface and denaturation conditions.

1 Introduction

The elucidation of the structure, dynamics and self assembly of biopolymers has been the subject of many experimental, theoretical and computational studies over the last several decades. [1, 2] More recently, powerful single-molecule (SM) techniques have emerged which make it possible to explore those questions with an unprecedented level of detail. [3–55] SM fluorescence resonance energy transfer (FRET), [56–60] in particular, has been established as a unique probe of conformational structure and dynamics. [26–55] In those SM-FRET experiments, one measures the efficiency of energy transfer between a donor dye molecule and an acceptor dye molecule, which label specific sites of a macromolecule. The rate constant for FRET from donor to acceptor is assumed to be given by the Förster theory, namely: [59, 61–64]

$$k_{ET}(R) = k_D \left(\frac{R_0}{R} \right)^6 \quad , \tag{1}$$

where k_D^{-1} is the fluorescence life-time of the free donor, R is the distance between donor and acceptor, and R_0 is a parameter that depends on the choice of donor-acceptor pair and other experimental conditions. [64] The strong dependence of the FRET efficiency on the donor-acceptor distance therefore

I. Burghardt et al. (eds.), *Energy Transfer Dynamics in Biomaterial Systems*, Springer Series in Chemical Physics 93, DOI 10.1007/978-3-642-02306-4_3,

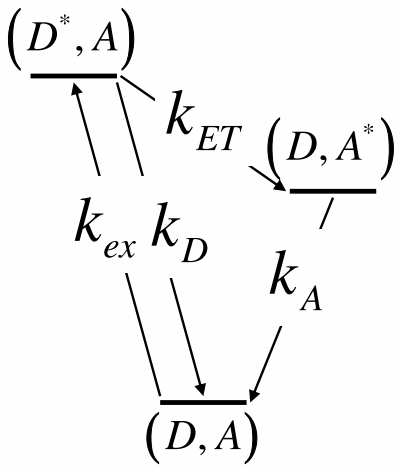

Fig. 1: A schematic view of the donor-acceptor photophysics. D/A and D^*/A^* correspond to the ground and excited donor/acceptor, respectively. It is assumed that only the donor is photoexcited at the rate of k_{ex}. k_{ET} is the donor-to-acceptor energy transfer rate constant, and k_D/k_A are the free donor/acceptor fluorescence rate constants.

makes it possible to obtain information on the underlying conformational structure and dynamics from SM-FRET measurements.

In a typical SM-FRET experiment, one photoexcites the donor dye at a rate of $k_{ex} \sim 10^8 s^{-1}$. The photoexcited donor either fluoresces back to the ground state, with a rate constant k_D ($\sim 10^9 s^{-1}$), or is quenched by nonradiatively transferring its energy to the acceptor, with a rate constant k_{ET} (Cf. Fig. 1). In the case where energy transfer (ET) from donor to acceptor takes place, emission of a fluorescence photon by the excited acceptor, with rate constant k_A ($\sim 10^9 s^{-1}$), follows. The fluorescence photon from the donor is typically blue-shifted relative to that from the acceptor, so that they can be detected in a selective manner. While the rate constants k_D and k_A are typically insensitive to the conformational state of the macromolecule, the ET rate constant k_{ET} is strongly dependent on the conformational state of the macromolecule at the time when ET takes place (Cf. Eq. (1)). The probability per excitation event for quenching via ET is given by:

$$E = \frac{k_{ET}}{k_{ET} + k_D} \equiv \frac{k_{ET}}{k} \quad , \tag{2}$$

where $k^{-1} = (k_{ET} + k_D)^{-1}$ is the donor fluorescence life-time. The probability for the complimentary donor fluorescence event is given by:

$$F = 1 - E = \frac{k_D}{k_{ET} + k_D} = \frac{k_D}{k} \quad . \tag{3}$$

The measurement of the FRET efficiency of a freely-diffusing single molecule is limited by the time it spends within the focal volume. Extending the time of the measurement is often achieved by spatially confining the macromolecule. One popular strategy for achieving this is by attaching the biopolymer to a surface. Thus, a self-consistent interpretation of SM FRET experiments also calls for a better understanding of how surface-immobilization impacts the conformational structure and dynamics of the macromolecule.

In the present paper, we review recent work in our group that aimed at understanding the relationship between quantities that can be measured via SM FRET and the underlying conformational structure and dynamics of freely diffusing and surface-immobilized protein molecules. [54, 55, 65, 66] Our approach differs from that employed by other researchers in order to interpret SM FRET measurements [49–53, 67] in the following respects:

- It is based on Langevin dynamics simulations of an off-lattice heteropolymer-like model of the polypeptide chain which is characterized by a a well-defined native state.
- It includes a detailed consideration of the impact of different types of surface-immobilization schemes and different denaturation conditions on the results obtained via SM FRET measurements.
- It puts special emphasis on the rather unique ability of SM FRET measurements to provide information on conformational dynamics and it correlation with conformational structure.

The various aspects of our approach are demonstrated below within the context of a two-stranded coiled-coil polypeptide model that was designed to mimic the disulfide cross-linked two-stranded coiled-coil from the yeast transcription factor GCN4 [68–74] which was used by Hochstrasser and coworkers in their pioneering SM-FRET experiment. [30, 33]

The plan of the remainder of this paper is as follows. Different ways of measuring conformational structure and dynamics via single-molecule FRET are described in Sec. 2 and demonstrated on the two-stranded coiled-coil polypeptide model in Sec. 3. The results are summarized and discussed in Sec. 4.

2 Measurement of conformational structure and dynamics via single-molecule FRET

2.1 Conformational structure

In a *time-resolved ensemble-averaged FRET* experiment, one measures the donor fluorescence, following the simultaneous photo-excitation of a large

number of donor molecules. [75] The ensemble-averaged fluorescence decay can then be described by:

$$\overline{I}(\tau) = \int_0^\infty dR P(R) e^{-k_D\left[1+\left(\frac{R_0}{R}\right)^6\right]\tau} \quad . \tag{4}$$

Here, $P(R)$ corresponds to the probability density of R at the time of excitation, and $\left(k_D\left[1+(R_0/R)^6\right]\right)^{-1}$ is the R-dependent life-time of the donor's excited state. It is important to note that R typically changes on the time scales of $\sim \mu s$, which is considerably longer than the donor's fluorescence life-time ($\sim ns$), thereby justifying the assumption that R is frozen during the fluorescence process. Thus, at least in principle, one may obtain the distribution of donor-acceptor distance, $P(R)$, from the ensemble-averaged fluorescence decay, $\overline{I}(\tau)$, via the relationship in Eq. (4). However, the inversion of $\overline{I}(\tau)$ to obtain $P(R)$ is numerically unstable. More specifically, writing $\overline{I}(\tau)$ in terms of the probability density of k_{ET}: [76]

$$\overline{I}(\tau) = e^{-k_D\tau} \int_0^\infty dk_{ET} P(k_{ET}) e^{-k_{ET}\tau} \quad , \tag{5}$$

shows that $\overline{I}(\tau)$ corresponds to the Laplace transform of $P(k_{ET})$. Thus, extracting $P(k_{ET})$ from $\overline{I}(\tau)$ corresponds to calculating its inverse Laplace transform, which is known to be numerically unstable (i.e., small errors in $\overline{I}(\tau)$ will be exponentially amplified in $P(k_{ET})$). This problem is usually bypassed by assuming a certain ad-hoc functional form of $P(R)$, such as a linear combination of Gaussians, and best fitting the parameters via a least square procedure.

SM-FRET experiments are typically performed by using a dual-channel detection scheme. More specifically, one photo-excites the donor with CW radiation or a train of pulses, while simultaneously detecting the fluorescence photons from the donor *and* acceptor in a selective manner. The fraction of photons detected in the acceptor channel, over a given time averaging window of length T_W, provides a direct measure of the time-averaged FRET efficiency, which we will denote by $E(T_W)$. One may then *define* a time-averaged and T_W-dependent donor-acceptor distance, which will be denoted by $\langle R\rangle_{T_W}$, such that

$$E(T_W) \equiv \frac{1}{1+[\langle R\rangle_{T_W}/R_0]^6} \quad . \tag{6}$$

It should be noted that in the limit where T_W is very short in comparison to the time scale of conformational dynamics, R remains fixed during the time interval T_W and $E(T_W)$ therefore reduces to its instantaneous value,$E = \{1+[R/R_0]^6\}^{-1}$. In such a case, there is a direct and exact relationship between the probability distribution of E and $P(R)$:

$$P(R) = P\left(E_{ET} = (1+[R/R_0]^6)^{-1}\right) \frac{d}{dR}(1+[R/R_0]^6)^{-1} \quad . \tag{7}$$

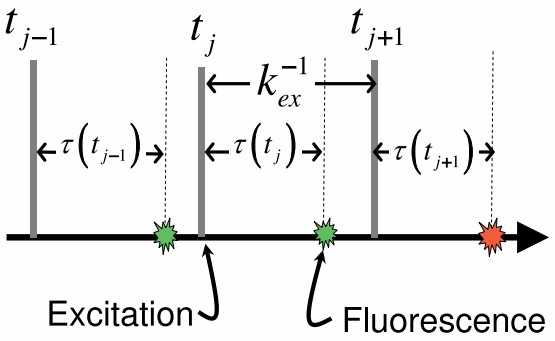

Fig. 2: A schematic view of an experimental setup for measuring the dynamical variable $\tau(t)$. A single macromolecule is subjected to a train of short pulses with a repetition rate k_{ex}. $\tau(t_j)$ is defined as the time interval between photoexcitation of the donor at time t_j and the emission of a fluorescence photon by either the donor (green) or the acceptor (red).

Thus, whereas ensemble-averaged time-resolved FRET measurements can yield $P(R)$ in an *indirect* manner, SM FRET measurements can yield $P(R)$ in a *direct* manner, but only if T_W is very short in comparison to the time scale of conformational dynamics.

2.2 Conformational dynamics

One way of extracting information regarding the time scale of conformational dynamics is by considering the following quantity: [33]

$$D(j;T_W) = [\langle R\rangle_{T_W}(j+1) - \langle R\rangle_{T_W}(j)]^2/T_W \quad . \tag{8}$$

Here, $\langle R\rangle_{T_W}(j)$ and $\langle R\rangle_{T_W}(j+1)$ correspond to the averaged value of R on the subsequent j and $(j+1)$-th time windows. Thus, $D(j;T_W)$ can be thought of as the square of the displacement of the window-time-averaged donor-acceptor distance when going from one window to the next, divided by the time window length T_W. In the analysis below we will employ the following definition of the time-window-averaged donor-acceptor distance:

$$\langle R\rangle_{T_W} = \frac{1}{T_W}\int_0^{T_W} d\tau R(\tau) \quad . \tag{9}$$

Although this *convenient* definition of $\langle R\rangle_{T_W}$ is somewhat different from that employed in the context of SM-FRET [Cf. Eq. (6)], one does not expect this distinction to modify the main observations reported below.

The time scale of conformational dynamics can be obtained from the T_W-dependence of $D(j;T_W)$. When T_W is much shorter than the time scale of

conformational dynamics, $\langle R\rangle_{T_W}(j)$ can be assumed to be constant within the time-window so that $D(j;\delta t) = [R(t_j + T_W) - R(t_j)]^2/T_W \approx T_W \dot{R}^2(t_j)$, where $\dot{R}(t_j)$ is the instantaneous time derivative of R. Thus, as T_W becomes vanishingly small so does $D(j;T_W)$. The opposite extreme corresponds to the case where T_W is very large in comparison to the characteristic time scale of conformational dynamics. In this case, the ergodic hypothesis implies that averaging R over the time window is equivalent to taking the ensemble average, namely $\langle R\rangle_{T_W} = \overline{R}$. Thus, $D(j,T_W)$ will vanish since $\langle R\rangle_{T_W}(j+1) = \langle R\rangle_{T_W}(j) = \overline{R}$. The facts that $D(j,T_W)$ is non-negative and vanishes at the limits $T_W \to 0$ and $T_W \to \infty$ imply that the average value of $D(j;T_W)$, $\bar{D}(T_W)$, will exhibit a turnover behavior as a function of T_W. The value of T_W at the turnover and its width therefore correspond to the the time-scale and dynamical range of conformational dynamics, respectively.

Another way of obtaining the characteristic time scale and dynamical range of conformational dynamics is from the equilibrium correlation functions of the FRET efficiency:

$$\langle F^{z_1}(t_1)F^{z_2}(t_2)\rangle = k_D^{z_1+z_2}\langle k^{-z_1}(t_1)k^{-z_2}(t_2)\rangle \tag{10}$$

where $z_1, z_2 > 0$. A related correlation function can be defined by considering the variable $\tau(t)$, which is defined as the time delay between photoexcitation of the donor at time t and the emission of a fluorescence photon by either donor or acceptor (Cf. Fig. 2). The time-delay $\tau(t)$ can then be viewed as a dynamical variable. The important point is that the correlation function of this single-photon dynamical variable can be related to the FRET efficiency correlation function via the following general relationship (the proof of this relation can be found in Ref. [65]).

$$\langle \tau_1^{z_1-1}\tau_2^{z_2-1}\rangle_D = \frac{\Gamma(z_1)\Gamma(z_2)}{k_D^{z_1+z_2-2}}\frac{\langle F_1^{z_1}F_2^{z_2}\rangle}{\langle F_1F_2\rangle} = \Gamma(z_1)\Gamma(z_2)\frac{\langle k_1^{-z_1}k_2^{-z_2}\rangle}{\langle k_1^{-1}k_2^{-1}\rangle} \quad , \tag{11}$$

where $\Gamma(z)$ is the familiar Gamma function. The main advantage of measuring $\langle \tau_1^{z_1-1}\tau_2^{z_2-1}\rangle_D$ over directly measuring $\langle F^{z_1}(t_1)F^{z_2}(t_2)\rangle$ lies in the fact that $\langle \tau_1^{z_1-1}\tau_2^{z_2-1}\rangle_D$ only requires a single photon per data point and can therefore be obtained with significantly better time resolution.

Finally, we note that the above mentioned two ways for extracting the time scale and dynamical range of conformational dynamics can be related via the following identity:

$$T_W\bar{D}(T_W) \equiv 2[\langle R^2\rangle - \langle R(t)R(t+T_w)\rangle] \tag{12}$$

Thus, measuring $T_W\bar{D}(T_W)$ as a function of T_W is equivalent to probing the correlation function $\langle R(t)R(t+T_w)\rangle$, which is in turn closely related to the correlation function in Eq. (10).

2.3 Correlation between conformational structure and dynamics

A unique feature of SM-FRET experiments is their ability to provide information on the *correlations between structure and dynamics*. One way of extracting this information is by monitoring the distribution of $\langle R \rangle_{T_W}$ as a function of T_W. [30] Correlations between conformational structure and the time scale on which it moves can be obtained from the different values of T_W at which different subsets of the ensemble which are characterized by different values of R reach the ergodic limit.

Information on the correlation between structure and dynamics can also be obtained from the correlation between $D(j;T_W)$ and $\langle R \rangle_{T_W}(j)$ [Cf. Eq. (8)]. As mentioned above, $D(j;T_W)$ follows a turnover behavior as a function of T_W, and the value of T_W at the turnover corresponds to a "characteristic" time scale of conformational dynamics. Thus, one may obtain information on the correlation between structure and dynamics by averaging $D(j;T_W)$ over the subset of conformations that correspond to the same value of $\langle R \rangle_{T_W}(j)$, instead of over the ensemble of all the conformations. We will denote this conditional average by $D(\langle R \rangle_{T_W})$.

3 Application to a model of a two-stranded coiled-coil polypeptide

3.1 Model and simulation techniques

In this section, we analyze in detail the information obtained via SM FRET measurements in the case of a two-stranded coiled-coil polypeptide model under different denaturation and surface-immobilization conditions.. To this end, we employed a 78-bead off-lattice model of the polypeptide backbone as a chain consisting of connected spherical beads. All the beads are assumed to have the same mass m and to be centered on the α-carbon of the corresponding amino acid residues. The beads are also assumed to be either hydrophobic (B) or hydrophilic (L). They were arranged along the chain in the following sequence: $(LLBLLBB)_5LLB - LL - BLL(BBLLBLL)_5$. The sequences $(LLBLLBB)_5LLB$ and $BLL(BBLLBLL)_5$ are designed to form a five-turn helix in the folded state, while the intermediate LL sequence provides a flexible link between the two helices.

The interaction potentials between beads were adopted from Refs. [77,78], and are briefly described below for the sake of completeness. The intramolecular potential energy of the freely diffusing protein is given by

$$V = V_{BL} + V_{BA} + V_{DIH} + V_{HB} + V_{NB} \quad , \tag{13}$$

where V_{BL}, V_{BA}, V_{DIH}, V_{HB}, and V_{NB} correspond to the bond-length, bond-angle, dihedral-angle, hydrogen-bond and nonbonding potentials, respectively. The bond-length potential, V_{BL}, imposes connectivity along the chain via

a spring potential of the form $v_{BL}(r) = \frac{1}{2}\ k_r(r-a)^2$ between subsequent beads, where $k_r = 100\epsilon/a^2$. Here, ϵ is the average strength of the hydrophobic interaction which is used as the unit of energy (see below). The bending potential, V_{BA}, is assumed to be harmonic in the bending angle, with a force constant $k_\theta = 20\epsilon/\mathrm{rad}^2$ and an equilibrium angle of 105°.

The dihedral-angle potential, V_{DIH}, is given by

$$V_{DIH} = \sum_{j=1}^{N-3} \left[A(1-\cos\phi_j) + B(1+\cos 3\phi_j) + C(1-\sin\phi_j)\right], \tag{14}$$

where $N = 78$ and ϕ_j is the angle between the planes defined by beads $(j, j+1, j+2)$ and $(j+1, j+2, j+3)$. Here, $A = \epsilon$, $B = 1.6\epsilon$ and $C = 2\epsilon$ [78]. It should be noted that this dihedral potential provides the main driving force for helix formation. The flexibility of the turn region that links the two helices is introduced by setting the dihedral potential energy of these beads to zero.

The hydrogen-bond potential is given by

$$V_{HB} = -\frac{\epsilon}{3} \sum_{i=1}^{N-4} e^{-\alpha_{hb}(\cos^2\Phi_i + \cos^2\Psi_i)} \quad . \tag{15}$$

Here, $\cos\Phi_i = (\boldsymbol{r}_{OH} \cdot \boldsymbol{r}_{i,i+1})/|\boldsymbol{r}_{OH}||\boldsymbol{r}_{i,i+1}|$ and $\cos\Psi_i = (\boldsymbol{r}_{OH} \cdot \boldsymbol{r}_{i+3,i+4})/|\boldsymbol{r}_{OH}||\boldsymbol{r}_{i+3,i+4}|$, where $r_{i,j}$ is the distance between the i-th and j-th beads along the backbone, and $\boldsymbol{r}_{OH}$ is the vector pointing from the virtual CO group on the i-th residue to the virtual NH group on the $(i+4)$-th residue. [78]

The nonbonding potential, V_{NB}, is given by

$$V_{NB} = \sum_{k=1}^{N-3} \sum_{l=k+3}^{N} v_{NB}(r_{k,l}) \tag{16}$$

where

$$v_{NB}(r) = 4\epsilon \left[\left(\frac{a}{r}\right)^{12} - \lambda \left(\frac{a}{r}\right)^{6}\right] \quad . \tag{17}$$

The L-L and L-B nonbonding interactions are assumed to be *purely repulsive* and therefore correspond to $\lambda = 0$, while the B-B nonbonding interaction is assumed to be *attractive* and corresponds to $\lambda = 1$.

Reduced units are used throughout, where the units of mass, energy, length and time are given by $m \sim 3 \times 10^{-22}$g, $\epsilon \sim 1.0$kcal/mol, $a \sim 5 \times 10^{-8}$m and $\tau = \sqrt{ma^2/\epsilon} \sim 3$ps, respectively.

The conformational dynamics is assumed to be governed by a Langevin equation of the form

$$m\frac{d^2\boldsymbol{r}_j}{dt^2} = -\zeta\frac{d\boldsymbol{r}_j}{dt} - \boldsymbol{\nabla}_j V + \boldsymbol{f}_j \quad . \tag{18}$$

Here, $\boldsymbol{r}_j$ is the position of the j-th bead $(j = 1, \ldots N)$, $-\boldsymbol{\nabla}_j V$ and $\boldsymbol{f}_j$ are the systematic and random forces it is subject to, respectively, and ζ is the

friction coefficient, which is set to 0.05 in all the simulations reported in this paper. Eq. (18) is integrated via the Verlet algorithm [79,80]. Temperature is introduced via the variance of the Gaussian random force, which is assumed to be delta-correlated. The integration time step is given by $\delta t = 0.005$.

The value of ζ used here corresponds to $\sim 10^{-3}$ of its value in room temperature aqueous solutions. [80] On the one hand, using such weak friction improves the sampling efficiency in the simulations and does not affect equilibrium structural properties. On the other hand, the dynamical properties that we observe may be different from those probed by SM-FRET techniques, which would not be able to resolve conformational dynamics on such fast time scales. Thus, the relevance of the following analysis of dynamical properties relies on the assumption that increasing the friction will not significantly alter our main conclusions. It is interesting to note in this context that the folding mechanism in similar models has been observed to be relatively insensitive to the value of the friction coefficient. [81]

We have determined the native conformation of the polypeptide by the multiple slow cooling method [78]. To this end, we generated 50 trajectories with random initial configurations at a high temperature ($T_h = 1.5\epsilon/k_B$), and propagated them in time while decreasing the temperature by $0.02\epsilon/k_B$ after every 5×10^5 time steps. The conformation with the lowest energy at the lowest temperature ($T_l = 0.02\epsilon/k_B$) is then used to define the native state.

The temperature was held fixed at $T = 0.40$(which is lower than the folding temperature) in all the simulations reported in this paper. Denaturation by a chemical agent was assumed to take effect by weakening the interactions that promote forming native contacts. One way to bring about denaturation is by weakening the attractive nonbonding B-B interactions, [54] which represent a major driving force for folding. [82] We will refer to the ensemble of unfolded conformations obtained by following this route as "unfolded state α". In this case, the folded and unfolded states correspond to setting λ in the B-B interaction potential, Eq. (17), equal to 1 or 0, respectively. Intermediate states can be obtained by setting λ to values between 0 and 1. A midpoint can be defined at $\lambda = 0.50$, where the fractions of folded and unfolded conformations are found to be 0.43 and 0.57, respectively, in the case of a freely diffusing polypeptide.

It is important to note that weakening the B-B interactions does not disrupt the helical structure. The two arms of the polypeptide therefore retain their helical structure in unfolded state α. However, the isolated helices in coiled-coils are believed to be unstable in aqueous solution because the hydrophobic residues are on one face of the helix. [83] We therefore also consider another scenario where the presence of the denaturant also disrupts the helical structure. This can be achieved by weakening the dihedral *and* nonbonding interactions. Weakening the dihedral interactions is achieved by adjusting the values of A, B and C in Eq. (14). We will refer to the ensemble of unfolded conformations obtained by setting A, B and C to zero as "unfolded state β". The midpoint along the denaturation curve can be defined by setting λ and

$\{A, B, C\}$ to 0.55 times their values in the native state. The fractions of folded and unfolded conformations are found to be 0.37 and 0.63, respectively, in the case of a freely diffusing polypeptide.

The results reported below were obtained from equilibrium simulations that were performed for a single polypeptide which is either freely diffusing or surface-immobilized. The surface was assumed to be planar, and to consist of beads of diameter a that were arranged on a 2D square lattice with distance a between nearest neighbors. Surface-immobilization was introduced by fixing the position of the 40-th bead such that it lies a distance a above a surface bead. The interaction between the polypeptide and surface beads is described by a pair-wise potential of the form:

$$v_{SP}^{k}(r) = 4\epsilon_s \left[\left(\frac{a}{r}\right)^{12} - \lambda_s^k \left(\frac{a}{r}\right)^{6} \right] \quad , \tag{19}$$

where $k = L, B$. Here, r is the distance between the polypeptide bead and the surface bead. The interaction between the L beads and the surface is assumed to be *purely repulsive* and corresponds to setting $\lambda_s^L = 0$ in Eq. (19). The interaction between the B beads and the surface depends on the hydrophobicity of the surface. Thus, setting λ_s^B equal to zero in Eq. (19) corresponds to the case of a repulsive (hydrophilic) surface, and increasing the value of λ_s^B corresponds to making the surface more sticky (i.e., making it more hydrophobic). The results reported below were obtained for $\lambda_s^B = 0$ and $\lambda_s^B = 0.9$, respectively. which are referred to as *repulsive surface* and *attractive surface*, respectively.

Equilibrium properties under each set of conditions were obtained by averaging over 10 trajectories. Each trajectory starts with an equilibration period of 10^5 time steps, followed by a data collection period of 5×10^5 time steps in the folded state and 5×10^7 time steps at the midpoint and unfolded states. Error bars were assumed to be given by one standard deviation.

Finally, the simulation of the stochastic streams of emitted fluorescence photons was performed via kinetic Monte Carlo simulations. It should be noted that each stochastic trajectory of R as obtained from the Langevin dynamics simulation of the polypeptide gives rise to an ensemble of stochastic photon streams. The kinetic Monte Carlo simulation of the photon streams was carried out via the algorithm of Makarov and Matiu. [84] More specifically, the residence time in state (D^*, A) following photoexcitation is given by $-\ln(\eta)/(k_D + k_{ET})$, where η is a random number between 0 and 1. Following this, the system makes a transition to either the ground state, with probability $F = k_D/(k_D + k_{ET})$, or the state (D, A^*), with probability $E = k_{ET}/(k_D + k_{ET})$. It should be noted that the value of k_{ET} at the time of the transition depends on the instantaneous value of R, which obviously differs from one stochastic trajectory of R to another. In the case where the system ends up in state (D, A^*), its residence time in this state is given by $-\ln(\eta)/k_A$, after which it makes a transition back to the ground state.

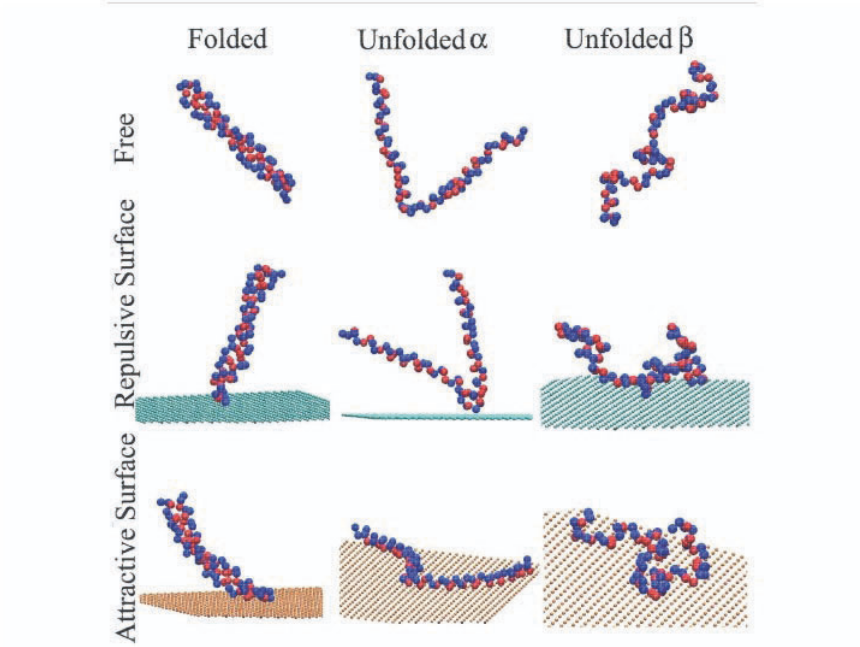

Fig. 3: Typical conformations of the model polypeptide under different conditions.

3.2 Conformational structure

The native state conformation of the freely diffusing polypeptide is seen to be a helical dimer (Cf. Fig. 3). Assuming that the donor-acceptor distance R is given by the end-to-end distance, the corresponding distribution of R clearly shows that surface-immobilization does not affect the conformations in the folded state, regardless of whether the surface is repulsive or attractive (Cf. Fig. 4). This can be explained by the fact that the two helices are held together by the attractive nonbonding B-B interactions so that the B residues form a hydrophobic core, and therefore cannot effectively interact with the surface.

The two helical arms become uncoiled in unfolded state α, which is the result of turning off the attractive nonbonding B-B interactions (Cf. Fig. 3). However, the helical structure of the two arms is retained in this unfolded state. The corresponding R distributions are clearly influenced by immobilization, as well as by the type of surface (Cf. Fig. 4). In comparison to the freely diffusing polypeptide, the R distribution in unfolded state α on the attractive surface is seen to be more asymmetrical and shifted to longer values of R. The opposite trend is observed in the case of the repulsive surface, where the distribution becomes more symmetrical and shifts to lower values

of R in comparison to the freely diffusing polypeptide. The asymmetry of the R distribution results from the relative rigidity of the helical arms, which implies that conformations with larger values of R are more likely. The increased *symmetry* and shift to *shorter* values of R in the case of a repulsive surface can be explained by the exclusion of stretched conformations where the two helical arms lie on opposite sides of the surface. The increased *asymmetry* and shift to *larger* values of R in the case of an attractive surface can be explained by the transition from a 3D space of conformations in the case of a freely diffusing polypeptide to a 2D space of conformations in the case of the attractive surface.

The chain loses its helical structure in unfolded state β, as a result of turning off the dihedral angle potential. The polypeptide in unfolded state β effectively reduces into a stiff Gaussian chain with excluded volume effects. Indeed, the R distributions are symmetrical and of Gaussian shape. Their dependence on immobilization and the type of surface is similar to that we previously reported in the case of a free-jointed homopolymer model. [55] The shift of the distribution to larger values of R when going from the freely diffusing polypeptide to the attractive surface-immobilized polypeptide is consistent with the scaling laws for a Gaussian chain. [85] More specifically, one expects $\langle R \rangle = 26$ and 14 in 2D and 3D, respectively, which is consistent with the distributions reported in Fig 4.

Finally, we consider the behavior of the polypeptide chain at the midpoint of the denaturation curves. The corresponding R distributions for the freely diffusing polypeptide and the attractive surface-immobilized polypeptide are very similar, and significantly different from the repulsive surface case (Cf. Fig. 4). Generally speaking, the spatial confinement associated with the repulsive surface leads to less unfolding at the midpoint. The similarity in the extent of unfolding between the freely diffusing case and the attractive surface case indicates that it is relatively insensitive to the dimensionality of the conformational space.

3.3 Conformational dynamics

The characteristic time scale and dynamical range of conformational dynamics can be estimated from the equilibrium correlation functions of the end-to-end distance R:

$$C(t) = \langle R(t)R(0) \rangle - \langle R \rangle^2 \quad . \tag{20}$$

This correlation function is shown under different conditions in Fig. 5. In the folded state, the decay of the correlation function is characterized by a relatively narrow dynamical range and short time scales, on the order of ~ 1. The rapid decay of $C(t)$ in this case can be attributed to fluctuations around the native conformation, within the corresponding basin of attraction. The fact that those fluctuations are fast is consistent with the fact that this is a rapid two-state folder. More specifically, the native conformation is expected

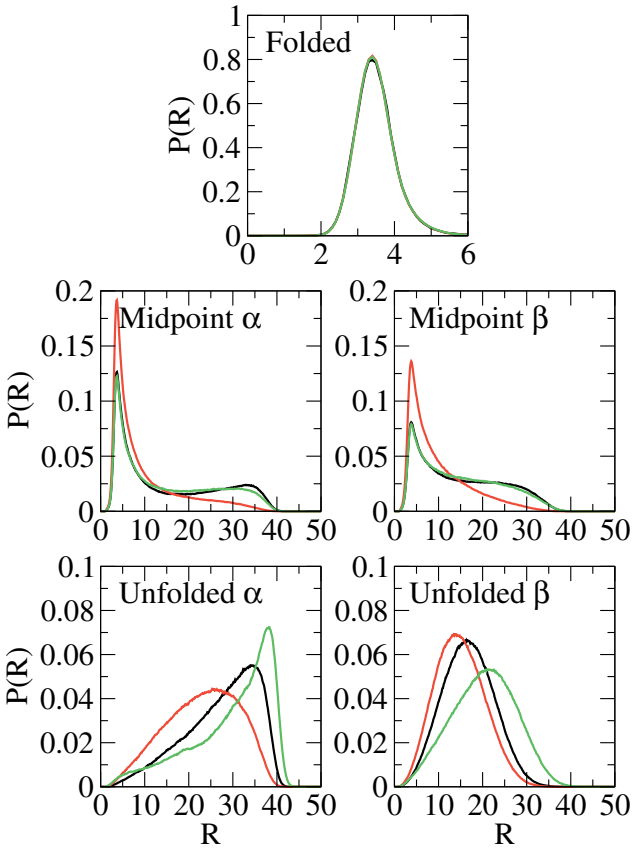

Fig. 4: Distributions of end-to-end distance, R, under different conditions. Black, red and green correspond to the cases of free diffusion, repulsive surface-immobilization and attractive surface-immobilization, respectively. The results were converged to within an error bar of 5%.

to be significantly more stable in comparison to neighboring conformations, such that small displacements relative to it will give rise to strong returning forces. The behavior of $C(t)$ in the folded state is also seen to be unaffected by surface-immobilization.

In the case of the unfolded (either α or β) freely diffusing polypeptide, $C(t)$ is seen to decay on time scales of 10-100, which are significantly slower and correspond to a wider dynamical range in comparison to the folded state. This is consistent with the fact that the underlying interactions are of the excluded volume type, which are short-ranged so that the dynamics is mostly diffusive and relatively slow. Immobilization on a repulsive surface does not alter $C(t)$, since the surface-polypeptide interactions are very similar to the intramolecular interactions in this case. However, $C(t)$ is observed to decay

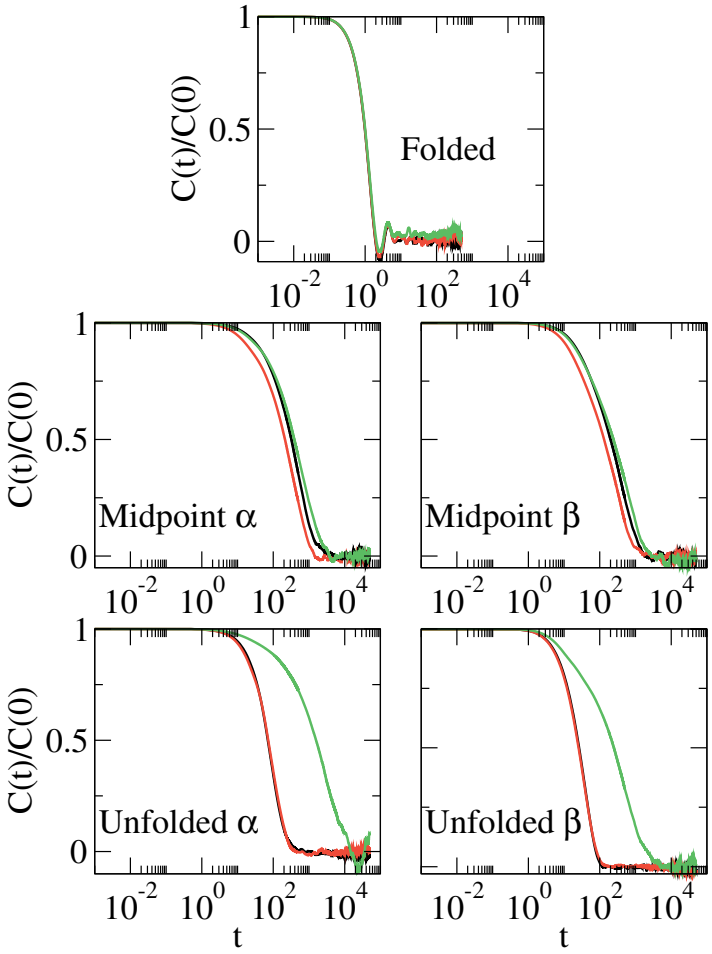

Fig. 5: Time correlation functions of the end-to-end distance, R, under different conditions. Black, red and green correspond to the cases of free diffusion, repulsive surface-immobilization and attractive surface-immobilization, respectively.

more slowly and on a wider dynamical range of $10^2 - 10^4$ when the unfolded polypeptide is immobilized on an attractive surface. The slow-down in this case can be attributed to the relatively large barriers that one needs to overcome when detaching segments of the polypeptide from the surface, which is necessary for rearranging the conformation.

The decay of $C(t)$ in the midpoint state (either α or β) is characterized by an even wider dynamical range. The short time scales in the cases of freely diffusing and repulsive surface-immobilized polypeptides are attributed to dynamics within the folded and unfolded sub-populations mentioned above. An

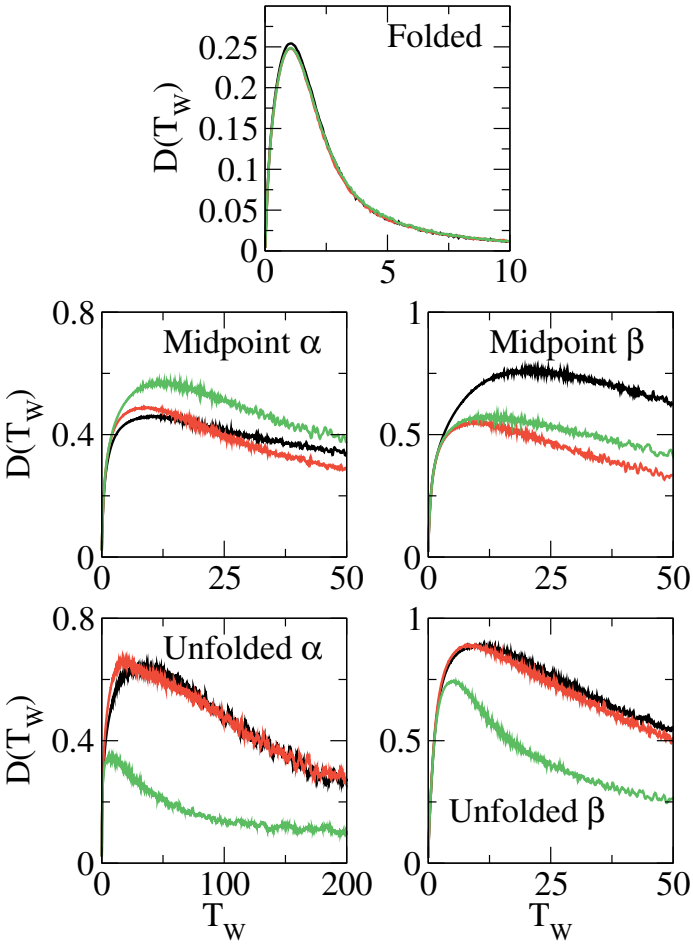

Fig. 6: $D(T_W)$ as a function of T_W under different conditions. Black, red and green correspond to the cases of free diffusion, repulsive surface-immobilization and attractive surface-immobilization, respectively. The results were converged to within an error bar of 9%

additional slower component that corresponds to time scales of $10^2 - 10^4$ is attributed to transitions between the unfolded and folded states (the average first passage time for the unfolded-folded transition in the case of unfolded state α is $\sim 10^3$). $C(t)$ is also seen to be rather insensitive to surface-immobilization, regardless of whether it is repulsive or attractive. This can be attributed to the fact that the transitions between the folded and unfolded states are dominated by intramolecular interactions rather than by polypeptide-surface interactions.

One way of obtaining information on the time scale of conformational dynamics from SM FRET measurements is via the T_W-dependence of the average $D(j;T_W)$ (see Eq. (8)), which is given by:

$$D(T_W) = \lim_{N_W \to \infty} \frac{1}{N_W} \sum_{j=1}^{N_W} D(j;T_W) \quad , \tag{21}$$

where N_W is the overall number of time windows. In Fig. 6, we show $D(T_W)$ as a function of T_W under different conditions. As expected, it exhibits a turnover behavior. The results in the case of the folded state are consistent with rapid conformational dynamics, a relatively narrow dynamical range, and insensitivity to surface-immobilization. The results in the case of unfolded states α and β of the freely diffusing or repulsive surface-immobilized polypeptide are consistent with slower conformational dynamics and a wider dynamical range. The results at the corresponding midpoint states are consistent with an even wider dynamical range, which is rather insensitive to surface-immobilization. These features are similar to the conclusions obtained based on the corresponding R correlation functions (Cf. Fig. 5). However, the turnover in the case of the unfolded state on the attractive surface suggests faster dynamics and a narrower dynamical range than on the repulsive surface, which appears to contradict the behavior of the corresponding $C(t)$ (Cf. Fig. 4). This difference implies that $D(T_W)$ and $C(t)$ do not always convey the same dynamical information. In this case, $D(T_W)$ starts out smaller and drops faster because of its sensitivity to the motion of the polypeptide relative to the surface. The latter has a narrow dynamical range and occurs on a fast time scale, since the interactions between the polypeptide and the attractive surface are similar to the intramolecular interactions in the native state. Indeed, $D(T_W)$ of the unfolded attractive surface-immobilized polypeptide is observed to be rather similar to that in the folded state.

It should also be noted that, for the same value of T_W, $D(T_W)$ in the folded state is *smaller* than that in the unfolded state. This observation is consistent with the fact that the dynamics in the folded state is in fact *faster* than that in the unfolded state. It should also be noted that the values of $D(T_W)$ in the folded and unfolded states are rather similar in the case of the attractive surface. This is due to the above mentioned rapid dynamics of the unfolded polypeptide relative to the attractive surface.

Finally, the correlation functions $\langle \tau_1 \tau_2 \rangle_D$ (see Eq. (11)) are shown on a semilog plot in Figs. 7 and 8, as obtained for the following values of the parameters: (1) Folded state: $k_D = k_A = 2000$, $k_{ex} = 200$; (2) Unfolded state α: $k_D = k_A = 200$, $k_{ex} = 20$; (3) Unfolded state β: $k_D = k_A = 200$, $k_{ex} = 20$. The results reported in those two figures differ with respect to the choice of R_0 (see Eq. (1)). More specifically, in Fig. 7, we have chosen values of R_0 in the vicinity of the maximum of the corresponding distributions of the end-to-end distance, namely $R_0 = 3.6$ in the folded state, $R_0 = 25$ in unfolded state α and $R_0 = 15$ in unfolded state β. Under those conditions, we

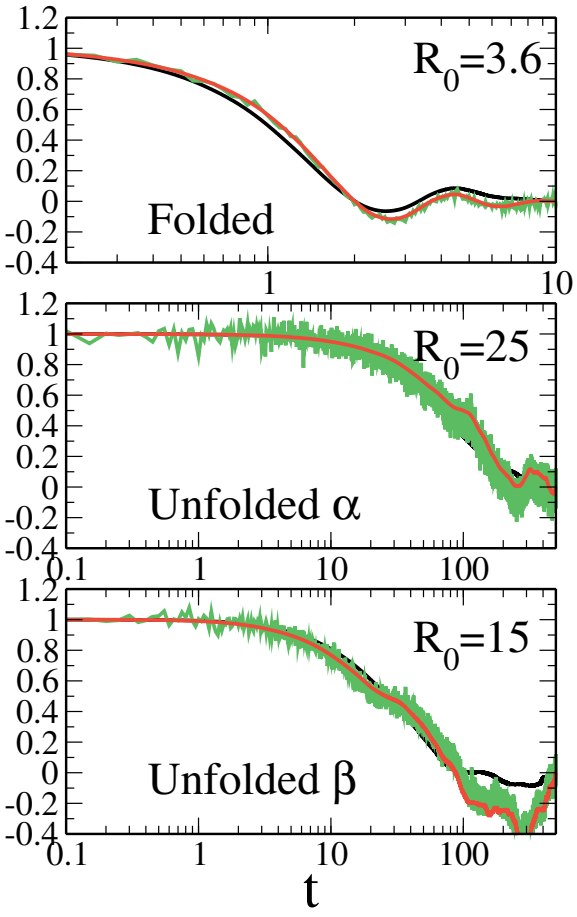

Fig. 7: The correlation function $\langle \tau_1 \tau_2 \rangle_D$ as obtained from kinetic Monte Carlo simulations for the polypeptide model (green). The normalized correlations functions $\langle k_1^{-2} k_2^{-2} \rangle$ (red) and $\langle R_1 R_2 \rangle$ (black) are also shown for the sake of comparison. All correlation function are normalized so that their initial value is equal to 1. The following parameters were used under different conditions: (1) Folded state: $k_D = k_A = 2000$, $k_{ex} = 200$, $R_0 = 3.6$; (2) Unfolded state α: $k_D = k_A = 200$, $k_{ex} = 20$, $R_0 = 25$; (3) Unfolded state β: $k_D = k_A = 200$, $k_{ex} = 20$, $R_0 = 15$.

observe that $\langle \tau_1 \tau_2 \rangle_D$ is proportional to $\langle k_1^{-2} k_2^{-2} \rangle$ and that $\langle \tau_1 \tau_2 \rangle_D$ does indeed reflect the time scales of conformational dynamics as manifested in the end-to-end distance autocorrelation function. In contrast, the results in Fig. 8 were obtained for larger values of R_0, namely $R_0 = 5.0$ in the folded state, $R_0 = 40$ in unfolded state α and $R_0 = 25$ in unfolded state β. Under those conditions, we observe that $\langle \tau_1 \tau_2 \rangle_D$ is not proportional to $\langle k_1^{-2} k_2^{-2} \rangle$ in the folded state and in unfolded state β and that $\langle \tau_1 \tau_2 \rangle_D$ does not accurately reflect the time

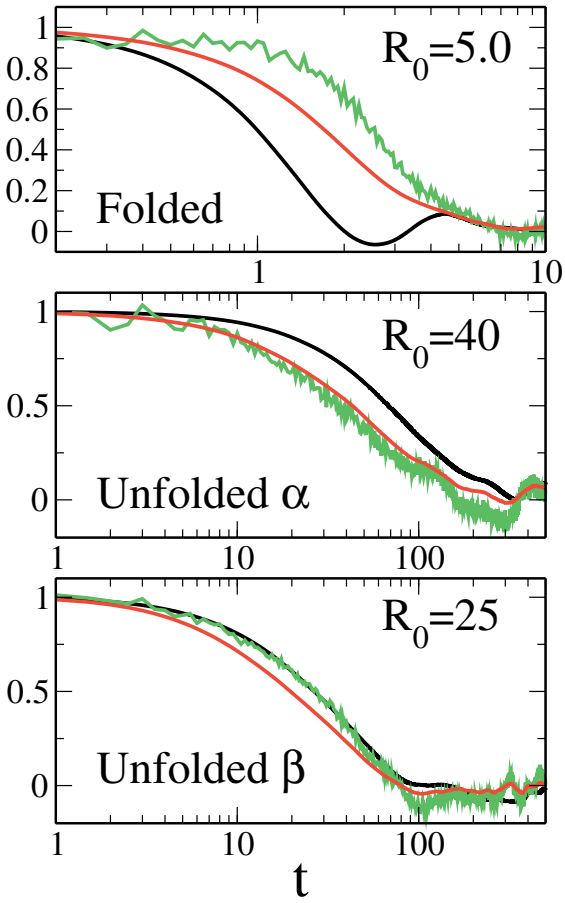

Fig. 8: The correlation function $\langle \tau_1 \tau_2 \rangle_D$ as obtained from kinetic Monte Carlo simulations for the polypeptide model (green). The normalized correlations functions $\langle k_1^{-2} k_2^{-2} \rangle$ (red) and $\langle R_1 R_2 \rangle$ (black) are also shown for the sake of comparison. All correlation function are normalized so that their initial value is equal to 1. The following parameters were used under different conditions: (1) Folded state: $k_D = k_A = 2000$, $k_{ex} = 200$, $R_0 = 5.0$; (2) Unfolded state α: $k_D = k_A = 200$, $k_{ex} = 20$, $R_0 = 40$; (3) Unfolded state β: $k_D = k_A = 200$, $k_{ex} = 20$, $R_0 = 25$.

scales of conformational dynamics in the folded state and unfolded state α, as manifested in the end-to-end distance autocorrelation function.

3.4 Correlation between conformational structure and dynamics

A unique feature of SM-FRET experiments is their ability to provide information on the *correlations between structure and dynamics*. One way of extracting this information is by monitoring the distribution of $\langle R \rangle_{T_W}$ as a

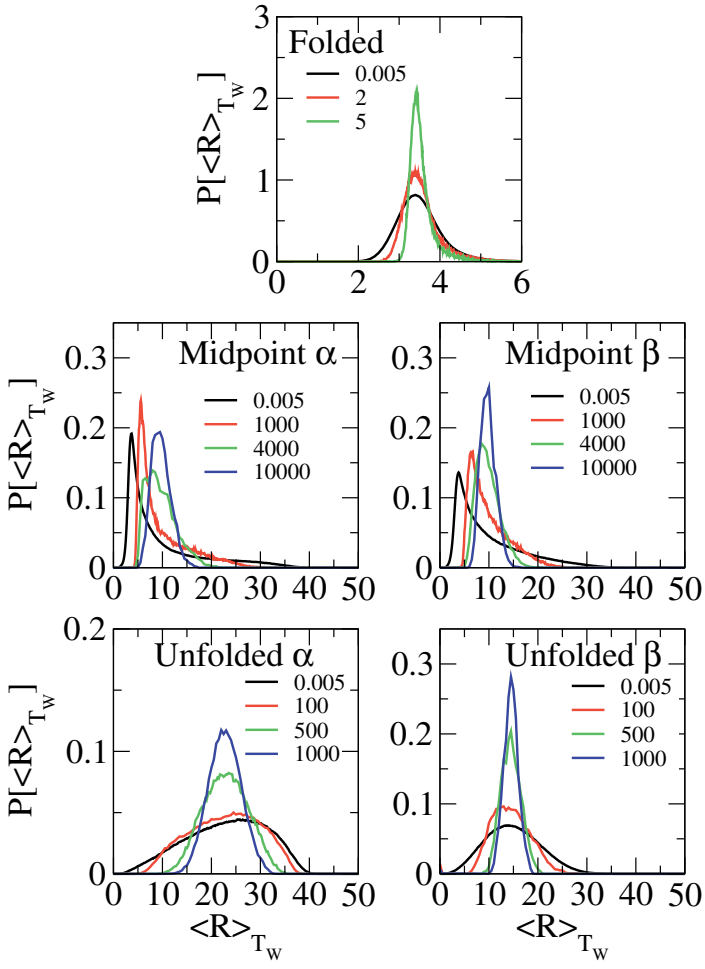

Fig. 9: The distributions of the time-window-averaged end-to-end distance for a freely diffusing polypeptide, as obtained for the indicated values of the averaging-time-window, T_W.

function of T_W. [30] The distributions of $\langle R \rangle_{T_W}$ obtained for a freely diffusing polypeptide using different values of T_W are presented in Fig. 9. The folded state is characterized by a relatively narrow distribution, which appears to be uni-modal and peaked at the relatively small value of R. The distribution becomes narrower when T_W is larger than the characteristic time scale of conformational dynamics in the folded state (~ 1). The distribution also becomes more asymmetrical with increasing T_W, which suggests that folded conformations with a *larger* value of R move on a *slower* time scale.

Unfolded state α is characterized by a wide uni-modal and *asymmetrical* distribution of R, with a slow rise and a sharp drop. The distribution becomes narrower and more symmetrical when the averaging time window is larger than the characteristic time scale of conformational dynamics in this unfolded state. This indicates a correlation between structure and dynamics, where *conformations that correspond to shorter R move on faster time scales.*

Unfolded state β is characterized by a wide uni-modal and *symmetrical* distribution of the end-to-end distance. The distribution narrows down *in a uniform manner* with increasing T_W. Thus, in the case of unfolded state β, one does *not* observe a correlation between R and the time scale of conformational dynamics. This behavior is similar to that previously observed in the case of a free-jointed homopolymer model. [54]

The midpoint states are characterized by a bi-modal distribution, with one narrow peak at the small R region, which corresponds to the folded sub-population, and another, wider, peak at the large R region, which corresponds to the unfolded sub-population. Distinguishing between the two peaks becomes easier with increasing T_W, as long as T_W^{-1} is larger than the transition rate between the folded and unfolded states. The $\langle R \rangle_{T_W}$ distribution changes from bi-modal to uni-modal when T_W^{-1} is smaller than the transition rate between the folded and unfolded states. The peak of the emerging uni-modal distribution corresponds to a value of R which is intermediate between the folded and unfolded states.

The distributions of $\langle R \rangle_{T_W}$ obtained for a polypeptide immobilized on the repulsive surface are presented in Fig. 10. As expected, the results in the folded state are not affected by surface immobilization. The $\langle R \rangle_{T_W}$ distributions in unfolded states α and β are also seen to follow the same general trends as for the freely diffusing polypeptide. The behavior at the two midpoint states is however rather different from that observed in the case of the freely diffusing polypeptide. More specifically, the $\langle R \rangle_{T_W}$ distribution is *not* bi-modal for all values of T_W considered. Thus, the geometrical constraint represented by the repulsive surface is sufficient for introducing a significant bias toward the folded state at the midpoint.

The distributions of $\langle R \rangle_{T_W}$ obtained for a polypeptide immobilized on the attractive surface are presented in Fig. 11. Surface-immobilization is seen once again not to affect the behavior of the folded state. In this case, surface immobilization is also seen to have a relatively minor effect on the behavior at the midpoint. However, the behavior in unfolded states α and β is clearly influenced by surface immobilization in this case. More specifically, the $\langle R \rangle_{T_W}$ distributions are hardly affected by the time-window-averaging for values of T_W that were seen to significantly modify the $\langle R \rangle_{T_W}$ distributions in the freely diffusing and repulsive surface-immobilized cases. This can be attributed to the slower dynamics of the unfolded polypeptide on the attractive surface. At the same time, conformations with a *small* value of R are still seen to move *faster* than conformations with a *large* value of R, as for the freely diffusing polypeptide.

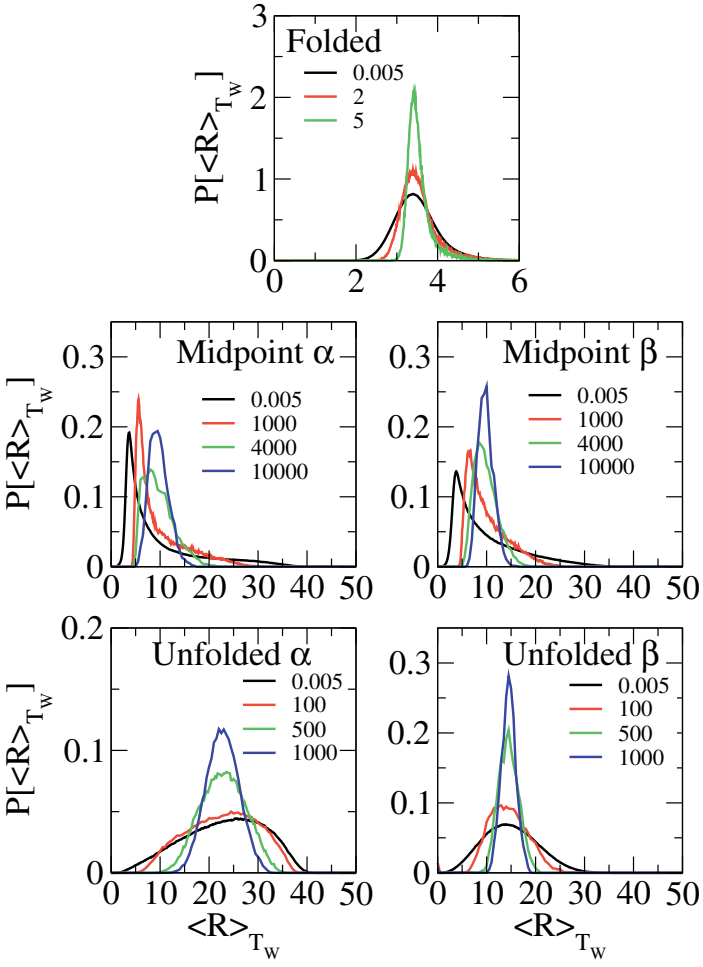

Fig. 10: The distributions of the time-window-averaged end-to-end distance for a repulsive-surface-immobilized polypeptide, as obtained for the indicated values of the averaging-time-window, T_W.

Finally, consider the correlation between structure and dynamics, as reflected in the correlation between $D(j;T_W)$ and $\langle R\rangle_{T_W}(j)$ [Cf. Eq. (8)]. As mentioned above, $D(j;T_W)$ follows a turnover behavior as a function of T_W, and the value of T_W at the turnover corresponds to a "characteristic" time scale of conformational dynamics. Thus, one may obtain information on the correlation between structure and dynamics by averaging $D(j;T_W)$ over the

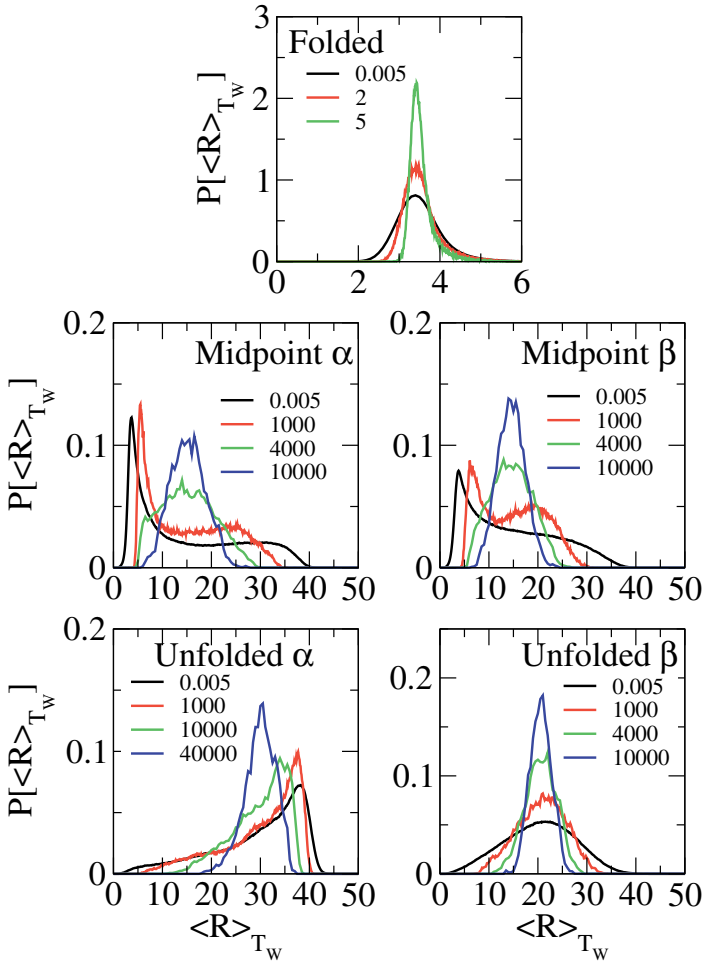

Fig. 11: The distributions of the time-window-averaged end-to-end distance for an attractive-surface-immobilized polypeptide, as obtained for the indicated values of the averaging-time-window, T_W.

subset of conformations that correspond to the same value of $\langle R\rangle_{T_W}(j)$, instead of over the ensemble of all the conformations. We will denote this conditional average by $D(\langle R\rangle_{T_W})$.

In Fig. 12, we show $D(\langle R\rangle_{T_W})$ as a function of $\langle R\rangle_{T_W}$ under different conditions. The values of T_W that were used to generate these plots correspond to the vicinity of the corresponding turnovers in Fig. 5, and are therefore comparable to the time scale of conformational dynamics. In the folded state, $D(\langle R\rangle_{T_W})$ is reminiscent of the corresponding inverted R distribution (Cf. Fig. 4). The fact that the lowest value of $D(\langle R\rangle_{T_W})$ corresponds to the native

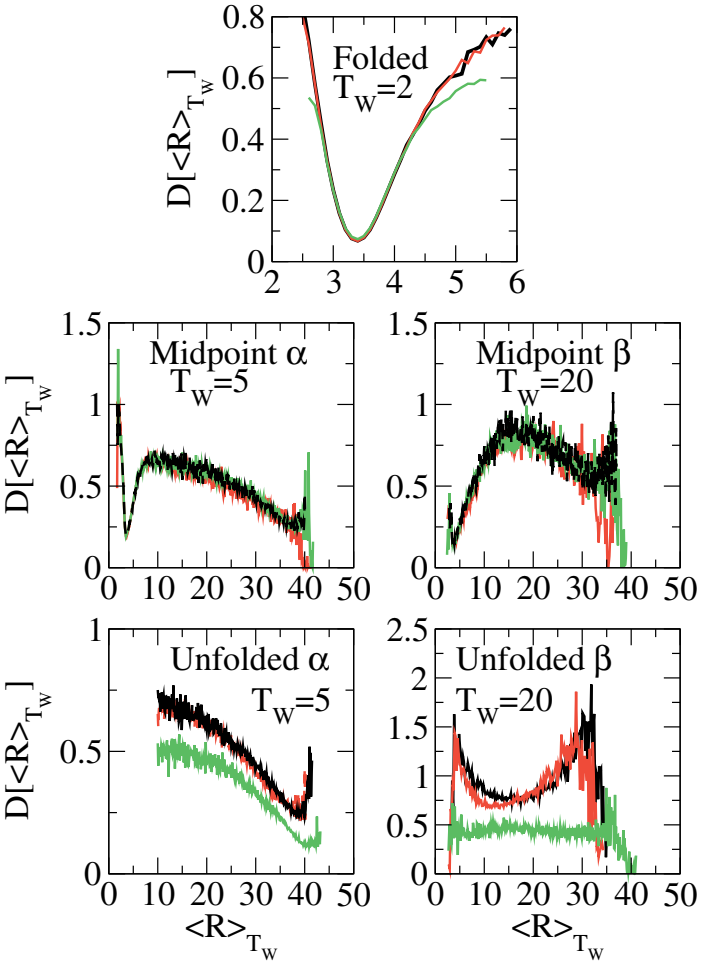

Fig. 12: The dependence of $D(\langle R\rangle_{T_W})$ on $\langle R\rangle_{T_W}$ under different conditions. Black, red and green correspond to the cases of free diffusion, repulsive surface-immobilization and attractive surface-immobilization, respectively.

state, suggests that the characteristic time scale for conformational dynamics is *faster* in the native conformation and its close vicinity. This is because the ergodic limit will be approached more rapidly, i.e. for lower values of T_W, in this case. It should be noted that a *smaller* value of $D(\langle R\rangle_{T_W})$ is correlated with *faster* dynamics of the corresponding subset of conformational states. This observation is consistent with the point of view that associates the native state with the minimum of a deep and narrow well on the protein's potential energy surface.

The correlation between structure and dynamics also persists in the midpoint and unfolded states. In the midpoint states $D(\langle R \rangle_{T_W})$ shows two minima, at the positions of the maxima in the corresponding R distributions of Fig. 4. In the unfolded states, $D(\langle R \rangle_{T_W})$ exhibits wide minima that coincide with the wide maxima of the corresponding R distribution of Fig. 4.

4 Discussion

The results reviewed in this paper provide a rather detailed picture of the signature of the underlying conformational structure and dynamics of a polypeptide on quantities that can be measured via SM FRET, including the effect of surface immobilization and denaturation. They clearly show that the fact that surface-immobilization does not impact the structure and dynamics of the protein in the native state does not imply that the same is true for the partially or fully denaturated protein. Indeed, surface-immobilization was seen to give rise to very significant shifts in distributions of structural quantities such as the end-to-end distance. Furthermore, the actual shift was seen to follow opposite trends depending on whether the protein-surface interactions are repulsive or attractive. It should be noted that the two types of surface-protein interactions that we have considered are rather simple and essentially amount to introducing different spatial confinement constraints (to half of the 3D space or to a 2D space in the cases of repulsive and attractive surfaces, respectively). Nevertheless, we believe that similar effects will emerge for other types of protein-surface interactions. In fact, comparing the results obtained for freely diffusing and surface-immobilized polypeptides at different points along the denaturation curve may be a useful way for figuring out the nature of surface-protein interactions. A related observation is that the correlation between structure and dynamics in the unfolded states can be rather sensitive to the denaturation mechanism. For example, while conformations with small end-to-end distance move on a faster time scale in unfolded state α, no such correlation was observed in unfolded state β. Thus, the existence of such a correlation provides evidence for residual secondary structure in the unfolded state.

It is also of interest to compare our results with experiment. The experimental study most closely related to the model considered here is the SM-FRET assay by Hochstrasser and co-workers on the disulfide cross-linked two-stranded coiled-coil from the yeast transcription factor GCN4. [30,33] Our results appear to be consistent with many of the experimental observations reported in Refs. [30, 33]. For example, surface-immobilization in the folded state has a rather small effect on the R distribution, the folded and unfolded states are seen to correspond to narrow and broad R distributions, respectively, and conformational dynamics is seen to be characterized by a wide dynamical range in the midpoint and unfolded states. Our analysis can also help in the interpretation of the experimental results. For example, surface-

immobilization is experimentally observed to significantly broaden the R distribution, and change it from asymmetrical with a slow rise and a sharp drop to a more symmetrical form. This trend is consistent with our predictions for the repulsive surface, but is clearly in conflict with our predictions for the attractive surface. Another example corresponds to the $\langle R \rangle_{T_W}$-dependence of $D(\langle R \rangle_{T_W})$ in the unfolded state, which shows a broad minimum similar to what is observed experimentally. Yet another example corresponds to the experimental observation that conformations with smaller values of the end-to-end distance move on faster time scales, [30] which is consistent with our results for unfolded state α, and may suggest residual helical structure in the unfolded state. Interestingly, this prediction appears to be in conflict with other experimental results which suggest that coiled-coils fold cooperatively, i.e. that the individual helices are unstable in the absence of native tertiary contacts. [70, 83] A possible explanation for this discrepancy is that surface-protein interactions stabilize the individual helices in the unfolded state.

Finally, we also find several discrepancies between our results and experiment. For example, surface-immobilization is experimentally observed to slow down conformational dynamics in the unfolded state, which would be consistent with our results in the case of an attractive surface. However, as mentioned above, the effect of surface-immobilization on the distribution of end-to-end distance is clearly inconsistent with this scenario. Furthermore, $\langle D \rangle_{T_W}$ is experimentally observed to be about an order of magnitude *smaller* in the unfolded state in comparison to the folded state. [33] Our results in the case of the freely diffusing polypeptide suggest that the value of $\langle D \rangle_{T_W}$ in the unfolded state should actually be *larger* than in the folded state. It is also interesting to note that while the authors of Ref. [33] argue that low values of $\langle D \rangle(T_W)$ are indicative of *slow* conformational dynamics, we find that the opposite is true. Thus, while our results are consistent with the idea that conformational dynamics in the unfolded state is *slower* than in the folded state, we find that this would lead to a smaller value of $\langle D \rangle(T_W)$ in the folded state. One may speculate that this discrepancy results from surface-immobilization. Indeed, we found that the value of $\langle D \rangle(T_W)$ obtained in the case of the attractive surface case can be significantly lower than in free solution (Cf. Fig. 5). Unfortunately, the results for the end-to-end distance distributions appear to be inconsistent with this possibility.

To summarize, the model used in this paper captures many important features of protein structure and dynamics and is indeed seen to reproduce many of the general trends observed in SM-FRET experiments. At the same time, we have also observed several intriguing discrepancies between the model predictions and the experimental results. One possibility is that these discrepancies originate from shortcomings of the model. For example, the SM-FRET measurements reported in Refs. [30, 33] were performed on a coiled-coil that was immobilized on a *positively charged* amino-silanized glass surface and involved charged dye molecules. This implies that the protein-surface and donor-acceptor interactions may be dominated by electrostatic forces. Our

model may not be able to fully account for the effects of such interactions. We have also assumed that the chemical denaturant operates by selectively weakening specific intramolecular interactions, which probably represents an oversimplification. More specifically, we have accounted for the fact that the formation of helical structure requires the formation of tertiary contacts by weakening the dihedral interactions in unfolded state β. A more accurate model would have to include a more realistic treatment of how a chemical denaturant such as urea destabilizes the native state structure. [82] Finally, we note that the experimental SM-FRET efficiency distributions reflect fluctuations due to sources other than conformational dynamics, including shot noise, spectral diffusion and dipole angle distributions. Those other sources of noise were not accounted for in the simulations reported in this paper. Further investigation of these issues is clearly desirable and will be the subject of future work.

Acknowledgement

The authors are grateful to the Petroleum Research Fund for financial support (through grant No. 36486-G).

References

1. Fersht, A. *Structure and Mechanism in Protein Science: A Guide to Enzyme Catalysis and Protein Folding;* Freeman and Company: New York, 1998.
2. Bloomfield, V. A.; Crothers, D. M.; Tinoco, I. *Nucleic Acids: Structures, Properties, and Functions;* University Science Books: Sausalito CA, 2000.
3. Edman, L.; Mets, Ü.; Rigler, R. *Proc. Natl. Acad. Sci. USA* **1996**, *93*, 6710.
4. Nie, S.; Zare, R. N. *Annu. Rev. Biophys. Struct* **1997**, *26*, 567.
5. Jia, Y.; Sytnik, A.; Li, L.; Vladimirov, S.; Cooperman, B. S.; Hochstrasser, R. M. *Proc. Natl. Acad. Sci. USA* **1997**, *94*, 7932.
6. Bopp, M. A.; Jia, Y.; haran, G.; Morlino, E. A.; Hochstrasser, R. M. *App. Phys. Lett.* **1998**, *73*, 7.
7. Xie, X. S.; Trautman, J. K. *Ann. Rev. Phys. Chem.* **1998**, *49*, 441.
8. Geva, E.; Skinner, J. L. *Chem. Phys. Lett.* **1998**, *288*, 225.
9. Lu, H. P.; Xun, L.; Xie, X. S. *Science* **1998**, *282*, 1877.
10. Weiss, S. *Science* **1999**, *283*, 1676.
11. Dahan, M.; Deniz, A. A.; Ha, T.; Chemla, D. S.; Schultz, P. G.; Weiss, S. *Chem. Phys.* **1999**, *247*, 85.
12. Hu, D.; Yu, J.; Wong, K.; Bagchi, B.; Rossky, P.; Barabara, P. F. *Nature* **2000**, *405*, 1030.
13. Moerner, W. E. *J. Phys. Chem. B* **2002**, *106*, 910.
14. Russel, R.; Zhuang, X. W.; Babcock, H. P.; Millet, I. S.; Doniach, S.; Chu, S.; Herschlag, D. *Proc. Natl. Acad. Sci. USA* **2002**, *99*, 155.
15. Yang, H.; Luo, G.; Karnchanaphanurach, P.; Louie, T.; Rech, I.; Cova, S.; Xun, L.; Xie, X. S. *Science* **2003**, *302*, 262.

16. Bartley, L. E.; Zhuang, X. W.; Das, R.; Chu, S.; Herschlag, D. *J. Mol. Biol* **2003**, *6*, 923.
17. Zhuang, X. W.; Reif, M. *Curr. Opin. Struct. Biol.* **2003**, *13*, 88.
18. Chu, S. *Phil. Trans. R. Soc. Lond. A* **2003**, *361*, 689.
19. Haran, G.; Vöhringer, P. *ChemPhysChem* **2005**, *6*, 755.
20. Sherman, E.; Haran, G. *Proc. Natl. Acad. Sci. USA* **2006**, *103*, 11539.
21. Ha, T. *Biochemistry* **2004**, *43*, 4055.
22. Kubelka, J.; Hofrichter, J.; Eaton, W. A. *Curr. Opin. Struct. Biol.* **2004**, *14*, 76.
23. Fernandez, J. M.; Li, H. *Chem. Phys.* **2004**, *303*, 1674.
24. Boukobza, E.; Sonnenfeld, A.; Haran, G. *J. Phys. Chem. B* **2001**, *105*, 12165.
25. Xie, Z.; Srividya, N.; Sosnick, T. R.; Pan, T.; Scherer, N. F. *Proc. Natl. Acad. Sci. USA* **2004**, *101*, 534.
26. Ha, T.; Enderle, T.; .; Oglertee, D. F.; Chemla, D. S.; Selvin, P. R.; Weiss, S. *Proc. Natl. Acad. Sci. USA* **1996**, *93*, 6264.
27. Ha, T.; Ting, A. Y.; Liang, J.; Denize, A. A.; Chemla, D. S.; Schultz, P. G.; Weiss, S. *Chem. Phys.* **1999**, *247*, 107.
28. Ha, T.; Ting, A. Y.; Liang, J.; Caldwell, D. B.; Denize, A. A.; Chemla, D. S.; Schultz, P. G.; Weiss, S. *Proc. Natl. Acad. Sci. USA* **1999**, *96*, 893.
29. Ha, T.; Zhuang, X.; Kim, H. D.; Orr, J. W.; Williamson, J. R.; Chu, S. *Proc. Natl. Acad. Sci. USA* **1999**, *96*, 9077.
30. Jia, Y.; Talaga, D. S.; Lau, W. L.; Lu, H. S. M.; DeGrado, W. F.; Hochstrasser, R. M. *Chem. Phys.* **1999**, *247*, 69.
31. Deniz, A. A.; Dahan, M.; Grunwell, J. R.; Ha, T.; Faulhaber, A. E.; Chemla, D. S.; Weiss, S.; Schultz, P. G. *Proc. Natl. Acad. Sci. USA* **1999**, *96*, 3670.
32. Ishii, Y.; Yoshida, T.; Funatsu, T.; Wazawa, T.; Yanagida, T. *Chem. Phys.* **1999**, *247*, 163.
33. Talaga, D. S.; Lau, W. L.; Roder, H.; Tang, J.; Jia, Y.; DeGrado, W. F.; Hochstrasser, R. M. *Proc. Natl. Acad. Sci. USA* **2000**, *97*, 13021.
34. Deniz, A. A.; Laurence, T. A.; Beligere, G. S.; Dahan, M.; Martin, A. B.; Chemla, D. S.; Dawson, P. E.; Schultz, P. G.; Weiss, S. *Proc. Natl. Acad. Sci. USA* **2000**, *97*, 5179.
35. Weiss, S. *Nature: Structural Biology* **2000**, *7*, 724.
36. Ying, L.; Wallace, M. L.; Balasubramainian, S.; Klenerman, D. *J. Phys. Chem. B* **2000**, *104*, 5171.
37. Brasselet, S.; Peterman, E. J. G.; Miyawaki, A.; Moerner, W. E. *J. Phys. Chem. B* **2000**, *104*, 3676.
38. Zhuang, X.; Kim, H.; Pereira, M. J.; Babcock, H. P.; Walter, N. G.; Chu, S. *Science* **2002**, *296*, 1473.
39. Schuler, B.; Lipman, E. A.; Eaton, W. A. *Nature* **2002**, *419*, 743.
40. Lipman, E. A.; Schuler, B.; Bakajin, O.; Eaton, W. A. *Science* **2003**, *301*, 1233.
41. Haran, G. *J. Phys.: Condens. Matter* **2003**, *15*, R1291.
42. Rhoades, E.; Gussakovsky, E.; Haran, G. *Proc. Natl. Acad. Sci. USA* **2003**, *100*, 3197.
43. Rhoades, E.; Cohen, M.; Schuler, B.; Haran, G. *J. Am. Chem. Soc.* **2004**, *126*, 14686.
44. Slaughter, B. D.; Allen, M. W.; Unruh, J. R.; Bieber-Urbauer, R. J.; Johnson, C. K. *J. Phys. Chem. B* **2004**, *108*, 10388.
45. Hodak, J. H.; Downey, C. D.; Fiore, J. L.; Pardi, A.; Nesbitt, D. J. *Proc. Natl. Acad. Sci. USA* **2005**, *102*, 10505.

46. Sabanayagam, C. R.; Eid, J. S.; Meller, A. *J. Chem. Phys.* **2005**, *123*, 224708.
47. Liu, H.-W.; Cosa, G.; Landes, C. F.; Zeng, Y.; Kovaleski, B. J.; Mullen, D. G.; Barany, G.; Musier-Forsyth, K.; Barbara, P. F. *Biophysical Journal* **2005**, *89*, 3470.
48. Kuzmenkina, E. V.; Heyes, C. D.; Nienhaus, G. U. *J. Mol. Biol.* **2006**, *257*, 313.
49. Srinivas, G.; Yethiraj, A.; Bagchi, B. *J. Phys. Chem. B* **2001**, *105*, 2475.
50. Srinivas, G.; Bagchi, B. *J. Chem. Phys.* **2002**, *116*, 837.
51. Srinivas, G.; Bagchi, B. *Phys. Chem. Comm.* **2002**, *5*, 59.
52. Yang, H.; Witkoskie, J. B.; Cao, J. S. *J. Chem. Phys.* **2002**, *117*, 11010.
53. Gopich, I. V.; Szabo, A. *J. Phys. Chem. B* **2003**, *107*, 5058.
54. Wang, D.; Geva, E. *J. Phys. Chem. B* **2005**, *109*, 1626.
55. Shang, J.; Geva, E. *J. Phys. Chem. B* **2005**, *109*, 16340.
56. Stryer, L.; Haugland, R. P. *Proc. Natl. Acad. Sci. USA* **1967**, *58*, 719.
57. Haas, E.; Wilchek, M.; Katchalski-Katzir, E.; Steinberg, I. Z. *Proc. Natl. Acad. Sci. USA* **1975**, *72*, 1807.
58. Selvin, P. R. *Meth. Enzymology* **1995**, *246*, 300.
59. Andrews, D. L.; Demidov, A. A. *Resonance energy transfer;* Wiley: New York, 1999.
60. Selvin, P. R. *Nature: Structural Biology* **2000**, *7*, 730.
61. Förster, T. *Ann. Physik* **1948**, *2*, 55.
62. Dexter, D. L. *J. Chem. Phys.* **1953**, *21*(5), 836.
63. Lakowicz, J. R. *Principles of fluorescence spectroscopy;* Plenum Publishing Corporation: New York, U.S.A., 1999.
64. Scholes, G. D. *Annu. Rev. Phys. Chem.* **2003**, *54*, 57.
65. Shang, J.; Geva, E. *J. Phys. Chem. B* **2007**, *111*, 4178.
66. Shang, J.; Geva, E. *J. Phys. Chem. B* **2007**, *111*, 4220.
67. Srinivas, G.; Yethiraj, A.; Bagchi, B. *J. Chem. Phys.* **2001**, *114*, 9170.
68. O'Shea, E. K.; Rutkowski, R.; Kim, P. S. *Science* **1989**, *243*, 538.
69. O'Shea, E. K.; Klemm, J. D.; Kim, P. S.; Alber, T. *Science* **1991**, *254*, 539.
70. Lumb, K. J.; Carr, C. M.; Kim, P. S. *Biochemistry* **1994**, *33*, 7361.
71. Zitzewitz, J. A.; Bilsel, O.; Luo, J.; Jones, B. E.; Matthews, C. R. *Biochemistry* **1995**, *34*, 12812.
72. Wendt, H.; Berger, C.; Baici, A.; Thomas, R. M.; Bosshard, H. R. *Biochemistry* **1995**, *34*, 4097.
73. Jelesarov, I.; Dürr, E.; Thomas, R. M.; Bosshard, H. R. *Biochemistry* **1998**, *37*, 7539.
74. Sosnick, T. R.; Jackson, S.; Wilk, R. R.; Englander, S. W.; Degrado, W. F. *Proteins: Structure, Function, and Genetics* **1996**, *24*, 427–432.
75. Ratner, V.; Sinev, M.; Haas, E. *J. Mol. Biol.* **2000**, *299*, 1383.
76. Lee, M.; Tang, J.; Hochstrasser, R. M. *Chem. Phys. Lett.* **2001**, *344*, 501.
77. Guo, Z.; Thirumalai, D. *J. Mol. Biol.* **1996**, *263*, 323–343.
78. Klimov, D. K.; Betancourt, M. R.; Thirumalai, D. *Folding and Design* **1998**, *3*, 481–496.
79. Honeycutt, J. D.; Thirumalai, D. *biopolymers* **1992**, *32*, 695.
80. Veithans, T.; Klimov, D.; Thirumalai, D. *Fol. Des.* **1996**, *2*, 1.
81. Klimov, D. K.; Thirumalai, D. *Phys. Rev. Lett.* **1997**, *79*, 317.
82. Walqwist, A.; Covell, D. G.; Thirumalai, D. *J. Am. Chem. Soc.* **1998**, *120*, 427.
83. Durr, E.; Jelesarov, I.; Bosshard, H. R. *Biochemistry* **1999**, *38*, 870.
84. Makarov, D. E.; Metiu, H. *J. Chem. Phys.* **1999**, *111*, 10126.
85. de Gennes, P. G. *Scaling concepts in polymer physics;* Cornell University Press: Cornell, U.S.A., 1979.

Part II

The Many Facets of DNA

Quantum Mechanics in Biology: Photoexcitations in DNA

Eric R. Bittner and Arkadiusz Czader

[1] Department of Chemistry and the Texas Center for Superconductivity, University of Houston, Houston, TX 77204 bittner@uh.edu
[2] Department of Chemistry and the Texas Center for Superconductivity, University of Houston, Houston, TX 77204

Abstract. We consider here the theoretical and quantum chemical description of the photoexcitated states in DNA duplexes. We discuss the motivation and limitations of an exciton model and use this as the starting point for more detailed excited state quantum chemical evaluations. In particular, we focus upon the role of interbase proton transfer between Watson/Crick pairs in localizing an excitation and then quenching it through intersystem crossing and charge transfer.

1 Quantum Biology

> But when a biochemist begins to use quantum-mechanical language ... we may justifiably suspect he is talking nonsense. H. C. Longuet-Higgins, "Quantum mechanics and biology", Biophys. J. **2**, 207-213 (1962).

At the risk of being too broad and perhaps too conservative, very few processes that occur in a biological system require a deep understanding of quantum theory. While all intermolecular forces and chemical structures are ultimately of quantum mechanical origin and their proper description does require the use of quantum theory, very few reactions are truly quantum mechanical. The reason is that in order for something to exhibit quantum like behavior, quanta of energy being exchanged must be discrete and large compared to the thermal energy. Thus, few ordinary chemical processes meet this criteria. Those that do, however, typically involve excitations of the electronic states, excitations of highly-local high-frequency vibrational modes, such as a CO group bound to the metal center on a heme, or tunneling of either an electron or proton between a donor and acceptor.

The quotation at the beginning of this section comes from an address given by H. C. Longuet-Higgins in the early 1960 at a workshop on "Emerging techniques in Biophysics". In it, he concludes that at the moment (in 1960) there was very little point in trying to conjure up a quantum theory to explain

I. Burghardt et al. (eds.), *Energy Transfer Dynamics in Biomaterial Systems*, Springer Series in Chemical Physics 93, DOI 10.1007/978-3-642-02306-4_4,

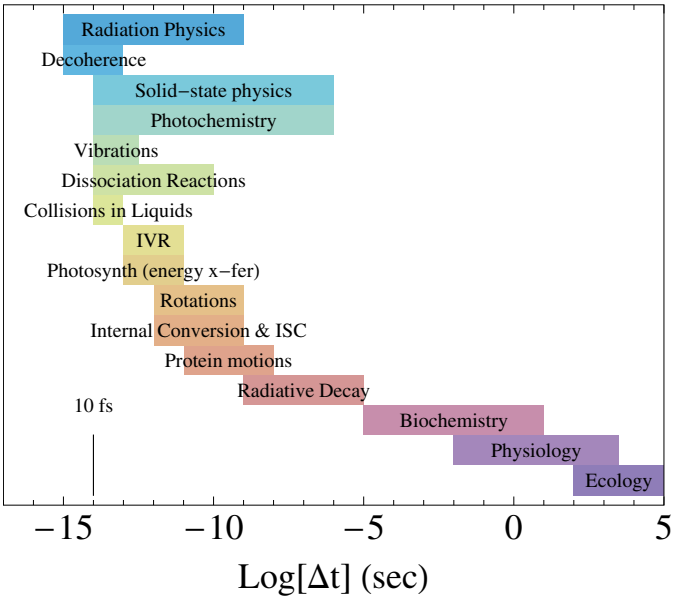

Fig. 1: Hierarchy of important photo-biophysical processes by typical timescales. The line at "10 fs" indicates the time-resolution of modern (2008) ultrafast spectroscopic experiments.

a particular biological process like enzyme catalysis. Perhaps one could cook up some strange quantum force that guides and directs the substrate to the reaction center that is without parallel in the non-biological world, but that seems highly unlikely since the forces that direct atoms and molecules are the same be it in an enzyme or in a jar of mustard. While quantum theory may provide a way to understand what happens once the substrate reaches the reaction center and quantum chemical investigations have greatly enriched our understanding of biochemical processes, the same quantum theory hold all living and non-living systems. For most biochemical and biophysical processes, there is an analogous non-biological process in solid-state or condensed matter physics.

On a more philosophical or meta-physical level, one may suspect that free will and consciousness may have some quantum mechanical origin rooted in the Heisenberg Uncertainty Principle. Perhaps at some neurological level an electron at a synapse exists in a superposition of two or more states that ultimately results in someone making some sort of decision. "Should I run for President, or not?" "Should I get married, or not?". Perhaps there are two states with eigenvalues "yes" or "no" that asymptotically lead to very different actions. Does quantum theory enter into our decision making process? Perhaps the brain itself acts as some sort of quantum computer taking

advantage of fact that a quantum state can be delocalized and hence sample multiple possible states at once and arrive at an answer far faster than a classical deterministic computer. While popular science and New Age gurus tout such claims, I highly doubt this is to be the case. First, thermal noise at ambient physiological conditions is certainly as much of a contribution to randomness as the fluctuations due to quantum uncertainty. Secondly, as we shall encounter in thinking about how long quantum coherence can survive in a condensed phase system, the lifetime of any quantum superposition state of an within a neuron is subject to the dielectric reorganization of the surrounding media. If we take this to the rotational reorganization time of water, we can easily suspect that the longest any electronic superposition my last is on the order of 10^{-12} seconds. This is a billion times shorter than the time scale for electrical synapses of 2.0×10^{-2} seconds. Any quantum information that could have been passed from neuron to neuron across the nexus junction has long decayed before the message is relayed.

What is true, however, is that the the optical and electro-optical properties of many biological and materials devices are determined by delocalized π-conjugated systems within their molecular frameworks. In living systems, π conjugated systems serve a variety of roles. In plants, the process of photosynthesis is triggered by the absorption of a photon by chlorophyl which initiates a series of ultrafast energy and electron transfer processes that ultimately converts the photoexcitation into chemical energy that can be used by the plant. This is perhaps the most important form of solar energy conversion in living systems. In fact, even though our current civilization derives most of its energy from the fossilized remains of plants and animals, the energy stored within the remaining coal, oil, and natural gas was originally harvested from the sun hundreds of millions years ago by some living plant or algae.

2 Excited state dynamics in DNA

It is generally agreed upon that life arose on the earth approximately 3.8 billion years ago. This is roughly 200 million years after the planet itself cooled. This in an of itself is remarkable since it indicates that in a relatively short time after the earth cooled and became a stable planet, the first identifiable traces of life began to appear. Evidence of this primitive bacteria can be found in certain rock out-croppings dating to this period.

However, before bacteria could evolve, the fundamental chemistry of life needed to be established. For this we need to turn back the clock to around 4.5 - 4.1 billion years ago where the earth's crust has cooled and solidified and the oceans and atmosphere begin to form. It is speculated that iron-sulfide synthesis along deep oceanic platelets may have lead to the synthesis of the first RNA and self-replicating molecules. Exactly how this chemical evolution came about remains an open question. It is possible that RNA may have used clays and similar self-replicating materials as substrates. Eventually, this

chemistry of self-replication would lead to replicating organisms. Such proto-lifeforms would require energy, food, and space and would eventually compete with each other for these vital resources. This competition naturally leads to a selection criteria where the organisms best capable of acquiring the necessary components would pass these traits on to their progeny through replication. Certainly, many trial chemistries would have been explored. Due to natural selection, the chemistries that are more faithful and efficient in replication have an evolutionary edge over chemistries that are more error prone and less efficient. At some point DNA based replication supplanted RNA based replication and became the dominant chemistry of life.

DNA is very stable with respect to the photochemical decay. This is remarkable since the base components of DNA: adenosine, thymine, cytosine, and guanine all are cyclic aromatic molecules with very large photo-absorption cross-sections in the ultraviolet range. Hence, the bases themselves are highly susceptible to photo-initiated chemical reactions. The path chosen by nature to protect DNA is through the very rapid decay pathways of the electronic excitation energy which prevents the localization of electronic energy. Given the importance of DNA in biological systems and its emerging role as a scaffold and conduit for electronic transport in molecular electronic devices, [1] DNA in its many forms is a well studied and well characterized system. What remains poorly understood, however, is the role that base-pairing and base-stacking plays in the transport and migration of the initial excitation along the double helix. [2–4]

The absorption of UV radiation by DNA initiates a number of photochemical reactions that can ultimately lead to carcinogenic mutations. [5–9] The UV absorption spectrum of DNA largely represents the weighted sum of the absorption spectra of it constituent bases. However, the distribution of the primary photochemical products of UV radiation, including bipyrimidine dimers, [10] is depends quite strongly upon base sequence, which implies some degree of coupling between the DNA bases. [3] Inasmuch as both the base stacking and base pairing are suspected to mediate the excess of electronic excitation energy, understanding of the excited-state dynamics is of primary importance for determining how the local environment affects the formation of DNA photolesions.

Recent work by various groups has underscored the different roles that base-stacking and base-pairing play in mediating the fate of an electronic excitation in DNA. [2, 3] Over 40 years ago, Löwdin discussed proton tunneling between bases as a excited state deactivation mechanism in DNA [11] and evidence of this was recently reported by Schultz *et al.* [12] In contrast, ultrafast fluorescence of double helix poly(dA)·poly(dT) oligomers by Crespo-Hernandez *et al.* [2] and by Markovitsi *et al.* [3] give compelling evidence that base-stacking rather than base-pairing largely determines the fate of an excited state in DNA chains composed of adenosine and thymine bases with long-lived intrastrand states forming when ever adenosine is stacked with itself or with thymine. However, there is considerable debate regarding whether or

not the dynamics can be explained via purely Frenkel exciton models [3,4,13] or whether charge-transfer (excimer) states play an intermediate role. [14]

Upon UV excitation, the majority of excited molecules shows a subpicosecund singlet lifetimes. [15–18] Owing to the technical difficulties in measuring the ultrashort lifetimes the study of the charge and excitation energy transfer in DNA has only recently received much of attention with the advances in the femtosecond spectroscopy. Although, so far, no clear picture of the excited -state deactivation mechanism has been offered by the experiment, two possible decay channels have been investigated. Kohler and coworkers in their recent study of the duplex poly(dA)·poly(dT) suggested that π-stacking of the DNA base determines the fate of a singlet electronic excited state. [2] Alternative decay mechanism involves interstrand hydrogen or proton transfer. Douhal and coworkers observed excited-state proton transfer in base pair mimincs in gas-phase. [19] The experimental results suggests that these very fast decay pathways play an important role in quenching the reactive decay channels and providing DNA with intrinsic photochemical stability. However, they do not provide a clear picture which arrangement of bases, pairing or stacking, is of primary importance.

3 Justification for a purely Exciton Model

Until recently, most theoretical investigations of excitation energy transfer in DNA helices has been within the Frenkel exciton model which treats the excitation as a coherent hopping process between adjacent bases. [20, 21] This model has tremendous appeal since it allows one to construct the global excited states (i.e of the complete chain) in terms of linear combinations of local excited states. The key parameter in the evaluation of the electronic excitation energy transfer (EET) is the electronic coupling between the individual bases. To a first-order approximation, the base to base coupling can be estimated using a dipole-dipole approximation in which the interaction between the donor and acceptor is calculated using only the transition dipole associated with each chromophore. While this approach is certainly suitable for cases in which the distance between the donor and acceptor sites is substantially greater than the molecular length scale. In case of double stranded DNA, where the DNA bases are in relatively close contact compared to their dimensions this approach leads to the neglect of the effect of the size and spatial extent of the interacting transition densities associated with each chromophore.

An important issue in the nature of the excited states in stacks of DNA bases is whether or not the states extended over a number of the bases are neutral Frenkel excitons or if they carry some degree of charge transfer character (exciplex or excimer).[3] [2–4] A purely excitonic model neglects configurations

[3] The simple distinction between an exciplex and an excimer is that an exciplex is a charge-separated state between two different species and and excimer is a charge-seperated state between two identical species.

in which the electron and hole reside on different sites and one can argue against excimer formation in stacked homodimers since the exciton binding energy ($\approx 0.4 - 0.5$ eV typical for conjugated organic species) is far greater than the difference in either electron affinities or ionization potentials of the stacked pair. [24, 25] Based upon the exciton stability criteria, exciplex states are only expected for stacked heterodimers (eg. AT, CG, etc...). The significance of the breakup of the exciton is twofold. First, it is well recognized that photoexcitation of adjacent stacked pyrimidine bases leads to the formation of *cis-syn* cyclobutane pyrimidine-dimer lesions. However, this dimerization occurs only in the triplet (rather than singlet) excited state. [8] Consequently, spin-flip must occur *ether* via spin-orbit coupling or via recombination of polaron pairs. [26] If we assume that the spins are decorrelated at some intermediate distance $r \propto e^2/\epsilon kT$ where the Coulomb energy is equal to the thermal energy, photoexcitation of a thymine sequence could rapidly result in a population of triplet excitons formed by exciton dissociation followed by geminate recombination. Secondly, the process is reversible and triplet reactivation of the dimer can lead to repair of the lesion.

3.1 Exciplexes, Excimers, and Excitons

It is constructive at some point to carefully define the difference between the various types of electronic states that arise when two molecules are brought into close contact, as in the case of the stacked bases in a DNA chain. Let us consider a simple model for understanding the various excited state configurations that can arise between stacked molecules. For the sake of simplicity, consider the following 4 electronic configurations:

$$\phi_1 = \otimes - \odot \tag{1}$$

$$\phi_2 = \odot - \otimes \tag{2}$$

$$\phi_3 = \oplus - \ominus \tag{3}$$

$$\phi_4 = \ominus - \oplus \tag{4}$$

where $-\otimes-$ denotes an electron/hole pair localized on the same base (i.e. a local exciton), $-\odot-$ denotes a base without an excitation, $-\oplus-$ denotes a base with an electron removed from its HOMO orbital (i.e. a hole) and $-\ominus-$ denotes a base with an electron placed in its LUMO orbital. For a homodimer in the absence of electron/hole interaction or ground-state polarization, these states are degenerate with energy equal to the LUMO-HOMO energy difference. Let us consider a simple Hubbard-like model where the electronic interaction, U corresponds to the exciton binding energy. We also will have two types of hopping terms, one in which the a local exciton $\otimes$ is transfered from one base to the other and a second hopping term for the swapping of the two charges. A schematic sketch of the relative placement of the energy levels is shown in Fig. 2. Under these assumptions, H can be written as the 4×4 matrix:

$$H = \begin{pmatrix} \Delta E_a - U & -J & -t & -t \\ -J & \Delta E_b - U & -t & -t \\ -t & -t & E_{Lb} - E_{Ha} & 0 \\ -t & -t & 0 & E_{La} - E_{Hb} \end{pmatrix}. \tag{5}$$

For a homo-dimer, $E_{La} - E_{Ha} = E_{Lb} - E_{Hb} = E_{La} - E_{Hb} = E_{Lb} - E_{Ha} = \Delta E$ and we take J, U, and t to be positive energies. By defining symmetrized states

$$\psi_1 = (\phi_1 - \phi_2)/\sqrt{2} \tag{6}$$

$$\psi_2 = (\phi_3 - \phi_4)/\sqrt{2} \tag{7}$$

$$\psi_3 = (\phi_1 + \phi_2)/\sqrt{2} \tag{8}$$

$$\psi_4 = (\phi_3 + \phi_4)/\sqrt{2} \tag{9}$$

H can be brought in to a block diagonal form

$$T.H.T^T = \begin{pmatrix} J - U & 0 & 0 & 0 \\ 0 & 0 & 0 & 0 \\ 0 & 0 & -(J+U) & -t \\ 0 & 0 & -t & 0 \end{pmatrix}. \tag{10}$$

and we take the energy-zero to be the LUMO-HOMO gap ΔE. The first two of these symmetrized states are purely excitonic or charge-transfer and do not depend upon the electron/hole hopping term. The eigenstates of the second block are mixed exciton/charge-transfer states

$$\psi_{\pm} = \cos(\theta)\psi_1 + \sin(\theta)\psi_2$$

where θ is now the mixing angle given by

$$\tan(2\theta) = \frac{2t}{(J+U)}.$$

with energy

$$E_{\pm} = \frac{1}{2}\left(-(J+U) \mp \sqrt{16t^2 + (J+U)^2}\right).$$

Typically for molecular dimers, the exciton binding energy $U \gg J$ and $J \approx t$. Thus, the lowest energy excited state will be dominated by excitonic-type configurations with some mixing with the charge-separated configurations. Consequently, to good approximation, these intrachain states can be considered to be Frenkel-type excitons.

Finally, let us consider how much of an energy off-set, ϵ_b, is required so that the lowest energy excited state is a charge-transfer state. For simplicity, we take the HOMO-LUMO gap on each monomer to be identical $E_{La} - E_{Ha} = E_{Lb} - E_{Hb} = \Delta E$ and thus, $E_{Lb} - E_{Ha} = \Delta E - 2\epsilon_b$ and $E_{La} - E_{Hb} = \Delta E + 2\epsilon_b$

$$H = \begin{pmatrix} \Delta E - U & -J & -t & -t \\ -J & \Delta E - U & -t & -t \\ -t & -t & \Delta E - 2\epsilon_b & 0 \\ -t & -t & 0 & \Delta E + 2\epsilon_b \end{pmatrix} \tag{11}$$

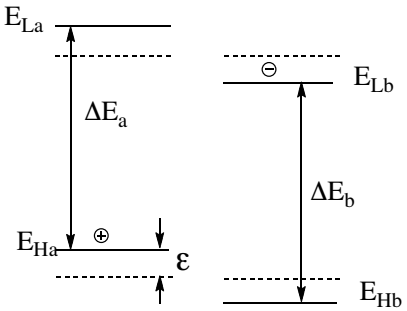

Fig. 2: Relative placement of HOMO and LUMO energy levels in a molecular dimer. The dashed lines indicate the energies for the homo-dimer. For the heterodimer, these levels are shifted up or down by ϵ so that the band off-set is 2ϵ. In the discussion, we assume that $\Delta E_a = \Delta E_b$. Shown also is the electron/hole configuration corresponding to state $\phi_3 = \oplus - \ominus$.

Again, using the symmetrized states above, we can transform this H into

$$\begin{pmatrix} \Delta E + J - U & 0 & 0 & 0 \\ 0 & \Delta E & 0 & -2\epsilon_b \\ 0 & 0 & \Delta E - J - U & -2t \\ 0 & -2\epsilon_b & -2t & \Delta E \end{pmatrix}. \tag{12}$$

The band off-set polarizes the system and it is convenient to transform the lower 3×3 submatrix into a basis defined by

$$\psi_+ = \phi_3 = \frac{1}{\sqrt{2}}(\psi_2 + \psi_4) \tag{13}$$

$$\psi_- = \phi_4 = \frac{1}{\sqrt{2}}(\psi_2 - \psi_4) \tag{14}$$

$$\psi_0 = \psi_3 \tag{15}$$

producing the tri-diagonal matrix

$$\begin{pmatrix} \Delta \mathrm{E} + 2\epsilon & \sqrt{2}t & 0 \\ \sqrt{2}t & \Delta \mathrm{E} - J - U & -\sqrt{2}t \\ 0 & -\sqrt{2}t & \Delta \mathrm{E} - 2\epsilon \end{pmatrix}. \tag{16}$$

Taking the hopping as a perturbation we can define the two energetically lowest states as

$$\psi_{exciton} \approx \psi_0 + \frac{\sqrt{2}t}{2\epsilon - (J+U)}\psi_+ \tag{17}$$

$$\psi_{exciplex} \approx \psi_+ - \frac{\sqrt{2}t}{2\epsilon - (J+U)}\psi_0 \tag{18}$$

When $2\epsilon < (U+J)$, the exciton state is lower in energy than the corresponding exciplex state. Also, we can see from this analysis how an exciplex state can acquire oscillator strength to the ground state through mixing with ψ_0. Taking $\epsilon \to 0$ as in the case of the homo-dimer,

$$\psi_{exciton} \approx \psi_0 + \frac{t}{(J+U)}(\phi_3 + \phi_4) \tag{19}$$

$$\psi_{excimer} \approx \frac{1}{\sqrt{2}}(\phi_3 + \phi_4) - \frac{\sqrt{2}t}{(J+U)}\psi_0 \tag{20}$$

Again, the excimer state acquires some oscillator strength due to mixing with purely excitonic configurations induced by the electron and hole hopping integrals. However, since the mixing is proportional to $t/(J+U)$ and $U \gg t$, this mixing is expected to be quite weak. On the other hand, at typical stacking distances, the transfer integral t could be significant and some degree of excimer formation could be expected.

While this analysis is compelling motivation for a purely excitonic model, one must bear in mind that we are neglecting the fact that the Coulomb integrals should be screened by the local environment. This begs the question: "Exactly what is the local environment about a base pair?" On one extreme, it is essentially salt water with a very high dielectric, on the other extreme they are in a low dielectric environment since they primarily interact with their conjugated heterocyclic neighbors. To understand the effect of screening, we next consider a simple screening model.

3.2 Onsager criteria for intrachain charge-separated species.

Having argued against the formation of intrachain charge separated species it is only fair at this point to provide an argument in favor of intrachain charge separation. For this, let us consider a DNA chain as a continuous and homogeneous dielectric medium and the electron/hole pair as a quasi-hydrogenic species. In order for complete charge separation to occur the electron and hole must be far enough apart so that their mutual attraction is less than the thermal energy. This distance is termed the Onsagar radius. If we consider this as a prototypical hydrogenic atom, then the virial theorem tells us that

$$\langle T \rangle = -\frac{1}{2}\langle V \rangle \tag{21}$$

Setting $\langle T \rangle = 3k_BT/2$ for a "free particle" moving in 3 dimensions and using the standard expectation values for a hydrogenic atom one finds that

$$r_c = \frac{e^2}{\epsilon}\frac{1}{2kT}a_o \tag{22}$$

where a_o is the Bohr radius of the electron/hole quasi-hydrogenic atom, e is the charge and ϵ is the dielectric constant of the material. In atomic units and 300K this comes out to be

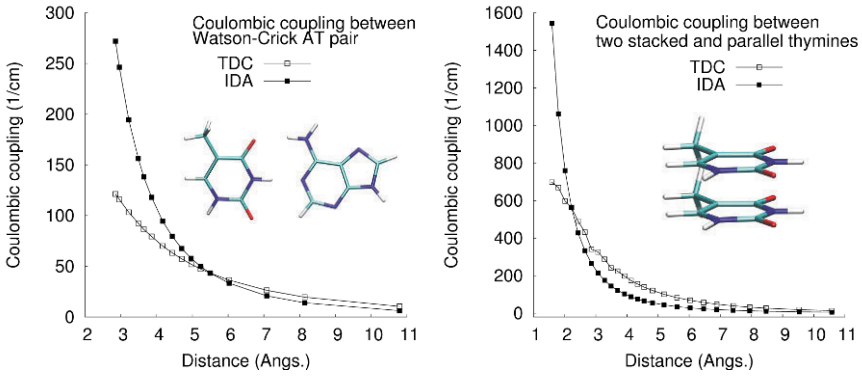

Fig. 3: Coulombic coupling between the lowest $\pi\pi^*$ transition moments of Watson Crick AT base pair (left) and two stacked and parallel Ts (right) as a function of the distance between the two bases. The distance is measured between N1 and N3 atoms of A and T, respectively, for the AT pair (left) and between the centers of the mases of the two Ts (right). (From Ref. [23])

$$r_c \approx \frac{1}{\epsilon} 535 a_o = \frac{1}{\epsilon} 278 \text{Å}$$

At 25°C, the dielectric constant of water is 78.4. In contrast, the typical dielectric constant of an organic *poly*-phenylene-type semiconductor is between 3 and 11. This implies that the r_c for charge separation along a DNA should be someplace in between 78.4 (due to the water surrounding the DNA chain) and 11 since the interior of the chain should looks more like stacked poly-aromatic hydrocarbons. In short, depending upon how exposed the low dielectric interior of the DNA chain is to the higher dielectric constant of the surrounding water, the Onsager radius can be between 25Åand 3.5Å, which does lend credence the formation of intrachain charge separated species; however, their presence should be highly sensitive the solvent environment and the average dielectric within the DNA helix.

3.3 Exciton coupling matrix elements

Molecules interact with each other at a distance via Coulomb forces determined by the shape and polarizibility of the electronic density surrounding each them. In general, we work in the limit that a given pair of molecules are far enough apart that electron exchange and correlation contributions can be safely ignored. Thus, the interaction can be written as

$$V_{ab} = \frac{1}{2} \int d^3 r_a \int d^3 r_b \frac{e^2 \rho_a(r_a) \rho_b(r_b)}{|r_a - r_b|} \tag{23}$$

where ρ_a and ρ_b are the transition densities of molecules A and B respectively between the initial and final electronic states. In loose terms, the transition

density can be thought of as the induced charge oscillations in the ground state electronic density in response to a linear oscillating driving force (i.e. the electro-magnetic field) at the transition frequency. If the distance, R, between A and B is large compared to the size of either molecule, a, we can safely expand the integrand in terms of its multipole moments and write

$$V_{ab} \approx V_{dd} + V_{dq} + V_{qd} + V_{qq} + \cdots$$

where V_{dd} is the "dipole-dipole" term, V_{qd} is the "quadrupole-dipole" interaction, and so forth. For $R \gg r$ we can truncate the multiple expansion at the first term and write the interaction in terms of the transition dipole moments of each molecule.

$$M = \frac{1}{R^3}\left(\boldsymbol{p}_A \cdot \boldsymbol{p}_B - \frac{3}{R^2}(\boldsymbol{p}_A \cdot \boldsymbol{R})(\boldsymbol{p}_B \cdot \boldsymbol{R})\right) \tag{24}$$

where $\boldsymbol{R}$ is a vector extending from the charge center of A the charge center of B. Setting this to be the z axis, we can write M as a function of the angles

$$\chi(\theta_a, \theta_b, \phi) = \sin\theta_a \sin\theta_b \cos\phi - 2\cos\theta_a \cos\theta_b \tag{25}$$

If all angles are statistically possible, one obtains the mean value

$$\overline{\chi^2} = 2/3 \tag{26}$$

for the orientation

However, for molecules that are in close proximity to each other, i.e. $R \approx r$, then we need to include essentially every term in the multipole expansion in order to accurately approximate the coupling. By far the most precise way to calculate the excitonic coupling elements is to directly integrate the Coulomb coupling matrix element between transition densities localized on the respective basis. [22] The basic ideas behind this approach are examined in the next chapter by Scholes. The accuracy is then limited only by the numerical quadrature in integrating the matrix element and by the level and accuracy of the quantum chemical approach used to construct the transition densities in the first place. The values of the Coulombic couplings between the lowest energy $\pi\pi^*$ transitions of the adenine and thymine and two π - stacked thymines as a function of distance between the bases (Fig. 3) were calculated using the TDC and IDA methods. The comparison of the coupling elements obtained with two methods (Fig. 3) shows a good agreement at a separation between the bases larger than 5 and 6 Å for AT pair and stacked THYs, respectively. At a shorter separations, in the range of 3-4 Å, which is typical for DNA structures, the agreement between IDA and TDC is very poor with the differences between calculated couplings in error larger than 100% in case of AT pair. The aforementioned good agreement between IDA and TDC at a large separation and poor agreement at shorter distances between nucleobases indicates that the shape and spatial extent of transition density

(Fig. 3) become important and cannot be neglected at distances between the bases typical for double helices DNA. The agreement between the two methods becomes very good in the limit of very large separation, (z >8 Å).

In Fig. 4 we show the delocalized $\pi\pi^*$ transition density differences for a stacked pentamer of 9H-adenine computed using an *ab initio* Hartree Fock description of the ground state followed by a CIS(D) description of the excitations. The configurations shown here are sampled from a molecular dynamics simulation of a dAdT oligomer in water in its B-form. From these calculations we see little evidence of charge transfer (excimer) states between stacked bases. None of the 20 excited states calculated at the CIS(D)/cc-pVDZ level have a charge transfer character. The lowest energy states can be most adequately classified as $n\pi*$ and $\pi\pi*$ states. Likewise the vertical excitation energies (VEE) of the AT base pair the VEEs of the former states of stacked pentamer are slightly lower than the VEEs of the latter states. The $\pi\pi*$ states with the largest oscillator strength are also the most delocalized, the corresponding molecular orbitals being delocalized over all five adenine bases. On the contrary, the $n\pi*$ states can be localized on a single thymine base. CIS(D) calculations on stacked adenosine pentamers based upon MD configurations give little evidence for excimer formation, although depending upon the instantaneous geometry of the chain, excitons may have a small static dipole due to differing degrees of localization of the occupied and virtual orbitals contributing to the configuration-interaction expansion of the excited state wave functions. The difference densities corresponding to the $\pi\pi*$ states of the pentamer with the largest oscillator strength are shown in Fig. 4. These calculations were performed in vacuum, consequently, it is entirely possible that contributions from solvent polarization, counter-charges, and near by water molecules could stabilize intrastrand excimer states even within a chain of identical bases. [27]

3.4 Exciton localization: disorder

The simplest Frenkel exciton model consists of diagonal energies ϵ_n representing the exciton energies of the individual bases with off-diagonal elements corresponding to the Coulomb coupling between exciton states, J

$$H_{exciton} = \sum_n |\phi_n\rangle\langle\phi_n|\epsilon_n + \sum_{n\neq m} |\phi_n\rangle\langle\phi_m|J_{nm}(\theta_{nm}). \tag{27}$$

Since short strands of DNA are fairly rigid, the electronic coupling terms are likely most sensitive to the base-base dihedral angle, θ_{ij} between adjacent bases. If we take the fluctuations in θ_{ij} to be $\delta\theta^2 = k_B T/I\Omega^2$ where I is the reduced moment of inertia of the AT base-pair and $\Omega = 25cm^{-1}$ is the torsional frequency. This gives an RMS angular fluctuation of about 5% about the avg. $\overline{\theta_{i,i+1}} = 35.4°$ helical angle. [28] Since this is a small angular deviation, we take the fluctuations in the electronic terms to be proportional to

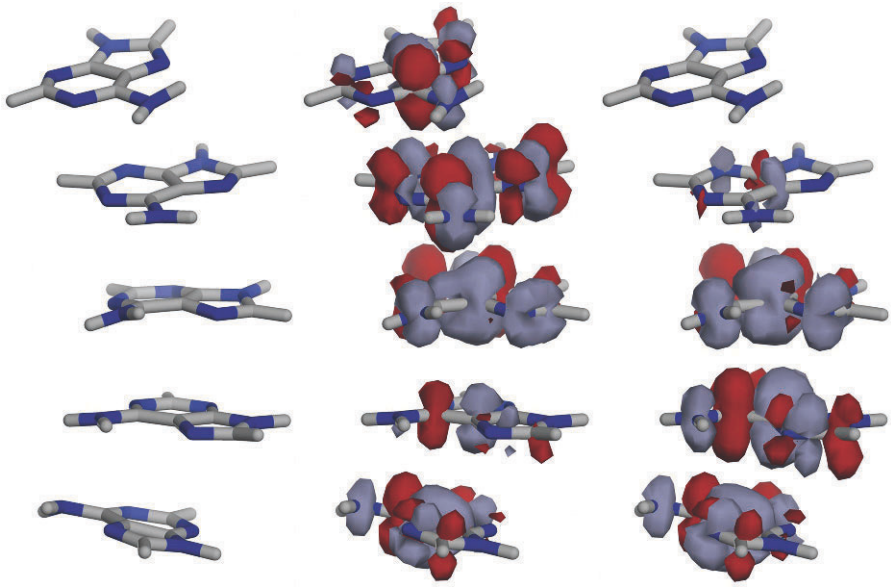

Fig. 4: The difference densities of stacked 9H-adenine pentamer (left) calculated at the CIS(D)/cc-pVDZ level corresponding to two different localized $\pi\pi*$ states (middle and right).

$\delta\theta^2$ and sample these terms from normal distributions about B-DNA average values. Such fluctuations in the electronic couplings are consistent with more robust estimates based upon combined molecular dynamics/quantum chemical simulations by our group. [23]

In Fig. 5 we computed the J_{nm} coupling matrix elements between each base for 12-base pair dAdT oligomer in water (in its B DNA form) over the course of an 80 ps molecular dynamics simulation and determined the Frenkel exciton states by diagonalizing Eq. 27. From these simulations, two states carried the majority of the oscillator strength, #13 corresponding to a exciton delocalized over the A side of the chain and the other #22 corresponding to an exciton delocalized over the T side of the chain. The spatial extent of the eigenstates was evaluated based on the participation ratio ($PR = 1/L_k$) of a given eigenstate, which indicates the number of coherently bound chromophores [29]. The participation ratio of the eigenstates <13> and <22> as a function of energy is ploted in Figure 5. The PR values for these two eigenstates of $(A)_{12}(T)_{12}$ calculated for 240 conformations taken from the MD simulations show large fluctuactions in the range of $2-10$. The higher energy eigenstate with index <22>, calculated using either IDA and TDC coupling elements, on average shows larger delocalization compared with the lower energy eigenstate number <13>. However, only for a handful configurations the value of PR exceeds the theoretical value of 8.4 (indicated by a dashed line in

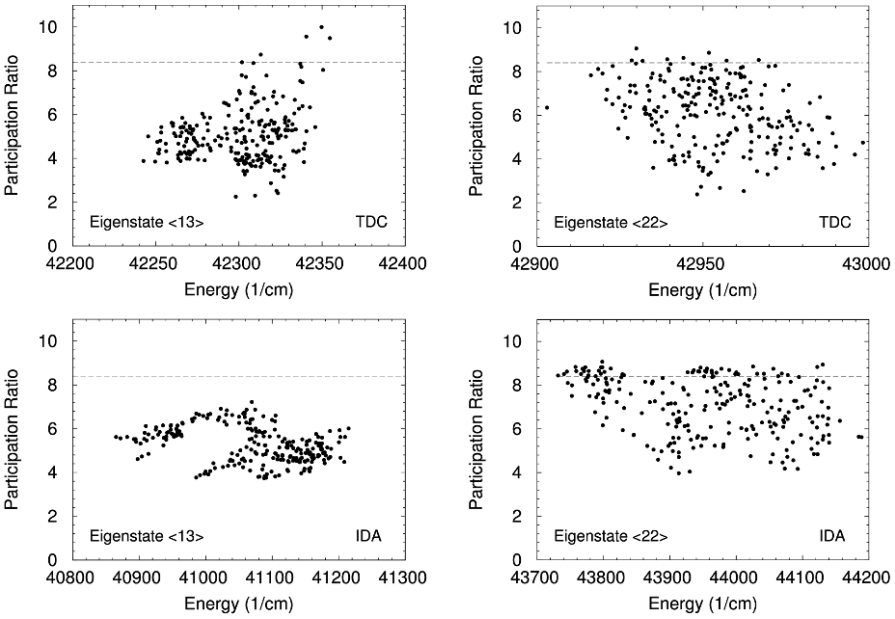

Fig. 5: Plot of the participation ratio of the eigenstate numbers <13> and <22> as a function of energy determined for 240 conformations of $(A)_{12}(T)_{12}$. (From Ref. [23])

Figure 5) corresponding to the completely delocalized exciton over one strand of the $(A)_{12}(T)_{12}$. This indicates that both eigenstates <13> and <22> which are localized on the transition associated with adenine remains localized on only one strand of the $(A)_{12}(T)_{12}$ composed of adenine nucleobases.

In Fig. 6 we consider a Gaussian noise model where we sampled the off-diagonal elements of Eq. 27 from normal deviates centered about the B DNA average values as computed using the transition density cube approach and assuming a fluctuation of 50 cm^{-1} between nearest neighbor bases consistent with our estimates based upon our MD simulation. In this case, we consider a 20 base-pair chain in order to eliminate any effect of the finite length of the chain and sample over 2000 individual realizations. Even though the gaussian-noise model does not include correlation between values of J_{nm}, it does a good job of reproducing the average inverse participation ratio compared to the molecular dynamics results.

This suggests that to first order the effect of disorder induced localization can be introduced into a reduced model for DNA by sampling the couplings from a normal distribution about the average B-DNA coupling. However, this may introduce too severe of an approximation when it comes to dynamics and transport related properties that may be sensitive to dynamical correlations amongst the coupling terms.

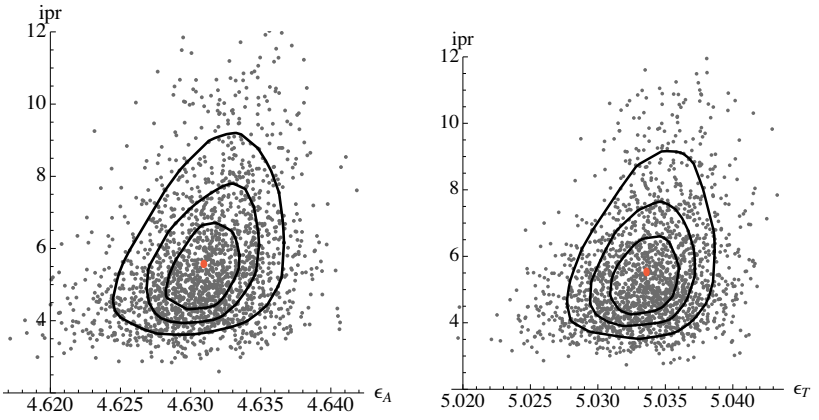

Fig. 6: Comparison of the localization length vs. exciton energy for a gaussian-noise model for dAdT.

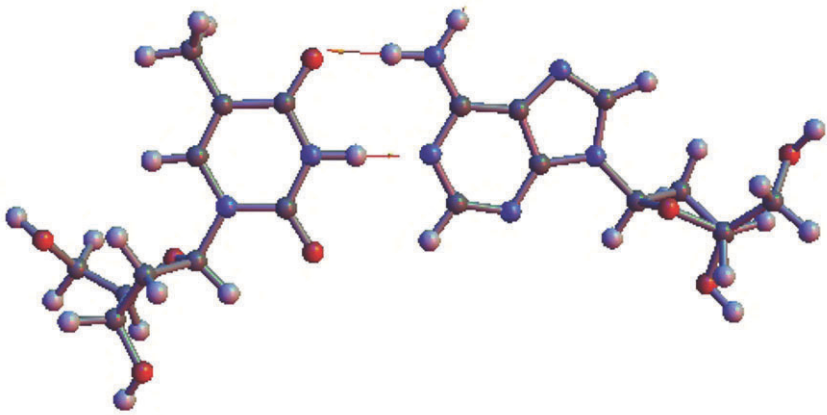

Fig. 7: Proton transfer reaction coordinate between amide/keto and imino/enol tautomer forms of the A-T base pair.

4 Role of proton transfer

Lastly we consider the role of proton transfer between the Watson Crick bases. As discussed above, experimental evidence supported by quantum chemical

calculations on *isolated* bases point to a significant role played by proton exchanges between bases in quenching photoexcitations. [12] In short, these studies indicate that the $\pi\pi^*$ states are strongly coupled to the proton transfer coordinate carrying the system from the (normal) amide/keto form to the (rare) imino/enol forms of the bases. For A-T, there are two hydrogen bonds between the two bases, one coming from the amine N in the 6 position on adenine and the carbonyl oxygen at the 4 position on thymine and the other between the N1 on adenine and the N3 on thymine. We can represent this as

$$A \left\{ \begin{array}{ccc} : H & \rightarrow & : \\ : & \leftarrow H & : \\ & & \end{array} \right\} T \rightarrow A^* \left\{ \begin{array}{ccc} : & & H : \\ : H & & : \\ & & \end{array} \right\} T^* \tag{28}$$

where : represent a pair of electrons. The other Watson/Crick pair has the following match up:

$$C \left\{ \begin{array}{ccc} : H & \rightarrow & : \\ : & \leftarrow H & : \\ : & H & : \end{array} \right\} G \rightarrow C^* \left\{ \begin{array}{ccc} : & & H : \\ : H & & : \\ & H & : \end{array} \right\} G^* \tag{29}$$

These rare tautomer forms A^*, T^*, C^* and G^* are of concern since it has been suggested that these may serve as a source for point mutations in DNA since the pyrimidine tautomer of one WC pair is now complementary to the purene of the other WC pair and vice versa. The genetic implication of these tautomer forms can be appreciated by considering the following scheme.

$$\begin{array}{ccccc} & & A-T & & \\ & & \downarrow & & \text{proton transfer} \\ & & A^*-T^* & & \\ & \swarrow & & \searrow & \text{replication} \\ & A^*-C & & G-T^* & \\ \swarrow & & \downarrow & & \downarrow \quad \searrow \\ A^*-C & & G-C & & G-C \quad G-T^* \end{array} \tag{30}$$

Here we show how an initial AT pair can be transformed in to a GC pair if the pair is in the tautomer form at the time of replication. One can see that after only two replication cycles, proton transfer can introduce a permanent point mutation where $AT \mapsto GC$ or $GC \mapsto AT$. In the ground state this is rare since thermodynamically only $1 : 10^9$ bases are in the tautomer form at any given time.

In Fig. 8 we plot the vertical excitation energies (VEE) of the lowest $n\pi^*$, localy excited $\pi\pi*$ excitonic states and charge transfer $\pi\pi*$ states of the Watson-Crick base pair calculated as a function of the N6-H distance of adenine at the CIS(D) level. The chemical structure of the dAdT base-pair is shown in the inset of Fig. 8 along with several key bond distances. In agreement with previous calculations both equilibrium structures were found

slightly buckled and propeller-twisted. Unless otherwise noted, all of our calculations were performed using Hartree-Fock (HF) theory with a high-quality basis (cc-pVDZ). Excited states were determined using a configuration interaction expansion of the wavefunction that included both single and double excitation terms. In addition, the distance between the two fragments, A and T, is shorter in the "rare" tautomer, a feature also calculated by Villani. [31] Particularly, the N6-H-O4 hydrogen bridge in the imino/enol-tautomer is shorter by 0.324 Å compared with the corresponding distance in the Watson/Crick structure.

The energy profile shown in Fig. 8 was constructed by moving the N6 proton of adenine toward thymine and reoptimizing all other bases geometrical parameters. These states are energetically very close together and resolving them accurately requires both large electronic bases-sets, accurate treatment of electronic-correlations, and the inclusion of virtual excitations. Furthermore the influence of these effects is magnified as the system is pushed towards the two conical intersections encountered as we stretch the r_{N6-H} bond. Finally, we found that there is is considerable interplay between the bases and the sugars that we could not simply replace them with methyl groups. The barrier for the double proton transfer dAdT $\rightarrow$ dA*dT* in the ground state calculated at the HF/cc-pVDZ is rather high, 31.1 kcal/mol, while the barrier for the reverse process dA*dT* $\rightarrow$ dAdT calculated at the same level amounts to 14.9 kcal/mol (Fig.8). Especially, the latter barrier is significantly higher compared with the values of 0.2 and 0.02 kcal/mol reported by Gorb et al [32] and Guallar et al, [33] respectively, for a AT base pair without sugars. However, reoptimization of the structures with sugars at the MP2/def-SV(P) level lowers the barriers for the forward and reverse processes to 18.2 and 2.0 kcal/mol respectively.

At the ground state equilibrium geometry, the calculated lowest energy excited state corresponds to the $n\pi*$ state with both the n and $\pi*$ orbitals completely localized on thymine. The $\pi\pi*$ exciton states are just about 0.2–0.4 eV above the $n\pi*$ state. We also determine that the state corresponding to the charge-transfer ($\pi\pi*$ CT) state is approximately 0.6 eV above the $\pi\pi*$ localized exciton states. The vertical excitation energy calculated at CIS(D) level are generally in good agreement with those calculated at the CC2 level for the AT base pair without sugars using similar quality basis set [34]. The primary configurations in all three $\pi\pi^*$ exciton states correspond to electron/hole excitations localized on either thymine or adenine bases. The weights of these configurations are by and large similar, below 50%, producing the $\pi\pi^*$ excited states delocalized over both bases with none of them entirely localized on just one base. The calculated vertical excitation energy of the $\pi\pi^*$ exciton states increase while the vertical excitation of the $\pi\pi*$ CT state decreases with increasing N6–H (adenine) bond distance up to 1.4 Å. As the adenine N6–H bond distance becomes longer this trend is reversed. Furthermore, the character of the excited states also changes. The $\pi\pi*$ exciton states become increasingly localized on just one base either adenine or thymine with the

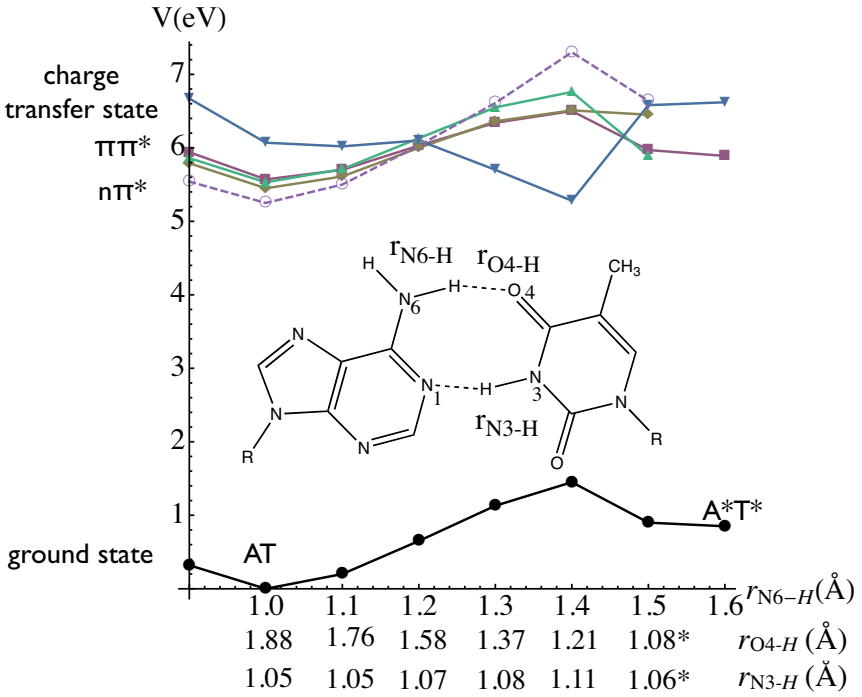

Fig. 8: *Ab initio* ground and excited state potential curves for a dAdT Watson/Crick nucleoside pair along the N6(A)–H stretching coordinate. At each point along the curve, the ground-state geometry was optimized constraining the sugars to their positions in a B-DNA chain.

contribution from the corresponding excitation greater than 80%. Ultimately, this is related to the formation of the tautomer, When the dAdT base pair geometry is reoptimized with the N6–H (adenine) bond distance $r_H = 1.5$ Å the N3 hydrogen of thymine moves over to the other side forming a covalent bond with the adenine N1 to form the imino/enol tautomer.

For purpose of developing a model for DNA excited sates we consider Hamiltonian consisting of interactions between the ground state of a Watson-Crick base pair and lowest energy localy excited (LE) and charge transfer (CT) $\pi\pi^*$ stetes, j_1 and j_2, respectively, on neighboring base pairs. The coupling between the LE and CT $\pi\pi^*$ states is denoted by j_2, while λ introduces coupling between two LE $\pi\pi^{**}$ states localized on neighboring base pairs. Such coupling suggest a The model hamiltonian for N-stacked Watson/Crick bases can be written in the form

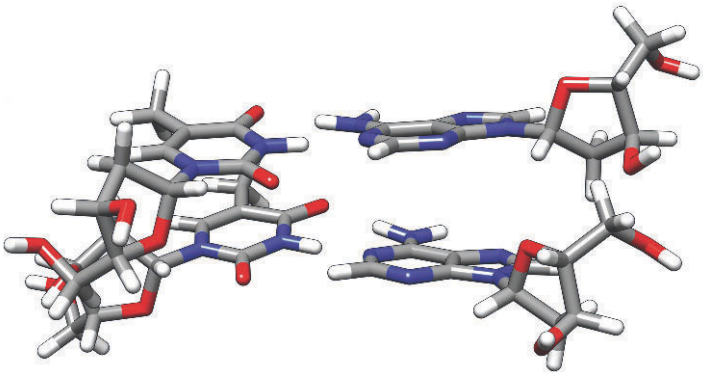

Fig. 9: Geometry of stacked AT nucleosides. In all calculations reported upon here we have fixed the positions of the atoms in the sugars to correspond to their atomic positions in the B-DNA configuration as generated by the X3DNA [35] program.

$$
\begin{aligned}
H &= H_{el} + H_{protons} \\
&= E_g|g\rangle\langle g| + \sum_{n=1}^{N} E_{xt}|e_n\rangle\langle e_n| + E_{ct}|c_n\rangle\langle c_n| + j_1(|e_n\rangle\langle c_n| + h.c.) \\
&+ \sum_{n=1}^{N} \lambda(|e_n\rangle\langle e_{n+1}| + h.c) \\
&+ \sum_{n=1}^{N} j_2(|c_n\rangle\langle g| + h.c) \\
&+ \sum_{n=1}^{N} r_n(g_1|e_n\rangle\langle e_n| + g_2|c_n\rangle\langle c_n|) \\
&+ \frac{1}{2}\sum_{n=1}^{N}(p_n^2 + r_n^2). \qquad (31)
\end{aligned}
$$

The diagonal elements of the model Hamiltonian were taken as the ground-state energy at equilibrium geometry of an isolated AT base pair (E_g), the vertical excitation energies of the localy excited (LE) $\pi\pi^*$ and charge transfer (CT) $\pi\pi^*$ states, $E_{e1,2}$ and $E_{c1,2}$ respectively. The indices 1 and 2 correspond to the respective AT monomers of the dimer. The coordinate r_n is a collective normal-mode coordinate corresponding to the symmetric stretch of the N6–H stretch on A and the N3–H stretch on T. In our model, r_n is taken to be both frequency and mass-scaled. The g_1 and g_2 electron/phonon couplings are related to the distortion molecule along the proton stretching coordinateof the excitonic state and charge-transfer state away from the initial equilibrium geometry of the ground-state. For g_1, we note in Fig. 8 that the geometry of the excitonic state is only slightly distorted and we set $g_1 = 0$. For g_2, we

assume that the ground-state minima corresponding to the imino/enol tautomer is diabatically related to the charge-transfer state in the amino/keto configuration. Thus, we set g_2 by requiring that the diabatic parabola for the charge-transfer state intersect the vertical energy of the charge-transfer state in the amino/keto configuration (E_2) and the ground-state energy (E_r) of the imino/enol configuration. In terms of the dimensionless (mass-frequency scaled variables) $g_2 = \sqrt{2(E_2 - E_r)}$. The off-diagonal coupling elements between the LE $\pi\pi^*$ states (λ) and between the CT and LE $\pi\pi^*$ states (j_2) were calculated using the Transition Density Cube (TDC) method described in [23]. The remaining off diagonal elements j_1 and j_3 were adjusted until satisfactory agreement with *ab initio* data was reached. While the model *certainly* over simplifies the details of the actual potential energy surfaces, we believe that it captures its salient topographical and topological features. A summary of these values is give in Table 1.

The model hamiltonian takes the following form (using dimensionless units for r_n). For a stacked A-T dimer, our model Hamiltonian takes the form:

$$H = \begin{pmatrix} E_g & j_1 & j_3 & j_1 & j_3 \\ j_1 & E_{e1} + g_1 r_1/2 & j_2 & \lambda & 0 \\ j_3 & j_2 & E_{c1} + g_2 r_1/2 & 0 & 0 \\ j_1 & 0 & 0 & E_{e2} + g_1 r_2/2 & j_2 \\ j_3 & 0 & 0 & j_2 & E_{c2} + g_2 r_2/2 \end{pmatrix} + H_{protons} \tag{32}$$

For a dimer, diagonalizing Eq.32 gives a series of 5 energy surfaces corresponding to the ground adiabatic electronic state and 4 excited states as functions of the two proton transfer coordinates r_1 and r_2 as shown in Fig. 10 First, the lowest surface is the potential surface for tautomerization in the ground state. Two minima occur at $(r_1, r_2) = (3, 0)$ and $(0, 3)$ corresponding to one base pair or the other in the tautomer form. However, both excitonic states are unstable with respect to the proton exchange coordinates. Once the system has moved away from the origin along one of the proton-transfer

Table 1: Model Parameters as derived from quantum chemical calculations.

E_1	5.625	Vertical excition energy
E_2	6.371	Vertical CT energy
E_r	1.4 eV	Tautomer energy
λ	200-400 cm^{-1}	coupling between stacked excitonic states
j_1	0	coupling between gs. and local $\pi\pi^*$
j_2	50cm^{-1}	coupling between local $\pi\pi^*$ and local CT
j_3	2500cm^{-1}	coupling between gs. and local CT
g_1	0	distortion of local $\pi\pi^*$
g_2	8	distortion of local CT (equivalent to geometry of tautomer)

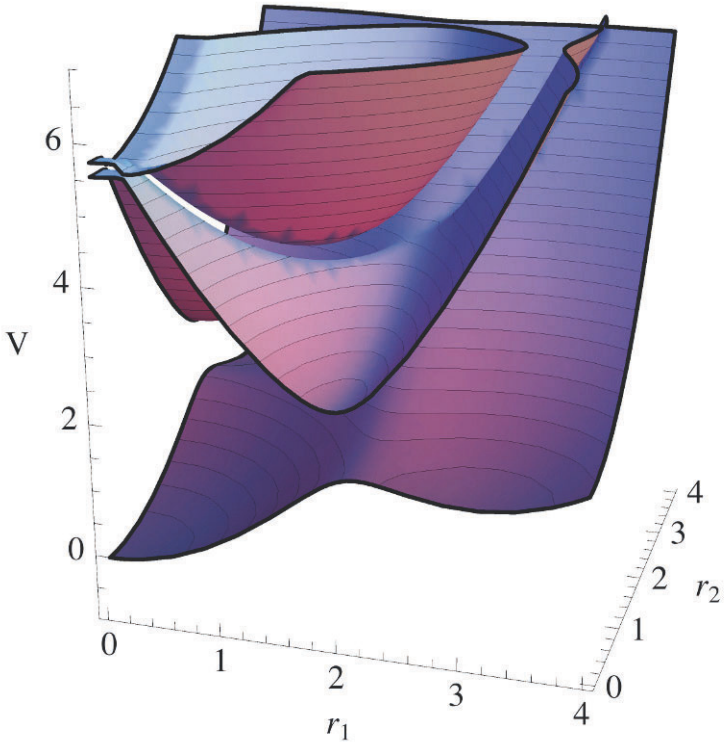

Fig. 10: The three-dimensional potential energy surface describing the motion of protons between N6(A) and O4(T) and between N3(T) and N1(A) shows two critical points in the ground state. The deeper minimum corresponds to the amine/keto structure of AT and a shallow one to the imine/enol structure (A*T*). Upon absorption of a UV photon the initaly delocalized excitonic states (1) undergo a rapid localization on ≈10 ps timescale for single bases and ≈100 ps timescale for stacked base pairs to form a charge transfer (CT) states. The subsequent CT states passing through a conical intersection are carried back to the ground state.

coordinates, the electronic states rapidly localize and we are carried towards the conical intersection between the local CT state and the ground state.

Let us assume that the lifetime of the delocalized state is limited by proton transfer between one of the base pairs such that as soon as one proton coordinate cross the XT/CT intersection, the delocalized state collapses to from a localized state. Assuming the usual Condon separation between the nuclear and electronic dynamics, we can write this within the non-adiabatic Marcus approximation

$$k_{loc} = \frac{2\pi}{\hbar}|V_{ab}|^2 \frac{1}{\sqrt{4\pi E_r k_B T}} e^{-(\Delta E + E_r)^2/(4E_r k_B T)} \tag{33}$$

where $V_{if} = j_2$ is the diabatic coupling. We can estimate this rate by setting the driving force ΔE to be the energy difference between the vertical exciton and the ground-state tautomer and the reorganization energy E_r as $E_r = E_{ct} - E_t$. This sets the time-scale for interbase electron transfer of $\tau = 1/k_{loc} =$ 10.3 ps. This gives a lower limit to the exciton lifetime since even a small error in our values can change this by a factor of 2 to 5. Moreover, for the delocalized case, the coupling matrix element will be at least proportional to the probability for finding the exciton on a given site, $V_{ab} \propto j_2\rho_n$. Thus, for the delocalized case where the exciton is extended over 3–5 bases we expect $\tau \approx 100$ to 250 ps.

In summary, this study combined with our previous study of exciton delocalization in B-DNA chains [23] proposes the following mechanism. Following vertical $\pi - \pi^*$ excitation of an adenosine, the exciton rapidly delocalizes between 3–4 neighboring stacked A's on a time-scale given by the exciton-exciton coupling, λ. The delocalization length is limited by the fact that λ is strongly modulated by the structural fluctuations of the DNA chain about its ideal B-DNA form. This initial delocalization occurs on the femtosecond time-scale. Next, these states are unstable with respect to the fluctuations of the stretching motions of the protons involved in the hydrogen-bonding between the Watson/Crick pairs. This causes a re-localization of the exciton to occur on the time-scale of 10s to 100s of pico-seconds. Subsequent relaxation to the ground-state occurs on a longer time scale as determined by the conical intersection between the CT and the ground-state.

5 Summary

The results described herein paint a similar picture to that described by recent ultrafast spectroscopic investigations of (dA).(dT) oligomers in that the initial excitonic dynamics is dominated by base-stacking type interactions rather than by inter-base couplings. Interchain transfer is multiple orders of magnitude slower than the intrachain transport of both geminate electron/hole pairs as excitons and independent charge-separated species. Indeed, for an exciton placed on the adenosine chain, our model predicts that exciton remains as a largely cohesive and geminate electron/hole pair wave function as it scatters along the adenosine side of the chain. Our model also highlights how the difference between the mobilities in the conduction and valence bands localized along each chain impact the excitonic dynamics by facilitating the break up of the thymidine exciton into separate mobile charge-carriers. In the actual physical system, the mobility of the free electron and hole along the chain will certainly be dressed by the polarization of the medium and reorganization of the lattice such that the coherent transport depicted here will be replaced by incoherent hopping between bases.

Isolating the photoexcitation to the originally excited chain minimizes the potential mutagenenic damage to the DNA sequence since it preserves the complementary chain as an undamaged back-up copy of the genetic information. It is fascinating to speculate whether or not the isolation of a photoexcitation and its photoproducts to the original chain was an early evolutionary selection criteria for the eventual emergence of DNA as the carrier of genetic information.

In conclusion, we present herein a rather compelling model for the short-time dynamics of the excited states in DNA chains that incorporates both charge-transfer and excitonic transfer. It is certainly not a complete model and parametric refinements are warranted before quantitative predictions can be established. For certain, there are various potentially important contributions we have left out: disorder in the system, the fluctuations and vibrations of the lattice, polarization of the media, dissipation, quantum decoherence. We hope that this work serves as a starting point for including these physical interactions into a more comprehensive description of this system.

Note added in proof: Since writing this chapter, we have preformed an extensive series of quantum chemical simulations based upon CIS(D)/cc-pVDZ with MP2 corrected ground states (same basis as used above) on stacks of 4 A-T base pairs in a PCM solvent cavity. Our results indicate that while the excitonic $\pi - \pi^*$ states are energetically lower than the corresponding intra-strand excimers in both single strand (poly A) and double strand DNA (polyA·polyT) as discussed herein, small variations in the hydrogen bonding can rapidly stabilizes the intrastrand excimer state. Similar effects can be seen in CIS(D)/cc-pVDZ calculations of stacked A's which include *explicit* water molecules hydrogen bonded to the bases. This strongly suggests that hydrogen bonding interactions also play a central role in the photophysics of this system.

Acknowledgements

This work was funded by the National Science Foundation and the Robert A. Welch Foundation. ERB also acknowledges the John Simon Guggenheim Foundation. The authors also wish to acknowledge the Texas Center for Learning and Computation (TLC2) for computer support.

References

1. Kelley, S. O.; Barton, J. K. *Science* **1999**, *283*, 375.
2. Crespo-Hernandez, C. E.; Cohen, B.; Kohler, B. *Nature* **2005**, *436*, 1141.
3. Markovitsi, D.; Onidas, D.; Gustovsson, T.; Talbot, F.; Lazzarotto, E. *J. Am. Chem. Soc.* **2005**, *127*, 17130.
4. Markovitsi, D.; Talbot, F.; Gustavsson, T.; Onidas, D.; Lazzarotto, E.; Marguet, S. *Nature* **2006**, *441*, E7.

5. Besaratinia, A.; Synold, T. W.; Chen, H.-H.; Chang, C.; Xi, B.; Riggs, A. *Proc Natl Acad Sci U S A* **2005**, *102*(29), 10058.
6. Sutherland, B. M.; Oliver, R.; Fuselier, C. O.; Sutherland, J. C. *Biochem.* **1976**, *15*(2), 402.
7. Callis, P. R. *Chem. Phys. Lett.* **1979**, *61*, 563–567.
8. Sinha, R. P.; Hädler, D.-P. *Photochem. Photobiol. Sci.* **2002**, *1*, 225–236.
9. Freeman, S. E.; Hacham, H.; Gange, R. W.; Maytum, D. J.; Sutherland, J. C.; Sutherland, B. M. *Proc Natl Acad Sci U S A* **1989**, *86*, 5605–5609.
10. Mouret, S.; Baudouin, C.; Charveron, M.; Favier, A.; Cadet, J.; Douki, T. *Proc Natl Acad Sci U S A* **2006**, *103*(37), 13765.
11. Löwdin, P. O. *Rev. Mod. Phys.* **1963**, *35*, 724.
12. Schultz, T.; Samoylova, E.; Radloff, W.; Ingolf, V. H.; Sobolewski, A. L.; Domcke, W. *Science* **2004**, *306*, 1765–8.
13. Emanuele, E.; Markovitsi, D.; Millie, P.; Zakrzewska, K. *ChemPhysChem* **2005**, *6*, 1387–1393.
14. Crespo-Hernandez, C. E.; Cohen, B.; Kohler, B. *Nature* **2006**, *441*, E8.
15. Pecourt, J.-M.; Peon, J.; Kohler, B. *J. Am. Chem. Soc.* **2001**, *123*.
16. Pecourt, J.-M.; Peon, J.; Kohler, B. *J. Am. Chem. Soc.* **2000**, *122*.
17. Gustavsson, T.; Sharonov, A.; Markovitsi, D. *Chemical Physics Letters* **2002**, *351*(3-4), 195–200.
18. Peon, J.; Zewail, A. H. *Chemical Physics Letters* **2001**, *348*(3-4), 255–262.
19. Douhal, A.; Kim, S. K.; Zewail, A. H. *Nature* **1995**, *378*, 260.
20. Shapiro, S. L.; Campillo, A. J.; Kollman, V. H.; Goad, W. B. *Optics Communications* **1975**, *15*, 308–10.
21. Suhai, S. *International Journal of Quantum Chemistry, Quantum Biology Symposium* **1984**, *11*, 223–35.
22. Krueger, B. P.; Scholes, G. D.; Fleming, G. R. *J. Phys. Chem. B* **1998**, *102*, 5378.
23. Czader, A.; Bittner, E. R. *The Journal of Chemical Physics* **2008**, *128*(3), 035101.
24. Brédas, J.-L.; Cornil, J.; Heeger, A. J. May **1996**, *8*(5), 447–452.
25. Karabunarliev, S.; Bittner, E. R. Aug **2003**, *119*(7), 3988–3995.
26. Karabunarliev, S.; Bittner, E. R. *Physical Review Letters* **2003**, *90*(5), 057402.
27. Santoro, F.; Barone, V.; Improta, R. *Proc Natl Acad Sci U S A* **2007**, *104*(24), 9931–9936.
28. McCammon, J. A.; Harvey, S. C. *Dynamics of proteins and nucleic acids;* Cambridge University Press: Cambridge, 2nd ed., 1987.
29. Bouvier, B.; Gustavsson, T.; Markovitsi, D.; Millie, P. *Chemical Physics* **2002**, *275*, 75–92.
30. Bittner, E. R. *The Journal of Chemical Physics* **2006**, *125*(9), 094909.
31. Villani, G. *Chemical Physics* **2005**, *316*, 1–8.
32. Gorb, L.; Podolyan, Y.; Dziekonski, P.; Sokalski, W. A.; Leszczynski, J. *J. AM. CHEM. SOC.* **2004**, *126*, 10119–10129.
33. Guallar, V.; Douhal, A.; Moreno, M.; Lluch, J. M. *J. Phys. Chem. A* **1999**, *103*, 6251–6256.
34. Perun, S.; Sobolewski, A. L.; Domcke, W. *J. Phys. Chem. A* **2006**, *110*, 9031–9038.
35. Lu, X.-J.; Olson, W. K. *Nucleic Acids Research* **2003**, *31*(17), 5108–5121.

Energy Flow in DNA Duplexes

Dimitra Markovitsi and Thomas Gustavsson

[1] Laboratoire Francis Perrin, CEA/DSM/IRAMIS/SPAM - CNRS URA 2453, CEA/Saclay, 91191 Gif-sur-Yvette, France dimitra.markovitsi@cea.fr
[2] Laboratoire Francis Perrin, CEA/DSM/IRAMIS/SPAM - CNRS URA 2453, CEA/Saclay, 91191 Gif-sur-Yvette, France thomas.gustavsson@cea.fr

Abstract. This chapter focuses on the singlet excited states of model DNA helices with simple base sequence: poly(dGdC).poly(dGdC), poly(dAdT).poly(dAdT) and poly(dA).poly(dT). We discuss their absorption spectra, which reflect the properties of Franck-Condon states, in connection with theoretical studies, performed in the frame of the exciton theory taking into account conformational disorder and spectral broadening. Then we turn to fluorescence properties studied using fluorescence upconversion and time-correlated single photon counting. We review the behavior of the fluorescence decays and we look more closely on the fluorescence anisotropy, explaining how this property can provide information on energy transfer in molecular systems and we show the results obtained in this way for the three examined polymeric helices. Finally, we present a qualitative model describing energy flow in DNA helices; this model involves population of excited states that are delocalized over a few bases, ultrafast (<100 fs) intraband scattering and emission from the lower part of the exciton band.

1 Motivations and simplifications

Two opposite motivations are put forward by researchers who are interested in the excited states of DNA components: on the one hand the stability of the genetic code and on the other the correlation between skin cancer and exposure to ultraviolet radiation. The former position is mainly justified by the extremely short lifetimes of the excited singlet $\pi\pi^*$ states of DNA monomeric components, the nucleotides: 2'-deoxyadenosine 5'-monophosphate (dAMP), thymidine 5'-monophosphate (TMP), 2'-deoxyguanosine 5'-monophosphate (dGMP), and 2'-deoxycytidine 5'-mono-phosphate (dCMP). Indeed, femtosecond spectroscopic measurements have shown that the deactivation of these excited states in aqueous solution takes place in less that 1 ps [1–6]. However, when these chromophores are organized in double helices, long-lived components are detected in the transient signals [7–13]. Although it has been suggested that such long-lived species correspond to UV-protecting excimers [8], there is no doubt that absorption of UV radiation by DNA bases does trigger

I. Burghardt et al. (eds.), *Energy Transfer Dynamics in Biomaterial Systems*, Springer Series in Chemical Physics 93, DOI 10.1007/978-3-642-02306-4_5,

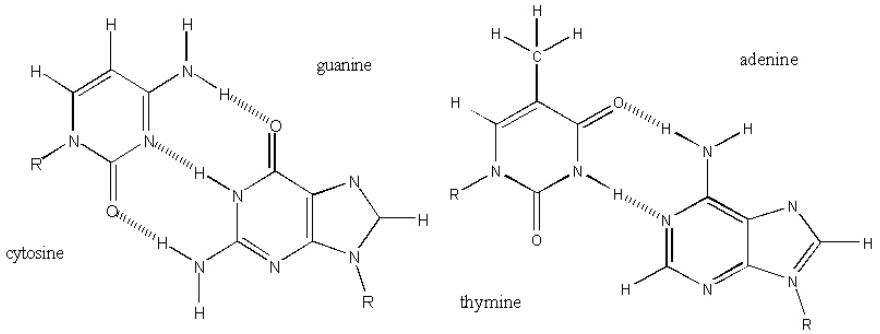

Fig. 1: Watson-Crick guanine-cytosine (G-C) and adenine-thymine (A-T) base-pairs.

photochemical reactions [14–17]. Fortunately, the action of repair enzymes reduces the probability for the appearance of carcinogenic mutations. But these reactions remain a major problem for the experimentalist who studies interaction of UV-induced processes in DNA helices. Therefore, specific care has to be taken in order to avoid photodamage during the collection of data, especially when high intensity lasers are used for their study [18]. The price to pay is simply the cost of large amounts of duplexes rendering these technically delicate experiments also awfully expensive.

No matters the philosophical considerations or concerns for public health, the fact is that the primary photoprocesses occurring in double helices following photon absorption by the letters of the genetic code remain still poorly understood. The methodology followed by us and other groups for their elucidation consists in studying model helices composed of only one type of base-pairs, guanine-cytosine or adenine-thymine Fig. 1, arranged in homopolymeric or alternating sequence (Fig. 2). Dealing with two chromophores instead of four and arranged in a repetitive manner simplifies somewhat this extremely complex problem. [19]

The above described model sequences have been studied both as oligomers [7, 8, 11–13, 19] and as polymers [9, 11, 20]. An increase in the size of the helix is known to reinforce its stability, as revealed by their melting curves [18] and attested by X-ray diffraction measurements in solution [21]. Therefore, in this chapter we focus on the polymeric duplexes poly(dGdC).poly(dGdC) [≡ 1000 base-pairs], poly(dAdT).poly(dAdT) [≡ 200-400 base-pairs] and poly(dA).poly(dT) [≡ 2000 base-pairs] studied by us. First we discuss the absorption spectra, which reflect the properties of Franck-Condon states, in connection with theoretical studies. Then we turn to fluorescence properties: fluorescence intensity decays (hereafter called simply "fluorescence decays"), fluorescence anisotropy decays and time-resolved fluorescence spectra. We

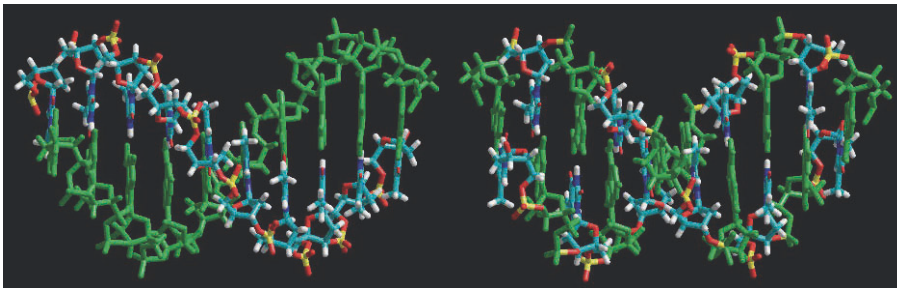

Fig. 2: Schematic representations of two model duplexes composed of homopolymeric and alternating adenine-thymine base-pairs; for clarity adenines are shown in green.

present the two techniques we use to study excited state relaxation, fluorescence upconversion (FU, also called sum-frequency generation technique) and time-correlated single photon counting (TCSPC). We discuss their respective advantages and drawbacks. We review the behavior of the fluorescence decays recorded by FU for the three types of base sequence. For one of these systems, poly(dA).poly(dT), which was more thoroughly studied [9, 10], we comment on the fluorescence spectra and the fluorescence decays recorded over a large time domain, from the femtosecond to the nanosecond time-scales. Finally, we look more closely on the fluorescence anisotropy, explaining how this property can provide information on energy transfer in molecular systems and we show the results obtained in this way for the three examined polymeric helices.

2 Absorption spectra: the *sine qua non* starting point

The knowledge of the excited states which are initially populated by the laser beam is a necessary condition in a time-resolved experiment aiming to elucidate energy flow in DNA helices. A commonly accepted idea since the 1960s is that excited states of DNA helices are localized on single bases because the DNA absorption spectrum resembles the sum of the spectra of its monomeric constituents. However, a careful inspection of the Fig. 3, where the spectrum of each polymeric duplex is compared with that of an equimolar mixture of the corresponding nucleotides, clearly shows that this is not the case. The most striking feature of the duplex spectra is the weaker values of the molar absorption coefficients around the maximum. This so-called DNA hypochromism has been largely exploited in biochemistry in order to study the stability of the duplexes by recording their melting curves (variation of the absorbance as a function of temperature). But for a long time this empirical observation was not correlated with the excited states properties although it was known that a loss of oscillator strength may result from interchromophore charge transfer states as evidenced in other systems (see for example Ref. [22]). The first attempt to rationalize DNA hypochromism was made by Starikow who studied

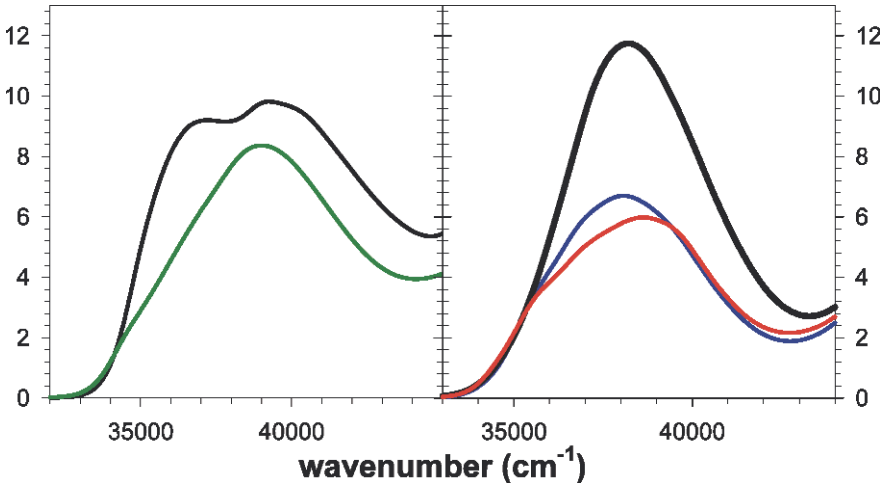

Fig. 3: Experimental absorption spectra obtained for poly(dGdC).poly(dGdC) (green), poly(dAdT).poly(dAdT) (blue) and poly(dA).poly(dT) (red) in phosphate buffer. Spectra in black correspond to an equimolar mixture of nucleotides (left: dGMP and dCMP; right: dAMP and dCMP). Molar absorption coefficients are given per base.

base-pairs and dimers of base pairs [23]. Later came a work by Varsano et al. [24] and more recently by Santoro et al. who reproduced the absorption spectrum of an adenine single strand [25]. To this date the calculation of realistic absorption spectra of duplexes including charge transfer interactions among bases remains an important challenge for theoreticians.

Besides charge transfer interactions, dipolar coupling between $\pi\pi^*$ transitions of bases may lead to delocalization of the excited states. In order to obtain some guidelines for our experimental studies, we have undertaken the calculation of excited Frank-Condon states within the framework of the exciton theory [26]. These studies were enriched by combining data from quantum chemistry and molecular dynamics calculations in collaboration with Krystyna Zakrzewska and Richard Lavery [26, 27, 27–29]. The general formalism is described in the Chapter by E. Bittner and A. Czader in the present volume.

Below we summarize the specific conditions used in our calculations, we underline the approximations made and we focus on the conclusions which are connected directly to experimental observables. Our calculations were performed for the alternating duplexes $(dCdG)_5.(dCdG)_5$ and $(dAdT)_5.(dAdT)_5$ and the homopolymeric one $(dA)_{10}.(dT)_{10}$.

We consider two electronic transitions for each guanine and adenine chromophore and one for each cytosine and thymine chromophore. The dipolar coupling among all the pairs of the thirty transitions was considered and

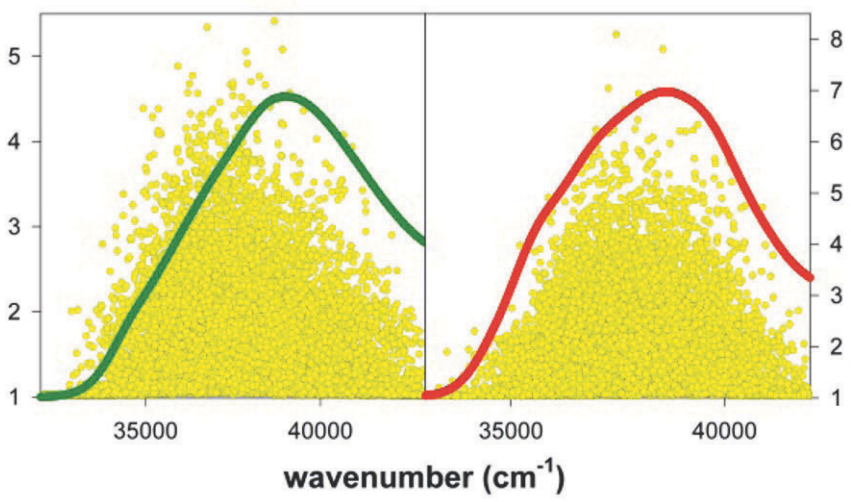

Fig. 4: Experimental absorption spectra of poly(dGdC).poly(dGdC) (green, left) and poly(dA).poly(dT) (red, right) shown together with the participation ratio of various eigenstates calculated for $(dCdG)_5.(dCdG)_5$ and $(dA)_{10}.(dT)_{10}$, respectively. The position of the circles corresponds to the excitation energy of the associated eigenstates resulting from diagonalization of 500 exciton matrices simulating diagonal disorder.

calculated using atomic transition charges (off-diagonal terms of the exciton matrix); we demonstrated that the point dipole approximation is not valid for closely lying bases (Fig. 4 in Ref. [26]). The geometry of the duplexes in their ground state was determined from molecular dynamics simulations including water and counter ions; one hundred conformations were calculated for each base sequence. The diagonal terms of the exciton matrix were represented by Gaussian functions whose maximum and width were derived from the absorption spectra of the nucleotides in solution.

The most important conclusions of this part are as follows:

- The dipolar coupling alone is capable to induce delocalization of the excited states over a few bases even in the presence of spectral broadening. The extent of the Franck-Condon states may reach up to 7-8 sites, but the participation ratio averaged over the ensemble of the eigenstates is close to two. However, it should be stressed that the calculated degrees of delocalization are underestimated because dispersion in diagonal terms was represented by the experimental spectral width including both homogeneous and inhomogeneous broadening.
- Although this type of modeling does not take into account orbital overlap and neglects higher order $\pi\pi^*$ transitions, the calculated spectra repro-

duce two trends observed in the experimental spectra. First, the spectrum of (dA)10(dT)10 is located to higher energies with respect to that of$(dA)_{10}.(dT)_{10}$ [27]. Second, the barycentre of the $(dCdG)_5.(dCdG)_5$ spectrum is blue-shifted compared to that of non interacting dGMP and dCMP (Fig. 3).

- The absorption spectrum of each duplex is the envelop of a large number of transitions corresponding to the energy distribution of the thirty eigenstates characterizing each conformation. Their dispersion in energy arises from both conformational disorder and spectral broadening, the latter contribution being by far more important.
- The most delocalized excited states are located near the absorption maximum (Fig. 4).

Having, thus demonstrated the delocalized nature of the Franck-Condon excited states, it was a challenge to probe experimentally the dynamics of energy transfer in the DNA helices.

3 Time-resolved fluorescence: one laser, two detection techniques

When deciding to study the dynamics of electronic excitation energy transfer in molecular systems by "conventional" spectroscopic techniques (in contrast to those based on non-linear properties such as photon echo spectroscopy) one has the choice between time-resolved fluorescence and transient absorption. This choice is not inconsequential because the two techniques do not necessarily monitor the same populations. Fluorescence is a very sensitive technique, in the sense that single photons can be detected. In contrast to transient absorption, it monitors solely excited state populations; this is the reason for our choice. But, when dealing with DNA components whose quantum yield is as low as 10^{-4}, [3,30] such experiments are far from trivial.

Our objective was to probe fluorescence over a time domain as large as possible. To this end we combined two different detection techniques, FU and TCSPC, allowing us to perform measurements from 100 fs to hundreds of nanoseconds. Notably, we use the same laser excitation source: the third harmonic of a titane:sapphire laser (267 nm, 100 fs). This is important because the excited state population is created under identical conditions in the two types of experiments. The time-resolution obtained after deconvolution of the recorded signals is 100 fs and 10 ps for FU and TCSPC, respectively. For reasons explained below, FU only detects emission corresponding to highly allowed transitions. TCSPC, on the other hand, is capable to monitor not only allowed but also very weak or forbidden transition. Therefore, particular care must be taken when merging data obtained by these two techniques as described in Ref. 10.

While TCSPC is a well-known and commercially available technique, our FU setup is "special" in the sense that it allows the recording not only decays

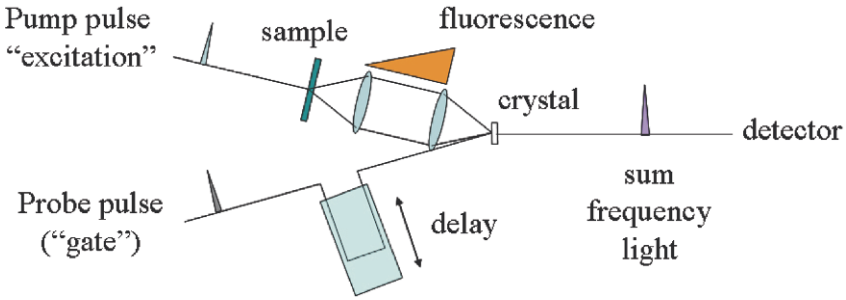

Fig. 5: Schematic view of a fluorescence upconversion setup.

but also time-resolved fluorescence spectra in the UV region [31]. FU is an all-optical pump-probe technique relying on ultrashort laser pulses, but contrary to the transient absorption technique, the probe pulse does not interrogate the photoexcited sample but the emitted fluorescence. This is realized by an optical mixing of the fluorescence and the probe pulse in a non-linear crystal. Since the sum-frequency generation is only active during the passage of the probe pulse, one can say that the probe pulse "opens a door" in the crystal providing an excellent time-resolution only limited by the temporal width of the laser pulse. Consequently, the photon flux during this time-window has to be very large, which is only the case of allowed transitions. A schematic view of a fluorescence upconversion setup is shown in Fig. 5. Examples of time-resolved spectra recorded by FU are shown in Fig. 6.

4 The unbearable complexity of the emission decays

The fluorescence decays of all three polymeric duplexes exhibit a strong dependence with the emission wavelength: as the wavelength increases the decays become slower. In the case of poly(dA).poly(dT), which has been studied systematically over a large time domain by both FU and TCSPC, at least four exponentials are needed for their fit [9, 10]. Most of the resulting time constants, ranging from 100 fs to a few nanoseconds, vary with the wavelength. Such parametric adjustments allow a quantitative description of the decays but they do not necessarily correspond to precise emitting states.

Despite the above mentioned complexity, it is possible to make some qualitative observations by focusing on the decays recorded by FU at 330 nm (30300 cm^{-1}) e.g. close to the maximum of the time-resolved spectra obtained by the same technique (Fig. 6). Fig. 7 shows the fluorescence decays

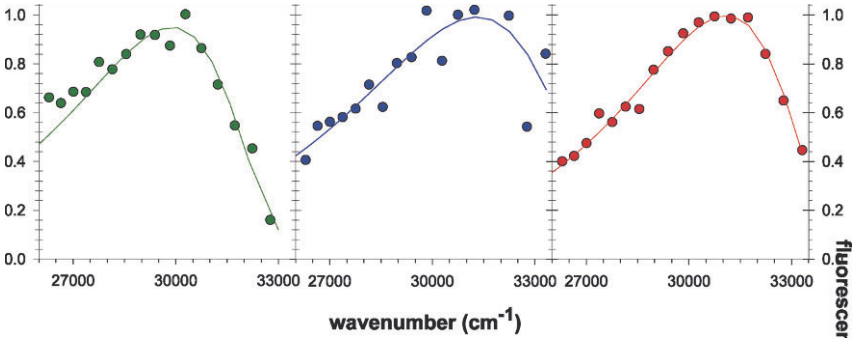

Fig. 6: Time-resolved fluorescence spectra obtained for poly(dGdC).poly(dGdC) (green), poly(dAdT).poly(dAdT) (blue) and poly(dA).poly(dT) (red) in phosphate buffer at zero-time. Circles correspond to experimental data and solid lines to fits with log-normal functions. Excitation wavelength: 267 nm.

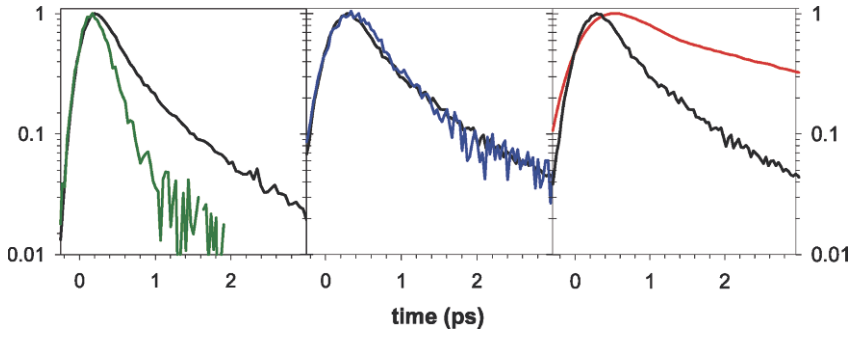

Fig. 7: Fluorescence decays obtained for poly(dGdC).poly(dGdC) (green), poly(dAdT).poly(dAdT) (blue) and poly(dA).poly(dT) (red) in phosphate buffer. Black signals correspond to an equimolar mixture of nucleotides (left: dGMP and dCMP; center and right: dAMP and TMP). Excitation wavelength: 267 nm. Emission wavelength: 330 nm.

recorded for the three examined polymers by FU with those obtained for an equimolar mixture of nucleotides. We remark a progression when going from poly(dGdC).poly(dGdC) to poly(dAdT).poly(dAdT) and poly(dA).poly(dT). Not only the decays of the duplexes become slower, but also their relation with the behavior of non-interacting chromophores is modified: the average lifetime is successively shorter, equal or longer indicating the presence of different sequence dependent deactivation processes.

As mentioned above, emission detected by FU is correlated with excited states carrying substantial oscillator strength. They correspond to $\pi\pi^*$ states, which may be delocalized or localized and have a partial charge transfer character. The signals in Fig. 7 reveal that the deactivation of $\pi\pi^*$ is accelerated in alternating G-C helices. An acceleration of the excited state dynamics within Watson-Crick G-C pairs was predicted by theoretical calculations who underlined the role of interbase proton transfer [32–34] and was confirmed by fluorescence measurement carried out for isolated base-pairs dissolved in chloroform [35]. The effect of mixed sequences on the excited state relaxation of oligomeric duplexes has been investigated recently by FU [36]. In spite of the growing number of experimental data of fluorescence decays of various DNA double strands, it is impossible to directly link them to an energy transfer process among bases.

Contrary to FU, the decays of the duplexes detected by TCSPC contain also contributions from excited states carrying very weak oscillator strength. These may be delocalized $\pi\pi^*$ exciton states located at the bottom of the exciton band, charge transfer states or combination of both. It is worth-noticing that in the case of poly(dA).poly(dT), a time constant equal to 2.3 ± 0.1 ns has been determined from the fit of the decays recorded at different wavelengths with exponential functions. Its weight increases with the wavelength with a maximum around 420 nm. These characteristics point towards emission from a fully developed excimer. Interestingly, its lifetime is much longer than the excimers detected in $(dA)_{18}\cdot(dT)_{18}$ (150 ps) by transient absorption [8].

5 Fluorescence anisotropy: a precious witness

As we explained in the previous section, fluorescence decays do not bring any direct evidence about energy transfer among DNA bases within a helix. In contrast, fluorescence anisotropy decays can provide this type of information. Such a possibility is based on the correlation of macroscopic observables to molecular parameters. On the molecular scale, r is related to the angle θ formed between the transition dipoles associated to photon absorption and photon emission:

$$r = 1/5(3\cos 2\theta - 1)$$

The limiting values of the fluorescence anisotropy are 0.4 and -0.2, corresponding to parallel and perpendicular absorption and emission dipoles, respectively. For a chromophore undergoing internal conversion, the change in angle between the two vectors can be instantaneous. It may also be caused by energy transfer or physical motion. On the laboratory scale, the time-resolved anisotropy decay is determined as:

$$r(t) = \frac{I(t)_{||} - I(t)_{\perp}(t)}{I(t)_{||} + 2I(t)_{\perp}(t)}$$

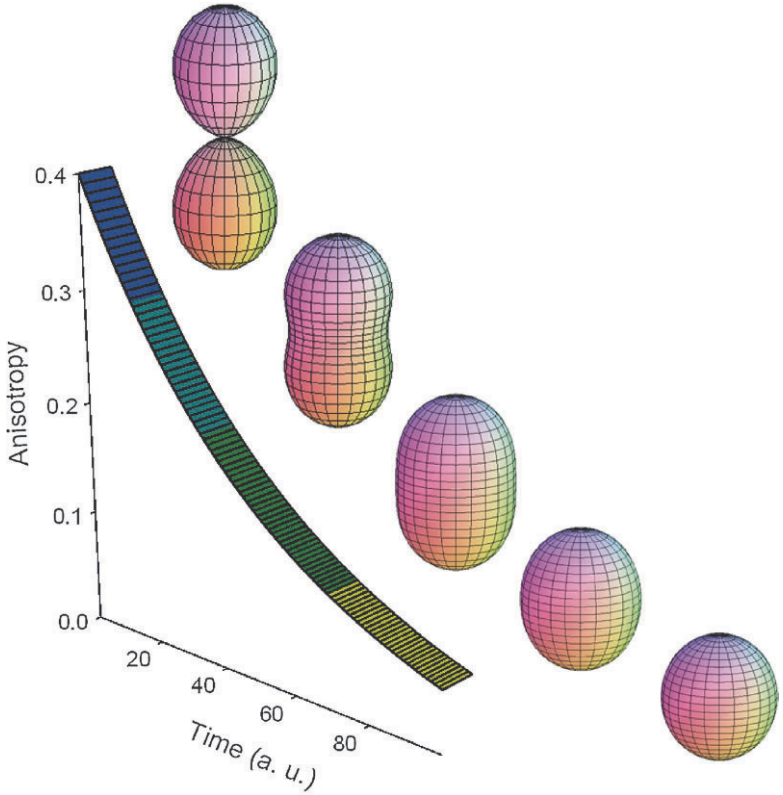

Fig. 8: Schematic view of the time-evolution of a spatial distribution of a transition dipole and the corresponding drop in fluorescence anisotropy.

where $I(t)_{||}$ and $I(t)_{\perp}$ are the fluorescence decays recorded by using at the detection side a polarizer respectively parallel or perpendicular to the polarization of the laser beam. In the case of fluid solutions, the anisotropic distribution of the emitting state of a given chromophore is gradually lost due to the rotational diffusion, which is evidently reflected by a drop in fluorescence anisotropy as depicted in Fig. 8.

The same effect is produced if, instead of physical rotation of the chromophore, energy transfer takes place among them. A randomization of the emitting dipoles in a three-dimensional space results to a limiting value of r equal to zero. If the transport process involves transition dipoles orthogonal to an axis, the limiting value of r is equal to 0.137. The loss of anisotropy

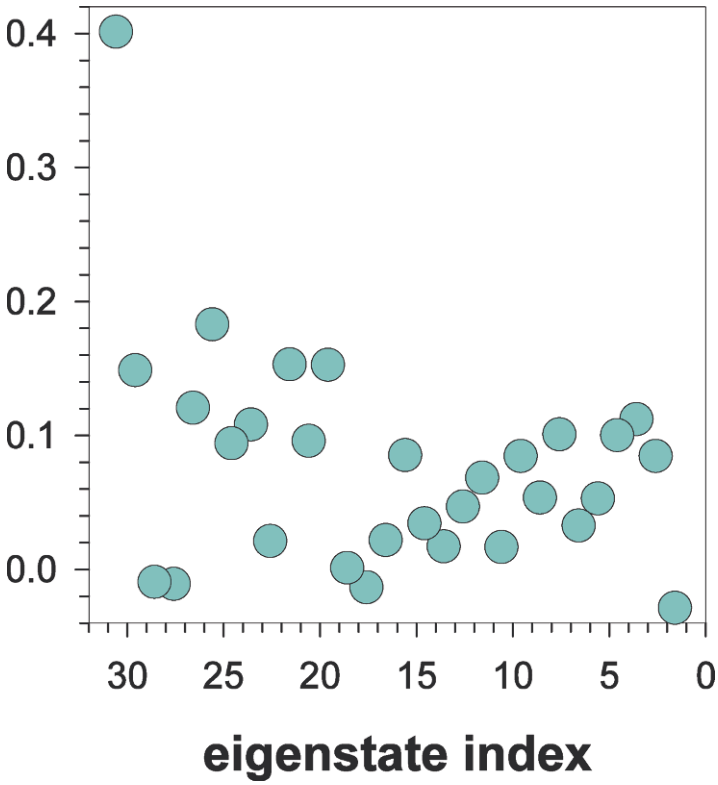

Fig. 9: "Fluorescence anisotropy" calculated for each one of the thirty eigenstates of $(dAdT)_5.(dAdT)_5$ with respect the highest eigenstate $\langle 30 \rangle$. This is defined as $r_{i,30} = 1/5(3cos2\theta_{i,30} - 1)$, where $\theta_{i,30}$ is the angle formed between the vectors of the transitions $< 0 > \rightarrow < k >$ and $< 0 > \rightarrow < 30 >$.

characterizes energy transfer involving either localized or delocalized excited states.

Fig. 9 shows the "fluorescence anisotropy" calculated for a given ground state conformation of $(dAdT)_5.(dAdT)_5$. We suppose that excitation populates only the highest eigenstate ($\langle 30 \rangle$). If emission arises from any of the lower eigenstates, r is expected to be drastically lower.

From an experimental point of view, if we want to establish whether a loss of anisotropy is due to rotational diffusion or to energy transfer, we must probe very short times when molecular motions are inhibited. This is precisely what we did by observing fluorescence anisotropy on the sub-picosecond time-

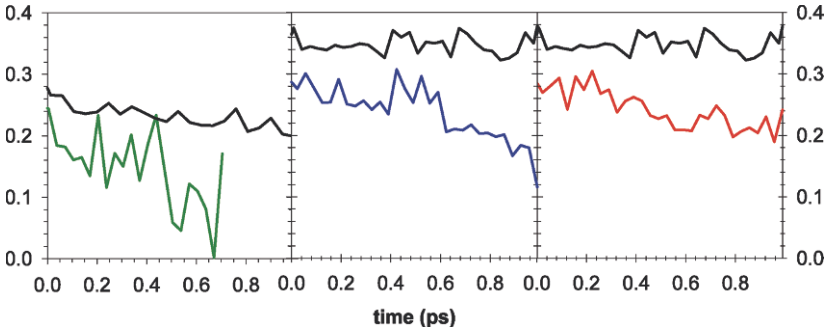

Fig. 10: Fluorescence anisotropy decays obtained for poly(dGdC).poly(dGdC) (green), poly(dAdT).poly(dAdT) (blue) and poly(dA).poly(dT) (red) in phosphate buffer. Black signals correspond to an equimolar mixture of nucleotides (left: dGMP and dCMP; center and right: dAMP and TMP). Excitation wavelength: 267 nm. Emission wavelength: 330 nm.

scale. Again it was important to compare the behavior of the helices with that of non-interacting chromophores. The r values of an equimolar mixture of nucleotides depend on the r values and the lifetimes of the purine and the pyrimidine composing each Watson-Crick pair. It is higher for the dAMP/TMP mixture compared to the dGMP/dCMP one (Fig. 10). The anisotropy of all three polymeric duplexes, the fluorescence anisotropy is clearly lower than that of non-interacting chromophores and it decays more rapidly. Knowing that rotational diffusion is much slower for double helices than for free nucleotides, the anisotropy decays clearly show that energy transfer takes place within the helices on the sub-picosecond time-domain. The anisotropy values detected for the helices are lower than that of the nucleotide mixture already at zero-time. This means that the onset of energy transfer occurs at times shorter than the 100 fs, time-resolution of our setup. Such an ultrafast energy transfer cannot take place via Förster transfer considering, in particular, the very large Stokes shift associated with the monomeric chromophores [3].

6 Just a qualitative picture...

The ensemble of the experimental results briefly reviewed here, e.g. steady-state absorption and fluorescence spectra, fluorescence decays, fluorescence anisotropy decays and time-resolved fluorescence spectra, allow us to draw a qualitative picture regarding the excited state relaxation in the examined polymeric duplexes. Our interpretation is guided by the theoretical calculation of the Franck-Condon excited states of shorter oligomers with the same base sequence.

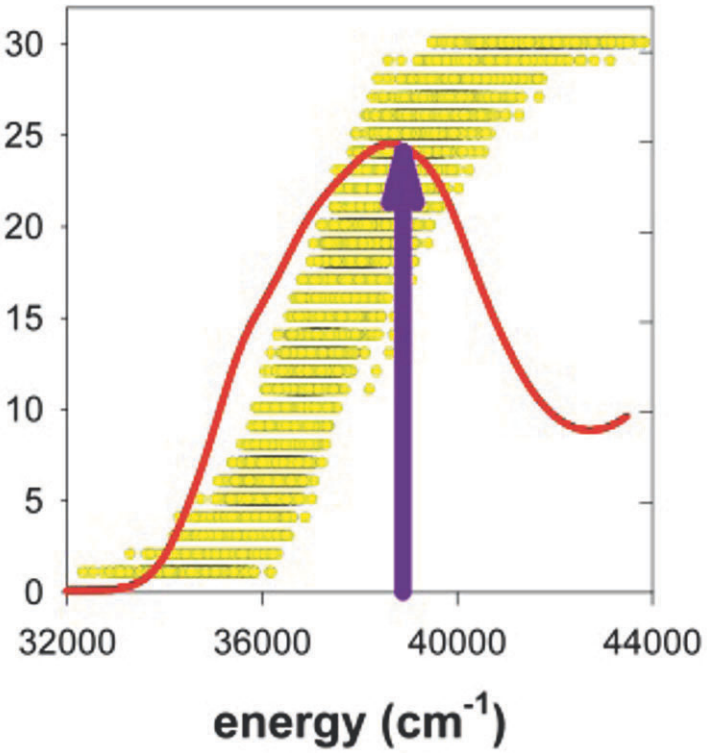

Fig. 11: Illustration of the excited state relaxation derived from experimental results obtained for poly(dA).poly(dT) by steady-state absorption and fluorescence spectroscopy, fluorescence upconversion and based on the modeling of the Franck-Condon excited states of $(dA)_{10}(dT)_{10}$. In red (full line): experimental absorption spectrum; yellow circles arranged at thirty steps represent the eigenstates, each circle being associated with a different helix conformation and chromophore vibrations.

The laser beam at 267 nm populates a large number of excited states, each one connected with a particular conformation of the helix and vibrations of the involved chromophores (simulated by the spectral width). Most of these states are delocalized over a few bases. Then, intraband scattering takes place and emission arises from excited states located at the bottom of the exciton band; these low-lying states have, in general, different polarization from the initially populated states and lead to a loss of anisotropy. Intraband scattering is obviously faster than 100 fs because, at that time, the anisotropy of the

helices is lower than that found for an equimolar mixture of nucleotides. In the case of poly(dA).poly(dT), this is also attested by the fact that the shape and quantum yield of the steady-state state fluorescence spectra do not vary with the excitation wavelength, proving that emission arises always from the same distribution of excited states no matters of the initially excited population. Moreover, the various emitting states have different lifetimes, explaining the wavelength dependence of the fluorescence properties. On the picosecond and nanosecond time-scales, conformational motions interfere with the purely electronic processes. These may result to localization of exciton states and formation of fully developed excimers and/or assist further energy transfer. The complexity of the fluorescence lifetimes reflects all these intricate processes.

The picture of energy flow drawn here is just qualitative. The development of theoretical models which started to appear [38, 39] is blatantly needed in order to get a detailed description of energy flow in DNA.

Acknowledgements

We gratefully acknowledge the contribution of our colleagues and co-workers who participated in this work: Akos Banyasz, Benjamin Bouvier, Delphine Onidas, Emanuela Emanuele, Elodie Lazzarotto, Sylvie Marguet, Fran cois-Alexandre Miannay, Philippe Millié, Alexei Sharonov and Francis Talbot from the Francis Perrin Laboratory; Richard Lavery and Krystyna Zakrzewska (Institut de Biologie et Chimie des Protéines, Lyon).

References

1. Pecourt, J.-M. L.; Peon, J.; Kohler, B. J. Am. Chem. Soc. 2000, 122, 9348-9349.
2. Pecourt, J.-M. L.; Peon, J.; Kohler, B. J. Am. Chem. Soc. 2001, 123, 10370-10378.
3. Onidas, D.; Markovitsi, D.; Marguet, S.; Sharonov, A.; Gustavsson, T. J. Phys. Chem. B 2002, 106, 11367- 11374.
4. Gustavsson, T.; Sharonov, A.; Markovitsi, D. Chem. Phys. Lett. 2002, 351, 195-200.
5. Gustavsson, T.; Sharonov, A.; Onidas, D.; Markovitsi, D. Chem. Phys. Lett. 2002, 356, 49-54.
6. Gustavsson, T.; Banyasz, A.; Lazzarotto, E.; Markovitsi, D.; Scalmani, G.; Frisch, M. J.; Barone, V.; Improta, R. J. Am. Chem. Soc. 2006, 128, 607-619.
7. Markovitsi, D.; Sharonov, A.; Onidas, D.; Gustavsson, T. ChemPhysChem 2003, 3, 303-305.
8. Crespo-Hernández, C. E.; Cohen, B.; Kohler, B. Nature 2005, 436, 1141-1144.
9. Markovitsi, D.; Onidas, D.; Gustavsson, T.; Talbot, F.; Lazzarotto, E. J. Am. Chem. Soc. 2005, 127, 17130-17131.
10. Markovitsi, D.; Gustavsson, T.; Talbot, F. Photochem. and Photobiol. Sci. 2007, 717 - 724.

11. Onidas, D.; Gustavsson, T.; Lazzarotto, E.; Markovitsi, D. Phys. Chem. Chem. Phys. 2007, 9, 5143-5148.
12. Onidas, D.; Gustavsson, T.; Lazzarotto, E.; Markovitsi, D. J. Phys. Chem. B 2007, 111, 9644-9650.
13. Buchvarov, I.; Wang, Q.; Raytchev, M.; Trifonov, A.; Fiebig, T. Proc. Natl. Acad. Sci. 2007, 104, 4794-4797.
14. Ravanat, J.-L.; Douki, T.; Cadet, J. J. Photochem. Photobiol., B: Biology 2001, 63, 1011-1344.
15. Douki, T. J. Photochem. Photobiol B: Biology 2006, 82, 45-52.
16. Malone, M. E.; Cullis, P. M.; Symons, M. C. R.; Parker, A. W. J. Phys. Chem. 1995, 99, 9299-9308.
17. Schreier, W. J.; Schrader, T. B.; Koller, F. O.; Gilch, P.; Crespo-Hernades, C.; Swaminathan, V. N.; Carell, T.; Zinth, W.; Kohler, B. Science 2007, 315, 625-629.
18. Markovitsi, D.; Onidas, D.; Talbot, F.; Marguet, S.; Gustavsson, T.; Lazzarotto, E. J. Photochem. Photobiol. A: Chem. 2006, 183, 1-8.
19. Markovitsi, D.; Talbot, F.; Gustavsson, T.; Onidas, D.; Lazzarotto, E.; Marguet, S. Nature 2006, 441, E7.
20. Miannay, F. A.; Banyasz, A.; Gustavsson, T.; Markovitsi, D. J. Am. Chem. Soc. 2007, 129, 14574-14575.
21. Zuo, X.; Cui, G.; Merz Jr., K. M.; Zhang, L.; Lewis, F. D.; Tiede, D. M. Proc. Natl. Acad. Sci. 2006, 103, 3534-3539.
22. Scholes, G. D.; Ghiggino, K. P. J. Phys. Chem. 1994, 98, 4580-4590.
23. Starikov, E. B. Modern Phys. Lett. B 2004, 18, 825-831.
24. Varsano, D.; Di Felice, R.; Marques, M. A. L.; Rubio, A. J. Phys. Chem. B 2006, 110, 7129-7138.
25. Santoro, F.; Barone, V.; Improta, R. Proc. Natl. Acad. Sci. 2007, 104, 9931-9936.
26. Bouvier, B.; Gustavsson, T.; Markovitsi, D.; Millié, P. Chem. Phys. 2002, 275, 75-92.
27. Bouvier, B.; Dognon, J. P.; Lavery, R.; Markovitsi, D.; Millié, P.; Onidas, D.; Zakrzewska, K. J. Phys. Chem. B 2003, 107, 13512-13522.
28. Emanuele, E.; Markovitsi, D.; Millié, P.; Zakrzewska, K. ChemPhysChem 2005, 6, 1387-1392.
29. Emanuele, E.; Zakrzewska, K.; Markovitsi, D.; Lavery, R.; Millie, P. J. Phys. Chem. B 2005, 109, 16109-16118.
30. Vigny, P.; Ballini, J. P. In Excited states in organic chemistry and biochemistry; Pullman, B., Goldblum, N., Eds.; D. Reidel Publishing Company: Doordrecht, Holland, 1977.
31. Gustavsson, T.; Cassara, L.; Gulbinas, V.; Gurzadyan, G.; Mialocq, J.-C.; Pommeret, S.; Sorgius, M.; van der Meulen, P. J. Phys. Chem. A 1998, 102, 4229-4245.
32. Sobolewski, A. L.; Domcke, W. Phys. Chem. Chem. Phys. 2004, 6, 2763-2771.
33. Sobolewski, A. L.; Domcke, W.; Hättig, C. Proc. Natl. Acad. Sci. 2005, 102, 17903-17906.
34. Groenof, G.; Schäfer, L. V.; Boggio-Pasqua, M.; Goette, M.; Grubmüller, H.; Robb, M. A. J. Am. Chem. Soc. 2007, 129, 6812-6819.
35. Schwalb, N.; Temps, F. J. Am. Chem. Soc. 2007, 129, 9272-9273.
36. Schwalb, N. K.; Temps, F. Science 2008, 322, 243-245.
37. Markovitsi, D.; Germain, A.; Millie, P.; Lécuyer, I.; Gallos, L.; Argyrakis, P.; Bengs, H.; Ringsdorf, H. J. Phys. Chem. 1995, 99, 1005-1017.

38. Bittner, E. R. J. Chem. Phys. 2006, 125, 094909 (1-12).
39. Bittner, E. R. J. Photochem. Photobiol. A: Chem. 2007, 190, 328-334.

Anharmonic Vibrational Dynamics of DNA Oligomers

O. Kühn, N. Došlić, G. M. Krishnan, H. Fidder, K. Heyne

[1] Institut für Physik, Universität Rostock, Universitätsplatz 3, 18055 Rostock, Germany
oliver.kuehn@uni-rostock.de
[2] Department of Physical Chemistry, Rudjer Bošković Institute, 10000 Zagreb, Croatia
[3] Institut für Chemie und Biochemie, Freie Universität Berlin, Takustr. 3, 14195 Berlin, Germany
[4] Institut für Physik, Freie Universität Berlin, Arnimallee, 14195 Berlin, Germany
heyne@physik.fu-berlin.de

Abstract. Combining two-color infared pump-probe spectroscopy and anharmonic force field calculations we characterize the anharmonic coupling patterns between fingerprint modes and the hydrogen-bonded symmetric ν_{NH_2} stretching vibration in adenine-thymine dA_{20}-dT_{20} DNA oligomers. Specifically, it is shown that the anharmonic coupling between the δ_{NH_2} bending and the $\nu_{C4=O4}$ stretching vibration, both absorbing around 1665 cm^{-1}, can be used to assign the ν_{NH_2} fundamental transition at 3215 cm^{-1} despite the broad background absorption of water.

1 Introduction

Vibrational energy redistribution and relaxation in complex systems depends on the network of anharmonically coupled vibrational states subject to fluctuations due to the interaction with some environment [1]. Focussing on hydrogen-bonded systems there is considerable evidence that the time scales for relaxation can be in the subpicosecond range pointing to a rather strong interaction, e.g., of the excited stretching vibration with other hydrogen bond (HB) related modes such as the bending and the low-frequency HB distance vibration as well as with the solvent [2–6].

One of the most prominent hydrogen-bonded systems is DNA. Despite numerous experimental and theoretical investigations on vibrational spectra of nucleic acid bases [7–13], information on inter- and intramolecular interactions in base pairs and DNA oligomers is still limited [14–25]. A recent example is the work on single adenine-uracil (AU) base pairs in the Watson-Crick geometry in solution, which showed an enhancement of vibrational energy

I. Burghardt et al. (eds.), *Energy Transfer Dynamics in Biomaterial Systems*, Springer Series in Chemical Physics 93, DOI 10.1007/978-3-642-02306-4_6,

relaxation of the NH stretching vibration by a factor of three as compared to the isolated uracil base [21].

DNA oligomers adopt different types of conformations, both in gas and condensed phases, such as the A, B, B', C, D, and Z form, depending on water and salt concentration, type of cations, pH, and base sequences [8, 12, 25–29]. In the condensed phase the conformations of DNA oligomers are stabilized by water molecules that form water networks, predominantly in the major and minor grooves, and near the phosphate groups of the backbone [12]. Among the different types of base sequences, adenine-thymine (AT) oligomers are special because they do not undergo transitions from the B to the A form upon reducing the water content. Instead, AT oligomers adopt the B' form at low water concentrations, with 4 to 6 water molecules per base pair that may be hydrogen-bonded to the oligomer [12,30–32]. In the B' form of the AT DNA oligomer two HBs are formed in the Watson-Crick configuration, i.e., between oxygen (O4) of the thymine and the NH_2 group of the adenine (N6), and between the NH group of the thymine (N3T) and the nitrogen atom of the adenine (N1), see Fig. 1.

Vibrational modes expected to be strongly influenced by the hydrogen-bonding in the DNA helix are the carbonyl stretches $\nu_{C2=O2}$ at 1716 cm^{-1} and $\nu_{C4=O4}$ at 1665 cm^{-1} and the amine bending δ_{NH_2} at 1665 cm^{-1} [7–9,14, 34–38]. Note, that in contrast to H_2O, in D_2O the δ_{ND_2} vibration of adenine and the carbonyl vibrations of thymine are decoupled, due to the frequency shift from δ_{NH_2} to δ_{ND_2} [22, 23]. The δ_{H_2O} vibration of water molecules in DNA samples typically absorbs in the same spectral region, i.e., around 1650 cm^{-1} [7, 35, 39]. A direct experimental assignment of ν_{NH_2} and ν_{NH} in AT DNA oligomers in the condensed phase is very difficult. Typically, symmetric and antisymmetric ν_{NH_2} stretching vibrations absorb around 3300 cm^{-1} [7]. However, the spectral range from 3050 to 3600 cm^{-1} is dominated by the strong absorption of the water OH stretching vibration. Reducing the water content of the DNA oligomers does not solve this problem, because at extremely low water contents the DNA oligomers do not adopt a well defined structure.

Ultrafast time-resolved infrared (IR) spectroscopy is ideally suited to address this issue as has been shown in studies of inter- and intramolecular couplings and energy relaxation dynamics in various hydrogen-bonded systems [2–4,40,41]. In this contribution we focus on shifts in oligomer vibrational modes induced by excitation of the $\nu_{C2=O2}$ or the $\nu_{C4=O4}$ / δ_{NH_2} oligomer fingerprint vibration. These shifts originate from inter- and intramolecular couplings among different vibrational modes of the DNA oligomer and depend on the strength of the couplings as well as the energy mismatch between different transitions. Related effects are particularly pronounced if overtones or combination modes match a fundamental vibrational transition (resonance enhancement). This already affects the linear absorption band shape, but also the vibrational relaxation dynamics [5]. A particular strength of the ultrafast IR pump-probe spectroscopy is the capability of uncovering vibrational

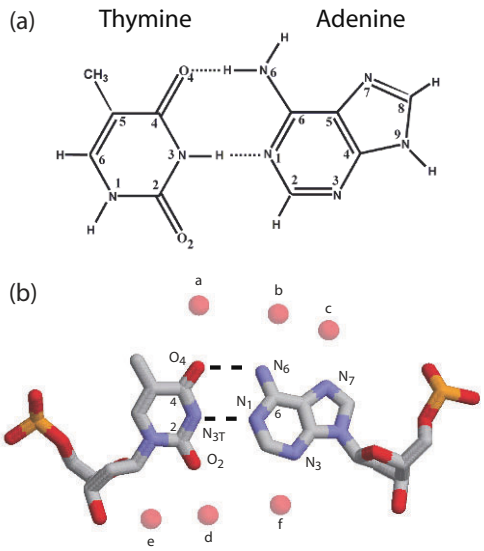

Fig. 1: (a) Scheme of the AT DNA Watson-Crick configuration. (b) Structure of a single AT DNA base pair in the Watson-Crick configuration of a dodecamer (taken from 428d.pdb [33]). The oxygen atoms of water molecules forming HBs to the nucleic acids are presented as spheres. Distances of the oxygen atoms of water molecules in the major groove a, b, and c to the O4, N6, and N7 atoms are 2.93 Å, 2.93 Å, and 2.80 Å, respectively. Water molecules d, e, and f of the minor groove have distances of 2.88 Å, 4.16 Å, and 2.61 Å to the O2 and N3 atoms, respectively. Intrastrand distances of the O2, O4, and N6 atoms to neighbooring thymine and adenine bases are 4.12 Å, 3.53 Å, and 3.34 Å, respectively.

spectral features not visible in linear spectroscopy due to excessive solvent absorption. This is demonstrated in the experiments presented here, where we excite oligomer vibrations between 1600 and 1760 cm^{-1} and probe for the oligomer ν_{NH_2} vibration in the region of 3050 - 3250 cm^{-1}, which is dominated by water absorption.

The experimental assignment of the adenine ν_{NH_2} vibration and the coupling pattern across the HBs is supported by quantum chemical calculations of anharmonic couplings which are used for obtaining fundamental transition frequencies for a set of relevant modes of a microsolvated gas phase AT model. In principle accurate theoretical modelling of the vibrational dynamics of DNA AT base pairs requires taking into account several effects: (i) The intermolecular double HB between adenine and thymine, (ii) The interaction between different base pairs along the DNA strand, (iii) The charges as well as the dynamics of the backbone, and (iv) The influence of water molecules

which may, for instance, make a HB to the base pair. Here, we are aiming to obtain a semiquantitative understanding of the transient band shifts, whereby it is assumed that they are dominated by effect (i), that is, the anharmonic coupling pattern due to the intermolecular HB. The effect of (ii)-(iv) can be of static nature, e.g., changes in the anharmonic frequencies and coupling constants, and also of dynamic nature, e.g., fluctuation of the energy levels. However, here we will only focus on the static influence of a well-defined environment determined by microsolvation of the AT base pair by several water molecules.

Isolated and microsolvated base pairs have been extensively studied theoretically, focussing in particular on the stability of different isomers, see, e.g. the work by Hobza and coworkers [42–44] as well as by Fonseca-Guerra et al. [45]. Although there is a number of reports on potential energy surfaces of base pairs in harmonic approximation, there appear to be only a few calculations addressing anharmonicity in the context of, e.g., proton transfer [10, 46, 47], the coupling to the intermolecular HB vibration [15] or the assignment of different gas phase isomers [48]. Most notable in this respect is the recent study of the anharmonic spectrum of a guanine-cytosine pair [49] as well as the development of a vibrational exciton model to describe nonlinear IR spectra involving DNA fingerprint modes [20, 22–25, 50].

This Chapter is organized as follows. In the next Section we will first discuss the effect of solvating water molecules on the anharmonic IR spectra of an isolated AT pair. In this context we will scrutinize the applicability of a dual level approach which combines different quantum chemistry methods within a correlation expansion of the potential energy surface (PES). For the case of two water molecules we will present an analysis of the anharmonic coupling patterns between the $\nu_{\mathrm{C2{=}O2}}$, $\nu_{\mathrm{C4{=}O4}}$ and $\delta_{\mathrm{NH_2}}$ vibrations and the symmetric $\nu_{\mathrm{NH_2}}$ mode in Section 2.2. Section 3 gives details on the experimental setup and presents results of two-color pump-probe spectra. Finally, we give a comparison between theory and experiment in Section 4 which leads us to the assignment of the $\nu_{\mathrm{NH_2}}$ fundamental transition.

2 Microsolvated AT Base Pairs

2.1 Fundamental Transitions Using a Dual Level Approach

In the following we present results on fundamental vibrational transitions of isolated AT base pairs microsolvated with 1-4 water molecules. The aim of this study is twofold: First to find out about overall changes of IR transitions of base pair modes due to the interaction with water molecules. And, second, to test the performance of a dual level approach combining density functional (DFT) and semiempirical PM3 data to expand the PES. Throughout we will assume that the deviations from equilibrium structures are small enough such

as to allow the use of normal mode coordinates $\mathbf{Q}$ for spanning the PES, i.e. $V = V(\mathbf{Q})$.

Under the conditions of the experiment there are 4 to 6 water molecules per AT pair which can form different HBs to the base pair (see also Fig. 1). Our interest will be in the IR transitions of the NH_2 and C4=O4 groups such that water situated in the major groove shall be of importance. However, for comparison we also consider a structure where a water molecule is on the C2=O2 side. There are several microsolvation studies which focussed on the effect of water on base pair properties such as interaction energies or HB lengths [43–45,51]. To our knowledge there is, however, no theoretical account on anharmonic IR spectra of HB related modes. The four structures which will be discussed in the following are shown in Figs. 2 and 3. They have been obtained by geometry optimization at the DFT/B3LYP level of theory with a 6-31++G(d,p) basis set using Gaussian 03 [52]. Notice that these are not necessarily the most stable structures at this level of theory (see also discussion in Ref. [44]). Our choice has been biased by the requirement that the water molecules should be close or even hydrogen-bonded to the considered target modes. The latter are shown in terms of their normal mode displacement vectors in Figs. 2 and 3 as well. The respective harmonic frequencies are compiled in Table 1.

In AT-H_2O, Fig. 2 (left column), the water molecule is hydrogen-bonded between the adenine N6-H and the N7 sites. This causes the ν_{NH_2} vibration to acquire some water stretching character lowering its harmonic frequency. The δ_{NH_2} vibration is only slightly mixed with some water motion and essentially constrained so that its frequency is blue-shifted. The next water molecule in AT-$(H_2O)_2$, Fig. 2 (right column), makes a HB to the oxygen of C4=O4 lowering the $\nu_{C4=O4}$ frequency slightly, but at the same time mixing this vibration with δ_{NH_2} type motions. For the case of three water molecules, Fig. 3 (left column), there is the possibility to form a hydrogen bonded water chain connecting the O4, N6-H, and N7 sites. This reduces the mixing of the ν_{NH_2} and water motions, but the δ_{NH_2} vibration contains a water bending now as does the $\nu_{C4=O4}$ mode. Adding another water at the C2=O2 site leads as expected to a shift of the $\nu_{C2=O2}$ transition only, Fig. 3 (right column). Overall we notice that the presence of solvating water molecules has the strongest impact on the δ_{NH_2} and $\nu_{C4=O4}$ vibrations, with the latter acquiring substantial δ_{NH_2} character.

So far we have only discussed harmonic frequencies. The effect of anharmonicity can be treated using either a Taylor expansion of the PES in terms of normal mode coordinates or by explicitly spanning the PES on a numerical grid. The discussion of anharmonic force constants is postponed to the following section. Here, we will focus on an explicit PES generated by means of the following correlation expansion, here written up to three-mode correlations, [53]

Table 1: Harmonic frequencies (in cm^{-1}) for the target modes of the different model structures as obtained using DFT/B3LYP with a 6-31++G(d,p) basis set. The displacement vectors for the solvated structures are shown in Figs. 2 and 3.

modes	AT	AT-H_2O	AT-$(H_2O)_2$	AT-$(H_2O)_3$	AT-$(H_2O)_4$
ν_{NH_2}	3410	3393	3401	3415	3410
$\nu_{C2=O2}$	1797	1794	1799	1799	1776
δ_{NH_2}	1689	1718	1720	1727	1727
$\nu_{C4=O4}$	1728	1731	1714	1720	1720

Table 2: Anharmonic frequencies (in cm^{-1}) for the target modes of the different model structures as obtained using Eq. (1) with the one mode potential generated by the DFT/B3LYP method with a 6-31++G(d,p) basis set and the two- and three-mode PES obtained by the PM3 approach.

mode	AT-H_2O	AT-$(H_2O)_2$	AT-$(H_2O)_3$	AT-$(H_2O)_4$
ν_{NH_2}	3326	3332	3307	3310
$\nu_{C2=O2}$	1803	1813	1797	1785
δ_{NH_2}	1732	1760	1777	1753
$\nu_{C4=O4}$	1701	1664	1635	1643

$$V(\mathbf{Q}) = \sum_i V^{(1)}(Q_i) + \sum_{i<j} V^{(2)}(Q_i, Q_j) + \sum_{i<j<k} V^{(3)}(Q_i, Q_j, Q_k)\,. \qquad (1)$$

Neglecting rotation [54], i.e. assuming that the kinetic energy operator is diagonal, the eigenstates of the respective Hamiltonian can be obtained by straightforward diagonalization using, e.g., the Lanczos method. For systems of the size of solvated base pairs the calculation of higher order correlation terms becomes rather expensive. Here, an interesting alternative are so-called dual level schemes where low-order correlation PES are calculated at a higher level of quantum chemistry than multi-mode correlation PES. For instance, Scheurer and coworker have combined MP2 and PM3 calculations to find a rather good description of IR spectra of a model peptide [55].

In Table 2 we present results of dual level calculations on 4D models including the target modes of Figs. 2 and 3. Here the one-mode potentials, $V^{(1)}(Q_i)$, have been calculated using the DFT method, while two- and three mode PES were generated using the semiempirical PM3 approach. Comparing these anharmonic results with the harmonic values in Table 1 we notice the following: The ν_{NH_2} vibration is strongly affected and red-shifts by about 70-100 cm^{-1} depending on the cluster size. The $\nu_{C2=O2}$ vibration is only slightly affected. Essentially, these two modes behave as expected. Except for the AT-H_2O case the δ_{NH_2} vibration is blue-shifted by about 40 cm^{-1}. The fundamental transition of the $\nu_{C4=O4}$ mode, on the other hand, is considerably

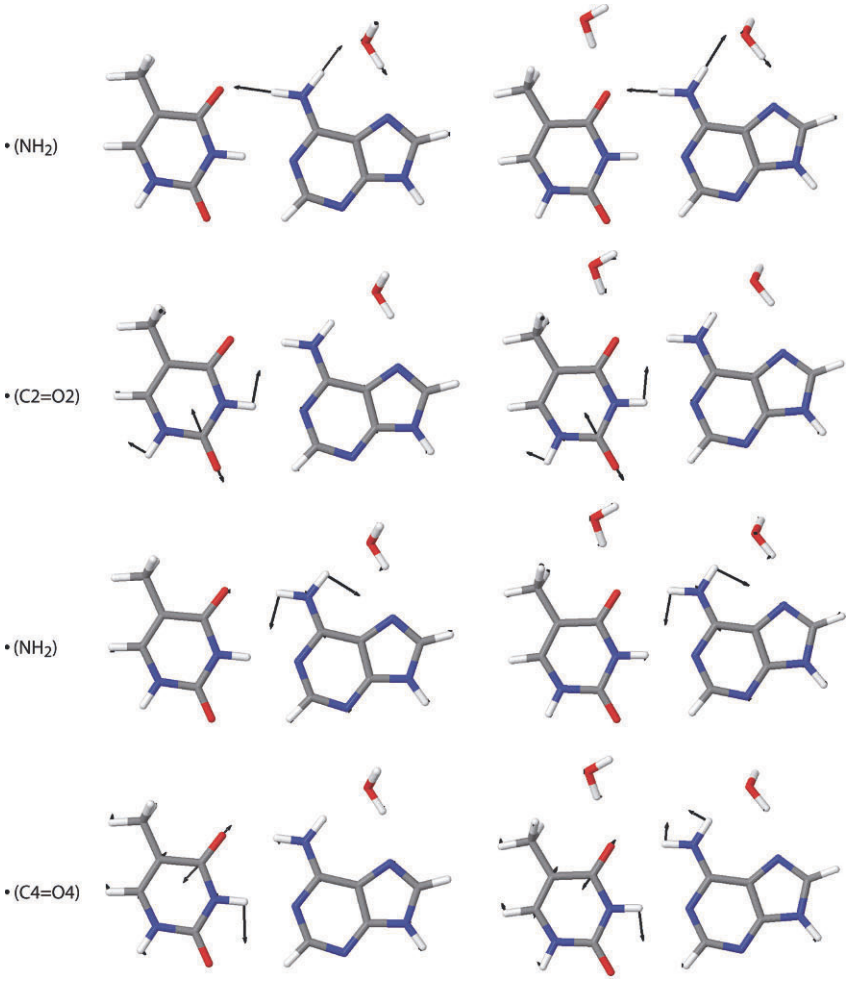

Fig. 2: Normal mode displacement vectors for the target modes as calculated in harmonic approximation of the AT-$(H_2O)_{n=1,2}$ PES using DFT/B3LYP with a 6-31++G(d,p) basis set.

red-shifted by about 30-80 cm^{-1}. In terms of the experimental assignment given in Table 6 below the $\nu_{C4=O4}$ agrees fairly well with experiment which puts this transition at 1665 cm^{-1} [7, 8, 14]. However, the δ_{NH_2} vibration is believed to absorb around 1665 cm^{-1} as well, which is at variance with the prediction of the dual level scheme. Moreover, in the harmonic case, but also in the fourth order anharmonic force field calculations reported below, the frequencies of $\nu_{C4=O4}$ and δ_{NH_2} are almost identical. It would be surprising if

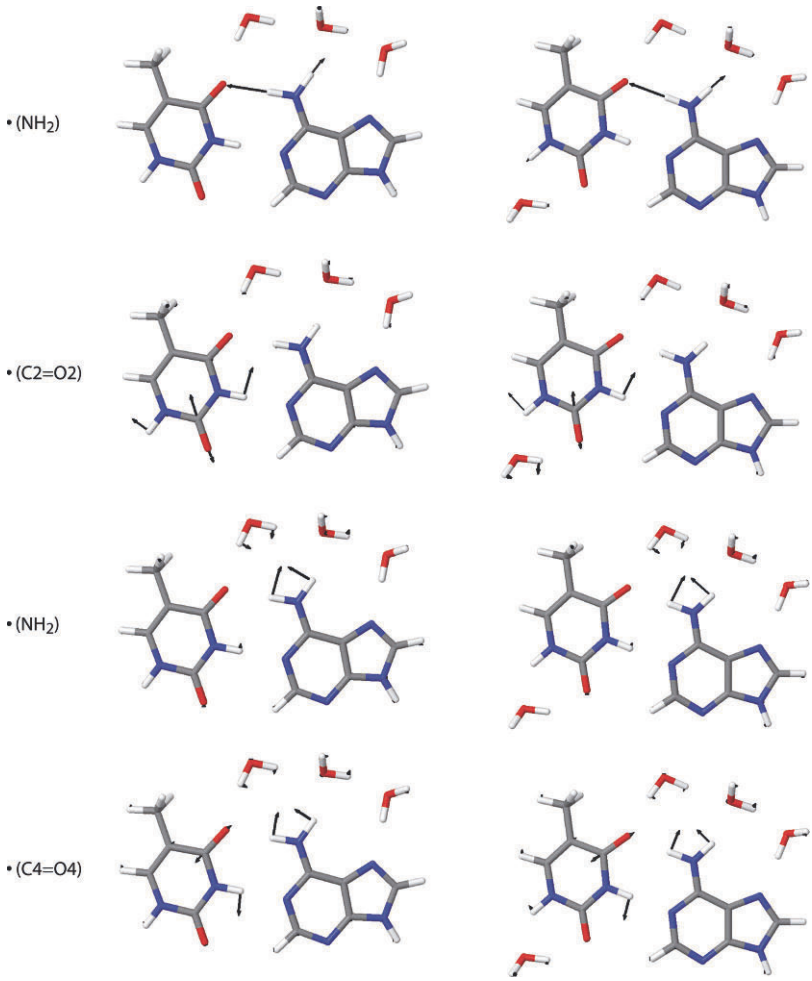

Fig. 3: Normal mode displacement vectors for the target modes as calculated in harmonic approximation of the AT-$(H_2O)_{n=3,4}$ PES using DFT/B3LYP with a 6-31++G(d,p) basis set.

the higher order anharmonic terms implicitly included in the PES expansion changes this situation to such an extent.

Since multimode calculations are rather expensive we have chosen to scrutinize the effect of the PM3 approximation by comparing different 2D models of AT-$(H_2O)_2$ at the full DFT, PM3, and dual level. The results are compiled in Table 3. The correlation between the ν_{NH_2} and δ_{NH_2} modes is rather well-desribed by the dual level scheme, the error being just a few cm^{-1}. The

Table 3: Comparison of anharmonic frequencies (in cm^{-1}) for the target modes of the AT-$(H_2O)_2$ model structures of different two-dimensional calculations and different levels of quantum chemistry (DFT: full DFT/B3LYP, 6-31++G(d,p); PM3: full PM3; DUAL: DFT one-mode and PM3 two-mode PES).

2D model	mode	DFT	PM3	DUAL
ν_{NH_2} ,δ_{NH_2}	ν_{NH_2}	3311	3154	3321
	δ_{NH_2}	1727	1950	1730
$\nu_{C2=O2}$, δ_{NH_2}	$\nu_{C2=O2}$	1796	1901	1796
	δ_{NH_2}	1742	1703	1742
$\nu_{C4=O4}$,δ_{NH_2}	$\nu_{C4=O4}$	1715	1807	1680
	δ_{NH_2}	1744	1671	1777

same holds true for the correlation between the $\nu_{C2=O2}$ and δ_{NH_2} modes. However, the hybrid scheme is performing poorly for the correlation between the $\nu_{C4=O4}$ and δ_{NH_2} modes and gives the frequency shifts of opposite sign also observed for the full 4D calculation in Table 2. The failure of the dual level scheme to describe the coupling of the $\nu_{C4=O4}$ stretching and δ_{NH_2} bending motion can be understood in terms of their considerable mixing as quantified by a normal mode internal coordinate decomposition. In general, an internal coordinate may contribute to the displacement along several normal modes. Analyzing the present situation using the scheme of Boatz and Gordon [56] the internal coordinate describing the NH_2 angle contributes to the decomposition of the δ_{NH_2} bending normal mode by only 29 %, while its contribution to the $\nu_{C4=O4}$ stretching normal mode (see also Fig. 2) and several purine ring deformations normal modes ranges between 15 and 17%. On the other hand, the internal NH_2 angle does not contribute to the decomposition of the $\nu_{C2=O2}$ and ν_{NH_2} normal modes which are 92% stretching of the C2=O2 bond and 82% and 17% stretchings of the N-H bonds, respectively.

2.2 Anharmonic Coupling Patterns

In this section we explore the second possibility to generate multidimensional PES, i.e. a Taylor expansion in terms of normal mode coordinate with respect to the geometry of the stable structure. Including terms up to fourth order we have (using dimensionless coordinates)

$$V(\mathbf{Q}) = \frac{1}{2!}\sum_i \hbar\omega_i Q_i^2 + \frac{1}{3!}\sum_{ijk} K_{ijk}^{(3)} Q_i Q_j Q_k + \frac{1}{4!}\sum_{ijkl} K_{ijkl}^{(4)} Q_i Q_j Q_k Q_l \,. \quad (2)$$

Third and fourth order anharmonic coupling constants are calculated using a combination of analytical second derivatives and finite differences [57]. Specifically, we have used the symmetric expressions [58]

Table 4: Harmonic and diagonal anharmonic force constants (in cm^{-1}) of the relevant system modes for AT-$(H_2O)_2$.

	ν_{NH_2}	$\nu_{C2=O2}$	δ_{NH_2}	$\nu_{C4=O4}$
ω	3401	1799	1713	1720
$K^{(3)}/3!$	-261	61	-19	-31
$K^{(4)}/4!$	24	5	4	2

Table 5: Third order coupling constants between the ν_{NH_2} mode and relevant fingerprint modes (in cm^{-1}) in AT-$(H_2O)_2$. The numbers in parentheses refer to the isolated AT case.

	$\nu_{C2=O2}$	δ_{NH_2}	$\nu_{C4=O4}$
$\nu_{C2=O2}$	-1 (-2)	5 (8)	0 (-2)
δ_{NH_2}		96 (87)	-66 (-17)
$\nu_{C4=O4}$			11 (2)

$$K^{(3)}_{ijk} = \frac{-K^{(+2)}_{ij} + 8K^{(+)}_{ij} - 8K^{(-)}_{ij} + K^{(-2)}_{ij}}{12\Delta Q_k}\,, \tag{3}$$

$$K^{(4)}_{ijkl} = \frac{K^{(++)}_{ij} + K^{(+-)}_{ij} - K^{(-+)}_{ij} + K^{(+-)}_{ij}}{4\Delta Q_k \Delta Q_l}\,. \tag{4}$$

Here, $K^{\pm}_{ij}$ is the Hessian calculated at displaced geometries where for the displacement we used $\Delta Q = 0.03$ for the cubic and $\Delta Q = 0.04$ for the quartic force field. Note that for the construction of the Hamiltonian we have neglected contributions which are off-resonant by more than $\sim$1000 cm^{-1}.

In the following we will focus on the case of two water molecules only, i.e. AT-$(H_2O)_2$, since this already contains the essential effect of hydrogen-bonding waters as discussed in the previous section. The diagonal force constants for the four target modes of Fig. 2 (right panel) are given in Table 4. Important third order anharmonic coupling constants involving the ν_{NH_2} mode are compiled in Table 5. As expected the diagonal anharmonic force constants are largest for the ν_{NH_2} mode. More interesting, however, is the coupling pattern between this mode and the fingerprint modes. Here, we observe two dominating Fermi-type resonance couplings: (i) to the bending overtone $2\delta_{NH_2}$ which is by far the strongest coupling, (ii) to the combination tone between the δ_{NH_2} and the $\nu_{C4=O4}$ modes. In Table 5 we also give the couplings for the isolated AT case. Notice that here only the $2\delta_{NH_2}$ overtone is strongly coupled. In other words, the presence of water establishes a new coupling channel. And, going back to Fig. 2 it requires a water molecule at the C4=O4 site which mixes the δ_{NH_2} and the $\nu_{C4=O4}$ modes.

Table 6: Anharmonic frequencies (in cm^{-1}) for the target modes of the AT-$(H_2O)_2$ model calculated using the anharmonic expansion, Eq. (2) and the DFT/B3LYP method with a 6-31++G(d,p) basis set. The 4D model is compared with a 6D model which includes in addition the most strongly coupled water stretching and bending modes at the N6-H site whose anharmonic frequencies are 3752 cm^{-1} and 1588 cm^{-1}, respectively. Also given are results for a 4D model which does not include water molecules [59]. The experimental assignment is shown as well (ν_{NH_2} from Ref. [59], the other modes from Refs. [7–9, 14, 34–38]).

mode	4D (AT)	4D	6D	exp.
ν_{NH_2}	3330	3297	3280	3215
$\nu_{C2=O2}$	1758	1796	1792	1716
δ_{NH_2}	1719	1718	1708	1665
$\nu_{C4=O4}$	1645	1709	1702	1665

The fundamental transition frequencies obtained from this 4D anharmonic force field are given in Table 6 which besides the experimental values contains frequencies calculated for a 6D model which additionally includes most strongly coupled water stretching and bending modes at the N6-H site [59]. Inspecting 4D and 6D cases we notice that the effect of explicit inclusion of water modes is only modest especially in comparison to the isolated case (4D(AT), see also Table 1). Given the simplicity of the model, the agreement between theory and experiment is rather reasonable with deviations being about 2% except for the $\nu_{C2=O2}$ mode whose frequency is about 4% above the experimental value. Perhaps this is not very surprising as the C2=O2 mode is close to the thymine N1 site where in DNA the base is linked to the backbone.

3 Experimental Section

3.1 Methods

AT DNA double strand oligomers with sodium counterions and a length of 20 base pairs were obtained from Biotherm, and were dissolved in water and dried on a CaF_2 window at 293 K in an atmosphere of 52% relative humidity (saturated solution of $NaHSO_4.H_2O$ at 20° Celsius [60]). This results in DNA samples with approximately 4 to 6 water molecules per base pair [37] (sample thickness $\sim$ 6.5 μm). It has been reported that under these conditions AT DNA oligomers adopt the B'-form [35]. Femtosecond time-resolved IR pump-probe experiments were performed with two independently tunable femtosecond pulses generated by parametric conversion processes pumped by a regenerative Ti:sapphire laser system (800 nm, repetition rate 1 kHz, pulse duration 100 fs) [61]. The central frequency of the pump pulse was varied from 1630 to 1760 cm^{-1} and the probe was centred around 1650 cm^{-1} or 3200

cm^{-1}. The cross correlation between pump and probe pulses had a temporal width of 130 fs (FWHM). With the used pump pulse energy of 1 μJ approximately 2% of the AT base pairs in the sample volume were excited. After interaction with the sample, the probe pulses were spectrally dispersed and detected with a HgCdTe detector array (resolution 5 cm^{-1}).

3.2 Experimental Results

The absorption between 3050 and 3600 cm^{-1} (see Fig. 4a and 5, solid line) is dominated by more than 85% by the broad OH stretching absorption of water molecules. Therefore, it is not possible to directly determine the ν_{NH_2} stretch absorption frequency of the DNA oligomer from this absorption spectrum. In the fingerprint region, the absorption of $\nu_{C2=O2}$ is located at 1716 cm^{-1} and the combined absorption of δ_{NH_2} and $\nu_{C4=O4}$ peaks at 1665 cm^{-1} (see Fig. 4a, solid line) [7,8,14,31,38,48]. Both the $\nu_{C4=O4}$ and the δ_{NH_2} vibration absorb at 1665 cm^{-1} and therefore cannot be excited separately in our experiment. Figure 5 shows results of femtosecond pump-probe experiments with excitation in the fingerprint region and probing between 3050 and 3600 cm^{-1}. Excitation with a broad pump pulse at 1740 cm^{-1} (FWHM 170 cm^{-1}) leads to an instantaneous spectrally narrow response around 3200 cm^{-1}. Furthermore, a spectrally broad response over the entire range of 3050 cm^{-1} to 3600 cm^{-1} is seen to increase on a picosecond time scale (see Fig. 5). At 1740 cm^{-1} the pump pulse mainly excites the $\nu_{C2=O2}$ stretching vibration. Given the photon energy and pulse intensity, two-photon excitation of vibrations around 3300 cm^{-1} is unlikely by the pump pulse. As a consequence, both the instantaneous and the increasing broad negative signal must result from exciting vibrations in the fingerprint region. The broad negative signal, which becomes positive above 3530 cm^{-1}, is known to correspond to the OH stretching vibration of hot bulk water. Excess energy in low frequency vibrations of water (e.g. librations) weakens the HB strength, resulting in an increase of the OH stretching force constant, and therefore in a higher OH stretching frequency [2, 62, 63]. The instantaneous narrow response around 3200 cm^{-1}, after excitation at 1740 cm^{-1}, decreases in time and should therefore correspond to a different process.

Figure 6 shows absorbance changes in the range between 3050 and 3250 cm^{-1}, upon excitation at 1630 cm^{-1} (FWHM 160 cm^{-1}), before and after subtraction of the spectrally broad 13 ps component of the hot water formation, obtained from a global fit. At 1630 cm^{-1} the pump pulse mainly excites the δ_{NH_2} and $\nu_{C4=O4}$ vibrations. An instantaneous bleach signal is observed with a maximum at 3215 cm^{-1} and a width of 50 cm^{-1}, which decays on a subpicosecond time scale. The perturbed free induction decay of this band gives a total dephasing time T_2 of 0.5 $\pm$ 0.1 ps, which corresponds to a homogeneous line width of 21 $\pm$ 5 cm^{-1}. This indicates that the origin of the observed 50 cm^{-1} width of the bleaching band is not caused by a single homogenously broadened absorption line. The maximum of the instantaneous

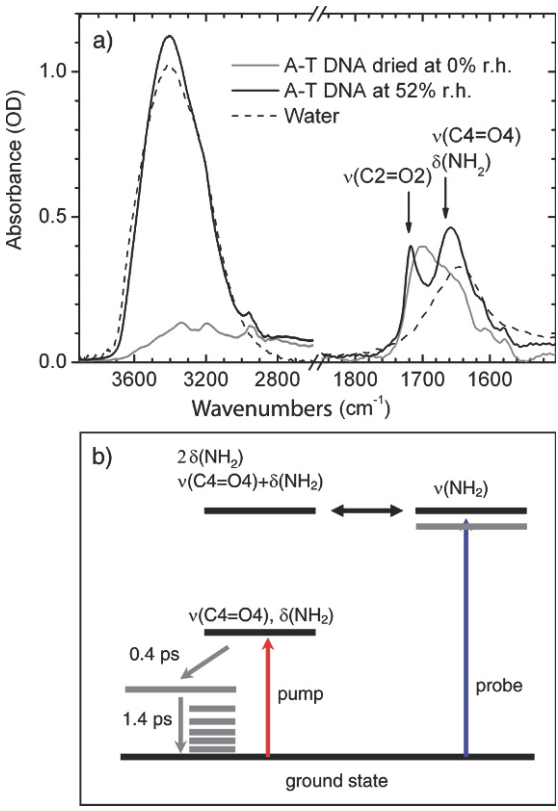

Fig. 4: (a) Absorption spectra of AT DNA oligomers prepared in 52% relative humidity (black solid line), neat water (dashed line), and AT DNA oligomers dried for two days in a N_2 atmosphere (gray solid line). (b) Scheme describing the two color IR pump-probe detection of the ν_{NH_2} stretching vibration in AT base pairs. Because of the anharmonic coupling between the $\nu_{C4=O4}$, δ_{NH_2}, and ν_{NH_2} vibrations, the ν_{NH_2} =0→1 transition is bleached upon excitation of the $\nu_{C4=O4}$ and δ_{NH_2} modes. Population of the excited state levels will locally heat the molecule, inducing a shift of the hot ground-state ν_{NH_2} transition.

response at 3215 cm^{-1} decays with a 0.6 ± 0.2 ps time constant. Around 3130 cm^{-1} a positive signature seems to be present for early delay times evolving into a negative band with a rise time of about 0.4 ps, that decays with a time constant of 1.4 ± 0.4 ps. The time constants characterizing the kinetics for various pump-probe wavelength combinations are summarized in Table 7.

In order to identify the origin of the instantaneous bleaching signal at 3215 cm^{-1} we compared transients at 3215 cm^{-1} after excitation at 1630 cm^{-1} and

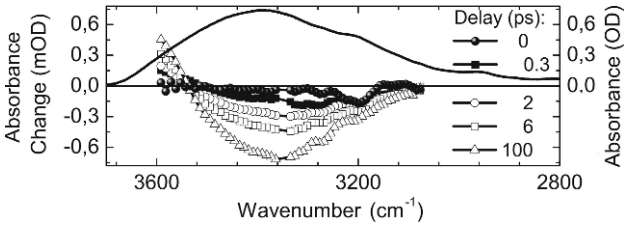

Fig. 5: Absorption spectrum of AT DNA oligomers around 3300 cm^{-1} (solid line) and absorbance difference spectra for several pump-probe delay times after excitation at 1740 cm^{-1} (FWHM 170 cm^{-1}). The picosecond OH stretching response of water ranges from 3600 to 3050 cm^{-1}. The spectrum at 0 ps delay time was obtained by averaging from -200 to 200 fs to eliminate nonabsorbing signal contributions.

1730 cm^{-1}, respectively, in Fig. 7. Excitation at 1730 cm^{-1} results in a $\approx$ 7 times weaker and barely visible instantaneous negative signal around 3215 cm^{-1}. In contrast, excitation around 1630 cm^{-1} result in a pronounced instantaneous signal around 3215 cm^{-1}. Comparing the two transients at 3215 cm^{-1}, we observe that, excitation at 1630 cm^{-1} leads to a three-exponential decay of the bleach with 0.6 ps, 3 ps, and 13 ps. A transient with similar time constants (0.9 ps, 4 ps, and 13 ps), but very different amplitudes is observed after pumping at 1730 cm^{-1}, where mainly the $\nu_{C2=O2}$ stretching vibration is excited. Thus, excitation in the spectral range of the $\nu_{C4=O4}$ / δ_{NH_2} vibrations results in significant instantaneous signals around 3215 cm^{-1}.

Experiments where both the pumping and probing takes place in the fingerprint region are presented in Fig. 8. In Fig. 8a the AT DNA oligomer sample was excited at 1760 cm^{-1} and probed between 1605 and 1740 cm^{-1}.

Table 7: Time constants of transients. r: rising signals; d: decaying signals.

mode	pump (cm^{-1}) (FWHM)	probe (cm^{-1})	time constants (ps)
ν_{NH_2}	1630 (160)	3215	(d) 0.6 ± 0.2 // (d) 3.0 ± 1.5 // (r) 13 ± 2
ν_{H_2O} [a]	1630 (160)	3130	(r) 0.4 ± 0.2 // (d) 1.4 ± 0.4 // (r) 13 ± 2
ν_{NH_2}	1730 (90)	3215	(d) 0.9 ± 0.4 // (r) 4.0 ± 1.5 // (r) 13
$\nu_{C2=O2}$	1760 (100)	1725	(d) 0.9 ± 0.1
$\nu_{C2=O2}$	1760 (100)	1685	(d) 0.7 ± 0.1
$\nu_{C2=O2}$	1630 (130)	1720	(d) 2.4 ± 0.2
$\nu_{C4=O4}$ / δ_{NH_2}	1630 (130)	1665	(d) 0.4 ± 0.1 // (d) 1.4 ± 0.4
δ_{H_2O}	1630 (130)	1650	(d) 0.2 ± 0.1 // (d) 1.0 ± 0.2
δ_{H_2O}	1630 (130)	1640	(r) 0.6 ± 0.1
$\nu_{C4=O4}$ / δ_{NH_2}	1630 (130)	1625	(d) 0.5 ± 0.1

[a] Suggested assignment (see text)

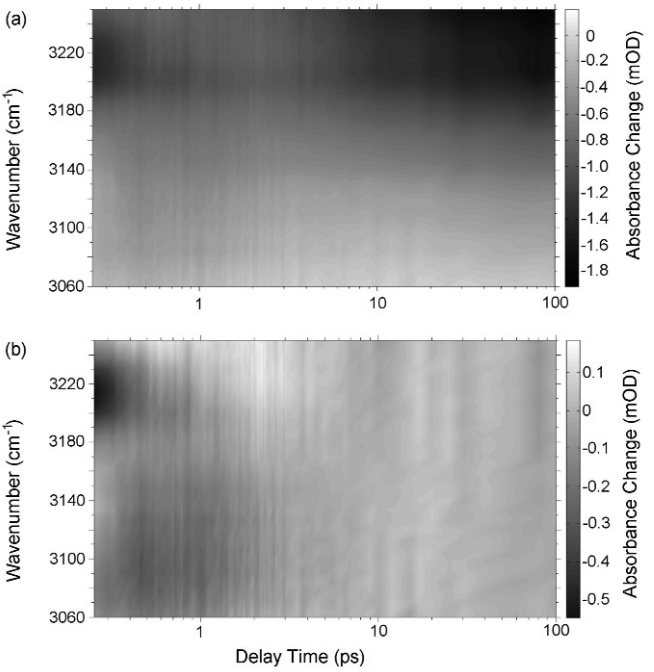

Fig. 6: (a) Contour plot of the absorbance change as a function of delay time on a log scale after excitation at 1630 cm^{-1} (FWHM 160 cm^{-1}). On the picosecond time scale the water response is visible. (b) Contour plot of the absorbance change after subtraction of the monoexponential 13 ps rise time of the hot water response. The negative peak around 3215 cm^{-1} is clearly visible for early delay times.

The pump-probe spectrum shows a negative band at 1725 cm^{-1} and a positive band at 1685 cm^{-1} . The band at 1725 cm^{-1} decays mono-exponentially with 0.9 ± 0.1 ps, while the band at 1685 cm^{-1} decays with 0.7 ± 0.1 ps. Transients at these frequency positions are presented together with their simulations in Fig. 9. The positive signal can be assigned to the $\nu_{C2=O2} = 1 \rightarrow 2$ transition. A similar lifetime was obtained by Zanni et al. for measurements on GC DNA oligomers with excitation in the same frequency region [20]. The difference between the 0.7 ps excited state lifetime and the 0.9 ps ground state recovery time signals is that the $\nu_{C2=O2}$ energy is first converted into excitation of lower frequency modes. As a consequence of this, the ground state absorption frequency is shifted due to anharmonic coupling to these lower frequency modes, and will not recover before these modes loose their excitation energy.

Results for excitation of the AT DNA oligomer at 1630 cm^{-1} , presented in Fig. 8b, show bleaching signals at the ground state absorption positions of the $\nu_{C2=O2}$ vibration (1716 cm^{-1}), the $\nu_{C4=O4}$ and δ_{NH_2} vibrations (both

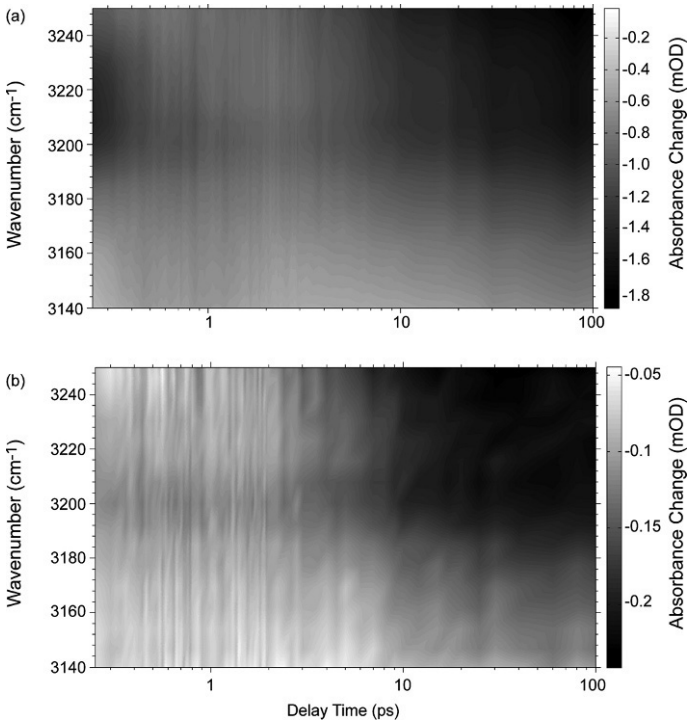

Fig. 7: (a) Contour plot of the absorbance change as a function of delay time after excitation at 1630 cm^{-1} (FWHM 160 cm^{-1}) from 3140 to 3250 cm^{-1}. The instantaneous negative signal at 3215 cm^{-1} as well as the dynamics of the hot water vibrations on a picosecond time scale is clearly visible. (b) Contour plot of the absorbance change after excitation at 1730 cm^{-1} (FWHM 90 cm^{-1}). The signals are much weaker. The picosecond dynamics of hot water vibrations is clearly visible, but the instantaneous response around 3215 cm^{-1} is negligible.

1665 cm^{-1}), and the water δ_{H_2O} vibration (1650 cm^{-1}) [7, 22, 31, 63]. The $\nu_{C2=O2}$ bleach recovers exponentially with 2.4 ± 0.2 ps on a significantly longer time scale than after direct $\nu_{C2=O2}$ excitation. This shows that there are at least two different energy relaxation pathways in DNA involving the $\nu_{C2=O2}$ vibration. For the $\nu_{C4=O4}$ / δ_{NH_2} vibrations biexponential recoveries were observed with 0.4 ± 0.1 ps and 1.4 ± 0.4 ps, and for the water δ_{H_2O} with 0.2 ± 0.1 ps and 1.0 ± 0.2 ps. For the bending vibration δ_{H_2O} of water molecules in bulk water a lifetime of 170 ± 30 fs [63] has been reported, which agrees with the fast component observed here for δ_{H_2O}. Instantaneous increased absorption signals below 1640 cm^{-1}, decay with a time constant of 0.5 ± 0.1 ps, matching the fast component of the $\nu_{C4=O4}$ / δ_{NH_2} bleach recovery. In addition, a positive band appears around 1640 cm^{-1}, rising in 0.6

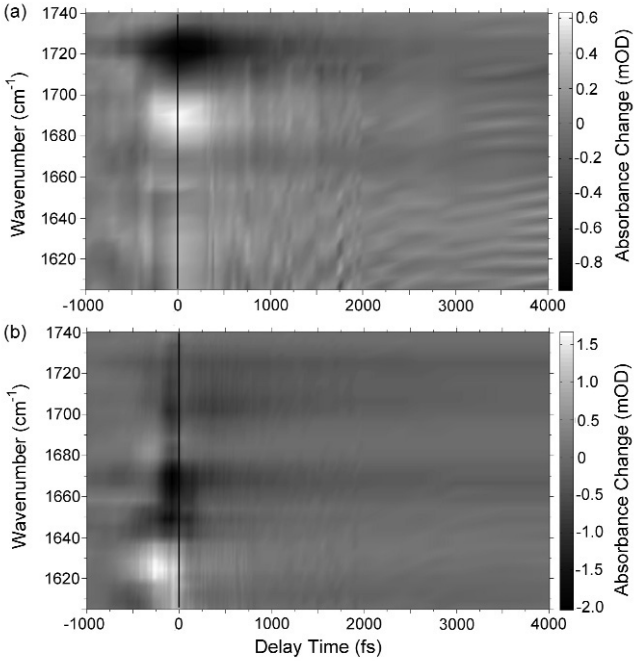

Fig. 8: (a) Contour plot of the absorbance change as a function of delay time after excitation at 1760 cm^{-1} (FWHM 100 cm^{-1}). (b) Contour plot in the same frequency range (1605 to 1740 cm^{-1}) after excitation at 1630 cm^{-1} (FWHM 160 cm^{-1}).

$\pm$ 0.1 ps. Signals at this spectral position have been assigned to the bending vibration of hot water molecules [63].

The dynamics of experiments with different pump frequencies in the fingerprint region, are compared to confirm that the bleach band at 3215 cm^{-1} originates from the ν_{NH_2} stretching vibration of adenine and not from water. First, we point out, that even the fastest recovery time of the bleach signal at 3215 cm^{-1} after excitation in the fingerprint region (where the water δ_{H_2O} also absorbs), is three times slower than the reported lifetime of the water δ_{H_2O} vibration [63]. Second, the width of the bleaching band at 3215 cm^{-1} of 50 cm^{-1} is considerably narrower than the 200 cm^{-1} estimate for the δ_{H_2O} overtone band of bulk water [64]. Having assigned the 3215 cm^{-1} bleaching signal to the AT DNA oligomer ν_{NH_2} vibration, we now compare the dynamics at this frequency for excitation at 1630 cm^{-1} and 1730 cm^{-1}, which correspond to the absorption bands of both the $\nu_{C4=O4}$ and δ_{NH_2} vibrations, and the $\nu_{C2=O2}$ vibration, respectively.

For both excitation frequencies the picosecond dynamics, shown in Fig. 7, can be modelled by the same 13 ps time constant, corresponding to the

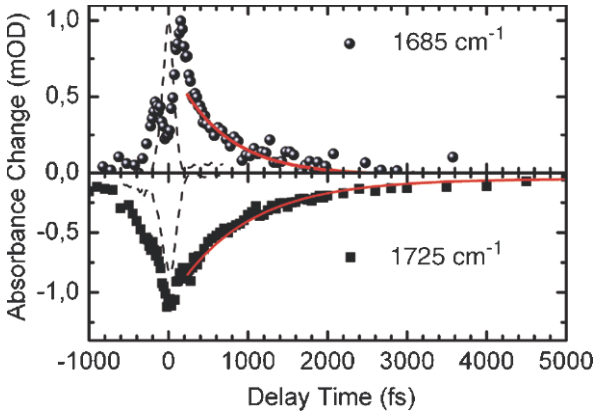

Fig. 9: Transients at 1685 cm^{-1} (circles) and 1725 cm^{-1} (squares) after excitation at 1760 cm^{-1} (FWHM 100 cm^{-1}). Solid lines represent fits with 0.7 ± 0.1 ps and 0.9 ± 0.1 ps time constants for 1685 and 1725 cm^{-1}, respectively. System response (dashed lines).

rise of hot water signal due to energy transfer from the DNA oligomer to the water molecules. However, the initial sub-picosecond dynamics are markedly different for these two excitation frequencies, further confirming that both signals can not be due to the overtone excitation of the water δ_{NH_2}. Although the absorption at both frequencies is comparable, the signal strength after excitation at 1630 cm^{-1} is in fact seven times stronger than after excitation at 1730 cm^{-1}, which indicates that the $\nu_{C2=O2}$ vibration couples substantially weaker to the ν_{NH_2} vibration than both the $\nu_{C4=O4}$ and the δ_{NH_2} vibration.

4 Discussion

A model summarizing the theoretical and experimental results is given in Fig. 4b. The calculated couplings of the $\nu_{C4=O4}$, δ_{NH_2}, and $\nu_{C2=O2}$ to the ν_{NH_2} vibration indicate that excitation of either of these modes should result in a bleaching signal due to the shifting of the $\nu_{NH_2}\ = 0 \rightarrow 1$ transition. The bleach signals in Fig. 7 around 3215 cm^{-1} agree with this theoretical result. Furthermore, the force constants in Table 5 predict that excitation of the $\nu_{C4=O4}$ and δ_{NH_2} vibrations should result in a larger shift of the ν_{NH_2} vibration than of the $\nu_{C2=O2}$ vibration. This is confirmed by the data in Fig. 7. Experimentally, one cannot distinguish between the contributions of the $\nu_{C4=O4}$ and δ_{NH_2} modes. From the force constants in Table 5, however, we conclude that excitation

of the δ_{NH_2} vibration is expected to have the most substantial effect on the shift of the ν_{NH_2} vibration. The agreement between theoretical predictions and IR pump-probe measurements allows us to assign the bleaching signal at 3215 cm^{-1} at least partially to the symmetric ν_{NH_2} vibration of adenine. This absorption band lies about 100 cm^{-1} lower in energy than the same mode in modified adenine-uracil Watson-Crick base pairs in solution [21]. The lower frequency of the hydrogen-bonded ν_{NH_2} vibration in DNA films compared to single AU base pairs in $CDCl_3$ solution can be rationalized by significant interactions with neighbouring base pairs and water molecules, that weaken the force constant. The theoretical results further show, that inclusion of water molecules leads to a HB between a water molecule and the NH_2 group of adenine, and therefore a coupling of the adenine ν_{NH_2} vibration and of the water bending vibration. Due to this coupling, this water molecule could act as a primary energy sink in energy disposal by DNA. Since the amount of water molecules and the coupling of water molecules to the nucleic acids is different for the major groove and the minor groove, one would expect different energy relaxation pathways with deviating time constants for energy flow from water to DNA and DNA to water, for both sides. Energy redistribution processes in DNA itself provide complex relaxation patterns as presented for the $\nu_{C2=O2}$ vibration.

In summary, the presented results demonstrate the capacity of combining IR-pump-probe methods with calculations on microsolvated base pairs to reveal information on hidden vibrational absorption bands. The simulation of real condensed phase dynamics of HBs, however, requires to take into account all intra- and intermolecular interactions mentioned in the Introduction. As far as DNA is concerned, Cho and coworkers have given an impressive account on the dynamics of the CO fingerprint modes [22–25]. Promising results for a single AU pair in deuterochloroform [21] have been reported recently using a QM/MM scheme [65].

Acknowledgment

We gratefully acknowledge financial support by the Deutsche Forschungsgemeinschaft (Sfb450) and the project MZOS 098-0352851-2921. We thank G. Kovacevic for his help concerning the normal mode decomposition. The experimental data have been recorded at the Max Born Institut für Nichtlineare Optik und Kurzzeitspektroskopie, Berlin, Germany.

References

1. V. May, O. Kühn, *Charge and Energy Transfer Dynamics in Molecular Systems, 2nd Revised and Enlarged Edition* (Wiley–VCH, Weinheim, 2004)
2. E.T.J. Nibbering, T. Elsaesser, Chem. Rev. **104**, 1887 (2004)

3. K. Heyne, E.T.J. Nibbering, T. Elsaesser, M. Petković, O. Kühn, J. Phys. Chem. A **108**, 6083 (2004)
4. E.T.J. Nibbering, J. Dreyer, O. Kühn, J. Bredenbeck, P. Hamm, T. Elsaesser, in *Analysis and control of ultrafast photoinduced reactions*, *Springer Series in Chemical Physics*, vol. 87, ed. by O. Kühn, L. Wöste (Springer Verlag, Heidelberg, 2007), p. 619
5. K. Giese, M. Petković, H. Naundorf, O. Kühn, Phys. Rep. **430**, 211 (2006)
6. Y. Maréchal, *The Hydrogen Bond and the Water Molecule* (Elsevier, Amsterdam, 2007)
7. M. Tsuboi, Applied Spectroscopy Reviews **3**, 45 (1969)
8. R. Clark, R. Hester, *Advances in Infrared and Raman Spectroscopy*, vol. 12 (Wiley Heyden Ltd., New York, 1985)
9. R. Letellier, M. Ghomi, E. Taillandier, J. Biomol. Struct. Dyn. **4**, 663 (1987)
10. J. Florián, V. Hrouda, P. Hobza, J. Am. Chem. Soc. **116**, 1457 (1994)
11. J. Florián, J. Leszczynski, B. Johnson, J. Mol. Struct. **349**, 421 (1995)
12. M. Ouali, H. Gousset, F. Geinguenaud, J. Liquier, J. GabarroArpa, M. LeBret, E. Taillandier, Nucleic Acids Res. **25**, 4816 (1997)
13. O. Shishkin, J. Sponer, P. Hobza, J. Mol. Struct. **477**, 15 (1999)
14. F. Howard, H. Miles, J. Biol. Chem. **240**, 801 (1965)
15. V. Spirko, J. Sponer, P. Hobza, J. Chem. Phys. **106**, 1472 (1997)
16. J. Sponer, H. Gabb, J. Leszczynski, P. Hobza, Biophys. J. **73**, 76 (1997)
17. M. Brandl, K. Lindauer, M. Meyer, J. Suhnel, Theor. Chem. Acc. **101**, 103 (1999)
18. J. Sponer, J. Leszczynski, P. Hobza, J. Mol. Struct.-Theochem **573**, 43 (2001)
19. E. Nir, C. Janzen, P. Imhof, K. Kleinermanns, M. de Vries, Phys. Chem. Chem. Phys. **4**, 740 (2002)
20. A. Krummel, P. Mukherjee, M. Zanni, J. Phys. Chem. B **107**, 9165 (2003)
21. S. Woutersen, G. Cristalli, J. Chem. Phys. **121**, 5381 (2004)
22. C. Lee, K. Park, M. Cho, J. Chem. Phys. **125**, 114508 (2006)
23. C. Lee, M. Cho, J. Chem. Phys. **125**, 114509 (2006)
24. C. Lee, K.H. Park, J.A. Kim, S. Hahn, M. Cho, J. Chem. Phys. **125**, 114510 (2006)
25. C. Lee, M. Cho, J. Chem. Phys. **126**, 145102 (2007)
26. W. Saenger, *Principles of Nucleic Acid Structure* (Springer-Verlag, New York, 1984)
27. V. Parvathy, S. Bhaumik, K. Chary, G. Govil, K. Liu, F. Howard, H. Miles, Nucleic Acids Res. **30**, 1500 (2002)
28. N. Pattabiraman, Biopolymers **25**, 1603 (1986)
29. A. Pichler, S. Rudisser, R. Winger, K. Liedl, A. Hallbrucker, E. Mayer, Chem. Phys. **258**, 391 (2000)
30. E. Taillandier, J. Ridoux, J. Liquier, W. Leupin, W. Denny, Y. Wang, G. Thomas, W. Peticolas, Biochemistry **26**, 3361 (1987)
31. M. Falk, K. Hartman, R. Lord, J. Am. Chem. Soc. **85**, 387 (1963)
32. J. Vargason, K. Henderson, P. Ho, Proc. Natl. Acad. Sci. **98**, 7265 (2001)
33. X. Shui, C.C. Sines, L. McFail-Isorn, D. VanDerveer, L.D. Williams, Biochemistry **37**, 16877 (1998)
34. H. Miles, Proc. Natl. Acad. Sci. **51**, 1104 (1964)
35. S. Adam, J. Liquier, J. Taboury, E. Taillandier, Biochemistry **25**, 3220 (1986)
36. J. Liquier, A. Akhebat, E. Taillandier, F. Ceolin, T. Dinh, J. Igolen, Spectrochim. Acta Part A **47**, 177 (1991)

37. G. Sutherland, M. Tsuboi, Proc. Royal Soc. London Series A **239**, 446 (1957)
38. M. Ghomi, R. Letellier, J. Liquier, E. Taillandier, Int. J. Biochem. **22**, 691 (1990)
39. J. Benevides, G. Thomas, Nucleic Acids Res. **11**, 5747 (1983)
40. M. Cowan, B. Bruner, N. Huse, J. Dwyer, B. Chugh, E. Nibbering, T. Elsaesser, R. Miller, Nature **434**, 199 (2005)
41. K. Heyne, N. Huse, J. Dreyer, E. Nibbering, T. Elsaesser, S. Mukamel, J. Chem. Phys. **121**, 902 (2004)
42. P. Jurecka, J. Sponer, J. Cerny, P. Hobza, Phys. Chem. Chem. Phys. **8**, 1985 (2006)
43. M. Kabelac, L. Zendlova, D. Reha, P. Hobza, J. Phys. Chem. B **109**, 12206 (2005)
44. M. Kabelac, P. Hobza, Phys. Chem. Chem. Phys. **9**, 903 (2007)
45. C. Fonseca-Guerra, F. Bickelhaupt, J. Snijders, E. Baerends, J. Am. Chem. Soc. **122**, 4117 (2000)
46. G. Villani, Chem. Phys. **316**, 1 (2005)
47. L. Gorb, Y. Podolyan, P. Dziekonski, W. Sokalski, J. Leszczynski, J. Am. Chem. Soc. **126**, 10119 (2004)
48. G.M. Krishnan, O. Kühn, Chem. Phys. Lett. **435**, 132 (2007)
49. B. Brauer, R. Gerber, M. Kabelac, P. Hobza, J. Bakker, A. Riziq, M. de Vries, J. Phys. Chem. A **109**, 6974 (2005)
50. A. Krummel, M. Zanni, J. Phys. Chem. B **110**, 13991 (2006)
51. A. Kumar, P.C. Mishra, S. Suhai, J. Phys. Chem. A **109**, 3971 (2005)
52. M.J. Frisch, G.W. Trucks, H.B. Schlegel, G.E. Scuseria, M.A. Robb, J.R. Cheeseman, J.A. Montgomery, Jr., T. Vreven, K.N. Kudin, J.C. Burant, J.M. Millam, S.S. Iyengar, J. Tomasi, V. Barone, B. Mennucci, M. Cossi, G. Scalmani, N. Rega, G.A. Petersson, H. Nakatsuji, M. Hada, M. Ehara, K. Toyota, R. Fukuda, J. Hasegawa, M. Ishida, T. Nakajima, Y. Honda, O. Kitao, H. Nakai, M. Klene, X. Li, J.E. Knox, H.P. Hratchian, J.B. Cross, V. Bakken, C. Adamo, J. Jaramillo, R. Gomperts, R.E. Stratmann, O. Yazyev, A.J. Austin, R. Cammi, C. Pomelli, J.W. Ochterski, P.Y. Ayala, K. Morokuma, G.A. Voth, P. Salvador, J.J. Dannenberg, V.G. Zakrzewski, S. Dapprich, A.D. Daniels, M.C. Strain, O. Farkas, D.K. Malick, A.D. Rabuck, K. Raghavachari, J.B. Foresman, J.V. Ortiz, Q. Cui, A.G. Baboul, S. Clifford, J. Cioslowski, B.B. Stefanov, G. Liu, A. Liashenko, P. Piskorz, I. Komaromi, R.L. Martin, D.J. Fox, T. Keith, M.A. Al-Laham, C.Y. Peng, A. Nanayakkara, M. Challacombe, P.M.W. Gill, B. Johnson, W. Chen, M.W. Wong, C. Gonzalez, J.A. Pople, *Gaussian 03, Revision B.04*. Gaussian Inc., Wallingford, CT (2004)
53. S. Carter, S.J. Culik, J.M. Bowman, J. Chem. Phys. **107**, 10458 (1997)
54. J.K.G. Watson, Mol. Phys. **15**, 479 (1968)
55. M. Bounouar, C. Scheurer, Chem. Phys. **323**, 87 (2006)
56. J.A. Boatz, M. S.Gordon, J. Phys. Chem. **93**, 1819 (1989)
57. W. Schneider, W. Thiel, Chem. Phys. Lett. **157**, 367 (1989)
58. A.G. Csaszar, in *Encyclopedia of Computational Chemistry*, ed. by P. v. Rague-Schleyer (John Wiley & Sons, Hoboken, 1998), p. 13
59. K. Heyne, G.M. Krishnan, O. Kühn, J. Phys. Chem. B **112**, 7909 (2008)
60. F. Obrien, J. Sci. Instr. Phys. Ind. **25**, 73 (1948)
61. R. Kaindl, M. Wurm, K. Reimann, P. Hamm, A. Weiner, M. Woerner, J. Opt. Soc. Am. B **17**, 2086 (2000)

62. H. Nienhuys, S. Woutersen, R. van Santen, H. Bakker, J. Chem. Phys. **111**, 1494 (1999)
63. N. Huse, S. Ashihara, E. Nibbering, T. Elsaesser, Chem. Phys. Lett. **404**, 389 (2005)
64. Z. Wang, A. Pakoulev, Y. Pang, D. Dlott, J. Phys. Chem. A **108**, 9054 (2004)
65. Y. Yan, G.M. Krishnan, O. Kühn, Chem. Phys. Lett. **464**, 230 (2008)

Simulation Study of the Molecular Mechanism of Intercalation of the Anti-Cancer Drug Daunomycin into DNA

Arnab Mukherjee, Richard Lavery, Biman Bagchi, and James T. Hynes

[1] Ecole Normale Supérieure, Chemistry Department, 24 Rue Lhomond, 75231 Paris Cedex 05, France, Arnab.Mukherjee@colorado.edu
[2] Institut de Biologie et Chimie des Protéines, CNRS UMR 5086 / Université de Lyon, 7 passage du Vercors, Lyon 69367, France, richard.lavery@ibcp.fr
[3] Solid State and Structural Chemistry Unit, Indian Institute of Science, Bangalore 560012, India, bbagchi@sscu.iisc.ernet.in
[4] Ecole Normale Supérieure, Department of Chemistry, CNRS UMR PASTEUR, 24 Rue Lhomond, 75231 Paris Cedex 05, France; Department of Chemistry and Biochemistry, University of Colorado, Boulder, CO 80309-0215, USA, hynes@chimie.ens.fr

Abstract. Intercalation of anti-cancer drugs into DNA is the insertion of the planar aromatic portion of the drug molecules between a pair of DNA basepairs, inducing certain local structural changes in the DNA and subsequently stopping its replication. Despite its importance, a detailed mechanistic understanding of this process at the molecular level is lacking. Here we recount some of the key aspects of our recent extensive simulation study addressed to this issue [A. Mukherjee, R. Lavery, B. Bagchi, and J. T. Hynes, J. Am. Chem. Soc. 130, 9747 (2008)]. In particular, we discuss the molecular aspects of the intercalation mechanism of a well-known anticancer drug daunomycin into a twelve basepair DNA with the help of a free energy landscape of the process constructed using extensive computer simulations (>0.3 μsec) with umbrella sampling techniques. The results give an intercalation free energy change (-12.3 kcal/mol) in reasonable agreement with experiment (-9.4 kcal/mol). They also point to a mechanism in which the drug first binds to the minor groove and then intercalates into the DNA in an activated process, in general agreement with experimental kinetic results.

1 Introduction

Anthracycline anti-cancer drug intercalation into DNA is a process in which the planar aromatic portion of the drug molecules inserts between a pair of DNA basepairs. This insertion subsequently leads to the stopping of DNA

I. Burghardt et al. (eds.), *Energy Transfer Dynamics in Biomaterial Systems*, Springer Series in Chemical Physics 93, DOI 10.1007/978-3-642-02306-4_7,

replication, resulting in cell death [1]. While aspects of the intercalation process have been studied over the years and important information has been gained (as indicated below), the molecular level mechanism of the intercalation is not known. In the present contribution, we recount some of the highlights of our recent computational study [2] aimed at providing new insights on the mechanism of the intercalation of the anthracycline drug daunomycin into DNA. No attempt is made here at completeness; the interested reader is referred to the original work [2] for further details and more extensive references.

The intercalation process has been the subject of extensive thermodynamic studies [3, 4], providing free energy, entropy and enthalpy differences between the intercalated and free states of various drug molecules. On the other hand, dynamic studies are far less common. Some different aspects of the intercalating molecules have been studied using ultrafast methods [5]. Kinetic studies of drug intercalation are few in number, and a consensus on the mechanism has not been reached [6, 7]. Thus, Chaires et al. [6] have proposed a three step model for daunomycin intercalation from the stopped flow association, while Rizzo et al. [7] have proposed a five step kinetic model.

Due to the complexity involved, theoretical studies related to intercalation [8, 9] are not common and have been restricted to a main focus of calculating the intercalation free energy, i.e., the free energy difference between intercalated and free states, using a continuum solvent approach [10,11]. These valuable studies have a number of limitations. They involve a very large cancellation of different contributions to the total free energy. Moreover, the molecular level role of water is missing in continuum solvent-based calculations. Finally, no information is provided about the mechanism of the intercalation.

Our study [2] addressed the question of the mechanism of DNA intercalation of the drug daunomycin (also known as daunorubicin [12]), widely used in various cancer treatments [13], by calculating a static free energy landscape for the process using an extensive set of all-atom simulations and umbrella sampling techniques [14]. This simulation study is a first effort to understand the intercalation process per se in atomistic detail and to elucidate its molecular aspects. It provides [2] an intercalation free energy in reasonable agreement with the experimental estimates, and points to a two-step mechanistic process in which daunomycin first goes, in a process downhill in free energy, to a minor groove-bound state and then crosses a barrier in an activated process to go to the intercalated state [2].

The outline of the remainder of this contribution is as follows. We describe the simulation approach in the next section and then discuss the results in Sect. 3, including a comparison with available experimental kinetic results. Finally, some concluding remarks are offered in Sect. 4.

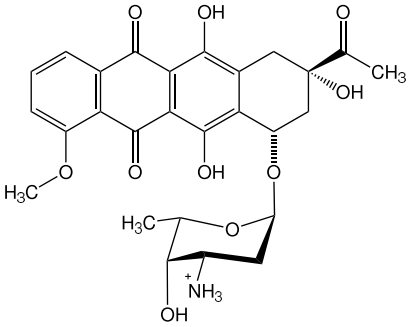

Fig. 1. Atomistic structure of daunomycin

2 Simulation Details

2.1 Construction of the Intercalated and the Minor Groove-bound States

The molecular structure of the anticancer drug daunomycin is shown in Fig. 1. It consists of an anthraquinone ring system (aglycon), the portion which intercalates into the DNA [15], and an amino sugar group (daunosamine), which stays in the DNA minor groove.

As described in more detail within, our actual calculations for the intercalation pathway proceeded in a "reverse" fashion. We calculated free energy changes as the drug was pulled out from the intercalated state and from a minor groove-bound state. The construction of these states is now discussed.

The crystal structure of the intercalated state of daunomycin-DNA was solved by Wang et al. [15] at 1.2 Å resolution and deposited in the protein data bank (PDB) [16] with PDB id 1D11. The crystal structure has a repeating unit of four base pairs $d(ACGT)_2$ in which two daunomycin molecules are intercalated between two separate CG base pairs. Using this crystal structure, we constructed a bigger, twelve basepair DNA. We kept the geometry of the three base pairs (ACG) intact and added four base pairs $d(CGCG)_2$ above and five base pairs $d(ACGCG)_2$ below using the DNA structure building and minimization program JUMNA [17] to construct a twelve basepair DNA. The complete DNA sequence is $d(GCGCACGTGCGC)_2$. As explained below, daunomycin was intercalated at the C6-G7 site, with the sugar group of daunomycin close to the A5 base pair.

Figure 2 shows the initial equilibrated intercalated state. The DNA sequence is $d(GCGCACGTGCGC)_2$. The intercalated structure's geometry is that of the B-DNA except for the 5th to 7th base pairs (A5 to G7), which stay close to the crystal structure used for the starting conformation, with a root mean square deviation of 3.2 Å for all the heavy atoms of those three basepairs. In this sequence, daunomycin is in contact with the strongest binding triplet sequence (A/T)CG [18, 19]. Moreover, due to the chosen sequence of the DNA, the intercalation site is flanked by the same sequence of basepairs in either direction, eliminating any related orientational preference of

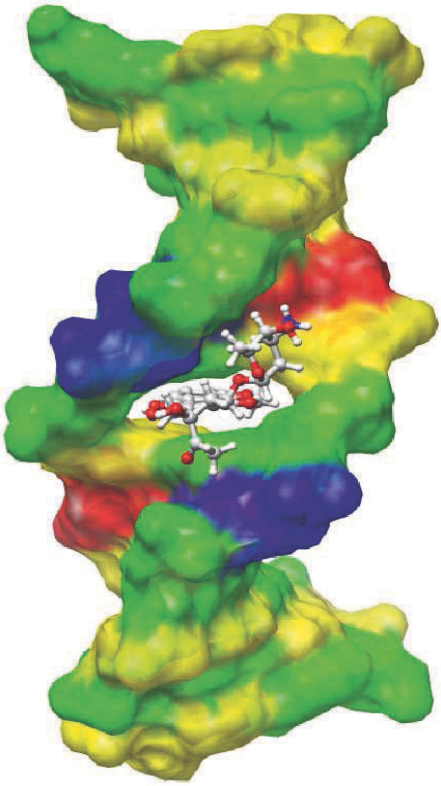

Fig. 2. Equilibrated structures of the intercalated state, plotted using Chimera. DNA is shown in a surface representation with residue-based color (yellow for C, green for G, red for A and blue for T), whereas daunomycin is represented via a ball and stick model with element-based CPK color.

the daunosamine sugar group. The four terminal base pairs on each DNA end were chosen as CG base pairs to increase overall stability [20].

Experimental studies [6,7] of the kinetics of daunomycin intercalation have indicated an initial bimolecular associated state which has been characterized as an intermediate "outside bound" state. Since a DNA minor groove-bound state is such a stable outside bound state and is known to be primary mode of binding for many other drugs [21], we constructed a minor groove-bound state of daunomycin and DNA as follows. Since the drug's binding in a minor groove does not affect the DNA structure, we constructed the DNA for the minor groove-bound state (Fig. 3) using the same sequence as that of the intercalated DNA with a complete B-DNA geometry using JUMNA [17]. The drug was then docked into the DNA minor groove using the docking program HEX [22]. Figure 3 shows the initial equilibrated structure of the minor groove-bound state.

2.2 Forcefield and Equilibration

All simulations were carried out with the GROMACS molecular dynamics simulation program [23] with some modification to perform the umbrella sampling

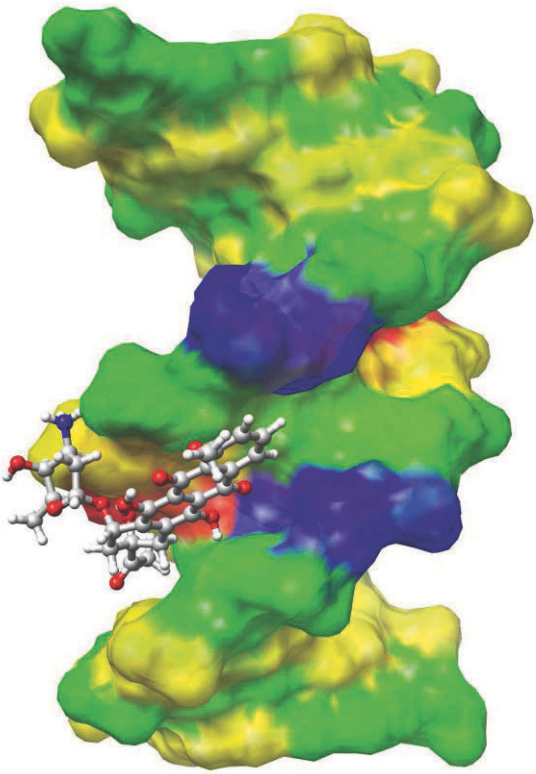

Fig. 3: Equilibrated structures of the minor groove-bound state, plotted using Chimera. Representation is same as used in Fig. 2.

along the chosen coordinate. Periodic boundary conditions were employed and Particle Mesh Ewald [24] was used for the long range electrostatic interactions. The AMBER94 force-field [25] was selected because it well describes B-DNA [20] (a refinement to the AMBER94 force-field has been published recently [26] which rectifies the problem of α/γ transition observed in DNA trajectories longer than those studied here), using AMBER ports in GROMACS [27]. Most daunomycin force-field parameters were obtained from AMBER94 [25], with those absent in AMBER94 obtained from AMBER99 [28] and GAFF [29]. The RESP charges of daunomycin were calculated using the antechamber module of AMBER7 molecular dynamics software [30] and Gaussian03 [31] using the Hartree-Fock method with the 6-31G* basis set.

The initial configurations of the intercalated and minor groove-bound states of the DNA/drug system were placed in a cubic box of side length 65 Å and then solvated by

TIP3P [32] water molecules. Twenty-two Na^+ ions and 1 Cl^- ion were placed randomly in the box to neutralize the DNA and positively charged daunomycin. In addition to the added ions, the system consists of 756 DNA atoms and 68 daunomycin atoms, solvated by 8822 water molecules, making a 27313 atom system. We also constructed a larger box of length 76.6 Å, which allowed us to study larger drug separations and to verify that the smaller box did not produce any artifacts in the energetic or structural features of the intercalation process.

After the initial configuration construction, we performed a standard equilibration protocol for DNA simulations [20]. The entire structure was minimized by the steepest descent method in order to avoid close atomic contacts, followed by slow constant volume heating to 300 K over 100 ps using 2.4 kcal/mol harmonic restraints. These restraints were slowly reduced to zero during a series of energy minimization and 50 ps equilibration steps at constant temperature (300 K) and pressure (1 bar) with a 0.2 ps coupling constant for both parameters. The final equilibration step was a 100 ps constant volume run.

2.3 Simulation Approach

The potential of mean force (PMF) gives the system free energy along a chosen reaction coordinate, and has for example recently been calculated in atomistic detail for protein - small molecule association [33]. In order to calculate this free energy and other reaction path quantities of the drug-DNA complex as a function of separation between the drug and the DNA, we carried out the simulations with an extra harmonic "umbrella potential" [14] acting on the drug-DNA separation X (sampling coordinate) along a particular vectorial direction [2]. Our coordinate choice was guided by (a) the necessity of pulling the drug out of the DNA intercalating center (IC), defined by the pair of base pairs involved in the intercalation, without affecting the drug's structure and (b) allowance of sampling of the drug on the minor groove side from where intercalation seems very likely to occur (given the experimentally observed position of the bulky daunomycin side chain in the minor groove following intercalation [15]). Related considerations [2] apply to the pulling out of the drug from the minor groove-bound state.

This sampling coordinate is measured by the projection (Fig. 4) of the vector $\boldsymbol{d}$ joining the center of mass (COM) of the IC to the COM of daunomycin onto a body-fixed unit vector $\hat{b}$, defined by the vector joining the COM of IC to the COM of two out of four ribose sugar groups (attached to the corresponding guanosine nucleotides) belonging to the intercalating set of base pairs which lie more towards the minor groove direction, i.e., $X = \hat{b} \cdot \boldsymbol{d}$. A harmonic umbrella potential $U = \frac{1}{2}k(X - X_0)^2$ is applied along the coordinate, with k the spring constant and X_0 the harmonic potential center.

With the equilibrated system, we began a series of canonical ensemble simulations by placing the umbrella potential center close to the intercalated

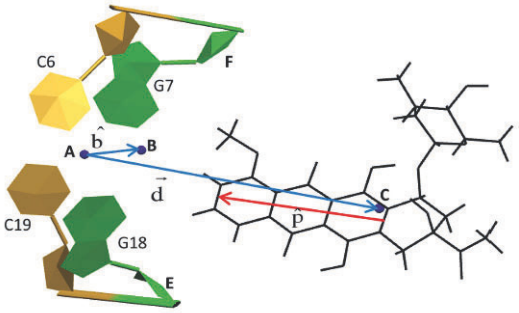

Fig. 4. Diagram of the body-fixed vector viewed along the DNA helical axis. "A" is the COM of the four bases as labeled (C6, G7, C19, G18). "B" is the COM of the sugar groups of G7 and G18 marked as "F" and "E". "C" is the COM of daunomycin. "AB" is the body-fixed vector $\hat{b}$ and "AC" is $\boldsymbol{d}$. $\hat{p}$ is the vector used to calculate an angle θ described in Fig. 7.

state and carrying out a 0.5 ns simulation. Subsequent simulations, each of 0.5 ns, were performed commencing with the previous simulation's end configuration by changing the umbrella potential center by only 0.4 to 0.5 Å to accelerate equilibration. For the intercalated to separated state transition, we performed 35 simulations, and for the minor groove-bound to separated state transition, 25 umbrella simulations were used. Bond lengths were constrained using the LINCS algorithm [34] and 2 fs integration time step was used for the simulations. The above 0.5 ns length for each umbrella simulation gave a far too large intercalation free energy ≈ -30 kcal/mol. Progressively increasing that length to 5 ns reduced this to ≈ 12 kcal/mol; the PMF calculated using all the umbrella simulations for various run lengths showed that the results varied with run lengths, so that convergence with 5 ns umbrella simulations was not guaranteed. To examine this, we took the final configurations of each 5 ns umbrella simulation and performed a further 2.5 ns simulation, with random initial velocities. The PMF calculated for various time lengths using these 2.5 ns trajectories produced an intercalation free energy -13.2 kcal/mol within ± 0.5 kcal/mol, indicating satisfactory convergence.

The slow convergence of the intercalation pathway can be reasonably linked to the large structural changes which are required in the DNA oligomer. Such changes are absent for the transition from separated to minor groove-bound drug, and an umbrella simulation length of 2.5 ns was found to be sufficient for a comparable convergence.

3 Results and Discussion

In the following, we discuss the simulation results [2] in terms of the transitions of the separated drug to the intercalated state and to the minor groove-bound state. We then discuss the minor groove-bound to intercalated state transition.

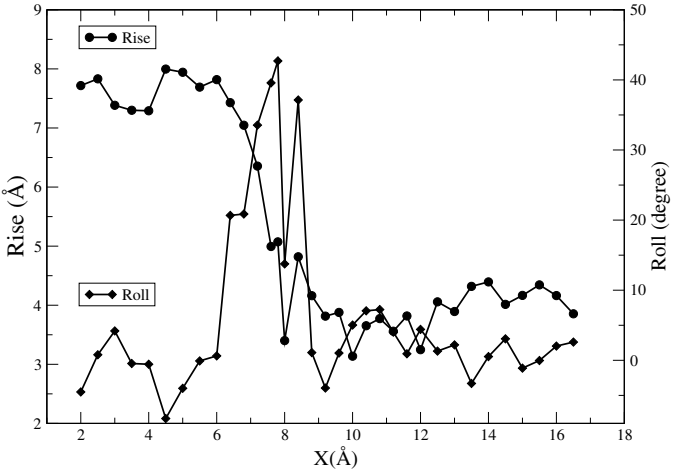

Fig. 5: Calculated changes in the average rise and roll angle of the separated to the intercalated state transition along the sampling coordinate X. Note that the roll angle increases earlier than the rise as the intercalating drug approaches.

3.1 Structural Changes in DNA during Intercalation: Rise and Roll

Although DNA obviously has a complicated structure, there are never-the-less six essential degrees of freedom (dof) of the base pair steps in terms of which the DNA structure can be described reasonably well [35]. The translational dof are the rise, shift, and slide, while the rotational dof are roll, tilt, and twist. These base pair step parameters provide a standard description of the base pair geometry defined by the Cambridge accord [36]. We monitored these parameters along each trajectory using the CURVES program [37]. Of these six parameters, the rise, roll and twist were found to be the important ones involved in the intercalation process [2]. Here we focus only on the first two of these parameters. The rise denotes the distance between two base pairs along the DNA helical axis; its value in normal B-DNA is ≈ 3.4 Å [38]. The roll is the angle made by two base pairs towards the minor groove side, and is close to zero in canonical B-DNA.

Figure 5 shows the average rise and roll values for each sampling window against the sampling coordinate X for the separated to intercalated state transition. Following the direction of the drug's approach from separated to intercalated state in this figure (i.e. from large to small X), the rise and roll values fluctuate around their normal values i.e., without any significant DNA structure change down to X $\approx$ 8.5 Å. For smaller X, first the roll angle starts to increase (implying opening towards the minor groove side of the double helix), followed by the increase in the rise. The 'front' part of the drug starts its insertion between the pair of base pairs around X=7.8 Å, where the roll angle has its maximum. Once the drug intercalates further into the DNA, the roll angle drops again to its normal value, allowing further increase in the rise. This sequence appears to be a natural one for the intercalation.

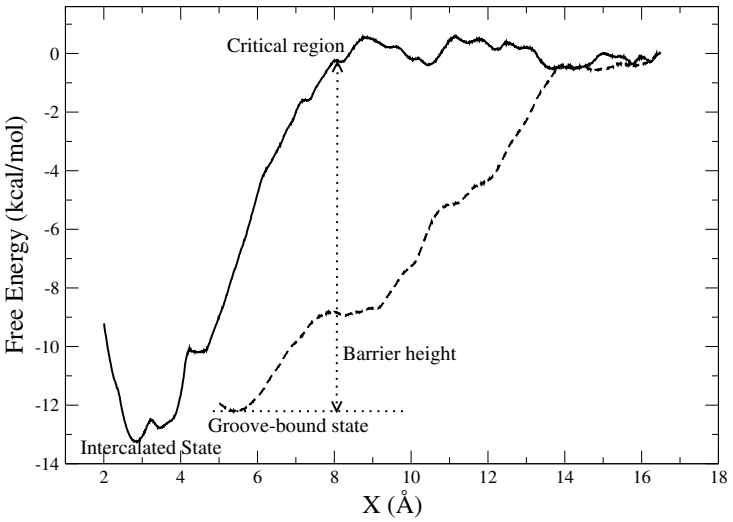

Fig. 6: Potential of mean force (PMF) along the sampling coordinate X leading to intercalation (solid line, X decreases as the drug approaches DNA) and leading to the minor groove-bound state transition (dashed line). The dotted line shows the barrier height for intercalation from the minor groove-bound state.

3.2 Potential of Mean Force of Intercalation

The umbrella sampling technique [14] allowed the obtaining of our sampling coordinate (X) probability distributions, which then were combined by the

weighted histogram analysis method (WHAM) [39, 40] to obtain the PMF or free energy along X. This is useful not only to understand the driving force for intercalation, but also to give some information on its kinetic aspects. Figure 6 (solid line) shows the PMF along X. The separated state (X=16.5 Å) is taken to have a reference zero value for the free energy.

Several features of the daunomycin intercalation free energy profile in Fig. 6 can be noted. First, the free energy minimum coincides with the crystal structure. Second, the PMF gives the difference in the free energy of the intercalated and separated states as -13.2 kcal/mol. In order to compare this with the experimental estimate of this intercalation free energy, we needed to include two corrections, connected to drug and ion concentrations [2]. With these two corrections, the resulting intercalation free energy is ≈ -12.3 kcal/mol, which is in reasonable agreement with the experimental value (≈-9.4 kcal/mol) [4].

We note parenthetically that the calculated [2] intercalation enthalpy -7.1 kcal/mol is also in reasonable agreement with the experimental estimate -8.2 kcal/mol [41], although as is well-known [42], such energetic calculations are subject to large uncertainties.

3.3 Minor Groove-bound State Analysis

We now investigate possible pathways of intercalation. To this end, we have created a minor groove-bound state which we consider a probable intermediate state in the intercalation process. Figure 6 shows the PMF of the separated state to the minor groove-bound state along the sampling coordinate X (dashed line), together with the corresponding PMF ending in the intercalated state for comparison.

Figure 6 indicates that the drug will first arrive at the minor groove-bound state following the minimum free energy path, i.e. there is a downhill free energy path to the minor groove when the daunomycin approaches the DNA from a completely separated state.

3.4 Minor Groove-bound to Intercalated State Transition

We next considered the transition from the groove-bound state to the intercalated state [2]. In order to intercalate starting from the former state, the drug needs to be oriented in such a way that the tip of the drug's planar aglycon portion (Fig. 1) could insert between the pair of base pairs. This criterion compels the drug to be in a correct orientation at a correct distance (X ≈ 8 Å, see below) from the intercalating base pairs. (Once the drug is intercalated, the orientation becomes automatically restricted due to the geometrical constraints imposed by the DNA.) The combination of distance and orientation could be termed a "critical" or "gate" region (defined below) through which the drug has to pass in order to intercalate. An estimate of the barrier height can be derived from Fig. 6 by noting that the free energy is downhill from

the critical region to the intercalated state. Therefore, the barrier height for the minor groove to intercalated state transition would be obtained from the difference of free energy at the critical region at X $\approx$ 8 Å ($\approx$ -0.3 kcal/mol) to the free energy of the minor groove-bound state (-12.2 kcal/mol) giving rise to a barrier of 11.9 kcal/mol. This value is fairly close to the experimental estimate of 14.9 kcal/mol calculated (see Sect. 3.6) using a rate constant in the kinetic model of Chaires et al. [6] A more detailed approach to the theoretical estimate of the barrier height is taken up next.

3.5 Two dimensional (2D) Free Energy Landscape of Daunomycin Intercalation

Simple geometric considerations, sketched in Fig. 7, indicate that a two dimensional (2D) description of the minor groove-bound to intercalated state transition for the drug is necessary, with attention to the orientation of the drug. Rigorous calculation of a 2D free energy surface for the present system is extremely difficult and time consuming. However, an approximate calculation can give insight into the reaction path not readily obtained in a 1D approach. We calculated [2] two 2D free energy surfaces from two independent sets of simulations, one leading to the intercalated state from the separated state and another leading to the minor groove-bound state from the separated state, using the probability distributions of X and an angle θ and combining the distributions using WHAM [39, 40]. The second dimension θ is the angle made by the body-fixed vector and the vector parallel to the aglycon plane pointing towards the tip of the drug (see Fig. 4), and is a useful parameter to distinguish the minor groove-bound state from the intercalated state (Fig. 7): θ is small ($<50°$) for the former and large ($>150°$) for the latter. The essential approximation is that no umbrella potential was used for θ. The angle is instead free to fluctuate, which naturally does not ensure sufficient sampling in all regions of the individual free energy surfaces. To approximately overcome this limitation, we combined the two 2D free energy surfaces into a single 2D free energy surface (Fig. 8), in which we averaged the values for each grid point wherever the two individual surfaces overlap.

The resulting free energy contour plot [2] Fig. 8 indicates that in order to intercalate, the drug first follows the minimum free energy path to the minor groove-bound state. It then - with accompanying DNA distortions - climbs up a free energy barrier by changing both distance and orientation to reach the critical region (loosely defined by X $\approx$ 8 Å and $\theta > 150°$), which serves a gate for the subsequent intercalated state, and finally descends to the intercalated state. From Fig. 8, the estimated free energy barrier for the minor groove-bound to intercalated state transition is 12 kcal/mol, very close to our estimate mentioned above.

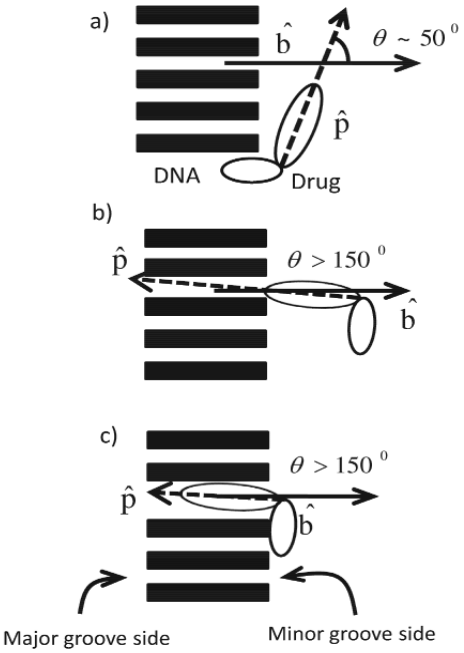

Fig. 7. Schematic picture for the angle θ for the (a) minor groove-bound state, (b) the critical region and (c) the intercalated state. The DNA is shown as a stack of bars and the drug is shown as a combination of two ellipses. θ is the angle for the dot product of unit vectors $\hat{b}$ and, $\hat{p}$. see Fig. 4.

3.6 Comparison with Experimental Kinetics Results

The calculations performed in ref. [2] and briefly summarized above for daunomycin intercalation into DNA give an overall intercalation free energy in reasonable agreement with experimental estimates. They have indicated a sequence of DNA roll and rise distortions (as well as changes in water H-bonds not discussed here; see ref. 2) associated with the process. These free energy calculations suggest that the overall mechanistic picture for the reaction pathway is, first, a downhill transition in free energy from the completely separated drug to a DNA minor groove-bound state, and second, an activated transition of the drug from this groove-bound state to the intercalated state, with a free energy barrier ≈11.9 kcal/mol (Fig. 6).

While these free energy calculations do not directly address the intercalation dynamics, we could nonetheless discuss [2] this mechanistic picture in the context of the two most extensive experimental kinetic studies [6,7] for daunomycin intercalation (which as noted in the Introduction are not in complete accord with each other). We do not enter into the details of this comparison here, but refer the reader to our original article [2]. Suffice it to say here that reasonable accord with some of the kinetics results of Chaires et al. [6] was obtained, and we assigned the first two steps of the three step mechanism of these authors in terms of the two step mechanism we have described above.

There is however a discrepancy in that Chaires et al. [6] proposed a final, third step. The final unimolecular step in the mechanism was postulated by

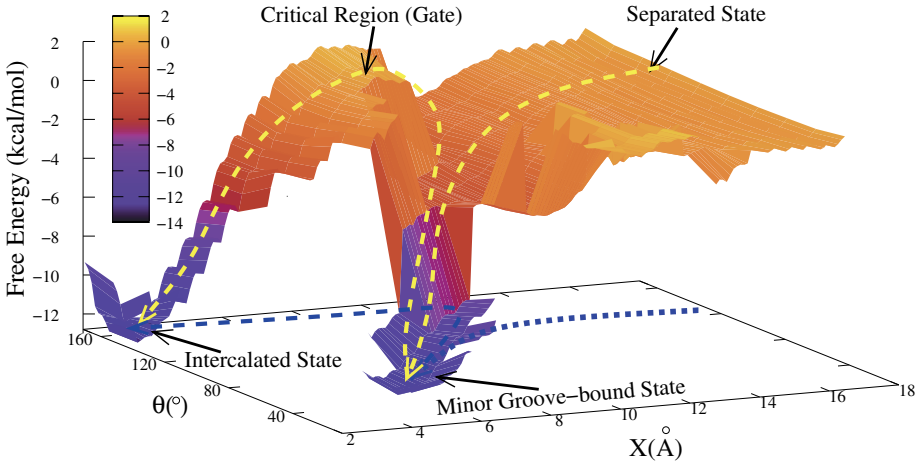

Fig. 8: Free energy landscape in the umbrella sampling coordinate X and the angle θ (see Figs. 4 and 7). The intercalated, minor groove-bound, and separated states are indicated, as is the critical region. The yellow (light grey) arrowed dashed lines (and their blue (black) projections onto the X-θ plane) are schematic guides to show the most probable path from separated → minor groove-bound → intercalated state through the critical region (see Fig. 7b). Due to the approximate nature of the calculations, it is not possible at this stage to say whether or not the small corrugations in the surface are physically meaningful.

these authors to be an activated readjustment of either the intercalated drug or the DNA in the presence of the intercalated drug. It is possible that the second and third steps observed by Chaires et al. represent a first intercalation to less stable site, followed by intercalation to the most stable site, whereas our calculations involve intercalation to the most stable site. Another possibility is the following. It is important to recall that in the PMF calculations of ref. [2] summarized here, the entire drug/DNA system is equilibrated at each sampling coordinate(s) value, as in Figs. 6 and 8. In such calculations, any nonequilibrium dynamical character of adjustments in the intercalated drug/DNA system would be absent. It is thus possible that the second and third step [6] in Chaires et al [6] are folded together, in an equilibrium path fashion, in the second, groove-bound state → intercalated state transition that we have found. This possibility is currently being investigated via appropriate nonequilibrium simulations, for which the study summarized here provides an important starting point.

4 Concluding Remarks

The extensive all-atom simulations of ref. [2] summarized here for daunomycin intercalation into DNA have given an overall intercalation free energy in reasonable agreement with experimental estimates. They indicate a sequence of DNA roll and rise distortions as well as changes in water H-bonds associated with the process. The free energy calculations suggest that the overall mechanistic picture for the reaction pathway is, first, a downhill transition in free energy from the completely separated drug to a DNA minor groove-bound state, and second, an activated transition of the drug from this groove-bound state to the intercalated state, with a free energy barrier ≈ 11.9 kcal/mol. Comparison with available kinetic results indicates reasonable quantitative agreement with this mechanistic picture, although the experiments suggest that the final intercalation step may be more complex than the one depicted in the present equilibrium path calculations. This issue is currently under investigation. Finally, one should note that the free energetically favorable minor groove-bound state that we have found need not be unique, and could be one representative of several possible "outside bound", i.e. non-intercalated, bound states in an experimental situation. This issue too is also under current investigation.

Acknowledgment

We thank P. Kiefer, D. Laage, S. Re, and J. Nandakumar for discussions. This work was supported by CEFIPRA-IFCPAR (Project No. 3105-1).

References

1. H. M. Berman, P. R. Young: Ann. Rev. Biophys. Bioeng. **10**, 87 (1981).
2. A. Mukherjee, R. Lavery, B. Bagchi, J. T. Hynes: J. Am. Chem. Soc. **130**, 9747 (2008).
3. D. P. Remeta, C. P. Mudd, R. L. Berger, K. J. Breslauer: Biochemistry **32**, 5064 (1993).
4. J. B. Chaires, S. Satyanarayana, D. Suh, I. Fokt, T. Przewloka, W. Priebe: Biochemistry **35**, 2047 (1996).
5. X. G. Qu, C. Z. Wan, H. C. Becker, D. P. Zhong, A. H. Zewail: Proc. Natl. Acad. Sci. U.S.A. **98**, 14212 (2001).
6. J. B. Chaires, N. Dattagupta, D. M. Crothers: Biochemistry**24**, 260 (1985).
7. V. Rizzo, N. Sacchi, M. Menozzi: Biochemistry **28**, 274 (1989).
8. M. Baginski, F. Fogolari, J. M. Briggs: J. Mol. Biol. **274**, 253 (1997).
9. M. Trieb, C. Rauch, F. R. Wibowo, B. Wellenzohn, K. R. Liedl: Nucl. Acids Res. **32**, 4696 (2004).
10. B. Honig, A. Nicholls: Science **268**, 1144 (1995).
11. J. M. Swanson, R. H. Henchman, J. A. McCammon: Biophys. J. **86**, 67 (2004).

12. A. DiMarco, M. Gaetani, P. Orezzi, B. Scarpinato, R. Silvestrini, M. Soldati, T. Dasdia, L. Valentini: Nature **201**, 706 (1964).
13. G. Minotti, P. Menna, E. Salvatorelli, G. Cairo, L. Gianni: Pharmacol Rev **56**, 185 (2004).
14. G. M. Torrie, J. P. Valleau: J. Comp. Phys. **23**, 187 (1977).
15. A. H.-J. Wang, G. Ughetto, G. J. Quigley, A. Rich: Biochemistry **26**, 1152 (1987).
16. H. M. Berman, J. Westbrook, Z. Feng, G. Gilliland, T. N. Bhat, H. Weissig, I. N. Shindya-lov, P. E. Bourne: Nucl. Acids Res. **28**, 235 (2000).
17. R. Lavery, K. Zakrzewska, H. Sklenar: Comput. Phys. Commun. **91**, 135 (1995).
18. J. B. Chaires, J. E. Herrera, M. J. Waring: Biochemistry **29**, 6145 (1990).
19. S. N. R. Piotr Cieplak, Peter D. J. Grootenhuis, Peter A. Kollman,: Biopolymers **29**, 717 (1990).
20. D. L. Beveridge, G. Barreiro, K. S. Byun, D. A. Case, T. E. Cheatham, S. B. Dixit, E. Giudice, F. Lankas, R. Lavery, J. H. Maddocks, R. Osman, E. Seibert, H. Sklenar, G. Stoll, K. M. Thayer, P. Varnai, M. A. Young: Biophys. J. **87**, 3799 (2004).
21. B. H. Geierstanger, D. E. Wemmer: Annu. Rev. Biophys. Biomolec. Struct. **24**, 463 (1995).
22. D. Mustard, D. W. Ritchie: Proteins **60**, 269 (2005). 15
23. H. J. C. Berendsen, D. v. d. Spoel, R. Vandrunen: Comput. Phys. Commun. **91**, 43 (1995).
24. T. Darden, D. York, L. Pedersen: J. Chem. Phys. **98**, 10089 (1993).
25. W. D. Cornell, P. Cieplak, C. I. Bayly, I. R. Gould, K. M. Merz Jr, D. M. Ferguson, D. C. Spellmeyer, T. Fox, J. C. Caldwell, P. A. Kollman: J. Am. Chem. Soc. **117**, 5179 (1995).
26. A. Perez, I. Marchan, D. Svozil, J. Sponer, T. E. Cheatham, 3rd, C. A. Laughton, M. Oroz-co: Biophys J **92**, 3817 (2007).
27. E. J. Sorin, V. S. Pande: Biophys. J. **88**, 2472 (2005).
28. J. Wang, P. Cieplak, P. A. Kollman: J. Comp. Chem. **21**, 1049 (2000).
29. J. Wang, R. M. Wolf, J. W. Caldwell, P. A. Kollman, D. A. Case: J. Com. Chem. **25**, 1157 (2004).
30. D. A. Case, D. A. Pearlman, J. W. Caldwell, T. E. Cheatham, III, J. Wang, W. S. Ross, C. L. Simmerling, T. A. Darden, K. M. Merz, R. V. Stanton, A. L. Cheng, J. J. Vincent, M. Crowley, V. Tsui, H. Gohlke, R. J. Radmer, Y. Duan, J. Pitera, I. Massova, G. L. Seibel, U. C. Singh, P. K. Weiner, P. A. Kollman, AMBER 7, (University of California, San Francisco., 2002).
31. M. J. Frisch, G. W. Trucks, H. B. Schlegel, G. E. Scuseria, M. A. Robb, J. R. Cheeseman, J. A. Montgomery, T. Vreven, K. N. Kudin, J. C. Burant, J. M. Millam, S. S. Iyengar, J. Tomasi, V. Barone, B. Mennucci, M. Cossi, G. Scalmani, N. Rega, G. A. Petersson, H. Nakatsuji, M. Hada, M. Ehara, K. Toyota, R. Fukuda, J. Hasegawa, M. Ishida, T. Nakajima, Y. Honda, O. Kitao, H. Nakai, M. Klene, X. Li, J. E. Knox, H. P. Hratchian, J. B. Cross, V. Bakken, C. Adamo, J. Jaramillo, R. Gomperts, R. E. Stratmann, O. Yazyev, A. J. Austin, R. Cammi, C. Pomelli, J. W. Ochterski, P. Y. Ayala, K. Morokuma, G. A. Voth, P. Salvador, J. J. Dannenberg, V. G. Zakrzewski, S. Dapprich, A. D. Daniels, M. C. Strain, O. Farkas, D. K. Malick, A. D. Rabuck, K. Raghavachari, J. B. Foresman, J. V. Ortiz, Q. Cui, A. G. Baboul, S. Clifford, J. Cioslowski, B. B. Stefanov, G. Liu, A. Liashenko, P. Piskorz, I. Komaromi, R. L. Martin, D. J.

Fox, T. Keith, M. A. Al-Laham, C. Y. Peng, A. Nanayakkara, M. Challacombe, P. M. W. Gill, B. Johnson, W. Chen, M. W. Wong, C. Gonzalez, J. A. Pople: Gaussian 03, Revision C.02. (2003).
32. W. L. Jorgensen: J. Am. Chem. Soc. **103**, 335 (1981).
33. H.-J. Woo, B. Roux: Proc. Natl. Acad. Sci. USA **102**, 6825 (2005).
34. B. Hess, H. Bekker, H. J. C. Berendsen, J. Fraaije: J. Comp. Chem. **18**, 1463 (1997).
35. D. Bhattacharya, M. Bansal: J. Biomol. Struct. Dyn. **6**, 93 (1988).
36. R. E. Dickerson, M. Bansal, C. R. Calladine, et al.: EMBO J. **8**, 1 (1989).
37. R. Lavery, H. Sklenar: J. Biomol. Struct. Dyn. **6**, 655 (1989).
38. W. Saenger: Principles of Nucleic Acid Structure, (Springer-Verlag, New York, 1984).
39. S. Kumar, D. Bouzida, R. H. Swendsen, P. A. Kollman, J. M. Rosenberg: J. Comp. Chem. **13**, 1011 (1992).
40. B. Roux: Comput. Phys. Commun. **91**, 275 (1995).
41. D. P. Remeta, C. P. Mudd, R. L. Berger, K. J. Breslauer: Biochemistry **30**, 9799 (1991).
42. P. Kollman: Chem. Rev. **93**, 2395 (1993).

Part III

Quantum Dynamics and Transport at Interfaces and Junctions

Ultrafast Photophysics of Organic Semiconductor Junctions

Irene Burghardt, Eric R. Bittner, Hiroyuki Tamura, Andrey Pereverzev, and John Glenn S. Ramon

[1] Département de Chimie, Ecole Normale Supérieure, 24 rue Lhomond, 75231 Paris cedex 05, France, irene.burghardt@ens.fr
[2] Department of Chemistry and Texas Center for Superconductivity, University of Houston, Houston, Texas 77204, USA, bittner@uh.edu
[3] Département de Chimie, Ecole Normale Supérieure, 24 rue Lhomond, 75231 Paris cedex 05, France, present address: Advanced Institute for Material Research, Tohoku University, 2-1-1 Katahira Aobaku Sendai, Japan, tamura.hiroyuki@orion.ocn.ne.jp
[4] Department of Chemistry and Texas Center for Superconductivity, University of Houston, Houston, Texas 77204, USA, andrey.pereverzev@mail.uh.edu
[5] Department of Chemistry and Texas Center for Superconductivity, University of Houston, Houston, Texas 77204, USA

Abstract. This contribution gives an overview of our recent studies of the electronic structure and ultrafast photophysics of semiconductor polymer junctions. We focus on the phonon-assisted exciton dissociation at donor-acceptor heterojunctions, using state-of-the-art electronic structure methods in conjunction with vibronic coupling models and multiconfigurational quantum dynamical techniques. The decay of the photogenerated exciton towards an interfacial charge-separated state is an ultrafast (femtosecond to picosecond scale) process which precedes photocurrent generation. We describe this process using a linear vibronic coupling model parametrized for two to three electronic states and 20-30 phonon modes. Several representative interface configurations are considered, which are shown to differ significantly in their cross-chain interactions but exhibit an efficient exciton dissociation in all cases investigated. The exciton decay depends critically on the presence of intermediate states and on the dynamical interplay between high-frequency (C=C stretch) and low-frequency (ring-torsional) modes. The resulting molecular-level picture of exciton dissociation could contribute to the design of efficient polymer junctions.

1 Introduction

The photophysics of semiconducting conjugated polymers is a key ingredient for the understanding and design of optoelectronic devices such as organic light-emitting diodes (OLEDs) and solar cells [1–10]. In view of these materials' composition of molecular building blocks, a natural approach is to

I. Burghardt et al. (eds.), *Energy Transfer Dynamics in Biomaterial Systems*, Springer Series in Chemical Physics 93, DOI 10.1007/978-3-642-02306-4_8,

interpret polymer photophysics by analogy with the photophysics and photochemistry of smaller organic species. One would thus typically expect vibrational relaxation and ultrafast internal conversion processes that lead to deexcitation on a femtosecond to picosecond time scale. These efficient deexcitation mechanisms are reflected, e.g., in Kasha's rule [11–13], a key rule of molecular photochemistry which states that fluorescence always occurs from the lowest excited state. (A related formulation known as the Kasha-Vavilov rule [14] states that the fluorescence quantum yield is independent of excitation frequency.) Even though exceptions to these rules occur – due to photophysical pathways that do not lead to the lowest excited state – their remarkable generality has been confirmed for a majority of organic systems. The Kasha-Vavilov rule has indeed been found to also hold for polymers of poly-phenylene-vinylene (PPV) type, according to the observations, e.g., of Ref. [15] which reports on the independence of the observed photoluminescence signal of the excitation wavelength.

However, beyond these similarities with conventional organic photochemistry, a host of new phenomena occur which reflect the extended nature of the conjugated π electronic system. This entails the formation of delocalized exciton states [6], along with excitation energy transfer (exciton migration) and dissociation of excitons to polaron pairs, i.e., formation of charge transfer states which are precursors of photocurrent carrying states. These processes can also be ultrafast and are expected to compete with the internal conversion pathways addressed above. Thus, the dissociation into charge carriers has been found to compete with the decay to the lowest excited state in PPV type systems, leading to a (partial) breakdown of Kasha's rule [16,17]. In all of these processes, both site-site interactions and electron-phonon coupling play a decisive role. Time-resolved experiments have provided evidence for the ultrafast [16, 18, 19] and coherent [20], quantum-mechanical nature of many of the processes involved. Very recent experiments indicate long-lived electronic coherences in the ultrafast exciton migration dynamics along polymer chains even at room temperature [21]. To provide an appropriate theoretical description of these dynamical phenomena, a perspective has to be adopted that interpolates between a molecular-level picture and a description in terms of a disordered, solid-like phase.

In the present contribution, we illustrate a molecular-level approach to the electronic structure and charge transfer dynamics at polymer heterojunctions [22–26], i.e., interfaces between phase-separated semiconducting polymer domains. So-called bulk heterojunctions [26] provide conditions for an extremely efficient charge separation at the interface; the advent of this type of heterojunctions in fact brought significant advances in device efficiency. In photovoltaic diode devices, the primary excitation is a photogenerated exciton stabilized by the electron-hole Coulombic interaction, with a typical binding energy of $\epsilon_B \sim 0.5$ eV [26–29], i.e., considerably larger than in inorganic semiconductors where ϵ_B typically lies in the 50 meV range. Due to the highly folded interfacial area in bulk heterojunction materials, the exciton has

an enhanced probability of reaching the interface within the diffusion length (typically $\sim$ 10 nm [28,30,31]). The exciton decay towards a charge-separated state ("exciplex") [26, 32, 33, 35–38] is largely determined by molecular-level electronic interactions at the interface. Recent time-resolved photoluminescence studies have shown that the exciton decay falls into a (sub)picosecond regime [32, 34].

In the following, we first give an account of the electronic structure side, summarizing recent time-dependent density functional theory (TD-DFT) calculations for interface fragments with different stacking geometries [41,43]. We then focus on the crucial role of electron-phonon coupling in mediating the ultrafast decay of the initially generated exciton to an interfacial charge transfer state. The currently accepted picture of the processes at a heterojunction involves the formation of both photoluminescent exciplex states and optically dark charge transfer states [41, 44]. The dynamical treatments which we describe here therefore include both 2-state and 3-state models which attempt to capture the relevant features of the dynamics. In the present analysis, we focus on the earliest events at the interface, which are followed by exciton regeneration and photocurrent generation [32,34,39,40] on longer time scales.

The approach adopted here combines high-level excited-state electronic structure calculations, vibronic coupling models that are adapted to the spatially extended nature of the system, and state-of-the-art techniques for the quantum dynamical description of electron-phonon coupling in high-dimensional systems. Using full quantum-dynamical calculations by the multi-configuration time-dependent Hartree (MCTDH) method [45–49] for 2-3 electronic states and 20-30 explicit phonon modes, a molecular-level picture of the exciton dissociation event is obtained. As detailed in Refs. [50–53], the exciton dissociation involves a coherent nonadiabatic transfer dynamics between the photogenerated exciton state and one or several charge transfer states; this process is found to be ultrafast ($\sim$100 fs–1 ps). A key factor in the dynamics is the interplay between high-frequency (C=C stretch) and low-frequency (ring-torsional) modes. Importantly, the exciton decay is found to be inefficient in the absence of the low-frequency modes [50, 51]. The dynamical mechanism is interpreted in terms of a hierarchical electron-phonon model which allows one to identify generalized reaction coordinates for the nonadiabatic process. This analysis highlights that the electron-phonon coupling is dominated by high-frequency modes, but the presence of low-frequency modes is crucial in mediating the transition to a charge-separated state. Further, the presence of intermediate states is favorable to the exciton dissociation, and the process is found to remain dynamically robust with respect to variation of the cross-chain interactions [53]. The ultrafast nature of the dynamics is in agreement with time-resolved spectroscopic observations [32].

In the remainder of this chapter, we first give an overview of electronic structure calculations for the donor-acceptor heterojunction systems under consideration (Sec. 2). We then introduce the electron-phonon coupling model adopted to describe the extended polymer system (Sec. 3), followed by an

account of the dynamical analysis based on a linear vibronic coupling Hamiltonian (Sec. 4). We employ, in particular, recently developed techniques by which a relevant set of effective modes is constructed that account for the short-time dynamics in high dimensional systems involving conical intersection topologies [51,54,55]. In Sec. 5, these methods are applied to the exciton dissociation at a heterojunction. Given that the systems under study typically involve high- vs. low frequency phonon distributions, we identify certain mechanistic aspects which should carry over to a related class of systems. Finally, Sec. 6 gives an outlook on possible extensions of the present analysis.

2 Overview of interfacial electronic states of polymer heterojunctions

Here, a brief summary is provided of the current understanding of the electronic structure properties of the heterojunction interface. We start with the basic picture of the energetics (Sec. 2.1), based on the offset between the frontier orbitals of the two polymer species; this offset triggers the dissociation of the photogenerated exciton if the exciton binding energy $\epsilon_B \sim 0.5$ eV can be overcome. To refine this picture, explicit electronic structure calculations are necessary, which pose a formidable challenge for the interfacial systems under consideration. Secs. 2.2 and 2.3 summarize recent efforts in this direction [41,43,44,56].

2.1 Energetics of a type-II heterojunction

The basic picture of the heterojunction energetics is formulated in terms of the offset between the frontier orbitals of the two polymer species, i.e., the respective highest occupied molecular orbitals (HOMOs) and lowest unoccupied molecular orbitals (LUMOs). The heterojunctions we are considering here are "type II" junctions [10,33], where the respective offsets between the HOMO and LUMO levels have the same sign and are of comparable magnitude, $\Delta E_{\mathrm{HOMO}} \sim \Delta E_{\mathrm{LUMO}} \sim \Delta E$. A schematic illustration is shown in Fig. 1. If the offset ΔE exceeds the exciton binding energy $\epsilon_B \sim 0.5$ eV, the photogenerated exciton (XT) is destabilized and tends to decay to an interfacial charge transfer state (CT) [3,23,28]. This is desirable for photovoltaic applications. Conversely, if $\Delta E < \epsilon_B$, the exciton is stable, and this is best suited for OLED applications. However, intermediate cases where $\Delta E \simeq \epsilon_B$ cannot straightforwardly be addressed in these terms. This applies, for example, to the TFB:F8BT junction [26,32,33,57] which we focus on in this chapter. Here, the interface is composed of the poly[9,9-dioctylfluorene-co-bis-N,N-(4-butyl-phenyl)-bis-N,N-phenyl-1,4-phenylenediamine] (TFB) and poly[9,9-dioctylfluorene-co-benzothiadiazole] (F8BT) polymer components, see Fig. 2 where the molecular structure of the junction is illustrated. For this system,

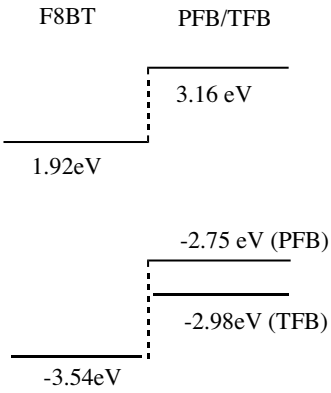

Fig. 1: Band offsets, i.e., relative HOMO/LUMO energies, for two representative type II polymer junctions, i.e., the TFB:F8BT and PFB:F8BT heterojunctions. Both are fluorene-based polymer materials [26, 33]. In this chapter, we focus on the TFB:F8BT junction.

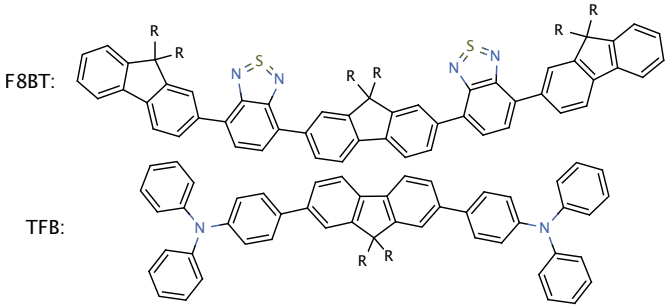

Fig. 2: Molecular structure of a model F8BT(top):TFB(bottom) polymer heterojunction in the "eclipsed" stacking configuration, see also Fig. 3. In the actual polymer, the residues are R = C_8H_{12}; in the calculations reported here, R = H was used (Adapted from Ref. [43]).

recent time-resolved photoluminescence studies suggest that both exciton decay and regeneration phenomena are observed [32, 34, 42], with the earliest events falling into the (sub)picosecond regime.

2.2 Electronic structure calculations of interfacial singlet states

Excited-state electronic structure calculations, even for small fragments of the polymer interfaces under consideration, are barely feasible using high-level *ab initio* methodology, and are a formidable task even if performed at a semiempirical level. This is all the more true if such calculations are to be carried out for a range of relevant geometries. Here, we summarize the results of Refs. [41, 43] for selected geometries, using single-excitation configuration interaction (CIS) and time-dependent density functional theory (TD-DFT) methods. The results of these studies are in qualitative agreement with semi-empirical calculations [44, 56].

In the calculations reported in Refs. [41, 43], a finite-sized fragment of the interface region is considered, composed of a F8BT moiety consisting of six co-monomer units (i.e., three benzothiadiazole (BT) units alternating with three fluorene (F) units) and a TFB moiety consisting of five co-monomer units (three F units alternating with two triarylamine units). The rationale for considering a finite portion of the interface region is that the delocalization length of the photogenerated exciton generally does not exceed a few monomer units [6, 29, 57, 58]. The CIS and TD-DFT methods were employed to determine the heterojunction excited states at the Franck-Condon geometry, either for the isolated TFB:F8BT or including a solvent modeled by a dielectric continuum [41].

Since intermolecular interactions at the interface play a key role, two representative interface structures were considered, which will be referred to as eclipsed (E) vs. staggered (S), see Fig. 3. These structures correspond to attractive vs. repulsive π-stacked interface configurations, which result from the following stacking patterns in the lowest-lying exciton state:

$$\text{attractive (E configuration):} \quad \begin{bmatrix} (-\mathbf{F8}^{\delta+} - \mathbf{BT}^{\delta-})_n \\ (-\mathbf{F8}^{\delta-} - \mathbf{TB}^{\delta+})_n \end{bmatrix} \tag{1}$$

$$\text{repulsive (S configuration):} \quad \begin{bmatrix} (-\mathbf{F8}^{\delta+} - \mathbf{BT}^{\delta-})_n \\ (-\mathbf{TB}^{\delta+} - \mathbf{F8}^{\delta-})_n \end{bmatrix} \tag{2}$$

As indicated by the partial charges, the F8 sub-unit acquires a net partial positive charge when co-polymerized with BT (in the F8BT moiety), but a net partial negative charge when co-polymerized with TB (in the TFB moiety) [34, 41]. This leads to a strongly attractive electrostatic interaction in the E configuration, but a repulsive interaction in the S configuration. Both structures were optimized in the electronic ground state using molecular mechanics force fields (i.e., the MM3 force field as implemented in TINKER [41]). Subsequently, CIS and TD-DFT calculations were carried out at this geometry. Geometry relaxation in the excited states was not accounted for. Overall, TD-DFT was found to give results that compare well with experimental absorption spectra [41] while CIS tends to significantly overestimate the relevant

excitation energies. However, due to the known deficiencies of TD-DFT in describing long-range charge transfer states, as a consequence of the local nature of the approximate exchange-correlation functionals [59], charge transfer state energies tend to be underestimated by about 0.5 eV [41].

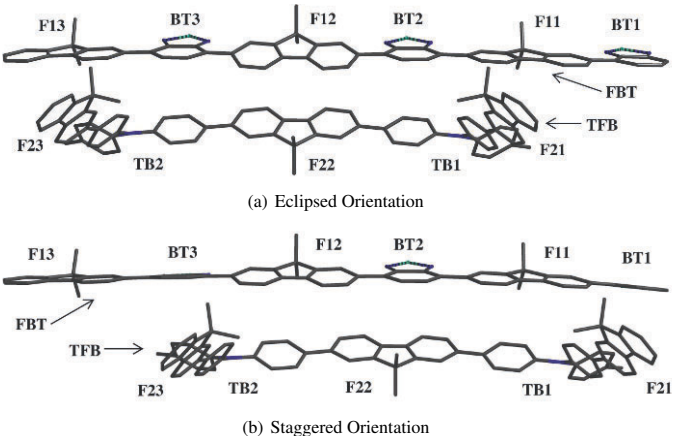

Fig. 3: TFB:F8BT structures (slightly tilted forward) showing two different orientations of the polymer constituents. In each, the FBT (top chain) consists of 3 fluorene (F) units and 3 benzothiadiazole (BT) units while the TFB (bottom chain) consists of 3 F units and 2 triarylamine (TB) units. These co-monomer units are labeled with indices. The eclipsed orientation (panel a) has the middle F units (F12 and F22) of both chains π-stacked while the staggered orientation (panel b) has the middle BT of FBT (BT2) and the middle F of TFB (F22) π-stacked, see Eqs. (1)-(2). Reprinted with permission from Ref. [41]. Copyright 2007, American Institute of Physics.

Fig. 4 illustrates the low-lying singlet states obtained from TD-DFT calculations for the E vs. S structures [41]. The observed states fall into two classes: excitonic states (XT), which feature electron-hole (e-h) configurations on the same polymer chain (FBT* or TFB*) and charge transfer states (CT), which feature e-h configurations on adjacent chains. In particular, the lowest-lying XT state is essentially of FBT* character, while the lowest-lying CT state corresponds to a TFB$^+$-FBT$^-$ inter-chain e-h configuration. In Fig. 4, these lowest-lying XT vs. CT states are highlighted. The XT $\rightarrow$ CT transition thus involves the inter-chain transfer of an electron from a TFB to an FBT unit.

Importantly, the excited electronic states are not of pure XT vs. CT character, and the observed admixtures of electronic state character strongly depend upon the interface geometry. While the XT states exhibit significantly larger oscillator strength and, hence, photoluminescence intensity, some of the nominal CT states can acquire non-negligible photoluminescence by intensity

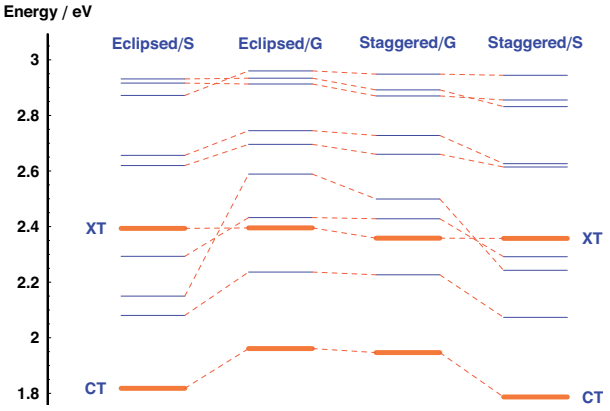

Fig. 4: Energy correlation diagram between the gas phase (/G) and solvated (toluene) (/S) lowest excited states in a TFB:F8BT model system calculated by TD-DFT (B3LYP/6-31G(d)). The eclipsed vs. staggered structures as shown in Fig. 3 are compared. The lowest-lying excitonic (XT) and charge transfer (CT) states are highlighted in red. Solvation effects tend to stabilize the CT state. Reprinted with permission from Ref. [41]. Copyright 2007, American Institute of Physics.

borrowing. For example, for the E configuration, the CT (1.96 eV) state is 92% TFB^+-FBT^- and 8% FBT^* in character while the XT (2.40 eV) state is 74% FBT^* and 26% TFB^+-FBT^- in character. Conversely, for the S configuration, the CT (1.95 eV) state is purely TFB^+-FBT^- while the XT (2.36 eV) state almost has a 1:1 admixture, i.e., 51% TFB^+-FBT^- and 49% FBT^*.

Thus a non-negligible FBT^* admixture (as in the E configuration) is thought to account for the luminescence of the lowest-lying CT state [41], which is characterized as a long-lived "exciplex" state that essentially corresponds to an inter-chain *e*-*h* pair pinned to the interface [44]. Other charge transfer states are optically dark; these states could be precursors to partially dissociated geminate *e*-*h* pairs that eventually contribute to the field-induced photocurrent observed in this system [34]. Indeed, as will be further discussed below, a picture which is solely based on the two dominant XT and CT states is not accurate enough to obtain a detailed understanding of the photophysical processes at the heterojunction.

2.3 Triplet states at the heterojunction

Finally, we briefly comment on the role of triplet states, a detailed characterisation of which has been given in Ref. [43]. Triplet states are generally lower in energy than their singlet counterparts, due to the exchange interaction which can lead to a stabilization of up to 0.5 eV. Since triplet states are optically

dark, they do not play a role in the photoexcitation process and subsequent ultrafast internal conversion events. Even on longer time scales, intersystem crossing (ISC) to form triplets is presumably not important. This is not only due to the fact that ISC is very slow in the absence of heavy atoms (of the order of 5 ns to 1 ms), but more importantly, is a consequence of the fact that the relevant spin-orbit matrix elements between singlet vs. triplet $\pi\pi^*$ states are generally zero [43].

Therefore, the only mechanism by which triplet generation is feasible is by recombination from bi-polaron like, charge separated states. This is comparable to direct electron-hole recombination in organic light-emitting diode (OLED) devices, where triplet formation indeed leads to a significant reduction in the theoretical efficiency of the device [60]. Using the results of TD-DFT calculations as reported above, we conclude that for TFB^+-FBT^- type states, the electron can essentially be assumed to be localized on an N 2p or S 3p orbital of the BT sub-unit. A "back of the envelope" estimate based on the spin-orbit coupling of hydrogenic systems then suggests that the time scale for spin flipping is around 700-800 ps. Since the TFB^+-FBT^- configuration appears as a significant admixture in the triplet exciton state of the eclipsed stacking (E) configuration, we expect spin interconversion to be more efficient in the E configuration.

It is tempting to speculate on the significance of the triplet states in these heterojunction systems. For OLED applications, triplets are generally undesirable since they are not emissive and hence potentially limit the efficiency of the device. However, for a heterojunction, it is possible that triplets pinned to the interface may undergo conversion to singlets and decay via exciplex or excitonic emission at long times. This would give an enhancement to the time-integrated emission and thereby account in part for the high electroluminescence efficiency reported for this system [26, 33].

3 Electron-phonon Hamiltonian

While the electronic structure calculations addressed in the preceding Section could in principle be used to construct the potential surfaces that are a prerequisite for dynamical calculations, such a procedure is in practice out of reach for large, extended systems like polymer junctions. At most, semiempirical calculations can be carried out as a function of selected relevant coordinates, see, e.g., the recent analysis of Ref. [44]. To proceed, we therefore resort to a different strategy, by constructing a suitably parametrized electron-phonon Hamiltonian model. This electron-phonon Hamiltonian underlies the two- and three-state diabatic models that are employed below (Secs. 4 and 5). The key ingredients are a lattice model formulated in the basis of localized Wannier functions and localized phonon modes (Sec. 3.1) and the construction of an associated diabatic Hamiltonian in a normal-mode representation (Sec. 3.2) [61].

3.1 Two-band configuration interaction lattice model

Following Refs. [61, 62], a two-band (valence and conduction band) configuration interaction model is introduced, using a basis of monoexcited configurations on the polymer chain. These correspond to electron-hole states $|\mathbf{n}\rangle = |n_e \bar{n}'_h\rangle = |n_e\rangle_C \otimes |\bar{n}'_h\rangle_V$ localized at sites n and n' of the chain. Here, $|n_e\rangle_C$ denotes a conduction-band (C) Wannier function (WF) localized at site n and occupied by an electron (e), while $|\bar{n}'_h\rangle_V$ denotes a valence-band (V) WF localized at site n' and occupied by a hole (h). The configurations $|\mathbf{n}\rangle$ thus correspond to neutral ($n_e = n'_h$) or charge transfer ($n_e \neq n'_h$) e-h pairs (excitons).

We now introduce creation and annihilation operators $a^\dagger_{\mathbf{n}}$ and $a_{\mathbf{n}}$ which create/annihilate e-h pairs at a given combination of sites $\mathbf{n} \equiv (n, n')$, i.e., $a^\dagger_{\mathbf{n}}|0\rangle = |\mathbf{n}\rangle = |n_e \bar{n}'_h\rangle$, where $|0\rangle$ is the ground state. Using these operators, a generic monoexcitation configuration interaction Hamiltonian can be formulated as follows in second quantization notation,

$$H_{\mathrm{el}} = \sum_{\mathbf{mn}} \Big(F_{\mathbf{mn}} + V_{\mathbf{mn}} \Big) a^\dagger_{\mathbf{m}} a_{\mathbf{n}} \tag{3}$$

Here, the $F_{\mathbf{mn}}$'s are one-particle matrix elements which yield the energy levels ($\mathbf{m} = \mathbf{n}$) and transfer integrals ($\mathbf{m} \neq \mathbf{n}$) for the e-h pairs composed of conduction electrons and valence holes,

$$F_{\mathbf{mn}} = \langle m_e | f | n_e \rangle \delta_{m'_h n'_h} - \langle \bar{m}'_h | f | \bar{n}'_h \rangle \delta_{m_e n_e} \tag{4}$$

The $V_{\mathbf{mn}}$'s of Eq. (3) contain two-particle interactions, including Coulomb, exchange, and dipole-dipole contributions, which are parameterized according to semi-empirical functional forms [61]. The parameters are adapted to PPV and are then transposed by scaling to other polymer species.

The electronic Hamiltonian H_{el} is now augmented by the electron-phonon interaction [61],

$$\begin{aligned} H &= H_{\mathrm{el}} + H_{\text{el-ph}} + H_{\mathrm{ph}} \\ &= \sum_{\mathbf{mn}} \Big(F_{\mathbf{mn}} + V_{\mathbf{mn}} \Big) a^\dagger_{\mathbf{m}} a_{\mathbf{n}} + \sum_{\mathbf{nm}} \sum_{l\alpha} \left(\frac{\partial F_{\mathbf{mn}}}{\partial q_{l\alpha}} \right) a^\dagger_{\mathbf{m}} a_{\mathbf{n}} q_{l\alpha} \\ &\quad + \sum_{ll'} \sum_{\alpha} \frac{1}{2} (\omega^2_{l\alpha}\, q^2_{l\alpha} + p^2_{l\alpha}) + \lambda_l q_{l\alpha} q_{l'\alpha} \delta_{l',l+1} \end{aligned} \tag{5}$$

The electron-phonon coupling term is constructed so as to account for the modulation of the band gap – stemming from the diagonal single-particle matrix elements of Eq. (4) – as a function of the $(l\alpha)$ phonon modes belonging to the αth phonon branch and lth site [29],

$$\left(\frac{\partial f_{mn}}{\partial q_{\ell\alpha}} \right) = \left(\frac{\partial \bar{f}_{mn}}{\partial q_{\ell\alpha}} \right) = \frac{S}{2} (2\hbar\omega^3)^{1/2} (\delta_{m\ell} + \delta_{n\ell}) \tag{6}$$

Here, S is the Huang-Rhys factor [63], which is related to the intensity of the 0-n vibronic transition, $I_{0-n} = e^{-S}S^n/n!$, and reflects the time-dependent Stokes shift associated with a given type of vibrational mode (e.g., $S \sim 0.6$ for the high-frequency C=C stretch modes [61,64,65]). For the class of systems studied here, two types of phonon modes are considered per monomer unit, i.e., high-frequency C=C stretch modes and low-frequency ring-torsional modes.

The parametrization for different polymer species is constructed by reference to the PPV case, by adjusting the relative HOMO and LUMO energies. For copolymer species which are not characterized by uniform sites, the site energies are varied along the chain. For the case of parallel chains, inter-chain single-particle terms are introduced, e.g., if the electrostatic coupling between the chains is strong. With regard to the electron-phonon coupling, it is assumed that no inter-chain phonon coupling terms occur.

3.2 Diabatic representation

Given the lattice Hamiltonian Eq. (5), which casts the interactions in terms of site-specific and site-site interaction terms, a complementary diabatic representation can be constructed which diagonalizes the Hamiltonian excluding the electron-phonon interaction, $H_0 = H_{\rm el} + H_{\rm ph}$. This leads to the form

$$H_{\rm dia} = \sum_a \epsilon_a |a\rangle\langle a| + \sum_{ab}\sum_\xi g_{ab\xi}\, x_\xi \left(|a\rangle\langle b| + |b\rangle\langle a|\right) + \frac{1}{2}\sum_\xi (\omega_\xi^2 x_\xi^2 + p_\xi^2) \tag{7}$$

Here, the x_ξ are normal mode coordinates. Note that off-diagonal electron-phonon coupling terms appear both in the representation Eq. (7) and in the excitonic site representation of Eq. (5).

The Hamiltonian Eq. (7) provides the basis for the quantum dynamical treatment to be detailed in the following sections, typically involving a parametrization for 20-30 phonon modes. Eq. (7) is formally equivalent to a class of linear vibronic coupling (LVC) Hamiltonians which have been used for the description of excited-state dynamics in molecular systems [66] as well as the Jahn-Teller effect in solid-state physics. In the following, we will elaborate on the general properties of the Hamiltonian Eq. (7) and on quantum dynamical calculations based on this Hamiltonian.

Regarding the parametrization of the Hamiltonian Eq. (7), the present approach relies on the parameters of the underlying lattice model Eq. (5). However, one could envisage an alternative approach, similar to the one described in Refs. [66–69] for small molecular systems, where a systematic diabatization is carried out based on supermolecular electronic structure calculations as described in Sec. 2.2.

4 Vibronic coupling in many dimensions: conical intersections and effective modes

The excited-state dynamics of the polymer systems studied here is a paradigm case of vibronic coupling in high-dimensional polyatomic systems. These systems are generally characterized by complex topologies of intersecting surfaces, involving in particular conical intersections (CoIn's) [66–69]. The linear vibronic coupling (LVC) Hamiltonian Eq. (7) is the simplest Hamiltonian which correctly accounts for the excited-state structure and topology. Generalizations of this Hamiltonian involve the inclusion of higher-order terms in a systematic Taylor expansion [66], or the embedding of the locally linearized structure into a correct representation of the overall adiabatic potential surfaces [70,71]. For the purpose of describing the polymer systems under consideration, the LVC model is appropriate since essentially small-amplitude motions are involved.

The LVC model further allows one to introduce coordinate transformations by which a set of relevant effective, or collective modes are extracted that act as generalized reaction coordinates for the dynamics. As shown in Refs. [54, 55,72], $n_{\mathrm{eff}} = n_{\mathrm{el}}(n_{\mathrm{el}}+1)/2$ such coordinates can be defined for an electronic n_{el}-state system, in such a way that the short time dynamics is completely described in terms of these effective coordinates. Thus, three effective modes are introduced for an electronic two-level system, six effective modes for a three-level system etc., for an arbitrary number of phonon modes that couple to the electronic subsystem according to the LVC Hamiltonian Eq. (7). In order to capture the dynamics on longer time scales, chains of such effective modes can be introduced [50,51,73]. These transformations, which are briefly summarized below, will be shown to yield a unique perspective on the excited-state dynamics of the extended systems under study.

4.1 LVC model and effective modes

We start by re-writing the generic Hamiltonian Eq. (7) for an electronic two-level system coupled to N nuclear modes,

$$\boldsymbol{H} = \boldsymbol{V}_{\Delta} + \sum_{i=1}^{N} \frac{\omega_i}{2}\left(p_i^2 + x_i^2\right)\mathbf{1} + \sum_{i=1}^{N} \begin{pmatrix} \kappa_i^{(1)}\, x_i & \lambda_i x_i \\ \lambda_i x_i & \kappa_i^{(2)}\, x_i \end{pmatrix} \tag{8}$$

where mass and frequency weighted coordinates were used for convenience. Here, $\mathbf{1}$ and $\boldsymbol{V}_{\Delta}$ denote the unit matrix and a coordinate-independent matrix of offsets, respectively. The diagonal ($\kappa_i^{(1,2)}$) and off-diagonal (λ_i) potential terms correspond to diabatic tuning and coupling terms [66]. The Hamiltonian Eq. (8) allows for the presence of a conical intersection (CoIn) topology at nuclear configurations where the diabatic couplings vanish and the adiabatic states become degenerate. A CoIn corresponds to an $(N-2)$-dimensional

hypersurface of degeneracy points of the adiabatic potential energy surfaces (PES). The degeneracy is lifted by displacements within the two-dimensional branching plane [66–69, 74].

The Hamiltonian Eq. (8) can alternatively be represented in terms of sum and difference parameters $\kappa^{(\pm)} = 1/2(\kappa_i^{(1)} \pm \kappa_i^{(2)})$,

$$\boldsymbol{H} = \boldsymbol{V}_{\Delta} + \sum_{i=1}^{N} \frac{\omega_i}{2}\left(p_i^2 + x_i^2\right)\mathbf{1} + \sum_{i=1}^{N} \kappa^{(+)}\, x_i + \begin{pmatrix} \kappa_i^{(-)}\, x_i & \lambda_i x_i \\ \lambda_i x_i & -\kappa_i^{(-)}\, x_i \end{pmatrix} \quad (9)$$

This illustrates that only the electron-phonon coupling terms associated with the $\kappa_i^{(-)}$ (tuning) and λ_i (coupling) parameters contribute to the lifting of the CoIn degeneracy [55, 74].

Following the analysis of Refs. [54,55,72], we now make use of the fact that the nuclear modes of the Hamiltonian Eq. (8) produce cumulative effects by their coupling to the electronic subsystem. From Eq. (9), the electron-phonon interaction can be absorbed into the following collective modes,

$$\begin{aligned} X_+ &= \sum_{i=1}^{N} \kappa_i^{(+)}\, x_i \\ X_- &= \sum_{i=1}^{N} \kappa_i^{(-)}\, x_i \\ X_{\Lambda} &= \sum_{i=1}^{N} \lambda_i\, x_i \end{aligned} \quad (10)$$

which represent collective shift (X_+), tuning (X_-), and coupling (X_{Λ}) effects. These modes entirely define the coupling to the electronic subsystem. The modes of Eq. (8) can be orthogonalized [54, 55, 72] so as to yield a set of effective coordinates (X_1, X_2, X_3). By introducing an orthogonal transformation in the full coordinate space, $\boldsymbol{X} = \boldsymbol{T}\boldsymbol{x}$, the remaining coordinates are identified as a complementary set of residual modes $(X_4, \ldots, X_N)$. These modes do not couple directly to the electronic subsystem but couple bilinearly to the effective modes.

The Hamiltonian in the new coordinates reads

$$\boldsymbol{H} = \boldsymbol{H}_{\text{eff}} + \boldsymbol{H}_{\text{res}} \quad (11)$$

with the 3-mode effective Hamiltonian part

$$\begin{aligned} \boldsymbol{H}_{\text{eff}} = \boldsymbol{V}_{\Delta} + \sum_{i=1}^{3} \frac{\Omega_i}{2}(P_i^2 + X_i^2)\ \mathbf{1} + \sum_{i,j=1,j>i}^{3} d_{ij}(P_iP_j + X_iX_j)\ \mathbf{1} \\ + \sum_{i=1}^{3} K_iX_i\mathbf{1} + \begin{pmatrix} D_1X_1 + D_2X_2 & \Lambda X_1 \\ \Lambda X_1 & -D_1X_1 - D_2X_2 \end{pmatrix} \end{aligned} \quad (12)$$

Here, a topology-adapted representation [55] was chosen, where (X_1, X_2) lift the degeneracy at the intersection and thus span the branching plane [74]. These modes are obtained by orthogonalizing the modes (X_-, X_Λ) of Eq. (10). The third mode X_3 is in turn orthogonal to (X_1, X_2) and carries information on the intersection space, i.e., the X_+ component of Eqs. (9)–(10). Alternative construction schemes are possible; in particular, the bilinear coupling terms can be eliminated within the three-mode subspace [54, 72].

The residual Hamiltonian $\boldsymbol{H}_{\rm res}$ contains the remaining $(N-3)$ modes, and their bilinear coupling to the effective modes,

$$\boldsymbol{H}_{\rm res} = \sum_{i=4}^{N} \frac{\Omega_i}{2}(P_i^2 + X_i^2)\mathbf{1} + \sum_{i=1}^{N}\sum_{j=4}^{N} d_{ij}\Big(P_iP_j + X_iX_j\Big)\mathbf{1} \qquad (13)$$

Using this transformation, it has been shown in Refs. [54,72] that the effective-mode Hamiltonian $\boldsymbol{H}_{\rm eff}$ by itself reproduces the short-time dynamics of the overall system exactly. This is reflected by an expansion of the propagator, for which it can be shown that the first few terms of the expansion – relating to the first three moments of the overall Hamiltonian – are exactly reproduced by the reduced-dimensional Hamiltonian $\boldsymbol{H}_{\rm eff}$.

The effective-mode transformation described here is closely related to earlier works which led to the construction of so-called interaction modes [75, 76] or cluster modes [77, 78] in Jahn-Teller systems. The approach of Refs. [54, 55, 72] generalizes these earlier analyses to the generic form – independent of particular symmetries – of the linear vibronic coupling Hamiltonian Eq. (8).

In Refs. [55, 79], the truncation at the level of $\boldsymbol{H}_{\rm eff}$ has been tested for several molecular systems exhibiting an ultrafast dynamics at CoIn's, and it was found that this approximation can give remarkably good results in reproducing the short-time dynamics. This is especially the case if a system-bath perspective is appropriate, and the effective-mode transformation is only applied to a set of weakly coupled bath modes [55,72]. In that case, the system Hamiltonian can take a more complicated form than given by the LVC model.

4.2 Hierarchical electron-phonon (HEP) representation

For the polymer systems studied here, the approximation defined by $\boldsymbol{H}_{\rm eff}$ is not necessarily sufficient, as demonstrated below (Sec. 5). We therefore resort to a strategy which generalizes the effective-mode approach in such a way that a chain of effective modes is generated, which successively unravel the dynamics as a function of time.

To this end, an additional orthogonal coordinate transformation is introduced, by which the bilinear couplings occurring in Eq. (13) are transformed to a band-diagonal form that only allows a coupling to the (three) nearest neighbors. By concatenating the effective-mode construction described in the previous section with this additional transformation in the residual-mode subspace,

a series of nth-order approximate Hamiltonians are generated [50, 51, 80],

$$\boldsymbol{H}^{(n)} = \boldsymbol{H}_{\text{eff}} + \sum_{l=1}^{n} \boldsymbol{H}_{\text{res}}^{(l)} \tag{14}$$

with the lth-order residual Hamiltonian

$$\boldsymbol{H}_{\text{res}}^{(l)} = \sum_{i=3l+1}^{3l+3} \frac{\Omega_i}{2}(P_i^2 + X_i^2)\mathbf{1} + \sum_{i=3l+1}^{3l+3} \sum_{j=i-3}^{i-1} d_{ij}\Big(P_i P_j + X_i X_j\Big)\mathbf{1} \tag{15}$$

For $(3 + 3n) = N$, Eqs. (14)-(15) yield an exact, transformed version of the original LVC Hamiltonian Eq. (8), as well as the effective-mode form Eqs. (11)-(13). We refer to this transformed LVC Hamiltonian as a hierarchical electron-phonon (HEP) model [50, 51, 80]. This form of the model is schematically illustrated in Fig. 5.

Successive orders $\boldsymbol{H}^{(n)}$ can be shown to correspond to successive orders in a moment (or cumulant) expansion of the propagator, which takes one to increasing times. Truncation of the chain at a given order n (i.e., $3 + 3n$ modes) leads to an approximate, lower-dimensional representation of the dynamical process, which reproduces the true dynamics up to a certain time. In Ref. [51], we have demonstrated explicitly that the nth-order ($3n+3$ mode) truncated HEP Hamiltonian exactly reproduces the first $(2n + 3)$rd order moments (cumulants) of the total Hamiltonian. A related analysis is given in Ref. [73].

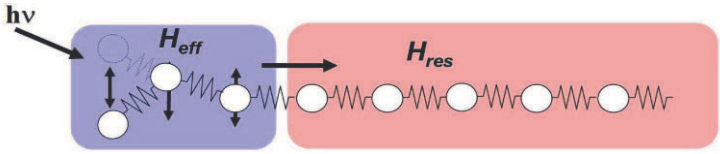

Fig. 5: Schematic illustration of the HEP construction. In addition to the transformation which identifies the three effective modes that couple directly to the electronic subsystem, further transformations are introduced for the residual bath in such a way that the chain-like representation of Eqs. (14)-(15) is obtained.

In the examples addressed below, for a two-band phonon distribution, the HEP scheme willl be shown to yield essential insight into the interplay between high-frequency (C=C stretch) and low-frequency (ring-torsional) modes of the polymer heterojunction model of Eq. (7).

4.3 Dissipative closure of the HEP model

If the phonon distribution of the model Eq. (8) spans a dense spectrum – as is generally the case for the extended systems under consideration, which are effectively infinite-dimensional – the dynamics induced by the Hamiltonian will eventually exhibit a dissipative character. However, the effective-mode construction demonstrates that the shortest time scales are fully determined by *few* effective modes, and by the coherent dynamics induced by these modes. The overall picture thus corresponds to a Brownian oscillator type dynamics, and is markedly non-Markovian [81, 82].

If the HEP chain is truncated at a given order, a natural approach to impose an irreversible character on the dynamics is to close the hierarchy by adding a dissipation mechanism, e.g., employing a Markovian master equation or a corresponding collection of explicit bath modes. By this technique, one prevents the occurrence of artificial recurrences that "propagate back" along the chain, and an effectively irreversible dynamics results. This scheme is known from Mori theory [83–86] as well as the Generalized Langevin Equation [82, 87] and translates to the following form of an nth-order system-bath Hamiltonian,

$$\begin{aligned} \boldsymbol{H}^{(n)}_{\mathrm{diss}} &= \boldsymbol{H}^{(n)} + \boldsymbol{H}^{(n)}_{\mathrm{bath}} \\ &= \boldsymbol{H}_{\mathrm{eff}} + \sum_{l=1}^{n} \boldsymbol{H}^{(l)}_{\mathrm{res}} + \boldsymbol{H}^{(n)}_{\mathrm{bath}} \end{aligned} \tag{16}$$

Here, $\boldsymbol{H}^{(n)}_{\mathrm{bath}}$ is an external bath Hamiltonian which generates a Markovian (Langevin-type) friction acting at the level of the highest order n of the hierarchy. In Ref. [88], we have constructed a hierarchy of approximate spectral densities representing the combined effect of the residual modes and bath modes; these converge towards the true spectral density as more chain modes are added in the residual space. One should again emphasize that the overall process is strongly non-Markovian [81, 82] even though the "end of the chain" undergoes a simple Markovian damping.

In Refs. [51, 53], we used an explicit representation of the bath in terms of a collection of oscillators which are bilinearly coupled to the last three members of the HEP hierarchy,

$$\boldsymbol{H}^{(n)}_{\mathrm{bath}} = \sum_{i=1}^{N_B} \frac{\omega_{B,i}}{2}(p^2_{B,i} + x^2_{B,i})\mathbf{1} + \sum_{i=n-3}^{n} \sum_{j=1}^{N_B} d^B_{ij} \Big(P_i p_j + X_i x_j \Big) \mathbf{1} \tag{17}$$

The coupling parameters d^B_{ij} are sampled according to a specified spectral density, which is here taken to be Ohmic [89–91]. More generally, the external bath itself can be taken to be non-Markovian. An example of this scheme is given in Fig. 8 of Sec. 5.1, for an Ohmic bath at zero temperature, i.e., exhibiting no thermal fluctuations. Here, the damping effect is generated by "quantum fluctuations" at $T = 0$ [90, 91].

More generally, a treatment which allows for the inclusion of temperature leads to a master equation of the form [88]

$$\frac{\partial \rho^{(n)}}{\partial t} = -\frac{i}{\hbar}[\boldsymbol{H}^{(n)}, \rho^{(n)}] + \boldsymbol{L}_{\rm diss}\rho^{(n)} \tag{18}$$

where $\boldsymbol{L}_{\rm diss}$ is a dissipative Liouvillian which can be derived from an explicit representation of the bath as given in Eq. (17). The density operator $\rho^{(n)}$ is a reduced density operator comprising all modes of the HEP hierarchy that are accounted for explicitly.

From the viewpoint of system-bath theory, the hierarchical structure of the HEP Hamiltonian thus allows for a flexible partitioning into system and bath subspaces. A chosen subset of effective modes can be absorbed into the system space, while approximations are introduced for the residual space. For a partitioning that identifies the electronic subsystem as the system part, the dynamics is generally non-Markovian and exhibits an inertial, coherent regime on short time scales. This coherent regime is determined by a limited number of effective environmental modes. The irreversible, multi-mode nature of the bath determines the dynamical behavior on intermediate and long time scales. Using cumulant expansion techniques [81], one can introduce a series of finite-dimensional bath propagators corresponding to successive orders of the HEP hierarchy, whose cumulant expansions are identical to the one of the full propagator up to a certain order.

4.4 Generalization to three and more states

A generalization of the effective-mode construction to three or more electronic states is straightforward, using a set of $n_{\rm eff} = n_{\rm el}(n_{\rm el}+1)/2$ effective modes as mentioned above. In Refs. [52, 53], we have thus employed a three-state representation with six effective modes, based on the following form of the Hamiltonian which generalizes Eq. (14),

$$\begin{aligned}\boldsymbol{H}^{(n)}(X_1,\ldots,X_{6n+6}) &= \boldsymbol{H}_{\rm eff}(X_1,\ldots,X_6) \\ &\quad + \sum_{l=1}^{n} \boldsymbol{H}^{(l)}_{\rm res}(X_{6l+1},\ldots,X_{6l+6})\end{aligned} \tag{19}$$

where the effective Hamiltonian reads as follows,

$$\begin{aligned}\boldsymbol{H}_{\rm eff} &= \sum_{i=1}^{6}\frac{\Omega_i}{2}(P_i^2+X_i^2)\mathbf{1} + \sum_{i=1}^{6}\begin{pmatrix} (K_i+D_i)X_i & \Lambda_i^{(12)}X_i & \Lambda_i^{(13)}X_i \\ \Lambda_i^{(12)}X_i & (K_i-D_i)X_i & \Lambda_i^{(23)}X_i \\ \Lambda_i^{(13)}X_i & \Lambda_i^{(23)}X_i & K_i^{(3)}X_i \end{pmatrix} \\ &\quad + \sum_{i=1}^{6}\sum_{j=i+1}^{6} d_{ij}\Big(P_iP_j + X_iX_j\Big)\mathbf{1} + \boldsymbol{C}\end{aligned} \tag{20}$$

The detailed derivation of $\boldsymbol{H}_{\text{eff}}$ is given in Ref. [53]. Here, two of the six modes (i.e., X_1 and X_2) are chosen as topology-adapted modes that span the branching plane for a chosen pair of electronic states (here, states 1 and 2). Each lth-order residual term now also comprises 6 modes,

$$\boldsymbol{H}_{\text{res}}^{(l)} = \sum_{i=6l+1}^{6l+6} \frac{\Omega_i}{2}(P_i^2 + X_i^2)\mathbf{1} + \sum_{i=6l+1}^{6l+6} \sum_{j=i-6}^{i-1} d_{ij}\Big(P_i P_j + X_i X_j\Big)\mathbf{1} \quad (21)$$

The moment conservation rules described above – i.e., conservation of the $(2n+3)$rd Hamiltonian moments (cumulants) at the nth order of the hierarchy – carry over to an arbitrary number of electronic states [51, 53, 73].

5 Quantum dynamics of exciton dissociation at a polymer heterojunction

The dynamics associated with the Hamiltonian Eq. (8) or its variants Eq. (11) and Eq. (14) can be treated at different levels, ranging from the explicit quantum dynamics to non-Markovian master equations and kinetic equations. In the present context, we will focus on the first aspect – an explicit quantum dynamical treatment – which is especially suited for the earliest, ultrafast events at the polymer heterojunction. Here, the coherent vibronic coupling dynamics dominates over thermally activated events. On longer time scales, the latter aspect becomes important, and kinetic approaches could be more appropriate.

In Refs. [50–53], we have used the MCTDH method [47–49] in order to calculate the femtosecond to picosecond scale evolution of the relevant state populations at the TFB:F8BT heterojunction. MCTDH is numerically exact and currently one of the most efficient methods for time-dependent quantum propagation for systems with many degrees of freedom. In the applications of Refs. [50–53], we have employed the method at a wavefunction level, using pure-state initial conditions and an explicit time propagation for all phonon modes. On longer time scales, the irreversible nature of the dynamics – due to the infinite-dimensional nature of the phonon mode space – can be accounted for by an augmented version of the model including a Markovian closure [51, 53], see Sec. 4.3. A related approach using a non-Markovian master equation formulation has been developed in Ref. [92]; this approach is able to capture both the coherent and dissipative aspects of the dynamics.

In the following, we summarize the pertinent results of our analysis of Refs. [50–53] where we applied the LVC Hamiltonian Eq. (1) in conjunction with a 20-30 mode phonon distribution composed of a high-frequency branch corresponding to C=C stretch modes and a low-frequency branch corresponding to ring-torsional modes. In all cases, the parametrization of the vibronic coupling models is based on the lattice model of Sec. 3.1 and the complementary diabatic representation of Sec. 3.2.

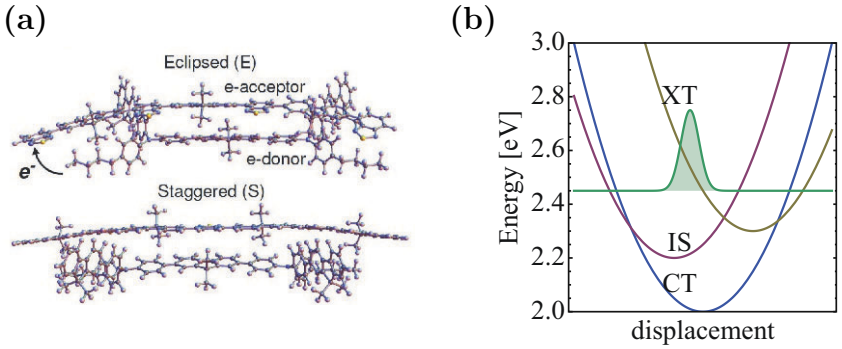

Fig. 6: Schematic illustration of the phonon-assisted exciton dissociation process. Due to the electronic state couplings, the photogenerated exciton (XT) wavepacket undergoes transitions to an interfacial charge transfer (CT) state, along with indirect XT → IS → CT transitions via an intermediate (IS) state (see panel (b)). In Ref. [52], the diabatic Hamiltonian of Eqs. (19)–(20) was parametrized for two relevant interface configurations (eclipsed (E) vs. staggered (S) as shown in panel (a)) which correspond to the configurations of Fig. 3.

In Refs. [50–53], two levels of analysis were successively addressed: (i) a two-state XT-CT model which is able to capture the basic features of the phonon-mediated exciton dissociation process; (ii) a three-state XT-IS-CT model which also comprises an intermediate state (IS), i.e., an additional charge transfer state whose presence can have a significant influence on the dynamics, see Fig. 6. In the latter case, comparative calculations for several interface configurations were carried out, leading to a realistic, molecular-level picture of the photophysical events at the heterojunction. In the following, we start with a summary of the findings reported in Refs. [50,51], where the two-state model was explored (Sec. 5.1). Following this, we address in more detail the analysis of Refs. [52,53] for the three-state model (Sec. 5.2).

5.1 Two-state XT-CT model

We now briefly summarize the key results of the analysis of Refs. [50,51] for a reduced XT-CT model of the TFB:F8BT heterojunction, using explicit quantum dynamical (MCTDH) calculations for a two-state model parametrized for 20-30 phonon modes. At this level of analysis, an ultrafast ($\sim$ 200 fs) XT state decay is predicted, followed by coherent oscillations, see Fig. 8 (trace "exact" in panel (a)). Further analysis in terms of an effective-mode model and the associated HEP decomposition (see Sec. 4.2) highlights several aspects:

i. The high-frequency vs. low-frequency modes appear in alternation at successive orders of the HEP hierarchy. The lowest order of the hierarchy, i.e., $\boldsymbol{H}^{(0)} = \boldsymbol{H}_{\rm eff}$ comprising modes (X_1, X_2, X_3), is entirely composed of high-frequency modes, reflecting that the high-frequency C=C stretch modes

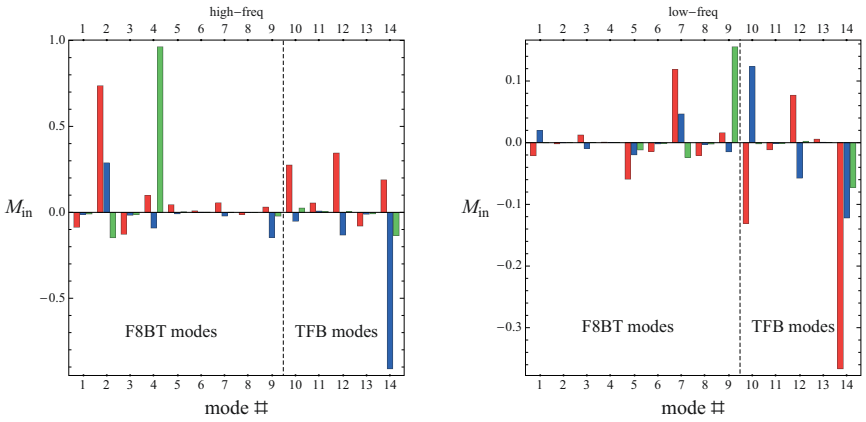

Fig. 7: For the two-state XT-CT model, the projection of the three effective modes (X_1, X_2, X_3) (shown in red, blue, and green, respectively) onto the primitive phonon modes $\{x_i\}$ is illustrated, for a model comprising 14 primitive high-frequency modes and 14 primitive low-frequency modes (i.e., 28 modes overall). Even though the projection involves contributions from both phonon bands, the low-frequency contributions are small, and all three effective modes are of high-frequency type. (Note the change in scale between the l.h.s. and the r.h.s. of the figure.) Furthermore, since the primitive modes are localized on the individual molecular units, the effective modes can be shown to be partially localized as well. Thus, two of the effective modes (shown in blue and green) are dominated by local contributions coming from either the F8BT chain or the TFB chain. The third mode (shown in red) exhibits contributions from both chains. (Reproduced from Ref. [93].)

dominate the coupling to the electronic subsystem. The next highest order, i.e., $\boldsymbol{H}_{\text{res}}^{(1)}$ comprising modes (X_4, X_5, X_6), is exclusively composed of low-frequency (ring torsional) modes. The second-order contribution $\boldsymbol{H}_{\text{res}}^{(2)}$ in turn consists again of high-frequency modes. At higher orders of the hierarchy, high-frequency and low-frequency components start to mix.

ii. From the branching plane representation of the potential in the (X_1, X_2) coordinates (see Sec. 4.1), one can infer that the system exhibits a conical intersection. However, the Franck-Condon geometry is found to lie significantly below this intersection, and the dynamics evolves in an extended avoided-crossing region in the vicinity of the intersection.

iii. Despite the predominance of the high-frequency modes in the electronic coupling, the low-frequency ring-torsional modes which appear at the order $\boldsymbol{H}_{\text{res}}^{(1)}$ of the mode hierarchy play a key role in the XT-CT transfer.

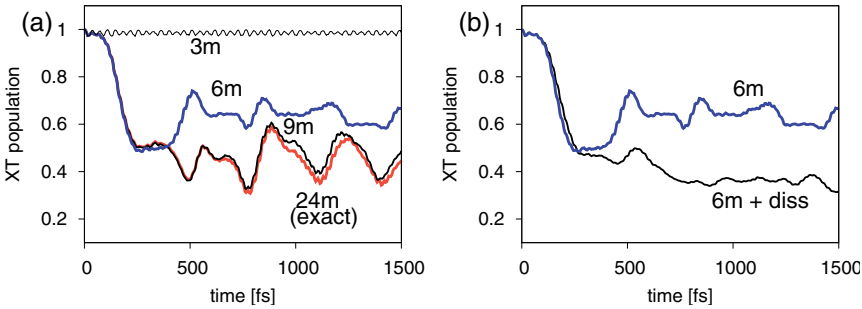

Fig. 8: Time-evolving XT state populations obtained from quantum dynamical (MCTDH) calculations for the 2-state model of Sec. 5.1, for different levels of the HEP hierarchy as compared with the full-dimensional (24-mode) result. Panel (a) shows the $\boldsymbol{H}^{(0)}$ approximation (3 modes) as compared with the $\boldsymbol{H}^{(1)}$ approximation (6 modes) and the $\boldsymbol{H}^{(2)}$ approximation (6 modes). Panel (b) presents a comparison with the $\boldsymbol{H}^{(1)}_{\rm diss}$ approximation including a Markovian closure as described in Sec. 4.3. Here, the coherent oscillations are largely damped out (adapted from Refs. [50, 51, 53]).

Indeed, exciton dissociation is observed to be inefficient in the absence of the low-frequency modes.

Figs. 7 and 8 illustrate the HEP analysis for the XT-CT model in more detail. Fig. 7 shows the decomposition of the first three modes of the hierarchy (X_1, X_2, X_3) into the primitive phonon modes [93]. As mentioned above, these modes constituting $\boldsymbol{H}_{\rm eff}$, are all of high-frequency type. Two of these effective modes can be seen to be localized on the TFB vs. F8BT moieties, whereas the third mode is delocalized over both chains.

Fig. 8 shows time-dependent state populations as obtained from quantum dynamical (MCTDH) calculations. While the full (here, 24 dimensional) model exhibits an ultrafast XT decay, no net decay is observed for the reduced 3-mode model truncated at the lowest level of the effective mode hierarchy. The dynamics is strongly diabatic if confined to the high-frequency subspace ($\boldsymbol{H}_{\rm eff}$) and involves repeated coherent crossings [51]. The dynamical interplay between the high-frequency and low-frequency modes is apparently a central feature of the process. To account for these effects, a treatment at the level of $\boldsymbol{H}^{(1)}$ is necessary, i.e., a six-mode model including the low-frequency modes. At the level of $\boldsymbol{H}^{(2)}$, the dynamics is found to be essentially exact. Similar conclusions can be drawn from a non-Markovian master equation approach [92, 93].

A qualitatively correct picture of the dynamics can indeed be obtained from a two effective-mode model – one high-frequency mode plus one low-

frequency mode – similarly to an early analysis by Halperin and Englman who proposed a two-frequency description of the Jahn-Teller coupling in solids [94]. A reduced-dimensional potential surface spanned by two relevant high-frequency vs. low-frequency modes shows that the XT-CT transition is essentially determined by low-frequency motion while the dynamics in the high-frequency direction remains diabatic [53].

An alternative explanation can be given in terms of a vibronic resonance effect, i.e., population transfer occurs due to the fact that the high-frequency subspace is tuned into resonance as a function of the low-frequency motions [88, 96]. This is very similar to resonant vibration-vibration coupling in liquids [95] where the transfer of vibrational excitation between solute species is mediated by low-frequency solvent modes.

Finally, we address the inclusion of dissipative effects in accordance with the discussion of Sec. 4.3. Dissipation is not expected to induce major changes in the dynamics, but its effect could be important in view of the fact that the finite-dimensional model under consideration tends to overemphasize coherent features on intermediate and long time scales. Fig. 8 (panel (b)) illustrates the effects of dissipation included at the level of the Markovian closure addressed in Sec. 4.3. We consider the $\boldsymbol{H}^{(1)}_{\rm diss}$ approximation according to Eq. (16), i.e., the HEP hierarchy is carried to the first order (thus including six modes) and the external bath is added so as to close the hierarchy at this order. Here, an explicit bath composed of 15 external modes is included, using an Ohmic spectral density. The bath is resonant with the low-frequency modes of the $\boldsymbol{H}^{(1)}_{\rm res}$ subspace, i.e., the bath is itself composed of low-frequency modes distributed according to an Ohmic spectral density. As expected, a pronounced attenuation of the coherent oscillatory behavior is observed. A realistic modeling of the exciton dissociation process is presumably intermediate between the strongly coherent, oscillatory evolution of Fig. 8a) and the partially damped dynamics of Fig. 8b).

5.2 Three-state XT-CT-IS model

While the two-state XT-CT model accounts for some of the essential features of the exciton dissociation process, a more detailed, molecular-level picture should include (i) intermediate electronic states that feature a non-negligible coupling to the XT and/or CT states, (ii) an ensemble of relevant interface configurations, as illustrated in Figs. 3 and 6. In Refs. [52, 53], these two aspects have been addressed. This analysis further allows one to verify whether the conclusions of the two-state analysis are corroborated by a more realistic treatment.

Regarding the role of intermediate states, we have focused on an additional charge transfer state which exhibits a non-negligible coupling to the exciton state and could therefore play a significant role in the exciton dissociation dynamics. Recent experimental studies provide strong indications that such an

intermediate state (here denoted IS) could contribute to photocurrent production [32]. In the semiempirical calculations of Ref. [44] for the same system, the CT state is identified as an exciplex state which remains "pinned" to the interface, while an additional charge transfer state is assigned as a potential photocurrent generating state (see the discussion of Sec. 2.2).

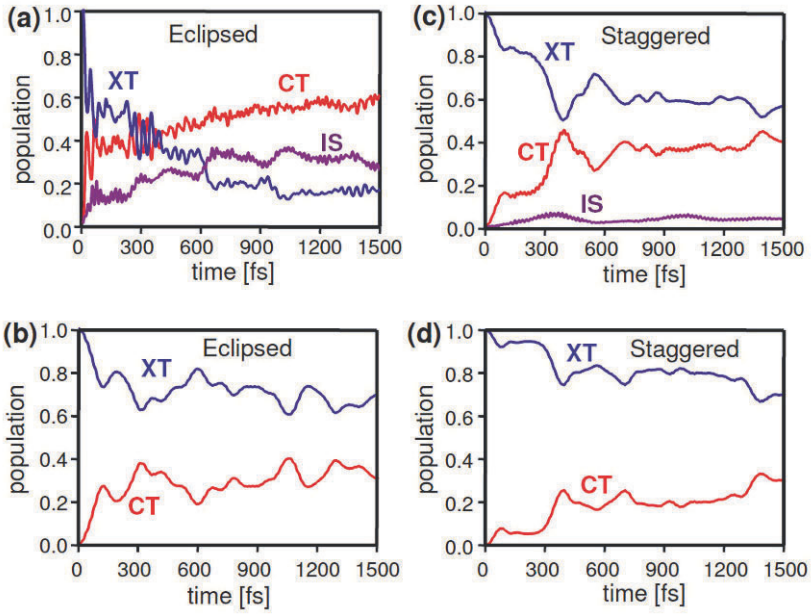

Fig. 9: Time-evolving state populations for the interface configurations of Fig. 3: (a) 3-state 28-mode wavepacket propagation for the E configuration, and (b) a complementary 2-state 28-mode calculation for the E configuration that was restricted to the XT-CT subspace; (c) and (d) are analogous calculations for the S configuration. Reproduced from Ref. [52]. Copyright 2008 by the American Physical Society.

In Refs. [52, 53], we have carried out a series of three-state simulations based on the model Eq. (20), including a comparative analysis of two representative interface structures at the TFB:F8BT heterojunction, i.e., the eclipsed (E) vs. staggered (S) configurations shown in Figs. 3 and 6. As mentioned above, the E vs. S configurations generate significantly different model parametrizations, pertaining to a strong-coupling vs. weak-coupling regime, respectively. As shown in Fig. 9, an ultrafast decay of the photogenerated exciton state is observed for both interface structures, even though the details of the dynamics differ in the two cases. Complementary calculations carried

out for a two-state model comprising the XT and CT states in the absence of the intermediate (IS) state (see panels (b) and (d) of Fig. 9), provide clear evidence that the intermediate "bridge" state plays an important role in accelerating the process.

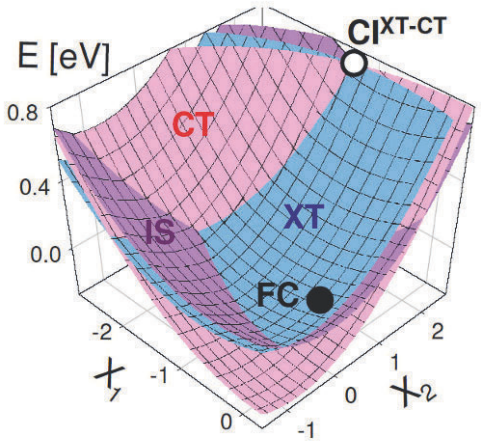

Fig. 10: For the 3-state model of Sec. 5.2., projections of the coupled diabatic XT, CT and IS potential surfaces (E configuration) onto the XT-CT branching plane are shown. The white and black circles indicate the conical intersection and Franck-Condon geometry, respectively. Reproduced from Ref. [52]. Copyright 2008 by the American Physical Society.

In order to obtain a reduced-dimensional picture of the dynamics and identify the roles of the respective phonon branches involved in the process, we again employ the HEP model. The hierarchy of effective modes – now with six modes at each level of $\boldsymbol{H}_{\text{eff}}$ and $\boldsymbol{H}_{\text{res}}^{(n)}$, see Eqs. (19)–(20) – again features the high-frequency vs. low-frequency modes in alternation. We therefore expect that the main dynamical features of the previous two-state model carry over to a more realistic treatment. Fig. 10 shows a projection of the diabatic states on the XT-CT branching plane. The inclusion of intermediate states generates a landscape of intersecting surfaces, thus opening various competing decay pathways. As pointed out above, the indirect XT → IS → CT pathway plays an important role and significantly accelerates the exciton dissociation. The IS state mediates the charge separation while also acting as a competing final state [53].

We conjecture that the dynamical robustness of the ultrafast exciton decay indeed results from the presence of multiple decay pathways. While the trans-

fer efficiency at individual avoided-crossing or conical intersection topologies can depend in a sensitive fashion on the molecular polymer structure, the ensemble of such structures is characterised by an efficient decay. The present approach suggests a systematic procedure by which a molecular-level analysis is carried out for such an ensemble of interface structures.

6 Discussion and Conclusions

In the analysis summarized here, we have attempted a molecular-level description of exciton dissociation at a polymer heterojunction, using a detailed electronic structure and quantum dynamical characterisation of the polymer interface. This study leads to detailed insight into the nature of the electron-phonon coupling mechanism which generates an ultrafast (fs–ps scale) exciton decay. The main ingredients of the analysis are (i) explicit electronic structure calculations (CIS and TD-DFT) for fragments of the polymer interface to determine the relevant electronic states and the Franck-Condon transition energies (Sec. 2), (ii) the construction of a linear vibronic coupling Hamiltonian which is initially set up in a localized site representation and then applied in a delocalized diabatic representation (Sec. 3), (iii) efficient multiconfigurational quantum dynamical techniques as applied to this linear vibronic coupling model, along with variants of the model which use the effective mode transformations described in Sec. 4. This analysis has led to the formulation of two-state and three-state model Hamiltonians involving the photogenerated exciton state and a charge-separated "exciplex" state, along with an additional, intermediate charge transfer state that could be relevant for photocurrent generation. This picture is in general agreement with other studies of the same system [44].

The effective mode decomposition described in Sec. 4 leads to a mechanistic interpretation of the vibronic coupling dynamics which involves both high-frequency (C=C stretch) and low-frequency (ring-torsional) modes. While the electron-phonon coupling is largely dominated by the subset of high-frequency modes, these modes taken by themselves cannot account for the ultrafast decay dynamics. The low-frequency ring-torsional modes which only appear at the second order of the HEP hierarchy (Sec. 5) are thus found to play a crucial role. The dynamical interplay of high- vs. low-frequency modes can be understood in terms of the nonadiabatic dynamics induced by the low-frequency motions via a vibronic resonance effect. The present picture points to the generic nature of the observed dynamical pattern for a two-band phonon distribution (see also Refs. [58, 97] which address the spectroscopic signature of both types of phonon modes in phenylene based polymers). A very similar dynamical mechanism could hold in related systems like carbon nanotubes [98].

The bulk heterojunction material exhibits an ensemble of interface configurations, such that spectroscopic observables and measurable photocurrents reflect statistically averaged properties (with the exception of observations

pertaining to single-molecule spectroscopy). Here, we have examined two representative configurations, i.e., the eclipsed (E) vs. staggered (S) configurations described in Sec. 2.2. These configurations differ significantly in the model parametrization, illustrating the importance of inter-chain interactions. The present analysis shows that even though the details of the exciton dissociation dynamics differ between these two configurations, an ultrafast process is observed in both cases. This suggests that the exciton dissociation process is dynamically robust. Given that this observation does not necessarily hold for the simpler two-state model of Sec. 5.1 (where the low-frequency modes do not always match the resonance window which guarantees that an efficient transfer occurs), we conjecture that the presence of intermediate states is of key importance.

The present approach has focused on the exciton dissociation event at the heterojunction, and does not account for exciton migration towards the interface region. This is justified by the fact that the highly filamented bulk heterojunction structure facilitates an immediate decay since the exciton is likely to reach the interface within its short diffusion length (of the order of 10 nm). Experimental observations for related polymer interfaces show that a considerable range of decay time scales can exist, reflecting an ultrafast decay of a subset of excitons, while longer time scales are associated with exciton states that are not localized in the immediate vicinity of the interface [102]. The present study focuses on the former subset of rapidly decaying states. However, site-site transfer could straightforwardly be included by returning to the lattice Hamiltonian of Sec. 3.1.

Further, the present analysis does not give a complete picture of all vibronic coupling pathways available to the system, but is primarily concerned with the intermolecular charge transfer at the heterojunction interface. Even though competing intramolecular internal conversion processes involving the monomer excited states could play a role (see the discussion of Sec. 1), the TD-DFT electronic structure calculations described in Sec. 2 confirm that the lowest-lying charge transfer states are of inter-chain character. The relevant states and their geometry dependence are described in a qualitatively correct way by the model Hamiltonian of Sec. 3, which builds upon a simplified electronic structure description in terms of monoexcited configurations. A more elaborate electronic structure picture for a range of geometries could lead to an even more complex scenario involving both inter- and intramolecular vibronic coupling pathways.

Finally, our analysis focuses on the primary events at the heterojunction and does not yet include a description of photocurrent production and the possible regeneration of excitons at the heterojunction. Both effects require going to longer time scales and accounting for finite temperatures. Exciton regeneration is in fact of crucial importance in the TFB:F8BT blend, since LEDs fabricated from this material have been shown to exhibit a remarkably large photoluminescence efficiency that must originate in secondary exciton formation [26, 32, 42].

The question as to how photocurrent is generated from either the exciplex states – i.e., long-lived charge-transfer excitons pinned to the interface – or from other charge transfer states (e.g., the intermediate state identified in our analysis [52] and related studies [44]) is currently an open issue. Recent experimental observations indicate that the dissociation of interfacial charge-transfer excitons constitutes the bottleneck for photocurrent generation [99–104]. A theoretical description that includes the prediction of photocurrent generation requires the use, e.g., of non-equilibrium Green's function techniques (see the Chapter by G. Cuniberti and collaborators in this volume) as combined with the vibronic coupling models described here. A detailed understanding of all phases of carrier generation, recombination, and transport is of paramount importance, especially in view of the fact that carrier generation and mobility are still the key limiting factors to device efficiency. The present analysis paves the way for such a complete *ab initio* picture of the processes at polymer junctions.

Acknowledgments

We thank Laura Herz for constructive discussions. This work was supported by the ANR-05-NANO-051-02 and ANR-NT05-3-42315 projects, by NSF grant CHE-0712981, and by the Robert Welch Foundation (E-1337).

References

1. R. H. Friend, R. W. Gymer, A. B. Holmes, J. H. Burroughes, R. N. Marks, C. Taliani, D. D. C. Bradley, D. A. Dos Santos, J. L. Brédas, M. Logdlund and W. R. Salaneck, Nature **397**, 121 (1999).
2. M. Granström, K. Petritsch, A. C. Arias, A. Lux, M. R. Andersson, and R. H. Friend, Nature **395**, 257 (1998).
3. J. J. M. Halls, J. Cornil, D. A. dos Santos, R. Silbey, D. H. Hwang, A. B. Holmes, J. L. Brédas, and R. H. Friend, Phys. Rev. B **60**, 5721 (1999).
4. L. Schmidt-Mende, A. Fechtenkötter, K. Müllen, E. Moons, R. H. Friend, and J. D. MacKenzie, Science **293**, 1119 (2001).
5. J. L. Brédas, D. Beljonne, V. Cropceanu, and J. Cornil, Chem. Rev. **104**, 4971 (2004).
6. G. D. Scholes and G. Rumbles, Nat. Mat. **5**, 683 (2006).
7. V. Cropceanu, J. Cornil, D. A. da Silva Filho, Y. Olivier, R. Silbey, and J.-L. Brédas, Chem. Rev. **107**, 926 (2007).
8. S. Günes, H. Neugebauer, and N. S. Sariciftci, Chem. Rev. **107**, 1324 (2007).
9. V. I. Arkhipov and H. Bässler, Phys. Stat. Sol. **201**, 1152 (2004).
10. *Organic Light-Emitting Devices*, eds. K. Müllen and U. Scherf, Wiley-VCH (2006).
11. M. Kasha, Discuss. Faraday Soc. **9**, 14 (1950).
12. N. J. Turro, *Modern Molecular Photochemistry*, University Science Books, 1991.

13. M. Klessinger and J. Michl, *Excited States and Photo-Chemistry of Organic Molecules*, Wiley-VCH, 1995.
14. S. I. Vavilov, Z. Phys. **42**, 311 (1927).
15. N. T. Harrison, G. R. Hayes, R. T. Philips, and R. H. Friend, Phys. Rev. Lett. **77**, 1881 (1996).
16. S. V. Frolov, Z. Bao, M. Wohlgenannt, and Z. V. Vardeny, Phys. Rev. B **65**, 205209 (2001).
17. C. Gadermaier, G. Cerullo, G. Sansone, G. Leising, U. Scherf, and G. Lanzani, Phys. Rev. Lett. **89**, 117402 (2002).
18. R. Kersting, U. Lemmer, R. F. Mahrt, K. Leo, H. Kurz, H. Bässler, and E. O. Göbel, Phys. Rev. Lett. **70**, 3820 (1993).
19. S. V. Frolov, Z. Bao, M. Wohlgenannt, and Z. V. Vardeny, Phys. Rev. Lett. **85**, 2196 (2000).
20. C. Cerullo, G. Lanzani, M. Muccini, C. Taliani, and S. De Silvestri, Phys. Rev. Lett. **83**, 231 (1999).
21. E. Collini and G. D. Scholes, Science **323**, 369 (2009).
22. G. Yu, J. Gao, J. C. Hummelen, F. Wudl, and A. J. Heeger, Science **270**, 1789 (1995).
23. J. J. M. Halls, C. A. Walsh, N. C. Greenham, E. A. Marseglia, R. H. Friend, S. C. Moratti, and A. B. Holmes, Nature **376**, 498 (1995).
24. C. Brabec, N. S. Sariciftci, and J. C. Hummelen, Adv. Funct. Mater. **11**, 15 (2001).
25. P. Peumans, S. Uchida, and S. R. Forrest, Nature **425**, 158 (2003).
26. A. C. Morteani, R. H. Friend, and C. Silva, in: *Organic Light-Emitting Devices*, p. 35, eds. K. Müllen and U. Scherf, Wiley-VCH (2006).
27. L. Sebastian and G. Weiser, Phys. Rev. Lett. **46**, 1156 (1981).
28. M. A. Stevens, C. Silva, D. M. Russell, and R. H. Friend, Phys. Rev. B **63**, 165213 (2001).
29. E. R. Bittner and J. Ramon, in *Quantum Dynamics of Complex Molecular Systems*, eds. D. A. Micha and I. Burghardt, Springer Chemical Physics Series, Vol. 83, Heidelberg, 2007.
30. J. Xue, B. P. Rand, S. Uchida, and S. R. Forrest, Adv. Mater. **17**, 66 (2005).
31. J. Halls, K. Pichler, R. H. Friend, S. Moratti, and A. Holmes, Appl. Phys. Lett. **68**, 3120 (1996).
32. A. C. Morteani, P. Sreearunothai, L. M. Herz, R. H. Friend, and C. Silva, Phys. Rev. Lett. **92**, 247402 (2004).
33. A. C. Morteani, A. S. Dhoot, J. S. Kim, C. Silva, N. C. Greenham, C. Murphy, E. Moons, S. Cina, J. H. Burroughes, and R. H. Friend, Adv. Mater. **15**, 1708 (2003).
34. P. Sreearunothai, A. C. Morteani, I. Avilov, J. Cornil, D. Beljonne, R. H. Friend, R. T. Phillips, C. Silva, and L. M. Herz, Phys. Rev. Lett. **96**, 117403 (2006).
35. S. A. Jenekhe and J. A. Osaheni, Science **265**, 765 (1994).
36. A. Weller, *The Exciplex*, Academic Press, New York, 1975.
37. T. Offermans, P. A. van Hal, S. C. J. Meskers, M. M. Koetse, and R. A. J. Janssen, Phys. Rev. B **72**, 045213 (2005).
38. I. R. Gould, R. H. Young, L. J. Mueller, A. C. Albrecht, and S. Farid, J. Am. Chem. Soc. **116**, 8188 (1994).
39. V. D. Mihailetchi, L. J. A. Koster, J. C. Hummelen, and P. W. M. Blom, Phys. Rev. Lett. **93**, 216601 (2004).

40. P. Parkinson, J. Lloyd-Hughes, M. B. Johnston, and L. M. Herz, Phys. Rev. B **78**, 115321 (2008).
41. J. Ramon and E. R. Bittner, J. Chem. Phys. **126**, 181101 (2007).
42. A. C. Morteani, R. H. Friend, and C. Silva, Chem. Phys. Lett. **391**, 81 (2004).
43. E. R. Bittner, I. Burghardt, and R. H. Friend, Chem. Phys. **357**, 159 (2009).
44. Y.-S. Huang, S. Westenhoff, I. Avilov, P. Sreearunothai, J. M. Hodgkiss, C. Deleener, R. H. Friend and D. Beljonne, Nat. Mat. **7**, 483 (2008).
45. H.-D. Meyer, U. Manthe, and L. S. Cederbaum, Chem. Phys. Lett. **165**, 73 (1990).
46. U. Manthe, H.-D. Meyer, and L. S. Cederbaum, J. Chem. Phys. **97**, 3199 (1992).
47. M. H. Beck, A. Jäckle, G. A. Worth, and H.-D. Meyer, Phys. Rep. **324**, 1 (2000).
48. G. A. Worth, M. H. Beck, A. Jäckle, and H. Meyer, 2006, The MCTDH Package, Version 8.2 (2000); H.-D. Meyer, Version 8.3 (2002). See http://www.pci.uni-heidelberg.de/tc/usr/mctdh/.
49. G. A. Worth, H.-D. Meyer, H. Köppel, L. S. Cederbaum, and I. Burghardt, Int. Rev. Phys. Chem. **27**, 569 (2008).
50. H. Tamura, E. R. Bittner, and I. Burghardt, J. Chem. Phys. **126**, 021103 (2007).
51. H. Tamura, E. R. Bittner, and I. Burghardt, J. Chem. Phys. **127**, 034706 (2007).
52. H. Tamura, J. Ramon, E. R. Bittner, and I. Burghardt, Phys. Rev. Lett. **100**, 107402 (2008).
53. H. Tamura, J. Ramon, E. R. Bittner, and I. Burghardt, J. Phys. Chem. B **112**, 495 (2008).
54. L. S. Cederbaum, E. Gindensperger, and I. Burghardt, Phys. Rev. Lett. **94**, 113003 (2005).
55. I. Burghardt, E. Gindensperger, and L. S. Cederbaum, Mol. Phys. **104**, 1081 (2006).
56. J. Ramon and E. R. Bittner, J. Phys. Chem. B **110**, 21001 (2006).
57. E. R. Bittner, J. Ramon, and S. Karabunarliev, J. Chem. Phys. **122**, 214719 (2005).
58. S. Tretiak, A. Saxena, R. L. Martin, and A. R. Bishop, Phys. Rev. Lett. **89**, 097402 (2002).
59. A. Dreuw and M. Head-Gordon, J. Am. Chem. Soc. **126**, 4007 (2004).
60. K. Müllen and U. Scherf, Eds., Organic Light-Emitting Devices, Springer Verlag, 1990.
61. S. Karabunarliev and E. R. Bittner, J. Chem. Phys. **118**, 4291 (2003).
62. P. Karadakov, J. L. Calais, and J. Delhalle, J. Chem. Phys. **94**, 8520 (1991).
63. S. Mukamel, Principles of Nonlinear Optical Spectroscopy, Oxford University Press, 1995.
64. A. L. T. Khan, P. Sreearunothai, L. M. Herz, M. J. Banach, and A. Kohler, Phys. Rev. B **69**, 085201 (2004).
65. S. Guha, J. D. Rice, Y. T. Yau, C. M. Martin, M. Chandrasekhar, H. R. Chandrasekhar, R. Guentner, P. S. de Freitas, and U. Scherf, Phys. Rev. B **67**, 125204 (2003).
66. H. Köppel, W. Domcke, and L. S. Cederbaum, Adv. Chem. Phys. **57**, 59 (1984).
67. *Conical Intersections*, ed. W. Domcke, D. R. Yarkony, and H. Köppel, World Scientific, New Jersey, 2004.
68. D. R. Yarkony, Rev. Mod. Phys. **68**, 985 (1996).
69. D. R. Yarkony, Acc. Chem. Res. **31**, 511 (1998).
70. H. Köppel and A. Thiel, J. Chem. Phys. **110**, 9371 (1999).

71. H. Köppel, J. Gronki, and S. Mahapatra, J. Chem. Phys. **115**, 2377 (2001).
72. E. Gindensperger, I. Burghardt, and L. S. Cederbaum, J. Chem. Phys. **124**, 144103 (2006).
73. E. Gindensperger, H. Köppel, and L. S. Cederbaum, J. Chem. Phys. **126**, 034106 (2007).
74. G. J. Atchity, S. S. Xantheas, and K. Ruedenberg, J. Chem. Phys. **95**, 1862 (1991).
75. Y. Toyozawa and M. Inoue, J. Phys. Soc. Jpn. **21**, 1663 (1966).
76. Y. Kayanuma and H. Nakayama, Phys. Rev. B **57**, 13099 (1998).
77. M. C. M. O'Brien, J. Phys. C **5**, 2045 (1971).
78. J. R. Fletcher, M. C. M. O'Brien, and S. N. Evangelou, J. Phys. A **13**, 2035 (1980).
79. E. Gindensperger, I. Burghardt, and L. S. Cederbaum, J. Chem. Phys. **124**, 144104 (2006).
80. I. Burghardt and H. Tamura, in: Dynamics of Open Quantum Systems, ed. K. H. Hughes (CCP6, Daresbury, 2006).
81. I. Burghardt, in *Quantum Dynamics of Complex Molecular Systems*, eds. D. A. Micha and I. Burghardt, Springer Chemical Physics Series, Vol. 83, Heidelberg, 2007.
82. E. Fick and G. Sauermann, *The Quantum Statistics of Dynamic Processes*, Springer Verlag, Berlin, 1990.
83. H. Mori, Prog. Theor. Phys. **34**, 399 (1965).
84. M. Dupuis, Prog. Theor. Phys. **37**, 502 (1967).
85. P. Grigolini and G. P. Parravicini, Phys. Rev. B **25**, 5180 (1982).
86. F. Shibata, M. Yasufuku, and C. Uchiyama, J. Phys. Soc. Jpn. **64**, 93 (1995).
87. S. A. Adelman, Adv. Chem. Phys. **53**, 61 (1983).
88. K. H. Hughes, C. D. Christ, and I. Burghardt, J. Chem. Phys. in press (2009).
89. U. Weiss, *Quantum Dissipative Systems*, World Scientific, Singapore, 1999.
90. M. Nest and H. Meyer, J. Chem. Phys. **119**, 24 (2003).
91. I. Burghardt, M. Nest, and G. A. Worth, J. Chem. Phys. **119**, 5364 (2003).
92. A. Pereverzev and E. R. Bittner, J. Chem. Phys. **125**, 104906 (2006).
93. A. Pereverzev, E. R. Bittner, and I. Burghardt, J. Chem. Phys., in press (2009).
94. B. Halperin and R. Englman, Phys. Rev. B **9**, 3364 (1973).
95. M. F. Herman, J. Chem. Phys. **109**, 2903 (1998).
96. H. Tamura, J. Chem. Phys., in press (2009).
97. S. Karabunarliev, M. Baumgarten, and E. R. Bittner, J. Chem. Phys. **114**, 5863 (2001).
98. B. F. Habenicht, H. Kamisaka, K. Yamashita, and O. V. Prezhdo, Nano Lett. **7**, 3260 (2007).
99. C. Yin, T. Kietzke, D. Neher, and H.-H. Hörhold, Appl. Phys. Lett. **90**, 092117 (2007).
100. R. A. Marsh, C. R. McNeill, A. Abrusci, A. R. Campbell, and R. H. Friend, Nano Lett. **8**, 1393 (2008).
101. C. R. McNeill, S. Westenhoff, C. Groves, R. H. Friend, and N. C. Greenham, J. Phys. Chem. C **111**, 19153 (2007).
102. L. W. Barbour, M. Hegadorn, S. Arzhantsev, and J. B. Asbury, J. Am. Chem. Soc. **129**, 15884 (2007).
103. V. I. Arkhipov, P. Heremans, and H. Bässler, Appl. Phys. Lett. **82**, 4605 (2003).
104. R. D. Pensack, K. M. Banyas, L. W. Barbour, M. Hegadorn, and J. B. Asbury, Phys. Chem. Chem. Phys. **11**, 2575 (2009).

Green Function Techniques in the Treatment of Quantum Transport at the Molecular Scale

D. A. Ryndyk, R. Gutiérrez, B. Song, and G. Cuniberti

[1] Institute for Theoretical Physics, University of Regensburg, D-93040 Regensburg, Germany, dmitry.ryndyk@physik.uni-regensburg.de
[2] Institute for Material Science and Max Bergmann Center of Biomaterials, Dresden University of Technology, D-01062 Dresden, Germany, rafael.gutierrez@tu-dresden.de
[3] Institute for Material Science and Max Bergmann Center of Biomaterials, Dresden University of Technology, D-01062 Dresden, Germany, present address: Shanghai Institute of Applied Physics, Chinese Academy of Sciences, Shanghai 201800 P. R. China, bosong@sinap.ac.cn
[4] Institute for Material Science and Max Bergmann Center of Biomaterials, Dresden University of Technology, D-01062 Dresden, Germany, g.cuniberti@tu-dresden.de

Abstract. The theoretical investigation of charge (and spin) transport at nanometer length scales requires the use of advanced and powerful techniques able to deal with the dynamical properties of the relevant physical systems, to explicitly include out-of-equilibrium situations typical for electrical/heat transport as well as to take into account interaction effects in a systematic way. Equilibrium Green function techniques and their extension to non-equilibrium situations via the Keldysh formalism build one of the pillars of current state-of-the-art approaches to quantum transport which have been implemented in both model Hamiltonian formulations and first-principle methodologies. In this chapter we offer a tutorial overview of the applications of Green functions to deal with some fundamental aspects of charge transport at the nanoscale, mainly focusing on applications to model Hamiltonian formulations.

1 Introduction

The natural limitations that are expected to arise by the further miniaturization attempts of semiconductor-based electronic devices have led in the past two decades to the emergence of the new field of molecular electronics, where electronic functions are going to be performed at the single-molecule level, see

I. Burghardt et al. (eds.), *Energy Transfer Dynamics in Biomaterial Systems*, Springer Series in Chemical Physics 93, DOI 10.1007/978-3-642-02306-4_9,

the recent overviews in Refs. [1–6]. The original conception which lies at the bottom of this fascinating field can be traced back to the paper by Ari Aviram and Mark Ratner in 1974 [7], where a single-molecule rectifying diode was proposed. Obviously, one of the core issues at stake in molecular electronics is to clarify the question whether single molecules (or more complex molecular aggregates) can support an electric current. To achieve this goal, extremely refined experimental techniques are required in order to probe the response of such a nano-object to external fields. The meanwhile paradigmatic situation is that of a single molecule contacted by two metallic electrodes between which a bias voltage is applied.

Recent experiments

Enormous progress has been achieved in the experimental realization of such nano-devices, we only mention the development of controllable single-molecule junctions [8]–[22] and scanning tunneling microscopy based techniques [23]–[44]. With their help, a plethora of interesting phenomena like rectification [18], negative differential conductance [9, 35], Coulomb blockade [10, 11, 15, 16, 21, 23], Kondo effect [11, 12], vibrational effects [10, 13, 14, 16, 21, 25, 31–33, 35, 36], and nanoscale memory effects [34, 39, 40, 42, 44], among others, have been demonstrated.

The traditional semiconductor nanoelectronics also remains at the forefront of modern research, in particular due to recent experiments with small quantum dots, where cotunneling effects were observed [45–47], as well as new rectification effects in double quantum dots, interpreted as spin blockade [48–51]. Note that semiconductor experiments are very well controlled at present time, so they play an important role as a benchmark for the theory.

Apart from single molecules, carbon nanotubes have also found extensive applications and have been the target of experimental and theoretical studies over the last years, see Ref. [52] for a very recent review. The expectations to realize electronics at the molecular scale also reached into the domain of bio-molecular systems, thus opening new perspectives for the field due to the specific self-recognition and self-assembling properties of biomolecules. For instance, DNA oligomers have been already used as templates in molecular electronic circuits [53–55]. Much less clear is, however, if bio-molecules, and more specifically short DNA oligomers could also act as wiring systems. Their electrical response properties are much harder to disclose and there is still much controversy about the factors that determine charge migration through such systems [56–64].

Theoretical methods

The theoretical treatment of transport at the nanoscale (see introduction in [65–70]) requires the combined use of different techniques which range from minimal model Hamiltonians, passing through semi-empirical methods up to

full first-principle methodologies. We mention here some important contributions, while we have no possibility to cite all relevant papers.

Model Hamiltonians can in a straightforward way select, out of the many variables that can control charge migration those which are thought to be the most relevant ones for a specific molecule-electrode set-up. They contain, however, in a sometimes not well-controlled way, many free parameters; hence, they can point at generic effects, but they must be complemented with other methodologies able to yield microscopic specific information. Semi-empirical methods can deal with rather large systems due to the use of special subsets of electronic states to construct molecular Hamiltonians as well as to the approximate treatment of interactions, but often have the drawback of not being transferable. *Ab initio* approaches, finally, can deal in a very precise manner with the electronic and atomic structure of the different constituents of a molecular junction (metallic electrodes, molecular wire, the interface) but it is not *a priori* evident that they can also be applied to strong non-equilibrium situations.

From a more formal standpoint, there are roughly two main theoretical frameworks that can be used to study quantum transport in nanosystems at finite voltage: generalized master equation (GME) [71,72] and nonequilibrium Green function (NGF) techniques [66, 73–76]. The former also lead to more simple rate equations in the case where (i) the electrode-system coupling can be considered as a weak perturbation, and (ii) off-diagonal elements of the reduced density matrix in the eigenstate representation (coherences) can be neglected due to very short decoherence times. Both approaches, the GME and NGF techniques, can yield formally exact expressions for many observables. For non-interacting systems, one can even solve analytically many models. However, once interactions are introduced - and these are the most interesting cases containing a very rich physics - different approximation schemes have to be introduced to make the problems tractable.

In this chapter, we will review mainly the technique of non-equilibrium Keldysh Green functions (NGF). This approach is able to deal with a very broad variety of physical problems related to quantum transport at the molecular scale. It can deal with strong non-equilibrium situations via an extension of the conventional GF formalism to the Schwinger-Keldysh contour [74] and it can also include interaction effects (electron-electron, electron-vibron, etc) in a systematic way (diagrammatic perturbation theory, equation of motion techniques). Proposed first time for the mesoscopic structures in the early seventies by Caroli et al. [77–80], this approach was formulated in an elegant way by Meir, Wingreen and Jauho [66, 81–84], see also Refs. [306, 307], who derived an exact expression for nonequilibrium current through an interacting nanosystem placed between large noninteracting leads in terms of the nonequilibrium Green functions of the nanosystem. Still, the problem of calculation of these Green functions is not trivial. We consider some possible approaches in the case of electron-electron and electron-vibron interactions. Moreover, as we will show later on, it can reproduce results obtained within

the master equation approach in the weak coupling limit to the electrodes (Coulomb blockade), but it can also go *beyond* this limit and cover intermediate coupling (Kondo effect) and strong coupling (Fabry-Perot) domains. It thus offer the possibility of dealing with different physical regimes in a unified way.

Now we review briefly some results obtained recently in the main directions of modern research: general nanoscale quantum transport theory, atomistic transport theory and applications to particular single-molecule systems.

General nanoscale quantum transport theory

On the way to interpretation of modern experiments with single-molecule junctions and STM spectroscopy of single molecules on surfaces, two main theoretical problems have to be solved. The first is development of appropriate models based on ab initio formulations. The second is an effective and scalable theory of quantum transport through multilevel interacting systems. We first consider the last problem, assuming that the model Hamiltonian is known. Quantum transport through *noninteracting* system can be considered using the famous Landauer-Büttiker method [85–94], which establishes the fundamental relation between the wave functions (scattering amplitudes) of a system and its conducting properties. The method can be applied to find the current through a noninteracting system or through an *effectively noninteracting* system, for example if the mean-field description is valid and the inelastic scattering is not essential. Such type of an electron transport is called coherent, because there is no phase-breaking and quantum interference is preserved during the electron motion across the system. In fact, coherence is initially assumed in many *ab initio* based transport methods (DFT+NGF, and others), so that the Landauer-Büttiker method is now routinely applied to any basic transport calculation through nanosystems and single molecules. Besides, it is directly applicable in many semiconductor quantum dot systems with weak electron-electron interactions. Due to simplicity and generality of this method, it is now widely accepted and is in the base of our understanding of coherent transport.

However, the peculiarity of single-molecule transport is just essential role of electron-electron and electron-vibron interactions, so that Landauer-Büttiker method is not enough usually to describe essential physics even qualitatively (see, however Refs. [303–305] for inelastic scattering effects).

During last years many new methods were developed to describe transport at finite voltage, with focus on correlation and inelastic effects, in particular in the cases when Coulomb blockade, Kondo effect and vibronic effects take place.

Vibrons (the localized phonons) are very important because molecules are flexible. The theory of electron-vibron interaction has a long history, but many questions it implies are not answered up to now. While the isolated

electron-vibron model can be solved exactly by the so-called polaron or Lang-Firsov transformation [95–97], the coupling to the leads produces a true many-body problem. The inelastic resonant tunneling of *single* electrons through the localized state coupled to phonons was considered in Refs. [98–103]. There the exact solution in the single-particle approximation was derived, ignoring completely the Fermi sea in the leads. At strong electron-vibron interaction and weak couplings to the leads the satellites of the main resonant peak are formed in the spectral function.

The essential progress in calculation of transport properties in the strong electron-vibron interaction limit has been made with the help of the master equation approach [104–112]. This method, however, is valid only in the limit of very weak molecule-to-lead coupling and neglects all spectral effects, which are the most important at finite coupling to the leads.

At strong coupling to the leads and the finite level width the master equation approach can no longer be used, and we apply alternatively the nonequilibrium Green function technique which have been recently developed to treat vibronic effects in a perturbative or self-consistent way in the cases of weak and intermediate electron-vibron interaction [113–130].

The case of intermediate and strong electron-vibron interaction *at intermediate coupling to the leads* is the most interesting, but also the most difficult. The existing approaches are mean-field [131–133], or start from the exact solution for the isolated system and then treat tunneling as a perturbation [134–140]. The fluctuations beyond mean-field approximations were considered in Refs. [141, 142]

In parallel, the related activity was in the field of single-electron shuttles and quantum shuttles [143–153]. Finally, based on the Bardeen's tunneling Hamiltonian method [154–158] and Tersoff-Hamann approach [159, 160], the theory of inelastic electron tunneling spectroscopy (IETS) was developed [113–116, 161–163].

The recent review of the electron-vibron problem and its relation to the molecular transport see in Ref. [164].

Coulomb interaction is the other important ingredient of the models, describing single molecules. It is in the origin of such fundamental effects as Coulomb blockade and Kondo efect. The most convenient and simple enough is Anderson-Hubbard model, combining the formulations of Anderson impurity model [165] and Hubbard many-body model [166–168]. To analyze such strongly correlated system several complementary methods can be used: master equation and perturbation in tunneling, equation-of-motion method, self-consistent Green functions, renormalization group and different numerical methods.

When the coupling to the leads is weak, electron-electron interaction results in Coulomb blockade, the sequential tunneling is described by the master equation method [169–176] and small cotunneling current in the blockaded regime can be calculated by the next-order perturbation theory [177–179]. This theory was used successfully to describe electron tunneling via discrete

quantum states in quantum dots [180–183]. Recently there were several attempts to apply master equation to multi-level models of molecules, in particular describing benzene rings [184–186].

To describe consistently cotunneling, level broadening and higher-order (in tunneling) processes, more sophisticated methods to calculate the reduced density matrix were developed, based on the Liouville - von Neumann equation [186–193] or real-time diagrammatic technique [194–201]. Different approaches were reviewed recently in Ref. [202].

The equation-of-motion (EOM) method is one of the basic and powerful ways to find the Green functions of interacting quantum systems. In spite of its simplicity it gives the appropriate results for strongly correlated nanosystems, describing qualitatively and in some cases quantitatively such important transport phenomena as Coulomb blockade and Kondo effect in quantum dots. The results of the EOM method could be calibrated with other available calculations, such as the master equation approach in the case of weak coupling to the leads, and the perturbation theory in the case of strong coupling to the leads and weak electron-electron interaction.

In the case of a single site junction with two (spin-up and spin-down) states and Coulomb interaction between these states (Anderson impurity model), the *linear conductance* properties have been successfully studied by means of the EOM approach in the cases related to Coulomb blockade [203, 204] and the Kondo effect [205]. Later the same method was applied to some two-site models [206–209]. Multi-level systems were started to be considered only recently [210, 211]. Besides, there are some difficulties in building the lesser GF in the nonequilibrium case (at finite bias voltages) by means of the EOM method [212–214].

The diagrammatic method was also used to analyze the Anderson impurity model. First of all, the perturbation theory can be used to describe weak electron-electron interaction and even some features of the Kondo effect [215]. The family of nonperturbative current-conserving self-consistent approximations for Green functions has a long history and goes back to the Schwinger functional derivative technique, Kadanoff-Baym approximations and Hedin equations in the equilibrium many-body theory [216–223]. Recently GW approximation was investigated together with other methods [224–227]. It was shown that dynamical correlation effects and self-consistency can be very important at finite bias.

Finally, we want to mention briefly three important fields of research, that we do not consider in the present review: the theory of Kondo effect [205, 228–234], spin-dependent transport [235–239], and time-dependent transport [83, 240–243].

Atomistic transport theory

Atomistic transport theory utilizes semi-empirical (tight-binding [244, 245, 301,302]) or *ab initio* based methods. In all cases the microscopic structure is taken into account with different level of accuracy.

The most popular is the approach combining density-functional theory (DFT) and NGF and known as DFT+NGF [246–268]. This method, however is not free from internal problems. First of all, it is essentially a mean-filed method neglecting strong local correlations and inelastic scattering. Second, density-functional theory is a ground state theory and e.g. the transmission calculated using static DFT eigenvalues will display peaks at the Kohn-Sham excitation energies, which in general do not coincide with the true excitation energies. Extensions to include excited states as in time-dependent density-functional theory, though very promising [269–271], are not fully developed up to date.

To improve DFT-based models several approaches were suggested, including inelastic electron-vibron interaction [121, 126, 272–279] or Coulomb interaction beyond mean-field level [280], or based on the LDA+U approache [281]. The principally different alternative to DFT is to use *an initio quantum chemistry* based many-body quantum transport approach [282–285].

Finally, transport in bio-molecules attracted more attention, in particular electrical conductance of DNA [286–290].

Outline

The review is organized as follows. In Section **2** we will first introduce the Green functions for non-interacting systems, and present few examples of transport through non-interacting regions. Then we review the master equation approach and its application to describe Coulomb blockade and vibron-mediated Franck-Condon blockade. In Section **3** the Keldysh NGF technique is developed in detail. In equilibrium situations or within the linear response regime, dynamic response and static correlation functions are related via the fluctuation-dissipation theorem. Thus, solving Dyson equation for the retarded GF is enough to obtain the correlation functions. In strong out-of-equilibrium situations, however, dynamic response and correlation functions have to be calculated simultaneously and are not related by fluctuation-dissipation theorems. The Kadanoff-Baym-Keldysh approach yield a compact, powerful formulation to derive Dyson and kinetic equations for non-equilibrium systems. In Sec. **4** we present different applications of the Green function techniques. We show how Coulomb blockade can be described within the Anderson-Hubbard model, once an appropriate truncation of the equation of motion hierarchy is performed (Sec. 4.A). Further, the paradigmatic case of transport through a single electronic level coupled to a local vibrational mode is discussed in detail within the context of the self-consistent Born approximation. It is shown that already this simple model can display non-trivial

physics (Sec. 4.B). Finally, the case of an electronic system interacting with a bosonic bath is discussed in Sec. 4.C where it is shown that the presence of an environment with a continuous spectrum can modified the low-energy analytical structure of the Green function and lead to dramatic changes in the electrical response of the system. We point at the relevance of this situation to discuss transport experiments in short DNA oligomers. We have not addressed the problem of the (equilibrium or non-equilibrium) Kondo effect, since this issue alone would require a chapter on its own due to the non-perturbative character of the processes leading to the formation of the Kondo resonance.

In view of the broadness of the topic, the authors were forced to do a very subjective selection of the topics to be included in this review as well as of the most relevant literature. We thus apologize for the omission of many interesting studies which could not be dealt with in the restricted space at our disposal. We refer the interested reader to the other contributions in this book and the cited papers.

2 From coherent transport to sequential tunneling (basics)

2.1 Coherent transport: single-particle Green functions

Nano-scale and molecular-scale systems are naturally described by discrete-level models, for example eigenstates of quantum dots, molecular orbitals, or atomic orbitals. But the leads are very large (infinite) and have a continuous energy spectrum. To include the lead effects systematically, it is reasonable to start from the discrete-level representation for the whole system. It can be made by the tight-binding (TB) model, which was proposed to describe quantum systems in which the localized electronic states play an essential role, it is widely used as an alternative to the plane wave description of electrons in solids, and also as a method to calculate the electronic structure of molecules in quantum chemistry.

A very effective method to describe scattering and transport is the Green function (GF) method. In the case of non-interacting systems and coherent transport single-particle GFs are used. In this section we consider the matrix Green function method for coherent transport through discrete-level systems.

(i) Matrix (tight-binding) Hamiltonian

The main idea of the method is to represent the wave function of a particle as a linear combination of some known *localized* states $\psi_\alpha(\mathbf{r}, \sigma)$, where α denote the set of quantum numbers, and σ is the spin index (for example, atomic orbitals, in this particular case the method is called LCAO – linear combination of atomic orbitals)

$$\psi(\xi) = \sum_\alpha c_\alpha \psi_\alpha(\xi), \tag{1}$$

here and below we use $\xi \equiv (\mathbf{r}, \sigma)$ to denote both spatial coordinates and spin.

Using the Dirac notations $|\alpha\rangle \equiv \psi_\alpha(\xi)$ and assuming that $\psi_\alpha(\xi)$ are orthonormal functions $\langle\alpha|\beta\rangle = \delta_{\alpha\beta}$ we can write the *single-particle matrix (tight-binding) Hamiltonian* in the Hilbert space formed by $\psi_\alpha(\xi)$

$$\hat{H} = \sum_\alpha (\epsilon_\alpha + e\varphi_\alpha)|\alpha\rangle\langle\alpha| + \sum_{\alpha\beta} t_{\alpha\beta}|\alpha\rangle\langle\beta|, \tag{2}$$

the first term in this Hamiltonian describes the states with energies ϵ_α, φ_α is the electrical potential, the second term should be included if the states $|\alpha\rangle$ are not eigenstates of the Hamiltonoian. In the TB model $t_{\alpha\beta}$ is the hopping matrix element between states $|\alpha\rangle$ and $|\beta\rangle$, which is nonzero, as a rule, for nearest neighbor sites. The two-particle interaction is described by the Hamiltonian

$$\hat{H} = \sum_{\alpha\beta,\delta\gamma} V_{\alpha\beta,\delta\gamma}|\alpha\rangle|\beta\rangle\langle\delta|\langle\gamma|, \tag{3}$$

in the two-particle Hilbert space, and so on.

The energies and hopping matrix elements in this Hamiltomian can be calculated, if the single-particle real-space Hamiltomian $\hat{h}(\xi)$ is known:

$$\epsilon_\alpha\delta_{\alpha\beta} + t_{\alpha\beta} = \int \psi^*_\alpha(\xi)\hat{h}(\xi)\psi_\beta(\xi)d\xi. \tag{4}$$

This approach was developed originally as an approximate method, if the wave functions of isolated atoms are taken as a basis wave functions $\psi_\alpha(\xi)$, but also can be formulated exactly with the help of Wannier functions. Only in the last case the expansion (1) and the Hamiltonian (2) are exact, but some extension to the arbitrary basis functions is possible. In principle, the TB model is reasonable only when *local* states can be orthogonalized. The method is useful to calculate the conductance of complex quantum systems in combination with *ab initio* methods. It is particular important to describe small molecules, when the atomic orbitals form the basis.

In the mathematical sense, the TB model is a discrete (grid) version of the continuous Schrödinger equation, thus it is routinely used in numerical calculations.

To solve the single-particle problem it is convenient to introduce a new representation, where the coefficients c_α in the expansion (1) are the components of a vector wave function (we assume here that all states α are numerated by integers)

$$\Psi = \begin{pmatrix} c_1 \\ c_2 \\ \vdots \\ c_N \end{pmatrix}, \tag{5}$$

and the eigenstates Ψ_λ are to be found from the matrix Schrödinger equation

$$\mathbf{H}\Psi_\lambda = E_\lambda \Psi_\lambda, \tag{6}$$

with the matrix elements of the single-particle Hamiltonian

$$H_{\alpha\beta} = \begin{cases} \epsilon_\alpha + e\varphi_\alpha, & \alpha = \beta, \\ t_{\alpha\beta}, & \alpha \neq \beta. \end{cases} \tag{7}$$

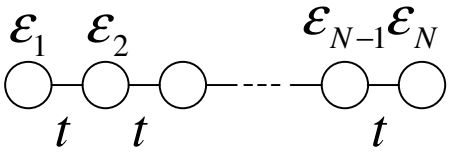

Fig. 1: A finite linear chain of single-level sites.

Now let us consider some typical systems, for which the matrix method is an appropriate starting point. The simplest example is a single quantum dot, the basis is formed by the *eigenstates*, the corresponding Hamiltonian is diagonal

$$\mathbf{H} = \begin{pmatrix} \epsilon_1 & 0 & 0 & \cdots & 0 \\ 0 & \epsilon_2 & 0 & \cdots & 0 \\ \vdots & \ddots & \ddots & \ddots & \vdots \\ 0 & \cdots & 0 & \epsilon_{N-1} & 0 \\ 0 & \cdots & 0 & 0 & \epsilon_N \end{pmatrix}. \tag{8}$$

The next typical example is a linear chain of single-state sites with only nearest-neighbor couplings (Fig. 1)

$$\boldsymbol{H} = \begin{pmatrix} \epsilon_1 & t & 0 & \cdots & 0 \\ t & \epsilon_2 & t & \cdots & 0 \\ \vdots & \ddots & \ddots & \ddots & \vdots \\ 0 & \cdots & t & \epsilon_{N-1} & t \\ 0 & \cdots & 0 & t & \epsilon_N \end{pmatrix}. \tag{9}$$

The method is applied as well to consider the semi-infinite leads. Although the matrices are formally infinite-dimensional in this case, we shall show below, that the problem is reduced to the finite-dimensional problem for the quantum system of interest, and the semi-infinite leads can be integrated out.

Finally, in the second quantized form the tight-binding Hamiltonian is

$$\hat{H} = \sum_\alpha (\epsilon_\alpha + e\varphi_\alpha)\, c_\alpha^\dagger c_\alpha + \sum_{\alpha\neq\beta} t_{\alpha\beta} c_\alpha^\dagger c_\beta. \tag{10}$$

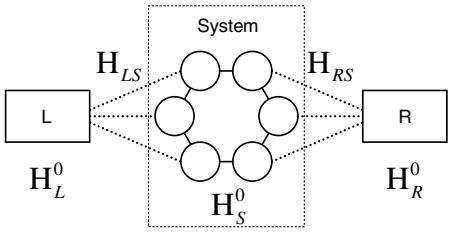

Fig. 2: A quantum system coupled to the left and right leads.

(ii) Matrix Green functions and contact self-energies

The solution of single-particle quantum problems, formulated with the help of a matrix Hamiltonian, is possible along the usual line of finding the wave-functions on a lattice, solving the Schrödinger equation (6). The other method, namely matrix Green functions, considered in this section, was found to be more convenient for transport calculations, especially when interactions are included.

The retarded *single-particle* matrix Green function $\boldsymbol{G}^R(\epsilon)$ is determined by the equation

$$[(\epsilon + i\eta)\boldsymbol{I} - \boldsymbol{H}]\,\boldsymbol{G}^R = \boldsymbol{I}, \tag{11}$$

where η is an infinitesimally small positive number $\eta = 0^+$.

For an isolated noninteracting system the Green function is simply obtained after the matrix inversion

$$\boldsymbol{G}^R = [(\epsilon + i\eta)\boldsymbol{I} - \boldsymbol{H}]^{-1}\,. \tag{12}$$

Let us consider the trivial example of a two-level system with the Hamiltonian

$$\boldsymbol{H} = \begin{pmatrix} \epsilon_1 & t \\ t & \epsilon_2 \end{pmatrix}. \tag{13}$$

The retarded GF is easy found to be ($\tilde{\epsilon} = \epsilon + i\eta$)

$$\boldsymbol{G}^R(\epsilon) = \frac{1}{(\tilde{\epsilon} - \epsilon_1)(\tilde{\epsilon} - \epsilon_2) - t^2} \begin{pmatrix} \tilde{\epsilon} - \epsilon_2 & t \\ t & \tilde{\epsilon} - \epsilon_1 \end{pmatrix}. \tag{14}$$

Now let us consider the case, when the system of interest is coupled to two contacts (Fig. 2). We assume here that the contacts are also described by the tight-binding model and by the matrix GFs. Actually, the semi-infinite contacts should be described by the matrix of infinite dimension. We shall consider the semi-infinite contacts in the next section.

Let us present the full Hamiltonian of the considered system in a following block form

$$\boldsymbol{H} = \begin{pmatrix} \boldsymbol{H}_L^0 & \boldsymbol{H}_{LS} & 0 \\ \boldsymbol{H}_{LS}^\dagger & \boldsymbol{H}_S^0 & \boldsymbol{H}_{RS}^\dagger \\ 0 & \boldsymbol{H}_{RS} & \boldsymbol{H}_R^0 \end{pmatrix}, \tag{15}$$

where $\boldsymbol{H}_L^0$, $\boldsymbol{H}_S^0$, and $\boldsymbol{H}_R^0$ are Hamiltonians of the left lead, the system, and the right lead separately. And the off-diagonal terms describe system-to-lead coupling. The Hamiltonian should be hermitian, so that

$$\boldsymbol{H}_{SL} = \boldsymbol{H}_{LS}^\dagger, \quad \boldsymbol{H}_{SR} = \boldsymbol{H}_{RS}^\dagger. \tag{16}$$

The Eq. (11) can be written as

$$\begin{pmatrix} \boldsymbol{E} - \boldsymbol{H}_L^0 & -\boldsymbol{H}_{LS} & 0 \\ -\boldsymbol{H}_{LS}^\dagger & \boldsymbol{E} - \boldsymbol{H}_S^0 & -\boldsymbol{H}_{RS}^\dagger \\ 0 & -\boldsymbol{H}_{RS} & \boldsymbol{E} - \boldsymbol{H}_R^0 \end{pmatrix} \begin{pmatrix} \boldsymbol{G}_L & \boldsymbol{G}_{LS} & 0 \\ \boldsymbol{G}_{SL} & \boldsymbol{G}_S & \boldsymbol{G}_{SR} \\ 0 & \boldsymbol{G}_{RS} & \boldsymbol{G}_R \end{pmatrix} = \boldsymbol{I}, \tag{17}$$

where we introduce the matrix $\boldsymbol{E} = (\epsilon + i\eta)\boldsymbol{I}$, and represent the matrix Green function in a convenient form, the notation of retarded function is omitted in intermediate formulas. Now our first goal is to find the system Green function $\boldsymbol{G}_S$ which defines all quantities of interest. From the matrix equation (17)

$$\left(\boldsymbol{E} - \boldsymbol{H}_L^0\right) \boldsymbol{G}_{LS} - \boldsymbol{H}_{LS} \boldsymbol{G}_S = 0, \tag{18}$$

$$-\boldsymbol{H}_{LS}^\dagger \boldsymbol{G}_{LS} + \left(\boldsymbol{E} - \boldsymbol{H}_S^0\right) \boldsymbol{G}_S - \boldsymbol{H}_{RS}^\dagger \boldsymbol{G}_{RS} = \boldsymbol{I}, \tag{19}$$

$$-\boldsymbol{H}_{RS} \boldsymbol{G}_S + \left(\boldsymbol{E} - \boldsymbol{H}_R^0\right) \boldsymbol{G}_{RS} = 0. \tag{20}$$

From the first and the third equations one has

$$\boldsymbol{G}_{LS} = \left(\boldsymbol{E} - \boldsymbol{H}_L^0\right)^{-1} \boldsymbol{H}_{LS} \boldsymbol{G}_S, \tag{21}$$

$$\boldsymbol{G}_{RS} = \left(\boldsymbol{E} - \boldsymbol{H}_R^0\right)^{-1} \boldsymbol{H}_{RS} \boldsymbol{G}_S, \tag{22}$$

and substituting it into the second equation we arrive at the equation

$$\left(\boldsymbol{E} - \boldsymbol{H}_S^0 - \boldsymbol{\Sigma}\right) \boldsymbol{G}_S = \boldsymbol{I}, \tag{23}$$

where we introduce the *contact self-energy* (which should be also called retarded, we omit the index in this chapter)

$$\boldsymbol{\Sigma} = \boldsymbol{H}_{LS}^\dagger \left(\boldsymbol{E} - \boldsymbol{H}_L^0\right)^{-1} \boldsymbol{H}_{LS} + \boldsymbol{H}_{RS}^\dagger \left(\boldsymbol{E} - \boldsymbol{H}_R^0\right)^{-1} \boldsymbol{H}_{RS}. \tag{24}$$

Finally, we found, that the retarded GF of a nanosystem coupled to the leads is determined by the expression

$$\boldsymbol{G}_S^R(\epsilon) = \left[(\epsilon + i\eta)\boldsymbol{I} - \boldsymbol{H}_S^0 - \boldsymbol{\Sigma}\right]^{-1}, \tag{25}$$

the effects of the leads are included through the self-energy.

Here we should stress the important property of the self-energy (24), it is determined only by the coupling Hamiltonians and the retarded GFs of the *isolated* leads $\boldsymbol{G}_i^{0R} = \left(\boldsymbol{E} - \boldsymbol{H}_R^0\right)^{-1}$ $(i = L, R)$

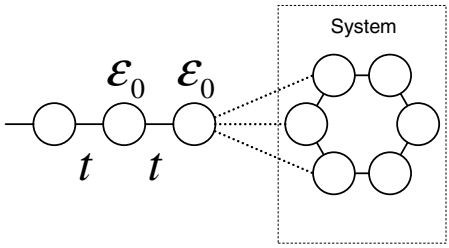

Fig. 3: A quantum system coupled to a semi-infinite 1D lead.

$$\boldsymbol{\Sigma}_i = \boldsymbol{H}_{iS}^{\dagger} \left(\boldsymbol{E} - \boldsymbol{H}_i^0\right)^{-1} \boldsymbol{H}_{iS} = \boldsymbol{H}_{iS}^{\dagger} \boldsymbol{G}_i^{0R} \boldsymbol{H}_{iS}, \tag{26}$$

it means, that the contact self-energy is independent of the state of the nanosystem itself and describes completely the influence of the leads. Later we shall see that this property conserves also for interacting system, if the leads are noninteracting.

Finally, we should note, that the Green functions considered in this section, are *single-particle* GFs, and can be used only for noninteracting systems.

(iii) Semi-infinite leads

Let us consider now a nanosystem coupled to a semi-infinite lead (Fig. 3). The direct matrix inversion can not be performed in this case. The spectrum of a semi-infinite system is continuous. We should transform the expression (26) into some other form.

To proceed, we use the relation between the Green function and the eigenfunctions Ψ_λ of a system, which are solutions of the Schrödinger equation (6). Let us define $\Psi_\lambda(\alpha) \equiv c_\lambda$ in the eigenstate $|\lambda\rangle$ in the sense of definition (5), then

$$G_{\alpha\beta}^R(\epsilon) = \sum_\lambda \frac{\Psi_\lambda(\alpha)\Psi_\lambda^*(\beta)}{\epsilon + i\eta - E_\lambda}, \tag{27}$$

where α is the TB state (site) index, λ denotes the eigenstate, E_λ is the energy of the eigenstate. The summation in this formula can be easy replaced by the integration in the case of a continuous spectrum. It is important to notice, that the eigenfunctions $\Psi_\lambda(\alpha)$ should be calculated for the separately taken semi-infinite lead, because the Green function of isolated lead is substituted into the contact self-energy.

For example, for the semi-infinite 1D chain of single-state sites ($n, m = 1, 2, ...$)

$$G_{nm}^R(\epsilon) = \int_{-\pi}^{\pi} \frac{dk}{2\pi} \frac{\Psi_k(n)\Psi_k^*(m)}{\epsilon + i\eta - E_k}, \tag{28}$$

with the eigenfunctions $\Psi_k(n) = \sqrt{2}\sin kn$, $E_k = \epsilon_0 + 2t\cos k$.

Let us consider a simple situation, when the nanosystem is coupled only to the end site of the 1D lead (Fig. 3). From (26) we obtain the matrix elements of the self-energy

$$\Sigma_{\alpha\beta} = V^*_{1\alpha} V_{1\beta} G^{0R}_{11}, \tag{29}$$

where the matrix element $V_{1\alpha}$ describes the coupling between the end site of the lead ($n = m = 1$) and the state $|\alpha\rangle$ of the nanosystem.

To make clear the main physical properties of the lead self-energy, let us analyze in detail the semi-infinite 1D lead with the Green function (28). The integral can be calculated analytically ([70], p. 213, [244])

$$G^R_{11}(\epsilon) = \frac{1}{\pi}\int_{-\pi}^{\pi} \frac{\sin^2 k dk}{\epsilon + i\eta - \epsilon_0 - 2t\cos k} = -\frac{\exp(iK(\epsilon))}{t}, \tag{30}$$

$K(\epsilon)$ is determined from $\epsilon = \epsilon_0 + 2t\cos K$. Finally, we obtain the following expressions for the real and imaginary part of the self-energy

$$\mathrm{Re}\Sigma_{\alpha\alpha} = \frac{|V_{1\alpha}|^2}{t}\left(\kappa - \sqrt{\kappa^2 - 1}\,[\theta(\kappa - 1) - \theta(-\kappa - 1)]\right), \tag{31}$$

$$\mathrm{Im}\Sigma_{\alpha\alpha} = -\frac{|V_{1\alpha}|^2}{t}\sqrt{1 - \kappa^2}\,\theta(1 - |\kappa|), \tag{32}$$

$$\kappa = \frac{\epsilon - \epsilon_0}{2t}. \tag{33}$$

The real and imaginary parts of the self-energy, given by these expressions, are shown in Fig. 4. There are several important general conclusion that we can make looking at the formulas and the curves.

(a) The self-energy is a complex function, the real part describes the energy shift of the level, and the imaginary part describes broadening. The *finite* imaginary part appears as a result of the continuous spectrum in the leads. The broadening is described traditionally by the matrix

$$\boldsymbol{\Gamma} = i\left(\boldsymbol{\Sigma} - \boldsymbol{\Sigma}^\dagger\right), \tag{34}$$

called *level-width function*.

(b) In the wide-band limit ($t \to \infty$), at the energies $\epsilon - \epsilon_0 \ll t$, it is possible to neglect the real part of the self-energy, and the only effect of the leads is level broadening. So that the self-energy of the left (right) lead is

$$\boldsymbol{\Sigma}_{L(R)} = -i\frac{\boldsymbol{\Gamma}_{L(R)}}{2}. \tag{35}$$

(iv) Transmission, conductance, current

After all, we want again to calculate the current through the nanosystem. We assume, as before, that the contacts are equilibrium, and there is the voltage V applied between the left and right contacts. The calculation of the

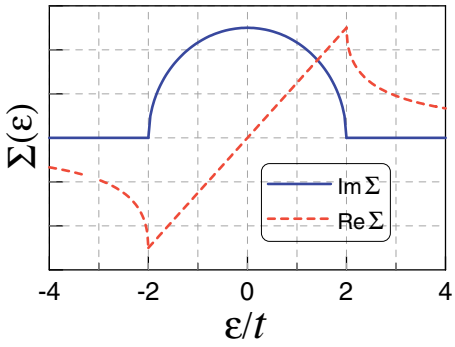

Fig. 4: Real and imaginary parts of the contact self-energy as a function of energy for a one-band one-dimensional lead.

current in a general case is more convenient to perform using the full power of the nonequilibrium Green function method. Here we present a simplified approach, valid for noninteracting systems only, following Paulsson [291].

Let us come back to the Schrödinger equation (6) in the matrix representation, and write it in the following form

$$\begin{pmatrix} \boldsymbol{H}_L^0 & \boldsymbol{H}_{LS} & 0 \\ \boldsymbol{H}_{LS}^\dagger & \boldsymbol{H}_S^0 & \boldsymbol{H}_{RS}^\dagger \\ 0 & \boldsymbol{H}_{RS} & \boldsymbol{H}_R^0 \end{pmatrix} \begin{pmatrix} \Psi_L \\ \Psi_S \\ \Psi_R \end{pmatrix} = E \begin{pmatrix} \Psi_L \\ \Psi_S \\ \Psi_R \end{pmatrix}, \tag{36}$$

where Ψ_L, Ψ_S, and Ψ_R are vector wave functions of the left lead, the nanosystem, and the right lead correspondingly.

Now we find the solution in the scattering form (which is difficult to call true scattering because we do not define explicitly the geometry of the leads). Namely, in the left lead $\Psi_L = \Psi_L^0 + \Psi_L^1$, where Ψ_L^0 is the eigenstate of $\boldsymbol{H}_L^0$, and is considered as known initial wave. The "reflected" wave Ψ_L^1, as well as the transmitted wave in the right lead Ψ_R, appear only as a result of the interaction between subsystems. The main trick is, that we find a *retarded* solution.

Solving the equation (36) with these conditions, the solution is

$$\Psi_L = \left(1 + \boldsymbol{G}_L^{0R} \boldsymbol{H}_{LS} \boldsymbol{G}_S^R \boldsymbol{H}_{LS}^\dagger\right) \Psi_L^0, \tag{37}$$

$$\Psi_R = \boldsymbol{G}_R^{0R} \boldsymbol{H}_{RS} \boldsymbol{G}_S^R \boldsymbol{H}_{LS}^\dagger \Psi_L^0 \tag{38}$$

$$\Psi_S = \boldsymbol{G}_S^R \boldsymbol{H}_{LS}^\dagger \Psi_L^0. \tag{39}$$

The physical sense of this expressions is quite transparent, they describe the quantum amplitudes of the scattering processes. Three functions Ψ_L, Ψ_S, and Ψ_R are equivalent together to the scattering state in the Landauer-Büttiker theory. Note, that $\boldsymbol{G}_S^R$ here is the full GF of the nanosystem including the lead self-energies.

Now the next step. We want to calculate the current. The partial (for some particular eigenstate $\Psi^0_{L\lambda}$) current from the lead to the system is

$$j_{i=L,R} = \frac{ie}{\hbar}\left(\Psi_i^\dagger \boldsymbol{H}_{iS}\Psi_S - \Psi_S^\dagger \boldsymbol{H}_{iS}^\dagger \Psi_i\right). \tag{40}$$

To calculate the total current we should substitute the expressions for the wave functions (37)-(39), and summarize all contributions [291]. As a result the Landauer formula is obtained. We present the calculation for the transmission function. First, after substitution of the wave functions we have for the partial current going through the system

$$\begin{aligned} j_\lambda = j_L = -j_R = &-\frac{ie}{\hbar}\left(\Psi_R^\dagger \boldsymbol{H}_{RS}\Psi_S - \Psi_S^\dagger \boldsymbol{H}_{RS}^\dagger \Psi_R\right) = \\ &-\frac{ie}{\hbar}\left(\Psi_L^{0\dagger} \boldsymbol{H}_{LS}\boldsymbol{G}_S^A \boldsymbol{H}_{RS}^\dagger \left(\boldsymbol{G}_R^{0\dagger} - \boldsymbol{G}_R^0\right)\boldsymbol{H}_{RS}\boldsymbol{G}_S^R \boldsymbol{H}_{LS}^\dagger \Psi_L^0\right) = \\ &\frac{e}{\hbar}\left(\Psi_L^{0\dagger} \boldsymbol{H}_{LS}\boldsymbol{G}_S^A \boldsymbol{\Gamma}_R \boldsymbol{G}_S^R \boldsymbol{H}_{LS}^\dagger \Psi_L^0\right). \end{aligned} \tag{41}$$

The full current of all possible left eigenstates is given by

$$I = \sum_\lambda j_\lambda = \sum_\lambda \frac{e}{\hbar}\left(\Psi_{L\lambda}^{0\dagger} \boldsymbol{H}_{LS}\boldsymbol{G}_S^A \boldsymbol{\Gamma}_R \boldsymbol{G}_S^R \boldsymbol{H}_{LS}^\dagger \Psi_{L\lambda}^0\right) f_L(E_\lambda), \tag{42}$$

the distribution function $f_L(E_\lambda)$ describes the population of the left states, the distribution function of the right lead is absent here, because we consider only the current from the left to the right.

The same current is given by the Landauer formula through the transmission function $\bar{T}(E)$

$$I = \frac{e}{h}\int_{-\infty}^{\infty} \overline{T}(E) f_L(E) dE. \tag{43}$$

If one compares these two expressions for the current, the transmission function at some energy is obtained as

$$\begin{aligned} \overline{T}(E) &= 2\pi \sum_\lambda \delta(E - E_\lambda)\left(\Psi_{L\lambda}^{0\dagger} \boldsymbol{H}_{LS}\boldsymbol{G}_S^A \boldsymbol{\Gamma}_R \boldsymbol{G}_S^R \boldsymbol{H}_{LS}^\dagger \Psi_{L\lambda}^0\right) \\ &= 2\pi \sum_\lambda \sum_\delta \delta(E - E_\lambda)\left(\Psi_{L\lambda}^{0\dagger} \boldsymbol{H}_{LS}\Psi_\delta\right)\left(\Psi_\delta^\dagger \boldsymbol{G}_S^A \boldsymbol{\Gamma}_R \boldsymbol{G}_S^R \boldsymbol{H}_{LS}^\dagger \Psi_{L\lambda}^0\right) \\ &= \sum_\delta \left(\Psi_\delta^\dagger \boldsymbol{G}_S^A \boldsymbol{\Gamma}_R \boldsymbol{G}_S^R \boldsymbol{H}_{LS}^\dagger \left(2\pi \sum_\lambda \delta(E - E_\lambda)\Psi_{L\lambda}^0 \Psi_{L\lambda}^{0\dagger}\right)\boldsymbol{H}_{LS}\Psi_\delta\right) \\ &= \mathrm{Tr}\left(\boldsymbol{\Gamma}_L \boldsymbol{G}_S^A \boldsymbol{\Gamma}_R \boldsymbol{G}_S^R\right). \end{aligned} \tag{44}$$

To evaluate the sum in brackets we used the eigenfunction expansion (27) for the left contact.

We obtained the new representation for the transmission formula, which is very convenient for numerical calculations

$$\overline{T} = \mathrm{Tr}\left(\hat{t}\hat{t}^{\dagger}\right) = \mathrm{Tr}\left(\boldsymbol{\Gamma}_L \boldsymbol{G}^A \boldsymbol{\Gamma}_R \boldsymbol{G}^R\right). \tag{45}$$

Finally, one important remark, at finite voltage the diagonal energies in the Hamiltonians $\boldsymbol{H}_L^0$, $\boldsymbol{H}_S^0$, and $\boldsymbol{H}_R^0$ are shifted $\epsilon_\alpha \to \epsilon_\alpha + e\varphi_\alpha$. Consequently, the energy dependencies of the self-energies defined by (26) are also changed and the lead self-energies are voltage dependent. However, it is convenient to define the self-energies using the Hamiltonians at zero voltage, in that case the voltage dependence should be explicitly shown in the transmission formula

$$\overline{T}(E) = \mathrm{Tr}\left[\boldsymbol{\Gamma}_L(E - e\varphi_L)\boldsymbol{G}^R(\epsilon)\boldsymbol{\Gamma}_R(E - e\varphi_R)\boldsymbol{G}^A(\epsilon)\right], \tag{46}$$

where φ_R and φ_L are electrical potentials of the right and left leads.

With known transmission function, the current I at finite voltage V can be calculated by the usual Landauer-Büttiker formulas (without spin degeneration, otherwise it should be multiplied additionally by 2)

$$I(V) = \frac{e}{h}\int_{-\infty}^{\infty} \overline{T}(E)\left[f_L(E) - f_R(E)\right] dE, \tag{47}$$

where the equilibrium distribution functions of the contacts should be written with corresponding chemical potentials μ_i, and electrical potentials φ_i

$$f_L(E) = \frac{1}{\exp\left(\frac{E-\mu_L-e\varphi_L}{T}\right)+1}, \quad f_R(E) = \frac{1}{\exp\left(\frac{E-\mu_R-e\varphi_R}{T}\right)+1}. \tag{48}$$

The zero-voltage conductance G is

$$G = \left.\frac{dI}{dV}\right|_{V=0} = -\frac{e^2}{h}\int_{-\infty}^{\infty} \overline{T}(E)\frac{\partial f^0(E)}{\partial E} dE, \tag{49}$$

where $f^0(E)$ is the equilibrium Fermi function

$$f^0(E) = \frac{1}{\exp\left(\frac{E-\mu}{T}\right)+1}. \tag{50}$$

2.2 Interacting nanosystems and master equation method

The single-particle matrix Green function method, considered in the previous section, can be applied only in the case of *noninteracting* electrons and without inelastic scattering. In the case of interacting systems, the other approach, known as the method of tunneling (or transfer) Hamiltonian (TH), plays an important role, and is widely used to describe tunneling in superconductors, in ferromagnets, effects in small tunnel junctions such as Coulomb blockade (CB), etc. The main advantage of this method is that it is easely combined with powerful methods of many-body theory. Besides, it is very convenient even for noninteracting electrons, when the coupling between subsystems is weak, and the tunneling process can be described by rather simple matrix elements.

Tunneling and master equation

(i) Tunneling (transfer) Hamiltonian

The main idea is to represent the Hamiltonian of the system (we consider first a single contact between two subsystems) as a sum of three parts: "left" $\hat{H}_L$, "right" $\hat{H}_R$, and "tunneling" $\hat{H}_T$

$$\hat{H} = \hat{H}_L + \hat{H}_R + \hat{H}_T, \tag{51}$$

$\hat{H}_L$ and $\hat{H}_R$ determine "left" $|Lk\rangle$ and "right" $|Rq\rangle$ states

$$\hat{H}_L \psi_k(\xi) = E_k \psi_k(\xi), \tag{52}$$

$$\hat{H}_R \psi_q(\xi) = E_q \psi_q(\xi), \tag{53}$$

below in this lecture we use the index k for left states and the index q for right states. $\hat{H}_T$ determines "transfer" between these states and is *defined* through matrix elements $V_{kq} = \langle Lk|\hat{H}_T|Rq\rangle$. With these definitions the single-particle tunneling Hamiltonian is

$$\hat{H} = \sum_{k\in L} E_k |k\rangle\langle k| + \sum_{q\in R} E_q |q\rangle\langle q| + \sum_{kq} \left[V_{qk}|q\rangle\langle k| + V^*_{qk}|k\rangle\langle q| \right]. \tag{54}$$

The method of the tunneling Hamiltonian was introduced by Bardeen [154], developed by Harrison [155], and formulated in most familiar second quantized form by Cohen, Falicov, and Phillips [156]. In spite of many very successful applications of the TH method, it was many times criticized for it's phenomenological character and incompleteness, beginning from the work of Prange [157]. However, in the same work Prange showed that the tunneling Hamiltonian is well defined in the sense of the perturbation theory. These developments and discussions were summarized by Duke [158]. Note, that the formulation equivalent to the method of the tunneling Hamiltonian can be derived exactly from the tight-binding approach.

Indeed, the tight-binding model assumes that the left and right states can be clearly separated, also when they are orthogonal. The difference with the continuous case is, that we restrict the Hilbert space introducing the tight-binding model, so that the solution is not exact in the sense of the continuous Schrödinger equation. But, in fact, we only consider physically relevant states, neglecting high-energy states not participating in transport.

Compare the tunneling Hamiltonian (54) and the tight-binding Hamiltonian (2), divided into left and right parts

$$\hat{H} = \sum_{\alpha\beta\in L} \tilde{\epsilon}_{\alpha\beta} |\alpha\rangle\langle\beta| + \sum_{\delta\gamma\in R} \tilde{\epsilon}_{\delta\gamma} |\delta\rangle\langle\gamma| + \sum_{\alpha\in L,\, \delta\in R} \left[V_{\delta\alpha}|\delta\rangle\langle\alpha| + V^*_{\delta\alpha}|\alpha\rangle\langle\delta| \right]. \tag{55}$$

The first two terms are the Hamiltonians of the left and right parts, the third term describes the left-right (tunneling) coupling. The equivalent matrix representation of this Hamiltonian is

$$\boldsymbol{H} = \begin{pmatrix} \boldsymbol{H}_L^0 & \boldsymbol{H}_{LR} \\ \boldsymbol{H}_{LR}^\dagger & \boldsymbol{H}_R^0 \end{pmatrix}. \tag{56}$$

The Hamiltonians (54) and (55) are essentially the same, only the first one is written in the eigenstate basis $|k\rangle$, $|q\rangle$, while the second in the tight-binding basis $|\alpha\rangle$, $|\beta\rangle$ of the left lead and $|\delta\rangle$, $|\gamma\rangle$ of the right lead. Now we want to transform the TB Hamiltonian (55) into the eigenstate representation.

Canonical transformations from the tight-binding (atomic orbitals) representation to the eigenstate (molecular orbitals) representation play an important role, and we consider it in detail. Assume, that we find two unitary matrices $\boldsymbol{S}_L$ and $\boldsymbol{S}_R$, such that the Hamiltonians of the left part $\boldsymbol{H}_L^0$ and of the right part $\boldsymbol{H}_R^0$ can be diagonalized by the canonical transformations

$$\bar{\boldsymbol{H}}_L^0 = \boldsymbol{S}_L^{-1} \boldsymbol{H}_L^0 \boldsymbol{S}_L, \tag{57}$$

$$\bar{\boldsymbol{H}}_R^0 = \boldsymbol{S}_R^{-1} \boldsymbol{H}_R^0 \boldsymbol{S}_R. \tag{58}$$

The left and right eigenstates can be written as

$$|k\rangle = \sum_\alpha S_{Lk\alpha} |\alpha\rangle, \tag{59}$$

$$|q\rangle = \sum_\delta S_{Rq\delta} |\delta\rangle, \tag{60}$$

and the first two free-particle terms of the Hamiltonian (54) are reproduced. The tunneling terms are transformed as

$$\bar{\boldsymbol{H}}_{LR} = \boldsymbol{S}_L^{-1} \boldsymbol{H}_{LR} \boldsymbol{S}_R, \tag{61}$$

$$\bar{\boldsymbol{H}}_{LR}^\dagger = \boldsymbol{S}_R^{-1} \boldsymbol{H}_{LR}^\dagger \boldsymbol{S}_L, \tag{62}$$

or explicitly

$$\sum_{\alpha \in L,\, \delta \in R} V_{\delta\alpha} |\delta\rangle\langle\alpha| = \sum_{kq} V_{qk} |q\rangle\langle k|, \tag{63}$$

where

$$V_{qk} = \sum_{\alpha \in L,\, \delta \in R} V_{\delta\alpha} S_{L\alpha k} S_{R\delta q}. \tag{64}$$

The last expression solve the problem of transformation of the tight-binding matrix elements into tunneling matrix elements.

For applications the tunneling Hamiltonian (54) should be formulated in the second quantized form. We introduce creation and annihilation *Schrödinger* operators $c_{Lk}^\dagger$, c_{Lk}, $c_{Rq}^\dagger$, c_{Rq}. Using the usual rules we obtain

$$\hat{H} = \hat{H}_L \left(\left\{ c_k^\dagger; c_k \right\} \right) + \hat{H}_R \left(\{ c_q^\dagger; c_q \} \right) + \hat{H}_T \left(\left\{ c_k^\dagger; c_k; c_q^\dagger; c_q \right\} \right), \tag{65}$$

$$\hat{H} = \sum_k (\epsilon_k + e\varphi_L(t)) c_k^\dagger c_k + \sum_q (\epsilon_q + e\varphi_R(t)) c_q^\dagger c_q + \sum_{kq} \left[V_{qk} c_q^\dagger c_k + V_{qk}^* c_k^\dagger c_q \right]. \tag{66}$$

It is assumed that left c_k and right c_q operators describe independent states and are anticommutative. For nonorthogonal states of the Hamiltonian $\hat{H}_l + \hat{H}_R$ it is not exactly so. But if we consider $\hat{H}_L$ and $\hat{H}_R$ as two independent Hamiltonians with independent Hilbert spaces we resolve this problem. Thus we again should consider (66) not as a true Hamiltonian, but as the formal expression describing the current between left and right states. In the weak coupling case the small corrections to the commutation relations are of the order of $|V_{qk}|$ and can be neglected. If the tight-binding formulation is possible, (66) is exact within the framework of this formulation. In general the method of tunneling Hamiltonian can be considered as a *phenomenological* microscopic approach, which was proved to give reasonable results in many cases, e.g. in the description of tunneling between superconductors and Josephson effect.

(ii) Tunneling current

The current from the state k into the state q is given by the golden rule

$$J_{k\to q} = e\Gamma_{qk} = \frac{2\pi e}{\hbar} |V_{qk}|^2 f_L(k) \left(1 - f_R(q)\right) \delta(E_k - E_q), \tag{67}$$

the probability $(1 - f_R(E_q))$ that the right state is unoccupied should be included, it is different from the scattering approach because left and right states are two independent states!

Then we write the total current as the sum of all partial currents from left states to right states and vice versa (note that the terms $f_L(k) f_R(q)$ are cancelled)

$$J = \frac{2\pi e}{\hbar} \sum_{kq} |V_{qk}|^2 \left[f(k) - f(q) \right] \delta(E_q - E_k). \tag{68}$$

For tunneling between two equilibrium leads distribution functions are simply Fermi-Dirac functions (48) and current can be finally written in the well known form (To do this one should multiply the integrand on $1 = \int \delta(E - E_q) dE$.)

$$J = \frac{e}{h} \int_{-\infty}^{\infty} T(E, V) \left[f_L(E) - f_R(E) \right] dE, \tag{69}$$

with

$$T(E, V) = (2\pi)^2 \sum_{qk} |V_{kq}|^2 \delta(E - E_k - e\varphi_L) \delta(E - E_q - e\varphi_R). \tag{70}$$

This expression is equivalent to the Landauer formula (47), but the transmission function is related now to the tunneling matrix element.

Now let us calculate the tunneling current as the time derivative of the number of particles operator in the left lead $\hat{N}_L = \sum_k c_k^\dagger c_k$. Current from the left to right contact is

$$J(t) = -e\left\langle \left(\frac{dN_L}{dt}\right)\right\rangle_S = -\frac{ie}{\hbar}\left\langle \left[\hat{H}_T, N_L\right]_-\right\rangle_S, \tag{71}$$

where $\langle ...\rangle_S$ is the average over time-dependent Schrödinger state. $\hat{N}_L$ commute with both left and right Hamiltonians, but not with the tunneling Hamiltonian

$$\left[\hat{H}_T, N_L\right]_- = \sum_{k'}\sum_{kq}\left[\left(V_{qk}c_q^\dagger c_k + V_{qk}^* c_q c_k^\dagger\right)c_{k'}^\dagger c_{k'}\right]_-, \tag{72}$$

using commutation relations

$$c_k c_{k'}^\dagger c_{k'} - c_{k'}^\dagger c_{k'} c_k = c_k c_{k'}^\dagger c_{k'} + c_{k'}^\dagger c_k c_{k'} = (c_k c_{k'}^\dagger + \delta_{kk'} - c_k c_{k'}^\dagger)c_{k'} = \delta_{kk'}c_k,$$

we obtain

$$J(t) = \frac{ie}{\hbar}\sum_{kq}\left[V_{qk}\left\langle c_q^\dagger c_k\right\rangle_S - V_{qk}^*\left\langle c_k^\dagger c_q\right\rangle_S\right]. \tag{73}$$

Now we switch to the Heisenberg picture, and average over initial time-independent *equilibrium* state

$$\left\langle \hat{O}(t)\right\rangle = Sp\left(\hat{\rho}_{eq}\hat{O}(t)\right), \quad \hat{\rho}_{eq} = \frac{e^{-H_{eq}/T}}{Sp\left(e^{-H_{eq}/T}\right)}. \tag{74}$$

One obtains

$$J(t) = \frac{ie}{\hbar}\sum_{kq}\left[V_{qk}\left\langle c_q^\dagger(t)c_k(t)\right\rangle - V_{qk}^*\left\langle c_k^\dagger(t)c_q(t)\right\rangle\right]. \tag{75}$$

It can be finally written as

$$J(t) = \frac{2e}{\hbar}\mathrm{Im}\left(\sum_{kq}V_{qk}\rho_{kq}(t)\right) = \frac{2e}{\hbar}\mathrm{Re}\left(\sum_{kq}V_{qk}G_{kq}^<(t,t)\right).$$

We define "left-right" density matrix or more generally lesser Green function

$$G_{kq}^<(t_1,t_2) = i\left\langle c_q^\dagger(t_2)c_k(t_1)\right\rangle.$$

Later we show that these expressions for the tunneling current give the same answer as was obtained above by the golden rule in the case of noninteracting leads.

(iii) Sequential tunneling and the master equation

Let us come back to our favorite problem – transport through a quantum system. There is one case (called *sequential tunneling*), when the simple formulas discussed above can be applied even in the case of resonant tunneling

Assume that a noninteracting nanosystem is coupled weakly to a thermal bath (in addition to the leads). The effect of the thermal bath is to break phase coherence of the electron inside the system during some time τ_{ph}, called *decoherence or phase-breaking time*. τ_{ph} is an important time-scale in the theory, it should be compared with the so-called "tunneling time" – the characteristic time for the electron to go from the nanosystem to the lead, which can be estimated as an inverse level-width function Γ^{-1}. So that the criteria of sequential tunneling is

$$\Gamma\tau_{ph} \ll 1. \tag{76}$$

The finite decoherence time is due to some inelastic scattering mechanism inside the system, but typically this time is shorter than the energy relaxation time τ_ϵ, and the distribution function of electrons inside the system can be nonequilibrium (if the finite voltage is applied), this transport regime is well known in semiconductor superlattices and quantum-cascade structures.

In the sequential tunneling regime the tunneling events between the left lead and the nanosystem and between the left lead and the nanosystem are independent and the current from the left (right) lead to the nanosystem is given by the golden rule expression (68). Let us modify it to the case of tunneling from the lead to a *single level* $|\alpha\rangle$ of a quantum system

$$J = \frac{2\pi e}{\hbar} \sum_k |V_{\alpha k}|^2 \left[f(k) - P_\alpha\right] \delta(E_\alpha - E_k), \tag{77}$$

where we introduce the probability P_α to find the electron in the state $|\alpha\rangle$ with the energy E_α.

(iv) Rate equations for noninteracting systems

Rate equation method is a simple approach base on the balance of incoming and outgoing currents. Assuming that the contacts are equilibrium we obtain for the left and right currents

$$J_{i=L(R)} = e\Gamma_{i\alpha} \left[f_i^0(E_\alpha) - P_\alpha\right], \tag{78}$$

where

$$\Gamma_{i\alpha} = \frac{2\pi}{\hbar} \sum_k |V_{\alpha k}|^2 \delta(E_\alpha - E_k). \tag{79}$$

In the stationary state $J = J_L = -J_R$, and from this condition the level population P_α is found to be

$$P_\alpha = \frac{\Gamma_{L\alpha} f_L^0(E_\alpha) + \Gamma_{R\alpha} f_R^0(E_\alpha)}{\Gamma_{L\alpha} + \Gamma_{R\alpha}}, \tag{80}$$

with the current

$$J = e\frac{\Gamma_{L\alpha}\Gamma_{R\alpha}}{\Gamma_{L\alpha}+\Gamma_{R\alpha}}\big(f_L^0(E_\alpha) - f_R^0(E_\alpha)\big). \tag{81}$$

It is interesting to note that this expression is exactly the same, as one can obtain for the resonant tunneling through a single level without any scattering. It should be not forgotten, however, that we did not take into account additional level broadening due to scattering.

(v) Master equation for interacting systems

Now let us formulate briefly a more general approach to transport through interacting nanosystems weakly coupled to the leads in the sequential tunneling regime, namely the master equation method. Assume, that the system can be in several states $|\lambda\rangle$, which are the eigenstates of an isolated system and introduce the distribution function P_λ – the probability to find the system in the state $|\lambda\rangle$. Note, that these states are *many-particle* states, for example for a two-level quantum dot the possible states are $|\lambda\rangle = |00\rangle, |10\rangle, 01|\rangle$, and $|11\rangle$. The first state is empty dot, the second and the third with one electron, and the last one is the double occupied state. The other non-electronic degrees of freedom can be introduce on the same ground in this approach. The only restriction is that some full set of eigenstates should be used

$$\sum_\lambda P_\lambda = 1. \tag{82}$$

The next step is to treat tunneling as a perturbation. Following this idea, the transition rates $\Gamma^{\lambda\lambda'}$ from the state λ' to the state λ are calculated using the Fermi golden rule

$$\Gamma^{fi} = \frac{2\pi}{\hbar}\left|\left\langle f|\hat{H}_T|i\right\rangle\right|^2 \delta(E_f - E_i). \tag{83}$$

Then, the kinetic (master) equation can be written as

$$\frac{dP_\lambda}{dt} = \sum_{\lambda'}\Gamma^{\lambda\lambda'}P_{\lambda'} - \sum_{\lambda'}\Gamma^{\lambda'\lambda}P_\lambda, \tag{84}$$

where the first term describes tunneling transition *into the state* $|\lambda\rangle$, and the second term – tunneling transition *out of the state* $|\lambda\rangle$.

In the stationary case the probabilities are determined from

$$\sum_{\lambda'}\Gamma^{\lambda\lambda'}P_{\lambda'} = \sum_{\lambda'}\Gamma^{\lambda'\lambda}P_\lambda. \tag{85}$$

For noninteracting electrons the transition rates are determined by the single-electron tunneling rates, and are nonzero only for the transitions between the states with the number of electrons different by one. For example,

transition from the state $|\lambda'\rangle$ with empty electron level α into the state $|\lambda\rangle$ with filled state α is described by

$$\Gamma^{n_\alpha=1\ n_\alpha=0} = \Gamma_{L\alpha} f_L^0(E_\alpha) + \Gamma_{R\alpha} f_R^0(E_\alpha), \tag{86}$$

where $\Gamma_{L\alpha}$ and $\Gamma_{R\alpha}$ are left and right level-width functions (79).

For interacting electrons the calculation is a little bit more complicated. One should establish the relation between *many-particle* eigenstates of the system and *single-particle* tunneling. To do this, let us note, that the states $|f\rangle$ and $|i\rangle$ in the golden rule formula (83) are actually the states of the whole system, including the leads. We denote the initial and final states as

$$|i\rangle = |\hat{k}_i, \lambda'\rangle = |\hat{k}_i\rangle|\lambda'\rangle, \tag{87}$$

$$|f\rangle = |\hat{k}_f, \lambda\rangle = |\hat{k}_f\rangle|\lambda\rangle, \tag{88}$$

where $\hat{k}$ is the occupation of the single-particle states in the lead. The parameterization is possible, because we apply the perturbation theory, and isolated lead and nanosystem are independent.

The important point is, that the leads are actually in the equilibrium mixed state, the single electron states are populated with probabilities, given by the Fermi-Dirac distribution function. Taking into account all possible single-electron tunneling processes, we obtain the incoming tunneling rate

$$\Gamma_{in}^{\lambda\lambda'} = \frac{2\pi}{\hbar} \sum_{ik\sigma} f_i^0(E_{ik\sigma}) \left| \left\langle i\bar{k}, \lambda \left| \bar{H}_T \right| ik, \lambda' \right\rangle \right|^2 \delta(E_{\lambda'} + E_{ik\sigma} - E_\lambda), \tag{89}$$

where we use the short-hand notations: $|ik, \lambda'\rangle$ is the state with occupied k-state in the $i-$th lead, while $|i\bar{k}, \lambda\rangle$ is the state with unoccupied k-state in the $i-$th lead, and all other states are assumed to be unchanged, E_λ is the energy of the state λ .

To proceed, we introduce the following Hamiltonian, describing single electron tunneling and charging of the nanosystem state

$$\hat{H}_T = \sum_{k\lambda\lambda'} \left[V_{\lambda\lambda' k} c_k X^{\lambda\lambda'} + V^*_{\lambda\lambda' k} c_k^\dagger X^{\lambda'\lambda} \right], \tag{90}$$

the Hubbard operators $X^{\lambda\lambda'} = |\lambda\rangle\langle\lambda'|$ describe transitions between eigenstates of the nanosystem.

Substituting this Hamiltonian one obtains

$$\Gamma_{in}^{\lambda\lambda'} = \frac{2\pi}{\hbar} \sum_{ik\sigma} f_i^0(E_{ik\sigma}) \left| V_{ik\sigma} \right|^2 \left| V_{\lambda\lambda' k} \right|^2 \delta(E_{\lambda'} + E_{ik\sigma} - E_\lambda). \tag{91}$$

In the important limiting case, when the matrix element $V_{\lambda\lambda' k}$ is k-independent, the sum over k can be performed, and finally

$$\Gamma_{in}^{\lambda\lambda'} = \sum_{i=L,R} \Gamma_i(E_\lambda - E_{\lambda'}) \left| V_{\lambda\lambda'} \right|^2 f_i^0(E_\lambda - E_{\lambda'}). \tag{92}$$

Similarly, the outgoing rate is

$$\Gamma_{out}^{\lambda\lambda'} = \sum_{i=L,R} \Gamma_i(E_{\lambda'} - E_\lambda) \left|V_{\lambda\lambda'}\right|^2 \left(1 - f_i^0(E_{\lambda'} - E_\lambda)\right). \tag{93}$$

The current (from the left or right lead to the system) is

$$J_{i=L,R}(t) = e \sum_{\lambda\lambda'} \left(\Gamma_{i\,in}^{\lambda\lambda'} P_{\lambda'} - \Gamma_{i\,out}^{\lambda\lambda'} P_{\lambda'}\right). \tag{94}$$

This system of equations solves the transport problem in the sequential tunneling regime.

Electron-electron interaction and Coulomb blockade

(i) Anderson-Hubbard and constant-interaction models

To take into account both discrete energy levels of a system and the electron-electron interaction, it is convenient to start from the general Hamiltonian

$$\hat{H} = \sum_{\alpha\beta} \tilde{\epsilon}_{\alpha\beta} d_\alpha^\dagger d_\beta + \frac{1}{2} \sum_{\alpha\beta\gamma\delta} V_{\alpha\beta,\gamma\delta} d_\alpha^\dagger d_\beta^\dagger d_\gamma d_\delta. \tag{95}$$

The first term of this Hamiltonian is a free-particle discrete-level model (10) with $\tilde{\epsilon}_{\alpha\beta}$ including electrical potentials. And the second term describes all possible interactions between electrons and is equivalent to the real-space Hamiltonian

$$\hat{H}_{ee} = \frac{1}{2} \int d\xi \int d\xi' \hat{\psi}^\dagger(\xi) \hat{\psi}^\dagger(\xi') V(\xi, \xi') \hat{\psi}(\xi') \hat{\psi}(\xi), \tag{96}$$

where $\hat{\psi}(\xi)$ are field operators

$$\hat{\psi}(\xi) = \sum_\alpha \psi_\alpha(\xi) d_\alpha, \tag{97}$$

$\psi_\alpha(\xi)$ are the basis single-particle functions, we remind, that spin quantum numbers are included in α, and spin indices are included in $\xi \equiv \boldsymbol{r}, \sigma$ as variables.

The matrix elements are defined as

$$V_{\alpha\beta,\gamma\delta} = \int d\xi \int d\xi' \psi_\alpha^*(\xi) \psi_\beta^*(\xi') V(\xi, \xi') \psi_\gamma(\xi) \psi_\delta(\xi'). \tag{98}$$

For pair Coulomb interaction $V(|\boldsymbol{r}|)$ the matrix elements are

$$V_{\alpha\beta,\gamma\delta} = \sum_{\sigma\sigma'} \int d\boldsymbol{r} \int d\boldsymbol{r}' \psi_\alpha^*(\boldsymbol{r}, \sigma) \psi_\beta^*(\boldsymbol{r}', \sigma') V(|\boldsymbol{r} - r'|) \psi_\gamma(\boldsymbol{r}, \sigma) \psi_\delta(\boldsymbol{r}', \sigma'). \tag{99}$$

Assume now, that the basis states $|\alpha\rangle$ are the states with definite spin quantum number σ_α. It means, that only one spin component of the wave function, namely $\psi_\alpha(\sigma_\alpha)$ is nonzero, and $\psi_\alpha(\bar{\sigma}_\alpha) = 0$. In this case the only nonzero matrix elements are those with $\sigma_\alpha = \sigma_\gamma$ and $\sigma_\beta = \sigma_\delta$, they are

$$V_{\alpha\beta,\gamma\delta} = \int d\boldsymbol{r} \int d\boldsymbol{r}' \psi^*_\alpha(\boldsymbol{r}) \psi^*_\beta(\boldsymbol{r}') V(|\boldsymbol{r} - r'|) \psi_\gamma(\boldsymbol{r}) \psi_\delta(\boldsymbol{r}'). \tag{100}$$

In the case of delocalized basis states $\psi_\alpha(\boldsymbol{r})$, the main matrix elements are those with $\alpha = \gamma$ and $\beta = \delta$, because the wave functions of two different states with the same spin are orthogonal in real space and their contribution is small. It is also true for the systems with localized wave functions $\psi_\alpha(\boldsymbol{r})$, when the overlap between two different states is weak. In these cases it is enough to replace the interacting part by the Anderson-Hubbard Hamiltonian, describing only density-density interaction

$$\hat{H}_{AH} = \frac{1}{2} \sum_{\alpha \neq \beta} U_{\alpha\beta} \hat{n}_\alpha \hat{n}_\beta. \tag{101}$$

with the Hubbard interaction defined as

$$U_{\alpha\beta} = \int d\boldsymbol{r} \int d\boldsymbol{r}' |\psi_\alpha(\boldsymbol{r})|^2 |\psi_\beta(\boldsymbol{r}')|^2 V(|\boldsymbol{r} - r'|). \tag{102}$$

In the limit of a single-level quantum dot (which is, however, a two-level system because of spin degeneration) we get the Anderson impurity model (AIM)

$$\hat{H}_{AIM} = \sum_{\sigma=\uparrow\downarrow} \epsilon_\sigma d^\dagger_\sigma d_\sigma + U \hat{n}_\uparrow \hat{n}_\downarrow. \tag{103}$$

The other important limit is the constant interaction model (CIM), which is valid when many levels interact with similar energies, so that approximately, assuming $U_{\alpha\beta} = U$ for any states α and β

$$\hat{H}_{AH} = \frac{1}{2} \sum_{\alpha \neq \beta} U_{\alpha\beta} \hat{n}_\alpha \hat{n}_\beta \approx \frac{U}{2} \left(\sum_\alpha \hat{n}_\alpha \right)^2 - \frac{U}{2} \left(\sum_\alpha \hat{n}^2_\alpha \right) = \frac{U\hat{N}(\hat{N} - 1)}{2}. \tag{104}$$

where we used $\hat{n}^2 = \hat{n}$.

Thus, the CIM reproduces the charging energy considered above, and the Hamiltonian of an isolated system is

$$\hat{H}_{CIM} = \sum_{\alpha\beta} \tilde{\epsilon}_{\alpha\beta} d^\dagger_\alpha d_\beta + E(N). \tag{105}$$

Note, that the equilibrium compensating charge density can be easily introduced into the AH Hamiltonian

$$\hat{H}_{AH} = \frac{1}{2} \sum_{\alpha \neq \beta} U_{\alpha\beta} \left(\hat{n}_\alpha - \bar{n}_\alpha \right) \left(\hat{n}_\beta - \bar{n}_\beta \right). \tag{106}$$

(ii) Coulomb blockade in quantum dots

Here we want to consider the Coulomb blockade in intermediate-size quantum dots, where the typical energy level spacing $\Delta\epsilon$ is not too small to neglect it completely, but the number of levels is large enough, so that one can use the constant-interaction model (105), which we write in the eigenstate basis as

$$\hat{H}_{CIM} = \sum_{\alpha} \tilde{\epsilon}_{\alpha} d_{\alpha}^{\dagger} d_{\alpha} + E(n), \tag{107}$$

where the charging energy $E(n)$ is determined in the same way as previously, for example by the expression (104). Note, that for quantum dots the usage of classical capacitance is not well established, although for large quantum dots it is possible. Instead, we shift the energy levels in the dot $\tilde{\epsilon}_{\alpha} = \epsilon_{\alpha} + e\varphi_{\alpha}$ by the electrical potential

$$\varphi_{\alpha} = V_G + V_R + \eta_{\alpha}(V_L - V_R), \tag{108}$$

where η_{α} are some coefficients, dependent on geometry. This method can be easily extended to include any self-consistent effects on the mean-field level by the help of the Poisson equation (instead of classical capacitances). Besides, if all η_{α} are the same, our approach reproduce again the the classical expression

$$\hat{E}_{CIM} = \sum_{\alpha} \epsilon_{\alpha} n_{\alpha} + E(n) + en\varphi_{ext}. \tag{109}$$

The *addition energy* now depends not only on the charge of the molecule, but also on the state $|\alpha\rangle$, in which the electron is added

$$\Delta E_{n\alpha}^{+}(n, n_{\alpha} = 0 \to n+1, n_{\alpha} = 1) = E(n+1) - E(n) + \epsilon_{\alpha}, \tag{110}$$

we can assume in this case, that the single particle energies are additive to the charging energy, so that the full quantum eigenstate of the system is $|n, \hat{n}\rangle$, where the set $\hat{n} \equiv \{n_{\alpha}\}$ shows weather the particular single-particle state $|\alpha\rangle$ is empty or occupied. Some arbitrary state $\hat{n}$ looks like

$$\hat{n} \equiv \{n_{\alpha}\} \equiv \big(n_1, n_2, n_3, n_4, n_5, ...\big) = \big(1, 1, 0, 1, 0, ...\big). \tag{111}$$

Note, that the distribution $\hat{n}$ defines also $n = \sum_{\alpha} n_{\alpha}$. It is convenient, however, to keep notation n to remember about the charge state of a system, below we use both notations $|n, \hat{n}\rangle$ and short one $|\hat{n}\rangle$ as equivalent.

The other important point is that the distribution function $f_n(\alpha)$ in the charge state $|n\rangle$ is not assumed to be equilibrium, as previously (this condition is not specific to quantum dots with discrete energy levels, the distribution function in metallic islands can also be nonequilibrium. However, in the parameter range, typical for classical Coulomb blockade, the tunneling time is much smaller than the energy relaxation time, and quasiparticle nonequilibrium effects are usually neglected).

With these new assumptions, the theory of sequential tunneling is quite the same, as was considered in the previous section. The master equation is [172, 180–182]

$$\frac{dp(n,\hat{n},t)}{dt} = \sum_{\hat{n}'} \left(\Gamma^{n\,n-1}_{\hat{n}\hat{n}'} p(n-1,\hat{n}',t) + \Gamma^{n\,n+1}_{\hat{n}\hat{n}'} p(n+1,\hat{n}',t) \right) - \sum_{\hat{n}'} \left(\Gamma^{n-1\,n}_{\hat{n}'\hat{n}} + \Gamma^{n+1\,n}_{\hat{n}'\hat{n}} \right) p(n,\hat{n},t) + I\left\{p(n,\hat{n},t)\right\}, \tag{112}$$

where $p(n,\hat{n},t)$ is now the probability to find the system in the state $|n,\hat{n}\rangle$, $\Gamma^{n\,n-1}_{\hat{n}\hat{n}'}$ is the transition rate from the state with $n-1$ electrons and single level occupation $\hat{n}'$ into the state with n electrons and single level occupation $\hat{n}$. The sum is over all states $\hat{n}'$, which are different by one electron from the state $\hat{n}$. The last term is included to describe possible inelastic processes inside the system and relaxation to the equilibrium function $p_{eq}(n,\hat{n})$. In principle, it is not necessary to introduce such type of dissipation in calculation, because the current is in any case finite. But the dissipation may be important in large systems and at finite temperatures. Besides, it is necessary to describe the limit of classical single-electron transport, where the distribution function of qausi-particles is assumed to be equilibrium. Below we shall not take into account this term, assuming that tunneling is more important.

While all considered processes are, in fact, single-particle tunneling processes, we arrive at

$$\frac{dp(\hat{n},t)}{dt} = \sum_{\beta} \left(\delta_{n_\beta 1} \Gamma^{n\,n-1}_{\beta} p(\hat{n}, n_\beta = 0, t) + \delta_{n_\beta 0} \Gamma^{n\,n+1}_{\beta} p(\hat{n}, n_\beta = 1, t) \right) - \sum_{\beta} \left(\delta_{n_\beta 1} \Gamma^{n-1\,n}_{\beta} + \delta_{n_\beta 0} \Gamma^{n+1\,n}_{\beta} \right) p(\hat{n}, t), \tag{113}$$

where the sum is over single-particle states. The probability $p(\hat{n}, n_\beta = 0, t)$ is the probability of the state equivalent to $\hat{n}$, but without the electron in the state β. Consider, for example, the first term in the right part. Here the delta-function $\delta_{n_\beta 1}$ shows, that this term should be taken into account only if the single-particle state β in the many-particle state $\hat{n}$ is occupied, $\Gamma^{n\,n-1}_{\beta}$ is the probability of tunneling from the lead to this state, $p(\hat{n}, n_\beta = 0, t)$ is the probability of the state $\hat{n}'$, from which the system can come into the state $\hat{n}$.

The transitions rates are defined by the same golden rule expressions, as before, but with explicitly shown single-particle state α

$$\Gamma^{n+1\,n}_{L\alpha} = \frac{2\pi}{\hbar} \left| \left\langle n+1, n_\alpha = 1 | \hat{H}_{TL} | n, n_\alpha = 0 \right\rangle \right|^2 \delta(E_i - E_f) = \frac{2\pi}{\hbar} \sum_k |V_{k\alpha}|^2 f_k \delta(\Delta E^+_{n\alpha} - E_k), \tag{114}$$

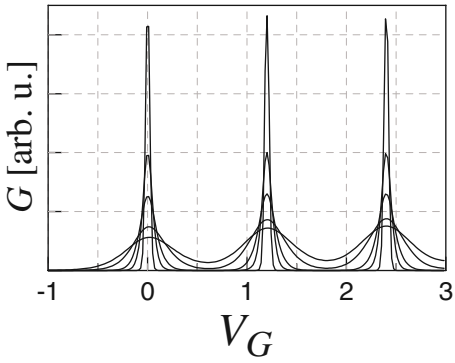

Fig. 5: Linear conductance of a QD as a function of the gate voltage at different temperatures $T = 0.01E_C$, $T = 0.03E_C$, $T = 0.05E_C$, $T = 0.1E_C$, $T = 0.15E_C$ (lower curve).

$$\Gamma_{L\alpha}^{n-1\,n} = \frac{2\pi}{\hbar}\left|\left\langle n-1, n_\alpha = 0|\hat{H}_{TL}|n, n_\alpha = 1\right\rangle\right|^2 \delta(E_i - E_f) = \frac{2\pi}{\hbar}\sum_k |V_{k\alpha}|^2 (1-f_k)\,\delta(\Delta E_{n-1\,\alpha}^{+} - E_k), \tag{115}$$

there is no occupation factors $(1 - f_\alpha)$, f_α because this state is assumed to be empty in the sense of the master equation (113). The energy of the state is now included into the addition energy.

Using again the level-width function

$$\Gamma_{i=L,R\,\alpha}(E) = \frac{2\pi}{\hbar}\sum_k |V_{ik,\alpha}|^2 \delta(E - E_k). \tag{116}$$

we obtain

$$\Gamma_{\alpha}^{n+1\,n} = \Gamma_{L\alpha} f_L^0(\Delta E_{n\alpha}^{+}) + \Gamma_{R\alpha} f_R^0(\Delta E_{n\alpha}^{+}), \tag{117}$$

$$\Gamma_{\alpha}^{n-1\,n} = \Gamma_{L\alpha}\left(1 - f_L^0(\Delta E_{n-1\,\alpha}^{+})\right) + \Gamma_{R\alpha}\left(1 - f_R^0(\Delta E_{n-1\,\alpha}^{+})\right). \tag{118}$$

Finally, the current from the left or right contact to a system is

$$J_{i=L,R} = e\sum_\alpha \sum_{\hat{n}} p(\hat{n})\Gamma_{i\alpha}\left(\delta_{n_\alpha 0} f_i^0(\Delta E_{n\alpha}^{+}) - \delta_{n_\alpha 1}(1 - f_i^0(\Delta E_{n\alpha}^{+}))\right). \tag{119}$$

The sum over α takes into account all possible single particle tunneling events, the sum over states $\hat{n}$ summarize probabilities $p(\hat{n})$ of these states.

(iii) Linear conductance

The linear conductance can be calculated analytically [172, 181]. Here we present the final result:

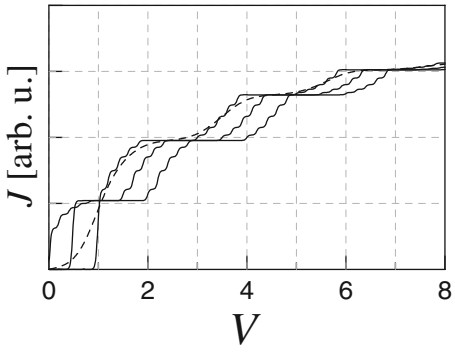

Fig. 6: Coulomb staircase.

$$G = \frac{e^2}{T} \sum_{\alpha} \sum_{n=1}^{\infty} \frac{\Gamma_{L\alpha}\Gamma_{R\alpha}}{\Gamma_{L\alpha} + \Gamma_{R\alpha}} P_{eq}(n, n_\alpha = 1) \left[1 - f^0(\Delta E^+_{n-1\,\alpha})\right], \tag{120}$$

where $P_{eq}(n, n_\alpha = 1)$ is the joint probability that the quantum dot contains n electrons and the level α is occupied

$$P_{eq}(n, n_\alpha = 1) = \sum_{\hat{n}} p_{eq}(\hat{n}) \delta \left(n - \sum_{\beta} n_\beta \right) \delta_{n_\alpha 1}, \tag{121}$$

and the equilibrium probability (distribution function) is determined by the Gibbs distribution in the grand canonical ensemble:

$$p_{eq}(\hat{n}) = \frac{1}{Z} \exp \left[-\frac{1}{T} \left(\sum_{\alpha} \tilde{\epsilon}_\alpha + E(n) \right) \right]. \tag{122}$$

A typical behaviour of the conductance as a function of the gate voltage at different temperatures is shown in Fig. 5. In the resonant tunneling regime at low temperatures $T \ll \Delta\epsilon$ the peak height is strongly temperature-dependent. It is changed by classical temperature dependence (constant height) at $T \gg \Delta\epsilon$.

(iv) Transport at finite bias voltage

At finite bias voltage we find new manifestations of the interplay between single-electron tunneling and resonant free-particle tunneling.

Now, let us consider the current-voltage curve of the differential conductance (Fig. 7). First of all, Coulomb staircase is reproduced, which is more pronounced, than for metallic islands, because the density of states is limited by the available single-particle states and the current is saturated. Besides, small additional steps due to discrete energy levels appear. This characteristic

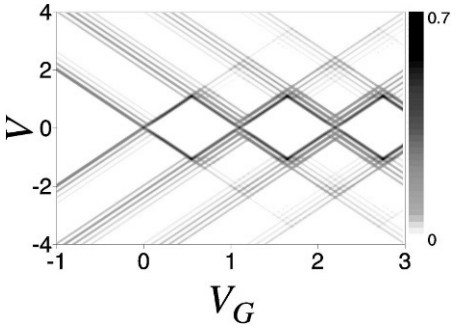

Fig. 7: Contour plot of the differential conductance.

behaviour is possible for large enough dots with $\Delta\epsilon \ll E_C$. If the level spacing is of the oder of the charging energy $\Delta\epsilon \sim E_C$, the Coulomb blockade steps and discrete-level steps look the same, but their statistics (position and height distribution) is determined by the details of the single-particle spectrum and interactions [182].

Finally, let us consider the contour plot of the differential conductance (Fig. 7). Ii is essentially different from those for the metallic island. First, it is not symmetric in the gate voltage, because the energy spectrum is restricted from the bottom, and at negative bias all the levels are above the Fermi-level (the electron charge is negative, and a negative potential means a positive energy shift). Nevertheless, existing stability patterns are of the same origin and form the same structure. The qualitatively new features are additional lines corresponding to the additional discrete-level steps in the voltage-current curves. In general, the current and conductance of quantum dots demonstrate all typical features of discrete-level systems: current steps, conductance peaks. Without Coulomb interaction the usual picture of resonant tunneling is reproduced. In the limit of dense energy spectrum $\Delta\epsilon \to 0$ the sharp single-level steps are merged into the smooth Coulomb staircase.

Vibrons and Franck-Condon blockade

(i) Linear vibrons

Vibrons are quantum local vibrations of nanosystems (Fig. 8), especially important in flexible molecules. In the linear regime the small displacements of the system can be expressed as linear combinations of the coordinates of the normal modes x_q, which are described by a set of independent linear oscillators with the Hamiltonian

$$\hat{H}_V^{(0)} = \sum_q \left(\frac{\hat{p}_q^2}{2m_q} + \frac{1}{2} m_q \omega_q^2 \hat{x}_q^2 \right). \tag{123}$$

The parameters m_q are determined by the microscopic theory, and $\hat{p}_q$ ($\hat{p}_q = -i\hbar\frac{\partial}{\partial x_q}$ in the x-representation) is the momentum conjugated to $\hat{x}_q$, $[\hat{x}_q, \hat{p}_q]_- = i\hbar$.

Let us outline briefly a possible way to calculate the normal modes of a molecule, and the relation between the positions of individual atoms and collective variables. We assume, that the atomic configuration of a system is determined mainly by the elastic forces, which are insensitive to the *transport* electrons. The dynamics of this system is determined by the *atomic* Hamiltonian

$$\hat{H}_{at} = \sum_n \frac{P_n^2}{2M_n} + W\left(\{\boldsymbol{R}_n\}\right), \tag{124}$$

where $W\left(\{\boldsymbol{R}_n\}\right)$ is the elastic energy, which includes also the static external forces and can be calculated by some *ab initio* method. Now define new generalized variables q_i with corresponding momentum p_i (as the generalized coordinates not only atomic positions, but also any other convenient degrees of freedom can be considered, for example, molecular rotations, center-of-mass motion, etc.)

$$\hat{H}_{at} = \sum_i \frac{p_i^2}{2m_i} + W\left(\{q_i\}\right), \tag{125}$$

"masses" m_i should be considered as some parameters. The equilibrium coordinates q_i^0 are defined from the energy minimum, the set of equations is

$$\frac{\partial W\left(\{q_i^0\}\right)}{\partial q_i} = 0. \tag{126}$$

The equations for linear oscillations are obtained from the next order expansion in the deviations $\Delta q_i = q_i - q_i^0$

$$\hat{H}_{at} = \sum_i \frac{p_i^2}{2m_i} + \sum_{ij} \frac{\partial^2 W\left(\{q_j^0\}\right)}{\partial q_i \partial q_j} \Delta q_i \Delta q_j. \tag{127}$$

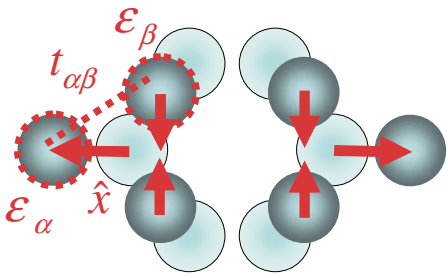

Fig. 8: A local molecular vibration. The empty circles show the equilibrium positions of the atoms. The energies ϵ_α, ϵ_β and the overlap integral $t_{\alpha\beta}$ are perturbed.

This Hamiltonian describes a set of coupled oscillators. Finally, applying the canonical transformation from Δq_i to new variables x_q (q is now the index of independent modes)

$$x_q = \sum_i C_{qi} q_i \tag{128}$$

we derive the Hamiltonian (123) together with the frequencies ω_q of vibrational modes.

It is useful to introduce the creation and annihilation operators

$$a_q^\dagger = \frac{1}{\sqrt{2}} \left(\sqrt{\frac{m_q \omega_q}{\hbar}} \hat{x}_q + \frac{i}{\sqrt{m_q \omega_q \hbar}} \hat{p}_q \right), \tag{129}$$

$$a_q = \frac{1}{\sqrt{2}} \left(\sqrt{\frac{m_q \omega_q}{\hbar}} \hat{x}_q - \frac{i}{\sqrt{m_q \omega_q \hbar}} \hat{p}_q \right), \tag{130}$$

in this representation the Hamiltonian of free vibrons is ($\hbar = 1$)

$$\hat{H}_V^{(0)} = \sum_q \omega_q a_q^\dagger a_q. \tag{131}$$

(ii) Electron-vibron Hamiltonian

A system without vibrons is described as before by a basis set of states $|\alpha\rangle$ with energies ϵ_α and inter-state overlap integrals $t_{\alpha\beta}$, the model Hamiltonian of a noninteracting system is

$$\hat{H}_S^{(0)} = \sum_\alpha \left(\epsilon_\alpha + e\varphi_\alpha(t) \right) d_\alpha^\dagger d_\alpha + \sum_{\alpha \neq \beta} t_{\alpha\beta} d_\alpha^\dagger d_\beta, \tag{132}$$

where $d_\alpha^\dagger$,d_α are creation and annihilation operators in the states $|\alpha\rangle$, and $\varphi_\alpha(t)$ is the (self-consistent) electrical potential (108). The index α is used to mark single-electron states (atomic orbitals) including the spin degree of freedom.

To establish the Hamiltonian describing the interaction of electrons with vibrons in nanosystems, we can start from the generalized Hamiltonian

$$\hat{H}_S = \sum_\alpha \tilde{\epsilon}_\alpha \left(\{x_q\} \right) d_\alpha^\dagger d_\alpha + \sum_{\alpha \neq \beta} t_{\alpha\beta} \left(\{x_q\} \right) d_\alpha^\dagger d_\beta, \tag{133}$$

where the parameters are some functions of the vibronic normal coordinates x_q. Note that we consider now only the electronic states, which were excluded previously from the Hamiltonian (124), it is important to prevent double counting.

Expanding to the first order near the equilibrium state we obtain

$$\hat{H}_{ev} = \sum_\alpha \sum_q \frac{\partial \tilde{\epsilon}_\alpha(0)}{\partial x_q} x_q d_\alpha^\dagger d_\alpha + \sum_{\alpha \neq \beta} \sum_q \frac{\partial t_{\alpha\beta}(0)}{\partial x_q} x_q d_\alpha^\dagger d_\beta, \tag{134}$$

where $\tilde{\epsilon}_\alpha(0)$ and $t_{\alpha\beta}(0)$ are unperturbed values of the energy and the overlap integral. In the quantum limit the normal coordinates should be treated as operators, and in the second-quantized representation the interaction Hamiltonian is

$$\hat{H}_{ev} = \sum_{\alpha\beta} \sum_{q} \lambda^q_{\alpha\beta} (a_q + a_q^\dagger) d_\alpha^\dagger d_\beta. \tag{135}$$

This Hamiltonian is similar to the usual electron-phonon Hamiltonian, but the vibrations are like localized phonons and q is an index labeling them, not the wave-vector. We include both diagonal coupling, which describes a change of the electrostatic energy with the distance between atoms, and the off-diagonal coupling, which describes the dependence of the matrix elements $t_{\alpha\beta}$ over the distance between atoms.

The full Hamiltonian

$$\hat{H} = \hat{H}_S^0 + \hat{H}_V + \hat{H}_L + \hat{H}_R + \hat{H}_T \tag{136}$$

is the sum of the noninteracting Hamiltonian $\hat{H}_S^0$, the Hamiltonians of the leads $\hat{H}_{R(L)}$, the tunneling Hamiltonian $\hat{H}_T$ describing the system-to-lead coupling, the vibron Hamiltonian $\hat{H}_V$ including electron-vibron interaction and coupling of vibrations to the environment (describing dissipation of vibrons).

Vibrons and the electron-vibron coupling are described by the Hamiltonian ($\hbar = 1$)

$$\hat{H}_V = \sum_q \omega_q a_q^\dagger a_q + \sum_{\alpha\beta} \sum_q \lambda^q_{\alpha\beta} (a_q + a_q^\dagger) d_\alpha^\dagger d_\beta + \hat{H}_{env}. \tag{137}$$

The first term represents free vibrons with the energy $\hbar\omega_q$. The second term is the electron-vibron interaction. The rest part $\hat{H}_{env}$ describes dissipation of vibrons due to interaction with other degrees of freedom, we do not consider the details in this chapter.

The Hamiltonians of the right (R) and left (L) leads read as usual

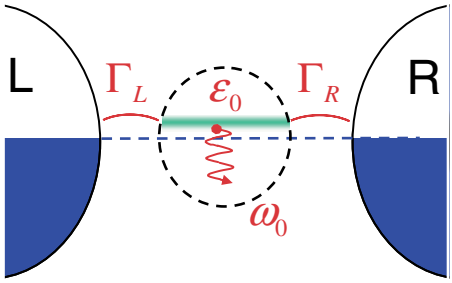

Fig. 9: Single-level electron-vibron model.

$$\hat{H}_{i=L(R)} = \sum_{k\sigma} (\epsilon_{ik\sigma} + e\varphi_i) c^{\dagger}_{ik\sigma} c_{ik\sigma}, \tag{138}$$

φ_i are the electrical potentials of the leads. Finally, the tunneling Hamiltonian

$$\hat{H}_T = \sum_{i=L,R} \sum_{k\sigma,\alpha} \left(V_{ik\sigma,\alpha} c^{\dagger}_{ik\sigma} d_{\alpha} + V^{*}_{ik\sigma,\alpha} d^{\dagger}_{\alpha} c_{ik\sigma} \right) \tag{139}$$

describes the hopping between the leads and the molecule. A direct hopping between two leads is neglected.

The simplest example of the considered model is a single-level model (Fig. 9) with the Hamiltonian

$$\hat{H} = \tilde{\epsilon}_0 d^{\dagger} d + \omega_0 a^{\dagger} a + \lambda \left(a^{\dagger} + a \right) d^{\dagger} d + \sum_{ik} \left[\tilde{\epsilon}_{ik} c^{\dagger}_{ik} c_{ik} + V_{ik} c^{\dagger}_{ik} d + h.c. \right], \tag{140}$$

where the first and the second terms describe free electron state and free vibron, the third term is electron-vibron interaction, and the rest is the Hamiltonian of the leads and tunneling coupling ($i = L, R$ is the lead index).

The other important case is a center-of-mass motion of molecules between the leads (Fig. 10). Here not the internal overlap integrals, but the coupling to the leads $V_{ik\sigma,\alpha}(x)$ is fluctuating. This model is easily reduced to the general model (137), if we consider additionaly two not flexible states in the left and right leads (two atoms most close to a system), to which the central system is coupled (shown by the dotted circles).

The tunneling Hamiltonian includes x-dependent matrix elements, considered in linear approximation

$$H_T = \sum_{i=L,R} \sum_{k\sigma,\alpha} \left(V_{ik\sigma,\alpha}(\hat{x}) c^{\dagger}_{ik\sigma} d_{\alpha} + h.c. \right), \tag{141}$$

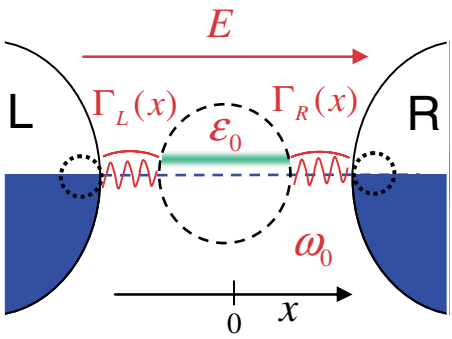

Fig. 10: A center-of-mass vibration.

$$V_{L,R}(x) = V_0 e^{\mp \hat{x}/L} \approx V_0 \left(1 \mp \frac{\hat{x}}{L}\right). \tag{142}$$

Consider now a single-level molecule ($\alpha \equiv 0$) and extend our system, including two additional states from the left ($\alpha \equiv l$) and right ($\alpha \equiv r$) sides of a molecule, which are coupled to the central state through x-dependent matrix elements, and to the leads in a usual way through $\Gamma_{L(R)}$. Then the Hamiltonian is of linear electron-vibron type

$$\hat{H}_{M+V} = \sum_{\alpha=l,0,r} (\epsilon_\alpha + e\varphi_\alpha)\, d_\alpha^\dagger d_\alpha + t_l(d_l^\dagger d_0 + h.c.) + t_r(d_r^\dagger d_0 + h.c.) + \\ + \omega_0 a^\dagger a + (a + a^\dagger)\left(\lambda_0 d_0^\dagger d_0 - \lambda_l(d_l^\dagger d_0 + h.c.) + \lambda_r(d_r^\dagger d_0 + h.c.)\right). \tag{143}$$

(iii) Local polaron and canonical transformation

Now let us start to consider the situation, when the electron-vibron interaction is strong. For an isolated system with the Hamiltonian, including only diagonal terms,

$$\hat{H}_{S+V} = \sum_\alpha \tilde{\epsilon}_\alpha d_\alpha^\dagger d_\alpha + \sum_q \omega_q a_q^\dagger a_q + \sum_\alpha \sum_q \lambda_\alpha^q (a_q + a_q^\dagger) d_\alpha^\dagger d_\alpha, \tag{144}$$

the problem can be solved exactly. This solution, as well as the method of the solution (canonical transformation), plays an important role in the theory of electron-vibron systems, and we consider it in detail.

Let's start from the simplest case. The single-level electron-vibron model is described by the Hamiltonian

$$\hat{H}_{S+V} = \tilde{\epsilon}_0 d^\dagger d + \omega_0 a^\dagger a + \lambda \left(a^\dagger + a\right) d^\dagger d, \tag{145}$$

where the first and the second terms describe free electron state and free vibron, and the third term is the electron-vibron interaction.

This Hamiltonian is diagonalized by the canonical transformation (called "Lang-Firsov" or "polaron") [95–97]

$$\bar{H} = \hat{S}^{-1} \hat{H} \hat{S}, \tag{146}$$

with

$$\hat{S} = \exp\left[-\frac{\lambda}{\omega_0}\left(a^\dagger - a\right) d^\dagger d\right], \tag{147}$$

the Hamiltonian (145) is transformed as

$$\bar{H}_{S+V} = \hat{S}^{-1} \hat{H}_{S+V} \hat{S} = \tilde{\epsilon}_0 \bar{d}^\dagger \bar{d} + \omega_0 \bar{a}^\dagger \bar{a} + \lambda \left(\bar{a}^\dagger + \bar{a}\right) \bar{d}^\dagger \bar{d}, \tag{148}$$

it has the same form as (145) with new operators, it is a trivial consequence of the general property

$$\hat{S}^{-1}\left(\hat{f}_1\hat{f}_2\hat{f}_3...\right)\hat{S} = (\hat{S}^{-1}\hat{f}_1\hat{S})(\hat{S}^{-1}\hat{f}_2\hat{S})(\hat{S}^{-1}\hat{f}_3\hat{S})... = \bar{f}_1\bar{f}_2\bar{f}_3... \tag{149}$$

and new single-particle operators are

$$\bar{a} = \hat{S}^{-1}a\hat{S} = a - \tfrac{\lambda}{\omega_0}d^\dagger d, \tag{150}$$

$$\bar{a}^\dagger = \hat{S}^{-1}a^\dagger\hat{S} = a^\dagger - \tfrac{\lambda}{\omega_0}d^\dagger d, \tag{151}$$

$$\bar{d} = \hat{S}^{-1}d\hat{S} = \exp\left[-\tfrac{\lambda}{\omega_0}\left(a^\dagger - a\right)\right]d, \tag{152}$$

$$\bar{d}^\dagger = \hat{S}^{-1}d^\dagger\hat{S} = \exp\left[\tfrac{\lambda}{\omega_0}\left(a^\dagger - a\right)\right]d^\dagger. \tag{153}$$

Substituting these expressions into (148) we get finally

$$\bar{H}_{S+V} = \left(\tilde{\epsilon}_0 - \frac{\lambda^2}{\omega_0}\right)d^\dagger d + \omega_0 a^\dagger a. \tag{154}$$

We see that the electron-vibron Hamiltonian (145) is equivalent to the free-particle Hamiltonian (154). This equivalence means that any quantum state $|\bar{\psi}_\lambda\rangle$, obtained as a solution of the Hamiltonian (154) is one-to-one equivalent to the state $|\psi_\lambda\rangle$ as a solution of the initial Hamiltonian (145), with the same matrix elements for any operator

$$\langle\bar{\psi}_\lambda|\bar{f}|\bar{\psi}_\lambda\rangle = \langle\psi_\lambda|\hat{f}|\psi_\lambda\rangle, \tag{155}$$

$$\bar{f} = \hat{S}^{-1}\hat{f}\hat{S}, \tag{156}$$

$$|\bar{\psi}_\lambda\rangle = \hat{S}^{-1}|\psi_\lambda\rangle. \tag{157}$$

It follows immediately that the eigenstates of the free-particle Hamiltonian are

$$|\bar{\psi}_{nm}\rangle = |n = 0, 1; m = 0, 1, 2, ...\rangle = (d^\dagger)^n\frac{(a^\dagger)^m}{\sqrt{m!}}|0\rangle, \tag{158}$$

and the eigen-energies are

$$E(n, m) = \left(\tilde{\epsilon}_0 - \frac{\lambda^2}{\omega_0}\right)n + \omega_0 m. \tag{159}$$

The eigenstates of the *initial* Hamiltonian (145) are

$$|\psi_{nm}\rangle = \hat{S}|\bar{\psi}_{nm}\rangle = e^{-\frac{\lambda}{\omega_0}(a^\dagger - a)d^\dagger d}(d^\dagger)^n\frac{(a^\dagger)^m}{\sqrt{m!}}|0\rangle, \tag{160}$$

with the same quantum numbers (n, m) and the same energies (159). This representation of the eigenstates demonstrates clearly the collective nature of the excitations, but it is inconvenient for practical calculations.

Now let us consider the polaron transformation (146)-(147) applied to the tunneling Hamiltonian

$$\hat{H}_T = \sum_{i=L,R} \sum_{k\sigma} \left(V_{ik\sigma} c^\dagger_{ik\sigma} d + V^*_{ik\sigma} d^\dagger c_{ik\sigma} \right) \tag{161}$$

The electron operators in the left and right leads $c_{ik\sigma}$ are not changed by this operation, but the dot operators d_α, $d^\dagger_\alpha$ are changed in accordance with (152) and (153). So that transformed Hamiltonian is

$$\bar{H}_T = \sum_{i=L,R} \sum_{k\sigma} \left(V_{ik\sigma} e^{-\frac{\lambda}{\omega_0}\left(a^\dagger - a\right)} c^\dagger_{ik\sigma} d + V^*_{ik\sigma} e^{\frac{\lambda}{\omega_0}\left(a^\dagger - a\right)} d^\dagger c_{ik\sigma} \right). \tag{162}$$

Now we see clear the problem: while the new dot Hamiltonian (154) is very simple and exactly solvable, the new tunneling Hamiltonian (162) is complicated. Moreover, instead of one linear electron-vibron interaction term, the exponent in (162) produces all powers of vibronic operators. Actually, we simply remove the complexity from one place to the other. This approach works well, if the tunneling can be considered as a perturbation, we consider it in the next section. In the general case the problem is quite difficult, but in the single-particle approximation it can be solved exactly [98–101].

To conclude, after the canonical transformation we have two equivalent models: (1) the initial model (145) with the eigenstates (160); and (2) the *fictional* free-particle model (154) with the eigenstates (158). We shall call this second model *polaron representation*. The relation between the models is established by (155)-(157). It is also clear from the Hamiltonian (148), that the operators $\bar{d}^\dagger$, $\bar{d}$, $\bar{a}^\dagger$, and $\bar{a}$ describe the initial electrons and vibrons in the fictional model.

(iv) Inelastic tunneling in the single-particle approximation

In this section we consider a special case of a *single particle transmission* through an electron-vibron system. It means that we consider a system coupled to the leads, but without electrons in the leads. This can be considered equivalently as the limit of large electron level energy ϵ_0 (far from the Fermi surface in the leads).

The inelastic *transmission matrix* $T(\epsilon', \epsilon)$ describes the probability that an electron with energy ϵ, incident from one lead, is transmitted with the energy ϵ' into a second lead. The transmission function can be defined as the total transmission probability

$$T(\epsilon) = \int T(\epsilon', \epsilon) d\epsilon'. \tag{163}$$

For a noninteracting single-level system the transmission matrix is

$$T^0(\epsilon', \epsilon) = \frac{\Gamma_R(\epsilon)\Gamma_L(\epsilon)\delta(\epsilon - \epsilon')}{(\epsilon - \epsilon_0 - \Lambda(\epsilon))^2 + (\Gamma(\epsilon)/2)^2}, \tag{164}$$

where $\Gamma(\epsilon) = \Gamma_L(\epsilon) + \Gamma_R(\epsilon)$ is the level-width function, and $\Lambda(\epsilon)$ is the real part of the self-energy.

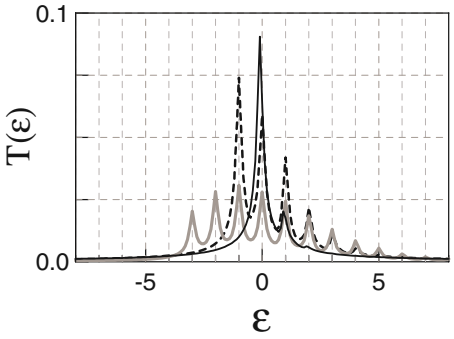

Fig. 11: Transmission function as a function of energy at different electron-vibron coupling: $g = 0.1$ (thin solid line), $g = 1$ (dashed line), and $g = 3$ (thick solid line), at $\Gamma = 0.1$.

We can do some general conclusions, based on the form of the tunneling Hamiltonian (162). Expanding the exponent in the same way as before, we get

$$\bar{H}_T = \sum_{i=L,R} \sum_{k\sigma} \left(V_{ik\sigma} c^\dagger_{ik\sigma} d \left[\alpha_0 + \sum_{m=1}^{\infty} \alpha_m \left((a^\dagger)^m + a^m \right) \right] + h.c. \right), \quad (165)$$

with the coefficients

$$\alpha_m = \left(-\frac{\lambda}{\omega_0} \right)^m \frac{e^{-(\lambda/\omega_0)^2/2}}{m!}. \quad (166)$$

This complex Hamiltonian has very clear interpretation, the tunneling of one electron from the right to the left lead is accompanied by the excitation of vibrons. The energy conservation implies that

$$\epsilon - \epsilon' = \pm m\omega_0, \quad (167)$$

so that the inelastic tunneling with emission or absorption of vibrons is possible.

The exact solution is possible in the wide-band limit. [98–101]

It is convenient to introduce the dimensionless electron-vibron coupling constant, known as the Huang-Rhys factor,

$$g = \left(\frac{\lambda}{\omega_0} \right)^2. \quad (168)$$

At zero temperature the solution is

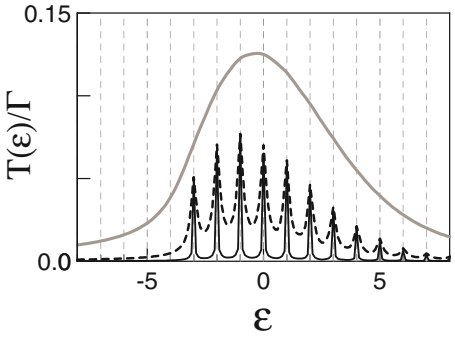

Fig. 12: Transmission function as a function of energy at different coupling to the leads: $\Gamma = 0.01$ (thin solid line), $\Gamma = 0.1$ (dashed line), and $\Gamma = 1$ (thick solid line), at $g = 3$.

$$T(\epsilon', \epsilon) = \Gamma_L \Gamma_R e^{-2g} \sum_{m=0}^{\infty} \frac{g^m}{m!} \delta(\epsilon - \epsilon' - m\omega_0) \times \left| \sum_{j=0}^{m} (-1)^j \frac{m!}{j!(m-j)!} \sum_{l=0}^{\infty} \frac{g^l}{l!} \frac{1}{\epsilon - \epsilon_0 + g\omega_0 - (j+l)\omega_0 + i\Gamma/2} \right|^2, \quad (169)$$

the total transmission function $T(\epsilon)$ is trivially obtain by integration over ϵ'. The representative results are presented in Figs. 11 and 12.

At finite temperature the general expression is too cumbersome, and we present here only the expression for the total transmission function

$$T(\epsilon) = \frac{\Gamma_L \Gamma_R}{\Gamma} e^{-g(1+2n_\omega)} \int_{-\infty}^{\infty} dt \times \exp\left(-\frac{\Gamma}{2}|t| + i(\epsilon - \epsilon_0 + g\omega_0)t - g\left[(1+n_\omega)e^{-i\omega_0 t} + n_\omega e^{i\omega_0 t}\right] \right), \quad (170)$$

where n_ω is the equilibrium number of vibrons.

(v) Master equation

When the system is weakly coupled to the leads, the polaron representation (154), (162) is a convenient starting point. Here we consider how the sequential tunneling is modified by vibrons.

The master equation for the probability $p(n, m, t)$ to find the system in one of the polaron eigenstates (158) can be written as

$$\frac{dp(n,m)}{dt} = \sum_{n'm'} \Gamma^{nn'}_{mm'} p(n', m') - \sum_{n'm'} \Gamma^{n'n}_{m'm} p(n, m) + I^V[p], \quad (171)$$

where the first term describes tunneling transition *into the state* $|n,m\rangle$, and the second term – tunneling transition *out of the state* $|n,m\rangle$, $I^V[p]$ is the vibron scattering integral describing the relaxation to equilibrium. The transition rates $\Gamma^{nn'}_{mm'}$ should be found from the Hamiltonian (162).

Taking into account all possible single-electron tunneling processes, we obtain the incoming tunneling rate

$$\begin{aligned}\Gamma^{10}_{mm'} &= \frac{2\pi}{\hbar}\sum_{ik\sigma} f_i^0(E_{ik\sigma})\left|\left\langle i\bar{k},1,m\left|\bar{H}_T\right|ik,0,m'\right\rangle\right|^2\delta(E_{0m'}+E_{ik\sigma}-E_{1m})\\ &= \frac{2\pi}{\hbar}\sum_{ik\sigma} f_i^0(E_{ik\sigma})\left|V_{ik\sigma}\right|^2\left|\left\langle m\left|e^{\frac{\lambda}{\omega_0}\left(a^\dagger-a\right)}\right|m'\right\rangle\right|^2\delta(E_{0m'}+E_{ik\sigma}-E_{1m})\\ &= \sum_{i=L,R}\Gamma_i(E_{1m}-E_{0m'})\left|M_{mm'}\right|^2 f_i^0(E_{1m}-E_{0m'}),\end{aligned} \tag{172}$$

where

$$M_{mm'} = \left\langle m\left|e^{\frac{\lambda}{\omega_0}\left(a^\dagger-a\right)}\right|m'\right\rangle \tag{173}$$

is the Franck-Condon matrix element. We use usual short-hand notations: $|ik,n,m\rangle$ is the state with occupied k-state in the $i-$th lead, n electrons, and m vibrons, while $|i\bar{k},n,m\rangle$ is the state with unoccupied k-state in the $i-$th lead, E_{nm} is the polaron energy (159).

Similarly, the outgoing rate is

$$\Gamma^{01}_{mm'} = \sum_{i=L,R}\Gamma_i(E_{1m'}-E_{0m})\left|M_{mm'}\right|^2\left(1-f_i^0(E_{1m'}-E_{0m})\right). \tag{174}$$

The current (from the left or right lead to the system) is

$$J_{i=L,R}(t) = e\sum_{mm'}\left(\Gamma^{10}_{imm'}p(0,m')-\Gamma^{01}_{imm'}p(1,m')\right). \tag{175}$$

The system of equations (171)-(175) solves the transport problem in the sequential tunneling regime.

(v) Franck-Condon blockade

Now let us consider some details of the tunneling at small and large values of the electro-vibron coupling parameter $g = \left(\frac{\lambda}{\omega_0}\right)^2$.

The matrix element (173) can be calculated analytically, it is symmetric in $m-m'$ and for $m<m'$ is

$$M_{m<m'} = \sum_{l=0}^{m}\frac{(-g)^l\sqrt{m!m'!}e^{-g/2}g^{(m'-m)/2}}{l!(m-l)!(l+m'-m)!}. \tag{176}$$

The lowest order elements are

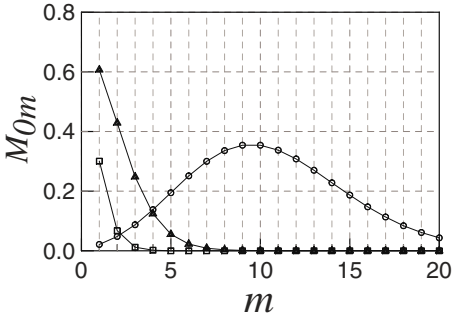

Fig. 13: Franck-Condon matrix elements M_{0m} for weak ($g = 0.1$, squares), intermediate ($g = 1$, triangles), and strong ($g = 10$, circles) electron-vibron interaction. Lines are the guides for eyes.

$$M_{0m} = e^{-g/2} \frac{g^{m/2}}{\sqrt{m!}}, \tag{177}$$

$$M_{11} = (1 - g)e^{-g/2}, \tag{178}$$

$$M_{12} = \sqrt{2g} \left(1 - \frac{g}{2}\right) e^{-g/2} ... \tag{179}$$

The characteristic feature of these matrix elements is so-called Franck-Condon blockade [107,108], illustrated in Fig. 13 for the matrix element M_{0m}. From the picture, as well as from the analytical formulas, it is clear, that in the case of strong electron-vibron interaction the tunneling with small change of the vibron quantum number is suppressed exponentially, and only the tunneling through high-energy states is possible, which is also suppressed at low bias voltage and low temperature. Thus, the electron transport through a system (linear conductance) is very small.

There are several interesting manifestations of the Franck-Condon blockade.

The *life-time* of the state $|n, m\rangle$ is determined by the sum of the rates of all possible processes which change this state in the assumption that all other states are empty

$$\tau_{nm}^{-1} = \sum_{n'm'} \Gamma_{m'm}^{n'n}. \tag{180}$$

As an example, let us calculate the life-time of the neutral state $|0, 0\rangle$, which has the energy higher than the charged ground state $|1, 0\rangle$.

$$\tau_{00}^{-1} = \sum_{n'm'} \Gamma_{m'0}^{n'0} = \sum_{m} \sum_{i=L,R} \Gamma_i(E_{1m} - E_{00}) \left|M_{m0}\right|^2 f_i^0(E_{1m} - E_{00}). \tag{181}$$

In the wide-band limit we obtain the simple analytical expression

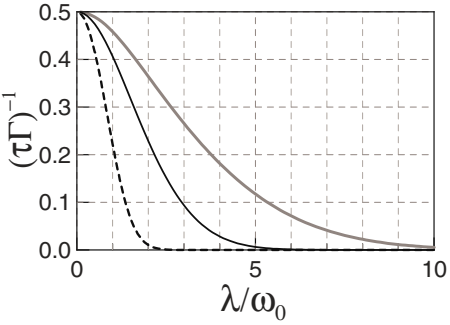

Fig. 14: The inverse life-time $(\tau\Gamma)^{-1}$ as a function of λ/ω_0 at optimal electron level position $\epsilon_0 = \lambda^2/2\omega_0$ for neutral state (thin solid line), and for the charged state (dashed line), and for the neutral state at other level position $\epsilon_0 = \lambda^2/4\omega_0$ (thick solid line).

$$\tau_{00}^{-1} = \Gamma \sum_m e^{-g} \frac{g^m}{m!} f^0 \left(\tilde{\epsilon}_0 - \frac{\lambda^2}{\omega_0} + \omega_0 m \right). \tag{182}$$

The corresponding expression for the life-time of the charged state (which can be excited by thermal fluctuations) is

$$\tau_{10}^{-1} = \Gamma \sum_m e^{-g} \frac{g^m}{m!} f^0 \left(-\tilde{\epsilon}_0 + \frac{\lambda^2}{\omega_0} + \omega_0 m \right). \tag{183}$$

The result of the calculation is shown in Fig. 14, it is clear seen that the tunneling from the state $|0,0\rangle$ to the charged state and from the state $|1,0\rangle$ to the neutral state is exponentially suppressed in comparison with the bare tunneling rate Γ at large values of the electron-vibron interaction constant λ. This *polaron memory effect* can be used to create nano-memory and nano-switches. At finite voltage the switching between two states is easy accessible through the excited vibron states. It can be used to switch between memory states [112].

The other direct manifestation of the Franck-Condon blockade, – suppression of the linear conductance, was considered in Refs. [107, 108].

3 Nonequilibrium Green function theory of transport

3.1 Standard transport model: a nanosystem between ideal leads

First of all, we formulate a standard discrete-level model to describe nanoscale interacting quantum systems (quantum dot, system of quantum dots, molecule, below "nanosystem", "central system", or simply "system") coupled to free

conduction electrons in the leads. We include the Coulomb interaction with the help of the Anderson-Hubbard Hamiltonan to be able to describe correlation effects, such as Coulomb blockade and Kondo effect, which could dominate at low temperatures. At high temperatures or weak interaction the self-consistent mean-field effects are well reproduced by the same model. Furthermore, electrons are coupled to vibrational modes, below we use the electron-vibron model introduced previously.

(i) The model Hamiltonian

The full Hamiltonian is the sum of the free system Hamiltonian $\hat{H}_S^{(0)}$, the inter-system electron-electron interaction Hamiltonian $\hat{H}_C$, the vibron Hamiltonian $\hat{H}_V$ including the electron-vibron interaction and coupling of vibrations to the environment (dissipation of vibrons), the Hamiltonians of the leads $\hat{H}_{R(L)}$, and the tunneling Hamiltonian $\hat{H}_T$ describing the system-to-lead coupling

$$\hat{H} = \hat{H}_S + \hat{H}_C + \hat{H}_V + \hat{H}_L + \hat{H}_R + \hat{H}_T. \tag{184}$$

An isolated noninteracting nanosystem is described as a set of discrete states $|\alpha\rangle$ with energies ϵ_α and inter-orbital overlap integrals $t_{\alpha\beta}$ by the following model Hamiltonian:

$$\hat{H}_S^{(0)} = \sum_\alpha \left(\epsilon_\alpha + e\varphi_\alpha(t)\right) d_\alpha^\dagger d_\alpha + \sum_{\alpha\neq\beta} t_{\alpha\beta} d_\alpha^\dagger d_\beta, \tag{185}$$

where $d_\alpha^\dagger$,d_α are creation and annihilation operators in the states $|\alpha\rangle$, and $\varphi_\alpha(t)$ is the effective (self-consistent) electrical potential. The index α is used to mark single-electron states (e.g. atomic orbitals) including the spin degree of freedom. In the eigenstate (molecular orbital) representation the second term is absent and the Hamiltonian is diagonal.

For molecular transport the parameters of a model are to be determined by *ab initio* methods or considered as semi-empirical. This is a compromise, which allows us to consider complex molecules with a relatively simple model.

The Hamiltonians of the right (R) and left (L) leads are

$$\hat{H}_{i=L(R)} = \sum_{k\sigma} (\epsilon_{ik\sigma} + e\varphi_i(t)) c_{ik\sigma}^\dagger c_{ik\sigma}, \tag{186}$$

$\varphi_i(t)$ are the electrical potentials of the leads, the index k is the wave vector, but can be considered as representing an other conserved quantum number, σ is the spin index, but can be considered as a generalized channel number, describing e.g. different bands or subbands in semiconductors. Alternatively, the tight-binding model can be used also for the leads, then (186) should be considered as a result of the Fourier transformation. The leads are assumed to be noninteracting and equilibrium.

The tunneling Hamiltonian

$$\hat{H}_T = \sum_{i=L,R} \sum_{k\sigma,\alpha} \left(V_{ik\sigma,\alpha} c^\dagger_{ik\sigma} d_\alpha + V^*_{ik\sigma,\alpha} d^\dagger_\alpha c_{ik\sigma} \right) \tag{187}$$

describes the hopping between the leads and the system. The direct hopping between two leads is neglected (relatively weak molecule-to-lead coupling case). Note, that the direct hoping between equilibrium leads can be easy taken into account as an additional independent current channel.

The Coulomb interaction inside a system is described by the Anderson-Hubbard Hamiltonian

$$\hat{H}_C = \frac{1}{2} \sum_{\alpha \neq \beta} U_{\alpha\beta} \hat{n}_\alpha \hat{n}_\beta. \tag{188}$$

This Hamiltonian is used usually only for the short-range part of Coulomb interaction. The long-range interactions can be better introduced through the self-consistent electrical potential φ_α, which is determined by the Poisson equation with the average electron density.

Vibrations and the electron-vibron coupling are described by the Hamiltonian

$$\hat{H}_V = \sum_q \hbar\omega_q a^\dagger_q a_q + \sum_{\alpha\beta} \sum_q \lambda^q_{\alpha\beta} (a_q + a^\dagger_q) d^\dagger_\alpha d_\beta + \hat{H}_e. \tag{189}$$

Here vibrations are considered as localized phonons and q is the index labeling them, not the wave-vector. The first term describes free vibrons with the energy $\hbar\omega_q$. The second term represents the electron-vibron interaction. The third term describes the coupling to the environment and the dissipation of vibrons. We include both diagonal coupling, which originates from a change of the electrostatic energy with the distance between atoms, and the off-diagonal coupling, which can be obtained from the dependence of the matrix elements $t_{\alpha\beta}$ over the distance between atoms.

(ii) Nonequilibrium current and charge

To connect the microscopic description of a system with the macroscopic (electrodynamic) equations and calculate the observables, we need the expressions for the nonequilibrium electrical charge of the system and the current between the system and the leads.

The charge in a nonequilibrium state is given by (Q_0 is the background charge)

$$Q_S(t) = e \sum_\alpha \left\langle d^\dagger_\alpha d_\alpha \right\rangle - Q_0. \tag{190}$$

To calculate the current we find the time evolution of the particle number operator $\hat{N}_S = \sum_\alpha d^\dagger_\alpha d_\alpha$ due to tunneling from the left ($i = L$) or right ($i = R$) contact.

The current *from* the left ($i = L$) or right ($i = R$) contact *to* the nanosystem is determined by (note, that we consider e as the charge of the electron (negative) or the hole (positive))

$$J_i(t) = -e\left\langle \left(\frac{dN_S}{dt}\right)_i \right\rangle = -\frac{ie}{\hbar}\left\langle [H_T^{(i)}, N_S] \right\rangle, \tag{191}$$

where

$$H_T^{(i)} = \sum_{k\sigma,\alpha}\left(V_{ik\sigma,\alpha}c_{ik\sigma}^\dagger d_\alpha + V_{ik\sigma,\alpha}^* d_\alpha^\dagger c_{ik\sigma}\right) \tag{192}$$

is the Hamiltonian of the coupling to the corresponding contact. The current is determined by this only part of the full Hamiltonian (136), because all other terms commute with $\hat{N}_S$.

Applying the commutation relation

$$\left[d_\alpha, d_\beta^\dagger d_\beta\right] = d_\alpha d_\beta^\dagger d_\beta - d_\beta^\dagger d_\beta d_\alpha = d_\alpha d_\beta^\dagger d_\beta + d_\beta^\dagger d_\alpha d_\beta = (d_\alpha d_\beta^\dagger + \delta_{\alpha\beta} - d_\alpha d_\beta^\dagger)d_\beta = \delta_{\alpha\beta}d_\alpha, \tag{193}$$

one obtains finally

$$J_i(t) = \frac{ie}{\hbar}\sum_{k\sigma,\alpha}\left[V_{ik\sigma,\alpha}\left\langle c_{ik\sigma}^\dagger d_\alpha\right\rangle - V_{ik\sigma,\alpha}^*\left\langle d_\alpha^\dagger c_{ik\sigma}\right\rangle\right]. \tag{194}$$

(iii) Density matrix and NGF

The averages of the operators in Eqs. (190) and (194) are the elements of the density matrix in the single-particle space

$$\rho_{\alpha\alpha}(t) = \left\langle d_\alpha^\dagger(t)d_\alpha(t)\right\rangle, \tag{195}$$

$$\rho_{\alpha,ik\sigma}(t) = \left\langle c_{ik\sigma}^\dagger(t)d_\alpha(t)\right\rangle. \tag{196}$$

It is possible, also, to express it as a two-time Green function at equal times

$$Q_S(t) = e\sum_\alpha \rho_{\alpha\alpha}(t) = -ie\sum_\alpha G_{\alpha\alpha}^<(t,t), \tag{197}$$

$$J_i(t) = \frac{2e}{\hbar}\mathrm{Im}\left(\sum_{k\sigma,\alpha}V_{ik\sigma,\alpha}\rho_{\alpha,ik\sigma}(t)\right) = \frac{2e}{\hbar}\mathrm{Re}\left(\sum_{k\sigma,\alpha}V_{ik\sigma,\alpha}G_{\alpha,ik\sigma}^<(t,t)\right), \tag{198}$$

where we define the system-to-lead lesser Green function

$$G_{\alpha,ik\sigma}^<(t_1,t_2) = i\left\langle c_{ik\sigma}^\dagger(t_2)d_\alpha(t_1)\right\rangle, \tag{199}$$

while nonequilibrium charge distribution of the molecule is determined by the system lesser function

$$G_{\alpha\beta}^<(t_1,t_2) = i\left\langle d_\beta^\dagger(t_2)d_\alpha(t_1)\right\rangle. \tag{200}$$

One can ask: what is the advantage to use the more complex two-time Green functions instead of density matrices? There are several reasons. First of all, NGF give, as we shall see below, a clear description of both density of states and distribution of particles over this states. Then, the equations of motion including interactions and the influence of environment can be obtained with the help of a diagrammatic technique, and (very important) all diagrammatic results of *equilibrium* theory can be easily incorporated. Retardation effects are conveniently taken into account by two-time Green functions. And, ... finally, one can always go back to the density matrix when necessary.

It is important to note, that the *single-particle* density matrix (195) should not be mixed up with the density matrix in the basis of *many-body eigenstates*.

In these review we consider different methods. The density matrix can be determined from the master equation. For Green functions the EOM method or Keldysh method can be applied. Traditionally, the density matrix is used in the case of very weak system-to-lead coupling, while the NGF methods are more successful in the description of strong and intermediate coupling to the leads. The convenience of one or other method is determined essentially by the type of interaction. Our aim is to combine the advantages of both methods.

3.2 Nonequilibrium Green functions: definition and properties

In the previous section we found, that the current through a system (as well as other observables) can be expressed through nonequilibrium Green functions. Here we give the definitions of retarded, advanced, lesser, and greater Green functions and consider some simple examples. We also introduce a very important concept of the Schwinger-Keldysh closed-time contour, and define contour Green functions. This section is a little bit technical, but we need these definitions in the next sections.

Spectral - retarded (G^R) and advanced (G^A) functions

(i) Definition

Retarded Green function for fermions is defined as

$$G^R_{\alpha\beta}(t_1,t_2) = -i\theta(t_1-t_2)\left\langle \left[c_\alpha(t_1), c^\dagger_\beta(t_2)\right]_+ \right\rangle, \tag{201}$$

where $c^\dagger_\alpha(t)$, $c_\alpha(t)$ are creation and annihilation time-dependent (Heisenberg) operators, $[c,d]_+ = cd + dc$ is the anti-commutator, $\langle ... \rangle$ denotes averaging over equilibrium state.

We use notations α, β, ... to denote single-particle quantum states, the other possible notation is more convenient for bulk systems

$$G^R(x_1,x_2) = -i\theta(t_1-t_2)\left\langle \left[c(x_1), c^\dagger(x_2)\right]_+ \right\rangle, \tag{202}$$

where $x \equiv \boldsymbol{r}, t, \sigma, ...$ or $x \equiv \boldsymbol{k}, t, \sigma, ...$, etc. Some other types of notations can be found in the literature, they are equivalent to (201).

The advanced function for fermions is defined as

$$G^A_{\alpha\beta}(t_1, t_2) = i\theta(t_2 - t_1) \left\langle \left[c_\alpha(t_1), c^\dagger_\beta(t_2) \right]_+ \right\rangle . \tag{203}$$

Finally, retarded and advanced functions for *bosons* can be defined as

$$\tilde{G}^R_{\alpha\beta}(t_1, t_2) = -i\theta(t_1 - t_2) \left\langle \left[a_\alpha(t_1), a^\dagger_\beta(t_2) \right]_- \right\rangle , \tag{204}$$

$$\tilde{G}^A_{\alpha\beta}(t_1, t_2) = i\theta(t_2 - t_1) \left\langle \left[a_\alpha(t_1), a^\dagger_\beta(t_2) \right]_- \right\rangle , \tag{205}$$

where $a^\dagger_\alpha(t)$, $a_\alpha(t)$ are creation and annihilation boson operators, $[a, b]_- = ab - ba$ is the commutator.

(ii) Discussion of averaging

The average value of any operator $\hat{O}$ can be written as $\langle \hat{O} \rangle = \langle t | \hat{O}^S | t \rangle$ in the Schrödinger representation or $\langle \hat{O} \rangle = \langle 0 | \hat{O}^H(t) | 0 \rangle$ in the Heisenberg representation, where $|0\rangle$ is some initial state. This initial state is in principle arbitrary, but in many-particle problems it is convenient to take this state as an equilibrium state, consequently without time-dependent perturbation we obtain usual equilibrium Green functions.

In accordance with this definition the Heisenberg operators $c_\alpha(t)$, $c^\dagger_\beta(t)$, etc. are equal to the time-independent Schrödinger operators at some initial time t_0: $c_\alpha(t_0) = c_\alpha$, etc. Density matrix of the system is assumed to be equilibrium at this time $\hat{\rho}(t_0) = \hat{\rho}_{eq}$. Usually we can take $t_0 = 0$ for simplicity, but if we want to use $t_0 \neq 0$ the transformation to Heisenberg operators should be written as

$$\hat{f}^H(t) = e^{i\hat{H}(t-t_0)} \hat{f}^S e^{-i\hat{H}(t-t_0)}. \tag{206}$$

In fact, the initial conditions are not important because of dissipation (the memory about the initial state is completely lost after the relaxation time). However, in some pathological cases, for example for free noninteracting particles, the initial state determines the state at all times. Note also, that the initial conditions can be more convenient formulated for Green functions itself, instead of corresponding initial conditions for operators or wave functions.

Nevertheless, thermal averaging is widely used and we define it here explicitly. If we introduce the basis of exact time-independent many-particle states $|n\rangle$ with energies E_n, the averaging over equilibrium state can be written as

$$\langle \hat{O} \rangle = \frac{1}{Z} \sum_n e^{-E_n/T} \left\langle n \left| \hat{O}^H(t) \right| n \right\rangle , \quad Z = \sum_n e^{-E_n/T}. \tag{207}$$

In the following when we use notations like $\left\langle \hat{O} \right\rangle$ or $\left\langle \Psi \left| \hat{O}(t) \right| \Psi \right\rangle$, we assume the averaging with density matrix (density operator) $\hat{\rho}$

$$\left\langle \hat{O} \right\rangle = Sp\left(\hat{\rho}\hat{O}\right), \tag{208}$$

for equilibrium density matrix and Heisenberg operators it is equivalent to (207).

(iii) Free-particle retarded function for fermions

Now consider the simplest possible example – retarded Green function for free particles (fermions).

The free-particle Hamiltonian has equivalent form if one uses Schrödinger or Heisenberg operators

$$\hat{H} = \sum_{\alpha} \epsilon_{\alpha} c_{\alpha}^{\dagger} c_{\alpha} = \sum_{\alpha} \epsilon_{\alpha} c_{\alpha}^{\dagger}(t) c_{\alpha}(t), \tag{209}$$

because (here we assume $t_0 = 0$)

$$\begin{aligned} c_{\alpha}^{\dagger}(t) c_{\alpha}(t) &= e^{i\hat{H}t} c_{\alpha}^{\dagger} e^{-i\hat{H}t} e^{i\hat{H}t} c_{\alpha} e^{-i\hat{H}t} \\ &= e^{i\hat{H}t} c_{\alpha}^{\dagger} c_{\alpha} e^{-i\hat{H}t} = c_{\alpha}^{\dagger} c_{\alpha}, \end{aligned} \tag{210}$$

where we used that $c_{\alpha}^{\dagger} c_{\alpha}$ is commutative with the Hamiltonian $\hat{H} = \sum_{\alpha} \epsilon_{\alpha} c_{\alpha}^{\dagger} c_{\alpha}$.

From the definitions (201) and (207)

$$\begin{aligned} &\left\langle \left[c_{\alpha}(t_1), c_{\beta}^{\dagger}(t_2) \right]_{+} \right\rangle = \left\langle c_{\alpha}(t_1) c_{\beta}^{\dagger}(t_2) + c_{\beta}^{\dagger}(t_2) c_{\alpha}(t_1) \right\rangle \\ &= \left\langle e^{i\hat{H}t_1} c_{\alpha}(t_1) e^{-i\hat{H}t_1} e^{i\hat{H}t_2} c_{\beta}^{\dagger}(t_2) e^{-i\hat{H}t_2} + e^{i\hat{H}t_2} c_{\beta}^{\dagger}(t_2) e^{-i\hat{H}t_2} e^{i\hat{H}t_1} c_{\alpha}(t_1) e^{-i\hat{H}t_1} \right\rangle \\ &= e^{i\epsilon_{\beta}t_2 - i\epsilon_{\alpha}t_1} \left\langle c_{\alpha} c_{\beta}^{\dagger} + c_{\beta}^{\dagger} c_{\alpha} \right\rangle = e^{-i\epsilon_{\alpha}(t_1 - t_2)} \delta_{\alpha\beta}, \end{aligned} \tag{211}$$

$$\begin{aligned} G_{\alpha\beta}^{R}(t_1, t_2) &= -i\theta(t_1 - t_2) \left\langle \left[c_{\alpha}(t_1), c_{\beta}^{\dagger}(t_2) \right]_{+} \right\rangle \\ &= -i\theta(t_1 - t_2) e^{-i\epsilon_{\alpha}(t_1 - t_2)} \delta_{\alpha\beta}, \end{aligned} \tag{212}$$

where we used some obvious properties of the creation and annihilation operators and commutation relations.

We consider also the other method, based on the equations of motion for operators. From Liouville – von Neumann equation we find (all c-operators are Heisenberg operators in the formula below, (t) is omitted for shortness)

$$i\frac{dc_\alpha(t)}{dt} = [c_\alpha(t), H]_- = \sum_\beta \epsilon_\beta \left[c_\alpha, c_\beta^\dagger c_\beta\right]_-$$
$$= \sum_\beta \epsilon_\beta \left(c_\alpha c_\beta^\dagger c_\beta - c_\beta^\dagger c_\beta c_\alpha\right) = \sum_\beta \epsilon_\beta \left(c_\alpha c_\beta^\dagger c_\beta + c_\beta^\dagger c_\alpha c_\beta\right)$$
$$= \sum_\beta \epsilon_\beta \left(c_\alpha c_\beta^\dagger + c_\beta^\dagger c_\alpha\right) c_\beta = \sum_\beta \epsilon_\beta \delta_{\alpha\beta} c_\beta = \epsilon_\alpha c_\alpha(t), \tag{213}$$

so that Heisenberg operators for free fermions are

$$c_\alpha(t) = e^{-i\epsilon_\alpha t} c_\alpha(0), \quad c_\alpha^\dagger(t) = e^{i\epsilon_\alpha t} c_\alpha^\dagger(0). \tag{214}$$

Substituting these expressions into (201) we obtain again (212). Note also that if we take $t_0 \neq 0$, then Heisenberg operators for free fermions are

$$c_\alpha(t) = e^{-i\epsilon_\alpha (t-t_0)} c_\alpha(t_0), \quad c_\alpha^\dagger(t) = e^{i\epsilon_\alpha (t-t_0)} c_\alpha^\dagger(t_0), \tag{215}$$

but the result for the Green functions is just the same, because

$$\left\langle \left[c_\alpha(t_1), c_\beta^\dagger(t_2)\right]_+ \right\rangle = \left\langle c_\alpha(t_1) c_\beta^\dagger(t_2) + c_\beta^\dagger(t_2) c_\alpha(t_1) \right\rangle =$$
$$= e^{i\epsilon_\beta (t_2 - t_0) - i\epsilon_\alpha (t_1 - t_0)} \left\langle c_\alpha c_\beta^\dagger + c_\beta^\dagger c_\alpha \right\rangle = e^{-i\epsilon_\alpha (t_1 - t_2)} \delta_{\alpha\beta}. \tag{216}$$

It is interesting to make a Fourier-transform of this function. In equilibrium two-time function $G^R_{\alpha\beta}(t_1, t_2)$ is a function of the time difference only, so that we define transform over time difference $(t_1 - t_2)$

$$G^R(\epsilon) = \int_0^\infty G^R(t_1 - t_2) e^{i(\epsilon + i0)(t_1 - t_2)} d(t_1 - t_2), \tag{217}$$

we add infinitely small positive complex part to ϵ to make this integral well defined in the upper limit (this is necessary for free particles without dissipation because function (212) oscillates at large times $\tau = t_1 - t_2$ and the integral (217) can not be calculated without $i0$ term. Then we obtain

$$G^R_{\alpha\beta}(\epsilon) = \frac{\delta_{\alpha\beta}}{\epsilon - \epsilon_\alpha + i0}. \tag{218}$$

More generally, transformation (217) can be considered as the Laplace transformation with complex argument $z = \epsilon + i\eta$.

For advanced function

$$G^A_{\alpha\beta}(t_1, t_2) = i\theta(t_2 - t_1) e^{-i\epsilon_\alpha (t_1 - t_2)} \delta_{\alpha\beta}, \tag{219}$$

the Fourier transform is given by

$$G^A(\epsilon) = \int_{-\infty}^0 G^A(t_1 - t_2) e^{i(\epsilon - i0)(t_1 - t_2)} d(t_1 - t_2), \tag{220}$$

with other sign of the term $i0$.

(iv) Spectral function

Finally, we introduce the important combination of retarded and advanced functions known as *spectral* or *spectral weight* function

$$A_{\alpha\beta}(\epsilon) = i\left(G^R_{\alpha\beta}(\epsilon) - G^A_{\alpha\beta}(\epsilon)\right), \tag{221}$$

in equilibrium case Fourier-transformed retarded and advanced functions are complex conjugate $G^A(\epsilon) = \left(G^R(\epsilon)\right)^*$, and $A_{\alpha\beta}(\epsilon) = -2\mathrm{Im}G^R_{\alpha\beta}(\epsilon)$.

For free fermions the spectral function is

$$A_{\alpha\beta}(\epsilon) = -2\mathrm{Im}\left(\frac{\delta_{\alpha\beta}}{\epsilon - \epsilon_\alpha + i0}\right) = 2\pi\delta(\epsilon - \epsilon_\alpha)\delta_{\alpha\beta}. \tag{222}$$

The result is transparent – the function $A_{\alpha\beta}(\epsilon)$ is nonzero only at particle eigen-energies, so that

$$\rho(\epsilon) = \frac{1}{2\pi}\mathrm{Sp}A_{\alpha\beta}(\epsilon) = \frac{1}{2\pi}\sum_\alpha A_{\alpha\alpha}(\epsilon) = \sum_\alpha \delta(\epsilon - \epsilon_\alpha) \tag{223}$$

is the usual energy density of states. Note that the imaginary part $i0$ is necessary to obtain this result, thus it is not only mathematical trick, but reflects the physical sense of a retarded Green function.

If we introduce finite relaxation time

$$G^R_{\alpha\beta}(\tau) = -i\theta(\tau)e^{-i\epsilon_\alpha\tau - \gamma\tau}\delta_{\alpha\beta}, \tag{224}$$

then the spectral function has familiar Lorentzian form

$$A_{\alpha\beta}(\epsilon) = \frac{2\gamma\delta_{\alpha\beta}}{(\epsilon - \epsilon_\alpha)^2 + \gamma^2}. \tag{225}$$

Finally, spectral function has a special property, so-called *sum rule*, namely

$$\int_{-\infty}^{\infty} A_{\alpha\beta}(\epsilon)\frac{d\epsilon}{2\pi} = \delta_{\alpha\beta}. \tag{226}$$

Kinetic - lesser ($G^<$) and greater ($G^>$) functions

(i) Definition

Spectral functions, described before, determine single-particle properties of the system, such as quasiparticle energy, broadening of the levels (life-time), and density of states. These functions can be modified in nonequilibrium state, but most important *kinetic* properties, such as distribution function, charge, and current, are determined by lesser Green function

$$G^<_{\alpha\beta}(t_1, t_2) = i\left\langle c^\dagger_\beta(t_2)c_\alpha(t_1)\right\rangle. \tag{227}$$

Indeed, the density matrix is the same as equal-time lesser function

$$\rho_{\alpha\beta}(t) = \left\langle c^\dagger_\beta(t) c_\alpha(t) \right\rangle = -iG^<_{\alpha\beta}(t,t). \tag{228}$$

the number of particles in state $|\alpha\rangle$ (distribution function) is

$$n_\alpha(t) = \left\langle c^\dagger_\alpha(t) c_\alpha(t) \right\rangle = -iG^<_{\alpha\alpha}(t,t), \tag{229}$$

the tunneling current is

$$\begin{aligned} J(t) &= \frac{ie}{\hbar} \sum_{kq} \left[V_{qk} \left\langle c^\dagger_q(t) c_k(t) \right\rangle - V^*_{qk} \left\langle c^\dagger_k(t) c_q(t) \right\rangle \right] \\ &= \frac{2e}{\hbar} \mathrm{Re} \left(\sum_{kq} V_{qk} G^<_{kq}(t,t) \right). \end{aligned} \tag{230}$$

In addition to the lesser the other (greater) function is used

$$G^>_{\alpha\beta}(t_1,t_2) = -i \left\langle c_\alpha(t_1) c^\dagger_\beta(t_2) \right\rangle. \tag{231}$$

For bosons lesser and greater functions are defined as

$$\tilde{G}^<_{\alpha\beta}(t_1,t_2) = -i \left\langle a^\dagger_\beta(t_2) a_\alpha(t_1) \right\rangle, \tag{232}$$

$$\tilde{G}^>_{\alpha\beta}(t_1,t_2) = -i \left\langle a_\alpha(t_1) a^\dagger_\beta(t_2) \right\rangle. \tag{233}$$

The name "lesser" originates from the time-ordered Green function, the main function in equilibrium theory, which can be calculated by diagrammatic technique

$$G_{\alpha\beta}(t_1,t_2) = -i \left\langle T \left(c_\alpha(t_1) c^\dagger_\beta(t_2) \right) \right\rangle, \tag{234}$$

$$G_{\alpha\beta}(t_1,t_2) = \begin{cases} -i \left\langle c_\alpha(t_1) c^\dagger_\beta(t_2) \right\rangle \text{ if } \quad t_1 > t_2 \Rightarrow \quad G_{\alpha\beta} \equiv G^>_{\alpha\beta}, \\ i \left\langle c^\dagger_\beta(t_2) c_\alpha(t_1) \right\rangle \quad \text{if } \quad t_1 < t_2 \Rightarrow \quad G_{\alpha\beta} \equiv G^<_{\alpha\beta}, \end{cases} \tag{235}$$

here additional sing minus appears for interchanging of fermionic creation-annihilation operators. Lesser means that $t_1 < t_2$.

From the definitions it is clear that the retarded function can be combined from lesser and greater functions

$$G^R_{\alpha\beta}(t_1,t_2) = \theta(t_1 - t_2) \left[G^>_{\alpha\beta}(t_1,t_2) - G^<_{\alpha\beta}(t_1,t_2) \right]. \tag{236}$$

(ii) Free-particle lesser function for fermions

Now let us consider again free fermions. Heisenberg operators for free fermions are ($t_0 = 0$)

$$c_\alpha(t) = e^{-i\epsilon_\alpha t} c_\alpha(0), \quad c_\alpha^\dagger(t) = e^{i\epsilon_\alpha t} c_\alpha^\dagger(0). \tag{237}$$

Lesser function is

$$\begin{aligned} G^<_{\alpha\beta}(t_1, t_2) =& i \left\langle c_\beta^\dagger(t_2) c_\alpha(t_1) \right\rangle = i e^{i\epsilon_\beta t_2 - i\epsilon_\alpha t_1} \left\langle c_\beta^\dagger c_\alpha \right\rangle \\ &= i e^{-i\epsilon_\alpha (t_1 - t_2)} f^0(\epsilon_\alpha) \delta_{\alpha\beta}, \end{aligned} \tag{238}$$

one sees that contrary to the retarded function, the lesser function is proportional to the distribution function, in equilibrium this is Fermi distribution function

$$f^0(\epsilon) = \frac{1}{e^{\frac{\epsilon - \mu}{T}} + 1}. \tag{239}$$

It is interesting to compare this answer with the result for *nonthermal* initial conditions. Assume that initial state is described by the density matrix $\rho^0_{\alpha\beta} = \left\langle c_\beta^\dagger c_\alpha \right\rangle$, now with nonzero off-diagonal elements. Time dependence of the density matrix is given by

$$\rho_{\alpha\beta}(t) = e^{i(\epsilon_\beta - \epsilon_\alpha)t} \rho^0_{\alpha\beta}. \tag{240}$$

We obtain the well known result that off-diagonal elements oscillate in time.

Now define Fourier-transform for lesser function ($\tau = t_1 - t_2$)

$$G^<(\epsilon) = \int_{-\infty}^{\infty} G^<(\tau) e^{i[\epsilon + i0\mathrm{sign}(\tau)]\tau} d\tau, \tag{241}$$

note that here we use Fourier-transform with complicated term $i0\mathrm{sign}(\tau)$, which makes this transformation consistent with previously introduced transformations (217) for retarded ($\tau > 0$) and (220) advanced ($\tau < 0$) functions.

Applying this transformation to (238) we obtain

$$\begin{aligned} G^<_{\alpha\beta}(\epsilon) =& i f^0(\epsilon_\alpha) \delta_{\alpha\beta} \int_{-\infty}^{\infty} e^{+i[\epsilon - \epsilon_\alpha + i0\mathrm{sign}(\tau)]\tau} d\tau \\ &= 2\pi i f^0(\epsilon_\alpha) \delta(\epsilon - \epsilon_\alpha) \delta_{\alpha\beta}. \end{aligned} \tag{242}$$

For free fermion greater functions one obtains

$$G^>_{\alpha\beta}(t_1, t_2) = -i e^{-i\epsilon_\alpha (t_1 - t_2)} (1 - f^0(\epsilon_\alpha)) \delta_{\alpha\beta}, \tag{243}$$

$$G^>_{\alpha\beta}(\epsilon) = -2\pi i (1 - f^0(\epsilon_\alpha)) \delta(\epsilon - \epsilon_\alpha) \delta_{\alpha\beta}. \tag{244}$$

(iii) Equilibrium case. Fluctuation-dissipation theorem

Now we want to consider some general properties of interacting systems. In equilibrium the lesser function is not independent and is simply related to the spectral function by the relation

$$G^{<}_{\alpha\beta}(\epsilon) = iA_{\alpha\beta}(\epsilon)f^0(\epsilon). \tag{245}$$

This relation is important because establish equilibrium initial condition for nonequilibrium lesser function, and propose useful Ansatz if equilibrium distribution function $f^0(\epsilon)$ is replaced by some unknown nonequilibrium function.

Here we prove this relation using *Lehmann representation* – quite useful method in the theory of Green functions. The idea of the method is to use exact many-particle eigenstates $|n\rangle$, even if they are not explicitly known.

Consider first the greater function. Using states $|n\rangle$ we represent this function as

$$G^{>}_{\alpha\beta}(t_1,t_2) = -i\left\langle c_\alpha(t_1)c^\dagger_\beta(t_2)\right\rangle = -\frac{i}{Z}\sum_n \left\langle n\left|e^{-\hat{H}/T}c_\alpha(t_1)c^\dagger_\beta(t_2)\right|n\right\rangle =$$

$$= -\frac{i}{Z}\sum_{nm} e^{-E_n/T}\langle n|c_\alpha|m\rangle\langle m|c^\dagger_\beta|n\rangle e^{i(E_n-E_m)(t_1-t_2)}. \tag{246}$$

In Fourie representation

$$G^{>}_{\alpha\beta}(\epsilon) = -\frac{2\pi i}{Z}\sum_{nm} e^{-E_n/T}\langle n|c_\alpha|m\rangle\langle m|c^\dagger_\beta|n\rangle\delta(E_n-E_m+\epsilon). \tag{247}$$

Similarly, for the lesser function we find

$$G^{<}_{\alpha\beta}(\epsilon) = \frac{2\pi i}{Z}\sum_{nm} e^{-E_m/T}\langle n|c^\dagger_\beta|m\rangle\langle m|c_\alpha|n\rangle\delta(E_m-E_n+\epsilon). \tag{248}$$

Now we can use these expressions to obtain some general properties of Green functions without explicit calculation of the matrix elements. Exchanging indices n and m in the expression (248) and taking into account that $E_m = E_n - \epsilon$ because of delta-function, we see that

$$G^{>}_{\alpha\beta}(\epsilon) = -e^{-\epsilon/T}G^{<}_{\alpha\beta}(\epsilon). \tag{249}$$

From this expression and relation (236), which can be written as

$$A_{\alpha\beta}(\epsilon) = i\left[G^{>}_{\alpha\beta}(\epsilon) - G^{<}_{\alpha\beta}(\epsilon)\right] \tag{250}$$

we derive (245).

Interaction representation

In the previous lectures we found that nonequilibrium Green functions can be quite easy calculated for free particles, and equations of motion for one-particle Green functions (the functions which are the averages of two creation-annihilation operators) can be formulated if we add interactions and time-dependent perturbations, but these equations include high-order Green functions (the averages of three, four, and larger number of operators). The equations can be truncated and formulated in terms of one-particle Green functions in some simple approximations. However, a systematic approach is needed to proceed with perturbation expansion and self-consistent methods (all together is known as *diagrammatic approach*). The main idea of the diagrammatic approach is to start from some "simple" Hamiltonian (usually for free particles) and, treating interactions and external fields as a perturbation, formulate perturbation expansion, and summarize all most important terms (diagrams) *in all orders of perturbation theory*. The result of such procedure gives, in principle, a *nonperturbative* description (ordinary mean-field theory is the simplest example). The starting point of the method is so-called *interaction representation*.

Let us consider the full Hamiltonian $\hat{H}$ as the sum of a *free-particle* time-independent part $\hat{H}_0$ and (possibly time-dependent) perturbation $\hat{V}(t)$ (note that this "perturbation" should not be necessarily small)

$$\hat{H} = \hat{H}_0 + \hat{V}(t). \tag{251}$$

We define new operators in *interaction representation* by

$$\hat{f}^I(t) = e^{i\hat{H}_0 t} \hat{f}^S e^{-i\hat{H}_0 t}, \tag{252}$$

where $\hat{f}^S$ is the time-independent Schrödinger operator. This is equivalent to the time-dependent Heisenberg operator, defined by the part $\hat{H}_0$ of the Hamiltonian. For a free-particle Hamiltonian $\hat{H}_0$ the operators $\hat{f}^I(t)$ can be calculated exactly.

A new wave function corresponding to (252) is

$$\Psi^I(t) = e^{i\hat{H}_0 t} \Psi^S(t). \tag{253}$$

It is easy to see that transformation (252), (253) is unitary transformation and conserves the average value of any operator

$$\langle \Psi^S | \hat{f}^S | \Psi^S \rangle = \langle \Psi^I | \hat{f}^I | \Psi^I \rangle. \tag{254}$$

Substituting (253) into the ordinary Schrödinger equation, we derive the equation

$$i \frac{\partial \Psi^I}{\partial t} = \hat{V}^I(t) \Psi^I, \tag{255}$$

where $\hat{V}^I(t) = e^{i\hat{H}_0 t}\hat{V}^S(t)e^{-i\hat{H}_0 t}$ is in the intreraction representation.

Equation (255) seems to be quite simple, however the operator nature of $\hat{V}$ makes this problem nontrivial. Indeed, consider a small time-step Δt. Then

$$\Psi(t+\Delta t) = \left[1 - i\hat{V}^S(t)\Delta t\right]\Psi(t) = \exp^{-i\hat{V}^S(t)\Delta t}\Psi(t), \tag{256}$$

linear in Δt term can be transformed into the exponent if we understand the exponential function of the operator in the usual way

$$\exp^{\hat{A}} = 1 + \hat{A} + \frac{1}{2!}\hat{A}^2 + ... + \frac{1}{n!}\hat{A}^n + ..., \tag{257}$$

and assume that only linear term should be taken at $\Delta t \to 0$.

If we now repeat this procedure at times t_i with step Δt, we obtain finally

$$\Psi^I(t) = \hat{S}(t,t_0)\Psi^I(t_0), \tag{258}$$

with

$$\hat{S}(t,t_0) = \prod_{t_i=t_0}^{t} \exp\left(-i\hat{V}^I(t_i)\Delta t\right), \tag{259}$$

this product, however, is not simply $\exp\left(-i\int_{t_0}^{t}\hat{V}^I(t')dt'\right)$ in the limit $\Delta t \to 0$, because operators $\hat{V}^I(t')$ are not commutative at different times, and for two noncommutative operators $\hat{A}$ and $\hat{B}$ $e^{\hat{A}+\hat{B}} \neq e^{\hat{A}}e^{\hat{B}}$.

In the product (259) operators at earlier times should be applied first, before operators at later times. In the limit $\Delta t \to 0$ we obtain

$$\hat{S}(t,t_0) = T\exp\left(-i\int_{t_0}^{t}\hat{V}^I(t')dt'\right), \tag{260}$$

where T is the time-ordering operator ("-" for fermionic operators)

$$T\left(\hat{A}(t_1)\hat{B}(t_2)\right) = \begin{cases} \hat{A}(t_1)\hat{B}(t_2) & \text{if} \quad t_1 > t_2, \\ \pm\hat{B}(t_2)\hat{A}(t_1) & \text{if} \quad t_1 < t_2. \end{cases} \tag{261}$$

Of cause, expression (260) is defined only in the sense of expansion (257). Consider for example the second-order term in the time-ordered expansion.

$$T\left[\int_{t_0}^{t}\hat{V}^I(t')dt'\right]^2 = T\left[\int_{t_0}^{t}\hat{V}^I(t')dt'\int_{t_0}^{t}\hat{V}^I(t'')dt''\right] =$$
$$= \int_{t_0}^{t}dt'\int_{t_0}^{t'}dt''\hat{V}^I(t')\hat{V}^I(t'') + \int_{t_0}^{t}dt''\int_{t_0}^{t''}dt'\hat{V}^I(t'')\hat{V}^I(t'). \tag{262}$$

If we exchange t' and t'' in the second integral, we see finally that

$$T\left[\int_{t_0}^{t}\hat{V}^I(t')dt'\right]^2 = 2\int_{t_0}^{t}dt'\int_{t_0}^{t'}dt''\hat{V}^I(t')\hat{V}^I(t''). \tag{263}$$

(i) Properties of $\hat{S}(t, t_0)$

$\hat{S}$ is the unitary operator and

$$\hat{S}^{-1}(t, t_0) = \hat{S}^{\dagger}(t, t_0) = \tilde{T} \exp\left(i \int_{t_0}^{t} \hat{V}^I(t') dt' \right), \tag{264}$$

where $\tilde{T}$ is time-anti-ordering operator. Some other important properties are

$$\hat{S}^{-1}(t, t_0) = \hat{S}(t_0, t), \tag{265}$$

$$\hat{S}(t_3, t_2)\hat{S}(t_2, t_1) = \hat{S}(t_3, t_1), \tag{266}$$

$$\hat{S}^{-1}(t_2, t_1)\hat{S}^{-1}(t_3, t_2) = \hat{S}^{-1}(t_3, t_1). \tag{267}$$

Finally, we need the expression of a Heisenberg operator, defined by the full Hamiltonian $\hat{H} = \hat{H}_0 + \hat{V}(t)$, through an operator in the interaction representation. The transformation, corresponding to (258), is given by

$$\hat{f}^H(t) = e^{-i\hat{H}_0 t_0} \hat{S}^{-1}(t, t_0) \hat{f}^I(t) \hat{S}(t, t_0) e^{i\hat{H}_0 t_0}, \tag{268}$$

and the state $\Psi^I(t_0)$ is related to the Heisenberg time-independent wave function by

$$\Psi^I(t_0) \equiv e^{i\hat{H}_0 t_0} \Psi^S(t_0) = e^{i\hat{H}_0 t_0} \Psi^H, \tag{269}$$

in accordance with our previous discussion of averaging we assume that at time $t = t_0$ Heisenberg operators coincide with time-independent Schrödinger operators $\hat{f}^H(t_0) = \hat{f}^S$, and Schrödinger wave function coincides at the same time with Heisenberg time-independent wave function $\Psi^S(t_0) = \Psi^H$. To avoid these additional exponents in (268) we can redefine the transformation to the interaction representation as

$$\hat{f}^I(t) = e^{i\hat{H}_0(t-t_0)} \hat{f}^S e^{-i\hat{H}_0(t-t_0)}, \tag{270}$$

in accordance with the transformation (206) for time-independent Hamiltonian. Previously we showed that free-particle Green functions are not dependent on t_0 for equilibrium initial condition, if we want to consider some nontrivial initial conditions, it is easier to formulate these conditions directly for Green functions. Thus below we shall use relations

$$\hat{f}^H(t) = \hat{S}^{-1}(t, t_0) \hat{f}^I(t) \hat{S}(t, t_0), \tag{271}$$

and

$$\Psi^I(t_0) \equiv \Psi^S(t_0) = \Psi^H. \tag{272}$$

(ii) Green functions in the interaction representation

Consider, for example, the lesser function

$$G^{<}_{\alpha\beta}(t_1,t_2) = i\left\langle c^{\dagger}_{\beta}(t_2)c_{\alpha}(t_1)\right\rangle = i\left\langle \Psi^H \left| c^{\dagger}_{\beta}(t_2)c_{\alpha}(t_1)\right| \Psi^H\right\rangle, \tag{273}$$

c-operators here are Heisenberg operators and they should be replaced by operators $c^I(t) \equiv \tilde{c}(t)$ in the interaction representation:

$$G^{<}_{\alpha\beta}(t_1,t_2) = i\left\langle \Psi^H \left| \hat{S}^{-1}(t_2,t_0)\tilde{c}^{\dagger}_{\beta}(t_2)\hat{S}(t_2,t_0)\hat{S}^{-1}(t_1,t_0)\tilde{c}_{\alpha}(t_1)\hat{S}(t_1,t_0)\right| \Psi^H\right\rangle. \tag{274}$$

Using properties of $\hat{S}$ operators, we rewrite this expression as

$$G^{<}_{\alpha\beta}(t_1,t_2) = i\left\langle \hat{S}(t_0,t_2)\tilde{c}^{\dagger}_{\beta}(t_2)\hat{S}(t_2,t_1)\tilde{c}_{\alpha}(t_1)\hat{S}(t_1,t_0)\right\rangle. \tag{275}$$

Schwinger-Keldysh time contour and contour functions

(i) Closed time-path integration

Now let us introduce one useful trick, so-called *closed time-path contour of integration*. First, note that the expression of the type

$$\hat{f}^H(t) = \hat{S}^{-1}(t,t_0)\hat{f}^I(t)\hat{S}(t,t_0) = \tilde{T}e^{i\int_{t_0}^{t}\hat{V}^I(t')dt'}\hat{f}^I(t)Te^{-i\int_{t_0}^{t}\hat{V}^I(t')dt'}, \tag{276}$$

can be written as

$$\hat{f}^H(t) = T_{C_t}\exp\left(-i\int_{C_t}\hat{V}^I(t')dt'\right)\hat{f}^I(t), \tag{277}$$

where the integral is taken along closed time contour from t_0 to t and then back from t to t_0

$$\int_{C_t}dt' = \int_{t_0}^{t}dt' + \int_{t}^{t_0}dt', \tag{278}$$

contour time-ordering operator T_{C_t} works along the contour C_t, it means that for times $t^{\rightarrow}$ it is usual time-ordering operator T, and for times $t^{\leftarrow}$ it is anti-time-ordering operator $\tilde{T}$. Symbolically

$$T_{C_t}\int_{C_t}dt' = T\int_{\rightarrow}dt' + \tilde{T}\int_{\leftarrow}dt'. \tag{279}$$

Consider now the application of this closed time-path contour to calculation of Green functions. It is convenient to start from the time-ordered function at $t_2 > t_1$

$$\left\langle T\left(\hat{B}(t_2)\hat{A}(t_1)\right)\right\rangle = \left\langle \hat{S}(t_0,t_2)\tilde{B}(t_2)\hat{S}(t_2,t_1)\tilde{A}(t_1)\hat{S}(t_1,t_0)\right\rangle, \tag{280}$$

here $\hat{A}(t)$ and $\hat{B}(t)$ are Heisenberg operators, $\tilde{A}(t)$ and $\tilde{B}(t)$ are operators in the interaction representation, in the case of fermionic operators the additional minus should be added for any permutation of two operators.

Using the properties of the $\hat{S}$-operator, we transform this expression as

$$\begin{aligned}\left\langle \hat{S}(t_0,t_2)\tilde{B}(t_2)\hat{S}(t_2,t_1)\tilde{A}(t_1)\hat{S}(t_1,t_0)\right\rangle \\ &= \left\langle \hat{S}^{-1}(t_2,t_0)\tilde{B}(t_2)\hat{S}(t_2,t_1)\tilde{A}(t_1)\hat{S}(t_1,t_0)\right\rangle \\ &= \left\langle \hat{S}^{-1}(\infty,t_0)\hat{S}(\infty,t_2)\tilde{B}(t_2)\hat{S}(t_2,t_1)\tilde{A}(t_1)\hat{S}(t_1,t_0)\right\rangle \\ &= \left\langle \hat{S}^{-1}T\left(\tilde{B}(t_2)\tilde{A}(t_1)\hat{S}\right)\right\rangle, \end{aligned} \tag{281}$$

where we defined operator

$$\hat{S} = \hat{S}(\infty, t_0). \tag{282}$$

Using contour integration, it can be written as

$$\left\langle T\left(\hat{B}(t_2)\hat{A}(t_1)\right)\right\rangle = \left\langle T_C\left(\hat{S}_C\tilde{B}(t_2^{\rightarrow})\tilde{A}(t_1^{\rightarrow})\right)\right\rangle, \tag{283}$$

$$\hat{S}_C = T_C \exp\left(-i\int_C \hat{V}^I(t')dt'\right), \tag{284}$$

contour C goes from t_0 trough t_1 and t_2, and back to t_0. If $t_2 > t_1$ it is obvious that contour ordering along $C^{\rightarrow}$ gives the terms from $\hat{S}(t_1,t_0)$ to $\hat{B}(t_2)$ in (280). The integral over the back path $C^{\leftarrow}$ gives

$$\begin{aligned} T_C \exp\left(-i\int_{\leftarrow} \hat{V}^I(t')dt'\right) = \tilde{T}\exp\left(-i\int_{t_2}^{t_0}\hat{V}^I(t')dt'\right) = \\ = \tilde{T}\exp\left(i\int_{t_0}^{t_2}\hat{V}^I(t')dt'\right) = \hat{S}^{-1}(t_2,t_0) = \hat{S}(t_0,t_2). \end{aligned} \tag{285}$$

For $t_2 < t_1$ the operators in (280) are reordered by T-operator and we again obtain (283).

The lesser and greater functions are not time-ordered and arguments of the operators are not affected by time-ordering operator. Nevertheless we can write such functions in the same form (283). The trick is to use one time argument from the forward contour and the other from the backward contour, for example

$$\left\langle \hat{B}(t_2)\hat{A}(t_1)\right\rangle = \left\langle T_C\left(\hat{S}_C\tilde{B}(t_2^{\leftarrow})\tilde{A}(t_1^{\rightarrow})\right)\right\rangle, \tag{286}$$

here the time t_1 is always before t_2.

(ii) Contour (contour-ordered) Green function

Now we are able to define *contour* or *contour-ordered* Green function – the useful tool of Keldysh diagrammatic technique. The definition is similar to the previous one

$$G^C_{\alpha\beta}(\tau_1,\tau_2) = -i\left\langle T_C\left(c_\alpha(\tau_1)c^\dagger_\beta(\tau_2)\right)\right\rangle, \tag{287}$$

where, however, τ_1 and τ_2 are contour times. This function includes all nonequilibrium Green functions introduced before. Indeed, depending on contour position of times we obtain lesser, greater, or time-ordered functions (below we give different notations used in the literature)

$$G^C_{\alpha\beta}(\tau_1,\tau_2) = \begin{cases} \tau_1,\tau_2 \in C^{\rightarrow}: & -i\left\langle Tc_\alpha(t_1)c^\dagger_\beta(t_2)\right\rangle \Longrightarrow \; G^{--} \; or \; G^T(t_1,t_2), \\ \tau_1 \in C^{\leftarrow}, \tau_2 \in C^{\rightarrow}: & -i\left\langle c_\alpha(t_1)c^\dagger_\beta(t_2)\right\rangle \Longrightarrow \; G^{+-} \; or \; G^{>}(t_1,t_2), \\ \tau_1 \in C^{\rightarrow}, \tau_2 \in C^{\leftarrow}: & i\left\langle c^\dagger_\beta(t_2)c_\alpha(t_1)\right\rangle \Longrightarrow \; G^{-+} \; or \; G^{<}(t_1,t_2), \\ \tau_1,\tau_2 \in C^{\leftarrow}: & -i\left\langle \tilde{T}c_\alpha(t_1)c^\dagger_\beta(t_2)\right\rangle \Longrightarrow \; G^{++} \; or \; G^{\tilde{T}}(t_1,t_2). \end{cases} \tag{288}$$

These four functions are not independent, from definitions it follows that

$$G^< + G^> = G^T + G^{\tilde{T}}, \tag{289}$$

and anti-hermitian relations

$$G^T_{\alpha\beta}(t_1,t_2) = -{G^T}^*_{\beta\alpha}(t_2,t_1), \tag{290}$$

$$G^<_{\alpha\beta}(t_1,t_2) = -{G^<}^*_{\beta\alpha}(t_2,t_1), \tag{291}$$

$$G^>_{\alpha\beta}(t_1,t_2) = -{G^>}^*_{\beta\alpha}(t_2,t_1). \tag{292}$$

It is more convenient to use retarded and advanced functions instead of time-ordered functions. There is a number of ways to express G^R and G^A through above defined functions

$$G^R = \theta(t_1-t_2)\left[G^> - G^<\right] = G^T - G^< = G^> - G^{\tilde{T}}, \tag{293}$$

$$G^A = \theta(t_2-t_1)\left[G^< - G^>\right] = G^T - G^> = G^< - G^{\tilde{T}}. \tag{294}$$

(iii) Contour Green function in the interaction representation

In the interaction representation one should repeat the calculations performed before and given the expressions (275), (280), and then replace usual times by contour times τ, so we obtain

$$\left\langle T_C\left(c_\alpha(\tau_1)c^\dagger_\beta(\tau_2)\right)\right\rangle = \left\langle T_C\left(\hat{S}(\tau_0,\tau_2)\tilde{c}^\dagger_\beta(\tau_2)\hat{S}(\tau_2,\tau_1)\tilde{c}_\alpha(\tau_1)\hat{S}(\tau_1,\tau_0)\right)\right\rangle. \tag{295}$$

Using contour integration, it can be written as

$$G^C_{\alpha\beta}(\tau_1,\tau_2) = -i\left\langle T_C\left(c_\alpha(\tau_1)c^\dagger_\beta(\tau_2)\right)\right\rangle = -i\left\langle T_C\left(\hat{S}_C\tilde{c}_\alpha(\tau_1)\tilde{c}^\dagger_\beta(\tau_2)\right)\right\rangle, \tag{296}$$

$$\hat{S}_C = T_C\exp\left(-i\int_C \hat{V}^I(t')dt'\right). \tag{297}$$

3.3 Current through a nanosystem: Meir-Wingreen-Jauho formula

Now we consider the central point of the NGF transport theory through nanosystems - the Meir-Wingreen-Jauho current formula [66,81,83]. This important expression shows that the current can be calculated, if the spectral and kinetic Green functions of the central system are known, and it is exact in the case of noninteracting leads. The details of the derivation can be found in the above cited papers, so we only briefly outline it.

(i) Derivation by the NGF method

In the absence of interactions in the leads (besides the tunneling) one can derive the following exact expression for the lead-system function:

$$G^<_{\alpha,ik\sigma}(\epsilon) = \sum_\beta V^*_{ik\sigma,\beta}\left[G^R_{\alpha\beta}(\epsilon)g^<_{ik\sigma}(\epsilon) + G^<_{\alpha\beta}(\epsilon)g^A_{ik\sigma}(\epsilon)\right], \tag{298}$$

where $g^<_{ik\sigma}(\epsilon)$ and $g^A_{ik\sigma}(\epsilon)$ are Green functions of *isolated* leads, Substituting it into (198), we obtain for the current

$$J_i(t) = \frac{2e}{\hbar}\int\frac{d\epsilon}{2\pi}\mathrm{Re}\left[\sum_{k\sigma,\alpha\beta} V_{ik\sigma,\alpha}V^*_{ik\sigma,\beta}\left[G^R_{\alpha\beta}(\epsilon)g^<_{ik\sigma}(\epsilon) + G^<_{\alpha\beta}(\epsilon)g^A_{ik\sigma}(\epsilon)\right]\right]. \tag{299}$$

For equilibrium right or left lead Green functions we obtain directly

$$g^<_{k\sigma}(t_1-t_2) = i\left\langle c^\dagger_{k\sigma}(t_2)c_{k\sigma}(t_1)\right\rangle = if^0_\sigma(\epsilon_{k\sigma})e^{-i(\epsilon_{k\sigma}+e\varphi)(t_1-t_2)}, \tag{300}$$

$$\begin{aligned} g^R_{k\sigma}(t_1-t_2) &= -i\theta(t_1-t_2)\left\langle\left[c_{k\sigma}(t_1),c^\dagger_{k\sigma}(t_2)\right]_+\right\rangle \\ &\quad + -i\theta(t_1-t_2)e^{-i(\epsilon_{k\sigma}+e\varphi)(t_1-t_2)}, \end{aligned} \tag{301}$$

$$\begin{aligned} g^A_{k\sigma}(t_1-t_2) &= i\theta(t_2-t_1)\left\langle\left[c_{k\sigma}(t_1),c^\dagger_{k\sigma}(t_2)\right]_+\right\rangle \\ &\quad + i\theta(t_2-t_1)e^{-i(\epsilon_{k\sigma}+e\varphi)(t_1-t_2)}, \end{aligned} \tag{302}$$

or after the Fourier transform

$$g^{<}_{k\sigma}(\epsilon) = \int g^{<}_{k\sigma}(t_1 - t_2) e^{i\epsilon(t_1-t_2)} d(t_1 - t_2) = 2\pi i f^0_\sigma(\epsilon_{k\sigma})\delta(\epsilon - \epsilon_{k\sigma} - e\varphi), \tag{303}$$

$$g^{>}_{k\sigma}(\epsilon) = -2\pi i[1 - f^0_\sigma(\epsilon_{k\sigma})]\delta(\epsilon - \epsilon_{k\sigma} - e\varphi), \tag{304}$$

$$g^{R}_{k\sigma}(\epsilon) = \frac{1}{\epsilon - \epsilon_{k\sigma} - e\varphi + i0}, \tag{305}$$

$$g^{A}_{k\sigma}(\epsilon) = \frac{1}{\epsilon - \epsilon_{k\sigma} - e\varphi - i0}, \tag{306}$$

$$f^0_\sigma(\epsilon) = \frac{1}{\exp\left(\frac{\epsilon-\mu_\sigma}{T}\right) + 1}. \tag{307}$$

Using the level-width function (below without *spin polarization* of the leads)

$$\begin{aligned} \Gamma_{i=L(R)}(\epsilon) \equiv \Gamma_{i\alpha\beta}(\epsilon) &= 2\pi \sum_{k\sigma} V_{ik\sigma,\beta} V^*_{ik\sigma,\alpha} \delta(\epsilon - \epsilon_{ik\sigma}) \\ &= 2\pi \sum_{\sigma} \rho_{i\sigma}(\epsilon) V_{i\sigma,\beta}(\epsilon) V^*_{i\sigma,\alpha}(\epsilon), \end{aligned} \tag{308}$$

and changing the momentum summation to the energy integration $\sum_k \Rightarrow \int \rho(\epsilon_k) d\epsilon_k$, we obtain the following expression for the current

$$J_{i=L,R} = \frac{ie}{\hbar} \int \frac{d\epsilon}{2\pi} \mathrm{Tr}\left\{ \Gamma_i(\epsilon - e\varphi_i) \left(\boldsymbol{G}^{<}(\epsilon) + f^0_i(\epsilon - e\varphi_i) \left[\boldsymbol{G}^{R}(\epsilon) - \boldsymbol{G}^{A}(\epsilon) \right] \right) \right\}, \tag{309}$$

where f^0_i is the equilibrium Fermi distribution function with chemical potential μ_i. Thus, we obtain the well-known Meir-Wingreen formula. Note, that we use explicitly the electrical potential of the leads in this expression. It is important to mention, that at finite voltage the arguments of the left and right level-width functions are changed in a different way, which means, in particular, that the known condition of proportional coupling $\Gamma_L = \lambda \Gamma_R$ can be fulfilled only in the wide-band limit, when both functions are energy independent.

(ii) Different forms of the MWJ formula

In a stationary state $J_R = -J_L = J$ and one can use the symmetric form

$$\begin{aligned} J = \frac{ie}{2\hbar} \int \frac{d\epsilon}{2\pi} \mathrm{Tr} \Big\{ \Big[\Gamma_L(\epsilon - e\varphi_L) - \Gamma_R(\epsilon - e\varphi_R) \Big] \boldsymbol{G}^{<}(\epsilon) + \\ + \Big[\Gamma_L(\epsilon - e\varphi_L) f^0_L(\epsilon - e\varphi_L) - \Gamma_R(\epsilon - e\varphi_R) f^0_R(\epsilon - e\varphi_R) \Big] \Big[\boldsymbol{G}^{R}(\epsilon) - \boldsymbol{G}^{A}(\epsilon) \Big] \Big\}. \end{aligned} \tag{310}$$

For the proportional coupling $\Gamma_L(\epsilon) = \lambda\Gamma_R(\epsilon)$ in *linear response* (φ_i dependence of Γ_i is ignored!)

$$J = \frac{2e}{\hbar}\int \frac{d\epsilon}{4\pi}\left[f_L^0(\epsilon - e\varphi_L) - f_R^0(\epsilon - e\varphi_R)\right]\mathrm{Tr}\left(\frac{\Gamma_L(\epsilon)\Gamma_R(\epsilon)}{\Gamma_L(\epsilon)+\Gamma_R(\epsilon)}\boldsymbol{A}(\epsilon)\right). \quad (311)$$

$\boldsymbol{A} = i(\boldsymbol{G}^R - \boldsymbol{G}^A)$ is the spectral function. This expression is valid for *nonlinear response* if the energy dependence of Γ can be neglected (wide band limit).

(iii) Noninteracting case

Finally, in the noninteracting case it is possible to obtain the usual Landauer-Büttikier formula with the transmission function

$$T(\epsilon) = \mathrm{Tr}\left[\Gamma_L(\epsilon - e\varphi_L)\boldsymbol{G}^R(\epsilon)\Gamma_R(\epsilon - e\varphi_R)\boldsymbol{G}^A(\epsilon)\right]. \quad (312)$$

This expression is equivalent to the one derived earlier by the single-particle Green function method.

We should stress once more that this formula is valid for finite voltage. Therefore, the voltage dependence of the level-width functions is important.

3.4 Nonequilibrium equation of motion method

Now we start to consider the case of interacting nanosystems. Although the MWJ current formula is exact, the problem to find the Green functions of the central region is sometimes highly nontrivial. At the present time there are several techniques developed to solve this problem.

Nonequilibrium equation of motion (NEOM) method is the simplest approximate approach. In spite of its simplicity, it is very useful in many cases, and is very convenient for numerical implementation. In this section we consider only a general formulation, some particular examples are considered further.

We start from the general definition of a Green function as the average of two Heisenberg operators $\hat{A}(t)$ and $\hat{B}(t)$, denoted as

$$\left\langle\!\left\langle \hat{A}(t_1), \hat{B}(t_2)\right\rangle\!\right\rangle^{R,A,<}.$$

The particular definitions of the averages for spectral and kinetic functions are

$$\left\langle\!\left\langle \hat{A}(t_1), \hat{B}(t_2)\right\rangle\!\right\rangle^{R} = -i\theta(t_1 - t_2)\left\langle\left[\hat{A}(t_1), \hat{B}(t_2)\right]_{\mp}\right\rangle, \quad (313)$$

where upper sign here and below is for boson functions, lower sign for fermions,

$$\left\langle\!\left\langle \hat{A}(t_1), \hat{B}(t_2)\right\rangle\!\right\rangle^{<} = -i\left\langle \hat{A}(t_1), \hat{B}(t_2)\right\rangle. \quad (314)$$

The equations of motion for NGF are obtained from the Heisenberg equation of motion for operators

$$i\frac{\partial \hat{A}}{\partial t} = \left[\hat{A}, \hat{H}\right]_- = \hat{A}\hat{H} - \hat{H}\hat{A}, \tag{315}$$

for any Heisenberg operator $\hat{A}(t)$. Here and below all Hamiltonians are *time-independent*. We consider the *stationary problem*.

(i) Spectral (retarded and advanced) functions

Let us start from a retarded function

$$\left\langle\!\left\langle \hat{A}(t_1), \hat{B}(t_2) \right\rangle\!\right\rangle^R = -i\theta(t_1 - t_2)\left\langle \left[\hat{A}(t_1), \hat{B}(t_2)\right]_\mp \right\rangle. \tag{316}$$

Taking the time derivative we obtain

$$i\frac{\partial}{\partial t_1}\left\langle\!\left\langle \hat{A}(t_1), \hat{B}(t_2) \right\rangle\!\right\rangle^R = \delta(t_1 - t_2)\left\langle \left[\hat{A}(t_1), \hat{B}(t_1)\right]_\mp \right\rangle + \left\langle\!\left\langle \left[\hat{A}(t_1), \hat{H}\right]_-, \hat{B}(t_2) \right\rangle\!\right\rangle^R \tag{317}$$

where the first term originates from the time-derivative of the θ-function, and the equation (315) is used in the second term.

In the stationary case the Fourier transform can be used

$$(\epsilon + i\eta)\left\langle\!\left\langle \hat{A}, \hat{B} \right\rangle\!\right\rangle^R_\epsilon = \left\langle \left[\hat{A}, \hat{B}\right]_\mp \right\rangle + \left\langle\!\left\langle \left[\hat{A}, \hat{H}\right]_-, \hat{B} \right\rangle\!\right\rangle^R_\epsilon. \tag{318}$$

Now let us assume that the Hamiltonian can be divided into "free particle" and "interaction" parts $\hat{H} = \hat{H}_0 + \hat{H}_1$, and $[\hat{A}, \hat{H}_0]_- = \hat{\epsilon}_0\hat{A}$. (The simple example. For the free particle Hamiltonian $\hat{H}_0 = \sum_\beta \epsilon_\beta d^\dagger_\beta d_\beta$ and the operator $\hat{A} = d^\dagger_\alpha$ one has $[\hat{A}, \hat{H}_0]_- = \sum_\beta \epsilon_\beta [d^\dagger_\alpha, d^\dagger_\beta d_\beta]_- = \epsilon_\alpha d^\dagger_\alpha$, $\hat{\epsilon}_0 = \epsilon_\alpha$ is simply a number. In general, $\hat{\epsilon}_0$ is some time-independent operator). So that

$$(\epsilon + i\eta - \hat{\epsilon}_0)\left\langle\!\left\langle \hat{A}, \hat{B} \right\rangle\!\right\rangle^R_\epsilon = \left\langle \left[\hat{A}, \hat{B}\right]_\mp \right\rangle + \left\langle\!\left\langle \left[\hat{A}, \hat{H}_1\right]_-, \hat{B} \right\rangle\!\right\rangle^R_\epsilon, \tag{319}$$

the second term includes interaction and can not be easy simplified.

It is convenient now to introduce the "free particle" function $\hat{g}^R_\epsilon$ as a solution of the equation

$$(\epsilon + i\eta - \hat{\epsilon}_0)\hat{g}^R_\epsilon = 1. \tag{320}$$

Now we multiply the right and left parts of (319) by $\hat{g}^R_\epsilon$. Using the function $\hat{g}^R(t) = \int \hat{g}^R_\epsilon e^{-i\epsilon t}\frac{d\epsilon}{2\pi}$ we can write the time-dependent solution of (317) as

$$\left\langle\!\left\langle \hat{A}(t_1), \hat{B}(t_2) \right\rangle\!\right\rangle^R = \hat{g}^R(t_1 - t_2)\left\langle \left[\hat{A}(t_1), \hat{B}(t_1)\right]_\mp \right\rangle + \int \hat{g}^R(t_1 - t')\left\langle\!\left\langle \left[\hat{A}(t'), \hat{H}_1\right]_-, \hat{B}(t_2) \right\rangle\!\right\rangle^R dt'. \tag{321}$$

(ii) EOM on the Schwinger-Keldysh contour

The calculation of the lesser functions by the EOM technique requires some care. To demonstrate it let us compare the EOM for retarded and lesser functions of free particles.

The equation for $g^R_{\alpha\beta}$ is (assuming the diagonal matrix $\tilde{\epsilon}_{\alpha\beta}$)

$$(\epsilon + i\eta - \tilde{\epsilon}_\alpha)\, g^R_{\alpha\beta} = \delta_{\alpha\beta}, \tag{322}$$

from which the free-particle Green function is easily obtained.

At the same time for the lesser function we have the equation

$$(\epsilon - \tilde{\epsilon}_\alpha)\, g^<_{\alpha\beta} = 0, \tag{323}$$

from which, however, the free-particle lesser function $g^<_{\alpha\beta} = 2\pi f_0(\epsilon)\delta(\epsilon - \epsilon_\alpha)\delta_{\alpha\beta}$ can not be obtained.

The problem can be generally resolved by using the EOM on the Schwinger-Keldysh time contour. Contour-ordered Green function is defined as

$$\left\langle\!\!\left\langle \hat{A}(\tau_1), \hat{B}(\tau_2) \right\rangle\!\!\right\rangle^C = -i\left\langle T_c\Big(\hat{A}(\tau_1), \hat{B}(\tau_2)\Big)\right\rangle, \tag{324}$$

where $\hat{A}(\tau_1)$ and $\hat{B}(\tau_2)$ are two Heisenberg operators, defined along the contour.

Taking the time derivative we obtain the equation

$$\begin{aligned} i\frac{\partial}{\partial\tau_1}\left\langle\!\!\left\langle \hat{A}(\tau_1), \hat{B}(\tau_2) \right\rangle\!\!\right\rangle^C &= \delta^c(\tau_1 - \tau_2)\left\langle \Big[\hat{A}(\tau_1), \hat{B}(\tau_1)\Big]_\mp \right\rangle \\ &\quad + \left\langle\!\!\left\langle \Big[\hat{A}(\tau_1), \hat{H}\Big]_-, \hat{B}(\tau_2) \right\rangle\!\!\right\rangle^C, \end{aligned} \tag{325}$$

in the stationary case this equation can be formally solved if one applies the Fourier transform along the contour, or perturbation expansion in the interaction representation (Niu et al. 1999). Using the free particle solution $\hat{g}^C(\tau_1 - \tau_2)$ we can write the time-dependent solution as

$$\begin{aligned} \left\langle\!\!\left\langle \hat{A}(\tau_1), \hat{B}(\tau_2) \right\rangle\!\!\right\rangle^C &= \hat{g}^C(\tau_1 - \tau_2)\left\langle \Big[\hat{A}(\tau_1), \hat{B}(\tau_1)\Big]_\mp \right\rangle \\ &\quad + \int \hat{g}^C(\tau_1 - \tau')\left\langle\!\!\left\langle \Big[\hat{A}(\tau'), \hat{H}_1\Big]_-, \hat{B}(\tau_2) \right\rangle\!\!\right\rangle^C d\tau'. \end{aligned} \tag{326}$$

(iii) Kinetic (lesser) function

Applying now the Langreth rules (see the next section for details), which shows, that from

$$C(\tau_1, \tau_2) = \int_C A(\tau_1, \tau_3) B(\tau_3, \tau_2) d\tau_3 \tag{327}$$

it follows

$$C^R(t_1,t_2) = \int A^R(t_1,t_3)B^R(t_3,t_2)dt_3, \tag{328}$$

$$C^<(t_1,t_2) = \int \left(A^R(t_1,t_3)B^R(t_3,t_2) + A^<(t_1,t_3)B^A(t_3,t_2)\right) dt_3, \tag{329}$$

we get (321) for the retarded function, and

$$\begin{aligned}\left\langle\!\left\langle \hat{A}(t_1), \hat{B}(t_2)\right\rangle\!\right\rangle^< &= \hat{g}^<(t_1-t_2)\left\langle \left[\hat{A}(t_1), \hat{B}(t_1)\right]_\mp \right\rangle \\ &+ \int \hat{g}^R(t_1-t')\left\langle\!\left\langle \left[\hat{A}(t'), \hat{H}_1\right]_-, \hat{B}(t_2)\right\rangle\!\right\rangle^< dt' \\ &+ \int \hat{g}^<(t_1-t')\left\langle\!\left\langle \left[\hat{A}(t'), \hat{H}_1\right]_-, \hat{B}(t_2)\right\rangle\!\right\rangle^A dt'\end{aligned} \tag{330}$$

for the lesser function. And the Fourier transform is

$$\left\langle\!\left\langle \hat{A}, \hat{B}\right\rangle\!\right\rangle_\epsilon^< = \hat{g}_\epsilon^<\left\langle \left[\hat{A}, \hat{B}\right]_\mp \right\rangle + \hat{g}_\epsilon^R\left\langle\!\left\langle \left[\hat{A}, \hat{H}_1\right]_-, \hat{B}\right\rangle\!\right\rangle_\epsilon^< + \hat{g}_\epsilon^<\left\langle\!\left\langle \left[\hat{A}, \hat{H}_1\right]_-, \hat{B}\right\rangle\!\right\rangle_\epsilon^A. \tag{331}$$

3.5 Kadanoff-Baym-Keldysh method

Now we review briefly the other approach. Kadanoff-Baym-Keldysh (KBK) method systematically extends the equilibrium many-body theory to the nonequilibrium case. Potentially, it is the most powerful approach. Below we give a simple introduction into the method, which is currently actively developed.

(i) Perturbation expansion and diagrammatic rules for contour functions

We found that Green functions can be written in the interaction representation with a help of the $\hat{S}$-operator. For example, time-ordered fermionic Green function is

$$G^T_{\alpha\beta}(t_1,t_2) = -i\left\langle T\left(c_\alpha(t_1)c^\dagger_\beta(t_2)\right)\right\rangle = -i\left\langle \hat{S}^{-1}T\left(\tilde{c}_\alpha(t_1)\tilde{c}^\dagger_\beta(t_2)\hat{S}\right)\right\rangle, \tag{332}$$

using "usual" $\hat{S}$-operator

$$\hat{S} = \hat{S}(\infty,t_0) = T\exp\left(-i\int_{t_0}^{\infty}\hat{V}^I(t')dt'\right), \tag{333}$$

or

$$G^T_{\alpha\beta}(t_1,t_2) = -i\left\langle T_C\left(\tilde{c}_\alpha(t_1^{\rightarrow})\tilde{c}^\dagger_\beta(t_2^{\rightarrow})\hat{S}_C\right)\right\rangle, \tag{334}$$

using "contour" $\hat{S}_C$-operator

$$\hat{S}_C = T_C\exp\left(-i\int_C\hat{V}^I(t')dt'\right). \tag{335}$$

We first consider the zero temperature case, when one can set $t_0 = -\infty$,

$$\hat{S} = \hat{S}(\infty, -\infty) = T \exp\left(-i \int_{-\infty}^{\infty} \hat{V}^I(t')dt'\right), \tag{336}$$

and assume that interaction is switched on and switched off at $t \to +\infty$ *adiabatically*. This condition is necessary to prevent excitation of the system from its ground state. The other necessary condition is that the perturbation is time-independent in the Schrödinger representation. In this case if the initial state $|\Psi(t = -\infty)\rangle = |\Psi_0\rangle$ is the ground state (of free particles), then the final state $|\Psi(t = +\infty)\rangle = \hat{S}|\Psi^0\rangle = e^{i\theta}|\Psi^0\rangle$ is also the ground state, only the phase can be changed. Now, using the average value of the $\hat{S}$-operator

$$\langle \hat{S} \rangle = \langle \Psi^0 | \hat{S} | \Psi^0 \rangle = e^{i\theta} \langle \Psi^0 | \Psi^0 \rangle = e^{i\theta}, \tag{337}$$

we obtain

$$\hat{S}|\Psi^0\rangle = \langle \hat{S} \rangle |\Psi^0\rangle, \tag{338}$$

and

$$\langle \Psi^0 | \hat{S}^{-1} = \frac{\langle \Psi^0 |}{\langle \hat{S} \rangle}. \tag{339}$$

So that (332) can be written as

$$G^T_{\alpha\beta}(t_1, t_2) = -i \frac{\left\langle T\left(\tilde{c}_\alpha(t_1)\tilde{c}^\dagger_\beta(t_2)\hat{S}\right)\right\rangle}{\langle \hat{S} \rangle}. \tag{340}$$

Now we can expand the exponent (note that S-operator is defined only in the sense of this expansion)

$$\begin{aligned} \hat{S} &= T \exp\left(-i \int_{-\infty}^{\infty} \hat{V}^I(t')dt'\right) \\ &= T \sum_{n=0}^{\infty} \frac{(-i)^n}{n!} \int_{-\infty}^{\infty} dt'_1 ... \int_{-\infty}^{\infty} dt'_n \; \hat{V}^I(t'_1)...\hat{V}^I(t'_n), \end{aligned} \tag{341}$$

and numerator and denominator of the expression (340) are

$$\begin{aligned} &\left\langle T\left(\tilde{c}_\alpha(t_1)\tilde{c}^\dagger_\beta(t_2)\hat{S}\right)\right\rangle \\ &\quad = \sum_{n=0}^{\infty} \frac{(-i)^n}{n!} \int_{-\infty}^{\infty} dt'_1 ... \int_{-\infty}^{\infty} dt'_n \left\langle T\tilde{c}_\alpha(t_1)\tilde{c}^\dagger_\beta(t_2)\hat{V}^I(t'_1)...\hat{V}^I(t'_n)\right\rangle, \end{aligned} \tag{342}$$

$$\langle \hat{S} \rangle = \sum_{n=0}^{\infty} \frac{(-i)^n}{n!} \int_{-\infty}^{\infty} dt'_1 ... \int_{-\infty}^{\infty} dt'_n \left\langle T\hat{V}^I(t'_1)...\hat{V}^I(t'_n)\right\rangle. \tag{343}$$

These expressions are used to produce the perturbation series.

The main quantity to be calculated is the contour Green function

$$G(1,2) \equiv G^C_{\alpha\beta}(\tau_1,\tau_2) = -i\left\langle T_C\left(c_\alpha(\tau_1)c^\dagger_\beta(\tau_2)\right)\right\rangle, \tag{344}$$

where τ_1 and τ_2 are contour times. Here $1_c \equiv \alpha, \tau_1$.

The general diagrammatic rules for contour Green functions are exactly the same as in the usual zero-temperature technique (we call it standard rules). The correspondence between diagrams and analytical expressions is established in the following way.

1. Open bare electron line is $iG_0(1,2)$.
2. Closed bare electron line is $n_0(1) \equiv n^{(0)}_\alpha(\tau_1)$.
3. Bare interaction line is $-iv(1,2)$.
4. Self-energy is $-i\Sigma(1,2)$.
5. Integration over internal vertices, and other standard rules.

(ii) Langreth rules

Although the basic equations and diagrammatic rules are formulated for contour Green functions, the solution of these equation and final results are much more transparent when represented by real-time spectral and kinetic functions.

As in the ordinary diagrammatic technique, the important role is played by the integration (summation) over space and contour-time arguments of Green functions, which is denoted as

$$\int d1_c \equiv \sum_\alpha \int_C d\tau_1. \tag{345}$$

After application of the Langreth rules, for real-time functions these integrals become

$$\int d1 \equiv \sum_\alpha \int_{-\infty}^{\infty} dt_1. \tag{346}$$

The Langreth rules show, for example, that from

$$C(\tau_1,\tau_2) = \int_C A(\tau_1,\tau_3)B(\tau_3,\tau_2)d\tau_3 \tag{347}$$

it follows

$$C^R(t_1,t_2) = \int A^R(t_1,t_3)B^R(t_3,t_2)dt_3, \tag{348}$$

$$C^<(t_1,t_2) = \int \big(A^R(t_1,t_3)B^<(t_3,t_2) + A^<(t_1,t_3)B^A(t_3,t_2)\big)dt_3. \tag{349}$$

The other important rules are: from

$$C(\tau_1, \tau_2) = A(\tau_1, \tau_2)B(\tau_1, \tau_2) \tag{350}$$

it follows

$$\begin{aligned} C^R(t_1, t_2) &= A^R(t_1, t_2)B^R(t_1, t_2) \\ &\quad + A^R(t_1, t_2)B^<(t_1, t_2) + A^<(t_1, t_2)B^R(t_1, t_2), \qquad (351) \\ C^<(t_1, t_2) &= A^<(t_1, t_2)B^<(t_1, t_2), \qquad (352) \end{aligned}$$

and from

$$C(\tau_1, \tau_2) = A(\tau_1, \tau_2)B(\tau_2, \tau_1) \tag{353}$$

it follows

$$\begin{aligned} C^R(t_1, t_2) &= A^R(t_1, t_2)B^<(t_2, t_1) + A^<(t_1, t_2)B^A(t_2, t_1), \qquad (354) \\ C^<(t_1, t_2) &= A^<(t_1, t_2)B^>(t_2, t_1). \qquad (355) \end{aligned}$$

(iii) First-order self-energy and polarization operator

Consider, as an example, the first order expression for the self-energy, shown in Fig. 15. Following the diagrammatic rules, we find

$$\Sigma_1(1, 2) = \delta(1 - 2) \int v(1, 3)n_0(3)d3 + iv(1, 2)G_0(1, 2), \tag{356}$$

where the first term is the Hartree contribution, which can be included into the unperturbed Green function $G_0(1, 2)$. This expression is actually symbolic, and translation from contour (Keldysh-time) to real-time functions is necessary. Using the Langreth rules, one obtains

$$\begin{aligned} \Sigma_1^R(1, 2) =& \delta(1^+ - 2) \int v^R(1, 3)n_0(3, 3)d3 + iv^R(1, 2)G_0^R(1, 2) \\ &+ iv^<(1, 2)G_0^R(1, 2) + iv^R(1, 2)G_0^<(1, 2), \qquad (357) \\ \Sigma_1^<(1, 2) &= iv^<(1, 2)G_0^<(1, 2). \qquad (358) \end{aligned}$$

There is no Hartree term for lesser function, because the times τ_1 and τ_2 are always at the different branches of the Keldysh contour, and the δ-function $\delta(\tau_1 - \tau_2)$ is zero.

In the stationary case and using explicit matrix indices, we have, finally ($\tau = t_1 - t_2$!, not to mix with the Keldysh time)

$$\begin{aligned} \Sigma_{\alpha\beta}^{R(1)}(\tau) &= \delta(\tau^+)\delta_{\alpha\beta} \textstyle\sum_\gamma \tilde{v}_{\alpha\gamma}^R(0)n_\gamma^{(0)} \\ +iv_{\alpha\beta}^R(\tau)G_{\alpha\beta}^{R(0)}\tau) &+ iv_{\alpha\beta}^<(\tau)G_{\alpha\beta}^{R(0)}(\tau) + iv_{\alpha\beta}^R(\tau)G_{\alpha\beta}^{<(0)}(\tau), \qquad (359) \end{aligned}$$

$$\Sigma_{\alpha\beta}^{<(1)}(\tau) = iv_{\alpha\beta}^<(\tau)G_{\alpha\beta}^{<(0)}(\tau), \tag{360}$$

and we define the Fourier transform of the bare interaction

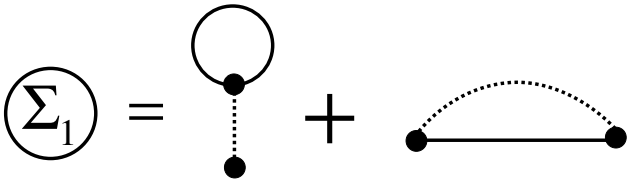

Fig. 15: Diagrammatic representation of the first-order self-energy.

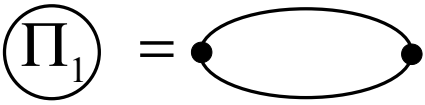

Fig. 16: Diagrammatic representation of the first-order polarization operator.

$$\tilde{v}^R_{\alpha\gamma}(0) = \int v^R_{\alpha\gamma}(\tau)d\tau. \tag{361}$$

Finally, the Fourier transforms are

$$\Sigma^{R(1)}_{\alpha\beta}(\epsilon) = \delta_{\alpha\beta}\sum_\gamma \tilde{v}^R_{\alpha\gamma}(0)n^{(0)}_\gamma$$
$$+ i\int \frac{d\epsilon'}{2\pi}\left[v^R_{\alpha\beta}(\epsilon')G^{R(0)}_{\alpha\beta}(\epsilon-\epsilon') + v^<_{\alpha\beta}(\epsilon')G^{R(0)}_{\alpha\beta}(\epsilon-\epsilon') + v^R_{\alpha\beta}(\epsilon')G^{<(0)}_{\alpha\beta}(\epsilon-\epsilon')\right], \tag{362}$$

$$\Sigma^{<(1)}_{\alpha\beta}(\epsilon) = i\int \frac{d\epsilon'}{2\pi}v^<_{\alpha\beta}(\epsilon')G^{<(0)}_{\alpha\beta}(\epsilon-\epsilon'). \tag{363}$$

The second important function is the polarization operator ("self-energy for interaction"), showing in Fig. 16. Following the diagrammatic rules, we find

$$\Pi_1(1,2) = -iG_0(1,2)G_0(2,1), \tag{364}$$

note the order of times in this expression.

Using the Langreth rules,

$$\Pi^R_1(1,2) = iG^R_0(1,2)G^<_0(2,1) + iG^<_0(1,2)G^A_0(2,1), \tag{365}$$

$$\Pi^<_1(1,2) = iG^<_0(1,2)G^>_0(2,1). \tag{366}$$

And in the stationary case, restoring the matrix indices

$$\Pi^{R(1)}_{\alpha\beta}(\epsilon) = -i\left[G^{R(0)}_{\alpha\beta}(\tau)G^{<(0)}_{\beta\alpha}(-\tau) + G^{<(0)}_{\alpha\beta}(\tau)G^{A(0)}_{\beta\alpha}(-\tau)\right], \tag{367}$$

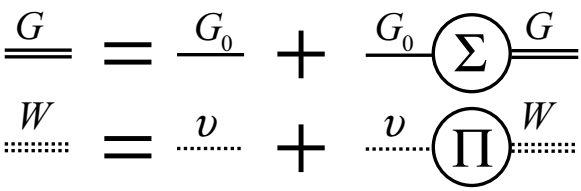

Fig. 17: Diagrammatic representation of the Dyson equations.

$$\Pi^{<(1)}_{\alpha\beta}(\epsilon) = -iG^{<(0)}_{\alpha\beta}(\tau)G^{>(0)}_{\beta\alpha}(-\tau). \tag{368}$$

In the Fourier representation

$$\Pi^{R(1)}_{\alpha\beta}(\tau) = -i\int \frac{d\epsilon'}{2\pi}\left[G^{R(0)}_{\alpha\beta}(\epsilon')G^{<(0)}_{\beta\alpha}(\epsilon'-\epsilon) + G^{<(0)}_{\alpha\beta}(\epsilon')G^{A(0)}_{\beta\alpha}(\epsilon'-\epsilon)\right], \tag{369}$$

$$\Pi^{<(1)}_{\alpha\beta}(\tau) = -i\int \frac{d\epsilon'}{2\pi}G^{<(0)}_{\alpha\beta}(\epsilon')G^{>(0)}_{\beta\alpha}(\epsilon'-\epsilon). \tag{370}$$

These expressions are quite general and can be used for both electron-electron and electron-vibron interaction.

For Coulomb interaction the bare interaction is is $v(1,2) \equiv U_{\alpha\beta}\delta(\tau_1^+ - \tau_2)$, so that

$$v^R(1,2) \equiv U_{\alpha\beta}\delta(t_1^+ - t_2), \tag{371}$$

$$v^<(1,2) = 0. \tag{372}$$

(iv) Self-consistent equations

The diagrams can be partially summed in all orders of perturbation theory. The resulting equations are known as Dyson equations for the dressed Green function $G(1,2)$ and the effective interaction $W(1,2)$ (Fig. 17). Analytically these equations are written as

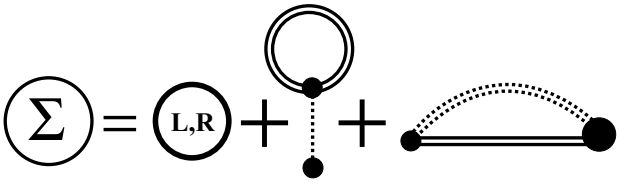

Fig. 18: Diagrammatic representation of the full self-energy.

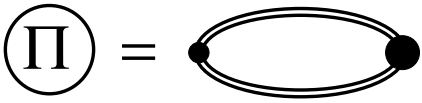

Fig. 19: Diagrammatic representation of the full polarization operator.

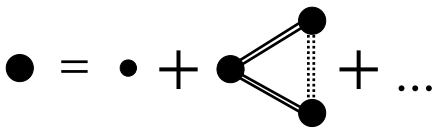

Fig. 20: Diagrammatic representation of the vertex function.

$$G(1,2) = G_0(1,2) + \int\int G_0(1,3)\Sigma(3,4)G(4,2)d3d4, \tag{373}$$

$$W(1,2) = v(1,2) + \int\int v(1,3)\Pi(3,4)W(4,2)d3d4. \tag{374}$$

In the perturbative approach the first order (or higher order) expressions for the self-energy and the polarization operator are used. The other possibility is to summarize further the diagrams and obtain the self-consistent approximations (Figs. 18,19), which include, however, a new unknown function, called vertex function. We shall write these expressions analytically, including the Hartree-Fock part into unperturbed Green function $G_0(1,2)$.

$$\Sigma'(1,2) = i\int\int W(1,3)G(1,4)\Gamma(3;4,2)d3d4, \tag{375}$$

$$\Pi(1,2) = -i\int\int G(1,3)G(4,1)\Gamma(2;3,4)d3d4. \tag{376}$$

The equation for the vertex function can not be closed diagrammatically (Fig. 20). Nevertheless, it is possible to write close set of equations (*Hedin's equations*), which are exact equations for full Green functions written through a functional derivative. Hedin's equations are equations (373)-(376) and the equation for the vertex function

$$\Gamma(1;2,3) = \delta(1,2)\delta(1,3) + \int\int\int\int G(4,6)G(7,5)\Gamma(1;6,7)\frac{\delta\Sigma(2,3)}{\delta G(4,5)}d4d5d6d7. \tag{377}$$

4 Applications

4.1 Coulomb blockade

In Section **2** we have seen that Coulomb blockade phenomena mediated by electron-electron interactions on a quantum dot can be dealt within a straightforward way by using master equation (ME) approaches, which are based on Fermi's Golden Rule. [172, 176, 180–185] However, due to its intrinsic perturbative character in the lead-dot coupling, ME techniques cannot cover the whole interaction range from weak-coupling (Coulomb blockade), intermediate coupling (Kondo physics), up to strong coupling (Fabry-Perot physics). It is thus of methodological and practical interest to develop schemes which allow, in a systematic way, to describe the three mentioned regimes also in out-of-equilibrium situations. As stated in the introduction, we believe that Green function techniques are such a tool; in this section we will show how a non-equilibrium treatment of the Hubbard-Anderson model together with appropriate approximations allow us to reproduce the well-known Coulomb blockade stability diagrams obtained with the master equation approach (see also Section **2**). For the sake of simplicity we will deal with the problem of single and double-site dots in the CB regime, although the method can be straightforwardly extended to multi-level systems. Our purpose is to study the problem of a two site donor/acceptor molecule in the CB regime within the NGF as a first step to deal with the phenomenology of a rigid multilevel island. The nuclear dynamics (vibrations) always present in molecular junctions could be then modularly included in this theory. Our method can be calibrated on the well-studied double quantum dot problem [176,192] and could be possibly integrated in the density functional theory based approaches to molecular conductance. The Kondo regime would require a separate treatment involving more complex decoupling schemes and will be thus left out of this review, for some new results see Ref. [213] (EOM method) and Refs. [224–226] (the self-consistent GW approximation).

The *linear conductance* properties of a single site junction (SSJ) with Coulomb interactions (Anderson impurity model), have been extensively studied by means of the EOM approach in the cases related to CB [203, 204] and the Kondo effect. [205] Later the same method was applied to some two-site models. [206–208, 214] Multi-level systems were started to be considered only recently. [210,211] For out-of-equilibrium situations (finite applied bias), there are some methodological unclarified issues for calculating correlation functions using EOM techniques. [212–214] We have developed an EOM-based method which allows to deal with the finite-bias case in a self-consistent way. [209]

Nonequilibrium EOM formalism

(i) The Anderson-Hubbard Hamiltonian

We consider the following model Hamiltonian (which can be called the multilevel Anderson impurity model, the Hubbard model, or the quantum cluster model)

$$\hat{H} = \sum_{\alpha\beta} \tilde{\epsilon}_{\alpha\beta} d^\dagger_\alpha d_\beta + \frac{1}{2} \sum_{\alpha\beta} U_{\alpha\beta} \hat{n}_\alpha \hat{n}_\beta + \sum_{ik\sigma} \tilde{\epsilon}_{ik\sigma} c^\dagger_{ik\sigma} c_{ik\sigma} + \sum_{ik\sigma,\alpha} \left(V_{ik\sigma,\alpha} c^\dagger_{ik\sigma} d_\alpha + h.c. \right), \tag{378}$$

electrical potentials are included into the energies $\tilde{\epsilon}_{ik\sigma} = \epsilon_{ik\sigma} + e\varphi_i(t)$ and $\tilde{\epsilon}_{\alpha\alpha} = \epsilon_{\alpha\alpha} + e\varphi_\alpha(t)$.

This model is quite universal, describing a variety of correlated electron systems coupled to the leads: the Anderson impurity model, the multilevel quantum dot with diagonal noninteracting Hamiltonian $\tilde{\epsilon}_{\alpha\beta}$, a system (cluster) of several quantum dots, when the off-diagonal matrix elements of $\tilde{\epsilon}_{\alpha\beta}$ describe hopping between individual dots, and, finally, the 1D and 2D quantum point contacts.

(ii) EOM for Heisenberg operators

Using the Hamiltonian (378) one derives

$$i\frac{\partial c_{ik\sigma}}{\partial t} = \left[c_{ik\sigma}, \hat{H} \right]_- = \tilde{\epsilon}_{ik\sigma} c_{ik\sigma} + \sum_\alpha V_{ik\sigma,\alpha} d_\alpha, \tag{379}$$

$$i\frac{\partial c^\dagger_{ik\sigma}}{\partial t} = -\tilde{\epsilon}_{ik\sigma} c^\dagger_{ik\sigma} - \sum_\alpha V^*_{ik\sigma,\alpha} d^\dagger_\alpha, \tag{380}$$

$$i\frac{\partial d_\alpha}{\partial t} = \sum_\beta \tilde{\epsilon}_{\alpha\beta} d_\beta + \sum_{\beta\neq\alpha} U_{\alpha\beta} \hat{n}_\beta d_\alpha + \sum_{ik\sigma} V^*_{ik\sigma,\alpha} c_{ik\sigma}, \tag{381}$$

$$i\frac{\partial d^\dagger_\alpha}{\partial t} = -\sum_\beta \tilde{\epsilon}_{\alpha\beta} d^\dagger_\beta - \sum_{\beta\neq\alpha} U_{\alpha\beta} \hat{n}_\beta d^\dagger_\alpha - \sum_{ik\sigma} V_{ik\sigma,\alpha} c^\dagger_{ik\sigma}, \tag{382}$$

$$i\frac{\partial \hat{n}_\gamma}{\partial t} = \sum_{ik\sigma} \left[-V_{ik\sigma,\gamma} c^\dagger_{ik\sigma} d_\gamma + V^*_{ik\sigma,\gamma} d^\dagger_\gamma c_{ik\sigma} \right] + \sum_\beta \tilde{\epsilon}_{\gamma\beta} d^\dagger_\gamma d_\beta - \sum_\alpha \tilde{\epsilon}_{\alpha\gamma} d^\dagger_\alpha d_\gamma. \tag{383}$$

These equations look like a set of ordinary differential equations, but are, in fact, much more complex. The first reason is, that there are the equations for *operators*, and special algebra should be used to solve it. Secondly, the number of $c_{ik\sigma}$ operators is infinite! Because of that, the above equations are not all sufficient, but are widely used to obtain the equations for Green functions.

(iii) Spectral (retarded and advanced) functions

Now we follow the general NEOM method described in the Section **3**. Using (381), we get the equation for $G^R_{\alpha\beta} = -i\left\langle \left[d_\alpha, d^\dagger_\beta\right]_+ \right\rangle_\epsilon$

$$(\epsilon + i\eta)G^R_{\alpha\beta} - \sum_\gamma \tilde{\epsilon}_{\alpha\gamma} G^R_{\gamma\beta} = \delta_{\alpha\beta} + \sum_{\gamma\neq\alpha} U_{\alpha\gamma} G^{(2)R}_{\alpha\gamma,\beta} + \sum_{ik\sigma} V^*_{ik\sigma,\alpha} G^R_{ik\sigma,\beta} \quad (384)$$

which includes two new functions: $G^{(2)R}_{\alpha\gamma,\beta}$ and $G^R_{ik\sigma,\beta}$.

The equation for $G^R_{ik\sigma,\beta}$ is closed (includes only the function $G^R_{\alpha\beta}$ introduced before)

$$(\epsilon + i\eta - \tilde{\epsilon}_{ik\sigma})G^R_{ik\sigma,\beta} = \sum_\delta V_{ik\sigma,\delta} G^R_{\delta\beta}. \quad (385)$$

The equation for

$$G^{(2)R}_{\alpha\gamma,\beta}(t_1 - t_2) = -i\theta(t_1 - t_2)\left\langle \left[d_\alpha(t_1)\hat{n}_\gamma(t_1), d^\dagger_\beta(t_2)\right]_+ \right\rangle$$

is more complicated

$$\begin{aligned}
&(\epsilon + i\eta)G^{(2)R}_{\alpha\gamma,\beta} - \sum_\delta \tilde{\epsilon}_{\alpha\delta} G^{(2)R}_{\delta\gamma,\beta} = n_\gamma \delta_{\alpha\beta} + (\delta_{\alpha\beta} - \rho_{\alpha\beta})\delta_{\beta\gamma} \\
&+ \sum_\delta U_{\alpha\delta} \left\langle\!\!\left\langle \hat{n}_\delta d_\alpha \hat{n}_\gamma; d^\dagger_\beta \right\rangle\!\!\right\rangle^R + \sum_{ik\sigma} V^*_{ik\sigma,\alpha} \left\langle\!\!\left\langle c_{ik\sigma} n_\gamma; d^\dagger_\beta \right\rangle\!\!\right\rangle^R + \\
&+ \sum_{ik\sigma} V^*_{ik\sigma,\gamma} \left\langle\!\!\left\langle d_\alpha d^\dagger_\gamma c_{ik\sigma}; d^\dagger_\beta \right\rangle\!\!\right\rangle^R - \sum_{ik\sigma} V_{ik\sigma,\gamma} \left\langle\!\!\left\langle d_\alpha c^\dagger_{ik\sigma} d_\gamma; d^\dagger_\beta \right\rangle\!\!\right\rangle^R \\
&+ \sum_\delta \tilde{\epsilon}_{\gamma\delta} \left\langle\!\!\left\langle d_\alpha d^\dagger_\gamma d_\delta; d^\dagger_\beta \right\rangle\!\!\right\rangle^R - \sum_\delta \tilde{\epsilon}_{\delta\gamma} \left\langle\!\!\left\langle d_\alpha d^\dagger_\delta d_\gamma; d^\dagger_\beta \right\rangle\!\!\right\rangle^R . \quad (386)
\end{aligned}$$

The equation (386) is not closed again and produces new Green functions of higher order. And so on. These sequence of equations can not be closed in the general case and should be truncated at some point. Below we consider some possible approximations. The other important point is, that average populations and lesser Green functions should be calculated self-consistently. In equilibrium (linear response) these functions are easy related to the spectral functions. But at finite voltage they should be calculated independently.

(iv) Kinetic (lesser) function

Following the same way, as for the retarded functions (using only the definitions of NGF and Heisenberg equations of motion) one derives instead of (384)-(386)

$$\epsilon G^<_{\alpha\beta} - \sum_\gamma \tilde{\epsilon}_{\alpha\gamma} G^<_{\gamma\beta} = \sum_{\gamma\neq\alpha} U_{\alpha\gamma} G^{(2)<}_{\alpha\gamma,\beta} + \sum_{ik\sigma} V^*_{ik\sigma,\alpha} G^<_{ik\sigma,\beta}, \quad (387)$$

$$(\epsilon - \tilde{\epsilon}_{ik\sigma})G^{<}_{ik\sigma,\beta} = \sum_{\delta} V_{ik\sigma,\delta} G^{<}_{\delta\beta}, \tag{388}$$

$$\begin{aligned}
\epsilon G^{(2)<}_{\alpha\gamma,\beta} - \sum_{\delta} \tilde{\epsilon}_{\alpha\delta} G^{(2)<}_{\delta\gamma,\beta} &= \sum_{\delta\neq\alpha} U_{\alpha\delta} \left\langle\!\!\left\langle \hat{n}_{\delta} d_{\alpha} \hat{n}_{\gamma}; d^{\dagger}_{\beta} \right\rangle\!\!\right\rangle^{<} + \\
+ \sum_{ik\sigma} V^{*}_{ik\sigma,\alpha} \left\langle\!\!\left\langle c_{ik\sigma} n_{\gamma}; d^{\dagger}_{\beta} \right\rangle\!\!\right\rangle^{<} &+ \sum_{ik\sigma} V^{*}_{ik\sigma,\gamma} \left\langle\!\!\left\langle d_{\alpha} d^{\dagger}_{\gamma} c_{ik\sigma}; d^{\dagger}_{\beta} \right\rangle\!\!\right\rangle^{<} \\
&- \sum_{ik\sigma} V_{ik\sigma,\gamma} \left\langle\!\!\left\langle d_{\alpha} c^{\dagger}_{ik\sigma} d_{\gamma}; d^{\dagger}_{\beta} \right\rangle\!\!\right\rangle^{<} \\
+ \sum_{\delta} \tilde{\epsilon}_{\gamma\delta} \left\langle\!\!\left\langle d_{\alpha} d^{\dagger}_{\gamma} d_{\delta}; d^{\dagger}_{\beta} \right\rangle\!\!\right\rangle^{<} &- \sum_{\delta} \tilde{\epsilon}_{\delta\gamma} \left\langle\!\!\left\langle d_{\alpha} d^{\dagger}_{\delta} d_{\gamma}; d^{\dagger}_{\beta} \right\rangle\!\!\right\rangle^{<}.
\end{aligned} \tag{389}$$

To find $G^{<}_{ik\sigma,\beta}$ we should divide the right parts by $(\epsilon - \tilde{\epsilon}_{ik\sigma})$, which is not well defined at $\epsilon = \tilde{\epsilon}_{ik\sigma}$. In the section **3** we considered the general prescription to avoid this problem, we use the equation (331), and instead of (388)we obtain

$$G^{<}_{ik\sigma,\beta} = g^{R}_{ik\sigma} \sum_{\delta} V_{ik\sigma,\delta} G^{<}_{\delta\beta} + g^{<}_{ik\sigma} \sum_{\delta} V_{ik\sigma,\delta} G^{A}_{\delta\beta}. \tag{390}$$

The equations (387) and (389) can be used without modifications because they include the imaginary parts (dissipation) from the lead terms.

At this point we stop the general consideration, and introduce a powerful *Ansatz* for the NGF which is related both to the equation-of-motion (EOM) method and to the Dyson equation approach. [209] From the knowledge of the Green functions we then calculate the transport observables. For clarity, we first describe our method in the more familiar problem of a single site junction, which is the well-known Anderson impurity model. Then we apply it to a double quantum dot. The equations obtained below by the heuristic mapping method can be obtained straightforward from the general NEOM equations derived in this section using the same approximations as in the mapping method.

Anderson impurity model (single site)

The Anderson impurity model is used to describe the Coulomb interaction on a single site:

$$H = H_{\mathrm{D}} + \sum_{\alpha} (H_{\alpha} + H_{\alpha\mathrm{D}}),$$

where

$$H_{\mathrm{D}} = \sum_{\sigma} \epsilon_{\sigma} d_{\sigma}^{\dagger} d_{\sigma} + \frac{1}{2} U n_{\sigma} n_{\bar{\sigma}},$$
$$H_{\alpha} = \sum_{k,\sigma} \epsilon_{k,\sigma}^{\alpha} c_{\alpha,k,\sigma}^{\dagger} c_{\alpha,k,\sigma},$$
$$H_{\alpha\mathrm{D}} = \sum_{k,\sigma} \left(V_{\alpha,k,\sigma} c_{\alpha,k,\sigma}^{\dagger} d_{\sigma} + V_{\alpha,k,\sigma}^{*} d_{\sigma}^{\dagger} c_{\alpha,k,\sigma} \right),$$

where d and c are the operators for electrons on the dot and on the left ($\alpha = \mathrm{L}$) and the right ($\alpha = \mathrm{R}$) lead, U is the Coulomb interaction parameter, ϵ_{σ} is the σ level of the quantum dot, while $\epsilon_{k,\sigma}^{\alpha}$ is the spin σ level of lead α in k space, $\sigma = \uparrow, \downarrow$. With the help of the EOM and the truncation approximation, we can get a closed set of equations for the retarded and advanced GFs $G_{\sigma,\tau}^{\mathrm{r/a}}$ [66,204]

$$(\omega - \epsilon_{\sigma} - \Sigma_{\sigma}^{\mathrm{r/a}}) G_{\sigma,\tau}^{\mathrm{r/a}} = \delta_{\sigma,\tau} + U G_{\sigma,\tau}^{(2)\mathrm{r/a}}, \tag{391a}$$
$$(\omega - \epsilon_{\sigma} - U - \Sigma_{\sigma}^{\mathrm{r/a}}) G_{\sigma,\tau}^{(2)\mathrm{r/a}} = \langle n_{\bar{\sigma}} \rangle \delta_{\sigma,\tau}, \tag{391b}$$

where $G_{\sigma,\tau}^{\mathrm{r/a}} = \langle\langle d_{\sigma} | d_{\tau}^{\dagger} \rangle\rangle^{\mathrm{r/a}}$, $G_{\sigma,\tau}^{(2)\mathrm{r/a}} = \langle\langle n_{\bar{\sigma}} d_{\sigma} | d_{\tau}^{\dagger} \rangle\rangle^{\mathrm{r/a}}$ and

$$\Sigma_{\sigma}^{\mathrm{r/a}}(\omega) = \Sigma_{\mathrm{L},\sigma}^{\mathrm{r/a}} + \Sigma_{\mathrm{R},\sigma}^{\mathrm{r/a}} = \sum_{\alpha,k} \frac{|V_{\alpha,k,\sigma}|^2}{\omega - \epsilon_{k,\sigma}^{\alpha} \pm \mathrm{i}0^{+}} \tag{392}$$

are the electron self-energies.

(i) Mapping on retarded Green functions

For retarded GFs, from the EOM method, and with the help of Eqs. (391a) and (391b), we can get

$$G^{\mathrm{r}} = G_0^{\mathrm{r}} + G_0^{\mathrm{r}} U G^{(2)\mathrm{r}} = G_0^{\mathrm{r}} + G_0^{\mathrm{r}} \Sigma^{\mathrm{EOM}} G^{(1)\mathrm{r}},$$

where G^{r} is single-particle GF matrix

$$G^{\mathrm{r}} = \begin{pmatrix} G_{\uparrow,\uparrow}^{\mathrm{r}} & G_{\uparrow,\downarrow}^{\mathrm{r}} \\ G_{\downarrow,\uparrow}^{\mathrm{r}} & G_{\downarrow,\downarrow}^{\mathrm{r}} \end{pmatrix},$$

and $G_{\sigma,\tau}^{(1)\mathrm{r}} = G_{\sigma,\tau}^{(2)\mathrm{r}} / \langle n_{\bar{\sigma}} \rangle$. G_0^{r} describes the single-particle spectrum without Coulomb interaction, but including the effects from the electrodes. $\Sigma_{\sigma,\tau}^{\mathrm{EOM}} = U \langle n_{\bar{\sigma}} \rangle$ is the Hartree-like self-energy of our model. Since there is only Coulomb interaction on the site with the levels ϵ_{σ}, the Fock-like self-energy is vanishing.

Alternatively, by means of the Dyson equation and the second-order truncation approximation, taking Hartree-like self-energies $\Sigma_{\sigma,\tau}^{\mathrm{H}} = U \langle n_{\bar{\sigma}} \rangle$ ($= \Sigma_{\sigma,\tau}^{\mathrm{EOM}}$), we can also get the retarded GFs as follows

$$G^{\mathrm{r}} = G_0^{\mathrm{r}} + G_0^{\mathrm{r}} \Sigma^{\mathrm{H}} G_1^{\mathrm{r}}, \tag{393}$$

where $G_1^{\rm r} = G_0^{\rm r} + G_0^{\rm r}\Sigma^{\rm H}G_0^{\rm r}$ is the first-order truncation GF.

Within the level of the second-order truncation approximation, we see that there is a map between the EOM results and the Dyson results:

$$\begin{array}{ccccc} G^{\rm r} & = & G_0^{\rm r} & + & G_0^{\rm r}\,\Sigma^{\rm H}\,G^{(1){\rm r}} \qquad \text{(EOM)}, \\ \updownarrow & & & & \updownarrow \\ G^{\rm r} & = & G_0^{\rm r} & + & G_0^{\rm r}\,\Sigma^{\rm H}\,G_1^{\rm r} \qquad \text{(Dyson)}. \end{array} \tag{394a, 394b}$$

Eqs. (394) prompts a way to include further many-particle effects into the Dyson equation, Eq. (394b), by replacing the *Dyson-first-order* retarded Green function $G_1^{\rm r}$ with the EOM $G^{(1)r}$. Then one obtains already the correct results to describe CB while keeping the Hartree-like self-energy.

(ii) Mapping on contour and lesser Green functions

Introducing now the contour GF $\check{G}$, we can get the Dyson equation as follows [66, 73, 74, 76]

$$\check{G} = \check{G}_0 + \check{G}_0\check{\Sigma}\check{G}, \tag{395}$$

where $\check{\Sigma}$ is the self-energy matrix [66].

According to the approximation for the retarded GF in Eq. (393), we take the second-order truncation on Eq. (395), and then get

$$\check{G} = \check{G}_0 + \check{G}_0\check{\Sigma}^{\rm H}\check{G}_1,$$

where $\check{G}_1 = \check{G}_0 + \check{G}_0\check{\Sigma}^{\rm H}\check{G}_0$ is the first-order contour GF, and $\check{G}_0$ has already included the lead broadening effects.

Similar to the mapping in Eq. (394), we perform an *Ansatz* consisting in substituting the *Dyson-first-order* $G_1^{\rm r/a/<}$ with the EOM one $G^{(1){\rm r/a/<}}$ to consider more many-particle correlations, while the EOM self-energy is used for the *Dyson* equation for consistency:

$$\begin{array}{lll} \check{G} = \check{G}_0 + \check{G}_0\ \check{\Sigma}^{\rm H}\ \check{G}_1 & & \text{(Dyson)}, \\ \updownarrow & \uparrow & \\ \check{G} & \check{G}^{(1)} & \text{(EOM)}. \end{array} \tag{396}$$

Then, using the Langreth theorem [66] we get the lesser GF,

$$\begin{aligned} G^{<} &= G_0^{<} + G_0^{\rm r}\Sigma^{{\rm H},{\rm r}}G^{(1)<} + G_0^{<}\Sigma^{{\rm H},{\rm a}}G^{(1){\rm a}} \\ &= G_0^{<} + G_0^{\rm r}UG^{(2)<} + G_0^{<}UG^{(2){\rm a}} \end{aligned} \tag{397}$$

where $G_0^{\rm r/a/<}$ are GFs for $U = 0$, *but* including the lead broadening effects, *i.e.*

$$\begin{aligned} G_0^{<} &= g_0^{<} + g_0^{\rm r}\Sigma^{<}G_0^{\rm a} + g_0^{<}\Sigma^{\rm a}G_0^{\rm a} + g_0^{\rm r}\Sigma^{\rm r}G_0^{<}, \\ G_0^{\rm r/a} &= g_0^{\rm r/a} + g_0^{\rm r/a}\Sigma^{\rm r/a}G_0^{\rm r/a}, \end{aligned}$$

with $g_0^{\mathrm{r/a/<}}$ the free electron GF, and

$$\Sigma^{\mathrm{r/a/<}} = \begin{pmatrix} \Sigma_{\uparrow}^{\mathrm{r/a/<}} & 0 \\ 0 & \Sigma_{\downarrow}^{\mathrm{r/a/<}} \end{pmatrix},$$

$\Sigma_\sigma^< = \mathrm{i}\sum_\alpha \Gamma_\alpha f_\alpha(\omega)$, and $\Gamma_\alpha = \mathrm{i}(\Sigma_\alpha^{\mathrm{r}} - \Sigma_\alpha^{\mathrm{a}})$, $f_\alpha(\omega) = f(\omega - \mu_\alpha)$, f is the equilibrium Fermi function and μ_α is the electro-chemical potential in lead α; $\Sigma_\alpha^{\mathrm{r/a}}$ are the retarded/advanced electron self-energies from Eq. (392) and $G_{\sigma,\tau}^{(1)\mathrm{r/a/<}} = G_{\sigma,\tau}^{(2)\mathrm{r/a/<}}/\langle n_{\bar{\sigma}}\rangle$. Performing the same *Ansatz* on the double-particle GF, from Eq. (391b) we can get

$$G^{(2)<} = G^{(2)\mathrm{r}}\Sigma^{(2)<}G^{(2)\mathrm{a}}, \tag{398}$$

with $\Sigma_\sigma^{(2)<} = \Sigma_\sigma^</\langle n_{\bar{\sigma}}\rangle$.

The lesser GFs in Eq. (397) can also be obtained directly from the general formula [66]

$$G^< = G_0^< + G_0^{\mathrm{r}}\Sigma^{\mathrm{r}}G^< + G_0^{\mathrm{r}}\Sigma^<G^{\mathrm{a}} + G_0^<\Sigma^{\mathrm{a}}G^{\mathrm{a}},$$

with the help of the *Ansatz* in Eq. (396). It should be noted that Eq. (397) is very different from the lesser GF formula,

$$G^< = G^{\mathrm{r}}\Sigma^<G^{\mathrm{a}}, \tag{399}$$

with the self-energy $\Sigma^<$ containing *only* contributions from the electrodes. The equation (399) is widely used for both first-principle [236, 255, 258] and model Hamiltonian calculations. [207]

The numerical calculation results of conductance dependence on the bias and gate voltages by the two different NGF Eqs. (397) and (399) are shown in Fig. 21. As we can see in the left panel, the adoption of Eq. (399) results in an incorrectly symmetry-breaking in the gate potential. This wrong behavior is corrected in the right panel where Eq. (397) has been used.

Note, that the expressions for the retarded and lesser functions, described above, can be obtained in a more formal way by the EOM method formulated on the Keldysh contour.

(iii) Comparison with the master equation result

In the single site model with two (spin-up and spin-down) levels it is possible to make the direct comparison between our *Ansatz* and the master equation methods. For the latter, we used the well known master equations for quantum dots [180, 181].

In the Fig. 22 the typical curves of the differential conductance as a function of the bias voltage at fixed gate voltage obtained by the two methods are shown together: there is basically no difference in the results obtained by these two methods. In the Fig. 23 the contour plot of the differential conductance

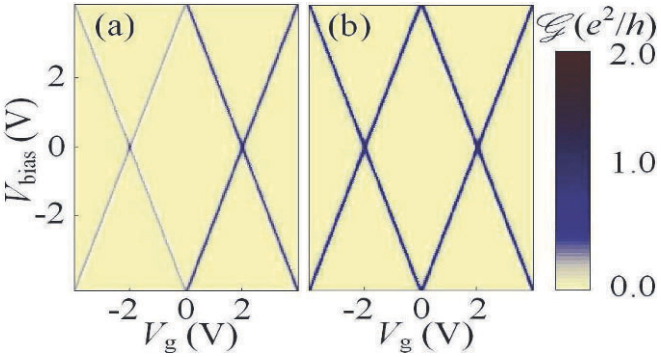

Fig. 21: Stability diagram of a SSJ with $\epsilon_\sigma = 2.0$ eV, $U = 4.0$ eV, $\Gamma_{\rm L} = \Gamma_{\rm R} = 0.05$ eV. (a) The incorrect result obtained by means of the widely used formula in Eq. (399) for the lesser GF is not symmetric for levels ϵ_σ and $\epsilon_\sigma + U$. (b) Results obtained by means of our *Ansatz* in Eq. (397) shows correctly symmetric for levels ϵ_σ and $\epsilon_\sigma + U$.

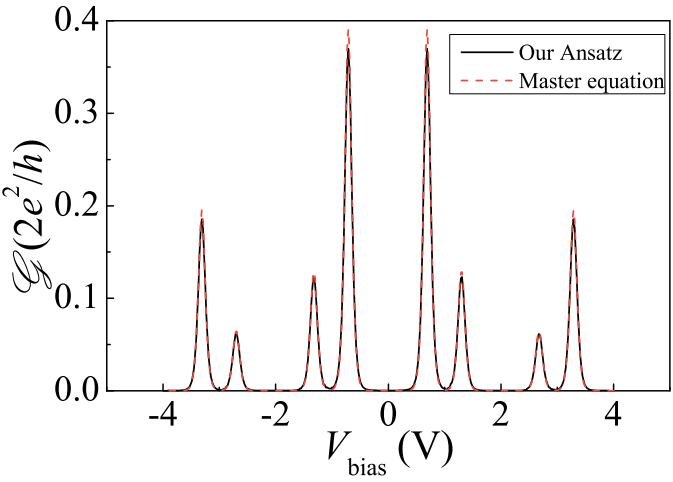

Fig. 22: The comparison of the master equation method and our *Ansatz* for the differential conductance of the two level model with $\epsilon_\uparrow = -0.35$ eV, $\epsilon_\downarrow = -0.65$ eV, $U = 1.0$ eV, $V_{\rm g} = 1.0$ V, $\Gamma_{\rm L} = \Gamma_{\rm R} = 0.05$ eV.

obtained by our *Ansatz* is shown. We do not present here the contour plot obtained by the master equation method because it looks exactly the same.

It is quite clear from the presented figures that our *Ansatz* and the master equation method give essentially the same results in the limit of weak coupling

to the leads. The systematic investigation of the deviations between the two methods at stronger tunneling will be presented in a separate publication.

It is important that our *Ansatz* can be applied straightforwardly to multilevel systems in the case when the exact eigenstates of an isolated system are unknown and the usage of the master equation method is not easy. In this paper we consider the simplest example of such a system, namely a double site case.

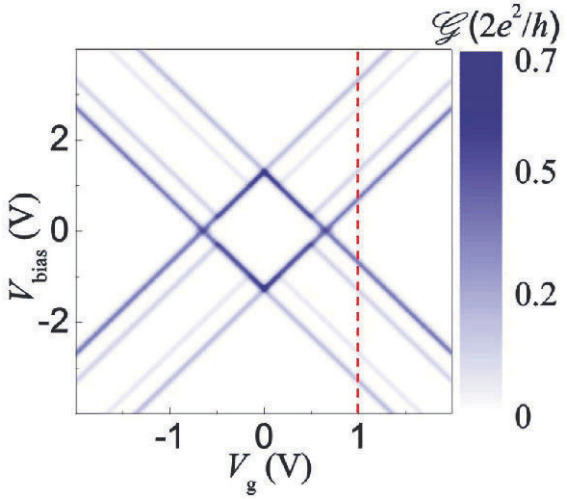

Fig. 23: Stability diagram (the contour plot of the differential conductance) calculated by our *Ansatz* for the two level model with parameters as in Fig. 22. The latter is indicated with a dash line at $V_g = 1.0$ V.

Double quantum dot (two sites)

We now return to the investigation of the DSJ system (Fig. 24) with Coulomb interaction on each site. The Hamiltonian is expressed as follows,

$$H = H_D + H_t + \sum_\alpha (H_\alpha + H_{\alpha D}),$$

where

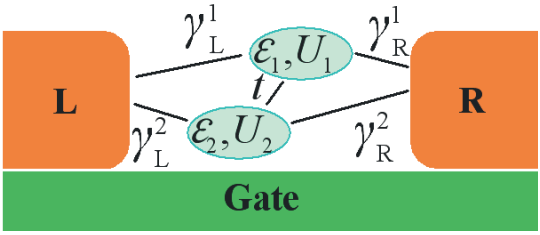

Fig. 24: The general configuration of a double site junction. The levels $\epsilon_{1,2}$ with charging energies $U_{1,2}$ are connected via t and coupled to the electrodes via the linewidth injection rates γ_α^i.

$$H_{\rm D} = \sum_{i,\sigma} \epsilon_{i,\sigma} d_{i,\sigma}^\dagger d_{i,\sigma} + \frac{U_i}{2} n_{i,\sigma} n_{i,\bar{\sigma}},$$

$$H_t = \sum_{i \neq j,\sigma} \frac{t}{2} (d_{i,\sigma}^\dagger d_{j,\sigma} + d_{j,\sigma}^\dagger d_{i,\sigma}),$$

$$H_{\alpha,\sigma} = \sum_{k,\sigma} \epsilon_{k,\sigma}^{(\alpha)} c_{\alpha,k,\sigma}^\dagger c_{\alpha,k,\sigma},$$

$$H_{\alpha{\rm D},\sigma} = \sum_{k,\sigma} \left(V_{\alpha,k,\sigma} c_{\alpha,k,\sigma}^\dagger d_{i,\sigma} + V_{\alpha,k,\sigma}^* d_{i,\sigma}^\dagger c_{\alpha,k,\sigma} \right),$$

with $i, j = 1, 2$ indicate the site, t is the constant for electron hopping between different sites.

With the help of the EOM, and by means of the truncation approximation on the double-particle GFs, we obtain the closed form for the retarded GFs as follows

$$(\omega - \epsilon_{i,\sigma} - \Sigma_{i,\sigma}^{\rm r}) G_{i,\sigma;j,\tau}^{(U,t){\rm r}} = \delta_{i,j}\delta_{\sigma,\tau} + U_i G_{i,\sigma;j,\tau}^{(2)(U,t){\rm r}} + t\, G_{i,\sigma;j,\tau}^{(U,t){\rm r}}, \tag{400a}$$

$$(\omega - \epsilon_{i,\sigma} - U_i - \Sigma_{i,\sigma}^{\rm r}) G_{i,\sigma;j,\tau}^{(2)(U,t){\rm r}} = \langle n_{i,\bar{\sigma}} \rangle \delta_{i,j}\delta_{\sigma,\tau} + t\, n_{i,\bar{\sigma}} G_{i,\sigma;j,\tau}^{(U,t){\rm r}}, \tag{400b}$$

where the DSJ retarded GFs are defined as

$$G_{i,j;\sigma,\tau}^{(U,t){\rm r}} = \langle\langle d_{i,\sigma} | d_{j,\tau}^\dagger \rangle\rangle^{\rm r}, \tag{401}$$

$$G_{i,j;\sigma,\tau}^{(2)(U,t){\rm r}} = \langle\langle n_{i,\bar{\sigma}} d_{i,\sigma} | d_{j,\tau}^\dagger \rangle\rangle^{\rm r}. \tag{402}$$

Here $\bar{i}$ means 'NOT i', and $\Sigma_{i,\sigma}^{\rm r}$ are the electron self-energy from leads.

From Eqs. (400a), (400b) and performing the same *Ansatz* as in the case of SSJ, we can obtain the DSJ lesser GFs with Coulomb-interaction effects as follows

$$G^{(U,t)<}(\omega) = (1 + G^{(U,t){\rm r}} \Sigma_t^{\rm r}) G^{(U)<} (1 + \Sigma_t^{\rm a} G^{(U,t){\rm a}}) + G^{(U,t){\rm r}} \Sigma_t^< G^{(U,t){\rm a}}, \tag{403}$$

with

$$\Sigma_t^{\mathrm{r}} = \Sigma_t^{\mathrm{a}} = \begin{pmatrix} 0 & t & 0 & 0 \\ t & 0 & 0 & 0 \\ 0 & 0 & 0 & t \\ 0 & 0 & t & 0 \end{pmatrix},$$

and $\Sigma_t^{<} = 0$. $G^{(U)<}$ is the DSJ lesser GF with the same form as Eq. (397), but taking

$$U = \begin{pmatrix} U_1 & 0 & 0 & 0 \\ 0 & U_2 & 0 & 0 \\ 0 & 0 & U_1 & 0 \\ 0 & 0 & 0 & U_2 \end{pmatrix}, \ \Gamma_\alpha = \begin{pmatrix} \gamma_\alpha^1 & 0 & 0 & 0 \\ 0 & \gamma_\alpha^2 & 0 & 0 \\ 0 & 0 & \gamma_\alpha^1 & 0 \\ 0 & 0 & 0 & \gamma_\alpha^2 \end{pmatrix}, \tag{404}$$

where γ_α^i indicates the line width function of lead α to site i, and U_i is the charging energy at site i. $G^{\mathrm{r/a}}$ and $G^{(2)\mathrm{r/a}}$ are the GF matrix from Eqs. (400a) and (400b). Here, in order to distinguish different GFs, we introduce the subscript '(U,t)' for the one with both Coulomb interaction U and inter-site hopping t, while '(U)' for the one only with Coulomb interaction.

For our models, the lesser GFs in Eq. (397), (398) and (403), which are obtained with help of our *Ansatz*, can also be obtained by the EOM NEGF formula (331) within the same truncation approximation.

The current can be generally written as [81]

$$J = \frac{\mathrm{i}e}{2\hbar} \int \frac{d\epsilon}{2\pi} \mathrm{Tr}\{(\Gamma_{\mathrm{L}} - \Gamma_{\mathrm{R}}) G^{(U,t)<} + [f_{\mathrm{L}}(\omega)\Gamma_{\mathrm{L}} - f_{\mathrm{R}}(\omega)\Gamma_{\mathrm{R}}](G^{(U,t)\mathrm{r}} - G^{(U,t)\mathrm{a}})\},$$

where the lesser GF is given by Eq. (403). The differential conductance is defined as

$$\mathcal{G} = \frac{\partial J}{\partial V_{\mathrm{bias}}},$$

where the bias voltage is defined as $V_{\mathrm{bias}} = (\mu_{\mathrm{R}} - \mu_{\mathrm{L}})/e$.

(i) Serial configuration

By taking $\gamma_L^2 = \gamma_R^1 = 0$, we obtain a serial DSJ, which could describe the kind of molecular quantum junctions like the ones studied in Ref. [18]. First, at small bias voltages, the conductance with the two gate voltages V_{g_1} and V_{g_2} was calculated, and the relative stability diagram was obtained as shown in Fig. 25. Because of the double degeneracy (spin-up and spin-down) considered for each site and electrons hopping between the dots, there are eight resonance-tunnelling regions. This result is consistent with the master-equation approach. [176]

Further, we studied the nonequilibrium current for large bias-voltages (Fig. 26). Because $\epsilon_{1,\sigma}$ and $\epsilon_{2,\sigma}$ are taken as asymmetric, for the case without Coulomb interaction, the I-V curve is asymmetric for $\pm V_{\mathrm{bias}}$, and there are one step and one maximum for the current. The step contributes to one peak for the conductance. When we introduce the Coulomb interaction to the

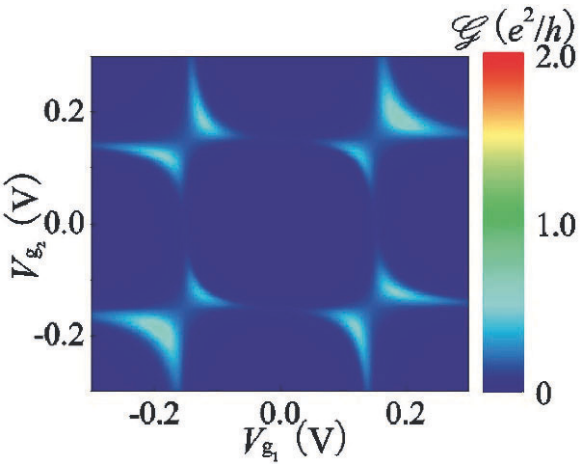

Fig. 25: Stability diagram of a serial DSJ with $\epsilon_{1,\sigma} = \epsilon_{2,\sigma} = -0.15$ eV, $U_1 = U_2 = 0.3$ eV, $t = 0.05$ eV, $\gamma_{\rm L}^1 = \gamma_{\rm R}^2 = 0.02$ eV, $\gamma_{\rm L}^2 = \gamma_{\rm R}^1 = 0$,$V_{\rm bias} = 0.005V$. The maximums of conductance are observed when the levels of the first site ($\epsilon_{1,\sigma}$ or $\epsilon_{1,\sigma} + U$) are overlapped with the levels of the second site ($\epsilon_{2,\sigma}$ or $\epsilon_{2,\sigma} + U$), and with the Fermi energy in the leads. The splitting of the four maximums is due to the hopping between the dots.

system, the one conductance peak is split into several: two peaks, one pseudo-peak and one dip, while the current maximum comes to be double split (see Fig. 26). The origin of this is in the effective splitting of the degenerate level when one of the spin states is occupied and the other is empty. When both spin states are occupied, the degeneracy is restored.

This process can be illustrated by the help of Fig. 27. At zero bias-voltage, $\epsilon_{2,\sigma}$ is occupied and $\epsilon_{1,\sigma}$ is empty. Then we start to increase the bias voltage. a) The level $\epsilon_{2,\sigma} + U$ is first opened for transport. It will contribute the first peak for conductance. b) Further, the levels $\epsilon_{2,\sigma}$ and $\epsilon_{1,\sigma}$ come into the transport window between the left and the right Fermi levels, resulting in the second peak. c) When the level $\epsilon_{1,\sigma} + U$ comes into play, only a pseudo-peak appears. This is because there is only a little possibility for electrons to occupy the level $\epsilon_{1,\sigma}$ under positive bias voltage. d) Levels $\epsilon_{2,\sigma} + U$ and $\epsilon_{1,\sigma}$ meet, which results in electron resonant-tunnelling and leads to the first maximum of the current. Then a new level $\epsilon_{1,\sigma} + U$ appears over the occupied $\epsilon_{1,\sigma}$ due to the Coulomb interaction. e) The meeting of $\epsilon_{2,\sigma}$ and $\epsilon_{1,\sigma}$ results in electron resonant tunnelling. It means that $\epsilon_{1,\sigma}$ will be occupied, which leads to the appearance of a new level $\epsilon_{1,\sigma} + U$. Then $\epsilon_{2,\sigma} + U$ meets $\epsilon_{1,\sigma} + U$ and another resonant tunnelling channel is opened for electrons. The two channels result in the second current maximum. f) finally, the level $\epsilon_{1,\sigma} + U$ disappears if the level $\epsilon_{1,\sigma}$ is empty. This means that a dip appears in the conductance.

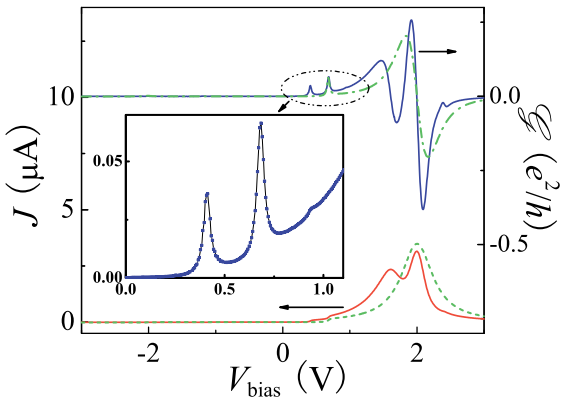

Fig. 26: Current and conductance vs. bias-voltage of a DSJ far from equilibrium with parameters $\epsilon_{1,\sigma} = 0.5$ eV, $\epsilon_{2,\sigma} = -0.5$ eV, $U_1 = U_2 = U = 0.2$ eV, $t = 0.07$ eV, $\gamma_{\rm L}^1 = \gamma_{\rm R}^2 = 0.03$ eV, $V_{\rm g_2} = -V_{\rm g_1} = V_{\rm bias}/4$ and $V_{\rm R} = -V_{\rm L} = V_{\rm bias}/2$. The red curve represents the current, while the blue the conductance. The inset is the blow-up for the conductance peak split. The dash and dot-dash curves are for current and conductance with $U = 0$, respectively.

It should be noted that the characteristics of serial DSJ in Fig. 26 have showed some reasonable similarities to experiments of a single-molecule diode. [18]

(ii) Parallel configuration

If on the other hand, the two sites are symmetrically connected to the electrodes, possibly with a small inter-dot hopping, but with charging energies U_1 and U_2 fixed to different scales for transport. The resulting stability diagram contains both interference effects for parallel pathways and an overlap of U_1 and U_2 stability diagrams, which we refer to a nesting characteristic. (see Fig. 28).

The physics of the *weak* lines in the figure can be understood by the help of charging effects. For simplicity, here we would ignore the site index i. In the region of large positive gate voltage at zero bias voltage, $\epsilon_\uparrow$ and $\epsilon_\downarrow$ are all empty, which means that the two levels are degenerate. Therefore adding a bias voltage, first, there will be two channels ($\epsilon_\uparrow$ and $\epsilon_\downarrow$) opened for current (thick lines). After then, one level ϵ_σ (spin-up or spin-down) is occupied, while the other obtains a shift for Coulomb interaction: $\epsilon_{\bar\sigma} \rightarrow \epsilon_{\bar\sigma} + U$. Therefore, when the bias voltage is further increased to make the Fermi-window boundary meeting level $\epsilon_{\bar\sigma} + U$, only one channel is opened for the current, which results

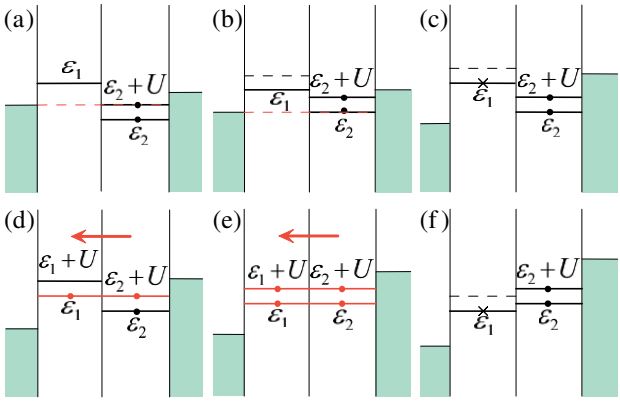

Fig. 27: Processes involved in the transport characteristics in figure 26. $\epsilon_1 \equiv \epsilon_{1,\sigma}$, $\epsilon_2 \equiv \epsilon_{2,\sigma}$, The red line indicates electron resonant-tunnelling. a) The first conductance peak. b) The second conductance peak. c) The pseudo-peak of conductance. d) The first current maximum, and the red line indicates resonant tunnelling of electrons. e) The second current maximum for electron resonant tunnelling. f) The dip of conductance.

in the *weak* lines in Fig. 28, which is the characteristic of CB. The similar case appears in the region of large negative gate voltages.

Finally, we have introduced a powerful *Ansatz* for the lesser Green function, which is consistent with both the Dyson-equation approach and the equation-of-motion approach. By using this *Ansatz* together with the standard equation-of-motion technique for the retarded and advanced Green functions, we obtained the NGF for both the single and the double site junctions in the Coulomb blockade regime *at finite voltages* and calculated the transport observables. The method can be applied to describe self-consistently transport through single molecules with strong Coulomb interaction and arbitrary coupling to the leads.

To test our method, we have analyzed the CB stability diagrams for a SSJ and a DSJ. Our results are all consistent with the results of experiments and the master-equation approach. We showed, that the improved lesser Green function gives better results for weak molecule-to-contact couplings, where a comparison with the master equation approach is possible.

For the serial configuration of a DSJ, such as a donor/acceptor rectifier, the *I*-*V* curves maintain a diode-like behavior, as it can be already inferred by coherent transport calculations. [265] Besides, we predict that as a result of charging effects, one conductance peak will be split into three peaks and one dip, and one current maximum into two. For a DSJ parallel configuration, due to different charging energies on the two dot sites, the stability diagrams show peculiar nesting characteristics.

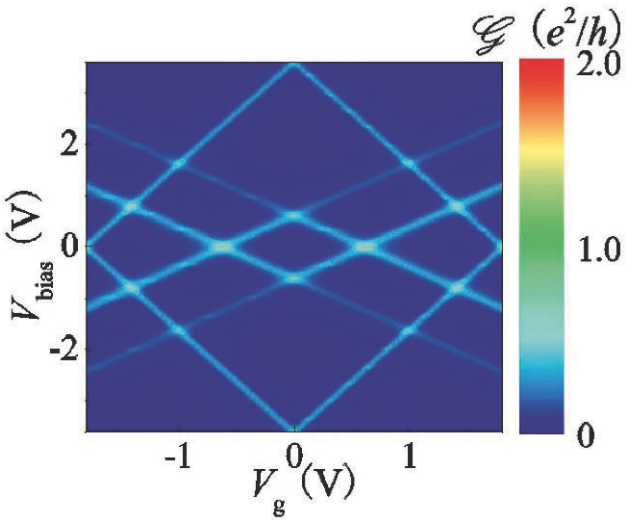

Fig. 28: Nested stability diagram of a parallel DSJ with parameters $\epsilon_{1,\sigma} = -1.8$ eV, $\epsilon_{2,\sigma} = -0.3$ eV, $U_1 = 3.6$ eV, $U_2 = 0.6$ eV $t = 0.001$ eV, $\gamma_{\rm L}^1 = \gamma_{\rm R}^1 = 0.04$ eV, $\gamma_{\rm L}^2 = \gamma_{\rm R}^2 = 0.05$ eV, $V_{\rm g_2} = V_{\rm g_1}/2 = V_{\rm g}/2$ and $V_{\rm R} = -V_{\rm L} = V_{\rm bias}/2$. See discussion in the text.

4.2 Nonequilibrium vibrons

Though the electron-vibron model described in the Section II has a long history, the many questions it implies are not answered up to now. While the isolated electron-vibron model can be solved exactly by the so-called polaron or Lang-Firsov transformation [95–97], the coupling to the leads produces a true many-body problem. The inelastic resonant tunneling of *single* electrons through the localized state coupled to phonons was first considered in Refs. [98–101]. There, the exact solution in the single-particle approximation was derived, ignoring completely the Fermi sea in the leads. At strong electron-vibron couplings and weak couplings to the leads, satellites of the main resonant peak are formed in the spectral function (Fig. 11). The number of the relevant side-bands is determined by the well known Huang-Rhys factor [292] $g = (\lambda/\omega_0)^2$. The question which remains is whether these side-bands can be observed in the differential conductance, when the coupling to all electrons in the leads should be taken into account simultaneously. New theoretical treatments were presented recently in Refs. [84, 102–109, 111, 112, 117, 118, 120–129, 132–136, 138–140, 164, 209, 274–279, 288–290].

In parallel, the theory of inelastic scanning tunneling spectroscopy was developed [113–116, 161–163]. For a recent review of the electron-vibron problem and its relation to charge transport at the molecular scale see Ref. [164]. Note the related problem of quantum shuttle [143, 145, 147, 149].

Many interesting results by the investigation of quantum transport in the strong electron-vibron coupling limit has been achieved with the help of the master equation approach [104, 106–109]. This method, however, is valid only in the limit of very weak molecule-to-lead coupling and neglects all spectral effects, which are the most important at finite coupling to the leads.

Nonequilibrium Dyson-Keldysh method

(i) The model electron-vibron Hamiltonian

We use the minimal transport model described in the previous sections. For convenience, we present the Hamiltonian here once more. The full Hamiltonian is the sum of the molecular Hamiltonian $\hat{H}_M$, the Hamiltonians of the leads $\hat{H}_{R(L)}$, the tunneling Hamiltonian $\hat{H}_T$ describing the molecule-to-lead coupling, the vibron Hamiltonian $\hat{H}_V$ including electron-vibron interaction and coupling of vibrations to the environment (describing dissipation of vibrons)

$$\hat{H} = \hat{H}_M + \hat{H}_V + \hat{H}_L + \hat{H}_R + \hat{H}_T. \tag{405}$$

A molecule is described by a set of localized states $|\alpha\rangle$ with energies ϵ_α and inter-orbital overlap integrals $t_{\alpha\beta}$ by the following model Hamiltonian:

$$\hat{H}_M^{(0)} = \sum_\alpha \left(\epsilon_\alpha + e\varphi_\alpha(t)\right) d_\alpha^\dagger d_\alpha + \sum_{\alpha\neq\beta} t_{\alpha\beta} d_\alpha^\dagger d_\beta. \tag{406}$$

Vibrations and the electron-vibron coupling are described by the Hamiltonian [120–122, 124] ($\hbar = 1$)

$$\hat{H}_V = \sum_q \omega_q a_q^\dagger a_q + \sum_{\alpha\beta}\sum_q \lambda_{\alpha\beta}^q (a_q + a_q^\dagger) d_\alpha^\dagger d_\beta. \tag{407}$$

Here vibrations are considered as localized phonons and q is an index labeling them, not the wave-vector. The first term describes free vibrons with the energy ω_q. The second term represents the electron-vibron interaction. We include both diagonal coupling, which describes a change of the electrostatic energy with the distance between atoms, and the off-diagonal coupling, which describes the dependence of the matrix elements $t_{\alpha\beta}$ over the distance between atoms.

The Hamiltonians of the right (R) and left (L) leads read

$$\hat{H}_{i=L(R)} = \sum_{k\sigma} (\epsilon_{ik\sigma} + e\varphi_i) c_{ik\sigma}^\dagger c_{ik\sigma}, \tag{408}$$

$\varphi_i(t)$ are the electrical potentials of the leads. Finally, the tunneling Hamiltonian

$$\hat{H}_T = \sum_{i=L,R}\sum_{k\sigma,\alpha} \left(V_{ik\sigma,\alpha} c_{ik\sigma}^\dagger d_\alpha + \text{h.c.} \right) \tag{409}$$

describes the hopping between the leads and the molecule. A direct hopping between two leads is neglected.

(ii) Keldysh-Dyson equations and self-energies

We use the nonequilibrium Green function (NGF) method, as introduced in Section III. The current in the left ($i = L$) or right ($i = R$) contact to the molecule is described by the expression

$$J_{i=L,R} = \frac{ie}{\hbar}\int \frac{d\epsilon}{2\pi}\mathrm{Tr}\left\{\mathbf{\Gamma}_i(\epsilon - e\varphi_i)\left(\mathbf{G}^<(\epsilon) + f_i^0(\epsilon - e\varphi_i)\left[\mathbf{G}^R(\epsilon) - \mathbf{G}^A(\epsilon)\right]\right)\right\}, \tag{410}$$

where $f_i^0(\epsilon)$ is the equilibrium Fermi distribution function with chemical potential μ_i, and the level-width function is

$$\mathbf{\Gamma}_{i=L(R)}(\epsilon) = \mathit{\Gamma}_{i\alpha\beta}(\epsilon) = 2\pi\sum_{k\sigma} V_{ik\sigma,\beta}V^*_{ik\sigma,\alpha}\delta(\epsilon - \epsilon_{ik\sigma}).$$

The lesser (retarded, advanced) Green function matrix of a nonequilibrium molecule $\mathbf{G}^{<(R,A)} \equiv G^{<(R,A)}_{\alpha\beta}$ can be found from the Dyson-Keldysh equations in the integral form

$$\mathbf{G}^R(\epsilon) = \mathbf{G}_0^R(\epsilon) + \mathbf{G}_0^R(\epsilon)\mathbf{\Sigma}^R(\epsilon)\mathbf{G}^R(\epsilon), \tag{411}$$

$$\mathbf{G}^<(\epsilon) = \mathbf{G}^R(\epsilon)\mathbf{\Sigma}^<(\epsilon)\mathbf{G}^A(\epsilon), \tag{412}$$

or from the corresponding equations in the differential form (see e.g. Refs. [123, 124] and references therein).

Here

$$\mathbf{\Sigma}^{R,<} = \mathbf{\Sigma}_L^{R,<(T)} + \mathbf{\Sigma}_R^{R,<(T)} + \mathbf{\Sigma}^{R,<(V)} \tag{413}$$

is the total self-energy of the molecule composed of the tunneling (coupling to the left and right leads) self-energies

$$\mathbf{\Sigma}^{R,<(T)}_{j=L,R} \equiv \mathit{\Sigma}^{R,<(T)}_{j\alpha\beta} = \sum_{k\sigma}\left\{V^*_{jk\sigma,\alpha}G^{R,<}_{jk\sigma}V_{jk\sigma,\beta}\right\}, \tag{414}$$

and the vibronic self-energy $\mathbf{\Sigma}^{R,<(V)} \equiv \mathit{\Sigma}^{R,<(V)}_{\alpha\beta}$.

For the retarded tunneling self-energy $\mathbf{\Sigma}_i^{R(T)}$ one obtains

$$\mathbf{\Sigma}_i^{R(T)}(\epsilon) = \mathbf{\Lambda}_i(\epsilon - e\varphi_i) - \frac{\mathrm{i}}{2}\mathbf{\Gamma}_i(\epsilon - e\varphi_i), \tag{415}$$

where $\mathbf{\Lambda}_i$ is the real part of the self-energy, which usually can be included in the single-particle Hamiltonian $\hat{H}_M^{(0)}$, and $\mathbf{\Gamma}_i$ describes level broadening due to coupling to the leads. For the corresponding lesser function one finds

$$\mathbf{\Sigma}_i^{<(T)}(\epsilon) = \mathrm{i}\mathbf{\Gamma}_i(\epsilon - e\varphi_i)f_i^0(\epsilon - e\varphi_i). \tag{416}$$

In the standard self-consistent Born approximation, using the Keldysh technique, one obtains for the vibronic self-energies [106, 117, 118, 120–122, 124, 164]

$$\mathbf{\Sigma}^{R(V)}(\epsilon) = \frac{i}{2}\sum_q \int \frac{d\omega}{2\pi}\left(\mathbf{M}^q \mathbf{G}^R_{\epsilon-\omega}\mathbf{M}^q D^K_{q\omega} + \right.$$

$$\left. + \mathbf{M}^q \mathbf{G}^K_{\epsilon-\omega}\mathbf{M}^q D^R_{q\omega} - 2D^R_{q\omega=0}\mathbf{M}^q \mathrm{Tr}\left[\mathbf{G}^<_\omega \mathbf{M}^q\right]\right), \tag{417}$$

$$\mathbf{\Sigma}^{<(V)}(\epsilon) = i\sum_q \int \frac{d\omega}{2\pi}\mathbf{M}^q \mathbf{G}^<_{\epsilon-\omega}\mathbf{M}^q D^<_{q\omega}, \tag{418}$$

where $\mathbf{G}^K = 2\mathbf{G}^< + \mathbf{G}^R - \mathbf{G}^A$ is the Keldysh Green function, and $\mathbf{M}^q \equiv M^q_{\alpha\beta}$.

If vibrons are noninteracting, in equilibrium, and non-dissipative, then the vibronic Green functions write:

$$D^R_0(q,\omega) = \frac{1}{\omega - \omega_q + \mathrm{i}0^+} - \frac{1}{\omega + \omega_q + \mathrm{i}0^+}, \tag{419}$$

$$D^<_0(q,\omega) = -2\pi\mathrm{i}\left[(f^0_B(\omega_q)+1)\delta(\omega+\omega_q) + f^0_B(\omega_q)\delta(\omega-\omega_q)\right], \tag{420}$$

where the equilibrium Bose distribution function is

$$f^0_B(\omega) = \frac{1}{\exp(\omega/T) - 1}. \tag{421}$$

In the Migdal model the retarded vibron function is calculated from the Dyson-Keldysh equation

$$D^R(q,\omega) = \frac{2\omega_q}{\omega^2 - \omega_q^2 - 2\omega_q \Pi^R(q,\omega)}, \tag{422}$$

where $\Pi(q,\omega)$ is the polarization operator (boson self-energy). The equation for the lesser function (quantum kinetic equation in the integral form) is

$$(\Pi^R_{q\omega} - \Pi^A_{q\omega})D^<_{q\omega} - (D^R_{q\omega} - D^A_{q\omega})\Pi^<_{q\omega} = 0, \tag{423}$$

this equation in the stationary case considered here is algebraic in the frequency domain.

The polarization operator is the sum of two parts, environmental and electronic: $\Pi^{R,<}_{q\omega} = \Pi^{R,<(\mathrm{env})}_{q\omega} + \Pi^{R,<(\mathrm{el})}_{q\omega}$.

The environmental equilibrium part of the polarization operator can be approximated by the simple expressions

$$\Pi^{R(\mathrm{env})}(q,\omega) = -\frac{i}{2}\gamma_q \mathrm{sign}(\omega), \tag{424}$$

$$\Pi^{<(\mathrm{env})}(q,\omega) = -i\gamma_q f^0_B(\omega)\mathrm{sign}(\omega), \tag{425}$$

where γ_g is the vibronic dissipation rate, and $f^0_B(\omega)$ is the equilibrium Bose-Einstein distribution function.

The electronic contribution to the polarization operator within the SCBA is

$$\Pi^{R(\mathrm{el})}(q,\omega) = -i\int \frac{d\epsilon}{2\pi}\mathrm{Tr}\left(\mathbf{M}^q\mathbf{G}^<_\epsilon\mathbf{M}^q\mathbf{G}^A_{\epsilon-\omega} + \mathbf{M}^q\mathbf{G}^R_\epsilon\mathbf{M}^q\mathbf{G}^<_{\epsilon-\omega}\right), \quad (426)$$

$$\Pi^{<(\mathrm{el})}(q,\omega) = -i\int \frac{d\epsilon}{2\pi}\mathrm{Tr}\left(\mathbf{M}^q\mathbf{G}^<_\epsilon\mathbf{M}^q\mathbf{G}^>_{\epsilon-\omega}\right). \quad (427)$$

We obtained the full set of equations, which can be used for numerical calculations.

Single-level model: spectroscopy of vibrons

The isolated single-level electron-vibron model is described by the Hamiltonian

$$\hat{H}_{M+V} = (\epsilon_0 + e\varphi_0)d^\dagger d + \omega_0 a^\dagger a + \lambda\left(a^\dagger + a\right)d^\dagger d, \quad (428)$$

where the first and the second terms describe the free electron state and the free vibron, and the third term is electron-vibron minimal coupling interaction.

The electrical potential of the molecule φ_0 plays an important role in transport at finite voltages. It describes the shift of the molecular level by the bias voltage, which is divided between the left lead (tip), the right lead (substrate), and the molecule as $\varphi_0 = \varphi_R + \eta(\varphi_L - \varphi_R)$ [293]. We assume the simplest linear dependence of the molecular potential ($\eta = const$), but its nonlinear dependence [294] can be easily included in our model.

Here we assume, that the vibrons are in equilibrium and are not excited by the current, so that the self-consistent Born approximation is a good starting point. The vibron Green function are assumed to be equilibrium with the broadening defined by the external thermal bath, see for details Refs. [117, 118, 120, 124, 164].

For the single-level model all equations are significantly simplified. Combining J_L and J_R the expression for the current can be written for energy independent $\Gamma_{L(R)}$ (wide-band limit) as

$$J = \frac{e}{h}\frac{\Gamma_L\Gamma_R}{\Gamma_R+\Gamma_L}\int d\epsilon A(\epsilon)\left[f^0(\epsilon - e\varphi_L) - f^0(\epsilon - e\varphi_R)\right]. \quad (429)$$

It looks as simple as the Landauer-Büttiker formula, but it is not trivial, because the spectral density $A(\epsilon) = -2\mathrm{Im}G^R(\epsilon)$ now depends on the distribution function of the electrons in the fluctuating molecule and hence the applied voltage, $\varphi_L = -\varphi_R = V/2$ [123]. Indeed, $G^R(\epsilon)$ can be found from (201)

$$G^R(\epsilon) = \frac{1}{\epsilon - \tilde{\epsilon}_0 - \Sigma^{R(V)}(\epsilon) + i(\Gamma_L+\Gamma_R)/2}, \quad (430)$$

where $\Sigma^{R(V)}(\epsilon)$ is a functional of the electron distribution function inside a molecule. Actually, the lesser function $G^<(\epsilon)$ is used in the quantum kinetic

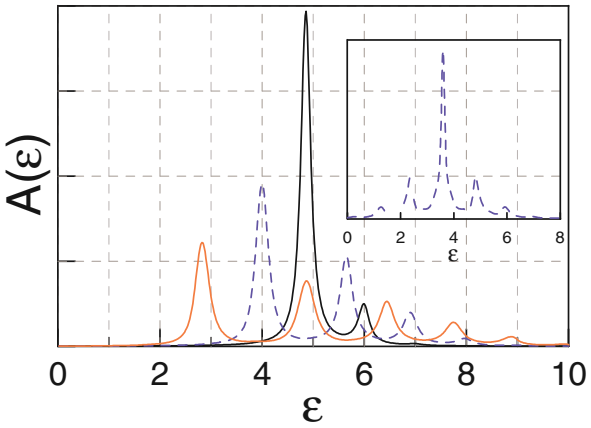

Fig. 29: Spectral function at different electron-vibron couplings: $\lambda/\omega_0 = 0.4$ (black), $\lambda/\omega_0 = 1.2$ (blue, dashed), and $\lambda/\omega_0 = 2$ (red); at $\epsilon_0/\omega_0 = 5$, $\Gamma_L/\omega_0 = \Gamma_R/\omega_0 = 0.1$. In the insert the spectral function at $\lambda/\omega_0 = 1.2$ is shown at finite voltage, when the level is partially filled. Energies are in units of $\hbar\omega_0$.

formalism as a distribution function. In the single-level case the usual distribution function can be introduced through the relation

$$G^<(\epsilon) = iA(\epsilon)f(\epsilon). \tag{431}$$

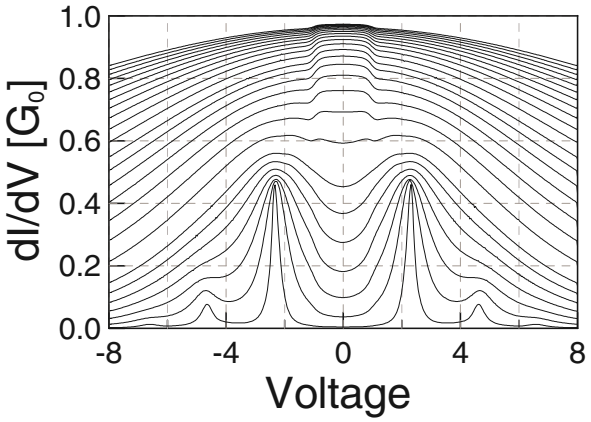

Fig. 30: Differential conductance of a *symmetric* junction ($\eta = 0.5$, $\Gamma_R = \Gamma_L$) at different molecule-to-lead coupling, from $\Gamma_L/\omega_0 = 0.1$ (lower curve) to $\Gamma_L/\omega_0 = 10$ (upper curve), $\lambda/\omega_0 = 1$, $\epsilon_0/\omega_0 = 2$. Voltage is in the units of $\hbar\omega_0/e$.

Note the essential difference between symmetric ($\Gamma_L = \Gamma_R$) and asymmetric junctions. It is clear from the noninteracting solution of the transport problem. Neglecting for a moment the vibron self-energies, we obtain the noninteracting distribution function

$$f(\epsilon) = \frac{\Gamma_L f_L^0(\epsilon - e\varphi_L) + \Gamma_R f_R^0(\epsilon - e\varphi_R)}{\Gamma_L + \Gamma_R}. \tag{432}$$

For strongly asymmetric junctions (e.g. $\Gamma_L \ll \Gamma_R$) the distribution function remains close to the equilibrium function in the right lead $f_R^0(\epsilon - e\varphi_R)$, thus essentially simplifying the solution. While for symmetric junctions the distribution function has the double-step form and is very different from the equilibrium one.

A typical example of the spectral function at zero voltage is shown in Fig. 29. At finite voltage it should be calculated self-consistently. In the insert the spectral function of the symmetric junction at finite voltage is shown, it is changed essentially because the distribution function is changed.

Let us discuss a general picture of the vibronic transport in symmetric and asymmetric single-molecule junctions, provided in experiments with the molecular bridges and STM-to-molecule junctions, respectively. The differential conductance, calculated at different molecule-to-lead coupling, is shown in Fig. 30 (symmetric) and Fig. 31 (asymmetric). At weak coupling, the vibronic side-band peaks are observed, reproducing the corresponding peaks in the spectral function. At strong couplings the broadening of the electronic state hides the side-bands, and new features become visible. In the symmetric junction, a suppression of the conductance at $V \simeq \pm\hbar\omega_0$ takes place as a result of inelastic scattering of the coherently transformed from the left lead to the right lead electrons. In the asymmetric junction (Fig. 31), the usual IETS increasing of the conductance is observed at a negative voltage $V \simeq -\hbar\omega_0$, this feature is weak and can be observed only in the incoherent tail of the resonant conductance. We conclude, that the vibronic contribution to the conductance can be distinguished clearly in both coherent and tunneling limits.

Now let us discuss the particular situation of STS experiments [32, 33, 35, 36]. Here we concentrate mainly on the dependence on the tip-to-molecule distance [33]. When the tip (left lead in our notations) is far from the molecule, the junction is strongly asymmetric: $\Gamma_L \ll \Gamma_R$ and $\eta \to 0$, and the conductance is similar to that shown in Fig. 31. When the tip is close to the molecule, the junction is approximately symmetric: $\Gamma_L \approx \Gamma_R$ and $\eta \approx 0.5$, and the conductance curve is of the type shown in Fig. 30. We calculated the transformation of the conductance from the asymmetric to symmetric case (Fig. 32). It is one new feature appeared in asymmetric case due to the fact that we started from a finite parameter $\eta = 0.2$ (in the Fig. 31 $\eta = 0$), namely a single peak at negative voltages, which is shifted to smaller voltage in the symmetric junction. The form and behavior of this peak is in agreement with experimental results [33].

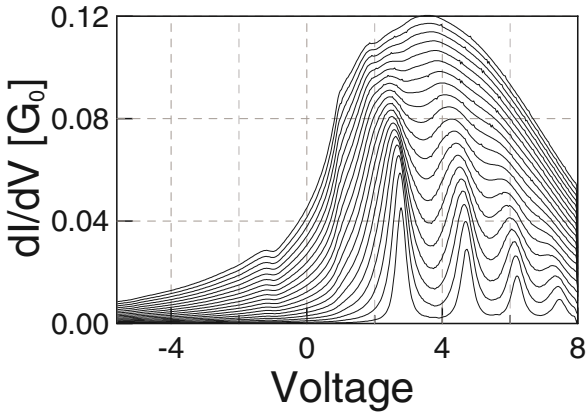

Fig. 31: Differential conductance of an *asymmetric* junction ($\eta = 0$, $\Gamma_R = 20\Gamma_L$) at different molecule-to-lead coupling, from $\Gamma_R/\omega_0 = 0.2$ (lower curve) to $\Gamma_R/\omega_0 = 4$ (upper curve), $\lambda/\omega_0 = 2$, $\epsilon_0/\omega_0 = 5$. The voltage is in the units of $\hbar\omega_0/e$

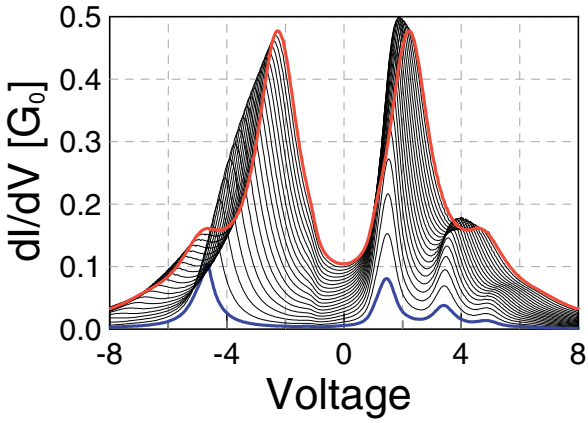

Fig. 32: Differential conductance at different molecule-to-STM coupling (see the text), from *asymmetric* junction with $\Gamma_L/\omega_0 = 0.025$, $\Gamma_R/\omega_0 = 0.5$ and $\eta = 0.2$ (lower curve, blue thick line) to *symmetric* junction with $\Gamma_L/\omega_0 = \Gamma_R/\omega_0 = 0.5$ and $\eta = 0.5$ (upper curve, red thick line), $\lambda/\omega_0 = 1$, $\epsilon_0/\omega_0 = 2$. Voltage is in the units of $\hbar\omega_0/e$

In conclusion, at weak molecule-to-lead (tip, substrate) coupling the usual vibronic side-band peaks in the differential conductance are observed; at stronger coupling to the leads (broadening) these peaks are transformed into step-like features. A vibronic-induced decreasing of the conductance with voltage is observed in high-conductance junctions. The usual IETS feature (in-

creasing of the conductance) can be observed only in the case of low off-resonant conductance. By changing independently the bias voltage and the tip position, it is possible to determine the energy of molecular orbitals and the spectrum of molecular vibrations. In the multi-level systems with strong electron-electron interaction further effects, such as Coulomb blockade and Kondo effect, could dominate over the physics which we address here; these effects have to be included in a subsequent step.

Multi-level model: nonequilibrium vibrons

Basically there are two main nonequilibrium effects: the electronic spectrum modification and excitation of vibrons (quantum vibrations). In the weak electron-vibron coupling case the spectrum modification is usually small (which is dependent, however, on the vibron dissipation rate, temperature, etc.) and the main possible nonequilibrium effect is the excitation of vibrons at finite voltages. We have developed an analytical theory for this case [124]. This theory is based on the self-consistent Born approximation (SCBA), which allows to take easily into account and calculate nonequilibrium distribution functions of electrons and vibrons.

If the mechanical degrees of freedom are coupled strongly to the environment (dissipative vibron), then the dissipation of molecular vibrations is determined by the environment. However, if the coupling of vibrations to the leads is weak, we should consider the case when the vibrations are excited by the current flowing through a molecule, and the dissipation of vibrations is also determined essentially by the coupling to the electrons. Here , we show that the effects of vibron emission and vibronic instability are important especially in the case of electron-vibron resonance.

We simplify the equations and obtain some analytical results in the *vibronic quasiparticle approximation*, which assumes weak electron-vibron coupling limit and weak external dissipation of vibrons:

$$\gamma_q^* = \gamma_q - 2\mathrm{Im}\Pi^R(\omega_q) \ll \omega_q. \tag{433}$$

So that the spectral function of vibrons can be approximated by the Dirac δ, and the lesser function reads

$$D^<(q,\omega) = -2\pi i \left[(N_q+1)\delta(\omega+\omega_q) + N_q\delta(\omega-\omega_q)\right], \tag{434}$$

where N_q is (nonequilibrium) number of vibrations in the q-th mode. So, in this approximation the spectrum modification of vibrons is not taken into account, but the possible excitation of vibrations is described by the nonequilibrium N_q. The dissipation of vibrons is neglected in the spectral function, but is taken into account later in the kinetic equation for N_q. A similar approach to the single-level problem was considered recently in [106, 113–118]. The more general case with broadened equilibrium vibron spectral function seems to be not very interesting, because in this case vibrons are not excited.

Nevertheless, in the numerical calculation it can be easy taken into consideration.

From the general quantum kinetic equation for vibrons, we obtain in this limit

$$N_q = \frac{\gamma_q N_q^0 - \mathrm{Im}\Pi^<(\omega_q)}{\gamma_q - 2\mathrm{Im}\Pi^R(\omega_q)}. \tag{435}$$

This expression describes the number of vibrons N_q in a nonequilibrium state, $N_q^0 = f_B^0(\omega_q)$ is the equilibrium number of vibrons. In the linear approximation the polarization operator is independent of N_q and $-2\mathrm{Im}\Pi^R(\omega_q)$ describes additional dissipation. Note that in equilibrium $N_q \equiv N_q^0$ because $\mathrm{Im}\Pi^<(\omega_q) = 2\mathrm{Im}\Pi^R(\omega_q) f_B^0(\omega_q)$. See also detailed discussion of vibron emission and absorption rates in Refs. [113–116].

For weak electron-vibron coupling the number of vibrons is close to equilibrium and is changed because of *vibron emission* by nonequilibrium electrons, N_q is roughly proportional to the number of such electrons, and the distribution function of nonequilibrium electrons is not change essentially by the interaction with vibrons (perturbation theory can be used). The situation changes, however, if nonequilibrium dissipation $-2\mathrm{Im}\Pi^R(\omega_q)$ is *negative*. In this case the number of vibrons can be essentially larger than in the equilibrium case (*vibronic instability*), and the change of electron distribution function should be taken into account self-consistently.

In the stationary state the *nonlinear* dissipation rate

$$\gamma_q^* = \gamma_q - 2\mathrm{Im}\Pi^R(\omega_q) \tag{436}$$

is positive, but the nonequilibrium contribution to dissipation $-2\mathrm{Im}\Pi^R(\omega_q)$ remains negative.

Additionally to the vibronic quasiparticle approximation, the *electronic quasiparticle approximation* can be used when the coupling to the leads is weak. In this case the lesser function can be parameterized through the number of electrons F_η *in the eigenstates of the noninteracting molecular Hamiltonian* $H_M^{(0)}$

$$G^<_{\alpha\beta} = i\sum_{\gamma\eta} A_{\alpha\gamma} S_{\gamma\eta} F_\eta S^{-1}_{\eta\beta}, \tag{437}$$

we introduce the unitary matrix $\mathbf{S}$, which transfer the Hamiltonian $\mathbf{H} \equiv H^{(0)}_{M\alpha\beta}$ into the diagonal form $\tilde{\mathbf{H}} = \mathbf{S}^{-1}\mathbf{H}\mathbf{S}$, so that the spectral function of this diagonal Hamiltonian is

$$\tilde{A}_{\delta\eta}(\epsilon) = 2\pi\delta(\epsilon - \tilde{\epsilon}_\delta)\delta_{\delta\eta}, \tag{438}$$

where $\tilde{\epsilon}_\delta$ are the eigenenergies.

Note that in the calculation of the self-energies and polarization operators we can not use δ-approximation for the spectral function (this is too rough

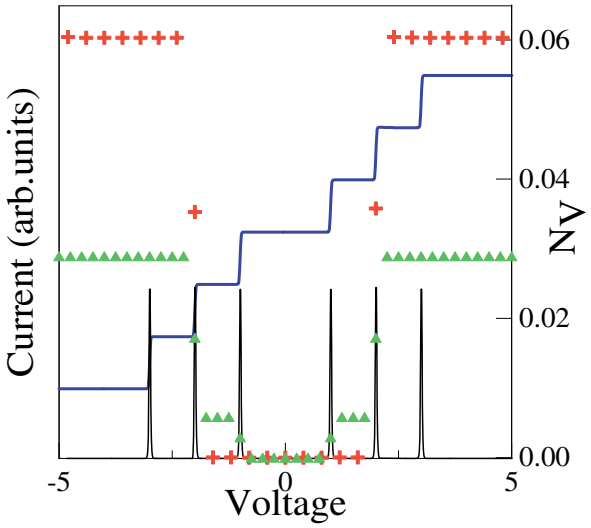

Fig. 33: Vibronic emission in the symmetric multilevel model: voltage-current curve, differential conductance, and the number of excited vibrons in the off-resonant (triangles) and resonant (crosses) cases (details see in the text).

and results in the absence of interaction out of the exact electron-vibron resonance). So that in the calculation we use actually (437) with broadened equilibrium spectral function. This approximation can be systematically improved by including nonequilibrium corrections to the spectral function, which are important near the resonance. It is important to comment that for stronger electron-vibron coupling *vibronic side-bands* are observed in the spectral function and voltage-current curves at energies $\tilde{\epsilon}_\delta \pm n\omega_q$, we do not consider these effects in the rest of our paper and concentrate on resonance effects.

After correspondingly calculations we obtain finally

$$N_q = \frac{\gamma_q N_q^0 - \sum_{\eta\delta} \kappa_{\eta\delta}(\omega_q) F_\eta (F_\delta - 1)}{\gamma_q - \sum_{\eta\delta} \kappa_{\eta\delta}(\omega_q)(F_\eta - F_\delta)}, \tag{439}$$

where coefficients $\kappa_{\eta\delta}$ are determined by the spectral function and electron-vibron coupling in the diagonal representation

$$\kappa_{\eta\delta}(\omega_q) = \int \frac{d\epsilon}{2\pi} \tilde{M}^q_{\eta\delta} \tilde{A}_{\delta\delta}(\epsilon - \omega_q) \tilde{M}^q_{\delta\eta} \tilde{A}_{\eta\eta}(\epsilon), \tag{440}$$

$$F_\eta = \frac{\tilde{\Gamma}_{L\eta\eta} f^0_{L\eta} + \tilde{\Gamma}_{R\eta\eta} f^0_{R\eta} + \sum_{q\eta} \left[\zeta^{-q}_{\eta\delta} F_\delta N_q + \zeta^{+q}_{\eta\delta} F_\delta (1 + N_q) \right]}{\tilde{\Gamma}_{L\eta\eta} + \tilde{\Gamma}_{R\eta\eta} + \sum_{q\eta} \left[\zeta^{-q}_{\eta\delta} (1 - F_\delta + N_q) + \zeta^{+q}_{\eta\delta} (F_\delta + N_q) \right]}, \tag{441}$$

$$\zeta^{\pm q}_{\eta\delta} = \tilde{M}^{q}_{\eta\delta}\tilde{A}_{\delta\delta}(\tilde{\epsilon}_\eta \pm \omega_q)\tilde{M}^{q}_{\delta\eta}, \tag{442}$$

here $\tilde{\Gamma}_{i\eta\eta}$ and $f^0_{i\eta}$ are the level width matrix in the diagonal representation and Fermi function at energy $\tilde{\epsilon}_\eta - e\varphi_i$.

These kinetic equations are similar to the usual golden rule equations, but are more general.

Now let us consider several examples of vibron emission and vibronic instability.

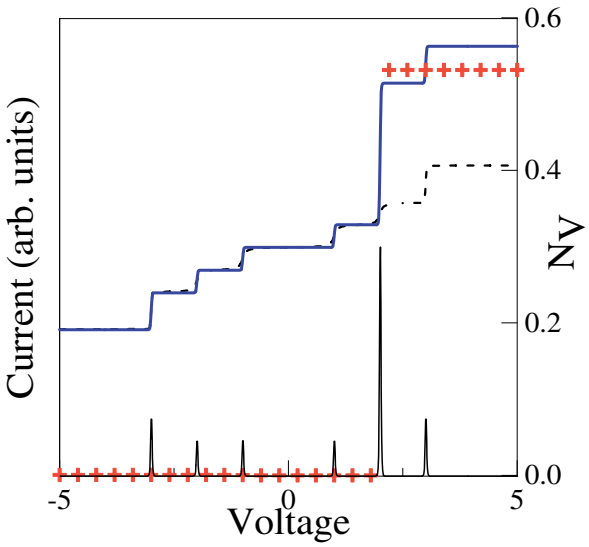

Fig. 34: Vibronic instability in an asymmetric multilevel model: voltage-current curve, differential conductance, and the number of excited vibrons (crosses). Dashed line show the voltage-current curve without vibrons (details see in the text).

First we consider the most simple case, when the instability is not possible and only vibron emission takes place. This corresponds to a negative imaginary part of the electronic polarization operator: $\mathrm{Im}\Pi^{R)}(\omega_q) < 0$. From the Eq. (440) one can see that for any two levels with the energies $\tilde{\epsilon}_\eta > \tilde{\epsilon}_\delta$ the coefficient $\kappa_{\eta\delta}$ is larger than $\kappa_{\delta\eta}$, because the spectral function $\tilde{A}_{\delta\delta}(\epsilon)$ has a maximum at $\epsilon = \tilde{\epsilon}_\delta$. The contribution of $\kappa_{\eta\delta}(\omega_q)(F_\eta - F_\delta)$ is negative if $F_\eta < F_\delta$. This takes place in equilibrium, and in nonequilibrium for transport through *symmetric* molecules, when higher energy levels are populated after lower levels. The example of such a system is shown in Fig. 33. Here we consider a simple three-level system ($\tilde{\epsilon}_1 = 1$, $\tilde{\epsilon}_2 = 2$, $\tilde{\epsilon}_3 = 3$) coupled symmetrically to the leads ($\Gamma_{L\eta} = \Gamma_{R\eta} = 0.01$). The current-voltage curve is the same with and without vibrations in the case of symmetrical coupling to the leads and in the weak electron-vibron coupling limit (if we neglect change of

the spectral function). The figure shows how vibrons are excited, the number of vibrons N_V in the mode with frequency ω_0 is presented in two cases. In the off-resonant case (green triangles) N_V is very small comparing with the resonant case ($\omega_0 = \tilde{\epsilon}_2 - \tilde{\epsilon}_1$, red crosses, the vertical scale is changed for the off-resonant points). In fact, if the number of vibrons is very large, the spectral function and voltage-current curve are changed. We shall consider this in a separate publication.

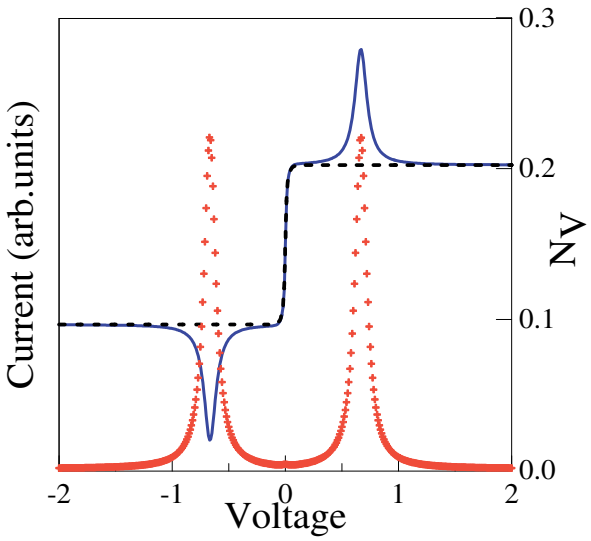

Fig. 35: Floating level resonance: voltage-current curve and the number of excited vibrons (crosses). Dashed line show the voltage-current curve without vibrons (details see in the text).

Now let us consider the situation when the imaginary part of the electronic polarization operator can be positive: $\mathrm{Im}\Pi^R(\omega_q) > 0$. Above we considered the normal case when the population of higher energy levels is smaller than lower levels. The opposite case $F_2 > F_1$ is known as inversion in laser physics. Such a state is unstable if the total dissipation γ_q^* (436) is negative, which is possible only in the nonstationary case. As a result of the instability, a large number of vibrons is excited, and in the stationary state γ_q^* is positive. This effect can be observed for transport through *asymmetric* molecules, when higher energy levels are populated *before* lower levels. The example of a such system is shown in Fig. 34. It is the same three-level system as before, but the first and second levels are coupled not symmetrically to the leads ($\Gamma_{L1} = 0.001$, $\Gamma_{R1} = 0.1$, $\Gamma_{L2} = 0.1$, $\Gamma_{R2} = 0.001$). The vibron couple resonantly these levels ($\omega_q = \tilde{\epsilon}_2 - \tilde{\epsilon}_1$). The result is qualitatively different from the symmetrical case.

The voltage-current curve is now asymmetric, a large *step* corresponds to the resonant level with inverted population.

Note the importance of the off-diagonal electron-vibron coupling for the resonant effects. If the matrix $\tilde{\mathbf{M}}$ in the eigen-state representation is diagonal, there is no resonant coupling between different electronic states.

Finally, let us consider the important case, when initially symmetric molecule becomes asymmetric when the external voltage is applied. The reason for such asymmetry is simply that in the external electric field left and right atoms feel different electrical potentials and the position of the levels $\epsilon_\alpha = \epsilon_\alpha^{(0)} + e\varphi_\alpha$ is changed (float) with the external voltage. The example of a such system is shown in Fig. 35. Here we consider a two-level system, one level is coupled electrostatically to the left lead $\tilde{\epsilon}_1 \propto \varphi_L$, the other level to the right lead $\tilde{\epsilon}_2 \propto \varphi_R$, the tunneling coupling to the leads also is not symmetrical ($\Gamma_{L1} = 0.1$, $\Gamma_{R1} = 0.001$, $\Gamma_{L2} = 0.001$, $\Gamma_{R2} = 0.1$). The frequency of the vibration, coupling these two states, is $\omega_0 = 1$. When we sweep the voltage, a *peak* in the voltage-current curve is observed when the energy difference $\tilde{\epsilon}_1 - \tilde{\epsilon}_2 \propto eV$ is going through the resonance $\tilde{\epsilon}_1 - \tilde{\epsilon}_2 \approx \omega_0$.

4.3 Coupling to a vibrational continuum: dissipation and renormalization

The model Hamiltonian

In the previous section we have dealt with a simple, but nevertheless physically rich, model describing the interaction of an electronic level with some specific vibrational mode confined to the quantum dot. We have seen how to apply in this case the Keldysh non-equilibrium techniques described in Section III within the self-consistent Born and Migdal approximations. The latter are however appropriate for the weak coupling limit to the vibrational degrees of freedom. In the opposite case of strong coupling, different techniques must be applied. For equilibrium problems, unitary transformations combined with variational approaches can be used, in non-equilibrium only recently some attempts were made to deal with the problem. [139]

In this section we will consider the case of a multi-level electronic system in interaction with a bosonic bath [288, 289]. We will use unitary transformation techniques to deal with the problem, but will only focus on the low-bias transport, so that strong non-equilibrium effects can be disregarded. Our interest is to explore how the *qualitative* low-energy properties of the electronic system are modified by the interaction with the bosonic bath. We will see that the existence of a continuum of vibrational excitations (up to some cut-off frequency) dramatically changes the analytic properties of the electronic Green function and may lead in some limiting cases to a qualitative modification of the low-energy electronic spectrum. As a result, the I-V characteristics at low bias may display "metallic" behavior (finite current) even if the isolated electronic system does exhibit a band gap. The model to be discussed below

has been motivated by the very exciting electrical transport measurements on short poly(dG)-poly(dC) DNA molecular wires carried out at the group of N. Tao some time ago [60]. Peculiar in these experiments was the large measured currents -up to 150 nA at 0.8 V- at low voltages, which stood in strong contrast to the usually accepted view that DNA should behave as an insulator at low applied bias. Further, a power-law length scaling of the linear conductance with increasing wire length was demonstrated, indicating that long-range charge transport was possible. Since the experiments were carried out in an aqueous solution, the possibility of a solvent-induced modification of the low-energy transport properties of the wire lied at hand, although additional factors like internal vibrations could also play a role.

The proposed model is based on an earlier work [286] and assumes, within a minimal tight-binding picture, that the DNA electronic states can be qualitatively classified into extended (conducting) and localized (non-conducting) states. The former may correspond e.g. to the π-orbital stack of the base pairs, the latter to energetically deeper lying (w.r.t. the frontier orbitals) base-pair states or sugar-phosphate backbone states. A further assumption is that any modification of the conducting states through the environment only takes place through a coupling to the non-conducting set. The tight-binding electronic Hamiltonian for N sites can then be written as (see also Fig. 36):

$$\mathcal{H}_{\mathrm{el}} = \epsilon_b \sum_j b_j^\dagger b_j - t_{||} \sum_j \left[b_j^\dagger b_{j+1} + \mathrm{H.c.} \right] + \epsilon \sum_j c_j^\dagger c_j - t_\perp \sum_j \left[b_j^\dagger c_j + \mathrm{H.c.} \right] = \mathcal{H}_{\mathrm{C}} + \mathcal{H}_{\mathrm{b}} + \mathcal{H}_{\mathrm{C\text{-}b}}. \tag{443}$$

Hereby $\mathcal{H}_{\mathrm{C}}$ and $\mathcal{H}_{\mathrm{b}}$ are the Hamiltonians of the extended and localized states (called in what follows "backbone" states for simplicity), respectively, and $\mathcal{H}_{\mathrm{C\text{-}b}}$ is the coupling between them. $t_{||}$ and $t_\perp$ are hopping integrals along the central chain (extended states) and between the localized states and the central chain, respectively. If not stated otherwise, the on-site energies will be later set equal to zero to simplify the calculations. Notice that this model displays a gap in the electronic spectrum roughly proportional to the transversal coupling $t_\perp$. This can be easely seen by looking at the limit $N \to \infty$ which leads to a periodic system. In this case, the Hamiltonian can be analytically diagonalized and two energy dispersion curves are obtained, which are given by $E_\pm(k) = t_{||} \cos(k) \pm \sqrt{t_\perp^2 + t_{||}^2 \cos^2(k)}$. The direct gap between the two bands is simply $\delta = 2\sqrt{t_\perp^2 + t_{||}^2}$. Since this model further shows electron-hole symmetry, two electronic manifolds (bands in the limit of $N \to \infty$) containing N states each, are symmetrically situated around the Fermi level, which is taken as the zero of energy.

The gap is obviously temperature independent and furthermore it is expected that transport at energies $E < \delta$ will be strongly suppressed due to the absence of electronic states to suport charge propagation. As a result,

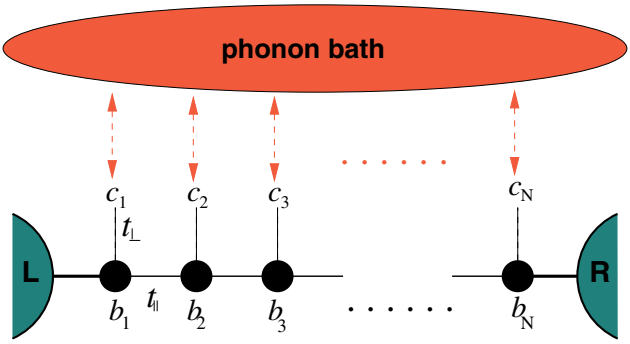

Fig. 36: Schematic drawing of a DNA molecular wire in contact with a dissipative environment. The central chain (extended states) with N sites is connected to semi-infinite left (L) and right (R) electronic reservoirs. The bath only interacts with the side chain sites (c), which we call for simplicity backbone sites, but which collectively stay for non-conducting, localized electronic states. The Hamiltonian associated with this model is given by Eqs. (443), (444), and (445) in the main text.

the linear conductance should display a strong exponential dependence as a function of the chain length N. In view of this behavior, an immediate issue that arises is how stable this electronic structure, *i.e.* two electronic manifolds separated by a gap, is against the coupling to an environment. This is an issue which reaches farther than the problem of charge transport in DNA wires, since it addresses the interaction of an open quantum mechanical system with a countable number of electronic energy levels to a continuum of states ("universe"). A generic example of such a situation is the measurement process in quantum mechanics. It is well-known that the interaction with complex environments is a source of dissipation and decoherence in quantum mechanical systems. [71] Concerning more specifically the case of DNA (and proteins), there is broad experimental evidence that the molecule dynamics follows the solvent dynamics over a broad temperature range. Especially, conformational changes, low-energy vibrational excitations and the corresponding temperature dependences turn out to be very sensitive to the solvents dynamics. [295] We will thus consider the vibrational degrees of freedom of counterions and hydration shells of the solvent as a dynamical bath able to break the electronic phase coherence and additionally to act as a dissipative environment. We do not consider specific features of the environment but represent it in a generic way by a bosonic bath of M harmonic oscillators. Then, the previous Hamiltonian can be extended to:

$$\mathcal{H}_{\rm W} = \mathcal{H}_{\rm el} + \sum_{\alpha} \Omega_\alpha B_\alpha^\dagger B_\alpha + \sum_{\alpha,j} \lambda_\alpha c_j^\dagger c_j (B_\alpha + B_\alpha^\dagger) = \mathcal{H}_{\rm el} + \mathcal{H}_{\rm B} + \mathcal{H}_{\text{c-B}}, \quad (444)$$

where $\mathcal{H}_{\rm B}$ and $\mathcal{H}_{\text{c-B}}$ are the phonon bath Hamiltonian and the (localized) state-bath interaction, respectively. B_α is a bath phonon operator and λ_α

denotes the electron-phonon coupling. Note that we assume a local coupling of the bath modes to the electronic density at the side chain. Later on, the thermodynamic limit ($M \to \infty$) in the bath degrees of freedom will be carried out and the corresponding bath spectral density introduced, so that at this stage we do not need to further specify the set of bath frequencies Ω_α and coupling constants λ_α. Obviously, the bath can be assumed to be in thermal equilibrium and be described by a canonical partition function.

To complete the formulation of the model, we have to include the interaction of the system with electronic reservoirs in order to describe charge transport along the same lines as before. We assume, as usual, a tunnel-type Hamiltonian with the form:

$$\mathcal{H} = \mathcal{H}_{\rm W} + \sum_{\boldsymbol{k}\in{\rm L,R},\sigma} \epsilon_{\boldsymbol{k}\sigma} d^\dagger_{\boldsymbol{k}\sigma} d_{\boldsymbol{k}\sigma} + \sum_{\boldsymbol{k}\in{\rm L},\sigma} (V_{\boldsymbol{k},1}\, d^\dagger_{\boldsymbol{k}\sigma}\, b_1 + {\rm H.c.}) + \sum_{\boldsymbol{k}\in R,\sigma} (V_{\boldsymbol{k},N}\, d^\dagger_{\boldsymbol{k}\sigma}\, b_N + {\rm H.c.}) = \mathcal{H}_{\rm W} + \mathcal{H}_{\rm L/R} + \mathcal{H}_{\rm L\text{-}C} + \mathcal{H}_{\rm R\text{-}C}. \quad (445)$$

The Hamiltonian of Eq. (445) is the starting point of our investigation. For a weak charge-bath coupling, a perturbative approach similar to the second order Born approximation, as described in the previous section can be applied. We expect, however, qualitative new effects rather in the opposite limit of strong coupling to the bath. To deal with this problem, a unitary transformation, the Lang-Firsov (LF) transformation, can be performed on the Hamiltonian of Eq. (445), which allows to eliminate the linear charge-vibron interaction $\mathcal{H}_{\rm c\text{-}B}$. In the limiting case of an isolated system with a single electron (or hole) this transformation becomes exact and allows for a full decoupling of electronic and vibronic propagators, see e.g. Ref. [97]. In the present case, this transformation is not exact and further approximations have to be introduced in order to make the problem tractable.

The generator of the LF transformation is given by

$$S = \sum_{\alpha,j} (\lambda_\alpha/\Omega_\alpha) c^\dagger_j c_j (B_\alpha - B^\dagger_\alpha)$$

and $S^\dagger = -S$. In the transformed Hamiltonian $\bar{\mathcal{H}} = {\rm e}^{\,S}\mathcal{H}{\rm e}^{\,-S}$ the linear coupling to the bath is eliminated. One should notice that in $\bar{\mathcal{H}}$ only the "backbone" part of the Hamiltonian is modified since the conducting state operators b_ℓ as well as the lead operators $d_{\boldsymbol{k}\sigma}$ are invariant with respect to the above transformation. The new Hamiltonian reads:

$$\bar{\mathcal{H}} = \mathcal{H}_{\rm C} + \mathcal{H}_{\rm L/R} + \mathcal{H}_{\rm B} + \mathcal{H}_{\rm L/R\text{-}C} + (\epsilon - \Delta) \sum_j c^\dagger_j c_j - t_\perp \sum_j \Big[b^\dagger_j c_j \mathcal{X} + {\rm H.c.} \Big],$$

$$\mathcal{X} = \exp\left[\sum_\alpha \frac{\lambda_\alpha}{\Omega_\alpha} (B_\alpha - B^\dagger_\alpha) \right], \quad \Delta = \sum_\alpha \frac{\lambda^2_\alpha}{\Omega_\alpha}. \quad (446)$$

As a result of the LF we get a shift of the onsite energies (polaron shift or reorganization energy in electron transfer theory) and a renormalization of

both the tunneling and of the transversal coupling Hamiltonian via the bosonic operators $\mathcal{X}$. There is also an additional electron-electron interaction term which we will not be concerned with in the remaining of this section and is thus omitted. Since we are mainly interested in qualitative statements, we will assume the wide-band approximation in the coupling to the electrodes which is equivalent to substituting the electrode self-energies by a purely imaginary constant, i.e. $\Sigma_{\mathrm{L,R}} \approx -\mathrm{i}\,\Gamma_{\mathrm{L,R}}$. We are thus not interested in specific features of the electrode electronic structure.

To further proceed, let us now introduce two kinds of retarded thermal Green functions related to the central chain $G_{j\ell}(t)$ and to the "backbones" $P_{j\ell}(t)$, respectively (taking $\hbar = 1$):

$$G_{j\ell}(t,t') = -i\Theta(t-t')\left\langle \left[b_j(t), b_\ell^\dagger(t')\right]_+ \right\rangle, \tag{447}$$

$$P_{j\ell}(t,t') = -i\Theta(t-t')\left\langle \left[c_j(t)\mathcal{X}(t), c_\ell^\dagger(t')\mathcal{X}^\dagger(t')\right]_+ \right\rangle,$$

where Θ is the Heaviside function. Notice that the P-Green function doe not have a pure electronic character but also contains the bath operators $\mathcal{X}$. For a full out-of-equilibrium calculation, the full Keldysh formalism including lesser- and greater-GF would also be needed. However, as we will briefly show below, the final expression for the electrical current at low applied voltages and for small transversal coupling $t_\perp$ will only include the retarded propagators.

We now use the equation of motion technique (EOM) to obtain an expression for the GF $G_{j\ell}(t)$. We first remark that in the time domain two EOM can be written, depending on which time argument in the double-time GF the time derivative will act. One thus obtains in general:

$$\mathrm{i}\,\partial_t G(t,t') = \left\langle \left[b(t), b^\dagger(t')\right]_+ \right\rangle \delta(t-t') + (([b(t), H]\,|b^\dagger(t'))).$$

$$G(t,t')[-\mathrm{i}\,\partial_{t'}] = \left\langle \left[b(t), b^\dagger(t')\right]_+ \right\rangle \delta(t-t') - ((b(t)|\left[b^\dagger(t'), H\right])).$$

The EOM for the GF $G_{j\ell}(t)$ reads then in the energy space:

$$\sum_n \left[G_0^{-1}(E)\right]_{\ell n} G_{nj}(E) = \delta_{\ell j} - t_\perp((c_\ell \mathcal{X}|b_j^\dagger)) \tag{448}$$

$$\left[G_0^{-1}(E)\right]_{\ell n} = (E-\epsilon_b)\delta_{n\ell} + t_{||}(\delta_{n,\ell+1} + \delta_{n,\ell-1}) - \Sigma_{\mathrm{L}}\delta_{\ell 1}\delta_{n1} - \Sigma_{\mathrm{R}}\delta_{\ell N}\delta_{nN}$$

$$\Sigma_{\mathrm{L(R)}} = \sum_{\boldsymbol{k}\in L(R)} \frac{|V_{\boldsymbol{k},1(N)}|^2}{E - \epsilon_{\boldsymbol{k}} + \mathrm{i}\,0^+} \approx -\mathrm{i}\,\Gamma_{\mathrm{L,R}}$$

In the next step, EOM for the "right" time argument t' of the GF $Z^{\mathcal{X}}_{\ell j}(t,t')((c_\ell(t)\mathcal{X}(t)|b_j^\dagger(t')))$ can be written. This leads to:

$$\sum_m Z^{\mathcal{X}}_{\ell m}(E)\left[G_0^{-1}(E)\right]_{mj} = -t_\perp((c_\ell\mathcal{X}|c_j^\dagger\mathcal{X}^\dagger)) = -t_\perp P_{\ell j}(E) \tag{449}$$

Inserting Eq. (449) into Eq. (448) we arrive at the matrix equation:

$$\boldsymbol{G}(E) = \boldsymbol{G}_0(E) + \boldsymbol{G}_0(E)\boldsymbol{\Sigma}_{\mathrm{B}}(E)\boldsymbol{G}_0(E),$$

which can be transformed into a Dyson-like equation when introducing the irreducible part $\boldsymbol{\Sigma}_{\mathrm{B}}(E) = \boldsymbol{\Sigma}_{\mathrm{B}}^{\mathrm{irr}}(E) + \boldsymbol{\Sigma}_{\mathrm{B}}^{\mathrm{irr}}(E)\boldsymbol{G}_0(E)\boldsymbol{\Sigma}_{\mathrm{B}}^{\mathrm{irr}}(E) + \ldots$:

$$\boldsymbol{G}(E) = \boldsymbol{G}_0(E) + \boldsymbol{G}_0(E)\boldsymbol{\Sigma}_{\mathrm{B}}^{\mathrm{irr}}(E)\boldsymbol{G}(E), \tag{450}$$

or equivalently:

$$\begin{aligned} \boldsymbol{G}^{-1}(E) &= \boldsymbol{G}_0^{-1}(E) - t_\perp^2 \boldsymbol{P}(E) \\ \boldsymbol{G}_0^{-1}(E) &= E\mathbf{1} - \mathcal{H}_{\mathrm{C}} - \Sigma_{\mathrm{L}}(E) - \Sigma_{\mathrm{R}}(E). \end{aligned} \tag{451}$$

$\boldsymbol{\Sigma}_{\mathrm{B}}^{\mathrm{irr}}(E) = t_\perp^2 \boldsymbol{P}(E)$ is the crucial contribution to the GF since it contains the influence of the bosonic bath. Note that $\boldsymbol{\Sigma}_{\mathrm{B}}^{\mathrm{irr}}(E)$ includes the transversal hopping $t_\perp$ to all orders, the leading one being $t_\perp^2$.

In the next step, an expression for the electrical current flowing through the system must be derived. Using the results of Sec. 2, we can directly write the following expression:

$$\begin{aligned} I = \frac{2e}{h} \int dE\, \mathrm{Tr}(f_{\mathrm{L}}(E) - f_{\mathrm{R}}(E))\, t(E) \\ + t_\perp^2 \frac{2e}{h} \int dE\, \left\{ \mathrm{Tr}[\boldsymbol{\Sigma}_{\mathrm{L}}^{>} \boldsymbol{P}^{<} - \boldsymbol{\Sigma}_{\mathrm{L}}^{<} \boldsymbol{P}^{>}] - (L \leftrightarrow R) \right\}. \end{aligned} \tag{452}$$

The first summand has the same form as Landauer's expression for the current with an effective transmission function $t(E) = \mathrm{Tr}[\boldsymbol{G}^\dagger \boldsymbol{\Gamma}_{\mathrm{R}} \boldsymbol{G} \boldsymbol{\Gamma}_{\mathrm{R}}]$. However, the reader should keep in mind that the GFs appearing in this expression do contain the full dressing by the bosonic bath and hence, $t(E)$ does not describe elastic transport. The remaining terms contain explicitly contributions from the bath. It can be shown after some transformations that the leading term is proportional to $(t_\perp^2)^2$ so that within a perturbative approach in $t_\perp$ and at low bias it can be approximately neglected. We therefore remian with the exression $I = \frac{2e}{h} \int dE\, \mathrm{Tr}(f_{\mathrm{L}}(E) - f_{\mathrm{R}}(E))\, t(E)$ to obtain the current.

To remain consistent with this approximation, the bath selfenergy should also be treated to order $t_\perp^2$, more explicitly:

$$\begin{aligned} P_{\ell j}(t,t') &= ((c_\ell(t)\mathcal{X}(t) | c_j^\dagger(t')\mathcal{X}^\dagger(t'))) \\ &\approx -\mathrm{i}\,\theta(t-t') \left\{ \left\langle c_\ell(t) c_j^\dagger(t') \right\rangle \left\langle \mathcal{X}(t)\mathcal{X}^\dagger(t') \right\rangle + \left\langle c_j^\dagger(t') c_\ell(t) \right\rangle \left\langle \mathcal{X}^\dagger(t')\mathcal{X}(t) \right\rangle \right\} \\ &\approx -\mathrm{i}\,\delta_{\ell j}\theta(t-t') \left\{ \left\langle c_j(t) c_j^\dagger(t') \right\rangle \left\langle \mathcal{X}(t)\mathcal{X}^\dagger(t') \right\rangle + \left\langle c_j^\dagger(t') c_j(t) \right\rangle \left\langle \mathcal{X}^\dagger(t')\mathcal{X}(t) \right\rangle \right\} \\ &= -\mathrm{i}\,\delta_{\ell j}\theta(t-t') \mathrm{e}^{-\mathrm{i}\,(\epsilon - \Delta)\,t} \left\{ (1-f_{\mathsf{c}}) \mathrm{e}^{-\Phi(t)} + f_{\mathsf{c}} \mathrm{e}^{-\Phi(-t)} \right\}. \end{aligned} \tag{453}$$

In the previous expression we have replaced the full averages of the "backbone" operators by their zero order values (free propagators). $\mathrm{e}^{-\Phi(t)} =$

$\left\langle \mathcal{X}(t)\mathcal{X}^{\dagger}(0)\right\rangle_{\mathrm{B}}$ is a dynamical bath correlation function to be specified later on. The average $\langle\cdot\rangle_{\mathrm{B}}$ is performed over the bath degrees of freedom. f_{c} is the Fermi function at the backbone sites. In what follows we consider the case of empty sites by setting $f_{\mathsf{c}} = 0$. The Fourier transform $P_{\ell j}(E)$ reads then:

$$P_{\ell j}(E) = -\mathrm{i}\,\delta_{\ell j}\int_0^{\infty} \mathrm{d}t\,\mathrm{e}^{\,\mathrm{i}\,(E+\mathrm{i}\,0^{+})t}\,\mathrm{e}^{\,-\mathrm{i}\,(\epsilon-\Delta)\,t}\,\left[(1-f_{\mathsf{c}})\mathrm{e}^{\,-\Phi(t)} + f_{\mathsf{c}}\mathrm{e}^{\,-\Phi(-t)}\right] \tag{454}$$

In order to get closed expressions for the bath thermal averages it is appropriate to introduce a bath spectral density [71] defined by :

$$J(\omega) = \sum_{\alpha}\lambda_{\alpha}^{2}\delta(\omega-\Omega_{\alpha}) = J_0(\frac{\omega}{\omega_{\mathrm{c}}})^{s}\mathrm{e}^{\,-\omega/\omega_{\mathrm{c}}}\Theta(\omega), \tag{455}$$

where ω_{c} is a cut-off frequency related to the bath memory time $\tau_{\mathrm{c}} \sim \omega_{\mathrm{c}}^{-1}$. It is easy to show that the limit $\omega_{\mathrm{c}} \to \infty$ corresponds to a Markovian bath, *i.e.* $J(t) \sim J_0\delta(t)$. Using this *Ansatz*, $\Phi(t)$ can be written as:

$$\Phi(t) = \int_0^{\infty}\mathrm{d}\omega\,\frac{J(\omega)}{\omega^2}\left[1-\mathrm{e}^{\,-\mathrm{i}\,\omega t} + 2\frac{1-\cos\omega t}{\mathrm{e}^{\,\beta\omega}-1}\right]. \tag{456}$$

Although the integral can be performed analytically [71], we consider $\Phi(t)$ in some limiting cases where it is easier to work directly with Eq. (456).

Limiting cases

We use now the results of the foregoing section to discuss the electronic transport properties of our model in some limiting cases for which analytic expressions can be derived. We will discuss the mean-field approximation and the weak-coupling regime in the electron-bath interaction as well as to elaborate on the strong-coupling limit. Furthermore, the cases of ohmic ($s = 1$) and superohmic ($s = 3$) spectral densities are treated.

(i) Mean-field approximation

The mean-field approximation is the simplest one and neglects bath fluctuations contained in $P(E)$. The MFA can be introduced by writing the phonon operator $\mathcal{X}$ as $\langle\mathcal{X}\rangle_{\mathrm{B}} + \delta\mathcal{X}$ in $\mathcal{H}_{\text{C-c}}$ in Eq. (446), *i.e.*

$$\mathcal{H}_{\text{C-b}}^{\mathrm{MF}} = -t_{\perp}\sum_{j}\left[b_j^{\dagger}c_j\,\langle\mathcal{X}\rangle_{\mathrm{B}} + \mathrm{H.c.}\right] + O(\delta\mathcal{X}).$$

As a result a real, static and temperature dependent term in Eq. (451) is found:

$$\boldsymbol{G}^{-1}(E) = \boldsymbol{G}_0^{-1}(E) - t_{\perp}^{2}\,\frac{|\,\langle\mathcal{X}\rangle_{\mathrm{B}}\,|^2}{E-\epsilon+\Delta+\mathrm{i}\,0^{+}}\mathbf{1}, \tag{457}$$

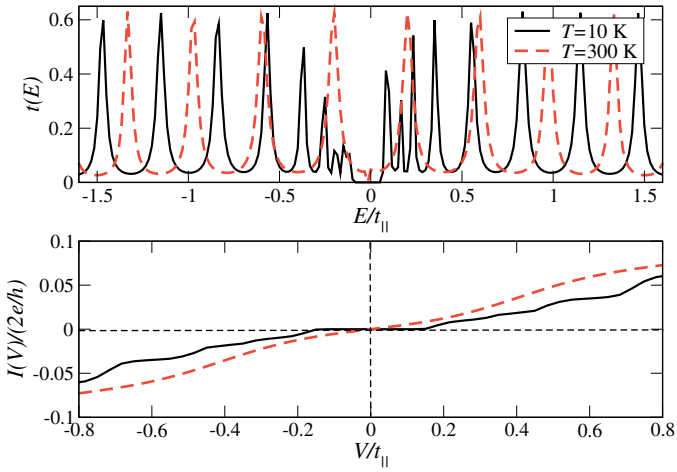

Fig. 37: Electronic transmission and corresponding current in the mean-field approximation for two different temperatures. Parameters: $N = 20, J_0/\omega_c = 0.12, t_\perp/t_{||} = 0.5, \Gamma_{L/R}/t_{||} = 0.5$.

where $|\langle \mathcal{X} \rangle_B|^2 = e^{-2\kappa(T)}$ and $\kappa(T)$ is given by:

$$\kappa(T) = \int_0^\infty \frac{d\omega}{\omega^2} J(\omega) \coth \frac{\omega}{2k_B T}. \tag{458}$$

The effect of the MF term is thus to scale the bare transversal hopping $t_\perp$ by the exponential temperature dependent factor $e^{-\kappa(T)}$.

In the case of an ohmic bath, $s = 1$, the integrand in $\kappa(T)$ scales as $1/\omega^p$, $p = 1, 2$ and has thus a logarithmic divergence at the lower integration limit. Thus, the MF contribution would vanish. In other words, no gap would exist on this approximation level.

In the superohmic case ($s = 3$) all integrals are regular. One obtains $\Delta = \int d\omega\, \omega^{-1} J(\omega) = \Gamma(s-1) J_0 = 2J_0$, with $\Gamma(s)$ being the Gamma function and $\kappa(T)$ reads:

$$\kappa(T) = \frac{2J_0}{\omega_c} \left[2 \left(\frac{k_B T}{\omega_c} \right)^2 \zeta_H \left(2, \frac{k_B T}{\omega_c} \right) - 1 \right]. \tag{459}$$

$\zeta_H(s, z) = \sum_{n=0}^\infty (n + z)^{-s}$ is the Hurwitz ζ-function, a generalization of the Riemann ζ-function. [296]

It follows from Eq. (17) that $\kappa(T)$ behaves like a constant for low temperatures ($k_B T/\omega_c < 1$), $\kappa(T) \sim J_0/\omega_c$, while it scales linear with T in the high-temperature limit ($k_B T/\omega_c > 1$), $\kappa(T) \sim J_0/\omega_c (1 + 2k_B T/\omega_c)$).

For $J_0 \neq 0$ and at zero temperature the hopping integral is roughly reduced to $t_\perp e^{-\frac{J_0}{\omega_c}}$ which is similar to the renormalization of the hopping in Holstein's

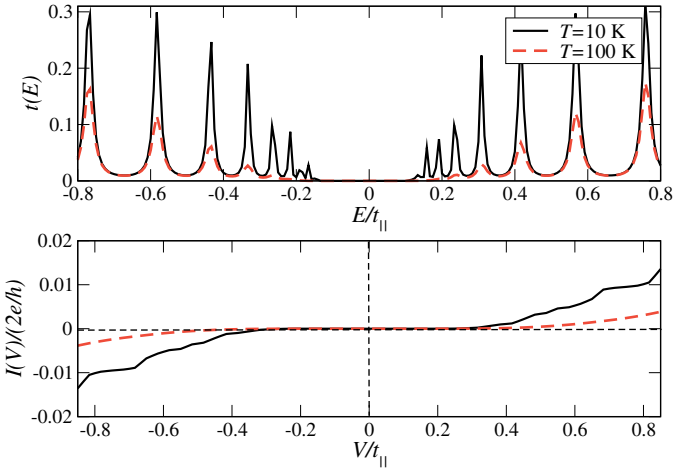

Fig. 38: Electronic transmission and corresponding current in the weak-coupling limit with ohmic dissipation ($s = 1$) in the bath. Parameters: $N = 20, J_0/\omega_c = 0.2, t_\perp/t_{||} = 0.6, \Gamma_{L/R}/t_{||} = 0.5$

polaron model [297], though here it is $t_\perp$ rather than $t_{||}$ the term that is rescaled. At high temperatures $t_\perp$ is further reduced ($\kappa(T) \sim T$) so that the gap in the electronic spectrum finally collapses and the system becomes "metallic", see Fig. 37. An appreciable temperature dependence can only be observed in the limit $J_0/\omega_c < 1$; otherwise the gap would collapse already at zero temperature due to the exponential dependence on J_0. We further remark that the MFA is only valid in this regime ($J_0/\omega_c < 1$), since for $J_0/\omega_c \gg 1$ multiphonon processes in the bath, which are not considered in the MFA, become increasingly relevant and thus a neglection of bath fluctuations is not possible.

(ii) Beyond MF: weak-coupling limit

As a first step beyond the mean-field approach let's first consider the weak-coupling limit in $\boldsymbol{P}(E)$. For $J_0/\omega_c < 1$ and not too high temperatures ($k_B T/\omega_c < 1$) the main contribution to the integral in Eq. (456) comes from long times $t \gg \omega_c^{-1}$. With the change of variables $z = \omega t$, $\Phi(t)$ can be written as:

$$\Phi(t) = J_0 \omega_c^{-s} t^{1-s} \int_0^\infty \mathrm{d}z\, z^{s-2} \mathrm{e}^{-\frac{z}{\omega_c t}} \times \left(1 - \mathrm{e}^{-\mathrm{i}\, z} + 2\frac{1-\cos z}{\mathrm{e}^{z\frac{\beta\omega_c}{\omega_c t}} - 1}\right). \tag{460}$$

As far as $\omega_c t \gg \beta\omega_c$ this can be simplified to:

$$\Phi(t) \approx J_0 \omega_c^{-s} t^{1-s} \int_0^\infty \mathrm{d}x\, z^{s-2} \mathrm{e}^{-\frac{z}{\omega_c t}} \times \left(1 - \mathrm{e}^{-\mathrm{i}\, z} + 2\frac{\beta\omega_c}{\omega_c t}\frac{1-\cos z}{z}\right). \tag{461}$$

Since in the long-time limit the low-frequency bath modes are giving the most important contribution we may expect some qualitative differences in the ohmic and superohmic regimes. For $s = 1$ we obtain $\Phi(t) \sim \pi \frac{J_0}{\omega_c} \frac{k_B T}{\omega_c}(\omega_c t)$ which leads to ($\Delta(s = 1) = J_0$):

$$\boldsymbol{G}^{-1}(E) = \boldsymbol{G}_0^{-1}(E) - t_\perp^2 \frac{1}{E + J_0 + \mathrm{i}\,\pi \frac{J_0}{\omega_c} k_B T}\mathbf{1}, \tag{462}$$

i.e. there is only a pure imaginary contribution from the bath. For the simple case of $N = 1$ (a two-states model) one can easily see that the gap approximately scales as $\sqrt{k_B T}$; thus it grows with increasing temperature. This is shown in Fig. 38, where we also see that the intensity of the transmission resonances strongly goes down with increasing temperature. The gap enhancement is induced by the suppression of the transmission peaks of the frontier orbitals, i. e. those closest to the Fermi energy.

For $s = 3$ and $k_B T/\omega_c < 1$, $\Phi(t)$ takes a nearly temperature independent value proportional to J_0/ω_c. As a result the gap is slightly reduced ($t_\perp \to t_\perp \mathrm{e}^{-J_0/\omega_c}$) but, because of the weak-coupling condition, the effect is rather small.

From this discussion we can conclude that in the weak-coupling limit ohmic dissipation in the bath induces an enhancement of the electronic gap while superohmic dissipation does not appreciably affect it. In the high-temperature limit $k_B T/\omega_c > 1$ a short-time expansion can be performed which yields similar results to those of the strong-coupling limit (see next section), [298] so that we do not need to discuss them here. Note farther that the gap obtained in the weak-coupling limit is an "intrinsic" property of the electronic system; it is only quantitatively modified by the interaction with the bath degrees of freedom. We thus trivially expect a strong exponential dependence of $t(E = E_F)$, typical of virtual tunneling through a gap. Indeed, we find $t(E = E_F) \sim \exp(-\beta L)$ with $\beta \sim 2 - 3\,\mathring{A}^{-1}$.

(iii) Beyond MF: strong coupling limit (SCL)

In this section we elaborate on the strong-coupling regime, as defined by the condition $J_0/\omega_c > 1$. In the SCL the main contribution to the time integral in Eq. (456) arises from short times. Hence a short-time expansion of $\Phi(t)$ may already give reasonable results and it allows, additionally, to find an analytical expression for $\boldsymbol{P}(E)$. At $t \ll \omega_c^{-1}$ we find,

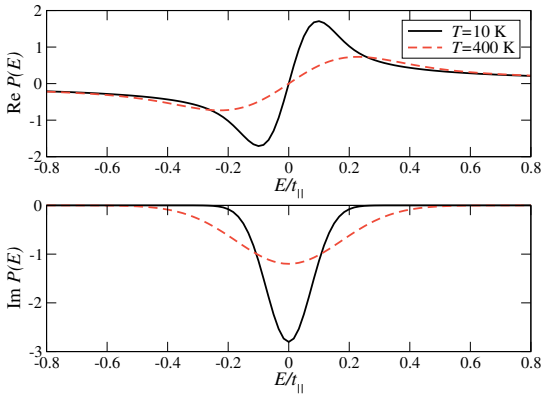

Fig. 39: Temperature dependence of the real and imaginary parts of $P(E)$ for $N = 20$, $J_0/\omega_c = 10, t_\perp/t_{||} = 0.4, \Gamma_{L/R}/t_{||} = 0.5$. With increasing temperature the slope of the real part near $E = 0$ decreases and the imaginary part broadens and loses intensity. A similar qualitative dependence on J_0 was found (not shown).

$$
\begin{aligned}
\Phi(t) &\approx \mathrm{i}\,\Delta\, t + (\omega_c t)^2\,\kappa_0(T) \qquad (463)\\
P_{\ell j}(E) &= -\mathrm{i}\,\delta_{\ell j}\int_0^\infty \mathrm{d}t\,\mathrm{e}^{\,\mathrm{i}\,(E-\epsilon+\mathrm{i}\,0^+)t}\,\mathrm{e}^{\,-(\omega_c t)^2\kappa_0(T)}\\
&= -\mathrm{i}\,\delta_{\ell j}\,\frac{\sqrt{\pi}}{2}\frac{1}{\omega_c\sqrt{\kappa_0(T)}}\,\exp\left(-\frac{(E-\epsilon+\mathrm{i}\,0^+)^2}{4\omega_c^2\kappa_0(T)}\right)\\
&\quad\times\left(1+\mathrm{erf}\left[\frac{\mathrm{i}\,(E-\epsilon+\mathrm{i}\,0^+)}{2\omega_c\sqrt{\kappa_0(T)}}\right]\right),\\
\kappa_0(T) &= \frac{1}{2\omega_c^2}\int_0^\infty \mathrm{d}\omega J(\omega)\coth\frac{\omega}{2k_BT}.
\end{aligned}
$$

Before presenting the results for the electronic transmission, it is useful to first consider the dependence of the real and imaginary parts of $\boldsymbol{P}(E)$ on temperature and on the reduced coupling constant J_0/ω_c. Both functions are shown in Fig. 39. We see that around the Fermi level at $E = 0$ the real part is approximately linear, $\mathrm{Re}\,P(E) \sim E$ while the imaginary part shows a Lorentzian-like behavior. The imaginary part loses intensity and becomes broadened with increasing temperature or J_0, while the slope in the real part decreases when k_BT or J_0 are increased.

If we neglect for the moment the imaginary part (the dissipative influence of the bath), we can understand the consequences of the real part being nonzero around the Fermi energy, *i.e.* in the gap region of the model of Ref. [286]. The solutions of the non-linear equation $\det|(E - t_\perp^2\,\mathrm{Re}\,P(E))\mathbf{1} - \mathcal{H}_C| = 0$ give the new poles of the Green function of the system in presence of the phonon bath. For comparison, the equation determining the eigenstates *without* the bath is simply $\det|(E - t_\perp^2/E)\mathbf{1} - \mathcal{H}_C| = 0$. It is just the $1/E$ de-

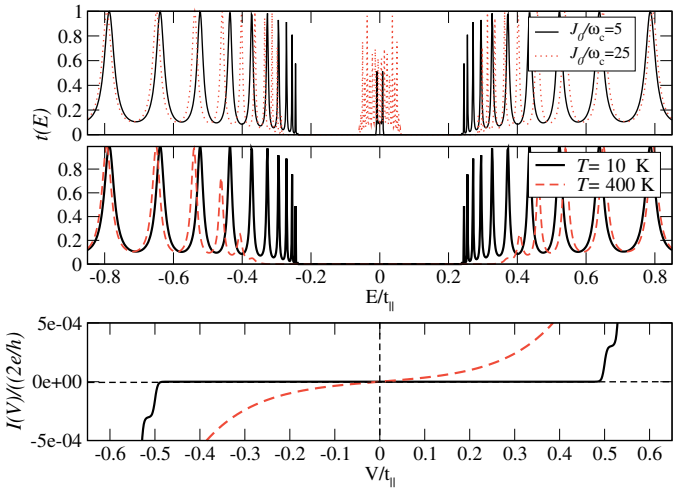

Fig. 40: $\mathrm{Im}\, P(E) = 0$; the intensity of the resonances on the central narrow band is strongly dependent on J_0/ω_c and $k_\mathrm{B}T$ (not shown). Temperature dependence of $t(E)$ with full inclusion of $P(E)$ (middle panel) and corresponding current (lower panel) for $N = 20$, $J_0/\omega_c = 5, t_\perp/t_{||} = 0.5, \Gamma_{\mathrm{L/R}}/t_{||} = 0.2$. The pseudo-gap increases with temperature.

pendence near $E = 0$ that induces the appearance of two electronic bands of states separated by a gap. In our present study, however, $\mathrm{Re}\, P(E \to 0)$ has no singular behavior and additional poles of the Green function may be expected to appear in the low-energy sector. This is indeed the case, as shown in Fig. 40 (upper panel). We find a third band of states around the Fermi energy, which we may call a polaronic band because it results from the strong interaction between an electron and the bath modes. The intensity of this band as well as its band width strongly depend on temperature and on J_0. When $k_\mathrm{B}T$ (or J_0) become large enough, these states spread out and eventually merge with the two other side bands. This would result in a transmission spectrum similar of a gapless system.

This picture is nevertheless not complete since the imaginary component of $P(E)$ has been neglected. Its inclusion leads to a dramatic modification of the spectrum, as shown in Fig. 40 (middle panel). We now only see two bands separated by a gap which basically resembles the semiconducting-type behavior of the original model. The origin of this gap or rather *pseudo-gap* (see below) is however quite different. It turns out that the imaginary part of $P(E)$, being peaked around $E = 0$, strongly suppresses the transmission resonances belonging to the third band. Additionally, the frontier orbitals on the side bands, *i.e.* orbitals closest to the gap region, are also strongly damped, this effect becoming stronger with increasing temperature ($\mathrm{Im}\, P(E)$ broadens). This latter effect has some similarities with the previously discussed

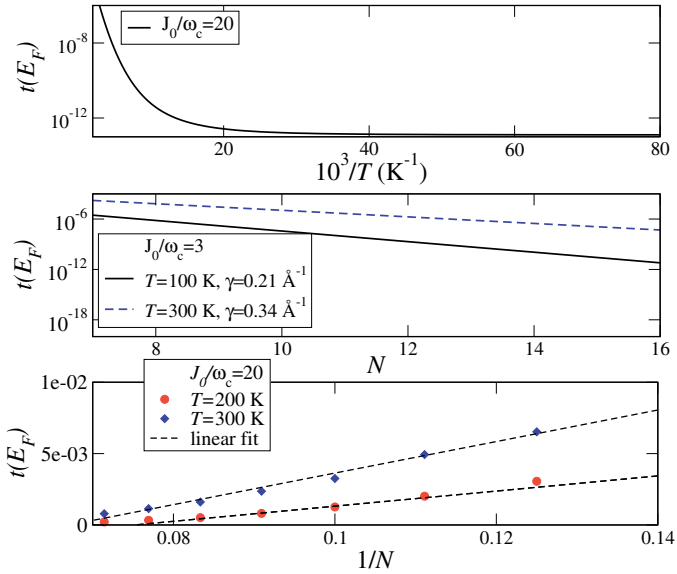

Fig. 41: Upper panel: Arrhenius plot for $t(E_F)$. Parameters: $N = 20$, $t_{||} = 0.6\,eV$, $t_\perp/t_{||} = 0.2$, $\Gamma_{\mathrm{L/R}}/t_{||} = 0.3$. Middle and lower panels: Length dependence of $t(E_F)$ at different temperatures for two different strengths of the electron-bath coupling J_0/ω_c. The electronic coupling parameters are the same as in the upper panel.

weak-coupling regime. Note, however, that the new electronic manifold around the Fermi energy does not appear in the weak-coupling regime. We further stress that the density of states around the Fermi level is not exactly zero (hence the term pseudo-gap); the states on the polaronic manifold, although strongly damped, contribute nevertheless with a finite temperature dependent background to the transmission. As a result, with increasing temperature, a crossover from "semiconducting" to "metallic" behavior in the low-voltage region of the I-V characteristics takes place, see Fig. 40 (lower panel). The slope in the I-V plot becomes larger when $t_\perp$ is reduced, since the side bands approach each other and the effect of $\mathrm{Im}\,P(E)$ is reinforced.

In Fig. 41 (top panel) an Arrhenius plot of the transmission at the Fermi energy is shown, which suggests that activated transport is the physical mechanism for propagation at low energies. Increasing the coupling to the phonon bath makes the suppression of the polaronic band around $E = 0$ less effective ($\mathrm{Im}\,P(E \sim 0)$ decreases) so that the density of states around this energy becomes larger. Hence the absolute value of the transmission will also increase. On the other side, increasing $t_\perp$ leads to a reduction of the transmission at the Fermi level, since the energetic separation of the side bands increases with $t_\perp$.

A controversial issue in transport through molecular wires is the actual length dependence of the electron transfer rates or correspondingly, of the linear conductance. This is specially critical in the case of DNA nanowires [56,57,59]. Different functional dependences have been found in charge transfer experiments ranging from strong exponential behavior related to superexchange mediated electron transfer [56] to algebraic dependences typical of thermal activated hopping [57, 59]. As far as transport experiments are concerned, the previously mentioned experiments at the group of N. Tao [60] reported an algebraic length dependence of the conductance for poly(GC) oligomers in solution. We have investigated the length dependence of $t(E_F)$ and found for the strong dissipative regime $J_0/\omega_c > 1$, an exponential law for energies close to E_F, $t(E_F) \sim \exp(-\gamma N)$. At the first sight, this might be not surprising since a gap in the spectrum does exist. Indeed, in the absence of the bath, *i.e.* with an intrinsic gap, we get decay lengths γ_{coh} of the order of 2 AA^{-1}. However, as soon as the interaction with the bath is included, we find values of γ much smaller than expected for virtual tunneling, ranging from 0.15 $Å^{-1}$ to 0.4 $Å^{-1}$. Additionally, γ is strongly dependent on the strength of the electron-bath coupling J_0/ω_c as well as on temperature; γ is reduced when J_0/ω_c or k_BT increases, since in both cases the density of states within the pseudo-gap increases. Remarkably, a further increase of the electron-bath coupling eventually leads to an algebraic length dependence, see lower panel of Fig. 41.

The studies presented in this section indicate that the presence of a complex environment, which induces decoherence and dissipation, can dramatically modify the electronic response of a nanowire coupled to electrodes. Electron transport on the low-energy sector of the transmission spectrum is supported by the formation of (virtual) polaronic states. Though strongly damped, these states manifest nonetheless with a finite density of states inside the bandgap and mediate thermally activated transport.

5 Conclusions and Perspectives

In this chapter we have reviewed the method of nonequilibrium Green functions and few selected applications to problems related with charge transport at the molecular scale. Hereby we have only focused on minimal model Hamiltonian formulations which build a very appropriate starting point to illustrate the power and range of validity of such techniques. We have showed how this approach can be used to deal with a variety of physical systems, covering both noninteracting and interacting cases. Thus, so different issues as coherent transport, Coulomb blockade phenomena, charge-vibron interaction, coupling to dissipative environments, and the Kondo effect (not addressed in this review) can be in principle treated on the same footing. Specially, the existence of well-developed diagrammatic techniques allows for a systematic treatment of interactions in nanoscale quantum systems. For the sake of

space, we did not deal with applications of NGF techniques to spin-dependent transport, a field that has been increasingly attracting the attention of the physical community in the past years due to its potential applications in quantum information theory and quantum computation [299, 300]. For the same reason, the implementation of NGF into first-principle based approaches was not discussed neither. This is nevertheless a crucial methodological issue, since system-specific and realistic information about molecule-metal contact details, charge transfer effects, modifications of the molecular electronic structure and configuration upon contacting, the electrostatic potential distribution in a device, etc can only be obtained via a full *ab initio* description of transport. For charge transport through noninteracting systems this has been accomplished some years ago by combining NGF with DFT methods. The inclusion of interactions, however, represents a much stronger challenge and has been mainly carried out, within the self-consistent Born-approximation, for the case of tunneling charges coupling to vibrational excitations in the molecular region. Also there were some efforts to include dynamical correlations into DFT-based approach. Much harder and till the present not achieved at all is the inclusion of electronic correlation effects, responsible for many-particle effects like Coulomb blockade or the Kondo effect, in a non-equilibrium transport situation. DFT-based techniques, being essentially mean-field theories, cannot deal in a straightforward way with such problems and have to be improved, e.g. within the LDA+U approaches. For the case of equilibrium transport, a generalization of the Landauer formula including correlations has been recently formulated as well as first attempts to go beyond the linear response regime; for strong out-of-equilibrium situations this will be, in our view, one of the most demanding issues that the theoretical "transport" community will be facing in the coming years.

Acknowledgments

The authors acknowledge the collaboration with Miriam del Valle, Marieta Gheorghe, Michael Hartung, Sudeep Mandal, and Soumya Mohapatra, with whom part of the work reviewed here was done. We appreciate very useful and illuminating discussions with Andrea Donarini, Pino D'Amico, Dietrich Förster, Milena Grifoni, Joachim Keller, Abraham Nitzan, Norbert Nemec, Danny Porath, Florian Pump, Klaus Richter, Eugen Starikow, and Juyeon Yi. We thank Antti-Pekka Jauho, Alessandro Pecchia, Tomáš Novotný, Hassan Raza, and Kristian Thygesen for their comments.

Funding by the EU through grant FET-IST-2001-38951 (international collaboration "DNA-based nanoelectronic devices (DNAnanoDEVICES)"), by the DFG through grant CU 44/3-2 (international collaboration "Single molecule based memories"), by the Volkswagen Stiftung under Grant No. I/78 340, by the DFG Graduated School "Nonlinearity and Nonequilibrium in Condensed Matter" GRK-638, by the DFG Priority Program "Quantum

Transport at the Molecular Scale" SPP1243, and by Collaborative Research Center SFB 689 is acknowledged. We also thank the Vielberth Foundation, the Minerva Foundation, the German Exchange Program (DAAD), the Humboldt foundation, and the German-Israeli foundation (GIF) for financial support. Computing time provided by the ZIH at the Dresden University of Technology is acknowledged.

References

1. M.A. Reed, J.M. Tour, Sci. Am. **282**, 86 (2000)
2. C. Joachim, J.K. Gimzewski, A. Aviram, Nature **408**, 541 (2000)
3. M.A. Ratner, Mater. today **5**, 20 (2002)
4. A. Nitzan, M.A. Ratner, Science **300**, 1384 (2003)
5. G. Cuniberti, G. Fagas, K. Richter (eds.), *Introducing Molecular Electronics*, *Lecture Notes in Physics*, vol. 680 (Springer-Verlag, 2005)
6. C. Joachim, M.A. Ratner, PNAS **102**, 8801 (2005)
7. A. Aviram, M.A. Ratner, Chem. Phys. Lett. **29**, 277 (1974)
8. M.A. Reed, C. Zhou, C.J. Muller, T.P. Burgin, J.M. Tour, Science **278**, 252 (1997)
9. J. Chen, M.A. Reed, A.M. Rawlett, J.M. Tour, Science **286**, 1550 (1999)
10. H. Park, J. Park, A.K.L. Lim, E.H. Anderson, A.P. Alivisatos, P.L. McEuen, Nature **407**, 57 (2000)
11. J. Park, A.N. Pasupathy, J.I. Goldsmit, C. Chang, Y. Yaish, J.R. Petta, M. Rinkoski, J.P. Sethna, H.D. Abruna, P.L. McEuen, D.C. Ralph, Nature **417**, 722 (2002)
12. W. Liang, M.P. Shores, M. Bockrath, J.R. Long, H. Park, Nature **417**, 725 (2002)
13. R.H.M. Smit, Y. Noat, C. Untiedt, N.D. Lang, M.C. van Hemert, J.M. van Ruitenbeek, Nature **419**, 906 (2002)
14. J. Kushmerick, J. Lazorcik, C. Patterson, R. Shashidhar, D. Seferos, G. Bazan, Nano Letters **4**, 639 (2004)
15. L.H. Yu, D. Natelson, Nano Lett. **4**, 79 (2004)
16. L.H. Yu, Z.K. Keane, J.W. Ciszek, L. Cheng, M.P. Stewart, J.M. Tour, D. Natelson, Phys. Rev. Lett. **93**, 266802 (2004)
17. X. Xiao, B. Xu, N.J. Tao, Nano Lett. **4**, 267 (2004)
18. M. Elbing, R. Ochs, M. Koentopp, M. Fischer, C. von Hänisch, F. Weigend, F. Evers, H.B. Weber, M. Mayor, PNAS **102**, 8815 (2005)
19. L. Venkataraman, J.E. Klare, I.W. Tam, C. Nuckolls, M.S. Hybertsen, M.L. Steigerwald, Nano Lett. **6**, 458 (2006)
20. M. Poot, E. Osorio, K. O'Neill, J.M. Thijssen, D. Vanmaekelbergh, C.A. van Walree, L.W. Jenneskens, H.S.J. van der Zant, Nano Lett. **6**, 1031 (2006)
21. E.A. Osorio, K. O'Neill, N. Stuhr-Hansen, O.F. Nielsen, T. Bjrnholm, H.S.J. van der Zant, Adv. Mater. **19**, 281 (2007)
22. E. Lörtscher, H.B. Weber, H. Riel, Phys. Rev. Lett. **98**, 176807 (2007)
23. D. Porath, Y. Levi, M. Tarabiah, O. Millo, Phys. Rev. B **56**, 9829 (1997)
24. B.C. Stipe, M.A. Rezaei, W. Ho, S. Gao, M. Persson, B.I. Lundqvist, Phys. Rev. Lett. **78**, 4410 (1997)

25. J.R. Hahn, W. Ho, Phys. Rev. Lett. **87**, 196102 (2001)
26. Y. Kim, T. Komeda, M. Kawai, Phys. Rev. Lett. **89**, 126104 (2002)
27. W. Ho, J. Chem. Phys. **117**, 11033 (2002)
28. N. Nilius, T.M. Wallis, W. Ho, Science **297**, 1853 (2002)
29. N. Nilius, T.M. Wallis, M. Persson, W. Ho, Phys. Rev. Lett. **90**, 196103 (2003)
30. S.W. Hla, K.F. Braun, B. Wassermann, K.H. Rieder, Phys. Rev. Lett. **93**, 208302 (2004)
31. N. Liu, N.A. Pradhan, W. Ho, J. Chem. Phys. **120**, 11371 (2004)
32. X.H. Qiu, G.V. Nazin, W. Ho, Phys. Rev. Lett. **92**, 206102 (2004)
33. S.W. Wu, G.V. Nazin, X. Chen, X.H. Qiu, W. Ho, Phys. Rev. Lett. **93**, 236802 (2004)
34. J. Repp, G. Meyer, F.E. Olsson, M. Persson, Science **305**, 493 (2004)
35. J. Repp, G. Meyer, S.M. Stojković, A. Gourdon, C. Joachim, Phys. Rev. Lett. **94**, 026803 (2005)
36. J. Repp, G. Meyer, S. Paavilainen, F.E. Olsson, M. Persson, Phys. Rev. Lett. **95**, 225503 (2005)
37. G.V. Nazin, X.H. Qiu, W. Ho, Phys. Rev. Lett. **95**, 166103 (2005)
38. N.A. Pradhan, N. Liu, C. Silien, W. Ho, Phys. Rev. Lett. **94**, 076801 (2005)
39. B.Y. Choi, S.J. Kahng, S. Kim, H. Kim, H.W. Kim, Y.J. Song, J. Ihm, Y. Kuk, Phys. Rev. Lett. **96**, 156106 (2006)
40. M. Martin, M. Lastapis, D. Riedel, G. Dujardin, M. Mamatkulov, L. Stauffer, P. Sonnet, Phys. Rev. Lett. **97**, 216103 (2006)
41. S.W. Wu, N. Ogawa, W. Ho, Science **312**, 1362 (2006)
42. F.E. Olsson, S. Paavilainen, M. Persson, J. Repp, G. Meyer, Phys. Rev. Lett. **98**, 176803 (2007)
43. A. Bannani, C. Bobisch, R. Moller, Science **315**, 1824 (2007)
44. P. Liljeroth, J. Repp, G. Meyer, Science **317**, 1203 (2007)
45. R. Schleser, T. Ihn, E. Ruh, K. Ensslin, M. Tews, D. Pfannkuche, D.C. Driscoll, A.C. Gossard, Phys. Rev. Lett. **94**, 206805 (2005)
46. M. Sigrist, T. Ihn, K. Ensslin, D. Loss, M. Reinwald, W. Wegscheider, Phys. Rev. Lett. **96**, 036804 (2006)
47. M. Sigrist, T. Ihn, K. Ensslin, M. Reinwald, W. Wegscheider, Phys. Rev. Lett. **98**, 036805 (2007)
48. K. Ono, D.G. Austing, Y. Tokura, S. Tarucha, Science **297**, 1313 (2002)
49. A.C. Johnson, J.R. Petta, C.M. Marcus, M.P. Hanson, A.C. Gossard, Phys. Rev. B **72**, 165308 (2005)
50. B. Muralidharan, S. Datta, Phys. Rev. B **76**, 035432 (2007)
51. J. Inarrea, G. Platero, A.H. MacDonald, Phys. Rev. B **76**, 085329 (2007)
52. J.C. Charlier, X. Blase, S. Roche, Rev. Mod. Phys. **79**, 677 (2007)
53. J. Richter, M. Mertig, W. Pompe, I. Monch, H.K. Schackert, Appl. Phys. Lett. **78**, 536 (2001)
54. M. Mertig, L. Colombi Ciacchi, R. Seidel, W. Pompe, A. De Vita, Nano Lett. **2**, 841 (2002)
55. K. Keren, R.S. Berman, E. Buchstab, U. Sivan, E. Braun, Science **302**, 1380 (2003)
56. E. Meggers, M.E. Michel-Beyerle, B. Giese, J. Am. Chem. Soc. **120**, 12950 (1998)
57. S.O. Kelley, J.K. Barton, Science **283**, 375 (1999)
58. D. Porath, A. Bezryadin, S. de Vries, C. Dekker, Nature **403**, 635 (2000)

59. C.R. Treadway, M.G. Hill, J.K. Barton, Chem. Phys. **281**, 409 (2002)
60. B. Xu, P. Zhang, X. Li, N. Tao, Nanolett. **4**(6), 1105 (2004)
61. R. Gutierrez, R. Bulla, G. Cuniberti, in *Modern methods for theoretical physical chemistry of biopolymers*, ed. by S. Tanaka, J. Lewis, E. Starikov (Elsevier, 2006)
62. R. Gutierrez, D. Porath, G. Cuniberti, in *Charge transport in disordered solids with applications in electronics*, ed. by S. Baranowski (John Wiley & Sons Inc., 2006)
63. D. Porath, G. Cuniberti, R.D. Felici, Topics in current chemistry **237**, 183 (2004)
64. E. Shapir, H. Cohen, A. Calzolari, C. Cavazzoni, D.A. Ryndyk, G. Cuniberti, A. Kotlyar, R. Di Felice, D. Porath, Nature Materials **7**, 68 (2008)
65. S. Datta, *Electronic Transport in Mesoscopic Systems* (Cambridge University Press, Cambridge, 1995)
66. H. Hauge, A.P. Jauho, *Quantum Kinetics in Transport and Optics of Semiconductors*, *Springer Series in Solid-State Physics*, vol. 123 (Springer, 1996)
67. D.K. Ferry, S.M. Goodnick, *Transport in Nanostructures* (Cambridge University Press, Cambridge, 1997)
68. T. Dittrich, P. Hänggi, G. Ingold, G. Schön, W. Zwerger, *Quantum dissipation and transport* (Wiley-VCH, 1998)
69. H. Bruus, K. Flensberg, *Many-body quantum theory in condensed matter physics* (Oxford University Press, Oxford, 2004)
70. S. Datta, *Quantum transport: atom to transistor* (Cambridge University Press, Cambridge, 2005)
71. U. Weiss, *Quantum Dissipative Systems*, *Series in Modern Condensed Matter Physics*, vol. 10 (World Scientific, 1999)
72. H.P. Breuer, F. Petruccione, *The theory of open quantum systems* (Oxford University Press, Oxford, 2002)
73. L. Kadanoff, G. Baym, *Quantum Statistical Mechanics* (Benjamin, New York, 1962)
74. L.V. Keldysh, Zh. Eksp. Teor. Fiz. **47**, 1515 (1964). [Sov. Phys. JETP **20**, 1018 (1965)]
75. D. Langreth, in *Linear and Nonlinear Electron Transport in Solids*, ed. by J. Devreese, E. van Doren (Plenum, New York, 1976)
76. J. Rammer, H. Smith, Rev. Mod. Phys. **58**, 323 (1986)
77. C. Caroli, R. Combescot, P. Nozieres, D. Saint-James, J. Phys. C: Solid St. Phys. **4**, 916 (1971)
78. C. Caroli, R. Combescot, D. Lederer, P. Nozieres, D. Saint-James, J. Phys. C: Solid St. Phys. **4**, 2598 (1971)
79. R. Combescot, J. Phys. C: Solid St. Phys. **4**, 2611 (1971)
80. C. Caroli, R. Combescot, P. Nozieres, D. Saint-James, J. Phys. C: Solid St. Phys. **5**, 21 (1972)
81. Y. Meir, N.S. Wingreen, Phys. Rev. Lett. **68**, 2512 (1992)
82. N.S. Wingreen, A.P. Jauho, Y. Meir, Phys. Rev. B **48**, 8487 (1993)
83. A.P. Jauho, N.S. Wingreen, Y. Meir, Phys. Rev. B **50**, 5528 (1994)
84. A.P. Jauho, Journal of Physics: Conference Series **35**, 313 (2006)
85. R. Landauer, IBM J. Res. Develop. **1**, 223 (1957)
86. R. Landauer, Phil. Mag. **21**, 863 (1970)
87. E.N. Economou, C.M. Soukoulis, Phys. Rev. Lett. **46**, 618 (1981)

88. D.S. Fisher, P.A. Lee, Phys. Rev. B **23**, 6851 (1981)
89. M. Büttiker, Y. Imry, R. Landauer, S. Pinhas, Phys. Rev. B **31**, 6207 (1985)
90. M. Büttiker, Phys. Rev. Lett. **57**, 1761 (1986)
91. R. Landauer, IBM J. Res. Develop. **32**, 306 (1988)
92. M. Büttiker, IBM J. Res. Develop. **32**, 317 (1988)
93. A.D. Stone, A. Szafer, IBM J. Res. Develop. **32**, 384 (1988)
94. H.U. Baranger, A.D. Stone, Phys. Rev. B **40**, 8169 (1989)
95. I.G. Lang, Y.A. Firsov, Sov. Phys. JETP **16**, 1301 (1963)
96. A.C. Hewson, D.M. Newns, Japan. J. Appl. Phys. **Suppl. 2, Pt. 2**, 121 (1974)
97. G. Mahan, *Many-Particle Physics*, 2nd edn. (Plenum, New York, 1990)
98. L.I. Glazman, R.I. Shekhter, Zh. Eksp. Teor. Fiz. **94**, 292 (1988). [Sov. Phys. JETP **67**, 163 (1988)]
99. N.S. Wingreen, K.W. Jacobsen, J.W. Wilkins, Phys. Rev. Lett. **61**, 1396 (1988)
100. N.S. Wingreen, K.W. Jacobsen, J.W. Wilkins, Phys. Rev. B **40**, 11834 (1989)
101. M. Jonson, Phys. Rev. B **39**, 5924 (1989)
102. M. Cízek, M. Thoss, W. Domcke, Phys. Rev. B **70**, 125406 (2004)
103. M. Cízek, Czech. J. of Phys. **55**, 189 (2005)
104. S. Braig, K. Flensberg, Phys. Rev. B **68**, 205324 (2003)
105. V. Aji, J.E. Moore, C.M. Varma, cond-mat/0302222 (2003)
106. A. Mitra, I. Aleiner, A.J. Millis, Phys. Rev. B **69**, 245302 (2004)
107. J. Koch, F. von Oppen, Phys. Rev. Lett. **94**, 206804 (2005)
108. J. Koch, M. Semmelhack, F. von Oppen, A. Nitzan, Phys. Rev. B **73**, 155306 (2006)
109. J. Koch, F. von Oppen, A.V. Andreev, Phys. Rev. B **74**, 205438 (2006)
110. K.C. Nowack, M.R. Wegewijs, cond-mat/0506552 (2005); M. R. Wegewijs, K. C. Nowack, New J. Phys. **7**, 239 (2005)
111. A. Zazunov, D. Feinberg, T. Martin, Phys. Rev. B **73**, 115405 (2006)
112. D.A. Ryndyk, P. D'Amico, G. Cuniberti, K. Richter, arXiv:0802.2808, Phys. Rev. B **78**, 085409 (2008)
113. S. Tikhodeev, M. Natario, K. Makoshi, T. Mii, H. Ueba, Surf. Sci. **493**, 63 (2001)
114. T. Mii, S. Tikhodeev, H. Ueba, Surf. Sci. **502**, 26 (2002)
115. T. Mii, S. Tikhodeev, H. Ueba, Phys. Rev. B **68**, 205406 (2003)
116. S. Tikhodeev, H. Ueba, Phys. Rev. B **70**, 125414 (2004)
117. M. Galperin, M.A. Ratner, A. Nitzan, Nano Lett. **4**, 1605 (2004)
118. M. Galperin, M.A. Ratner, A. Nitzan, J. Chem. Phys. **121**, 11965 (2004)
119. M. Galperin, A. Nitzan, M.A. Ratner, D.R. Stewart, J. Phys. Chem. B **109**, 8519 (2005)
120. T. Frederiksen, Inelastic electron transport in nanosystems. Master's thesis, Technical University of Denmark (2004)
121. T. Frederiksen, M. Brandbyge, N. Lorente, A.P. Jauho, Phys. Rev. Lett. **93**, 256601 (2004)
122. M. Hartung, Vibrational effects in transport through molecular junctions. Master's thesis, University of Regensburg (2004)
123. D.A. Ryndyk, J. Keller, Phys. Rev. B **71**, 073305 (2005)
124. D.A. Ryndyk, M. Hartung, G. Cuniberti, Phys. Rev. B **73**, 045420 (2006)
125. D.A. Ryndyk, G. Cuniberti, Phys. Rev. B **76**, 155430 (2007)
126. M. Paulsson, T. Frederiksen, M. Brandbyge, Phys. Rev. B **72**, 201101 (2005). [Erratum: **75**, 129901(E) (2007)]

127. M. Paulsson, T. Frederiksen, M. Brandbyge, J. Phys.: Conf. Series **35**, 247 (2006)
128. P.I. Arseyev, N.S. Maslova, JETP Lett. **82**, 297 (2005)
129. P.I. Arseyev, N.S. Maslova, JETP Lett. **84**, 93 (2006)
130. A. Zazunov, R. Egger, C. Mora, T. Martin, Phys. Rev. B **73**, 214501 (2006)
131. A.C. Hewson, D.M. Newns, J. Phys. C: Solid State Phys. **12**, 1665 (1979)
132. M. Galperin, M.A. Ratner, A. Nitzan, Nano Lett. **5**, 125 (2005)
133. P. D'Amico, D.A. Ryndyk, G. Cuniberti, K. Richter, arXiv:0806.1633, New J. Phys. **10**, 085002 (2008)
134. P. Král, Phys. Rev. B **56**, 7293 (1997)
135. U. Lundin, R.H. McKenzie, Phys. Rev. B **66**, 075303 (2002)
136. J.X. Zhu, A.V. Balatsky, Phys. Rev. B **67**, 165326 (2003)
137. A.S. Alexandrov, A.M. Bratkovsky, Phys. Rev. B **67**(23), 235312 (2003)
138. K. Flensberg, Phys. Rev. B **68**, 205323 (2003)
139. M. Galperin, M.A. Ratner, A. Nitzan, Phys. Rev. B **73**, 045314 (2006)
140. A. Zazunov, T. Martin, Phys. Rev. B **76**, 033417 (2007)
141. A. Mitra, I. Aleiner, A.J. Millis, Phys. Rev. Lett. **94**, 076404 (2005)
142. D. Mozyrsky, M.B. Hastings, I. Martin, Phys. Rev. B **73**, 035104 (2006)
143. L.Y. Gorelik, A. Isacsson, M.V. Voinova, B. Kasemo, R.I. Shekhter, M. Jonson, Phys. Rev. Lett. **80**, 4526 (1998)
144. D. Boese, H. Schoeller, Europhys. Lett. **54**, 668 (2001)
145. D. Fedorets, L.Y. Gorelik, R.I. Shekhter, M. Jonson, Europhys. Lett. **58**, 99 (2002)
146. D. Fedorets, Phys. Rev. B **68**, 033106 (2003)
147. D. Fedorets, L.Y. Gorelik, R.I. Shekhter, M. Jonson, Phys. Rev. Lett. **92**, 166801 (2004)
148. K.D. McCarthy, N. Prokof'ev, M.T. Tuominen, Phys. Rev. B **67**, 245415 (2003)
149. T. Novotný, A. Donarini, A.P. Jauho, Phys. Rev. Lett. **90**, 256801 (2003)
150. T. Novotný, A. Donarini, C. Flindt, A.P. Jauho, Phys. Rev. Lett. **92**, 248302 (2004)
151. Ya. M. Blanter, O. Usmani, Yu. V. Nazarov, Phys. Rev. Lett. **93**, 136802 (2004)
152. A.Y. Smirnov, L.G. Mourokh, N.J.M. Horing, Phys. Rev. B **69**, 155310 (2004)
153. N.M. Chtchelkatchev, W. Belzig, C. Bruder, Phys. Rev. B **70**, 193305 (2004)
154. J. Bardeen, Phys. Rev. Lett. **6**, 57 (1961)
155. W.A. Harrison, Phys. Rev. **123**, 85 (1961)
156. M.H. Cohen, L.M. Falicov, J.C. Phillips, Phys. Rev. Lett. **8**, 316 (1962)
157. R.E. Prange, Phys. Rev. **131**, 1083 (1963)
158. C.B. Duke, *Tunneling in solids* (Academic Press, New York, 1969). Chapter VII
159. J. Tersoff, D.R. Hamann, Phys. Rev. Lett. **50**, 1998 (1983)
160. J. Tersoff, D.R. Hamann, Phys. Rev. B **31**, 805 (1985)
161. B.N.J. Persson, A. Baratoff, Phys. Rev. Lett. **59**, 339 (1987)
162. M.A. Gata, P.R. Antoniewicz, Phys. Rev. B **47**, 13797 (1993)
163. H. Raza, arXiv:cond-mat/0703236 (2007)
164. M. Galperin, M.A. Ratner, A. Nitzan, J. Phys.: Condens. Matter **19**, 103201 (2007)
165. P.W. Anderson, Phys. Rev. **124**, 41 (1961)
166. J. Hubbard, Proc. R. Soc. London Ser. A **276**, 238 (1963)
167. J. Hubbard, Proc. R. Soc. London Ser. A **277**, 237 (1964)

168. J. Hubbard, Proc. R. Soc. London Ser. A **281**, 401 (1964)
169. D.V. Averin, K.K. Likharev, J. Low Temp. Phys. **62**(3/4), 345 (1986)
170. D.V. Averin, K.K. Likharev, in *Mesoscopic phenomena in solids*, ed. by B.L. Altshuler, P.A. Lee, R.A. Webb (Elsevier, Amsterdam, 1991), p. 173
171. H. Grabert, M.H. Devoret (eds.), *Single charge tunneling*, *NATO ASI Series B*, vol. 294 (Plenum, 1992)
172. H. van Houten, C.W.J. Beenakker, A.A.M. Staring, in *Single charge tunneling. NATO ASI Series B. Vol. 294*, ed. by H. Grabert, M.H. Devoret (Plenum, 1992), p. 167
173. L.P. Kouwenhoven, C.M. Markus, P.L. McEuen, S. Tarucha, R.M. Westervelt, N.S. Wingreen, in *Mesoscopic electron transport*, ed. by L.L. Sohn, L.P. Kouwenhoven, G. Schön (Kluwer, 1997), NATO ASI Series E: Applied Sciences, p. 105
174. H. Schoeller, in *Mesoscopic electron transport*, ed. by L.L. Sohn, L.P. Kouwenhoven, G. Schön (Kluwer, 1997), NATO ASI Series E: Applied Sciences, p. 291
175. G. Schön, in *Quantum dissipation and transport* (Wiley-VCH, 1998)
176. W.G. van der Wiel, S. De Franceschi, J.M. Elzerman, T. Fujisawa, S. Tarucha, L.P. Kouwenhoven, Rev. Mod. Phys. **75**, 1 (2002)
177. D.V. Averin, A.A. Odintsov, Phys. Lett. A **140**(5), 251 (1989)
178. D.V. Averin, Y.V. Nazarov, Phys. Rev. Lett. **65**, 2446 (1990)
179. D.V. Averin, Y.V. Nazarov, *Macroscopic quantum tunneling of charge and cotunneling* (Plenum, 1992), *NATO ASI Series B*, vol. 294, chap. 6, p. 217
180. D.V. Averin, A.N. Korotkov, K.K. Likharev, Phys. Rev. B **44**, 6199 (1991)
181. C.W.J. Beenakker, Phys. Rev. B **44**, 1646 (1991)
182. J. von Delft, D.C. Ralph, Phys. Rep. **345**, 61 (2001)
183. E. Bonet, M.M. Deshmukh, D.C. Ralph, Phys. Rev. B **65**, 045317 (2002)
184. M.H. Hettler, W. Wenzel, M.R. Wegewijs, H. Schoeller, Phys. Rev. Lett. **90**, 076805 (2003)
185. B. Muralidharan, A.W. Ghosh, S. Datta, Phys. Rev. B **73**, 155410 (2006)
186. G. Begemann, D. Darau, A. Donarini, M. Grifoni, Phys. Rev. B **77**, 201406 (2008)
187. E.G. Petrov, V. May, P. Hanggi, Chem. Phys. **296**, 251 (2004)
188. E.G. Petrov, V. May, P. Hanggi, Chem. Phys. **319**, 380 (2005)
189. E.G. Petrov, V. May, P. Hanggi, Phys. Rev. B **73**, 045408 (2006)
190. F. Elste, C. Timm, Phys. Rev. B **71**, 155403 (2005)
191. U. Harbola, M. Esposito, S. Mukamel, Phys. Rev. B) **74**, 235309 (2006)
192. J.N. Pedersen, B. Lassen, A. Wacker, M.H. Hettler, Phys. Rev. B **75**, 235314 (2007)
193. L. Mayrhofer, M. Grifoni, Eur. Phys. J. B **56**, 107 (2007)
194. H. Schoeller, G. Schön, Phys. Rev. B **50**, 18436 (1994)
195. J. König, H. Schoeller, G. Schön, Phys. Rev. Lett. **76**, 1715 (1996)
196. J. König, J. Schmid, H. Schoeller, G. Schön, Phys. Rev. B **54**, 16820 (1996)
197. J. König, H. Schoeller, G. Schön, Phys. Rev. Lett. **78**, 4482 (1997)
198. J. König, H. Schoeller, G. Schön, Phys. Rev. B **58**, 7882 (1998)
199. A. Thielmann, M.H. Hettler, J. König, G. Schön, Phys. Rev. B **68**, 115105 (2003)
200. A. Thielmann, M.H. Hettler, J. Konig, G. Schon, Phys. Rev. Lett. **95**, 146806 (2005)

201. J. Aghassi, A. Thielmann, M.H. Hettler, G. Schon, Phys. Rev. B **73**, 195323 (2006)
202. C. Timm, Phys. Rev. B **77**, 195416 (2008)
203. C. Lacroix, J. Phys. F: Metal Phys. **11**, 2389 (1981)
204. Y. Meir, N.S. Wingreen, P.A. Lee, Phys. Rev. Lett. **66**, 3048 (1991)
205. Y. Meir, N.S. Wingreen, P.A. Lee, Phys. Rev. Lett. **70**, 2601 (1993)
206. C. Niu, L.J. Liu, T.H. Lin, Phys. Rev. B **51**, 5130 (1995)
207. P. Pals, A. MacKinnon, J. Phys.: Condens. Matter **8**, 5401 (1996)
208. S. Lamba, S.K. Joshi, Phys. Rev. B **62**, 1580 (2000)
209. B. Song, D.A. Ryndyk, G. Cuniberti, Phys. Rev. B **76**, 045408 (2007)
210. J.J. Palacios, L. Liu, D. Yoshioka, Phys. Rev. B **55**, 15735 (1997)
211. L. Yi, J.S. Wang, Phys. Rev. B **66**, 085105 (2002)
212. C. Niu, D.L. Lin, T.H. Lin, J. Phys.: Condens. Matter **11**, 1511 (1999)
213. R. Swirkowicz, J. Barnas, M. Wilczynski, Phys. Rev. B **68**, 195318 (2003)
214. B.R. Bulka, T. Kostyrko, Phys. Rev. B **70**, 205333 (2004)
215. T. Fujii, K. Ueda, Phys. Rev. B **68**, 155310 (2003)
216. J. Schwinger, PNAS **37**, 452
217. P.C. Martin, J. Schwinger, Phys. Rev. **115**, 1342 (1959)
218. G. Baym, L.P. Kadanoff, Phys. Rev. **124**, 287 (1961)
219. G. Baym, Phys. Rev. **127**, 1391 (1962)
220. L. Hedin, Phys. Rev. **139**, A796 (1965)
221. F. Aryasetiawany, O. Gunnarsson, Rep. Prog. Phys. **61**, 237 (1988)
222. J.A. White, Phys. Rev. B **45**, 1100
223. G. Onida, L. Reining, A. Rubio, Rev. Mod. Phys. **74**, 601 (2002)
224. K.S. Thygesen, A. Rubio, J. Chem. Phys. **126**, 091101 (2007)
225. K.S. Thygesen, Phys. Rev. Lett. **100**, 166804 (2008)
226. K.S. Thygesen, A. Rubio, Phys. Rev. B **77**, 115333 (2008)
227. X. Wang, C.D. Spataru, M.S. Hybertsen, A.J. Millis, Phys. Rev. B **77**, 045119 (2008)
228. L.I. Glazman, M.E. Raikh, Pis'ma Zh. Eksp. Teor. Fiz. **47**, 378 (1988). [JETP Lett. **47**, 452 (1988)]
229. T.K. Ng, P.A. Lee, Phys. Rev. Lett. **61**, 1768 (1988)
230. S. Hershfield, J.H. Davies, J.W. Wilkins, Phys. Rev. B **46**, 7046 (1992)
231. N.S. Wingreen, Y. Meir, Phys. Rev. B **49**, 11040 (1994)
232. R. Aguado, D.C. Langreth, Phys. Rev. Lett. **85**, 1946 (2000)
233. T.S. Kim, S. Hershfield, Phys. Rev. B **63**, 245326 (2001)
234. M. Plihal, J.W. Gadzuk, Phys. Rev. B **63**, 085404 (2001)
235. S. Sanvito, A.R. Rocha, J. of Comp. and Theor. Nanoscience **3**, 624 (2006)
236. A.R. Rocha, V.M. García-Suárez, S. Bailey, C. Lambert, J. Ferrer, S. Sanvito, Phys. Rev. B **73**, 085414 (2006)
237. W.J.M. Naber, S. Faez, W.G. van der Wiel, J. Phys. D: Applied Physics **40**, R205 (2007)
238. Y. Ke, K. Xia, H. Guo, Phys. Rev. Lett. **100**, 166805 (2008)
239. Z. Ning, Y. Zhu, J. Wang, H. Guo, Phys. Rev. Lett. **100**, 056803 (2008)
240. M. Grifoni, P. Hänggi, Phys. Rep. **304**, 229 (1998)
241. S. Kohler, J. Lehmann, P. Hänggi, Phys. Rep. **406**, 379 (2005)
242. R. Sanchez, E. Cota, R. Aguado, G. Platero, Phys. Rev. B **74**, 035326 (2006)
243. J. Maciejko, J. Wang, H. Guo, Phys. Rev. B **74** (2006)
244. G. Cuniberti, G. Fagas, K. Richter, Chem. Phys. **281**, 465 (2002)

245. T.N. Todorov, J. Phys.: Condens. Matter **14**, 3049 (2002)
246. J. Taylor, H. Guo, J. Wang, Phys. Rev. B **63**, 121104 (2001)
247. J. Taylor, H. Guo, J. Wang, Phys. Rev. B **63**, 245407 (2001)
248. P.S. Damle, A.W. Ghosh, S. Datta, Phys. Rev. B **64**, 201403 (2001)
249. Y. Xue, S. Datta, M.A. Ratner, J. Chem. Phys. **115**, 4292 (2001)
250. Y. Xue, S. Datta, M.A. Ratner, Chem. Phys. **281**, 151 (2002)
251. Y. Xue, M.A. Ratner, Phys. Rev. B **68**, 115406 (2003)
252. Y. Xue, M.A. Ratner, Phys. Rev. B **68**, 115407 (2003)
253. A. Di Carlo, M. Gheorghe, P. Lugli, M. Sternberg, G. Seifert, Th. Frauenheim, Physica B **314**, 86 (2002)
254. Th. Frauenheim, G. Seifert, M. Elstner, T. Niehaus, C. Köhler, M. Amkreutz, M. Sternberg, Z. Hajnal, A. Di Carlo, S. Suhai, J. Phys.: Condens. Matter **14**, 3015 (2002)
255. M. Brandbyge, J.L. Mozos, P. Ordejón, J. Taylor, K. Stokbro, Phys. Rev. B **65**, 165401 (2002)
256. J. Taylor, M. Brandbyge, K. Stokbro, Phys. Rev. B **68**, 121101 (2003)
257. Y.J. Lee, M. Brandbyge, M.J. Puska, J. Taylor, K. Stokbro, R.M. Nieminen, Phys. Rev. B **69**, 125409 (2004)
258. A. Pecchia, A. Di Carlo, Rep. Prog. Phys. **67**, 1497 (2004)
259. S.H. Ke, H.U. Baranger, W. Yang, Phys. Rev. B **70**, 085410 (2004)
260. S.H. Ke, H.U. Baranger, W. Yang, Phys. Rev. B **71**, 113401 (2005)
261. S.H. Ke, H.U. Baranger, W. Yang, J. Chem. Phys. **122**, 074704 (2005)
262. S.H. Ke, H.U. Baranger, W. Yang, J. Chem. Phys. **123**, 114701 (2005)
263. R. Liu, S.H. Ke, W. Yang, H.U. Baranger, J. Chem. Phy. **124**, 024718 (2006)
264. S.H. Ke, H.U. Baranger, W. Yang, J. Chem. Phys. **127**, 144107 (2007)
265. F. Pump, G. Cuniberti, Surf. Sci. **601**, 4109 (2007)
266. M. del Valle, R. Gutiérrez, C. Tejedor, G. Cuniberti, Nature Nanotechnology **2**, 176 (2007)
267. A. Pecchia, G. Romano, A. Di Carlo, Phys. Rev. B **75**, 035401 (2007)
268. A. Pecchia, G. Penazzi, L. Salvucci, A. Di Carlo, New Journal of Physics **10**, 065022 (2008)
269. N. Sai, M. Zwolak, G. Vignale, M. Di Ventra, Phys. Rev. Lett. **94**, 186810 (2005)
270. S. Kurth, G. Stefanucci, C.O. Almbladh, A. Rubio, E.K.U. Gross, Phys. Rev. B **72**, 035308 (2005)
271. M. Di Ventra, R. D'Agosta, Phys. Rev. Lett. **98**, 226403 (2007)
272. A. Pecchia, A.D. Carlo, A. Gagliardi, S. Sanna, T. Frauenheim, R. Gutierrez, Nano Letters **4**, 2109 (2004)
273. N. Sergueev, D. Roubtsov, H. Guo, Phys. Rev. Lett. **95**, 146803 (2005)
274. M. Paulsson, T. Frederiksen, M. Brandbyge, Nano Lett. **6**, 258 (2006)
275. T. Frederiksen, M. Paulsson, M. Brandbyge, A.P. Jauho, Phys. Rev. B **75**, 205413 (2007)
276. T. Frederiksen, N. Lorente, M. Paulsson, M. Brandbyge, Phys. Rev. B **75**, 235441 (2007)
277. A. Gagliardi, G. Romano, A. Pecchia, A.D. Carlo, T. Frauenheim, T.A. Niehaus, New Journal of Physics **10**, 065020 (2008)
278. H. Raza, E.C. Kan, arXiv:0802.2357 (2008)
279. H. Raza, K.H. Bevan, D. Kienle, Phys. Rev. B **77**, 035432 (2008)
280. A. Ferretti, A. Calzolari, R. Di Felice, F. Manghi, Phys. Rev. B **72**, 125114 (2005)

281. V.I. Anisimov, J. Zaanen, O.K. Andersen, Phys. Rev. B **44**, 943 (1991)
282. P. Delaney, J.C. Greer, Phys. Rev. Lett. **93**, 036805 (2004)
283. P. Delaney, J.C. Greer, Int. J. Quantum Chem. **100**, 1163 (2004)
284. G. Fagas, P. Delaney, J.C. Greer, Phys. Rev. B **73**, 241314 (2006)
285. M. Albrecht, B. Song, A. Schnurpfeil, J. Appl. Phys. **100**, 013702 (2006)
286. G. Cuniberti, L. Craco, D. Porath, C. Dekker, Phys. Rev. B **65**, 241314 (2002)
287. R. Gutierrez, G. Fagas, K. Richter, F. Grossmann, R. Schmidt, Europhys. Letters **62**, 90 (2003)
288. R. Gutierrez, S. Mandal, G. Cuniberti, Nano Letters **5**, 1093 (2005)
289. R. Gutierrez, S. Mandal, G. Cuniberti, Phys. Rev. B **71**, 235116 (2005)
290. R. Gutiérrez, S. Mohapatra, H. Cohen, D. Porath, G. Cuniberti, Phys. Rev. B **74**, 235105 (2006)
291. M. Paulsson, cond-mat/0210519 (2002)
292. K. Huang, A. Rhys, Proc. R. Soc. London Ser. A **204**, 406 (1950)
293. S. Datta, W. Tian, S. Hong, R. Reifenberger, J.I. Henderson, C.P. Kubiak, Phys. Rev. Lett. **79**, 2530 (1997)
294. T. Rakshit, G.C. Liang, A.W. Gosh, M.C. Hersam, S. Datta, Phys. Rev. B **72**, 125305 (2005)
295. G. Caliskan, D. Mechtani, J.H. Roh, A. Kisliuk, A.P. Sokolov, S. Azzam, M.T. Cicerone, S. Lin-Gibson, I. Peral, The Journal of Chemical Physics **121**, 1978 (2004)
296. I.S. Gradshteyn, I.M. Ryzhik, *Table of Integrals, Series and Products* (Academic Press, 2000)
297. T. Holstein, Ann. Phys. N.Y. **8**, 325 (1959)
298. P. Ao, S. Grundberg, J. Rammer, Phys. Rev. B **53**, 10042 (1996)
299. M.A. Nielsen, I.L. Chuang, *Quantum Computation and Quantum Information* (Cambridge University Press, 2000)
300. D. Bouwmeester, A.K. Ekert, A. Zeilinger, *The Physics of Quantum Information: Quantum Cryptography, Quantum Teleportation, Quantum Computation* (Springer, 2000)
301. P. R. Levstein, H. M. Pastawski, J. L. D'Amato, J. Phys.: Cond. Matter **2**, 1781 (1990)
302. H.M. Pastawski, E. Medina, Rev. Mex. Fisica **47s1**, 1 (2001), cond-mat/0103219
303. J. L. D'Amato and H. M. Pastawski, Phys. Rev. B **41**, 7411 (1990)
304. H. M. Pastawski, L. E. F. Foa Torres, E. Medina, Chem. Phys. **281**, 257 (2002)
305. L. E. F. Foa Torres, H. M. Pastawski, E. Medina, EPL **73**, 1 (2006)
306. H. M. Pastawski, Phys. Rev. B **44**, 6329 (1991); **46**, 4053 (1992)
307. E. Runge, H. Ehrenreich, Phys. Rev. B **45**, 9145 (1992)

Part IV

New Methods for Open Systems Dynamics

Time-Local Quantum Master Equations and their Applications to Dissipative Dynamics and Molecular Wires

Ulrich Kleinekathöfer

School of Engineering and Science, Jacobs University Bremen, Campusring 1, 28759 Bremen, Germany u.kleinekathoefer@jacobs-university.de

Abstract. The dynamics in open quantum systems is often described by quantum master equations (QMEs). Here a certain class of these master equations, the so-called time-local or time-convolutionless QMEs, are reviewed in combination with a decomposition of the spectral density which describes the coupling between system and environment. Details of the derivations are given jointly together with applications to damped harmonic oscillators, calculation of absorption spectra on one side, and molecular wires on the other side. In the first class of applications the environment consists of a bosonic heat bath while in the second case the environments are fermionic particle reservoirs.

1 Introduction

Open quantum systems have attracted much attention over the last decades. While most of the studies dealt with systems coupled to bosonic heat baths, recently systems coupled to fermionic reservoirs describing for example molecular wires have been in the focus of many investigations. This chapter will not try to give a concise overview of the available literature but will focus on a particular approach: time-local (TL) quantum master equations (QMEs) and in particular their combination with specific forms of the spectral density.

To determine the dynamics of a system coupled to an environment is a formidable task which can only be solved analytically for a few basic examples. Among these are the damped harmonic oscillator serving as an example for the coupling to a bosonic bath [1] and the resonant level model as an example for the coupling to fermionic reservoirs [2]. There is a huge variety of formalisms developed to treat such systems. Exact treatments are for example possible by using the path integral technique [3] or the self-consistent hybrid schemes [4,5]. Also alternative approaches such as the surrogate Hamiltonian formalism for spin baths are possible [6]. Furthermore, a huge number of perturbative approaches are known either based on the Nakajima-Zwanzig identity [7–9] or on the Hashitsume-Shibata-Takahashi identity [10, 11]. In these theories the

I. Burghardt et al. (eds.), *Energy Transfer Dynamics in Biomaterial Systems*, Springer Series in Chemical Physics 93, DOI 10.1007/978-3-642-02306-4_10,

time evolution of the complete system plus environment is projected onto the relevant part of the system, leading to an explicit equation of motion for the relevant system alone. In rare cases the Nakajima-Zwanzig identity can be used to calculate the dynamics exactly [12]. However, in most cases perturbative treatments have to be invoked. A famous and widely used example of such a perturbative treatment is the so-called Redfield formalism [13–17] which is second order in the system-bath interaction part of the Hamiltonian.

Basically the perturbative techniques can be grouped into two classes: time-local (TL) and time-nonlocal (TNL) techniques, based on the Nakajima-Zwanzig or the Hashitsume-Shibata-Takahashi identity, respectively. Within the TL methods the QME of the relevant system depends only on the actual state of the system, whereas within the TNL methods the QME also depends on the past evolution of the system. This chapter concentrates on the TL formalism but also shows comparisons between TL and TNL QMEs. An important way how to go beyond second-order in perturbation theory is the so-called hierarchical approach by Tanimura, Kubo, Shao, Yan and others [18–26]. The hierarchical method originally developed by Tanimura and Kubo [18] (see also the review in Ref. [26]) is based on the path integral technique for treating a reduced system coupled to a thermal bath of harmonic oscillators. Most interestingly, Ishizaki and Tanimura [27] recently showed that for a quadratic potential the second-order TL approximation coincides with the exact result. Numerically a hint in this direction was already visible in simulations for individual and coupled damped harmonic oscillators [28].

In this chapter the work of our group in the direction of TL QMEs is reviewed. Before going into the details of QMEs, issues concerning spectral densities and correlation functions important for the present approach are discussed for both, bosonic as well as fermionic environments. In section 3, QMEs for dissipative quantum dynamics are derived and applied to model systems, but also to more complicated ones. It is shown that non-Markovian effects might also appear in static absorption spectra. Molecular wires and the electron transport through them is the topic of section 4 while some concluding remarks are given in the last section. The chapter is completed by an appendix containing simple derivations of the Nakajima-Zwanzig and the Hashitsume-Shibata-Takahashi identities. The Planck constant $\hbar$ is set to unity throughout this chapter.

2 Spectral densities and correlations functions

By using special forms of the so-called spectral density $J(\omega)$ it is possible to treat memory effects in QMEs. The spectral density $J(\omega)$ contains information on the frequencies of the environmental modes and their coupling to the system. Tanimura and coworkers [18, 20, 26] were the first to do calculations along the lines described here using spectral densities of Drude shape. This spectral densities lead to bath correlation functions with purely exponential

time dependence (see also [29]). Spectral densities which are not of this specific form can be fitted as a sum of Lorentzians. This way bath correlation functions with exponential time-dependencies are obtained. Among the first to use to use a fitted form of the bath correlation function were Korolkov, Paramonov and Manz [30,31] though their form included an extra fitting parameter. Meier and Tannor derived an approach based on the time-nonlocal Nakajima-Zwanzig identity in which an arbitrary spectral density is being fitted by a sum of Lorentzians [32]. By now this technique has been applied successfully in different approaches and to several applications as described, for example, in Refs. [29,33–38]. However, in special cases such as the Drude spectral density, the present scheme can be employed even without the numerical decomposition of the spectral density. For a bosonic bath of harmonic oscillators with mass m_i and frequency ω_i the spectral density function is defined as [3]

$$J(\omega) = \frac{\pi}{2} \sum_i \frac{c_i^2}{m_i \omega_i} \, \delta(\omega - \omega_i) \tag{1}$$

where c_i determines the coupling strength between the system and the ith environmental mode. Usually one assumes an infinite number of bath oscillators and therefore a continuous spectral density. Many different forms of the spectral density are discussed and applied in the literature either based on model assumptions or based on the analysis of numerical calculations (for example in Ref. [39]). The numerical decomposition of the spectral density proposed by Meier and Tannor [32] is given by

$$J(\omega) = \sum_{k=1}^{n} p_k \frac{\omega}{[(\omega + \Omega_k)^2 + \Gamma_k^2][(\omega - \Omega_k)^2 + \Gamma_k^2]} \tag{2}$$

with arbitrary real parameters p_k, Ω_k, and Γ_k. For the Ohmic spectral density with exponential cut-off $J(\omega) = \eta\omega \exp(-\omega/\omega_c)$ the fit parameters are given in table 1 of the paper by Meier and Tannor [32] together with a plot of the original and the fitted spectral densities. For an accurate fit three terms ($n = 3$) in Eq. (2) were needed in this case. Also more complicated spectral densities like $J(\omega) = \eta\omega^2/(2\omega_c^3) \exp(-\omega/\omega_c)$ which start quadratically in ω for small ω could be fitted using nine terms [36]. 20 terms are necessary for the spectral density for a light-harvesting systems obtained from molecular dynamics simulations [37].

2.1 Bosonic bath

To describe the effect of the environment one usually needs to determine the bath correlation function $C(t)$. Let us start discussing this function for a bosonic bath where the subscript "Ph" indicates a bath of phonons. Using the numerical decomposition of the spectral density Eq. (2) together with the theorem of residues one obtains the complex bath correlation functions

$$C(t) = \int_{-\infty}^{\infty} \frac{d\omega}{\pi} J_{\mathrm{Ph}}(\omega) n_B(\omega) e^{i\omega t} = \int_{-\infty}^{\infty} \frac{d\omega}{\pi} J_{\mathrm{Ph}}(\omega) \frac{e^{i\omega t}}{e^{\beta\omega} - 1}$$
$$= \sum_{k=1}^{n} \frac{p_k}{4\Omega_k \Gamma_k} \left\{ e^{i\Omega_k^+ t} n_B(\Omega_k^+) + e^{-i\Omega_k^- t} (n_B(\Omega_k^-) + 1) \right\}$$
$$+ \frac{2i}{\beta} \sum_{k=1}^{n'} J_{\mathrm{Ph}}(i\nu_k) e^{-\nu_k t} \tag{3}$$

using $\Omega_k^+ = \Omega_k + i\Gamma_k$, $\Omega_k^- = \Omega_k - i\Gamma_k$, the Bose-Einstein distribution $n_B(\omega)$ and the Matsubara frequencies $\nu_k = 2\pi k/\beta$. For simplicity, the spectral density has been extended to negative frequencies through $J(-\omega) = -J(\omega)$. In principle, the sum over the Matsubara terms is an infinite one. But for all practical purposes the sum can be truncated at some finite value n'. For very low temperatures a larger number of terms might be needed. In the version above we used the complex representation of the correlation function. Below we will also make use of separate real and imaginary parts of the correlation functions defined as

$$C(t) = a(t) - ib(t) = \int_{-\infty}^{\infty} \frac{d\omega}{2\pi} J_{\mathrm{Ph}}(\omega) \cos(\omega t) \coth\left(\frac{\beta\omega}{2}\right)$$
$$-i \int_{-\infty}^{\infty} \frac{d\omega}{2\pi} J_{\mathrm{Ph}}(\omega) \sin(\omega t) \tag{4}$$

with

$$a(t) = \sum_{k=1}^{n} \frac{p_k}{8\Omega_k \Gamma_k} \left\{ \coth(\beta\Omega_k^-/2) e^{-i\Omega_k^- t} + \coth(\beta\Omega_k^+/2) e^{i\Omega_k^+ t} \right\}$$
$$+ \frac{2i}{\beta} \sum_{k=1}^{n'} J_{\mathrm{Ph}}(i\nu_k) e^{-\nu_k t} \tag{5}$$

and

$$b(t) = \sum_{k=1}^{n} \frac{ip_k}{8\Omega_k \Gamma_k} \left\{ e^{-i\Omega_k^- t} - e^{i\Omega_k^+ t} \right\}. \tag{6}$$

The important property of this form of the correlation function is the fully exponential time-dependence which enables further analytical treatment. As in Ref. [32] we introduce the abbreviations

$$a(t) = \sum_{k=1}^{n_r} \alpha_k^{\mathrm{r}} e^{\gamma_k^{\mathrm{r}} t} \tag{7}$$

and

$$b(t) = \sum_{k=1}^{n_i} \alpha_k^{\mathrm{i}} e^{\gamma_k^{\mathrm{i}} t} \tag{8}$$

with $n_r = 2n + n'$ and $n_i = 2n$.

2.2 Fermionic reservoirs

Similar to the case of the bosonic bath, one may also define correlation functions in the case of fermionic reservoirs . In contrast to the former case, two different correlation functions will be introduced since there are also two different parts of the system-reservoir interaction: one creates and one annihilates an electron in the wire. The correlation functions are given by

$$C_{21}(t) = \int_0^\infty \frac{\mathrm{d}\omega}{\pi} J_{\mathrm{R}}(\omega)\, n_F(\omega - E_F) e^{i\omega t} \ , \tag{9}$$

$$C_{12}(t) = \int_0^\infty \frac{\mathrm{d}\omega}{\pi} J_{\mathrm{R}}(\omega)\, n_F(-\omega + E_F) e^{-i\omega t}. \tag{10}$$

The spectral density for the reservoir is denoted by J_{R}. There are two basic differences to the bosonic correlation function. The lower bound of the integrals is zero and not infinity and one has to introduce the Fermi energy E_F. By shifting the energy scale and therefore shifting the Fermi energy, one can make sure that the integrands vanish for negative ω. Accordingly one can extend the lower limits of the integrals to minus infinity and use the theorem of residues yielding

$$C_{12}(t) = \sum_{k=1}^{m} \frac{p_k}{4\Omega_k \Gamma_k} n_F(-\Omega_k^- + E_F) e^{-i\Omega_k^- t} - \frac{2i}{\beta} \sum_{k=0}^{m'} J_{\mathrm{R}}(\nu_k^*) e^{-i\nu_k^* t} \ , \tag{11}$$

$$C_{21}(t) = \sum_{k=1}^{m} \frac{p_k}{4\Omega_k \Gamma_k} n_F(\Omega_k^+ - E_F) e^{i\Omega_k^+ t} - \frac{2i}{\beta} \sum_{k=0}^{m'} J_{\mathrm{R}}(\nu_k) e^{i\nu_k t} \ , \tag{12}$$

with the abbreviations $\Omega_k^+ = \Omega_k + i\Gamma_k$ and $\Omega_k^- = \Omega_k - i\Gamma_k$ and $\nu_k = i\frac{2\pi k + \pi}{\beta} + E_F$. One has to note that the ν_k are now complex generalizations of the Matsubara frequencies including the Fermi energy as an additional argument. Since in general ν_k is non-zero for $k = 0$ the sum over the Matsubara terms has to start at $k = 0$. Similar to the case of bosonic baths the abbreviations $C_{12}(t) = \sum_{k=0}^{m+m'} a_{12}^k e^{\gamma_{12}^k t}$ and $C_{21}(t) = \sum_{k=0}^{m+m'} a_{21}^k e^{\gamma_{21}^k t}$ are introduced. The Matsubara sum can be truncated to a finite number of terms depending on the temperature of the reservoir.

3 Dissipative dynamics

After discussing the properties of the environments, let us now turn to the dynamics of a system in a dissipative environment, i.e. a system coupled to a bosonic bath . The case of fermionic reservoirs will be treated in the next section.

3.1 Model and quantum master equation

For a system-plus-bath complex the Hamiltonian is given by

$$H = H_{\rm S} + H_{\rm B} + H_{\rm SB} + H_{\rm ren} \ . \tag{13}$$

Denoting the coordinate of the system by q and the momentum by p, which both might be multi-dimensional variables in the general case, the system Hamiltonian is given by

$$H_{\rm S} = \frac{p^2}{2M} + V(q,t) \ , \tag{14}$$

where M defines the mass of the system. As indicated, the potential part $V(q,t)$ might be explicitly time-dependent. As is usually the case in system-plus-bath models, the Hamiltonian of the bath is assumed to be the sum of harmonic oscillators with mass m_i and frequency ω_i

$$H_{\rm B} = \frac{1}{2}\sum_{i=1}^{N}\left(\frac{p_i^2}{m_i} + m_i\omega_i^2 x_i^2\right) \ . \tag{15}$$

The other two terms in Eq. (13) are the interaction Hamiltonian $H_{\rm SB}$ which is assumed to be separable

$$H_{\rm SB} = \sum_k K_k(q)\sum_i c_{ik}x_i \tag{16}$$

where the c_{ik} denote coupling constants. The operators $K_k(q)$ are the system parts of the system-bath coupling operator. In addition, one often adds a renormalization term that compensates for artificial shifts of the system frequencies due to the interaction term [3]

$$H_{\rm ren} = \sum_{mn} K_m(q)K_n(q)\sum_i \frac{c_{im}c_{in}}{m_i\omega_i^2} = \sum_{mn} K_m(q)K_n(q)\mu_{mn} \ . \tag{17}$$

In the case of only one non-vanishing $K_m(q)$ and if the dissipation is assumed to be bilinear (i.e. $K(q) = -q$), Eqs. (13)-(17) lead to the so-called Caldeira-Leggett Hamiltonian

$$H = \frac{p^2}{2M} + V(t) + W(q,t) + \frac{1}{2}\sum_{i=1}^{N}\left[\frac{p_i^2}{m_i} + m_i\omega_i^2\left(x_i - \frac{c_i}{m_i\omega_i^2}q\right)^2\right] \ . \tag{18}$$

This standard Hamiltonian has been discussed in a tremendous number of publications under various aspects and will also be used in the examples described here.

Having established the Hamiltonian, the next step is to derive an equation of motion for the density matrix. One can start with the Liouville-von Neumann equation for the complete system-plus-bath density matrix $\sigma(t)$

$$i\frac{\partial}{\partial t}\sigma(t) = [H, \sigma(t)] = \mathcal{L}\sigma(t). \tag{19}$$

The solution of this equation would give the time-evolution of all system as well as bath degrees of freedom. This is often unnecessary and leads to a huge number of equations. Therefore one normally introduces the reduced density matrix $\rho(t)$ of the system degrees of freedom only.

Two different starting points of deriving equations of motion for the reduced density matrix $\rho(t)$ are the Nakajima-Zwanzig identity [7–9] and Hashitsume-Shibata-Takahashi identity [10, 11]. Derivations for these two identities are given in the appendix since they are key identities for the present approach and can be derived in a rather straightforward manner. The Nakajima-Zwanzig identity is the starting point for the TNL approach which is known under different names in the literature. Often it is called chronological time ordering prescription (COP) [40–42], time-convolution approach [43], or also Mori formalism [44]. Since the usual formal solution of the Liouville equation contains only chronologically ordered operators, the operators in this formalism are naturally time-ordered. Invoking a perturbation expansion of the system-bath coupling to second order one obtains a TNL QME [14,32,45]. This approach has been very popular but will not be the main focus of the current contribution due to reasons discussed below.

The time-local approach is based on the Hashitsume-Shibata-Takahashi identity and is also denoted as time-convolutionless formalism [43], partial time ordering prescription (POP) [40–42], or Tokuyama-Mori approach [46]. This can be derived formally from a second-order cumulant expansion of the time-ordered exponential function and yields a resummation of the COP expression [40, 42]. Sometimes the approach is also called the time-dependent Redfield theory [47]. As was shown by Gzyl [48] the time-convolutionless formulation of Shibata et al. [10, 11] is equivalent to the antecedent version by Fuliński and Kramarczyk [49, 50]. Using the Hashitsume-Shibata-Takahashi identity whose derivation is reviewed in the appendix, one yields in second-order in the system-bath coupling [51]

$$\frac{d\rho(t)}{dt} = -i\mathcal{L}_{\mathrm{S}}^{\mathrm{eff}}\rho(t) + \int_0^t dt' \mathcal{K}(t')\rho(t) \ , \tag{20}$$

where

$$\mathcal{K}(t') = \sum_k \mathcal{L}_k^- \mathcal{U}_{\mathrm{S}}(t,t') \left[a(t-t')\mathcal{L}_k^- - b(t-t')\mathcal{L}_k^+\right] \mathcal{U}_{\mathrm{S}}^\dagger(t,t') \tag{21}$$

$$\mathcal{L}_{\mathrm{S}}^{\mathrm{eff}} = [H_{\mathrm{S}} + H_{\mathrm{ren}}, \bullet\,], \quad \mathcal{L}_k^- = -i\,[K_k, \bullet\,], \quad \mathcal{L}_k^+ = [K_k, \bullet\,]_+ \tag{22}$$

and the free time evolution superoperator of the relevant system

$$\mathcal{U}_{\mathrm{S}}(t,t') = T_+ \exp\left\{-i\int_{t'}^{t} \mathrm{d}\tau \mathcal{L}_{\mathrm{S}}(\tau)\right\} \tag{23}$$

with the time-ordering operator T_+. In the expressions above no term stemming from the initial correlations was taken into account and the initial state $\sigma(t=0) = \rho(t=0)\rho_{\mathrm{B}}^{\mathrm{eq}}$ was assumed to be separable. In a realistic simulation one would have to include an excitation process into the simulation to account for initial correlations.

We want to note in passing that one can obtain the TL QME by making the approximate substitution [47]

$$\rho(t') = \mathcal{U}_{\mathrm{S}}^{\dagger}(t,t')\rho(t) \tag{24}$$

in the TNL equation, i.e. by neglecting the influence of dissipation on the time propagation of the density matrix within the integral. This transforms the integro-differential equation in the TNL formalism into one which is local in time. Both the TNL and the TL approach are second order in the system-bath coupling and we want to stress again that it is not easy to see if one of them is superior. For very small system-bath coupling strength the TNL, the TL and the Markovian approach are of course becoming identical. Using the real and imaginary parts of the correlation function and carrying out the commutators $\mathcal{L}_k^-$ and $\mathcal{L}_k^+$ one can define the following time dependent operators

$$\Lambda_k^r(t) = \int_0^t dt' a(t-t')\mathcal{U}_{\mathrm{S}}(t,t')K_k, \tag{25}$$

$$\Lambda_k^i(t) = \int_0^t dt' b(t-t')\mathcal{U}_{\mathrm{S}}(t,t')K_k \tag{26}$$

and

$$\Lambda_k(t) = \Lambda_k^{\mathrm{r}}(t) - i\Lambda_k^{\mathrm{i}}(t). \tag{27}$$

With these identities one can obtain an EOM for the reduced density matrix [29, 37]

$$\frac{\partial}{\partial t}\rho(t) = -i\mathcal{L}_{\mathrm{S}}^{\mathrm{eff}}\rho(t) - \sum_k \Big[K_k\Lambda_k(t)\rho(t) + \rho(t)\Lambda_k^{\dagger}(t)K_k - K_k\rho(t)\Lambda_k^{\dagger}(t) - \Lambda_k(t)\rho(t)K_k\Big]. \tag{28}$$

This expression will be used in the following for time-independent as well as time-dependent system Hamiltonians.

At this point a remark is in order concerning the notion of "non-Markovian" which is not used consistently in literature. Here we term non-Markovian everything which is beyond the Markov approximation in the TNL formalism. The Markov approximation normally consists of two parts [14, 16] starting from the TNL description: changing the equations in such a way that the density matrix is independent of the integration variable and moving the upper limit of the integration to infinity. In the original meaning of Markovian, a master equation can already be called Markovian if no time-convolution terms are present as in the TL approach. Here we use the former notion.

3.2 Time-independent systems

As a first step we take a closer look at time-independent system Hamiltonians. In these cases, the energy representation can be employed without any further approximation. In the following Greek letters will be used for the eigenstate representation, i.e. eigenenergies E_μ and eigenstates $|\mu\rangle$, etc. For a time-independent Hamiltonian, the matrix elements of the operators Λ_k can be calculated in this representation with transition frequencies $\omega_{\mu\nu}$. Taking advantage of the decomposition of the spectral density and a change of integration variables one obtains [29, 37]

$$\langle\mu|\,\Lambda_k\,|\nu\rangle = \langle\mu|\,K_k\,|\nu\rangle \int_0^t dt' C(t') e^{-i\omega_{\mu\nu}t'} = \langle\mu|\,K_k\,|\nu\rangle\,\Theta^+(t,\omega_{\mu\nu}) \tag{29}$$

in which the complex function $\Theta^+(t,\omega_{\mu\nu})$ is given by

$$\begin{aligned}\Theta^+(t,\omega_{\mu\nu}) = &\sum_j^{n_\mathrm{r}} \alpha_j^\mathrm{r} \frac{1}{\gamma_j^\mathrm{r} - i\omega_{\mu\nu}} \left[e^{(\gamma_j^\mathrm{r} - i\omega_{\mu\nu})t} - 1\right] \\ &-i\sum_j^{n_\mathrm{i}} \alpha_j^\mathrm{i} \frac{1}{\gamma_j^\mathrm{i} - i\omega_{\mu\nu}} \left[e^{(\gamma_j^\mathrm{i} - i\omega_{\mu\nu})t} - 1\right].\end{aligned} \tag{30}$$

Here we followed the notation of Ref. [52] for $\Theta^+(t,\omega_{\mu\nu})$ and used Eqs. (5) and (6) for the correlation functions $a(t)$ and $b(t)$. In the case of non-Markovian treatments $\Theta^+(t,\omega_{\mu\nu})$ has to be calculated at every moment in time instead of only once as in the Markovian limit. The Markovian limit of these expressions can easily be obtained by moving the upper integration boundary in Eq. (29) to infinity [16]. In both, the Markovian as well as the non-Markovian case, the evaluation of the matrix elements (30) does not contain any numerical integration anymore.

3.3 Time-dependent systems

For systems with time-dependent Hamiltonians one cannot use the eigenstate representation to easily solve the problem. Even an instantaneous diagonalization at every moment in time does not cure this problem because one would

have to correct for time-dependent basis functions in this case. A solution of this problem is a scheme with auxiliary quantities as developed by Meier and Tannor for the TNL-QME [32]. In the TL approach one has to define auxiliary operators instead of auxiliary density matrices [38]

$$\Lambda_k^{\mathrm{r}}(t) = \int_0^t dt' e^{\gamma_k^{\mathrm{r}} t'} \mathcal{U}_{\mathrm{S}}(t,t') K \ , \tag{31}$$

$$\Lambda_k^{\mathrm{i}}(t) = \int_0^t dt' e^{\gamma_k^{\mathrm{r}} t'} \mathcal{U}_{\mathrm{S}}(t,t') K \ . \tag{32}$$

Using these operators, the TL-QME can be written as

$$\frac{d\rho(t)}{dt} = -i\mathcal{L}_{\mathrm{S}}^{\mathrm{eff}}\rho(t) + \mathcal{L}_- \left(i \sum_{k=1}^{n_r} [\rho(t)\Lambda_k^{\mathrm{r}}(t) - \Lambda_k^{\mathrm{r}}(t)\rho(t)] - \sum_{k=1}^{n_i} [\rho(t)\Lambda_k^{\mathrm{i}}(t) + \Lambda_k^{\mathrm{i}}(t)\rho(t)] \right) \ . \tag{33}$$

Taking the time derivative of $\Lambda_k^{\mathrm{r}}(t)$ and $\Lambda_k^{\mathrm{i}}(t)$ the following differential equations can be found

$$\frac{d\Lambda_k^{\mathrm{r}}}{dt} = (\gamma_k^{\mathrm{r}} - i\mathcal{L}_{\mathrm{S}})\Lambda_k^{\mathrm{r}} + K \ , \tag{34}$$

$$\frac{d\Lambda_k^{\mathrm{i}}}{dt} = (\gamma_k^{\mathrm{i}} - i\mathcal{L}_{\mathrm{S}})\Lambda_k^{\mathrm{r}} + K \ . \tag{35}$$

These equations are representation independent and are valid for an arbitrary time-dependence of the system Hamiltonian as, for example, in the case of strong laser driving. In a suitable representation, the coupled set of differential equations Eqs. (33) to (35) can be solved numerically, for example, using a Runge-Kutta scheme. As already mentioned in the Introduction, Yan and coworkers [33–35] independently developed a similar approach starting at a correlation function which is assumed to be of the form Eqs. (5) and (6).

3.4 Example: damped harmonic oscillator

Memory effects play an important role for the description of dynamical effects in open quantum systems. As mentioned above, Meier and Tannor [32] developed a time-nonlocal scheme employing the numerical decomposition of the spectral density. The TL approach as discussed above as well as the approaches by Yan and coworkers [33–35] use similar techniques. Few systems exist for which exact solutions are available and can serve as test beds for the various theories. Among them is the damped harmonic oscillator for which a path-integral solution exists [1]. In the simple model of an initially excited

state of the oscillator, the Hamiltonian is time-independent and both methods described above, using the analytic matrix elements for the operators Λ_k^{r} and Λ_k^{i} as well as their solutions of the corresponding differential equations, can be used. In Ref. [29] the different non-Markovian theories were compared among each other as well as to each other, to the Markovian limit neglecting memory effects and to exact path integral calculations. For weak to moderate damping strengths and short bath correlation times, good agreement between the exact calculations and the non-Markovian results was obtained. For this study a spectral density of Drude form

$$J(\omega) = \frac{\eta\omega}{1 + (\omega/\omega_d)^2} \tag{36}$$

was used. As can be seen in Fig. 1 , for large bath correlation times, i.e. small cut-off frequencies of the spectral density, severe differences between the non-Markovian TNL and the TL versions can be observed. Comparing

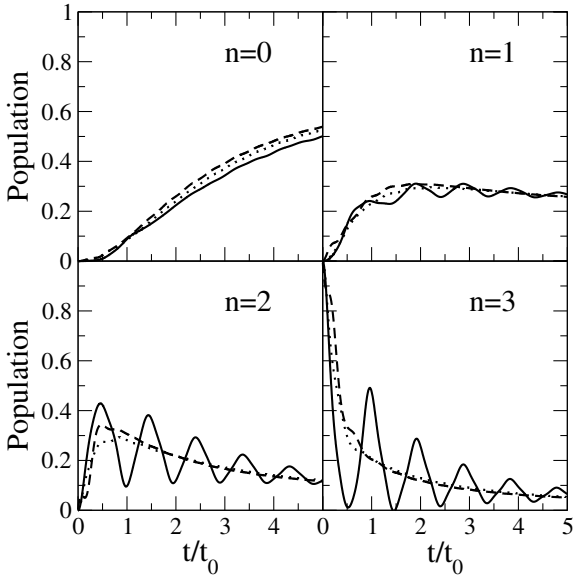

Fig. 1: Population dynamics of a damped harmonic oscillator. The populations of the ground state ($n = 0$) up to the third excited state ($n = 3$) are shown while initially all population is in the third excited state. The parameters are $\omega_d = \omega_0/2$, $\eta = 0.544\omega_0$, and $\beta = 1/\omega_0$. The results for the TNL theory are shown by the solid curve, those for the TL approach by the dotted curve and those of the Markovian limit by the dashed curve. (Reproduced from Ref. [29]. Copyright 2004, American Institute of Physics.)

the expectation values and standard deviations of the coordinate operator

to the exact solutions [1], no clear conclusion could be reached if the TL or if the TNL scheme is more accurate. The problem is that those expectation values are only averaged quantities and most of the difference between the TL and TNL formalisms were washed out. To see the reasons for these differences we recently performed higher-order perturbative treatments of the same system [53]. This higher-order treatment was based on a hierarchical method developed by the groups of Yan and Shao [23,25]. This formulation is very similar to the earlier one proposed by Tanimura and coworkers [18,20,26]. Fig. 2

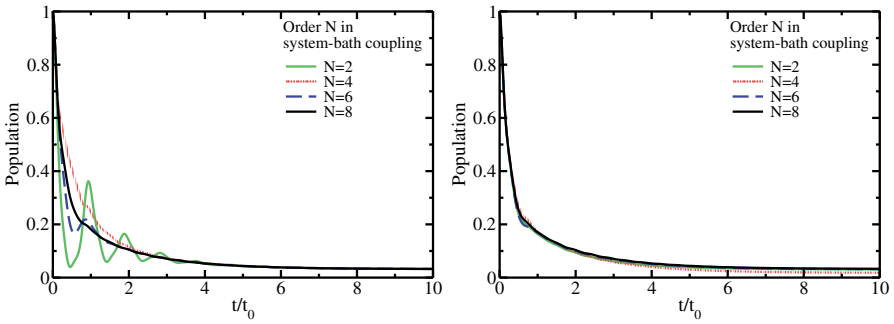

Fig. 2: Population dynamics of the third excited state for TL (left) and TNL (right) truncation in different orders N of the system-bath coupling calculated using a Drude spectral density with $\eta = 0.544$ and $\omega_d = 0.5$ a.u. (Reproduced from Ref. [28]. Copyright 2007, American Institute of Physics.)

shows the population dynamics for the third excited state and the long bath correlation for the same parameters as in Fig. 1. This time the TL and TNL approaches are displayed in different panels showing results up to eighth order in the system-bath coupling strength. As can be seen clearly, the oscillations in the TNL second order results are artificial and vanish using higher order terms. Actually, as shown recently by Ishizaki and Tanimura [27] second-order TL is exact for bosonic environments and, taking higher-order contributions into account, this additional small but non-vanishing terms even introduce inaccuracies. In addition, the hierarchical method was applied to calculate the time evolution of the reduced density matrix of two coupled harmonic oscillators coupled to a thermal bath [53]. Calculations to several orders in the system-bath coupling with two different truncation schemes were performed. The respective density matrices were then used to calculate the time evolution of the population dynamics as well as the variance in the coordinate. It could clearly be seen that for the initial state chosen, the population dynamics for one or two coupled damped harmonic oscillators converges faster in the TL approach while the variance of the coordinate converges faster in the TNL formalism [53].

One point which has not been addressed in the example of the time-independent harmonic oscillator is the non-perturbative treatment of the time dependence in the system Hamiltonians. Both the TL and the TNL non-Markovian theories employ auxiliary operators or density matrices, respectively, and can be applied in strongly driven systems [29, 32]. This point will be shown to be very important in the examples for the molecular wires under the influence of strong laser fields.

3.5 Absorption spectra

Interestingly enough, one sees differences between the various variants of Markovian and non-Markovian theories already in static linear absorption spectra. In the regime of second-order perturbation theory in the coupling to the electromagnetic field the linear absorption line-shape $I(\omega)$ can be calculated from the Fourier transform of the dipole-dipole correlation function as

$$I(\omega) \propto \mathrm{Re} \int_0^\infty dt\, e^{i\omega t}\ \mathrm{tr}\left\{\sigma_{\mathrm{eq}}\left[\hat{\mu}(t), \hat{\mu}\right]\right\}\ , \tag{37}$$

where $\hat{\mu}(t)$ denotes the dipole operator which is evolving according to the Hamiltonian of the unperturbed system and σ_{eq} is the equilibrium density matrix of the full system. As an example in Ref. [37] the linear absorption spectrum of an ensemble of B850 rings of the light-harvesting system LH2 of purple bacteria (*Rhodospirillum molischianum*) [37] was calculated. As can be seen in Fig. 3 in the ensemble average calculated using 3000 samples over a random site disorder, the deviations between the various theories is small. But again, for configurations with longer bath correlation times, the TL theory shows extra features not present in the TL and Markovian results. This might become very important in calculating spectra for single molecule setups. In Ref. [37] the influence of static disorder on the line shape in the ensemble average was further demonstrated and the results of the calculations compared to experimental data.

In addition to non-Markovian theories also the modified Redfield theory was applied to determine the absorption spectra of light-harvesting systems [37]. Moreover a time-dependent modified Redfield theory was employed to calculate the linear absorption spectra for an ensemble of B850 rings [53]. This theory is an extension of the standard modified Redfield theory without invoking the Markov approximation. The results for the modified Redfield theory with and without Markov approximation were compared to the spectra obtained from TL second-order perturbation theory sometimes also called "time-dependent Redfield theory". The influence of the shape of the spectral density on the linear absorption spectrum was again demonstrated for single samples and in the ensemble average. Stronger damping clearly leads to further broadening, especially in the high-energy part of the static absorption line shapes [53].

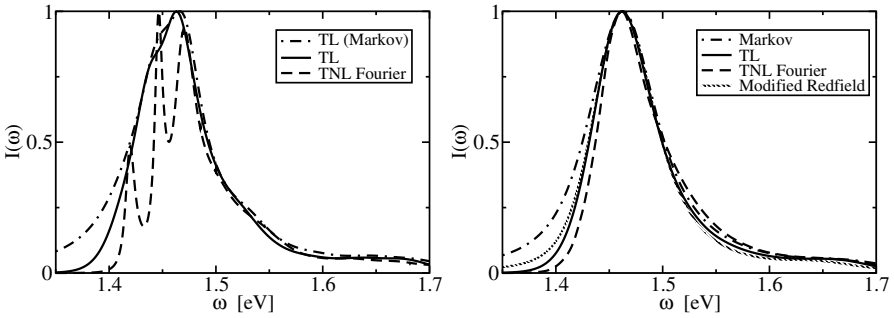

Fig. 3: Absorption spectra of one sample of B850 calculated with different methods for an Ohmic spectral density with $\eta = 3.37$ and $\omega_c = 0.027$ eV. Left: Methods with Markov approximation, i.e. Redfield theory with and without secular approximation and TL method. Right: TL with and without Markov approximation, TNL and modified Redfield method. (Reproduced from Ref. [37]. Copyright 2006, American Institute of Physics.)

4 Molecular wires

In the previous chapter the system was coupled to a thermal phononic bath. In another type of open quantum systems the relevant system is coupled to fermionic reservoirs [38]. The prime applications of this model are molecular wires and quantum dot systems in which the relevant system describes a molecule or a set of quantum dots and the reservoirs the electronic contacts. Although in the following the focus lies on molecular wires, most of the statements are also true for quantum dots at this level of description. Concerning possible systems, recent theoretical investigations discuss trans-polyacetylene oligomers [54] or oligophenylene molecules [55] as candidates for an experimental implementation of light-induced effects. It is also shown how to derive tight-binding models for such systems. To theoretically investigate the effect of time-dependent fields on molecular junctions one can, for example, apply non-equilibrium Green's functions [56] but in most approaches so far the coupling of the wire to the leads was treated perturbatively [38, 57–63].

4.1 Model and quantum master equation

As for the case of a bosonic bath, the Hamiltonian describing the molecular junction is separated into the relevant system $H_{\rm S}(t)$, describing the wire, the field-matter interaction $H_{\rm F}(t)$ and reservoirs $H_{\rm R}$ modeling the leads

$$H(t) = H_{\rm S}(t) + H_{\rm F}(t) + H_{\rm R} + H_{\rm SR} \ , \tag{38}$$

with wire-lead coupling $H_{\rm SR}$. The wire consists of N sites coupled to each other by a hopping element Δ. The electrons in the molecular wire at site n

are created (annihilated) by $c_n^\dagger$ (c_n) and therefore the tight-binding description of the wire reads

$$H_{\mathrm{S}}(t) = \sum_n \varepsilon_n c_n^\dagger c_n - \Delta \sum_n (c_n^\dagger c_{n+1} + c_{n+1}^\dagger c_n) + U \sum_n c_n^\dagger c_n c_{n+1}^\dagger c_{n+1} \ . \quad (39)$$

The on-site energy contributions are described by the first term and the nearest-neighbor hopping is contained in the second. The last term denotes an electron-electron interaction term with strength U. For simplicity electron spin has been neglected but can be incorporated in a straightforward manner [64]. Denoting the dipole operator, which will be detailed below, by μ the coupling between the wire and the laser field $E(t)$ reads $H_{\mathrm{F}}(t) = -\mu E(t)$.

The environment of the wire consists of two electronic leads that are modeled by two independent reservoirs of uncorrelated electrons in thermal equilibrium. For each lead, the Hamiltonian H_{R} is given by $H_{\mathrm{R}} = \sum_q \omega_q b_q^\dagger b_q$ with $b_q^\dagger$ creating and b_q annihilating an electron in the corresponding reservoir mode $|q\rangle$ with energy ω_q. In further derivations we will only refer to the left lead but the formalism has to be applied as well to the right lead coupled to the last site N of the wire. The coupling of the left electronic lead with the first site of the wire is given by

$$H_{\mathrm{SR}} = \sum_{x=1}^{2} K_x \Phi_x = \sum_q (V_q c_1^\dagger b_q + V_q^* b_q^\dagger c_1) \quad (40)$$

with $\Phi_1 = \sum_q V_q b_q$, $\Phi_2 = \sum_q V_q^* b_q^\dagger$, $K_1 = c_1^\dagger$, $K_2 = c_1$, and a wire-lead coupling V_q for each reservoir mode.

As for the case of a bosonic bath, the starting point here is the TL approach and a TL QME based on a second-order perturbation theory in the molecule-lead coupling was developed for the reduced density matrix $\rho(t)$ of the molecule [38, 65]

$$\frac{\partial \rho(t)}{\partial t} = -i\mathcal{L}_{\mathrm{S}}(t)\rho(t) - i\mathcal{L}_{\mathrm{F}}\rho(t) - D(t)\rho(t) \ , \quad (41)$$

$$D(t)\rho(t) = \sum_{xx'} [K_x, \Lambda_{xx'}(t)\rho(t)] + \mathrm{H.\,c.} \quad (42)$$

with H. c. denoting the Hermitian conjugate and the auxiliary operators for the wire-lead coupling

$$\Lambda_{xx'}(t) = \int_{t_0}^{t} \mathrm{d}t' C_{xx'}(t-t') \mathcal{U}_{\mathrm{S}}(t,t') K_{x'} \ . \quad (43)$$

Here we employed the definitions $\mathcal{U}_{\mathrm{S}}(t,t') = T_+ \exp\left\{-i \int_{t'}^{t} \mathrm{d}\tau \, (\mathcal{L}_{\mathrm{S}}(\tau) + \mathcal{L}_{\mathrm{F}}(\tau))\right\}$, $\mathcal{L}_{\mathrm{S}}(\tau) = [H_{\mathrm{S}}(\tau), \bullet]$, $\mathcal{L}_{\mathrm{F}}(\tau) = [H_{\mathrm{F}}(\tau), \bullet]$ with the time-ordering operator T_+

and the reservoir correlation functions $C_{xx'}(t)$. To derive this shorter version of $D(t)\rho(t)$ in Eq. (42) compared to Refs. [38,65], one has to use the fact that $K_1 = K_2\dagger$ and observe that $U_{\rm S}(t,t')$ is a superoperator acting on $K_{x'}$ only. Under these circumstances the operator $\widehat{\Lambda}_{xx'}(t)$ equals $\Lambda^\dagger_{x'x}(t)$.

4.2 Auxiliary operators

As in the bosonic case, a simplified algorithm can be derived for time-independent system Hamiltonians. In eigenstate representation with eigenstates $|\mu\rangle, |\nu\rangle$ and transition frequencies $\omega_{\mu\nu}$ the matrix elements of $\Lambda_{xx'}(t)$ are given by

$$\langle\mu|\,\Lambda_{xx'}\,|\nu\rangle = \langle\mu|\,K_{x'}\,|\nu\rangle \int\limits_0^t dt' C_{xx'}(t') e^{-i\omega_{\mu\nu}t'} = \langle\mu|\,K_{x'}\,|\nu\rangle\,\Theta^+_{xx'}(t,\omega_{\mu\nu}) \tag{44}$$

with

$$\Theta^+_{xx'}(t,\omega_{\mu\nu}) = \sum_{k=0}^{m+m'} a^k_{xx'} \frac{1}{\gamma^k_{xx'} - i\omega_{\mu\nu}} \left[e^{(\gamma^k_{xx'} - i\omega_{\mu\nu})t} - 1\right] \tag{45}$$

where the expression $C_{12}(t) = \sum_{k=0}^{m+m'} a^k_{12} e^{\gamma^k_{12}t}$ and $C_{21}(t) = \sum_{k=0}^{m+m'} a^k_{21} e^{\gamma^k_{21}t}$ for the correlation functions were used as defined in subsection 2.2. So the treatment is of course very similar to that of the bosonic case and also the same comments concerning the Markovian limit apply.

For time-dependent systems again the purely exponential time-dependence of the correlation function allows the derivation of a set of differential equations for the auxiliary operators

$$\frac{\partial}{\partial t}\Lambda^k_{xx'}(t) = a^k_{xx'} K_{x'}\rho_{\rm S}(t) - i[H_{\rm S}(t), \Lambda^k_{xx'}(t)] + \gamma^k_{xx'}\Lambda^k_{xx'}(t) \tag{46}$$

with $\Lambda_{xx'}(t) = \sum_{k=0}^{m+m'} \Lambda^k_{xx'}(t)$. Thus in addition to the QME for $\rho(t)$ one has to propagate $m + m'$ differential equation for the auxiliary operators.

4.3 Switching electron transport with laser pulses

In molecular wire systems the population dynamics is of course an interesting quantity to analyze but probably the most interesting quantity is the electron current. Using the electron number operator of the left lead with the summation performed over the reservoir degrees of freedom $N_l = \sum_q b^\dagger_q b_q$, the expression for the current is given by [38]

$$\begin{aligned} I_l(t) &= e\frac{\rm d}{{\rm d}t}{\rm tr}\left\{N_l\rho_S(t)\right\} = -ie\,{\rm tr}\left\{[N_l, H(t)]\rho_{\rm S}(t)\right\} \\ &= 2e\,{\rm Re}\left({\rm tr}_{\rm S}\left\{c^\dagger_1\Lambda_{12}(t)\rho_{\rm S}(t) - c^\dagger_1\rho_{\rm S}(t)\Lambda^\dagger_{21}(t)\right\}\right)\,. \end{aligned} \tag{47}$$

Here e denotes the elementary charge. This equation describes the current $I_l(t)$ from the left lead into the molecule. A similar expression holds for $I_r(t)$ from the right lead into the molecule. In a steady state and after averaging over one period of the driving field, I_l and I_r have the same magnitude but opposite signs and therefore a total transient current through the molecular junction can be defined as $I(t) = (I_l(t) - I_r(t))/2$. The time-dependent average current "$\bar{I}(t)$" will be determined below by averaging $I(t)$ over five periods of the highly oscillating carrier field.

The advantage of the present QME for transport is the possibility to directly incorporate effects of laser fields. Molecular wires irradiated by laser fields do show some new interesting effects and in the future can lead to optical switching of electronic current which would open a whole new field of applications. Especially interesting about the theory above is the non-perturbative treatment of the laser-matter interaction. This can be done in a TL but also in a TNL formalism [66]. As the TL approach in second-order perturbation theory is exact in many instances of the bosonic case, we also prefer it for the case of fermionic reservoirs. Furthermore it allows for an easier definition of the current operator which is important for the coherent control theory (see below). In previous studies the non-perturbative treatment of the laser-matter interaction and therefore of strong-field effects was often performed using the Floquet theory for periodic driving. This restriction of periodic driving is not present in the current TL QME and pulsed driving can be studied.

In the context of molecular wires, the Floquet theory was especially employed to study the phenomenon of coherent destruction of tunneling (CDT) for monochromatic laser fields [57, 67–69] . For certain ratios of amplitude and frequency of the driving field, a destructive quantum effect leads to a vanishing current through the wire. Using the present QME it was shown [65] that the average current through the system can be suppressed also for pulsed driving as shown in Fig. 4. For different parameters of the model, which do not show a net current without any optical field, a Gaussian laser pulse could establish a temporary current. Electron interaction effects on the current can easily be incorporated in this QME formalism.

Interestingly enough, CDT cannot only suppress the current through systems consisting of two or more sites but also through molecular junctions in which only one site is needed to describe the molecule. In this case the current is suppressed inbetween junction and molecule and only works for small applied bias voltages. For larger voltages so-called photon-assisted states come into play and the current through those virtual states is not suppressed [70].

Moreover, instead of using a fixed laser pulse and calculating the resulting electron current one can employ the optimal control theory often used in the area of molecular and chemical physics [71, 72]. In this approach one first defines a target, i.e. a time-dependent current flow pattern, and then calculates backwards the driving field resulting in the target. So the laser field is determined in an inverse problem. The theory was applied in Ref. [73] and an example is shown in Fig. 5. Here the target contains a high-frequency car-

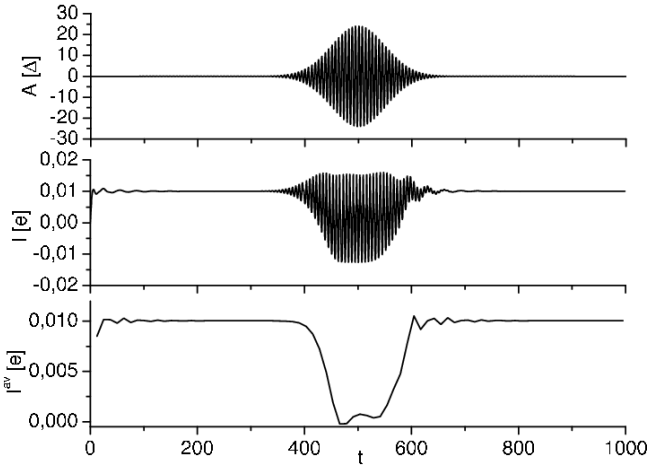

Fig. 4: The upper panel shows the Gaussian excitation pulse with a peak amplitude fulfilling the CDT condition. The resulting current is given in middle panel and its average over three periods of the fast pulse oscillations at the bottom. The on-site energies are equal and centered between the left and the right Fermi energy. (Reproduced from Ref. [38]. Copyright 2004, American Institute of Physics.)

rier wave and a pulse envelope. Averaging over five oscillatory periods of the carrier wave yields an efficient suppression of the current.

These examples show that there is a multitude of possible effects that laser field driving can have on the current through a molecular wire. In the upcoming years this will certainly become an interesting field of research, theoretically as well as experimentally. On the experimental side, the challenge is to focus the laser light onto the molecular junction with a width below the diffraction limit of the light. Nevertheless, the development of several techniques such as tip-enhanced near-field scanning optical microscopy [74], coupling of a laser field to an adsorbed molecule on a surface with the help of scanning tunneling microscopy [75] or the laser illumination of an molecule in a break-junction geometry [76] seems to be very promising.

5 Concluding remarks

Using a numerical decomposition of the spectral density which describes the coupling of the system to the environment allows one to develop TL and TNL non-Markovian QMEs. Using the hierarchical approach the results can be extended from second-order perturbation theory to higher orders to be able to study the convergence properties of the different approaches. As shown in the example for bosonic baths, the TL formalism shows numerically almost converged results. Actually, this numerical finding has been analytically proven

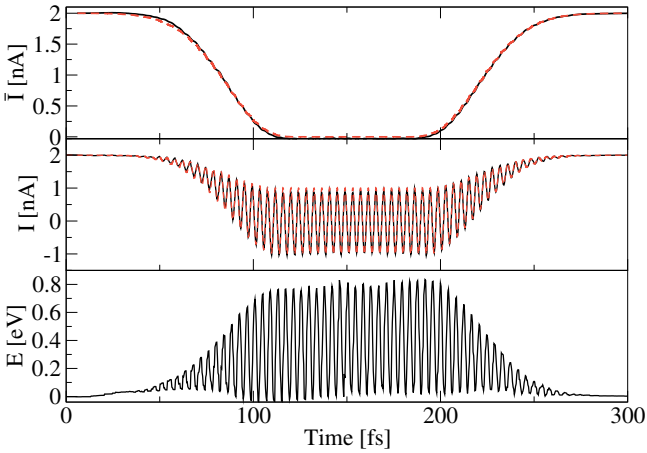

Fig. 5: A control target including a highly oscillating pattern. The control target (dashed) and the achieved current (solid) are displayed in the middle panel while in the top panel an average over five oscillatory periods is shown. The control field is given in the lowest part of the figure. (Reproduced from Ref. [73]. Copyright 2008 by the American Physical Society.)

to be correct, i.e. for bosonic bath the second-order TL QME coincides with the exact result [27]. For fermionic reservoirs no analysis in this direction has been made yet but would be of high importance for further studies along these lines.

Models describing the transport of electrons in molecular junctions have been shown to be quite powerful. Here the emphasis was put on time-dependent effects which can, for example, be triggered by external laser fields. If these fields are strong, a non-perturbative treatment of the laser-matter interaction is of large importance and is included in the presented TL QME. Also the connection of transport through molecular wires or coherent laser control scenarios may play an important role in the future.

Beyond the systems and applications described in this chapter, projection-operator methods can, for example, be used to study the dynamics near glass transitions [77] and the propagation of wave functions in systems with non-resonant transitions. The latter application has recently been analyzed in connection with the decomposition of the spectral density [78] showing the wide range of applicability of the proposed schemes.

Acknowledgement

The work briefly reviewed above was performed in collaboration with Markus Schröder, Sven Welack, Guangqi Li and Michael Schreiber. For suggestions to

improve the manuscript I thank Lisa Moevius and Ciprian Padurariu. Funding through the Deutsche Forschungsgemeinschaft is gratefully acknowledged.

Appendix

5.1 Nakajima-Zwanzig identity

Starting point for the derivation of the Nakajima-Zwanzig identity is the Lioville-von Neumann equation for the density operator σ of the complete system, i.e. relevant system plus environment. As stated before $\hbar \equiv 1$ is used and thus the QME reads

$$i\frac{d}{dt}\sigma(t) = \mathcal{L}\sigma(t) \tag{48}$$

with the Liouville operator $\mathcal{L}\bullet = [H, \bullet]$. For simplicity we restrict ourselves to time-independent Hamilton operators H in the following. For time-dependent Hamiltonians care has to be taken with respect to time ordering. To derive the Nakajima-Zwanzig identity out of this equation one introduces a projector P onto the relevant system. The sub- and superscripts E refer to the environment which corresponds to a heat bath for the bosonic case and to electron reservoirs for the fermionic case. In the context of the current chapter, this operator is usually defined as

$$\mathcal{P}\bullet = \rho_{\mathrm{eq}}^{\mathrm{E}} \otimes \mathrm{Tr}_{\mathrm{E}}(\bullet) \tag{49}$$

where ρ_{eq}^{E} is the equilibrium state of the environment with $\mathrm{Tr}_{\mathrm{E}}\rho_{\mathrm{eq}}^{\mathrm{E}} = 1$. Since the projector is idempotent, $\mathcal{P} = \mathcal{P}^2$, the complementary operator is given by $\mathcal{Q}$ with $\mathcal{P} + \mathcal{Q} = 1$. Nevertheless, for clarity reasons we will mainly stick to $\mathcal{P}$ and $1 - \mathcal{P}$ below.

In a first step one applies the projectors for the relevant and irrelevant part to the Lioville-von Neumann equation

$$i\frac{d}{dt}\mathcal{P}\sigma(t) = \mathcal{P}\mathcal{L}\sigma(t) = \mathcal{P}\mathcal{L}\mathcal{P}\sigma(t) + \mathcal{P}\mathcal{L}(1-\mathcal{P})\sigma(t) \tag{50}$$

$$i\frac{d}{dt}(1-\mathcal{P})\sigma(t) = (1-\mathcal{P})\mathcal{L}\sigma(t) = (1-\mathcal{P})\mathcal{L}\mathcal{P}\sigma(t) + (1-\mathcal{P})\mathcal{L}(1-\mathcal{P})\sigma(t) \tag{51}$$

Then the equation for the irrelevant part is formally integrated

$$\begin{aligned}(1-\mathcal{P})\sigma(t) = {} & \mathrm{e}^{-i(1-\mathcal{P})\mathcal{L}(t)}(1-\mathcal{P})\sigma(t_0) \\ & -i\int_0^t \mathrm{e}^{-i(1-\mathcal{P})\mathcal{L}(t-\tau)}(1-\mathcal{P})\mathcal{L}\mathcal{P}\sigma(\tau)\,d\tau\end{aligned} \tag{52}$$

which can be checked easily by differentiation. The result is plugged into the equation for the relevant part to obtain the Nakajima-Zwanzig identity

$$\begin{aligned}\frac{d}{dt}\mathcal{P}\sigma(t) = -i\mathcal{P}\mathcal{L}\mathcal{P}\sigma(t) - \int_0^t \mathcal{P}\mathcal{L}\mathrm{e}^{-i(1-\mathcal{P})\mathcal{L}(t-\tau)}(1-\mathcal{P})\mathcal{L}\mathcal{P}\sigma(\tau)\,d\tau \\ -i\mathcal{P}\mathcal{L}\mathrm{e}^{-i(1-\mathcal{P})\mathcal{L}(t-t_0)}(1-\mathcal{P})\sigma(t_0) \qquad (53)\end{aligned}$$

So within a few steps it is possible to derive the Nakajima-Zwanzig identity starting from the Lioville-von Neumann equation.

5.2 Hashitsume-Shibata-Takahashi identity

The Nakajima-Zwanzig identity is of course not the only way to proceed. Defining the operator $D(t)$ using

$$D(t) = i\int_0^t \mathrm{e}^{-i(1-\mathcal{P})\mathcal{L}(t-\tau)}(1-\mathcal{P})\mathcal{L}\mathcal{P}\mathrm{e}^{i\mathcal{L}(t-\tau)}\,d\tau\ , \qquad (54)$$

one can rewrite Eq. (52) to get

$$\begin{aligned}(1-\mathcal{P})\sigma(t) = \mathrm{e}^{-i(1-\mathcal{P})\mathcal{L}(t-0)}(1-\mathcal{P})\sigma(t_0) \\ -D(t)(\mathcal{P}\sigma(t) + (1-\mathcal{P})\sigma(t)\ . \qquad (55)\end{aligned}$$

Moving the terms proportional to $(1-\mathcal{P})\sigma(t)$ to the l.h.s. one gets

$$(1+D(t))(1-\mathcal{P})\sigma(t) = -D(t)\mathcal{P}\sigma(t) + \mathrm{e}^{-i(1-\mathcal{P})\mathcal{L}(t-t_0)}(1-\mathcal{P})\sigma(t_0) \quad (56)$$

Multiplying this equation by the inverse of $(1+D(t))$, an expression for the irrelevant part of the density matrix can be derived

$$(1-\mathcal{P})\sigma(t) = (1+D(t))^{-1}\left[-D(t)\mathcal{P}\sigma(t) + \mathrm{e}^{-i(1-\mathcal{P})\mathcal{L}(t-t_0)}(1-\mathcal{P})\sigma(t_0)\right] \quad (57)$$

Plugging this result into the differential equation for the relevant part, Eq. (50), the Hashitsume-Shibata-Takahashi identity can be obtained

$$\begin{aligned}\frac{d}{dt}\mathcal{P}\sigma(t) &= -i\mathcal{P}\mathcal{L}\left\{\mathcal{P}\sigma(t)\right. \\ &\quad + \left.(1+D(t))^{-1}\left[-D(t)\mathcal{P}\sigma(t) + \mathrm{e}^{-i(1-\mathcal{P})\mathcal{L}(t-t_0)}(1-\mathcal{P})\sigma(t_0)\right]\right\} \\ &= -i\mathcal{P}\mathcal{L}(1+D(t))^{-1}\left[\mathcal{P}\sigma(t) + \mathrm{e}^{-i(1-\mathcal{P})\mathcal{L}(t-t_0)}(1-\mathcal{P})\sigma(t_0)\right] \quad (58)\end{aligned}$$

with $D(t)$ defined in Eq. (54).

References

1. H. Grabert, P. Schramm, G.L. Ingold, Phys. Rep. **168**, 115 (1988)
2. H. Haug, A.P. Jauho, *Quantum Kinetics in Transport and Optics of Semiconductors*, 2nd edn. (Springer, Berlin, 2008)
3. U. Weiss, *Quantum Dissipative Systems*, 2nd edn. (World Scientific, Singapore, 1999)
4. H. Wang, M. Thoss, W.H. Miller, J. Chem. Phys. **115**, 2979 (2001)
5. M. Thoss, H. Wang, W.H. Miller, J. Chem. Phys. **115**, 2991 (2001)
6. D. Gelman, C.P. Koch, R. Kosloff, J. Chem. Phys. **121**, 661 (2004)
7. S. Nakajima, Prog. Theor. Phys. **20**, 948 (1958)
8. R. Zwanzig, in *Lectures in Theoretical Physics*, vol. 3, ed. by W.E. Brittin, B.W. Downs, J. Downs (Interscience, New York, 1961), vol. 3, p. 106
9. R. Zwanzig, Physica **30**, 1109 (1964)
10. N. Hashitsume, F. Shibata, M. Shingu, J. Stat. Phys. **17**, 155 (1977)
11. F. Shibata, Y. Takahashi, N. Hashitsume, J. Stat. Phys. **17**, 171 (1977)
12. Q. Shi, E. Geva, J. Chem. Phys. **119**, 12063 (2003)
13. A.G. Redfield, Adv. Magn. Reson. **1**, 1 (1965)
14. K. Blum, *Density Matrix Theory and Applications*, 2nd edn. (Plenum Press, New York, 1996)
15. W.T. Pollard, A.K. Felts, R.A. Friesner, Adv. Chem. Phys. **93**, 77 (1996)
16. V. May, O. Kühn, *Charge and Energy Transfer in Molecular Systems*, 2nd edn. (Wiley–VCH, Berlin, 2004)
17. A. Nitzan, *Chemical Dynamics in Condensed Phases: Relaxation, Transfer and Reactions in Condensed Molecular Systems* (Oxford University Press, Oxford, 2006)
18. Y. Tanimura, R. Kubo, J. Phys. Soc. Jpn. **58**, 101 (1989)
19. Y. Tanimura, Phys. Rev. A **41**, 6676 (1990)
20. Y. Tanimura, P.G. Wolynes, Phys. Rev. A **43**, 4131 (1991)
21. Y. Tanimura, S. Mukamel, J. Phys. Soc. Jpn. **63**, 66 (1994)
22. J. Shao, J. Chem. Phys. **120**, 5053 (2004)
23. Y.J. Yan, F. Yang, J. Shao, Chem. Phys. Lett. **395**, 216 (2004)
24. A. Ishizaki, Y. Tanimura, J. Phys. Soc. Jpn. **74**, 3131 (2005)
25. R.X. Xu, P. Cui, X.Q. Li, Y. Mo, Y.J. Yan, J. Chem. Phys. **122**, 041103 (2005)
26. Y. Tanimura, J. Phys. Soc. Jpn. **75**, 082001 (2006)
27. A. Ishizaki, Y. Tanimura, Chem. Phys. **347**, 185 (2008)
28. M. Schröder, M. Schreiber, U. Kleinekathöfer, J. Chem. Phys. **126**, 114102 (2007)
29. U. Kleinekathöfer, J. Chem. Phys. **121**, 2505 (2004)
30. M.V. Korolkov, J. Manz, G.K. Paramonov, J. Chem. Phys. **105**, 10874 (1996)
31. M.V. Korolkov, G.K. Paramonov, Phys. Rev. A **55**, 589 (1997)
32. C. Meier, D.J. Tannor, J. Chem. Phys. **111**, 3365 (1999)
33. R. Xu, Y.J. Yan, J. Chem. Phys. **116**, 9196 (2002)
34. R. Xu, Y. Mo, P. Cui, S.H. Lin, Y.J. Yan, in *Advanced Topics in Theoretical Chemical Physics*, *Progress in Theoretical Chemistry and Physics*, vol. 12, ed. by J. Maruani, R. Lefebvre, E. Brändas (Kluwer, Dordrecht, 2003), *Progress in Theoretical Chemistry and Physics*, vol. 12, p. 7
35. Y.J. Yan, R.X. Xu, Ann. Rev. Phys. Chem. **56**, 187 (2005)
36. U. Kleinekathöfer, I. Barvík, P. Heřman, I. Kondov, M. Schreiber, J. Phys. Chem. B **107**, 14094 (2003)

37. M. Schröder, U. Kleinekathöfer, M. Schreiber, J. Chem. Phys. **124**, 084903 (2006)
38. S. Welack, M. Schreiber, U. Kleinekathöfer, J. Chem. Phys. **124**, 044712 (2006)
39. A. Damjanović, I. Kosztin, U. Kleinekathöfer, K. Schulten, Phys. Rev. E **65**, 031919 (2002)
40. S. Mukamel, I. Oppenheim, J. Ross, Phys. Rev. A **17**, 1988 (1978)
41. D.R. Reichman, F.L.H. Brown, P. Neu, Phys. Rev. E **55**, 2328 (1997)
42. Y.J. Yan, Phys. Rev. A **58**, 2721 (1998)
43. H.P. Breuer, B. Kappler, F. Petruccione, Phys. Rev. A **59**, 1633 (1999)
44. V. Čápek, Physica A **203**, 495 (1994)
45. F. Haake, Springer Tracts Mod. Phys. **66**, 98 (1973)
46. V. Čápek, Physica A **203**, 520 (1994)
47. D. Egorova, M. Thoss, W. Domcke, H. Wang, J. Chem. Phys. **119**, 2761 (2003)
48. H. Gzyl, J. Stat. Phys. **26**, 679 (1981)
49. A. Fuliński, Phys. Lett. A **25**, 13 (1967)
50. A. Fuliński, W.J. Kramarczyk, Physica **39**, 575 (1968)
51. M. Tokuyama, H. Mori, Prog. Theor. Phys. **55**, 411 (1976)
52. W.T. Pollard, R.A. Friesner, J. Chem. Phys. **100**, 5054 (1994)
53. M. Schröder, M. Schreiber, U. Kleinekathöfer, J. Lumin. **125**, 126 (2007)
54. I. Franco, M. Shapiro, P. Brumer, Phys. Rev. Lett. **99**, 126802 (2007)
55. J.K. Viljas, F. Pauly, J.C. Cuevas, Phys. Rev. B **77**, 155119 (2008)
56. Y. Meir, N.S. Wingreen, Phys. Rev. Lett. **68**, 2512 (1992)
57. S. Kohler, J. Lehmann, P. Hänggi, Phys. Rep. **406**, 379 (2005)
58. X.Q. Li, J. Luo, Y.G. Yang, P. Cui, Y.J. Yan, Phys. Rev. B **71**, 205304 (2005)
59. I.V. Ovchinnikov, D. Neuhauser, J. Chem. Phys. **122**, 024707 (2005)
60. U. Harbola, M. Esposito, S. Mukamel, Phys. Rev. B **74**, 235309 (2006)
61. S. Welack, M. Esposito, U. Harbola, S. Mukamel, Phys. Rev. B **77**, 195315 (2008)
62. S. Welack, J.M. Maddox, M. Esposito, U. Harbola, S. Mukamel, Nano Lett. **8**, 1137 (2008)
63. V. May, O. Kühn, Nano Lett. **8**, 1095 (2008)
64. U. Kleinekathöfer, G.Q. Li, S. Welack, M. Schreiber, phys. stat. sol. (b) **243**, 3775 (2006)
65. U. Kleinekathöfer, G.Q. Li, S. Welack, M. Schreiber, Europhys. Lett. **75**, 139 (2006)
66. S. Welack, U. Kleinekathöfer, M. Schreiber, J. Lumin. **119 & 120**, 462 (2006)
67. J. Lehmann, S. Kohler, P. Hänggi, A. Nitzan, Phys. Rev. Lett. **88**, 228305 (2002)
68. A. Tikhonov, R.D. Coalson, Y. Dahnovsky, J. Chem. Phys. **117**, 567 (2002)
69. J. Lehmann, S. Camalet, S. Kohler, P. Hänggi, Chem. Phys. Lett. **368**, 282 (2003)
70. G.Q. Li, M. Schreiber, U. Kleinekathöfer, EPL **79**, 27006 (2007)
71. M. Shapiro, P. Brumer, Rep. Prog. Phys. **66**, 859 (2003)
72. T. Brixner, G. Gerber, ChemPhysChem **4**, 418 (2003)
73. G.Q. Li, S. Welack, M. Schreiber, U. Kleinekathöfer, Phys. Rev. B **77**, 075321 (2008)
74. A. Hartschuh, M.R. Beversluis, A. Bouhelier, L. Novotny, Phil. Trans. R. Soc. Lond. A **362**, 807 (2004)
75. S.W. Wu, N. Ogawa, W. Ho, Science **312**, 1362 (2006)
76. D.C. Guhr, D. Rettinger, J. Boneberg, A. Erbe, P. Leiderer, E. Scheer, Phys. Rev. Lett. **99**, 086801 (2007)
77. M. Tokuyama, Physica A **387**, 1926 (2008)
78. J. Liebers, U. Kleinekathöfer, V. May, Chem. Phys. **347**, 229 (2008)

Reduced Density Matrix Equations for Combined Instantaneous and Delayed Dissipation in Many-Atom Systems, and their Numerical Treatment

David A. Micha, Andrew S. Leathers

[1] Quantum Theory Project, Departments of Chemistry and Physics, University of Florida, Gainesville, FL 32611-8435, USA, micha@qtp.ufl.edu
[2] Quantum Theory Project, Departments of Chemistry and Physics, University of Florida, Gainesville, FL 32611-8435, USA, leathers@qtp.ufl.edu

Abstract. A many-atom system excited by light or by collisions, such as is found in the photo-excitation of a molecule adsorbed on a surface or in photosynthesis and vision, leads to energy dissipation on different time scales. A fast dissipation typically occurs due to electronic energy relaxation in the medium, while a slow (delayed) dissipation arises from vibrational energy relaxation. In what follows we briefly present a reduced density matrix treatment based on a self-consistent coupling of primary and secondary regions which includes their time correlation, in a generalization valid for an active medium. We also describe a numerical procedure based on an extended Runge-Kutta algorithm which can be applied to systems undergoing simultaneous fast and slow rates of dissipation. We illustrate our treatment with a realistic model for an adsorbate on a solid surface, $CO/Cu(001)$ photoexcited by a femtosecond pulse of light and relaxing by electronic and vibrational pathways. Results for the populations of vibronic states versus time show that they oscillate due to vibrational coupling through dissipative interaction with the substrate, and are therefore in coherent quantum states. The total populations of electronic states are however little affected by vibrational motions. The same formalism and numerical procedure can be followed for example in treatments of photoexcitation of chromophores in biomolecular systems.

1 Introduction

A many-atom system excited by light or by collisions, such as occurs in the photo-excitation of a molecule adsorbed on a surface or in photosynthesis and vision, leads to energy dissipation on different time scales. A fast dissipation typically occurs due to electronic energy relaxation in the medium, while a slow (delayed) dissipation arises from vibrational energy relaxation . Here we concentrate on localized phenomena where a relatively small number

I. Burghardt et al. (eds.), *Energy Transfer Dynamics in Biomaterial Systems*, Springer Series in Chemical Physics 93, DOI 10.1007/978-3-642-02306-4_11,

of atoms define a primary region of interest, while the medium comprises a secondary region or bath. A theoretical and computational treatment of these phenomena can be done in terms of a reduced density operator (RDOp) $\hat{\rho}$ satisfying a generalized Liouville-von Neumann equation , [1–5] which contains the hamiltonian of the primary region and also terms describing fluctuation and dissipative phenomena due to its coupling to the secondary region.

A convenient approximation in many applications is to assume that a region of interest with a RDOp $\hat{\rho}$ is in contact with a medium at thermal equilibrium. The system and medium are chosen so that the latter can be assumed to remain at equilibrium at all times, with a density operator $\hat{\gamma}_{eq}$. In this case it is possible to search for solutions of the equations starting from a factorized density operator for the whole system, $\hat{\Gamma} = \hat{\rho} \otimes \hat{\gamma}_{eq}$, in a procedure also called a Fano-factorization. [6] This however is not acceptable when the total system is subject to excitations which induce transitions among states of the medium. An example is a molecule adsorbed on a metal surface, excited by visible light which first creates electronic excitations in the substrate. In this case the active medium is described by a DOp evolving in time, and some of the common developments in the literature must be generalized.

In what follows we briefly present a treatment based on a self-consistent coupling of primary and secondary regions which includes their time correlation. This is done by transforming equations between the Schroedinger and interaction pictures of quantum mechanics, to introduce suitable approximations along lines found helpful in the special case of a secondary region at equilibrium. The formalism allows for treament of phenomena occurring with different time scales, where the medium contains both fast and slow variables compared to periods of motion in the primary region of interest. This leads to coexisting fast and slow dissipative phenomena, both of which can affect the long time behaviour of the system.

Fast dissipation is treated numerically within the Markoff approximation, which leads to differential equations in time, and dissipative rates most commonly written in the Redfield [9, 10] or Lindblad [11, 12] forms. Several numerical procedures have been introduced for dissipative dynamics within the Markoff approximation. The differential equations have been solved using a pseudospectral method [13], expansions of the Liouville propagator in terms of polynomials, [14–16] and continued fractions. [17]

More generally the formalism with both fast and slow dissipation leads to integrodifferential equations (IDEqs) of motion for the primary RDOp, which become coupled IDEqs in the time variable after expansions of operators in basis sets or on a numerical grid for variables. There are few numerical treatments of those IDEqs, including one where they have been solved expanding the integral kernel in Laguerre polynomials, [18] and another done by parametrizing the medium spectral density [19, 20]. The present contribution describes an extended Runge-Kutta algorithm [21] which can be applied quite generally for systems undergoing simultaneous fast and slow rates of dissipation. Numerical results for state populations and quantum coherences have

been obtained with this algorithm, which we developed and tested [22] and then used in an application to vibrational relaxation of an adsorbed CO . [23] Another approach for dissipative dynamics in open systems is based on the Feynman-Vernon path integral formulation, [24] but it is not being covered in this presentation. Reviews of this approach can be found in references [25,26].

In applications, it is desirable to start from a system of electrons and nuclei to take advantage of the different time scales of electronic and vibrational transitions, and to separate fast and slow dissipative phenomena. We have chosen to illustrate our treatment with a realistic model for an adsorbate on a solid surface, $CO/Cu(001)$, but the same numerical procedure can be followed for applications to many-atom systems arising, for example, in biomolecular applications. Instantaneous dissipation within the Lindblad formulation has been succesfully used in the description of dissipative dynamics of adsorbates. [27, 28] We have implemented an alternative treatment for the CO/Cu(001) system using a dissipative potential in the primary region of adsorption and a Lindblad-type treatment of fast electronic decay in the surrounding medium. [29,30] In our previous work we have compared calculations [23,31,32] with experimental results from femtosecond spectroscopy [33] and time-of flight measurements. [34] Those studies dealt only with fast dissipation in the case of femtosecond desorption, and only with slow dissipation of CO molecules vibrationally excited by collisions, with the system in its ground electronic state. Here we consider again CO/Cu(001) but now including both fast and slow dissipative processes. In this way we can describe the femtosecond excitation of the substrate metal which is known to create a vibrationally excited CO molecule on the electronically excited solid surface. Fast electronic excitation is accompanied by slow vibrational relaxation of the CO. The related delayed dissipation is given by a time integral with a memory term derived from the time-correlation of atomic displacements in the medium.

We present in Section 2 the formalism giving the equations for the reduced density operator and for competing instantaneous and delayed dissipation. Section 3 presents matrix equations in a form suitable for numerical work, and the details of the numerical procedure used to solve the integrodifferential equations with the two types of dissipative processes. In Section 4 on applications to adsorbates, results are shown for quantum state populations versus time for the dissipative dynamics of CO/Cu(001). The fast electronic relaxation to the ground electronic state is shown first without the slow relaxation of the frustrated translation mode of CO vibrations, for comparison with previous work, and this is followed by results with both fast and slow relaxation. In Section 5 we comment on the general conclusions that can be reached in problems involving both vibrational and electronic relaxation at surfaces.

2 Density operator treatment

2.1 Equation for the reduced density operator

A molecule M plus its bath B in an external field can be described as a total system with a Hamiltonian $\hat{H} = \hat{H}_M + \hat{H}_B + \hat{H}_{MB} + \hat{H}_{ext}(t)$ which may depend on time if the total system is subject to an external electromagnetic field, as indicated. Given this, the density operator $\hat{\Gamma}(t)$ for the system satisfies the Liouville-von Neumann (L-vN) equation,

$$i\hbar\partial\hat{\Gamma}/\partial t = \hat{H}(t)\hat{\Gamma}(t) - \hat{\Gamma}(t)\hat{H}(t) = [\hat{H}(t), \Gamma\hat{(t)}] \tag{1}$$

with the initial condition $\hat{\Gamma}(t_0) = \hat{\Gamma}_0$.

In the frequent cases where the molecule is strongly interacting with the medium, as in chemisorption, or when there is strong polarization of solvent shells by a charged or polar molecule, it is more convenient to redefine the region where the dynamics of interest occurs to include part of the medium. We begin by introducing a primary (p) region containing the molecule M and adjacent bath atoms, and a secondary (s) region including the remaining bath, both interacting with light (l). The Hamiltonian terms are regrouped into the form

$$\begin{aligned} \hat{H}(t) &= \hat{H}^0 + \hat{H}_{pl}(t) + \hat{H}_{sl}(t) \\ \hat{H}^0 &= \hat{H}_p(\boldsymbol{X}, \frac{\partial}{\partial \boldsymbol{X}}) + \hat{H}_s(\boldsymbol{Y}, \frac{\partial}{\partial \boldsymbol{Y}}) + \hat{H}_{ps}(\boldsymbol{X}, \boldsymbol{Y}) \end{aligned} \tag{2}$$

with $\boldsymbol{X}$ and $\boldsymbol{Y}$ sets of primary and secondary degrees of freedom, respectively. The interactions of p- and s-regions with light are given in the dipole approximation by

$$\hat{H}_{pl}(t) = -\hat{D}_p(\boldsymbol{X})\hat{\mathcal{E}}_{ext}(t) \tag{3}$$

and

$$\hat{H}_{sl}(t) = -\int d^3r\ \hat{\mathcal{E}}_{loc}(\boldsymbol{r}, t)\hat{P}_s(\boldsymbol{r}, \boldsymbol{Y}) \tag{4}$$

under the assumption that the dipole operator is a sum of the dipole $\hat{D}_p$ of the p-region, and the dipole per unit volume $\hat{P}_s$ in the s-region, both projections on the direction of the external electric field $\mathcal{E}_{ext}$ and its local value $\mathcal{E}_{loc}$ inside the s-region. This assumption can be verified as correct in practice by choosing a p-region of increasing size.

We consider a secondary region described in terms of stochastic physical properties subject to thermodynamical boundary conditions, with a non-equilibrium density operator $\hat{\Gamma}^{(s)}(t)$ in a general case. Our goal is to obtain equations of motion for the reduced density operator (RDOp) which follow from taking the trace of the density operator over the s-region degrees of freedom, so that $tr_s(\overline{\hat{\Gamma}}) = \hat{\rho}(t)$ describes the p-region. A perturbative treatment would not suffice for the present strong interactions between p- and s-regions.

Instead we begin with a selfconsistent field (SCF or mean field) molecular approximation, justified by the introduction of a stochastic description of the medium. We seek special solutions to the L-vN equation which can be factorized after averaging over initial conditions in the s-region (shown by overlines), so that $\overline{\hat{\Gamma}}(t) = \overline{\hat{\Gamma}^{(p)}}(t) \otimes \overline{\hat{\Gamma}^{(s)}}(t)$. Here both factors are normalized and $\overline{\hat{\Gamma}^p} = tr_s(\overline{\hat{\Gamma}}) = \hat{\rho}(t)$ is the RDOp for the p-region. This assumes that the s- and p- regions have been chosen so that their quantum entanglement can be neglected. A more accurate description takes the previous factorized form to be the leading term in an expansion of the total DOp, with the equations for the reminder obtained by a partitioning method for the DOp. [3, 7, 8]

To derive an equation for $\hat{\rho}(t)$, we start from the full L-vN equation for $\hat{\Gamma}(t)$, and transform it into an integrodifferential form to display correlations in the s-region. [1] We introduce the decomposition $\hat{H} = \hat{F}(t) + \hat{H}_F(t)$, where $\hat{F}$ stands for an effective Hamiltonian possibly dependent on time, to be defined in what follows, and $\hat{H}_F$ is a small residual energy operator. We define an interaction picture (IP) generated by the time evolution operator $\hat{U}_F(t,0) = exp_T[-(i/\hbar)\int_0^t dt'\ \hat{F}(t')]$and written in terms of a time-ordered exponential, and the operator $\hat{\Gamma}^{(I)}(t) = \hat{U}_F(t,0)^\dagger \hat{\Gamma}(t) \hat{U}_F(t,0)$. Other IP operators are similarly defined, and the RDOp in the IP is $\hat{\rho}^{(I)}(t) = tr_s[\hat{\Gamma}^{(I)}(t)]$. The equation of motion for $\hat{\Gamma}^{(I)}$ becomes

$$i\hbar\partial\hat{\Gamma}^{(I)}/\partial t = [\hat{H}_F^{(I)}, \hat{\Gamma}^{(I)}(t)] \tag{5}$$

Integrating to obtain $\hat{\Gamma}^{(I)}(t)$, replacing in the DEq and taking the trace over s-variables,

$$\begin{aligned} i\hbar\partial\hat{\rho}^{(I)}/\partial t &= tr_s([\hat{H}_F^{(I)}(t), \hat{\Gamma}^{(I)}(0)]) \\ &- (i/\hbar) tr_s([\hat{H}_F^{(I)}(t), \int_0^t dt'\ [\hat{H}_F^{(I)}(t'), \hat{\Gamma}^{(I)}(t')]] \end{aligned} \tag{6}$$

Here the first term to the right describes a rate of fluctuations for the given initial conditions, and the second term describes a rate of dissipation due to coupling back and forth between p- and s-regions. A similar equation can be written for the RDOp of the s-region, $tr_p[\hat{\Gamma}^{(I)}(t)]$, if needed.

To generate a first approximation valid for strongly coupled p- and s-regions, we'll construct solutions for a factorized density operator, $\overline{\hat{\Gamma}^{(I)}(t)} = \hat{\rho}^{(I)}(t) \otimes \hat{\gamma}^{(I)}(t)$, where $\hat{\gamma}^{(I)}$ is the IP form of $\overline{\hat{\Gamma}^{(s)}}(t)$. Insofar the s-region is large and with many degrees of freedom, we'll assume that on average $tr_s[\hat{H}_F^{(I)}(t)\gamma^{(I)}(0)] = 0$, so that the fluctuation rate does not appear in what follows. It can be restored in equations if needed.

To proceed it is convenient to make the choice of effective Hamiltonian

$$\begin{aligned} \hat{F} &= \hat{F}_p + \hat{F}_s - \langle\langle \hat{H}_{ps} \rangle\rangle \\ \hat{F}_p &= \hat{H}_p + \hat{G}_p \end{aligned} \tag{7}$$

with $\hat{G}_p = tr_s[\hat{H}_{ps}\hat{\Gamma}^{(s)}]$ and $\langle\langle \hat{H}_{ps}\rangle\rangle = tr[\hat{H}_{ps}\hat{\rho}\hat{\Gamma}^{(s)}]$, and similarly for the s-operators after interchanging p- and s- labels, so that $\hat{F}$ is an SCF Hamiltonian with an average equal to the instantaneous energy of the total system, involving the SCF potentials $\hat{G}_p(t)$ and $\hat{G}_s(t)$. This definition leads to $\hat{H}_F = \hat{H}_{ps} - (\hat{G}_p + \hat{G}_s) + \langle\langle \hat{H}_{ps}\rangle\rangle$, a residual coupling due to the non-SCF correlation of motions in the p- and s-regions that averages to zero at all times. In addition it follows that $\hat{U}_F(t,t') = \hat{U}_p(t,t')\hat{U}_s(t,t')$, so that the time evolution of primary and secondary regions generated by the effective Hamiltonian are decoupled. Analogous relations are valid in the IP.

These choices give the simple integrodifferential equation

$$i\hbar\partial\hat{\rho}^{(I)}/\partial t = -(i/\hbar)\int_0^t dt'\ tr_s([\hat{H}_F^{(I)}(t),[\hat{H}_F^{(I)}(t'),\hat{\rho}^{(I)}(t')\hat{\gamma}^{(I)}(t')]] \tag{8}$$

similar to the ones in published work, but now valid for an active medium and including its correlation with the system of interest. That can be described in terms of time correlation functions (TCFs) of the medium, but the TCFs must now involve an average over the non-equilibrium RDOp $\hat{\gamma}^{(I)}(t)$ of the s-region, instead of the usual average over an equilibrium $\hat{\gamma}_{eq}$ at a given temperature.

The effect of time correlations in the medium can be displayed working with a factorized coupling hamiltonian, which we choose here as $\hat{H}_{ps} = \hat{A}\hat{B}$, with $\hat{A} = \hat{A}^\dagger$ a hermitian operator dependent only on the p-variables, and similarly for $\hat{B}$ dependent only on s-variables. This expression can be easily generalized to include several factorized terms. It leads to a residual Hamiltonian $\hat{H}_F = (\hat{A} - \langle\langle A\rangle\rangle)(\hat{B} - \langle\langle B\rangle\rangle) = \Delta\hat{A}(t).\Delta\hat{B}(t)$. Turning to the IP, the equation of motion for the RDOp is

$$\begin{aligned}\partial\hat{\rho}^{(I)}/\partial t = -(1/\hbar^2)\int_0^t dt'\ tr_s([\Delta\hat{A}^{(I)}(t)\Delta\hat{B}^{(I)}(t),\\ [\Delta\hat{A}^{(I)}(t')\Delta\hat{B}^{(I)}(t'),\hat{\rho}^{(I)}(t')\hat{\gamma}^{(I)}(t')]]\end{aligned} \tag{9}$$

where the double commutator can be expanded to factor TCFs in the s-region. They are defined as the transient TCFs

$$\begin{aligned}C_{BB}(t,t';t') &= tr_s[\Delta\hat{B}^{(I)}(t)\Delta\hat{B}^{(I)}(t')\hat{\gamma}^{(I)}(t')]\\ C_{BB}(t',t;t') &= tr_s[\Delta\hat{B}^{(I)}(t')\Delta\hat{B}^{(I)}(t)\hat{\gamma}^{(I)}(t')]\end{aligned} \tag{10}$$

and contain an extra time variable relating to the RDOp of the s-region. It can be shown going back to the Schroedinger picture (SP) that $C_{BB}(t',t;t') = C_{BB}(t,t';t')^*$ and that they transform into standard TCFs when the s-region is at thermal equilibrium. The equation of motion

$$\begin{aligned}\partial\hat{\rho}^{(I)}/\partial t = -\ (1/\hbar^2)\int_0^t dt'\ \{C_{BB}(t,t';t')[\Delta\hat{A}^{(I)}(t),\Delta\hat{A}^{(I)}(t')\hat{\rho}^{(I)}(t')]\\ + C_{BB}(t',t;t')[\hat{\rho}^{(I)}(t')\Delta\hat{A}^{(I)}(t'),\Delta\hat{A}^{(I)}(t)]\}\end{aligned} \tag{11}$$

gives a compact expression generalizing the ones in the literature, to include an active medium.

Returning to the SP with the substitution $\hat{\rho}^{(I)}(t) = \hat{U}_p^{\dagger}(t,0)\hat{\rho}(t)\hat{U}_p(t,0)$ gives

$$\partial\hat{\rho}/\partial t = -(i/\hbar)[\hat{F}_p(t), \hat{\rho}(t)] - (1/\hbar^2)\int_0^t dt'\, \hat{\mathcal{M}}_p(t,t')\hat{\rho}(t') \quad (12)$$

$$\hat{\mathcal{M}}_p(t,t')\hat{\rho}(t) = C_{BB}(t,t';t')[\Delta\hat{A}(t), \hat{U}_p(t,t')\Delta\hat{A}(t')\hat{\rho}(t')\hat{U}_p(t,t')^{\dagger}]$$
$$+C_{BB}(t',t;t')[\hat{U}_p(t,t')\hat{\rho}(t')\Delta\hat{A}(t')\hat{U}_p(t,t')^{\dagger}, \Delta\hat{A}(t)]$$

for the general case where the effective hamiltonian in the p-region depends on time through the SCF interaction $\hat{G}_p(t)$. Here we have introduced a superoperator $\hat{\mathcal{M}}_p(t,t')$ which describes dissipative phenomena and allows for memory effects extending from the initial time $t = 0$ up to the time t at which the rate of the RDOp is calculated.

2.2 Competing Instantaneous and Delayed Dissipation

The dissipative superoperator $\hat{\mathcal{M}}_p(t,t')$ can in some cases be derived from the dynamics of the s-region, and constructed from information about the electronic and atomic structure of this region. Frequently the response and decay of electronic motions is faster than that of atomic motions, with the electronic dissipation occurring instantly (compared to the duration of a light pulse) and atomic dissipation showing delays. Here we consider situations where both are present, and describe the total system as made up of atomic cores and electronic charge distributions. In what follows we associate fast dissipation with electronic motions in the s-region, and slow dissipation with atomic motions there, but the treatment would be suitable to other types of degrees of freedom (such as in proton transfer) with their own time scales.

In general, couplings in $\hat{H}_F$ are sums of factorized terms, which can be used to express dissipative rates in terms of TCFs. The main features of dissipation rates can be discussed assuming that $\hat{H}_F$ contains a term with a s-region operator $\hat{B}^{(el)}$ dependent on fast electronic variables, and a term $\hat{B}^{(at)}$ dependent on slow atomic electronic variables. The TCFs appearing in the memory term are $C_{BB}^{(el,el)}$, $C_{BB}^{(at,at)}$, and $C_{BB}^{(el,at)}$. The TCFs of electronic motions with themselves and of atomic motions with themselves must be considered, but the cross time-correlation terms are small on the average because of their different time scales when s-region electrons are excited by visible light, and can be neglected. This leads to a memory superoperator with two terms. One of them contains as factors time-correlation of electronic motions in the s-region that decay rapidly due to electron-electron interactions there. The other one involves memory terms with slow vibrational TCFs of the s-region motions. Under these conditions we can write that

$$\hat{\mathcal{M}}_p(t,t') = \hat{\mathcal{M}}_p^{(el)}(t,t') + \hat{\mathcal{M}}_p^{(at)}(t,t') \quad (13)$$

where the first term describes fast dissipation, and the second gives one delayed dissipation . This leads to two separate rates of dissipation in the equation of motion for $\hat{\rho}$,

$$\partial\hat{\rho}/\partial t = -(i/\hbar)[\hat{F}_p(t), \hat{\rho}(t)] + (\partial\hat{\rho}/\partial t)_D^{(el)} + (\partial\hat{\rho}/\partial t)_D^{(at)} \tag{14}$$

which we analyze in what follows.

Instantaneous dissipation

The memory kernel for the p-region arising from its coupling to the electronic motions in the s-region is given in the IP by

$$\begin{aligned}\hat{\mathcal{M}}_p^{(el)}(t,t')\hat{\rho}^{(I)} = C_{BB}^{(el,el)}(t,t';t')[\Delta\hat{A}^{(I)}(t), \Delta\hat{A}^{(I)}(t')\hat{\rho}^{(I)}(t')] \\ + C_{BB}^{(el,el)}(t',t;t')[\hat{\rho}^{(I)}(t')\Delta\hat{A}^{(I)}(t'), \Delta\hat{A}^{(I)}(t)]\}\end{aligned} \tag{15}$$

This can be simplified when the relaxation of electronic motions is fast and the TCF for a fixed time t and earlier times t' satisfies

$$C_{BB}^{(el)}(t,t';t') \cong g(t).exp[-f(t).|t-t'|/\tau_s^{(el)}] \tag{16}$$

and $\| \partial\hat{\rho}^{(I)}/\partial t' \| << \| \hat{\rho}^{(I)} \| /\tau_s^{(el)}$ for $|t-t'| >> \tau_s^{(el)}$, a relaxation time constant. Then it is accurate to let $\hat{\rho}^{(I)}(t') \approx \hat{\rho}^{(I)}(t)$ in the the memory integral and to replace its upper limit with $t \to \infty$. Returning to the SP this gives

$$\begin{aligned}(\partial\hat{\rho}/\partial t)_D^{(el)} = -(1/\hbar^2)\{c(t)[\Delta\hat{A}(t)]^2\hat{\rho}(t) + c(t)^*\hat{\rho}(t)[\Delta\hat{A}(t)]^2 \\ -[c(t)+c(t)^*]\Delta\hat{A}(t)\hat{\rho}(t)\Delta\hat{A}(t)\} \\ c(t) = \int_0^\infty dt'\, C_{BB}^{(el,el)}(t,t';t')\end{aligned} \tag{17}$$

Therefore, rapid electronic motions lead to an instantaneous dissipative memory and $\overline{\hat{\mathcal{M}}_p^{el}(t,t')\hat{\rho}(t')}/\hbar = \delta(t-t')\hat{\mathcal{W}}_p^{(el)}(t)\hat{\rho}(t)$, in terms of a new time-dependent dissipative superoperator which gives a dissipative rate $(\partial\hat{\rho}/\partial t)_D^{(el)} = -\hat{\mathcal{W}}_p^{(el)}(t)\hat{\rho}(t)/(2\hbar)$ defined by the previous equation.

When the s-region can be assumed to remain at equilibrium, the dissipative superoperator $\hat{\mathcal{W}}_p^{(el)}$ does not depend on time and can be constructed as a so-called Lindblad-type dissipation expression, [11, 12]

$$(\frac{\partial\hat{\rho}}{\partial t})_D^{(el)} = -\frac{1}{2}\sum_k [\hat{L}_p^{(k)\dagger}\hat{L}_p^{(k)}, \hat{\rho}(t)]_+ - 2\hat{L}_p^{(k)}\hat{\rho}(t)\hat{L}_p^{(k)\dagger} \tag{18}$$

where the $\hat{L}_p^{(k)}$ are operators in the p-region constructed from information about relaxation and decoherence rates of each process k in the p-region induced by couplings to the electronic motions in the s-region; here the subscript

"+" indicates an anticommutator. This form maintains complete positivity and leads to a density operator $\hat{\rho}(t)$ of constant norm. It has been implemented for example to describe the relaxation of adsorbates. [27],

The dissipative superoperator $\hat{\mathcal{W}}_p^{(el)}$ can also be constructed from a dissipative potential operator $\hat{W}_p^{(el)}$ which describes the interaction of the p-region with the electrons in the s-region followed by a back interaction, [8] and therefore depends on the initial equilibrium temperature T of the s-region. This leads, for a general non-hermitian $\hat{W}_p^{(el)}$, to the expression

$$(\frac{\partial\hat{\rho}}{\partial t})_D^{(el)} = -\frac{1}{2\hbar}[\hat{W}_p^{(el)}\hat{\rho}(t) + \hat{\rho}(t)\hat{W}_p^{(el)\dagger} - (\hat{W}_p^{(el)} + \hat{W}_p^{(el)\dagger})^{1/2}\hat{\rho}(t)(\hat{W}_p^{(el)} + \hat{W}_p^{(el)\dagger})^{1/2}] \tag{19}$$

which appears in the equation for the RDOp and gives solutions with the required constant normalization. This will be called the *dissipative potential form* of the instantaneous dissipation, in what follows.

Delayed dissipation

For slow atomic motions, the dissipative kernel $\hat{\mathcal{M}}^{(at)}(t,t')$ can be constructed from the TCFs $C_{BB}^{(at,at)}(t,t';t')$ but the integral over t' in the equation of motion must be in principle kept between limits $t = 0$ and t, as given in a previous equation in the SP.

However, delayed dissipation typically occurs after the s-region has settled into its thermal equilibrium, with RDOp $\hat{\gamma}_{eq}$, and the more familiar equations for the dissipative rate can be used. Then $\hat{\mathcal{M}}^{(at)}(t,t')$ is obtained to second order from a p-s coupling $\hat{H}_{ps} = \sum_j \hat{A}_p^{(j)}\hat{B}_s^{(j)}$, with $tr_s(\hat{\Gamma}^{(s)}\hat{B}_s^{(j)}) = 0$ chosen for convenience, and can be written in terms of the time-correlation functions $C_s^{(jj')}(t,t') = \langle\langle\hat{B}_s^{(j)}(t)\hat{B}_s^{(j')}(t')\rangle\rangle = tr_s[\hat{B}_s^{(j)}(t)\hat{B}_s^{(j')}(t')\hat{\gamma}_{eq}]$ of the atomic motions in the s-region, [3] as

$$\hat{\mathcal{M}}_p^{(at)}(t,t')\hat{\rho}(t') = \sum_{jj'} C_s^{(jj')}(t,t')[\hat{A}_p^{(j)}, \hat{U}_p(t')\hat{A}_p^{(j')}\hat{\rho}(t-t')\hat{U}_p^{\dagger}(t')] - C_s^{(j'j)}(t',t)[\hat{A}_p^{(j)}, \hat{U}_p(t')\hat{\rho}(t-t')\hat{A}_p^{(j')}\hat{U}_p^{\dagger}(t')] \tag{20}$$

where $\hat{U}_p(t) = exp(-i\hat{F}_p^0 t/\hbar)$ is the time evolution operator in the p-region without light. This follows from our equation for $\hat{\mathcal{M}}_p^{(at)}(t,t')$ with the substitution $t' \to (t-t')$ in the integral over time.

Combining both types of dissipation gives the integrodifferential equation

$$\partial\hat{\rho}/\partial t = -(i/\hbar)[\hat{F}_p(t), \hat{\rho}(t)] - (1/2\hbar)\hat{\mathcal{W}}_p^{el}(t)\hat{\rho}(t) - (1/\hbar^2)\int_0^t dt'\ \hat{\mathcal{M}}_p^{(at)}(t,t')\hat{\rho}(t'), \tag{21}$$

which includes fast electronic dissipation and delayed atomic dissipation and is a linear integrodifferential equation in $\hat{\rho}$. The upper limit of the integral to the right must be kept equal to the time t for slow dissipation, instead of replacing it with $t \to \infty$ as done for fast dissipation.

3 Computational method

3.1 Matrix Equations in a Basis Set

Reintroducing the coupling of the p-region with light, and expanding Eq. (21) in a basis set of stationary states $\{\phi_\alpha, \alpha = 1...n\}$ with energies E_α in the p-region we have

$$\frac{d\boldsymbol{\rho}}{dt} = -\frac{i}{\hbar}[\mathbf{F}_p - \mathcal{E}(t)\mathbf{D}_p, \boldsymbol{\rho}(t)] - \frac{1}{2\hbar}\boldsymbol{\mathcal{W}}_p^{(el)}(t)\boldsymbol{\rho}(t) - \frac{1}{\hbar^2}\int_0^t dt' \boldsymbol{\mathcal{M}}_p^{(at)}(t,t')\boldsymbol{\rho}(t') \tag{22}$$

Here matrices of the operators $\hat{\rho}$, $\hat{F}_p$,and $\hat{D}_p$,have the same dimensions, $(n \times n)$, while the supermatrices $\mathcal{W}_p^{(el)}$ and $\mathcal{M}_p^{(at)}$ are four-index $n^2 \times n^2$ matrices, which follows from Eq.(20) using $n \times n$ matrices $\mathbf{A}_p^{(j)}$ and $\mathbf{U}_p$. This is a set of coupled ordinary IDEqs which can be solved quite generally with the numerical procedure that follows.

We introduce matrices in the p-basis, like $\mathbf{V} = [\langle\beta|\hat{V}_p|\alpha\rangle]$ and $\mathbf{W} = [\langle\beta|\hat{W}_p|\alpha\rangle]$. The Lindblad form of the dissipation rate can be constructed from state-to-state transition rates $r(\beta \leftarrow \alpha)$ in the p-region, induced by its interaction with the s-region, and the operator for the transition $k = (\beta \leftarrow \alpha)$ is

$$\hat{L}_p^{(k)} = |\beta\rangle[r(\beta \leftarrow \alpha)]^{1/2}\langle\alpha| \tag{23}$$

The Lindblad operators become matrices $\mathbf{L}_p^{(k)}$, and the Lindblad rate is then

$$(\frac{d\boldsymbol{\rho}}{dt})_D^{(el)} = -\frac{1}{2}\left(\sum_k [\mathbf{L}_p^{(k)\dagger}\mathbf{L}_p^{(k)}, \boldsymbol{\rho}(t)]_+ - 2\mathbf{L}_p^{(k)}\boldsymbol{\rho}(t)\mathbf{L}_p^{(k)\dagger}\right). \tag{24}$$

This choice leads to a constant $tr_p(\boldsymbol{\rho}) = 1$ normalization over time. For an s-region near equilibrium at temperature T, the rates satisfy the detailed balance relation $r(\beta \leftarrow \alpha)exp[-E_\alpha/(k_BT)] = r(\alpha \leftarrow \beta)exp[-E_\beta/(k_BT)]$.

Alternatively, the rate of instantaneous dissipation in the equation of the RDM is obtained from the dissipative potential form as

$$(\frac{d\boldsymbol{\rho}}{dt})_D^{(el)} = -\frac{1}{2\hbar}[\mathbf{W}\boldsymbol{\rho}(t) + \boldsymbol{\rho}(t)\mathbf{W}^\dagger - (\mathbf{W} + \mathbf{W}^\dagger)^{1/2}\boldsymbol{\rho}(t)(\mathbf{W} + \mathbf{W}^\dagger)^{1/2}] \tag{25}$$

where $\langle\beta|\hat{W}_p|\alpha\rangle_T/\hbar = r(\beta \leftarrow \alpha; T)$. This form of the dissipation rate also conserves the norm of the density operator.

For computational purposes it is sometimes convenient to introduce a diadic notation where a square $n \times n$ matrix with indices (j, k) is transformed into a column matrix with index J running from 1 to n^2. [7, 10] This transforms $\boldsymbol{\rho}$ to the $n^2 \times 1$ column matrix $\boldsymbol{\sigma}$ and allows us to write the commutators in terms of $n^2 \times n^2$ matrices $\mathbf{A}$ and $\mathbf{B}$, so that the equations are now of the diadic form

$$\frac{d\boldsymbol{\sigma}(t)}{dt} = \mathbf{A}(t)\boldsymbol{\sigma}(t) + \int_0^t dt' \mathbf{B}(t, t')\boldsymbol{\sigma}(t'). \tag{26}$$

3.2 Numerical Procedure

To begin, we write the integro-differential equation in a more compact form,

$$\frac{d\sigma}{dt} = f[t, \sigma(t), z(t)] \tag{27}$$

with

$$z(t) = \int_0^t K[t, t', \sigma(t')]dt' \tag{28}$$

An extended Runge-Kutta integration scheme from time t_n to $t_n + \Delta t$ employs an iterative procedure during time advancement, with the notation $Y_{n,j} = \sigma^{(j)}(t_n)$ for the $j - th$ iteration. With similar notation for other functions of time, and with $\Delta t = h$, the following algorithm can be used [21]

$$Y_{n,j} = \sigma_n + h \sum_{i=1}^{m} a_{j,i} f[t_n + c_i h, Y_{n,i}, \tilde{F}_n(t_n + c_i h) + hZ_{n,i}] \tag{29}$$

$$Z_{n,i} = \sum_{l=1}^{m} \bar{a}_{i,l} K(t_n + c_i h, t_n + c_l h, Y_{n.l}) \tag{30}$$

$$\tilde{F}_n(t) = h \sum_{l=0}^{n-1} \sum_{j=i}^{m} b_j K(t, t_l + c_j h, Y_{l,j}) \tag{31}$$

$$\sigma_{n+1} = \sigma_n + h \sum_{j=1}^{m} b_j f[t_n + c_j h, Y_{n,j}, \tilde{F}_n(t_n + c_j h) + hZ_{n,j}] \tag{32}$$

where m is the number of iteration stages of the method, and the column matrices $\mathbf{b}$=$[b_j]$, $\mathbf{c}$= $[c_j]$, and square matrices $\mathbf{a} = [a_{j,i}]$, $\bar{\mathbf{a}} = [\bar{a}_{i,l}]$ depend on the choice of the accuracy order in the Runge-Kutta method. The values chosen here are based on the standard fourth order RK method (RK4), $\mathbf{b}$= $(\frac{1}{6}, \frac{1}{3}, \frac{1}{3}, \frac{1}{6})$, $\mathbf{c}$= $(0, \frac{1}{2}, \frac{1}{2}, 1)$, and $\mathbf{a} = \bar{\mathbf{a}}$ is in lower diagonal form, with the only nonzero elements being $a_{21} = a_{32} = \frac{1}{2}$, $a_{43} = 1$.

The procedure gives a simple recursion because the **a** matrices are in lower diagonal form. Similar equations can be written for the original RDM $\boldsymbol{\rho}$ instead of the diadic form $\boldsymbol{\sigma}$. This recursive procedure has been previously tested by us for density matrix calculations and found to be reliable. [22]

4 Application to adsorbates

4.1 A model for adsorbates

We introduce the vibrational wavefunctions $\phi_{v_I}(x)$ for each electronic state I and work with the vibronic basis set $\{|I, v_I\rangle\}$ and matrices in this basis, like $\mathbf{V} = [\langle J, v_J|\hat{V}_p|I, v_I\rangle]$ and $\mathbf{W} = [\langle v_I|W_{IJ}|v_J\rangle]$. The dissipative potential form of the instantaneous dissipative rate in the RDM equation follows from **W** as given above.

The Lindblad form of the dissipative rate is obtained from state-to-state rates $r(J, v_J \leftarrow I, v_I; T)$ for of the adsorbate interacting with a medium at temperature T. The operator for the transition $k = (J, v_J \leftarrow I, v_I)$ is then constructed as $\hat{L}_p^{(k)} = |J, v_J\rangle[r(J, v_J \leftarrow I, v_I)]^{1/2}\langle I, v_I|$, corresponding to vibronic transitions in the p-region.

For the delayed dissipation rate, we'll use in Eq.(20) the form $\hat{H}_{ps} = \hat{A}\hat{B}$, with $\hat{A} = \hat{q} = \hat{x}/x_0$ a dimensionless displacement and $\hat{B} = 2\hbar\sum_j \kappa_j \hat{Q}_j$, suitable for a p-region with a single vibrational mode q, and where κ_j is a measure of its coupling strength with s-region mode Q_j of frequency ω_j. This coupling is present in both ground and excited electronic states, possibly with different values for κ in each electronic state. With this coupling, the memory matrices look like $M^{(I)}_{rs,cd} = \langle\langle \hat{B}(t)\hat{B}(0)\rangle\rangle q_{rs}q_{cd}$ for electronic state I and vibrational states $v_I = r, s, c, d$. In the applications, the density of normal modes in the substrates is large and it is better to use functions of a continuous vibrational frequency ω, obtained calculating $\kappa(\omega)$ from the pairs (κ_j, ω_j) by interpolation. In a model with a continuum of vibrational modes of frequencies ω for the substrate solid, the p-region displacement is coupled to normal vibrational displacements $\hat{Q}(\omega)$ in the s-region given by the boson (phonon superposition) operator $\hat{B} = 2\hbar\int d\omega g(\omega)\kappa(\omega)\hat{Q}(\omega)$, with $g(\omega)$ the density of vibrational modes per unit frequency. The TCF $\langle\langle \hat{B}(t)\hat{B}(0)\rangle\rangle$ follows from the spectral density $\omega^2 J(\omega) = 2g(\omega)|\kappa(\omega)|^2$, as

$$C(t) = \int_0^\infty d\omega\, \omega^2 J(\omega)[\cos(\omega t)\coth(\frac{\hbar\omega}{2k_B T}) - i\sin(\omega t)] \tag{33}$$

for the total system initially at temperature T.

4.2 CO/Cu(001) dissipative dynamics

We consider the system $CO/Cu(001)$ excited by a pulse of visible light, as an example where electronic and vibrational excitation and further relaxation of

CO on the Cu(001) surface can be used to elucidate the present treatment of a dissipative dynamics. Here we focus on the frustrated-translation vibrational mode of CO, parallel to the surface, with vibrational quantum numbers v_I for electronic states $I = g, e$. Absorption of a pulse of visible light leads to photodesorption of a small fraction of adsorbed CO , and leaves the remaining CO's on an electronically excited surface. This happens by indirect excitation of the CO adsorbate as illustrated in Figure 1. First, light is absorbed by the substrate and excites electrons there. They get rapidly de-excited with transfer of energy to the adsorbate (or p-) region. This interacts back with the substrate (or s-) region and goes from its excited vibronic states (e, v_e) to its ground vibronic states (g, v_g), which then slowly relax.

The fast desorption of CO in CO/Cu(001) has been measured [33] and also calculated. [30, 31] The collision induced vibrational excitation and following relaxation of CO on Cu(001) has also been experimentally explored using time-of-flight techniques, and has been analyzed in experiments [34] and theory. [23, 32] Our previous treatment of instantaneous electronic de-excitation of CO/Cu(001) after photoexcitation is extended here to include delayed vibrational relaxation of CO/Cu(001) in its ground electronic state. We show results for the density matrix, from calculations with the described numerical procedure for the integrodifferential equations.

We use the previously developed model, with two diabatic electronic states, $I = g, e$, and desorption by a pulse of light of wavelength 520 nm. [29, 31] The normal vibrational coordinates q_i of the p-region can be obtained in principle for the CO/Cu_6 cluster, but in practice a simpler description can be used. The vibrations perpendicular to the surface have a much larger energy spacing than the frustrated translation and do not get excited, and the frustrated translation is weakly coupled to the Cu displacements because of the large difference in masses. Therefore, here we concentrate on electronic and vibrational relaxation of the adsorbed molecule with axis perpendicular to the surface and its center of mass vibrating in a frustrated translation x parallel to the surface, with the distance Z from CO to the surface kept constant at $Z = Z_g$, and the orientation angles of CO, which change slowly, fixed at $\theta = 0$ and $\phi = 0$. The potential energy functions are then $V_{IJ}(x)$ and form a 2×2 matrix $\mathbf{V}(x)$ which is diagonal around $Z = Z_g$ in a basis of diabatic electronic states. Diagonal elements have the form $V_{II}(x) = M_{CO}\Omega_I^2/2 + \Delta V_I$, with parameters taken from [29].

The light absorbed first by the substrate (the s-region) creates there electronic excitations described by the $\hat{\Gamma}^{(s)}$ density operator. They in turn create a local electric field at the adsorbate (or p-) region, where the states $I = (g,\ e)$ are coupled by an SCF potential $G_{p,IJ}(x) = \mathcal{E}_p(t) sin(\omega_0 t) D_{IJ}(x)$, where D_{IJ} is a transition dipole and $\mathcal{E}_p$ is the envelope of the effective electric field in the p-region when the applied light pulse has frequency ω_0, as previously published. [30]

Furthermore, in our previous work [29,30] we constructed a dissipative potential energy 2×2 matrix $[W_{IJ}(x)]$ resulting from p-electric-dipole/s-electric-

dipole coupling. Its off-diagonal element $W_c = W_{ge}$ is used in the present calculations to obtain state-to-state rates $r(g, v_g \leftarrow e, v_e; T) = \langle v_g|W_{ge}|v_e\rangle_T/\hbar$ and $r(e, v_e \leftarrow g, v_g; T) = r(g, v_g \leftarrow e, v_e; T)exp\{-[E(e, v_e) - E(g, v_g)]/(k_B T)\}$ satisfying detailed balance.

After the adsorbed CO rapidly relaxes to its ground electronic state g due to electronic dissipation, the s-region reaches equilibrium at a temperature T, but the p-region is yet found in a distribution of vibrational states ϕ_r, with $r = v_g = 0, 1, 2, ...$The kernel matrix for delayed dissipation of vibrational energy has been given in terms of the dimensionless CO displacement $\hat{q} = \hbar^{1/2}/(m_{CO}\omega_V)^{1/2}\hat{x}$ for a frustrated translation of frequency ω_V and mass m_{CO} in the p-region.

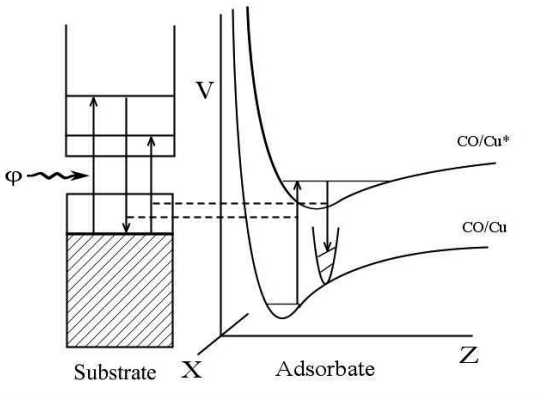

Fig. 1: Energy levels for $CO/Cu(001)$ showing the energy bands of the substrate and potential energy functions of the adsorbate CO with its axis perpendicular to the surface. The variable x refers to the frustrated-translation vibration of the center of mass of CO parallel to the surface, and q here is the distance from the center of mass of CO to the surface. Following an initial substrate photoexcitation, its de-excitation transfers energy into the adsorbate, which relaxes to the ground vibronic states.

The functions $\kappa(\omega)$ and $g(\omega)$ in $\hat{B} = 2\hbar \int d\omega g(\omega)\kappa(\omega)\hat{Q}(\omega)$ have been obtained from a Debye model of the substrate and are given in references [23, 32]. The matrix elements of the density operator for the ground electronic state are of the form $\rho_{gr,gs} = \rho^{(g)}_{r,s}$, and the dissipative superoperator is expressed in terms of four-index matrices $M^{(g)}_{rs,cd} = \langle\langle \hat{B}(t)\hat{B}(0)\rangle\rangle q_{rs}q_{cd}$. The equation of motion for the ground state density matrix is given in reference [23]. The present model assumes that the electronic relaxation from state e to g is so fast that vibrational relaxation plays a role only in the ground electronic state. Therefore the following results do not involve a density matrix $\rho_{er,es} = \rho^{(e)}_{r,s}$.

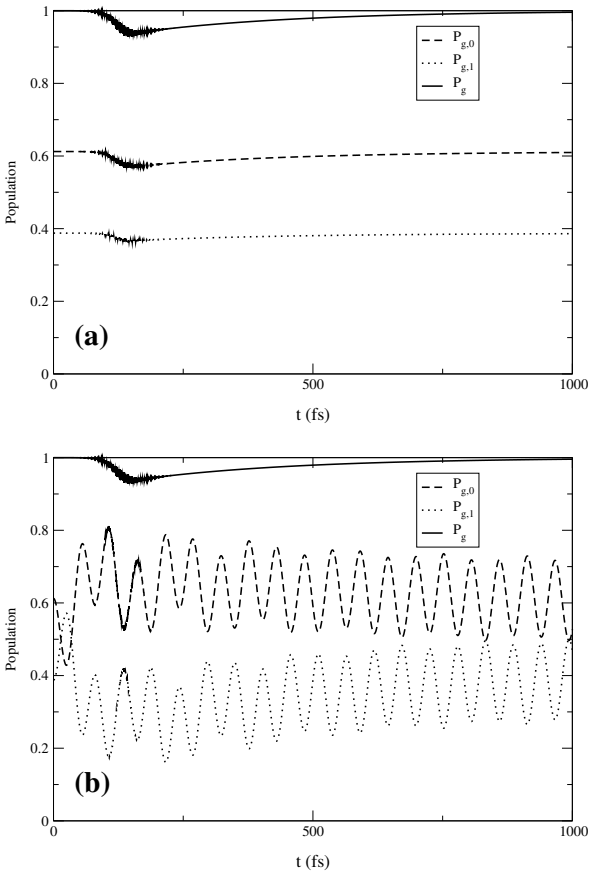

Fig. 2: (a) Populations of the ground electronic state of the adsorbate without delayed dissipation for two vibrational levels $r = v_g = 0, 1$, $P_{g,r}$ and their sum P_g; (b) Results with delayed dissipation, versus time. Here the alternating populations of states $r = v_g = 0, 1$ show quantum state coherence.

Results obtained from Eq.(22) and numerical solution of the RDM equation with the instantaneous dissipation from the dissipative potential formula, are in very good agreement with our previous results [29] using propagation of density amplitudes. The adsorbate state populations P_I reach at long times constant values, with $P_g(\infty) + P_e(\infty) = 1 - P_S(\infty)$ and P_S equal to the total population of the substrate, maintained by a steady interaction between p- and s-regions.

Presently we do our calculations with the Lindblad form of the instantaneous dissipation, to describe instead the relaxation of the adsorbate back

to the initial state with the substrate at thermal equilibrium, through the detailed balance relation for rates. In our calculations, the adsorbate starts in the ground electronic state with a thermalized distribution of vibrational states at 100 K and undergoes an electronic excitation by the light pulse. The present results, including now delayed dissipation, are shown in Figs. 2 for a gaussian light pulse centered at $t_0 = 100fs$ with a fluence of 3.0 mJ/cm^2 and a width of 100 fs (or 4.214×10^3 au(T)).

Figure 2a shows p-region populations $P_{g,r}(t) = \rho^{(g)}_{r,r}(t)$ of the ground electronic state and their sum $P_g = \sum_r \rho^{(g)}_{r,r}$, without delayed dissipation, versus time, while Fig. 2b includes delayed dissipation. In both cases the population of the ground electronic state is first rapidly depleted within 150 fs and then recovers after the pulse. Including the delayed dissipation causes only a slight decrease in the total population of the ground state. But we also see in Fig. 2b pronounced oscillations of the vibrational state populations caused by their dissipative coupling to the s-region. The coupling leads to quantum coherence of vibrational states of the adsorbate as shown by the interchange of their populations.

5 Conclusion

The present reduced density operator treatment allows for a general description of fluctuation and dissipation phenomena in an extended atomic system displaying both fast and slow motions, for a general case where the medium is evolving over time. It involves transient time-correlation functions of an active medium where its density operator depends on time. The treatment is based on a partition of the total system into coupled primary and secondary regions each with both electronic and atomic degrees of freedom, and can therefore be applied to many-atom systems as they arise in adsorbates or biomolecular systems.

Density operator equations were converted into coupled integrodifferential equations suitable for numerical processing, and an extended Runge-Kutta algorithm has been implemented for solving the matrix equations in diadic form. A similar procedure can be followed for the original density matrix.

As an illustration of the numerical treatment, the instantaneous dissipation due to fast electronic motions was constructed from the Lindblad expression in the treatment of CO/Cu(001), from decay and transition rates. The delayed dissipation, present for slow atomic vibrations of the medium, was given in terms of a memory kernel in the integrodifferential equation, calculated to second order in the coupling of the adsorbate and its environment.

Results for CO/Cu(001) were obtained with a model of electronic and vibrational transitions we have previously derived, with populations and quantum coherences calculated to compare with experimental results from femtosecond spectroscopy and time-of flight measurements. The present results show that the populations of individual vibronic states oscillate as a result

of their coupling through the medium and are therefore in coherent quantum states, but that total electronic populations are smoother over time and little changed by vibrational relaxation. The delayed relaxation due to vibrational motions of the medium has a small effect on total electronic populations of the adsorbate region at short times.

An accurate description of the photoexcitation dynamics of adsorbates or of biomolecular chromophores over times of the order of picoseconds or longer must account for two different mechanisms of relaxation: electronic and vibrational relaxation. The former one dominate at short times while the latter one dominate at longer times. The present treatment describes both processes within a single formulation, and should be applicable to a wide variety of physical systems.

Acknowledgements

This material is based upon work supported by the National Science Foundation under Grant No. 0607913.

References

1. K. Blum, *Density Matrix Theory and Applications, 2nd. edition* (Plenum Press, New York, 1981)
2. S. Mukamel, *Principles of Nonlinear Optical Spectroscopy* (Oxford Univ. Press, Oxford, England, 1995)
3. V. May and O. Kuhn "Charge and energy transfer dynamics in molecular systems" (Wiley-VCH, Weinheim, Germany, 2004)
4. A. Nitzan *Chemical Dynamics in Condensed Phases*(Oxford Univ. Press, Oxford, England, 2006)
5. D. A. Micha, A. Leathers, and B. Thorndyke in "Quantum Dynamics of Complex Molecular Systems" (Springer-Verlag, 2007) D. A. Micha and I. Burghardt, eds., pp. 165-194.
6. U. Fano, Rev. Modern Phys. **29**, 74 (1957)
7. P. O. Lowdin, Intern. J. Quantum Chem. Symp. **16**, 485 (1982)
8. D. A. Micha, Intern. J. Quantum Chem. **80**, 394 (2000)
9. A. G. Redfield, Adv. Magn. Reson. **1**, 1 (1965)
10. W. T. Pollard, A. K. Felts, and R. A. Friesner, Adv. Chem. Phys. **93**, 77 (1996)
11. G. Lindblad, Commun. Math. Phys. **48**, 119 (1976).
12. V. Gorini, A. Kossakowski, A., and E. C. G. Sudarshan, J. Math. Phys. **17**,821 (1976)
13. M. Berman, R. Kosloff, and H. Tal-Ezer, J. Phys. A **25**, 1283 (1992)
14. W. Huisinga, L. Pesce, R. Kosloff, and P. Saalfrank, J. Chem. Phys. **110**, 5538 (1999)
15. H. Guo and R. Q. Chen, J. Chem. Phys. **110**, 6626 (1999)
16. I. Kondov, U. Kleinekathofer, and M. Schreiber, J. Chem. Phys. **114**, 1497 (2001)

17. Y. Tanimura, J. Phys. Soc. Japan **75**, 082001 (2006)
18. T. Mancal, and V. May, Eur. Phys. J. B **18**, 633 (2000)
19. C. Meier and D. J. Tannor, J. Chem. Phys. **111** 3365 (1999)
20. U. Kleinekathofer, J. Chem. Phys. **121**, 2505 (2004)
21. H. Brunner and P. J. van der Houden, "The Numerical Solution of Volterra Equations" (North-Holland, New York, 1986)
22. A. S. Leathers and D. A. Micha, Chem. Phys. Lett. **415**, 46 (2005)
23. A. S. Leathers and D. A. Micha, J. Phys. Chem. A **110**, 749 (2006).
24. R. P. Feynman and F. L. Vernon Jr., Ann. Phys. **24**, 118 (1963)
25. N. Makri, Ann. Rev. Phys. Chem. **50**, 167 (1999)
26. G. A. Voth, Adv. Chem. Phys. **93**, 135 (1996)
27. P. Saalfrank and R. Kosloff, J. Chem. Phys. **105**, 2441 (1996)
28. H. Guo, P. Saalfrank and T. Seideman, Progr. Surf Sci. **62**, 239 (1999)
29. Z. Yi, D. A. Micha, and J. Sund, J. Chem. Phys. **110**, 10562 (1999)
30. D. A. Micha, A. Santana, and A. Salam, J. Chem. Phys. **116**, 5173 (2002).
31. D. A. Micha and A. Santana, J. Phys. Chem. A **107**, 7311 (2003).
32. J. L. Vega, R. Guantes, S. Miret-Artes, and D. A. Micha, J. Chem. Phys. **121**, 8580 (2004)
33. J. A. Prybyla and H. W. K. Tom and G.D. Aumiller, Phys. Rev. Lett. **68**, 503 (1992)
34. F. Hofmann and J. P. Toennies, Chem. Rev. **96** 1307 (1996)

Part V

New Methods for Mixing Quantum and Classical Mechanics

Quantum Dynamics in Almost Classical Environments

Robbie Grunwald, Aaron Kelly, and Raymond Kapral

[1] Chemical Physics Theory Group, Department of Chemistry, University of Toronto, Toronto, Ontario, M5S 3H6 Canada rgrunwal@chem.utoronto.ca
[2] Chemical Physics Theory Group, Department of Chemistry, University of Toronto, Toronto, Ontario, M5S 3H6 Canada akelly@chem.utoronto.ca
[3] Chemical Physics Theory Group, Department of Chemistry, University of Toronto, Toronto, Ontario, M5S 3H6 Canada rkapral@chem.utoronto.ca

Abstract. In this chapter we discuss approaches to solving quantum dynamics in the condensed phase based on the quantum-classical Liouville method. Several representations of the quantum-classical Liouville equation (QCLE) of motion have been investigated and subsequently simulated. We discuss the benefits and limitations of these approaches. By making further approximations to the QCLE, we show that standard approaches to this problem, i.e., mean-field and surface-hopping methods, can be derived. The computation of transport coefficients, such as chemical rate constants, represent an important class of problems where the QCL method is applicable. We present a general quantum-classical expression for a time-dependent transport coefficient which incorporates the full system's initial quantum equilibrium structure. As an example of the formalism, the computation of a reaction rate coefficient for a simple reactive model is presented. These results are compared to illuminate the similarities and differences between various approaches discussed in this chapter.

1 Introduction

The elucidation of real-time quantum molecular dynamics remains a challenging and fascinating problem of importance in physics, chemistry and biology. Current experimental techniques are beginning to allow one to probe dynamical events in previously unexplored regimes; for example, sub-femtosecond to picosecond time scales in condensed media. In order to describe such dynamics from both theoretical and numerical points of view, one is faced with a task that becomes exponentially more difficult with the number of degrees of freedom. For small systems, with roughly ten to one hundred particles, full quantum simulations can be carried out but at a large computational cost. In order to describe larger, more complicated systems we are forced to make approximations to full quantum mechanics in order to obtain dynamical in-

I. Burghardt et al. (eds.), *Energy Transfer Dynamics in Biomaterial Systems*, Springer Series in Chemical Physics 93, DOI 10.1007/978-3-642-02306-4_12,

formation. Indeed, in some instances a full quantum mechanical treatment is probably unnecessary. This is the case if one is interested in a small subset of system degrees of freedom whose quantum mechanical character is important, while the remainder of the system (environment) may be approximated by classical mechanics [1–3]. For example, a decomposition of this type is appropriate for a subsystem composed of light particles, like electrons or protons, interacting with a solvent of heavy molecules.

In this paper we restrict our consideration of such systems to descriptions based on quantum-classical Liouville dynamics [3]. We begin with a discussion of this equation and its properties. The quantum-classical Liouville equation describes the dynamics of a quantum subsystem coupled to an almost classical environment. The term "almost" used here and in the title refers to the fact that while the environment evolves by the classical equations of motion in the absence of coupling to the quantum subsystem, in the presence of coupling a description in terms of single classical trajectories is no longer possible. After this introduction, we outline a number of ways one may construct numerical solutions to this equation by projecting it onto different bases. In certain limits, making approximations, quantum-classical Liouville dynamics may be reduced to some commonly-used mixed quantum-classical approaches, in particular, mean field and surface hopping schemes, as well as the Wigner-Liouville approach. Quantum time correlation functions, which are related to transport properties, are then discussed. As an example, the computation of quantum chemical reaction rates is described in the penultimate section. Some perspectives on the work are given in conclusions.

2 Quantum-Classical Liouville Dynamics

The time evolution of a quantum mechanical system is governed by the quantum Liouville-von Neumann equation,

$$\frac{\partial}{\partial t}\hat{\rho}(t) = -\frac{i}{\hbar}[\hat{H}, \hat{\rho}(t)], \tag{1}$$

where $\hat{\rho}(t)$ is the density matrix, $\hat{H}$ is the total Hamiltonian, and the square brackets denote the commutator. Quantum-classical Liouville dynamics is an approximation to this equation that is appropriate for situations where the full quantum system may be partitioned into a quantum subsystem, and a classical environment. This partition is motivated by the observation that for many condensed phase processes the quantum mechanical character of only a few degrees of freedom need be taken into account to accurately describe the system's overall dynamics. To this end, we let $\hat{q} = \{\hat{q}_i\},\ i = 1, ..., n$ be a set of coordinate operators for the n subsystem degrees of freedom with mass m, while the remaining N environmental degrees of freedom with mass M have coordinate operators $\hat{Q} = \{\hat{Q}_i\},\ i = 1, ..., N$. The total Hamiltonian can then be written as

$$\hat{H} = \frac{\hat{P}^2}{2M} + \frac{\hat{p}^2}{2m} + \hat{V}(\hat{q}, \hat{Q}), \tag{2}$$

where we have written the momentum operators for the subsystem and environment as $\hat{p}$ and $\hat{P}$, respectively. In keeping with this partition scheme, the potential energy operator, $\hat{V}(\hat{q}, \hat{Q})$ can be decomposed into subsystem, environment, and coupling terms: $\hat{V}(\hat{q}, \hat{Q}) = \hat{V}_s(\hat{q}) + \hat{V}_e(\hat{Q}) + \hat{V}_c(\hat{q}, \hat{Q})$.

By performing a partial Wigner transform with respect to the coordinates of the environment, we obtain a classical-like phase space representation of those degrees of freedom. The subsystem coordinate operators are left untransformed, thus, retaining the operator character of the density matrix and Hamiltonian in the subsystem Hilbert space [4]. In order to take the partial Wigner transform of Eq. (1) explicitly, we express the Liouville-von Neumann equation in the $\{Q\}$ representation,

$$\frac{\partial \langle Q|\hat{\rho}(t)|Q'\rangle}{\partial t} = -\frac{i}{\hbar} \int dQ'' \left(\langle Q|\hat{H}|Q''\rangle \langle Q''|\hat{\rho}(t)|Q'\rangle - \langle Q|\hat{\rho}(t)|Q''\rangle \langle Q''|\hat{H}|Q'\rangle \right). \tag{3}$$

Using the definition of the Wigner transform [5] of the density matrix,

$$\hat{\rho}_W(R, P) = (2\pi\hbar)^{-3N} \int dZ \; e^{iP\cdot Z/\hbar} \langle R - \frac{Z}{2}|\hat{\rho}|R + \frac{Z}{2}\rangle, \tag{4}$$

and the formula for the partial Wigner transform of a product of two operators [6]

$$\left(\hat{A}\hat{B}\right)_W (R, P) = \hat{A}_W(R, P) e^{\hbar\Lambda/2i} \hat{B}_W(R, P), \tag{5}$$

Eq. (3) becomes

$$\frac{\partial \hat{\rho}_W(R, P, t)}{\partial t} = -\frac{i}{\hbar} \Big(\hat{H}_W(R, P) e^{\hbar\Lambda/2i} \hat{\rho}_W(R, P, t) - \hat{\rho}_W(R, P, t) e^{\hbar\Lambda/2i} \hat{H}_W(R, P) \Big). \tag{6}$$

The operator $\Lambda = \overleftarrow{\nabla}_P \cdot \overrightarrow{\nabla}_R - \overleftarrow{\nabla}_R \cdot \overrightarrow{\nabla}_P$ is the negative of the Poisson bracket operator, and the subscript W indicates the partial Wigner transform. The partial Wigner transform of the total Hamiltonian is written as,

$$\hat{H}_W(R, P) = \frac{P^2}{2M} + \frac{\hat{p}^2}{2m} + \hat{V}_W(\hat{q}, R). \tag{7}$$

The quantum-classical Liouville equation can be derived by formally expanding the operator on the right side of Eq. (6) to $\mathcal{O}(\hbar^0)$. One may justify [4] such an expansion for systems where the masses of particles in the environment are much greater than those of the subsystem, $M \gg m$. In this case the small parameter in the theory is $\mu = (m/M)^{1/2}$. This factor emerges in the equation of motion quite naturally through a scaling of the variables motivated

by the classical theory of Brownian motion. Through such an analysis [4], one obtains the quantum-classical Liouville (QCL) equation [3, 4, 7–15]

$$\begin{aligned}\frac{\partial \hat{\rho}_W(R,P,t)}{\partial t} &= -\frac{i}{\hbar}\left[\hat{H}_W(R,P), \hat{\rho}_W(R,P,t)\right] \\ &\quad + \frac{1}{2}(\{\hat{H}_W(R,P), \hat{\rho}_W(R,P,t)\} - \{\hat{\rho}_W(R,P,t), \hat{H}_W(R,P)\}) \\ &= -i\hat{\mathcal{L}}\hat{\rho}_W(R,P,t). \end{aligned} \tag{8}$$

The last line defines the mixed quantum-classical Liouville (super)operator $\hat{\mathcal{L}}$.

The QCL superoperator has many desirable features required to produce physical dynamics; it conserves total mass, energy, momentum and phase space volumes [4, 16, 17]. However, it does not provide a fully consistent treatment of mixed quantum-classical dynamics. The quantum-classical bracket defined by the right side of Eq. (8) does not possess a Lie algebraic structure since it fails to satisfy the Jacobi identity [16, 18]. A detailed discussion of the consequences of this lack of a Lie algebraic structure can be found in Ref. [16]. There have been attempts to construct quantum-classical brackets that possess a Lie algebraic structure [19, 20] although these constructions have been shown to have difficulties [21, 22]. In addition to these attempts, there have been more recent formulations of quantum-classical dynamics based on different premises that have a Lie algebraic structure [23]. In spite of these limitations the quantum-classical Liouville description is one of the most accurate, computationally tractable methods for the study of the quantum dynamics of large complex systems. In particular, we observe that it equivalent to the full quantum dynamics described by Eq. (1) for arbitrary quantum subsystems bilinearly coupled to harmonic baths. In addition, as we shall see, approximations to QCL dynamics yield mean field and surface-hopping schemes.

In the next section we describe how the QCL equation may be expressed in any basis that spans the subsystem Hilbert space. Here we observe that the subsystem may also be Wigner transformed to obtain a phase-space-like representation of the subsystem variables as well as those of the environment. Taking the Wigner transform of Eq. (8) over the subsystem, we obtain the quantum-classical Wigner-Liouville equation [24],

$$\begin{aligned}&\left[\frac{\partial}{\partial t} + i\mathcal{L}_\ell^{(0)} + i\mathcal{L}_{\rm h}^{(0)}\right]\rho_W(p,P,r,R,t) \\ &\quad = \frac{2}{\hbar(\pi\hbar)^n}\int ds\,\left[\int d\tilde{r}\; V(r-\tilde{r},R)\sin\left(\frac{2s\tilde{r}}{\hbar}\right)\right]\rho_W(p-s,P,r,R,t) \\ &\qquad + \int ds\; \Delta F(R,s)\frac{\partial}{\partial P}\rho_W(p-s,P,r,R,t), \end{aligned} \tag{9}$$

where the force $\Delta F(R,s)$ is defined as

$$\Delta F(R,s) = \frac{1}{(\pi\hbar)^n}\frac{\partial}{\partial R}\left[\int d\tilde{r}\;\cos(2s\tilde{r}/\hbar)V(r-\tilde{r},R)\right]. \tag{10}$$

The classical free streaming Liouville operators are $i\mathcal{L}_\ell^{(0)} = \frac{p}{m}\frac{\partial}{\partial r}$ and $i\mathcal{L}_{\rm h}^{(0)} = \frac{P}{M}\frac{\partial}{\partial R}$ for the light (ℓ) subsystem particles and (h) heavy environmental particles, respectively. The quantum-classical Wigner-Liouville equation (9) can be written in a more compact form,

$$\left[\frac{\partial}{\partial t} + i\mathcal{L}_\ell + i\mathcal{L}_{\rm h}\right]\rho_W(p,P,r,R,t) = \int ds\; K(s,P,r,R)\rho_W(p-s,P,r,R,t) \tag{11}$$

where $i\mathcal{L}_\ell = \frac{p}{m}\frac{\partial}{\partial r} + F_s(r)\frac{\partial}{\partial p}$ is the full classical Liouville operator for the subsystem and $i\mathcal{L}_{\rm h} = \frac{P}{M}\frac{\partial}{\partial R} + F_e(R)\frac{\partial}{\partial P}$ is the full classical Liouville operator for the environment. Here $F_s(r) = -\partial V_s(r)/\partial r$ and $F_e(R) = -\partial V_e(R)/\partial R$. The kernel $K(s,P,r,R)$ is the sum of two contributions, $K = K_\ell + K_{\rm h}$ with

$$\begin{aligned} K_{\rm h}(s,P,r,R) &= \frac{1}{(\pi\hbar)^n}\left\{\frac{\partial}{\partial R}\int d\tilde{r}\;\cos(2s\tilde{r}/\hbar)V_c(r-\tilde{r},R)\right\}\frac{\partial}{\partial P}, \\ K_\ell(s,P,r,R) &= -\frac{\partial V_s(r)}{\partial r}\frac{d\delta(s)}{ds} \\ &\quad + \frac{2}{\hbar(\pi\hbar)^n}\int d\tilde{r}\;[V_s(r-\tilde{r}) + V_c(r-\tilde{r},R)]\sin(\frac{2s\tilde{r}}{\hbar}). \end{aligned} \tag{12}$$

This equation gives the dynamics of the quantum-classical system in terms of phase space variables (R,P) for the bath and the Wigner transform variables (r,p) for the quantum subsystem. This equation cannot be simulated easily but can be used when a representation in a discrete basis is not appropriate. It is easy to recover a classical description of the entire system by expanding the potential energy terms in a Taylor series to linear order in $\tilde{r}$. Such classical approximations, in conjunction with quantum equilibrium sampling, are often used to estimate quantum correlation functions and expectation values. Classical evolution in this full Wigner representation is exact for harmonic systems since the Taylor expansion truncates.

3 Representations and Solutions

In many cases, in order to compute the dynamics of condensed phase systems, one invokes a basis representation for the quantum degrees of freedom in the system. Typically, one computes the dynamics of these systems in order to obtain quantities of interest, such as an average value, $\overline{A(t)} = {\rm Tr}\,[\hat{A}\hat{\rho}(t)]$, or a correlation function, as will be discussed below. Since such averages are basis independent one may project Eq. (8) onto any convenient basis. This is in principle a nice feature, and one that is often exploited to aid in calculations. However, it is important to note that the basis onto which one chooses to project the QCLE has important implications on how one goes about solving the resulting equations of motion. Ultimately the time-dependent average value of an observable is expressed as a trace over quantum subsystem

states and a phase space average over classical-like coordinates; this feature is intimately linked to constructing a solution using statistical mechanics. Trajectory-based simulation methods for computing phase-space averages are often sought once the system Hamiltonian is known in a given basis. However, other schemes have been proposed that do not rely on computing ensembles of trajectories [25, 26].

In this section we present the major basis representations that have been used in the literature to solve the QCLE. For each representation - subsystem, adiabatic, force, and mapping, respectively - we present the QCLE in the particular representation, and briefly describe the schemes used to solve the equation of motion in that particular basis. We discuss the strengths and shortcomings of each representation.

3.1 The subsystem basis

When partitioning a system into a subsystem and its environment, the Hamiltonian one obtains, Eq. (2), is composed of subsystem, environment, and coupling parts. Thus, representing the QCLE in the subsystem basis is a natural starting point.

Let us consider a simple partitioning of the total Hamiltonian into two parts; one containing terms corresponding to the isolated quantum subsystem only, $\hat{h}_s$, and a remainder that contains all the bath and coupling terms. The subsystem basis is then defined by the following eigenvalue problem, $\hat{h}_s|\alpha\rangle = \epsilon_\alpha|\alpha\rangle$, where $\hat{h}_s = \hat{p}^2/2m + \hat{V}_s(\hat{q})$. These basis states, and the associated energy eigenvalues, are independent of the coordinates of the environment. The quantum-classical Liouville superoperator when written in the subsystem basis is given by,

$$-i\mathcal{L}^s_{\alpha\alpha',\beta\beta'} = -i(\omega^s_{\alpha\alpha'} + L^s_{\alpha\alpha'})\delta_{\alpha\beta}\delta_{\alpha'\beta'} + \frac{i}{\hbar}(\delta_{\alpha\beta}V_c^{\beta'\alpha'} - V_c^{\alpha\beta}\delta_{\alpha'\beta'}) + \frac{1}{2}\left(\delta_{\alpha'\beta'}\frac{\partial V_c^{\alpha\beta}}{\partial R} + \delta_{\alpha\beta}\frac{\partial V_c^{\beta'\alpha'}}{\partial R}\right)\cdot\frac{\partial}{\partial P}, \tag{13}$$

where we have used the following notation for subsystem quantities: $\omega^s_{\alpha\alpha'} = (\epsilon_\alpha - \epsilon_{\alpha'})/\hbar$, $V_c^{\alpha\alpha'} = \langle\alpha|\hat{V}_c|\alpha'\rangle$, $iL^s_{\alpha\alpha'} = \frac{P}{M}\cdot\frac{\partial}{\partial R} + F_b(R)\cdot\frac{\partial}{\partial P}$, and $F_e(R) = -\partial V_e/\partial R$ is the force exerted by the environment. Also, this equation of motion has been derived from the linearized influence functional in a path integral representation expressed in this basis [15]. Thus, in this basis, QCL dynamics is equivalent to the linearized path integral formulation.

Donoso and Martens [13, 27] have developed a method for simulating the dynamics prescribed in this representation in the spirit of classical molecular dynamics. The algorithm is based on writing each element of the density matrix in the subsystem basis as a weighted sum over an ensemble of classical trajectories,

$$\rho_s^{\alpha\alpha'}(X,t) = \sum_{k=1}^{N_{\alpha\alpha'}} a_k^{\alpha\alpha'}(t)\delta(X - X_k^{\alpha\alpha'}(t)). \tag{14}$$

The ensemble contains $N_{\alpha\alpha'}$ classical trajectories of the type

$$X_k^{\alpha\alpha'}(t) = (R_k^{\alpha\alpha'}(t), P_k^{\alpha\alpha'}(t)),$$

with weight $a_k^{\alpha\alpha'}(t)$. Population transfer and phase oscillations in the subsystem occur via the time variation of the weights attributed to the ensemble. However, in this construction the density is not a smooth function of the phase space coordinates [13], so a smoothing process is implemented to obtain appropriately scaled gaussian wavepackets. A short time approximation of the propagator is then performed and the resulting equations of motion for the weights are numerically integrated, whilst the ensemble undergoes Hamiltonian dynamics. The results from simulations using this algorithm (called the semiclassical Liouville method) are generally in excellent agreement with exact quantum mechanical solutions for model problems. The method has also been applied to the computation of vibrational dephasing rates of the I_2 molecule in a low temperature Kr matrix and the results are in good agreement with experiment [28].

3.2 The adiabatic basis

In contrast to the subsystem representation, the adiabatic basis depends on the environmental coordinates. As such, one obtains a physically intuitive description in terms of classical trajectories along Born-Oppenheimer surfaces. A variety of systems have been studied using QCL dynamics in this basis. These include: the reaction rate and the kinetic isotope effect of proton transfer in a polar condensed phase solvent and a cluster [29–33], vibrational energy relaxation of a hydrogen bonded complex in a polar liquid [34], photodissociation of F_2 [35], dynamical analysis of vibrational frequency shifts in a Xe fluid [36], and the spin-boson model [37,38], which is of particular importance as exact quantum results are available for comparison.

The adiabatic basis is defined by the eigenvalue problem,

$$\hat{h}_W(R)|\alpha;R\rangle = E_\alpha(R)|\alpha;R\rangle,$$

where

$$\hat{h}_W(R) = \hat{H}_W(R,P) - P^2/2M$$

is the Hamiltonian for the subsystem in a static environment, and the adiabatic energies, $E_\alpha(R)$, depend parametrically on the coordinates of the environment, R. In this representation, the time evolution of an element of the density matrix,

$$\langle\alpha;R|\hat{\rho}_W(R,P,t)|\alpha';R\rangle = \rho_W^{\alpha\alpha'}(R,P,t),$$

is given by

$$\frac{\partial \rho_W^{\alpha\alpha'}(R,P,t)}{\partial t} = -i \sum_{\beta\beta'} \mathcal{L}_{\alpha\alpha',\beta\beta'} \rho_W^{\beta\beta'}(R,P,t), \tag{15}$$

where the evolution operator is now [4]

$$\begin{aligned} i\mathcal{L}_{\alpha\alpha',\beta\beta'} &= i\mathcal{L}^{(0)}_{\alpha\alpha'}\delta_{\alpha\beta}\delta_{\alpha'\beta'} - \mathcal{J}_{\alpha\alpha',\beta\beta'} \\ &= (i\omega_{\alpha\alpha'} + iL_{\alpha\alpha'})\delta_{\alpha\beta}\delta_{\alpha'\beta'} - \mathcal{J}_{\alpha\alpha',\beta\beta'}. \end{aligned} \tag{16}$$

The structure of $\mathcal{L}$ given above, consists of two distinct components; (i) classical propagation on mean surfaces accompanied by quantum mechanical phase oscillations with frequency $\omega_{\alpha\alpha'} = (E_\alpha - E_{\alpha'})/\hbar$, and (ii) nonadiabatic transitions accompanied by changes in the momentum of the environment in order to conserve energy. The classical Liouville operator

$$iL_{\alpha\alpha'} = \frac{P}{M}\cdot\frac{\partial}{\partial R} + \frac{1}{2}\left(F_W^{\alpha} + F_W^{\alpha'}\right)\cdot\frac{\partial}{\partial P}\,, \tag{17}$$

propagates the environmental coordinates via Hellmann-Feynman forces,

$$F_W^{\alpha} = -\langle\alpha;R|\frac{\partial \hat{V}_W(\hat{q},R)}{\partial R}|\alpha;R\rangle.$$

The operator, $\mathcal{J}$, responsible for nonadiabatic transitions may be written as follows,

$$\begin{aligned} \mathcal{J}_{\alpha\alpha',\beta\beta'} &= -\frac{P}{M}\cdot d_{\alpha\beta}\left(1+\frac{1}{2}S_{\alpha\beta}\cdot\frac{\partial}{\partial P}\right)\delta_{\alpha'\beta'} \\ &- \frac{P}{M}\cdot d^*_{\alpha'\beta'}\left(1+\frac{1}{2}S^*_{\alpha'\beta'}\cdot\frac{\partial}{\partial P}\right)\delta_{\alpha\beta}\,. \end{aligned} \tag{18}$$

where the quantity $S_{\alpha\beta}$ is defined as

$$S_{\alpha\beta} = F_W^{\alpha}\delta_{\alpha\beta} - F_W^{\alpha\beta}(\frac{P}{M}\cdot d_{\alpha\beta})^{-1} = E_{\alpha\beta}d_{\alpha\beta}(\frac{P}{M}\cdot d_{\alpha\beta})^{-1},$$

where $F_W^{\alpha\beta}$ are the off-diagonal matrix elements of the force and $d_{\alpha\beta}$ is the nonadiabatic coupling matrix element, $d_{\alpha\beta} = \langle\alpha;R|\frac{\partial}{\partial R}|\beta;R\rangle$. The presence of the nonadiabatic coupling matrix elements in this operator accounts for nonadiabatic transitions, which change the quantum state of the subsystem from a diagonal to an off-diagonal state or vice versa. The environment momentum derivative accounts for the energy transfer involved in the subsystem state change.

Shi and Geva [15] have also derived the QCLE in the adiabatic basis starting from the full path integral expression for the quantum mechanical problem. In this representation the derivation starts with the partial Wigner transform of the environmental degrees of freedom in contrast to what is done

in the subsystem basis. The final form of the equation is then obtained by expressing the adiabatic matrix elements of the partially Wigner transformed density, $\hat{\rho}_W^{\alpha\alpha'}(R,P;t+\epsilon)$ in terms of $\hat{\rho}_W^{\alpha\alpha'}(R,P;t)$, and linearizing the resulting system propagators. It is interesting to note that the choice of basis has consequences on the order of operations between the linearization and partial Wigner transform in the derivation of these equations. In the subsystem basis, the partial Wigner transform is a consequence of the linearization of the forward-backward action, however in the adiabatic case, the partial Wigner transform is applied to the equation of motion, and the propagators are subsequently linearized in order to obtain the QCLE.

It is easy to see how a trajectory picture of the dynamics emerges by applying the Dyson identity to the formal solution of Eq. (15). The iterative solution of the Dyson equation results in a series of trajectory segments. These segments consist of evolution along the surface $(\alpha\alpha')$, which may be adiabatic $(\alpha = \alpha')$ or the arithmetic mean of two adiabatic surfaces, $(\alpha \neq \alpha')$, governed by the propagator, $e^{-i(\omega_{\alpha\alpha'}+L_{\alpha\alpha'})t}$. Each subsequent term in the series includes this type of propagation interrupted by the nonadiabatic coupling operator, $\mathcal{J}$, an incremental number of times. Since, the operator $\mathcal{J}$ accounts for nonadiabatic transitions, these contributions represent trajectory segments that evolve along some surface, undergo a transition to a new surface, followed by subsequent evolution on this surface and so on.

The presence of the momentum derivatives in $\mathcal{J}$ makes the action of this operator difficult to simulate, because it acts on all functions to its right. This will generate a branching tree of trajectories. This difficulty is avoided by making the momentum-jump approximation. To see how this approximation is obtained, the following change of variables is made:

$$1 + \frac{1}{2} S_{\alpha\beta} \cdot \frac{\partial}{\partial P} = 1 + \Delta E_{\alpha\beta} M \frac{\partial}{\partial (P \cdot \hat{d}_{\alpha\beta})^2}. \tag{19}$$

For small $\Delta E_{\alpha\beta} M$ this expression corresponds to the linear expansion of the exponential translation operator $e^{\Delta E_{\alpha\beta} M \cdot \frac{\partial}{\partial (P \cdot \hat{d}_{\alpha\beta})^2}}$, whose action on a function $f(P)$ is a translation of the environment momentum by $\Delta E_{\alpha\beta} M$ along the component of the momentum that is parallel to the nonadiabatic coupling matrix element:

$$\begin{aligned} & e^{\Delta E_{\alpha\beta} M \cdot \frac{\partial}{\partial (P \cdot \hat{d}_{\alpha\beta})^2}} f(P) \\ & = e^{\Delta E_{\alpha\beta} M \cdot \frac{\partial}{\partial (P \cdot \hat{d}_{\alpha\beta})^2}} f\left((P \cdot \hat{d}_{\alpha\beta}^{\perp}) \hat{d}_{\alpha\beta}^{\perp} + \mathrm{sgn}(P \cdot \hat{d}_{\alpha\beta}) \sqrt{(P \cdot \hat{d}_{\alpha\beta})^2} \hat{d}_{\alpha\beta} \right) \\ & = f\left((P \cdot \hat{d}_{\alpha\beta}) \hat{d}_{\alpha\beta}^{\perp} + \mathrm{sgn}(P \cdot \hat{d}_{\alpha\beta}) \sqrt{(P \cdot \hat{d}_{\alpha\beta})^2 + \Delta E_{\alpha\beta} M} \hat{d}_{\alpha\beta} \right). \end{aligned} \tag{20}$$

The approximations surrounding the definition of the $\mathcal{J}$ operator comprise the momentum-jump approximation. This translation or shift of the momentum corresponds precisely to the amount of energy transferred during a transition

and thus satisfies energy conservation. In situations where there is insufficient kinetic energy available from the environment for the subsystem to make the transition, $\Delta E_{\alpha\beta} M/(P \cdot \hat{d}_{\alpha\beta})^2 > 1$, the transition is simply not allowed, and the evolution continues evolving on the surface it is on.

Several algorithms exist to simulate this evolution equation [14, 38–41]. The computation of observables in this approach is accomplished by Monte Carlo sampling configurations from the initial quantum equilibrium distribution followed by propagation of the observable by some algorithm [38, 40]. The sequential short time propagation algorithm [40] is one such algorithm where the propagator is divided into N propagators that act for a short time interval:

$$(e^{i\hat{\mathcal{L}}t})_{\alpha\alpha',\alpha_N\alpha'_N} = \sum_{(\alpha_1\alpha'_1)\ldots(\alpha_{N-1}\alpha'_{N-1})} \prod_{j=1}^{N} (e^{i\hat{\mathcal{L}}\Delta t_j})_{\alpha_{j-1}\alpha'_{j-1},\alpha_j\alpha'_j}. \tag{21}$$

The short-time propagators can be solved through application of the Dyson identity truncated to first order. The subsequent dynamics of the quantity of interest are obtained by propagating the classical variables along a surface that corresponds to the quantum state $(\alpha\alpha')$ followed by Monte Carlo sampling of the nonadiabatic transition events:

$$\begin{aligned}(e^{i\hat{\mathcal{L}}\Delta t_j})_{\alpha_{j-1}\alpha'_{j-1},\alpha_j\alpha'_j} \approx{}& \mathcal{W}_{\alpha_{j-1}\alpha'_{j-1}}(t_{j-1}, t_j) e^{iL_{\alpha_{j-1}\alpha'_{j-1}}\Delta t_j} \\ &\times \left(\delta_{\alpha_{j-1}\alpha_j}\delta_{\alpha'_{j-1}\alpha'_j} + \Delta t \mathcal{J}_{\alpha_{j-1}\alpha'_{j-1},\alpha_j\alpha'_j}\right). \end{aligned} \tag{22}$$

Simulations using this algorithm [40] and the Trotter-based scheme [38] are able to reproduce the exact quantum results for the spin-boson model, verifying its utility.

3.3 The force basis

When the quantum-classical Liouville equation is expressed in the adiabatic basis, the most difficult terms to simulate come from the off-diagonal force matrix elements, which give rise to the nonadiabatic coupling matrix elements. As described above, contributions coming from this term were computed using the momentum-jump approximation in the context of a surface-hopping scheme.

One way to simplify this term in the evolution equation is to make use of a basis that diagonalizes the force contribution [42]; i.e., we represent the quantum-classical Liouville equation in a basis $|i; R\rangle$ such that

$$-\langle i; R| \frac{\partial \hat{V}(R)}{\partial R} |j; R\rangle = F_F^i(R)\delta_{ij}, \tag{23}$$

where the subscript F is used to denote the force basis. Taking the matrix elements of Eq. (8) in this basis, we obtain

$$\frac{\partial \rho_F^{ij}(X,t)}{\partial t} = -\frac{i}{\hbar}\sum_k \left(\mathcal{H}_F^{ik}\rho_F^{kj}(t) - \rho_F^{ik}(t)\mathcal{H}_F^{kj}\right) - \left(\frac{P}{M}\cdot\frac{\partial}{\partial R} + \frac{1}{2}(F_F^i + F_F^j)\cdot\frac{\partial}{\partial P}\right)\rho_F^{ij}, \tag{24}$$

where $\mathcal{H}_F^{ij} = H_F^{ij} + i\hbar\frac{P}{M}\cdot d_{ij}^F$. Here d_{ij}^F is the nonadiabatic coupling matrix element in the force basis. It can be related to the usual nonadiabatic coupling matrix element in the adiabatic basis by inserting complete sets of adiabatic states:

$$d_{ij}^F = \sum_{\alpha\beta}\langle i;R|\alpha;R\rangle d_{\alpha\beta}\langle\beta;R|j;R\rangle. \tag{25}$$

Evolution governed by the last term in Eq. (24) is simple and can be solved in characteristics. The first term is responsible for coupling among the elements of the density matrix and its inclusion makes the computation of the dynamics a difficult task.

The quantum-classical Liouville equation in the force basis has been solved for low-dimensional systems using the multithreads algorithm [42,43]. Assuming that the density matrix is localized within a small volume of the classical phase space, it is written as linear combination of matrices located at L discrete phase space points as

$$\hat{\rho}_W(R,P,t) = \sum_{k=1}^{L}\hat{\rho}^{(k)}(t)\delta(R - R_k(t))\delta(P - P_k(t)). \tag{26}$$

The evolution equations for the quantities entering the right side of this equation are obtained by substitution into the quantum-classical Liouville equation. For a variety of one- and two-dimensional systems for which exact results are known, excellent agreement was found.

3.4 The mapping basis

The quantum-classical Liouville equation was expressed in the subsystem basis in Sec. 3.1. Based on this representation, it is possible to recast the equations of motion in a form where the discrete quantum degrees of freedom are described by continuous position and momentum variables [44–49]. In the mapping basis the eigenfunctions of the n-state subsystem can be replaced with eigenfunctions of n fictitious harmonic oscillators with occupation numbers limited to 0 or 1: $|\lambda\rangle \to |m_\lambda\rangle = |0_1,\cdots,1_\lambda,\cdots 0_n\rangle$. This mapping basis representation then makes use of the fact that the matrix element of an operator $\hat{B}_W(X)$ in the subsystem basis, $B_W^{\lambda\lambda'}(X)$, can be written in mapping form as $B_W^{\lambda\lambda'}(X) = \langle\lambda|\hat{B}_W(X)|\lambda'\rangle = \langle m_\lambda|\hat{B}_m(X)|m_{\lambda'}\rangle$, where

$$\hat{B}_m(X) = \sum_{\lambda\lambda'} B_W^{\lambda\lambda'}(X)\hat{a}_\lambda^\dagger\hat{a}_{\lambda'}. \tag{27}$$

The mapping annihilation and creation operators are given by

$$\hat{a}_\lambda = \sqrt{\frac{1}{2\hbar}}(\hat{q}_\lambda + i\hat{p}_\lambda), \quad \hat{a}^\dagger_\lambda = \sqrt{\frac{1}{2\hbar}}(\hat{q}_\lambda - i\hat{p}_\lambda). \tag{28}$$

The mapping basis has been exploited in quantum-classical calculations based on a linearization of the path integral formulation of quantum correlation functions in the LAND-map method [50–52].

Given this correspondence between the matrix elements of a partially Wigner transformed operator in the subsystem and mapping bases, we can express the quantum-classical Liouville equation in the continuous mapping coordinates [53]. The first step in this calculation is to introduce an n-dimensional coordinate space representation of the mapping basis,

$$\langle m_\lambda|\hat{B}_m(X)|m_{\lambda'}\rangle = \int dq dq' \langle m_\lambda|q\rangle\langle q|\hat{B}_m(X,t)|q'\rangle\langle q'|m_{\lambda'}\rangle, \tag{29}$$

and then write the coordinate space matrix elements in terms of Wigner transforms in the mapping space to obtain

$$\langle r - \frac{z}{2}|\hat{B}_m(X,t)|r + \frac{z}{2}\rangle = \frac{1}{(2\pi\hbar)^n}\int dp\, e^{-ipz/\hbar} B_m(x,X,t). \tag{30}$$

Carrying out the this change of representation on the quantum-classical Liouville equation and using the product rule formula for the Wigner transform of a product of operators, we obtain

$$\begin{aligned}\frac{d}{dt}\rho_m(x,X,t) = &-\frac{2}{\hbar}H_m \sin(\frac{\hbar\Lambda_m}{2})\rho_m(t) \\ &+\frac{\partial H_m}{\partial R}\cos(\frac{\hbar\Lambda_m}{2})\cdot\frac{\partial B_m(t)}{\partial P} - \frac{P}{M}\cdot\frac{\partial\rho_m(t)}{\partial R},\end{aligned} \tag{31}$$

where the negative of the Poisson bracket operator on the mapping phase space coordinates is defined as $\Lambda_m = \overleftarrow{\nabla_p}\cdot\overrightarrow{\nabla_r} - \overleftarrow{\nabla_r}\cdot\overrightarrow{\nabla_p}$. The Hamiltonian in the mapping basis is

$$H_m(x,X) = \frac{P^2}{2M} + V_e(R) + \frac{1}{2\hbar}\sum_{\lambda\lambda'} h_{\lambda\lambda'}(R)(r_\lambda r_{\lambda'} + p_\lambda p_{\lambda'} - \hbar\delta_{\lambda\lambda'}),$$

where $h_{\lambda\lambda'}(R) = \langle\lambda|\hat{p}^2/2m + V_s(\hat{q}) + V_c(\hat{q},R)|\lambda'\rangle$. Explicitly computing the exponential Poisson bracket operators, we find the quantum-classical Liouville equation in the mapping basis,

$$\begin{aligned}\frac{d}{dt}B_m(x,X,t) &= -\{H_m, B_m(t)\}_{x,X} \\ &+\frac{\hbar}{8}\sum_{\lambda\lambda'}\frac{\partial h_{\lambda\lambda'}}{\partial R}(\frac{\partial}{\partial r_{\lambda'}}\frac{\partial}{\partial r_\lambda} + \frac{\partial}{\partial p_{\lambda'}}\frac{\partial}{\partial p_\lambda})\cdot\frac{\partial}{\partial P}B_m(t) \\ &\equiv i\mathcal{L}_m B_m(t),\end{aligned} \tag{32}$$

where $\{A_m, B_m(t)\}_{x,X}$ denotes a Poisson bracket in the full mapping-bath phase space of the system.

The first term in the evolution operator has the form of a Poisson bracket and evolution under this part of the operator can be expressed in terms of characteristics. The corresponding set of ordinary differential equations is

$$\begin{aligned}
\frac{dr_\lambda(t)}{dt} &= \frac{1}{\hbar}\sum_{\lambda'} h_{\lambda\lambda'}(R(t))p_{\lambda'}(t),\\
\frac{dp_\lambda(t)}{dt} &= -\frac{1}{\hbar}\sum_{\lambda'} h_{\lambda\lambda'}(R(t))r_{\lambda'}(t),\\
\frac{dR(t)}{dt} &= \frac{P(t)}{M}, \quad \frac{dP(t)}{dt} = -\frac{\partial H_m}{\partial R(t)}.
\end{aligned} \tag{33}$$

The last term involves derivatives with respect to both mapping and environmental variables. Its contribution is difficult to compute. Calculations on the spin-boson model have shown that even if the last term is neglected, excellent agreement with the exact results for a wide range of system parameters is obtained [53].

4 Approximations to the QCL equation

The QCL approach discussed thus far in this chapter provides a good approximation to the quantum dynamics of condensed phase systems. Most often other approximate quantum-classical methods, such as mean field and surface-hopping schemes, have been commonly employed to treat the same class of problems as the QCLE. These methods are attractive due to their computational simplicity; however, many important quantum features, such as quantum coherence and correlations, are not properly handled in these approaches. In this section we discuss these methods and show that starting from the QCLE, an approximate theory in its own right, further approximations lead to these other approaches.

4.1 Mean field theory

Mean field theories of mixed quantum-classical systems are based on approximations that neglect correlations in Ehrenfest's equations of motion for the evolution of the position and momentum operators of the heavy-mass nuclear degrees of freedom. The approximate evolution equations take the form of Newton's equations of motion where the forces that the nuclear degrees of freedom experience involve mean forces determined from the time-evolving wave function of the system.

We now show how the mean field equations can be derived as an approximation to the quantum-classical Liouville equation (8) [9]. The Hamiltonian

can be written again as the sum of environmental, subsystem and interaction contributions,

$$\hat{H}_W = \frac{P^2}{2M} + V_e(R) + \frac{\hat{p}^2}{2m} + \hat{V}_s(\hat{q}) + \hat{V}_c(\hat{q}, R) = H_e(X) + \hat{H}_s(\hat{q}) + \hat{V}_c(\hat{q}, R).$$

In order to study the effects of neglecting correlations in this description of the dynamics, we define the reduced density matrices for the environment and subsystem, respectively, as

$$\rho_e(X,t) = \mathrm{Tr}'\hat{\rho}_W(X,t), \quad \hat{\rho}_s(t) = \int dX\ \hat{\rho}_W(X,t), \tag{34}$$

which are normalized so that $\int dX\ \rho_e(X,t) = 1$ and $\mathrm{Tr}'\hat{\rho}_s(t) = 1$. We also define the correlation density operator $\hat{\rho}_{cor}(X,t)$ by $\hat{\rho}_W(X,t) \equiv \hat{\rho}_s(t)\rho_e(X,t) + \hat{\rho}_{cor}(X,t)$. Given that the density operator satisfies the normalization $\mathrm{Tr}' \int dX\ \rho_W(X,t) = 1$, we have $\mathrm{Tr}' \int dX\ \rho_{cor}(X,t) = 0$.

If we substitute the above expression for $\hat{\rho}_W(X,t)$ into the quantum-classical Liouville equation we find

$$\hat{\rho}_s(t)\frac{\partial \rho_e(X,t)}{\partial t} + \rho_e(X,t)\frac{\partial \hat{\rho}_s(t)}{\partial t} + \frac{\partial \hat{\rho}_{cor}(X,t)}{\partial t} = -i\hat{\mathcal{L}}\hat{\rho}_s(t)\rho_e(X,t) - i\hat{\mathcal{L}}\hat{\rho}_{cor}(X,t). \tag{35}$$

To obtain the mean field equations, we make the assumption that all terms in this equation containing $\hat{\rho}_{cor}(X,t)$ can be neglected. Then, integration over X and use of the normalization conditions yields

$$\frac{\partial \hat{\rho}_s(t)}{\partial t} = -\frac{i}{\hbar}\Big[\hat{H}_s + \int dX\ \hat{V}_c\rho_e(X,t), \hat{\rho}_s(t)\Big], \tag{36}$$

while the trace over the quantum degrees of freedom gives

$$\frac{\partial \rho_e(X,t)}{\partial t} = \Big\{H_e + \mathrm{Tr}'\hat{V}_c\hat{\rho}_s(t), \rho_e(X,t)\Big\} = \Big\{H_{\mathrm{eff}}, \rho_e(X,t)\Big\}, \tag{37}$$

where $H_{\mathrm{eff}} = P^2/2M + V_{\mathrm{eff}}(R)$ and the effective potential is defined as $V_{\mathrm{eff}}(R) = V_e(R) + \mathrm{Tr}'\hat{V}_c\hat{\rho}_s(t)$. This equation can be solved in terms of characteristics. The density function takes the form $\rho_e(X,t) = \delta(X - X(t))$, where $X(t) = (R(t), P(t))$ satisfy Newtonian equations of motion,

$$\dot{R}(t) = \frac{P(t)}{M}, \quad \dot{P}(t) = -\frac{\partial V_{\mathrm{eff}}(R(t))}{\partial R(t)}. \tag{38}$$

Using $\rho_e(X,t) = \delta(X - X(t))$, we may write

$$\int dX\ \hat{V}_c(R)\rho_e(X,t) = \hat{V}_c(R(t)). \tag{39}$$

As a result, Eq. (36) is equivalent to the pair of Schrödinger equations,

$$i\hbar\frac{\partial|\psi(R(t),t)\rangle}{\partial t} = \Big(\hat{H}_s + \hat{V}_c(R(t))\Big)|\psi(R(t),t)\rangle, \tag{40}$$

and its adjoint. Equations (38) and (40) are the standard mean field equations of motion for a mixed quantum-classical system.

Thus, we see that in order to obtain the mean field equations of motion, the density matrix of the entire system is assumed to factor into a product of subsystem and environmental contributions with neglect of correlations. The quantum dynamics then evolves as a pure state wave function depending on the coordinates evolving in the mean field generated by the quantum density. As we have seen in the previous sections, these approximations are not valid and no simple representation of the quantum-classical dynamics is possible in terms of single effective trajectories. Consequently, in contrast to claims made in the literature [54], quantum-classical Liouville dynamics is not equivalent to mean field dynamics.

4.2 Surface-hopping dynamics

Surface-hopping methods provide a more accurate description of nonadiabatic dynamics since they do not force the system to evolve on the mean field determined by a superposition of quantum states. Instead, using a representation in adiabatic eigenstates, in surface-hopping dynamics the classical degrees of freedom evolve on single adiabatic surfaces with hops between these surfaces determined by probabilistic rules [55]. Consequently, the dynamics of the system is correctly described when the evolution takes the system in regions where coupling between quantum states is small or zero. The precise form of the surface-hopping method depends on the nature of the rule used to specify quantum transitions. The fewest switches algorithm of Tully [2, 56] is one of the most popular such schemes.

A connection between surface-hopping schemes and the dynamics prescribed by the QCLE may be established by considering the conditions under which it is reasonable to express the dynamics given by the QCLE in terms of evolution along single adiabatic surfaces or, equivalently, the evolution of diagonal matrix elements in the adiabatic representation. As we have seen, since coherence is described by the off-diagonal elements of the density matrix, the problem reduces to the examination of the conditions under which decoherence leads to rapid decay of the off-diagonal elements. Here we describe the quantum-classical master equation which results in surface-hopping-like trajectories. The full details are given in Ref. [57].

Starting from the QCLE expressed in the adiabatic basis, it is not difficult to derive a generalized master equation for the diagonal elements of the density matrix by formally solving the QCLE (15) in the adiabatic basis for the off-diagonal elements and substituting the resulting solution into the equation for the diagonal elements. The result is the non-Markovian equation,

$$\frac{\partial}{\partial t}\rho_d^\alpha(X,t) = -iL_\alpha\rho_d^\alpha(X,t) + \int_0^t dt' \sum_\beta \mathcal{M}_{\alpha\beta}(t')\rho_d^\beta(X,t-t'), \tag{41}$$

where the memory kernel operator $\mathcal{M}_{\alpha\beta}(t)$ is given by,

$$\mathcal{M}_{\alpha\beta}(t) = \sum_{\nu\nu',\mu\mu'} \mathcal{J}^{d,o}_{\alpha,\mu\mu'} \left(e^{-i\mathcal{L}^o(X)(t)}\right)_{\mu\mu',\nu\nu'} \mathcal{J}^{o,d}_{\nu\nu',\beta}\ , \tag{42}$$

and acts on all of the classical degrees of freedom that appear in functions to its right.

By considering the action of the operators given in Eq. (42) on functions to its right, the memory kernel operator may be reduced to a memory function.

$$M^{\alpha\beta}_{\alpha\beta}(X,t) = 2\mathrm{Re}\left[\mathcal{W}_{\alpha\beta}(t,0)\right] D_{\alpha\beta}(X) D_{\alpha\beta}(\bar{X}_{\alpha\beta,t}), \tag{43}$$

where $\mathcal{W}_{\alpha\beta}(t,0) = e^{-i\int_0^t d\tau \omega_{\alpha\beta}[R(\tau)]}$ is a phase factor, $D_{\alpha\beta} = (P/M)\cdot d_{\alpha\beta}(R)$, and the subscripts and superscripts on the memory function label the indices on the first and second D function respectively. The bar on the phase space variable X indicates the action of a momentum shift by the $\mathcal{J}$ operator, and the subscript notation indicates that X has been evolved along the surface $(\alpha\beta)$ for a time t. In this form, the memory function accounts for all coherent evolution segments in the dynamics.

Decoherence arising from interaction of the subsystem with an environment is incorporated into the evolution expression by averaging over an initial distribution of the environmental phase space coordinates. The resulting expression prescribes the evolution of the diagonal elements of the subsystem density matrix and contains the environmental average of the time dependent memory kernel. The environmental average provides a mechanism for decoherence and leads to decay of the memory kernel. In the absence of an environmental average, the memory kernel is a purely oscillatory function and does not decay. However, the environmentally averaged memory kernel does decay and, depending on the system under investigation, if there is a sufficient separation of time scales between the decay of the memory function and other relevant system relaxation times, a Markovian approximation on the memory term may be used. The resulting equation,

$$\begin{aligned}\frac{\partial}{\partial t}\rho_s^\alpha(X_0,t) = &-\int dX_e iL_\alpha e^{-i\hat{\mathcal{Q}}_e L_\alpha t}\hat{\mathcal{Q}}_e\rho_d^\alpha(X,0) - \langle iL_\alpha\rangle_e\rho_s^\alpha(X_0,t) \\ &-\int_0^t dt' \langle iL_\alpha e^{-i\hat{\mathcal{Q}}_e L_\alpha t'} i\hat{\mathcal{Q}}_e L_\alpha\rangle_e \rho_s^\alpha(X_0,t-t') \\ &+\sum_\beta m_{\alpha\beta}(X_0)\hat{j}_{\alpha\to\beta}\rho_s^\beta(X_0,t) - m_{\alpha\alpha}(X_0)\rho_s^\alpha(X_0,t)\ ,\end{aligned} \tag{44}$$

gives the evolution of the subsystem density matrix $\rho_s^\alpha(X_0,t) \equiv \int dX_e \rho^\alpha(X,t)$, where X_0 is the set of phase space variables of the subsystem. This expression

is still non-Markovian in character as a result of the projection of the evolution equation onto the subsystem. The final master equation is obtained by lifting the equation back into the full phase space to recover a fully Markovian master equation description:

$$\frac{d}{dt}\rho_d^\alpha(X,t) = -iL_\alpha\rho_d^\alpha(X,t) + \sum_\beta m_{\alpha\beta}(X_0)j_{\alpha\to\beta}\rho_d^\beta(X,t) - m_{\alpha\alpha}(X_0)\rho_d^\alpha(X,t). \tag{45}$$

where

$$m_{\alpha\beta}(X_0) = \int_0^\infty dt' \langle M_{\alpha\beta}^{\alpha\beta}(X,t')\rangle_e \ , \tag{46}$$

and $j_{\alpha\to\beta}$ is a momentum shift operator [57]. Note that the subscripts on the second memory term in Eq. (45) are the same. This term arises from the memory function corresponding to $\langle M_{\alpha\nu}^{\nu\alpha}(X,t)\rangle_e$, where the angle brackets indicate that the average over the environment has been performed. Trajectories accounted for by this term jump to the mean surface and then return to their original surface. Thus, the net effect is no jump, but a phase factor is introduced.

The master equation evolves the classical degrees of freedom on single adiabatic surfaces with instantaneous hops between them. Each single (fictitious) trajectory represents an ensemble of trajectories corresponding to different environment initial conditions. This choice of different environment coordinates for a given initial subsystem coordinate will result in different trajectories on the mean surface; the average over this collection of classical evolution segments results in decoherence. Consequently, this master equation in full phase space provides a description in terms of fictitious trajectories, each of which accounts for decoherence. When the approximations that lead to the master equation are valid, this provides a useful simulation tool since no oscillatory phase factors appear in the trajectory evolution.

The surface-hopping trajectories obtained in the adiabatic representation of the QCLE contain nonadiabatic transitions between potential surfaces including both single adiabatic potential surfaces and the mean of two adiabatic surfaces. This picture is qualitatively different from surface-hopping schemes [2, 56] which make the ansatz that classical coordinates follow some trajectory, $R(t)$, while the quantum subsystem wavefunction, expanded in the adiabatic basis, is evolved according to the time dependent Schrödinger equation. The potential surfaces that the classical trajectories evolve along correspond to one of the adiabatic surfaces used in the expansion of the subsystem wavefunction, while the subsystem evolution is carried out coherently and may develop into linear combinations of these states. In such schemes, the environment does not experience the force associated with the true quantum state of the subsystem and decoherence by the environment is not automatically taken into account. Nonetheless, these methods have provided com-

putationally tractable and, under the conditions outlined above, reasonable descriptions of nonadiabatic dynamics.

Coherence is created and destroyed in the QCLE through the action of the momentum-jump operator, $\hat{\mathcal{J}}$, and phase information is obtained for off-diagonal evolution segments through the phase term in the propagator (17). The master equation discussed above incorporates this decoherence mechanism in the environmental average of the memory kernel. Decoherence in the quantum subsystem of condensed phase systems is a well established phenomenon [58, 59] and should be accounted for in surface-hopping schemes. We note that various phenomenologically motivated prescriptions have been proposed to incorporate decoherence into the dynamics of the subsystem [56, 60–63].

5 Observables and correlation functions

Thus far we have focussed on the dynamics of quantum-classical systems. In practice, we are primarily interested instead in computing observables that can be compared eventually to experimentally obtainable quantities. To this end, consider the general quantum mechanical expression for the expectation value of an observable,

$$\begin{aligned}\overline{A(t)} &= \mathrm{Tr}(\hat{\rho}(t)\hat{A}) = \mathrm{Tr}(\hat{\rho}\hat{A}(t)) \qquad (47)\\ &= \mathrm{Tr}' \int dQ_1 dQ_2 \langle Q_1|\hat{A}(t)|Q_2\rangle\langle Q_2|\hat{\rho}(0)|Q_1\rangle \\ &= \mathrm{Tr}' \int dR dP\ \hat{A}_W(R,P,t)\hat{\rho}_W(R,P) = \mathrm{Tr}' \int dX \hat{A}_W(X,t)\hat{\rho}_W(X) \qquad (48)\end{aligned}$$

In the above expressions we have introduced the (primed) partial trace over the Hilbert space of the susbsystem, $\mathrm{Tr}'\hat{\rho}_W(R,P) = \rho_e(R,P)$, and the symbols Tr' and Tr_e refer to taking the partial trace over the subsystem and environment, respectively.

If we expand Eq. (47) in the coordinate $\{Q\}$-representation for the environmental degrees of freedom only we obtain the second line. Taking the Wigner representation for these degrees of freedom and finally, defining the general coordinate $X = (R, P)$ gives Eq. (48).

For a quantum mechanical system in thermal equilibrium a transport coefficient λ_{AB} may be determined from the time integral of a flux-flux correlation function [64].

$$\lambda_{AB} = \frac{1}{\beta}\int_0^\infty dt \langle \frac{i}{\hbar}[\dot{\hat{B}}(t), \hat{A}]\rangle \ , \qquad (49)$$

where $\dot{\hat{B}} = (i/\hbar)[\hat{H}, \hat{B}]$ is the flux of $\hat{B}$, and $\beta = (k_B T)^{-1}$. The equilibrium quantum canonical average is $\langle \cdots \rangle = Z_Q^{-1}\mathrm{Tr}\cdots e^{-\beta\hat{H}}$ where Z_Q is the partition function. The transport coefficient may then be obtained from the plateau value of $\lambda_{AB}(t)$ [65].

The quantum mechanical forms of the correlation function expressions for transport coefficients are well known and may be derived by invoking linear response theory [64] or the Mori-Zwanzig projection operator formalism [66,67]. However, we would like to evaluate transport properties for quantum-classical systems. We thus take the quantum mechanical expression for a transport coefficient as a starting point and then consider a limit where the dynamics is approximated by quantum-classical dynamics [68–70]. The advantage of this approach is that the full quantum equilibrium structure can be retained.

In simulations it is convenient to obtain the transport coefficient from the plateau value of $\lambda_{AB}(t)$. Writing Eq. (49) in detail, we can express the time-dependent transport coefficient $\lambda_{AB}(t)$ as,

$$\begin{aligned}\lambda_{AB}(t) &= \frac{1}{\beta}\int_0^t dt' \langle \dot{\hat{B}}(t); \dot{\hat{A}} \rangle \\ &= \frac{1}{\beta Z_Q}\int_0^\beta d\lambda \mathrm{Tr}\left(\dot{\hat{A}} e^{\frac{i}{\hbar}\hat{H}(i\hbar\lambda)} \hat{B}(t) e^{-\frac{i}{\hbar}\hat{H}(i\hbar\lambda)-\beta\hat{H}} \right). \end{aligned} \tag{50}$$

Here we have introduced the notation, $\langle \cdot;\cdot \rangle$, to indicate the Kubo transformed-correlation function. Rewriting the expression in the coordinate representation for the full system, $\{\mathcal{Q}\} = \{q\}\{Q\}$ (calligraphic symbols are used to denote variables for the entire system, subsystem plus bath),

$$\begin{aligned}\lambda_{AB}(t) = \frac{1}{\beta Z_Q}\int_0^\beta d\lambda \int d\mathcal{Q}_1 d\mathcal{Q}_1' d\mathcal{Q}_2 d\mathcal{Q}_2' \langle \mathcal{Q}_1|\dot{\hat{A}}|\mathcal{Q}_1'\rangle\langle \mathcal{Q}_1'|e^{\frac{i}{\hbar}\hat{H}(t+i\hbar\lambda)}|\mathcal{Q}_2\rangle \\ \times \langle \mathcal{Q}_2|\hat{B}|\mathcal{Q}_2'\rangle\langle \mathcal{Q}_2'|e^{-\beta\hat{H}-\frac{i}{\hbar}\hat{H}(t+i\hbar\lambda)}|\mathcal{Q}_1\rangle. \end{aligned} \tag{51}$$

Making a change of variables, $\mathcal{Q}_1 = \mathcal{R}_1 - \mathcal{Z}_1/2$, $\mathcal{Q}_1' = \mathcal{R}_1 + \mathcal{Z}_1/2$, etc., and then expressing the matrix elements in terms of the Wigner transforms of the operators, we have [69]

$$\begin{aligned}\lambda_{AB}(t) = \frac{1}{\beta}\int_0^\beta d\lambda \int d\mathcal{X}_1 d\mathcal{X}_2 (\dot{A})_W(\mathcal{X}_1) B_W(\mathcal{X}_2) \frac{1}{(2\pi\hbar)^{2\nu} Z_Q} \\ \times \int d\mathcal{Z}_1 d\mathcal{Z}_2 e^{-\frac{i}{\hbar}(\mathcal{P}_1\cdot\mathcal{Z}_1+\mathcal{P}_2\cdot\mathcal{Z}_2)} \left\langle \mathcal{R}_1 + \frac{\mathcal{Z}_1}{2}\left| e^{\frac{i}{\hbar}\hat{H}(t+i\hbar\lambda)} \right| \mathcal{R}_2 - \frac{\mathcal{Z}_2}{2} \right\rangle \\ \times \left\langle \mathcal{R}_2 + \frac{\mathcal{Z}_2}{2}\left| e^{-\beta\hat{H}-\frac{i}{\hbar}\hat{H}(t+i\hbar\lambda)} \right| \mathcal{R}_1 - \frac{\mathcal{Z}_1}{2} \right\rangle. \end{aligned} \tag{52}$$

Here we used the fact that the matrix element of an operator $\hat{A}$ can be expressed in terms of its Wigner transform $A_W(\mathcal{X})$ as

$$\left\langle \mathcal{R} - \frac{\mathcal{Z}}{2}\left|\hat{A}\right|\mathcal{R} + \frac{\mathcal{Z}}{2}\right\rangle = \frac{1}{(2\pi\hbar)^\nu}\int d\mathcal{P} e^{-\frac{i}{\hbar}\mathcal{P}\cdot\mathcal{Z}} A_W(\mathcal{X}), \tag{53}$$

where ν is the coordinate space dimension.

If we define the spectral density by,

$$W(\mathcal{X}_1,\mathcal{X}_2,t)=\frac{1}{(2\pi\hbar)^{2\nu}\,Z_Q}\int d\mathcal{Z}_1 d\mathcal{Z}_2 e^{-\frac{i}{\hbar}(\mathcal{P}_1\cdot\mathcal{Z}_1+\mathcal{P}_2\cdot\mathcal{Z}_2)}$$
$$\times\left\langle\mathcal{R}_1+\frac{\mathcal{Z}_1}{2}\left|e^{\frac{i}{\hbar}\hat{H}t}\right|\mathcal{R}_2-\frac{\mathcal{Z}_2}{2}\right\rangle\left\langle\mathcal{R}_2+\frac{\mathcal{Z}_2}{2}\left|e^{-\beta\hat{H}-\frac{i}{\hbar}\hat{H}t}\right|\mathcal{R}_1-\frac{\mathcal{Z}_1}{2}\right\rangle, \quad (54)$$

we can write the transport coefficient as

$$\lambda_{AB}(t)=\int d\mathcal{X}_1 d\mathcal{X}_2(\dot{A})_W(\mathcal{X}_1)B_W(\mathcal{X}_2)\overline{W}(\mathcal{X}_1,\mathcal{X}_2,t), \quad (55)$$

where

$$\overline{W}(\mathcal{X}_1,\mathcal{X}_2,t)=\frac{1}{\beta}\int_0^\beta d\lambda W(\mathcal{X}_1,\mathcal{X}_2,t+i\hbar\lambda)\,. \quad (56)$$

To take the quantum-classical limit of this general expression for the transport coefficient we partition the system into a subsystem and bath and use the notation $\mathcal{R}=(r,R)$, $\mathcal{P}=(p,P)$ and $\mathcal{X}=(r,R,p,P)$ where the lower case symbols refer to the subsystem and the upper case symbols refer to the bath. To make connection with surface-hopping representations of the quantum-classical Liouville equation [4], we first observe that $A_W(\mathcal{X}_1)$ can be written as

$$A_W(\mathcal{X}_1)=\int dz_1\; e^{\frac{i}{\hbar}p_1\cdot z_1}\langle r_1-\frac{z_1}{2}|\hat{A}_W(X_1)|r_1+\frac{z_1}{2}\rangle, \quad (57)$$

where $\hat{A}_W(X_1)$ is the *partial* Wigner transform of $\hat{A}$ over the bath degrees of freedom. We may now express the subsystem operators in the adiabatic basis to obtain,

$$A_W(\mathcal{X}_1)=\sum_{\alpha_1\alpha_1'}\int dz_1\; e^{\frac{i}{\hbar}p_1\cdot z_1}\langle r_1-\frac{z_1}{2}|\alpha_1;R_1\rangle A_W^{\alpha_1\alpha_1'}(X_1)\langle\alpha_1';R_1|r_1+\frac{z_1}{2}\rangle, \quad (58)$$

where $A_W^{\alpha_1\alpha_1'}(X_1)=\langle\alpha_1;R_1|\hat{A}_W(X_1)|\alpha_1';R_1\rangle$. Inserting this expression, and its analog for $B_W(\mathcal{X}_2)$, into Eq. (52) we have

$$\lambda_{AB}(t)=-\sum_{\alpha_1,\alpha_1',\alpha_2,\alpha_2'}\int\prod_{i=1}^{2}dX_i\; A_W^{\alpha_1\alpha_1'}(X_1)B_W^{\alpha_2\alpha_2'}(X_2)$$
$$\times\frac{\partial}{\partial t}\overline{W}^{\alpha_1'\alpha_1\alpha_2'\alpha_2}(X_1,X_2,t), \quad (59)$$

where the matrix elements of W are given by

$$W^{\alpha_1'\alpha_1\alpha_2'\alpha_2}(X_1,X_2,t)=\int\prod_{i=1}^{2}dZ_i e^{-\frac{i}{\hbar}(P_1\cdot Z_1+P_2\cdot Z_2)}\frac{1}{Z_Q}\frac{1}{(2\pi\hbar)^{2\nu_h}}$$
$$\times\langle\alpha_1';R_1|\langle R_1+\frac{Z_1}{2}|e^{\frac{i}{\hbar}\hat{H}t}|R_2-\frac{Z_2}{2}\rangle|\alpha_2;R_2\rangle$$
$$\times\langle\alpha_2';R_2|\langle R_2+\frac{Z_2}{2}|e^{-\frac{i}{\hbar}\hat{H}t''}|R_1-\frac{Z_1}{2}\rangle|\alpha_1;R_1\rangle\,, \quad (60)$$

with $t'' = t - i\beta\hbar$.

The quantum-classical limit of the transport coefficient is obtained by evaluating the evolution equation for the matrix elements of $\overline{W}$ in the quantum-classical limit. This limit was taken in Ref. [68] and the result is

$$\frac{\partial}{\partial t}\overline{W}^{\alpha_1'\alpha_1\alpha_2'\alpha_2}(X_1, X_2, t) = \frac{1}{2}\sum_{\beta_1'\beta_1\beta_2'\beta_2}\left(i\mathcal{L}_{\alpha_1'\alpha_1,\beta_1'\beta_1}(X_1)\delta_{\alpha_2'\beta_2'}\delta_{\alpha_2\beta_2} - i\mathcal{L}_{\alpha_2'\alpha_2,\beta_2'\beta_2}(X_2)\delta_{\alpha_1'\beta_1'}\delta_{\alpha_1\beta_1}\right) \times\overline{W}^{\beta_1'\beta_1\beta_2'\beta_2}(X_1, X_2, t)\ . \tag{61}$$

We use the first equality in Eq. (61), insert this into Eq. (59), and move the evolution operator $i\mathcal{L}(X_1)$ onto the $A_W(X_1)$ dynamical variable. Next, we use the second equality in Eq. (61) and formally solve the equation to obtain $\overline{W}(X_1, X_2, t) = e^{-i\mathcal{L}(X_2)t}\overline{W}(X_1, X_2, 0)$. Finally we substitute this form for $\overline{W}(X_1, X_2, t)$ into Eq. (59) and move the evolution operator to the dynamical variable $B_W(X_2)$. In the adiabatic basis, the action of the propagator $e^{-i\mathcal{L}(X_2)t}$ on $\hat{B}_W(X_2)$ is

$$B_W^{\alpha_2\alpha_2'}(X_2, t) = \sum_{\beta_2\beta_2'}\left(e^{-i\mathcal{L}(X_2)t}\right)_{\alpha_2\alpha_2',\beta_2\beta_2'} B_W^{\beta_2\beta_2'}(X_2)\ . \tag{62}$$

The result of these operations is

$$\lambda_{AB}(t) = \sum_{\alpha_1,\alpha_1',\alpha_2,\alpha_2'}\int\prod_{i=1}^{2} dX_i\ (i\mathcal{L}(X_1)A_W(X_1))^{\alpha_1\alpha_1'} \times B_W^{\alpha_2\alpha_2'}(X_2, t)\overline{W}^{\alpha_1'\alpha_1\alpha_2'\alpha_2}(X_1, X_2, 0). \tag{63}$$

This equation can serve as the basis for the computation of transport properties for quantum-classical systems. Note that full quantum effects are described by the initial value of $\overline{W}$.

6 Example reaction rate calculation

The rate coefficient of a reactive process is a transport coefficient of interest in chemical physics. It has been shown from linear response theory that this coefficient can be obtained from the reactive flux correlation function of the system of interest. This quantity has been computed extensively in the literature for systems such as proton and electron transfer in solvents as well as clusters [29, 32, 33, 56, 71–76], where the use of the QCL formalism has allowed one to consider quantum phenomena such as the kinetic isotope effect in proton transfer [31]. Here, we will consider the problem of formulating an expression for a reactive rate coefficient in the framework of the QCL theory. Results from a model calculation will be presented including a comparison to the approximate methods described in Sec. 4.

6.1 Simulation results

Consider a simple reactive process $A \rightleftharpoons B$. The quantum mechanical expression for the time dependent forward rate coefficient for such a process is given by,

$$k_{AB}(t) = -\frac{1}{n_A^{eq}} \int_0^t dt' \langle \delta\dot{\hat{N}}_B(t'); \delta\dot{\hat{N}}_A \rangle, \tag{64}$$

where the $\delta\hat{N}_i$ are the species operators representing the deviations of each species from their equilibrium number densities, and the angled brackets denote the Kubo transformed correlation function as defined in Eq. (50). This expression was derived previously by following the projection operator methods of Mori and Zwanzig in the linear response regime [77]. Following the discussion of the previous section, the quantum classical limit of this expression, (63) can be obtained and is given by [70]

$$k_{AB}(t) = \frac{1}{n_A^{eq}} \sum_{\alpha} \sum_{\alpha' \geq \alpha} (2 - \delta_{\alpha'\alpha}) \times \int dX \mathrm{Re} \left[N_B^{\alpha\alpha'}(X,t) W_A^{\alpha'\alpha}(X, \frac{i\hbar\beta}{2}) \right]. \tag{65}$$

Here, the integration over X_1 was performed in Eq. (63) to define $W_A^{\alpha\alpha'}(X, \frac{i\hbar\beta}{2})$ which is the integrated value of the combination of the spectral density function with the time independent operator. This spectral density function contains the quantum equilibrium structure of the system. $N_B^{\alpha\alpha'}(X,t)$ is the time evolved matrix element of the number operator for the product state B. Thus, to calculate the rate, one samples initial configurations from the quantum equilibrium distribution, and then computes the evolution of the number operator for product state B. The QCL evolution of the species operator is accomplished using one of the algorithms discussed in Sec. 3.2. Alternative approaches to the dynamics may also be used such as the further approximations to the QCLE discussed in Sec. 4.

The sampling of initial configurations from the spectral density function remains a challenging task as the structure of this function is complicated. By factoring this quantity into a subsystem and conditional environment distribution, $W_A^{\alpha'\alpha}(X, \frac{i\hbar\beta}{2}) = \rho_A^{\alpha'\alpha}(X_0)\rho_e^c(X_e; R_0)$, the problem simplifies. In particular, if the environment consists of harmonic oscillators, as is the case here, the exact form of the spectral density is known for the environment. For the subsystem, one can appeal to the fact that typically the barrier region, where the largest contribution to the dynamics in this problem take place, is approximately harmonic. Doing so, one is able to obtain an approximate analytic form of this function given by [78],

$$\rho_A^{\alpha'\alpha}(X_0) = \frac{ia}{Z_Q\pi^2}\int dZ_0 e^{-\frac{i}{\hbar}(P_0\cdot Z_0)}\sum_{\alpha_1\alpha_2} A^{\alpha'\alpha}_{\alpha_1\alpha_2}B_{\alpha_1\alpha_2}(0) \tag{66}$$
$$\times\Big[\delta_{\alpha_1\alpha_2}e^{-a(4R_0^2+Z_0^2)u_1'}2aM_0Z_0\tilde{u}_1^2$$
$$-d_{\alpha_1\alpha_2}(0)e^{-2a\left[\left(R_0+\frac{Z_0}{2}\right)^2u_1'+\left(R_0-\frac{Z_0}{2}\right)^2u_2'\right]}\sqrt{\tilde{u}_1\tilde{u}_2}\Big],$$

where $u_i' = u_i\mathrm{coth}u_i$, $\tilde{u}_i = u_i\mathrm{csch}u_i$, $u_i = \beta\hbar\omega_i/2$, ω_i is the barrier region frequency for the state α_i which may be real or imaginary, and $a = M_0/(2\beta\hbar^2)$. By numerically integrating over Z_0 we obtain the quantum mechanical equilibrium structure for the subsystem, $\hat{\rho}_0(X_0)$. Sampling from this distribution is performed from the harmonic part and subsequently reweighted by the remaining term. With this quantity, in conjunction with that for the environment and Eq. (65), the quantum mechanical rate-coefficient can be computed via computer simulation.

We consider the same reaction model used in previous studies as a simple model for a proton transfer reaction. [31, 57, 79] The subsystem consists of a two-level quantum system bilinearly coupled to a quartic oscillator and the bath consists of $\nu - 1 = 300$ harmonic oscillators bilinearly coupled to the non-linear oscillator but not directly to the two-level quantum system. In the subsystem representation, the partially Wigner transformed Hamiltonian for this system is,

$$\mathbf{H}_W = \begin{pmatrix} V_q(R_0)+\hbar\Omega & \hbar\gamma_0R_0 \\ \hbar\gamma_0R_0 & V_q(R_0)-\hbar\Omega \end{pmatrix} \tag{67}$$
$$+\left(\frac{P_0^2}{2M_0}+\sum_{j=1}^{\nu-1}\frac{P_j^2}{2M_j}+\frac{M_j\omega_j^2}{2}\left(R_j-\frac{c_j}{M_j\omega_j^2}R_0\right)^2\right)\mathbf{I}.$$

The solution of the eigenvalue problem, $\hat{h}_W(R)|\alpha;R_0\rangle = E_\alpha(R)|\alpha;R_0\rangle$, yields the adiabatic eigenstates, $|\alpha;R_0\rangle$, and eigenvalues

$$E_\alpha(R) = V_q(R_0) + V_e(R_e;R_0) \mp \hbar\sqrt{\Omega^2+(\gamma_0R_0)^2},$$

where 2Ω is the adiabatic energy gap. The parameters of this model characterize a harmonic environment with ohmic spectral density, [80] the details of which can be found elsewhere. [31, 68, 79] The reaction coordinate R_0 undergoes dynamics characteristic of a well defined barrier crossing process and product species operator $N_B^{\alpha\alpha'}(R_0) = \theta(R_0)\delta_{\alpha\alpha'}$ is initially diagonal in the adiabatic basis. Here $\theta(R_0)$ is the Heaviside function.

The plot in Fig. 1 shows the reaction rate computed via adiabatic versus nonadiabatic dynamics. The rate constant, given by the plateau value of the correlation function, is lower when nonadiabatic dynamics is considered. This reduction is due to enhanced barrier crossing as a result of motion on either the excited state or mean surfaces. This is seen more clearly in Fig. 2. When the

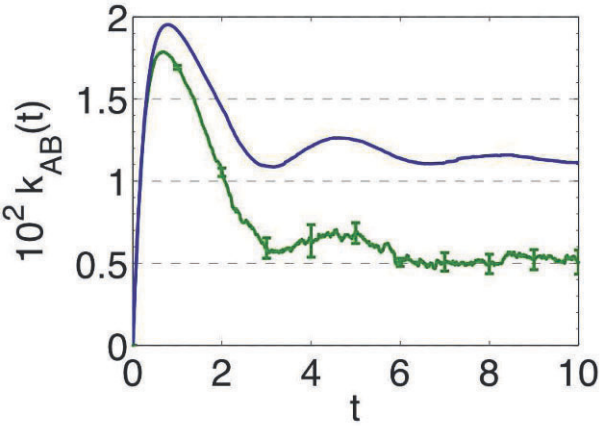

Fig. 1: Nonadiabatic vs adiabatic reaction rate for $\beta = 1.0$. The blue (upper) curve is the adiabatic result while the green (lower) curve is the nonadiabatic rate.

system is propagating on either the mean or excited state surface it is confined close to the barrier region such that it crosses the barrier more frequently. On the other hand, once the system jumps down to the ground state, it stabilizes in one of the wells such that recrossings are less frequent. The increase of recrossings due to dynamics on these surfaces leads to decay of the correlation function.

In Fig. 2 one can see the qualitative differences between the dynamics on the various surfaces. Although both excited state and mean surface evolution segments oscillate around the barrier, the mean surface segments are able to explore a wider region due to the broader structure of the mean free energy surface for this model. In contrast, the excited surface trajectories are narrowly confined to the barrier region where the probability of a transition is high. Thus, excited state trajectory segments are short lived. The evolution of trajectories along the mean surface is an important result in QCL dynamics as it entails the proper treatment of coherence that is lacking in surface-hopping approaches.

By inserting the form of the spectral density function discussed above into the rate coefficient expression, the second line of Eq. (65) may be replaced by

$$\int dX \mathrm{Re}\left[N_B^{\alpha\alpha'}(X,t) W_A^{\alpha'\alpha}(X, \frac{i\hbar\beta}{2})\right] = \int dX_0 \mathrm{Re}\left[\langle N_B^{\alpha\alpha'}\rangle_e(X_0,t)\rho_A^{\alpha'\alpha}(X_0, \frac{i\hbar\beta}{2})\right], \tag{68}$$

where the angle brackets indicate an average over the conditional equilibrium distribution, $\rho_e^c(X_e; R_0)$. In this form, the computation of the rate constant

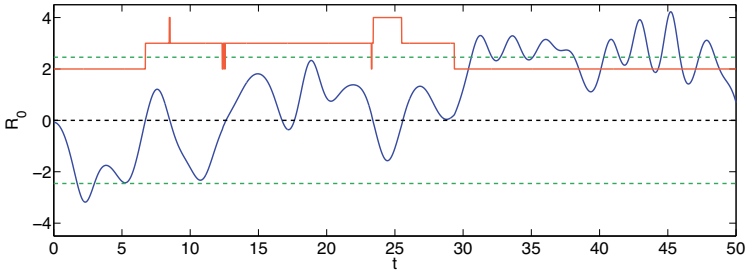

Fig. 2: A segment taken from the time series of a nonadiabatic trajectory. The blue curve is the times series for R_0, the red curve indicates the surface on which the trajectory is evolving, where a value of 2 on the R_0 axis corresponds to the ground state (1,1), 3 corresponds to the mean surface (1,2) or (2,1), and 4 corresponds to the excited state (2,2). During the evolution on the mean surface and excited state surface the trajectory is confined to the barrier region where it may cross the barrier. In contrast, when the trajectory is on the ground state surface the system stabilizes in one well or the other.

involves the bath averaged observable discussed in Sec. 4.2, allowing us to apply the master equation formalism discussed above.

In Fig. 3, the simulation results for the same model problem are presented using the QCLE, the master equation, Tully's surface-hopping approach, the mean field approach, and adiabatic dynamics. The algorithmic details of each approach can be found elsewhere [2, 40, 79].

From the figure we see that the surface-hopping result using Tully's algorithm is almost identical to the adiabatic rate for the parameters given here. By comparison to both the QCLE simulation and the master equation simulation, one can conclude that for this set of parameters this overestimates the reaction rate. The primary reason for the discrepancy is the manner in which coherence and decoherence is treated in the theory. Although the master equation also restricts motion to single adiabatic surfaces, the probability of hopping is obtained from a calculation that accounts for decoherence in a different manner. The prediction of the rate obtained by the mean-field approach, shown in the figure, underestimates the rate. This can be attributed to the neglect of correlations in the equations of motion as discussed in Sec. 4.1.

We remark that the simulation scheme for master equation dynamics has a number of attractive features when compared to quantum-classical Liouville dynamics. The solution of the master equation consists of two numerically simple parts. The first is the computation of the memory function which involves adiabatic evolution along mean surfaces. Once the transition rates are known as a function of the subsystem coordinates, the sequential short-time propagation algorithm may be used to evolve the observable or density. Since the dynamics is restricted to single adiabatic surfaces, no phase factors

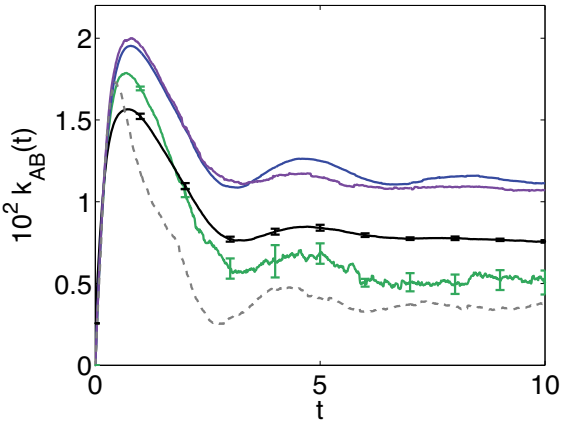

Fig. 3: Forward rate coefficient $k_{AB}(t)$ as a function of time for $\beta = 1.0$. The upper (blue) curve is the adiabatic rate, the purple curve is the result obtained by Tully's surface-hopping algorithm, the middle (black) curve is the quantum master equation result, the green curve is the QCL result, and the lowest dashed line (grey) is the result using mean-field dynamics.

enter this part of the calculation increasing the stability of the algorithm. For complicated reaction coordinates which are arbitrary functions of the environmental coordinates the calculation of the transition rates will be more difficult and time consuming. Of course, the validity of this scheme rests on the accuracy of the Markovian approximation to the memory kernel, which must be determined for the system under consideration.

7 Conclusions

We have presented some of the most recent developments in the computation and modeling of quantum phenomena in condensed phased systems in terms of the quantum-classical Liouville equation. In this approach we consider situations where the dynamics of the environment can be treated as if it were almost classical. This description introduces certain non-classical features into the dynamics, such as classical evolution on the mean of two adiabatic surfaces. Decoherence is naturally incorporated into the description of the dynamics. Although the theory involves several levels of approximation, QCL dynamics performs extremely well when compared to exact quantum calculations for some important benchmark tests such as the spin-boson system. Consequently, QCL dynamics is an accurate theory to explore the dynamics of many quantum condensed phase systems.

In practice, one's ability to model any realistic system via the QCLE depends on the appropriate choice of representation of the quantum system.

Each representation brings with it a unique set of challenges and limitations in the development of efficient algorithms for computing the dynamics as well as sampling initial configurations. For these reasons it is interesting to consider some of the earlier more approximate schemes such as the mean field and surface-hopping approaches. We have shown here that there are conditions under which the approximations underlying these methods are reasonable and thus one can take advantage of the computational simplicity involved in these schemes to obtain a computationally cheap solution to the problem. One, however, must keep in mind that the QCLE is already an approximate approach, and that these schemes involve further, often severe, approximations to the QCLE. An important outcome of this analysis is that the QCLE emerges as an analytic tool that one can use as a theoretical basis to evaluate alternative approaches to the problem of quantum dynamics in almost classical environments.

As quantum-classical dynamics is a rapidly emerging field of increasing importance, there are many areas in which further study is needed. For example, as was discussed in Sec. 4.2, the QCLE provides a useful framework to investigate the mechanism of decoherence in various scenarios. This fact allows one to assess the validity of a Markovian approximation to the generalized master equation. Another important area involves alternate representations of the QCLE. For example the mapping basis discussed in Sec. 3.4 is one such example where the use of harmonic oscillator states leads to dynamics in terms of classical trajectories involving new forces. The computational simplicity that this affords is obviously appealing. Although the structure of the higher order correlation terms in the equation of motion are not easily computed, in certain cases it has been shown to be negligible. Further research into this area will prove useful and may yield more stable algorithms allowing for the study of far more difficult systems. For example, an important problem of interest that still lacks a satisfactory solution is the simulation of quantum systems in the condensed phase interacting with a field. Through the use of appropriate choices of representations leading to improved algorithms, this type of problem may soon be solvable.

Acknowledgements

This work was supported in part by a grant from the Natural Sciences and Engineering Research Council of Canada. One of the authors (AK) acknowledges the support from the Walter C. Sumner foundation.

References

1. P. Pechukas. *Time-dependent semiclassical scattering theory .I. potential scattering. Phys. Rev.*, 181(1):166, 1969.

2. J. C. Tully. Molecular dynamics with electronic transitions. *J. Chem. Phys.*, 93(2):1061–1071, 1990.
3. R. Kapral. Progress in the theory of mixed quantum-classical dynamics. *Annu. Rev. Phys. Chem.*, 57:129–157, 2006.
4. R. Kapral and G. Ciccotti. Mixed quantum-classical dynamics. *J. Chem. Phys.*, 110:8919–8929, 1999.
5. E. Wigner. On the quantum correction for thermodynamic equilibrium. *Physical Review*, 40(5), 1932.
6. K. Imre, E. Özizmir, M. Rosenbaum, and P. F. Zweifel. Wigner method in quantum statistical mechanics. *Journal of Mathematical Physics*, 8(5):1097–1108, 1967.
7. I. V. Aleksandrov. The statistical dynamics of a system consisting of a classical and a quantum subsystem. *Z. Naturforsch.*, 36:902–850, 1981.
8. V. I. Gerasimenko. Correlation-less equations of motion of quantum-classical systems. *Repts. Acad. Sci. Ukr.SSR*, (10):64–67, 1981.
9. V. I. Gerasimenko. Dynamical equations of quantum-classical systems. *Theor. Math. Phys.*, 50:49–55, 1982.
10. W. Boucher and J. Traschen. Semiclassical physics and quantum fluctuations. *Phys. Rev. D*, 37(12):3522–3532, Jun 1988.
11. W.Y. Zhang and R. Balescu. Statistical mechanics of a spin polarized plasma. *J. Plasma Physics*, 40:199–213, 1988.
12. Y. Tanimura and S. Mukamel. Multistate quantum Fokker–Planck approach to nonadiabatic wave packet dynamics in pump–probe spectroscopy. *J. Chem. Phys.*, 101:3049, 1994.
13. C. C. Martens and J. Y. Fang. Semiclassical-limit molecular dynamics on multiple electronic surfaces. *J. Chem. Phys.*, 106(12):4918–4930, 1997.
14. I. Horenko, C. Salzmann, B. Schmidt, and C. Schutte. Quantum-classical liouville approach to molecular dynamics: Surface hopping gaussian phase-space packets. *J. Chem. Phys.*, 117(24):11075–11088, 2002.
15. Q. Shi and E. Geva. A derivation of the mixed quantum-classical Liouville equation from the influence functional formalism. *J. Chem. Phys.*, 121(8):3393–3404, 2004.
16. S. Nielsen, R. Kapral, and G. Ciccotti. Statistical mechanics of quantum-classical systems. *J. Chem. Phys.*, 115(13):5805–5815, 2001.
17. A. Sergi. Non-Hamiltonian commutators in quantum mechanics. *Phys. Rev. E*, 72(6):066125, Dec 2005.
18. L. L. Salcedo. Absence of classical and quantum mixing. *Phys. Rev. A*, 54(4):3657–3660, Oct 1996.
19. V. V. Kisil. A quantum-classical bracket from p-mechanics. *Europhys. Lett.*, 72(6):873–879, DEC 2005.
20. O. V. Prezhdo. A quantum-classical bracket that satisfies the Jacobi identity. *J. Chem. Phys.*, 124(20):201104, May 2006.
21. F. Agostini, S. Caprara, and G. Ciccotti. Do we have a consistent non-adiabatic quantum-classical mechanics? *EPL*, 78(3):30001, 2007.
22. L. L. Salcedo. Comment on "a quantum-classical bracket that satisfies the Jacobi identity". *J. Chem. Phys.*, 126(5), FEB 7 2007.
23. M.J.W. Hall and M. Reginatto. Interacting classical and quantum ensembles. *Phys. Rev. A*, 72(6), DEC 2005.
24. R. Kapral and A. Sergi. Quantum-classical Wigner-Liouville equation. *Ukr. Math. J.*, 57:749–756, 2005.

25. A. Sergi. Quantum-classical dynamics of wave fields. *J. Chem. Phys.*, 126:074109, 2007.
26. I. Burghardt, K. B. Moller, G. Parlant, L. S. Cederbaum and E. R. Bittner. Quantum hydrodynamics: Mixed states, dissipation and new hybrid quantum-classical approach. *Int. J. Quantum Chem.*, 100:1153–1162, 2004.
27. A. Donoso and C.C. Martens. Simulation of coherent nonadiabatic dynamics using classical trajectories. *J. Phys. Chem. A*, 102:4291–4300, 1998.
28. J. M. Riga, E. Fredj, and C. C. Martens. Simulation of vibrational dephasing of I[sub 2] in solid Kr using the semiclassical Liouville method. *J. Chem. Phys.*, 124(6):064506, 2006.
29. G. Hanna and R. Kapral. Quantum-classical Liouville dynamics of nonadiabatic proton transfer. *J. Chem. Phys.*, 122(24):244505, 2005.
30. G. Hanna and R. Kapral. Nonadiabatic dynamics of condensed phase rate processes. *Acc. Chem. Res.*, 39(1):21–27, Jan 2006.
31. H. Kim, G. Hanna, and R. Kapral. Analysis of kinetic isotope effects for nonadiabatic reactions. *J. Chem. Phys.*, 125:084509, 2006.
32. H. Kim and R. Kapral. Solvation and proton transfer in polar molecule nanoclusters. *J. Chem. Phys.*, 125(23), DEC 21 2006.
33. H. Kim and R. Kapral. Proton and deuteron transfer reactions in molecular nanoclusters. *ChemPhysChem*, 9(3):470–474, FEB 22 2008.
34. G. Hanna and E. Geva. Vibrational energy relaxation of a hydrogen-bonded complex dissolved in a polar liquid via the mixed quantum-classical lionville method. *J. Phys. Chem. B*, 112(13):4048–4058, APR 3 2008.
35. I. Horenko, B. Schmidt, and C. Schutte. A theoretical model for molecules interacting with intense laser pulses: The floquet-based quantum-classical Liouville equation. *The Journal of Chemical Physics*, 115(13):5733–5743, 2001.
36. C. M. Morales and W. H. Thompson. Mixed quantum-classical molecular dynamics analysis of the molecular-level mechanisms of vibrational frequency shifts. *J.Phys. Chem. A*, 111(25):5422–5433, JUN 28 2007.
37. D. Mac Kernan, G. Ciccotti, and R. Kapral. Surface-hopping dynamics of a spin-boson system. *J. Chem. Phys.*, 116(6):2346–2353, 2002.
38. D. Mac Kernan, G. Ciccotti, and R. Kapral. Trotter-based simulation of quantum-classical dynamics. *J. Phys. Chem. B*, 112:424, 2008.
39. M. Santer, U. Manthe, and G. Stock. Quantum-classical Liouville description of multidimensional nonadiabatic molecular dynamics. *J. Chem. Phys.*, 114(5):2001–2012, 2001.
40. D. Mac Kernan, R. Kapral, and G. Ciccotti. Sequential short-time propagation of quantum–classical dynamics sequential short-time propagation of quantum-classical dynamics. *J. Phys.: Condensed Matter*, 14:9069, 2002.
41. A. Sergi, D. Mac Kernan, G. Ciccotti, and R. Kapral. Simulating quantum dynamics in classical environments. *Theor. Chem. Acc.*, 110:49, 2003.
42. C. Wan and J. Schofield. Mixed quantum-classical molecular dynamics: Aspects of the multithread algorithm. *J. Chem. Phys.*, 113:7047, 2000.
43. C. Wan and J. Schofield. Solutions of mixed quantum-classical dynamics in multiple dimensions using classical trajectories. *J. Chem. Phys.*, 116:494–506, 2002.
44. J. Schwinger. In L. C. Biedenharm and H. V. Dam, editors, *Quantum theory of angular momentum*. Academic, New York, 1965.
45. H. D. Meyer and W. H. Miller. Classical analog for electronic degrees of freedom in non-adiabatic collision processes. *J. Chem. Phys.*, 70(7):3214–3223, 1979.

46. G. Stock. A semiclassical self-consistent-field approach to dissipative dynamics - the spin-boson problem. *J. Chem. Phys.*, 103(4):1561–1573, Jul 1995.
47. G. Stock and M. Thoss. Semiclassical description of nonadiabatic quantum dynamics. *Phys. Rev. Lett.*, 78(4):578–581, Jan 1997.
48. U. Muller and G. Stock. Consistent treatment of quantum-mechanical and classical degrees of freedom in mixed quantum-classical simulations. *J. Chem. Phys.*, 108(18):7516–7526, May 1998.
49. M. Thoss and G. Stock. Mapping approach to the semiclassical description of nonadiabatic quantum dynamics. *Phys. Rev. A*, 59(1):64–79, Jan 1999.
50. S. Bonella and D. F. Coker. Semiclassical implementation of the mapping Hamiltonian approach for nonadiabatic dynamics using focused initial distribution sampling. *J. Chem. Phys.*, 118(10):4370–4385, Mar 2003.
51. S. Bonella and D. F. Coker. LAND-map, a linearized approach to nonadiabatic dynamics using the mapping formalism. *J. Chem. Phys.*, 122(19):194102, 2005.
52. S. Bonella, D. Montemayor, and D.F. Coker. Linearized path integral approach for calculating nonadiabatic time correlation functions. *Proc. Natl. Acad. Sci.*, 102:6715–6719, 2005.
53. H. Kim, A. Nassimi, and R. Kapral. Quantum-classical Liouville dynamics in the mapping basis. *J. Chem. Phys.*, 2008. Submitted.
54. F. Zhan, Y. Lin, and B. Wu. Equivalence of two approaches for quantum-classical hybrid systems. *J. Chem. Phys.*, 128(20):204104, 2008.
55. J. C. Tully and R. K. Preston. Trajectory surface hopping approach to nonadiabatic molecular collisions: The reaction of H[sup +] with D[sub 2]. *J. Chem. Phys.*, 55(2):562–572, 1971.
56. S. Hammes-Schiffer and J. C. Tully. Proton transfer in solution: Molecular dynamics with quantum transitions. *J. Chem. Phys.*, 101(6):4657–4667, 1994.
57. R. Grunwald and R. Kapral. Decoherence and quantum-classical master equation dynamics. *J. Chem. Phys.*, 126(11):114109, 2007.
58. W. H. Zurek. Decoherence and the transition from quantum to classical. *Physics Today*, 44(10):36–44, Oct 1991.
59. B. J. Berne, G. Ciccotti, and D. F. Coker, editors. *Classical and Quantum Dynamics in Condensed Phase Simulations*. World Scientific, 1997.
60. F. Webster, E. T. Wang, P. J. Rossky, and R. A. Friesner. Stationary phase surface hopping for nonadiabatic dynamics: Two-state systems. *J. Chem. Phys.*, 100(7):4835–4847, 1994.
61. D.F. Coker and L. Xiao. Methods for molecular-dynamics with nonadiabatic transitions. *J. Chem. Phys.*, 102:496–510, 1995.
62. E. R. Bittner and P. J. Rossky. Quantum decoherence in mixed quantum-classical systems: Nonadiabatic processes. *J. Chem. Phys.*, 103(18):8130–8143, 1995.
63. O. V. Prezhdo and P. J. Rossky. Mean-field molecular dynamics with surface hopping. *J. Chem. Phys.*, 107(3):825–834, 1997.
64. R. Kubo. The fluctuation-dissipation theorem. *Rep. Prog. Phys.*, 29:255, 1966.
65. R. Kapral, S. Consta, and L. McWhirter. Chemical rate laws and rate constants. In B. J. Berne, G. Ciccotti, and D. F. Coker, editors, *Classical and Quantum Dynamics in Condensed Phase Simulations*, pages 583–616. World Scientific, 1998.
66. R. W. Zwanzig. *Statistical Mechanics of Irreversibility*, page 106. Wiley-Interscience, 1961.

67. H. Mori. Transport, collective motion, and Brownian motion. *Prog. Theor. Phys.*, 33(3):423, 1965.
68. A. Sergi and R. Kapral. Quantum-classical dynamics of nonadiabatic chemical reactions. *J. Chem. Phys.*, 118:8566–8575, 2003.
69. H. Kim and R. Kapral. Transport properties of quantum-classical systems. *J. Chem. Phys.*, 122:214105, 2005.
70. H. Kim and R. Kapral. Nonadiabatic quantum-classical reaction rates with quantum equilibrium structure. *J. Chem. Phys.*, 123:194108, 2005.
71. A. Warshel. Dynamics of reactions in polar-solvents - semi-classical trajectory studies of electron-transfer and proton-transfer reactions. *J. Phys. Chem.*, 86(12):2218–2224, 1982.
72. R. A. Marcus and N. Sutin. Electron transfers in chemistry and biology. *Biochim. Biophys. Acta*, 811(3):265–322, 1985.
73. D. Laria, G. Ciccotti, M. Ferrario, and R. Kapral. Molecular-dynamics study of adiabatic proton-transfer reactions in solution. *J. Chem. Phys.*, 97(1):378–388, 1992.
74. S. Hammes-Schiffer and J. C. Tully. Vibrationally enhanced proton transfer. *J. Phys. Chem.*, 99(16):5793–5797, 1995.
75. S. Consta and R. Kapral. Dynamics of proton transfer in mesoscopic clusters. *J. Chem. Phys.*, 104(12):4581–4590, 1996.
76. A. A. Kornyshev, M Tosi, and J Ulstrup, editors. *Electron and Ion transfer in Condensed Media*. World Sci., 1997.
77. G. Ciccotti, M. Ferrario, D. Laria, and R. Kapral. Simulation of classical and quantum activated process in the condensed phase. In L Reatto and F Manghi, editors, *Progress of Computational Physics of Matter: Methods, Software and Applications*. World Scientific, New Jersey, 1995.
78. H. Kim and R. Kapral. Quantum equilibrium structure for strong nonadiabatic coupling: Reaction rate enhancement. *Chem. Phys, Lett.*, 440(4-6):215–220, 2007.
79. R. Grunwald, H. Kim, and R. Kapral. Surface hopping dynamics and decoherence with quantum equilibrium structure. *J. Chem. Phys.*, 128(17), 2008.
80. K. Thompson and N. Makri. Rigorous forward-backward semiclassical formulation of many-body dynamics. *Phys. Rev. E*, 59(5):R4729–R4732, 1999.

Trajectory Based Simulations of Quantum-Classical Systems

S. Bonella, D. F. Coker, D. Mac Kernan, R. Kapral, and G. Ciccotti

[1] Dipartimento di Fisica, Università "La Sapienza", Piazzale Aldo Moro, 2, 00185 Roma, Italy. sara.bonella@roma1.infn.it
[2] Department of Chemistry, Boston University, 590 Commonwealth Avenue, Boston, Massachusetts, 02215, U.S.A. and School of Physics, University College Dublin, Belfield, Dublin 4, Ireland coker@bu.edu
[3] School of Physics, University College Dublin, Belfield, Dublin 4, Ireland. donal.mackernan@ucd.ie
[4] Chemical Physics Theory Group, Department of Chemistry, University of Toronto, Toronto, Ontario M5S3H6, Canada rkapral@cptg.chem.utoronto.ca
[5] Dipartimento di Fisica, Università "La Sapienza", Piazzale Aldo Moro, 2, 00185 Roma, Italy giovanni.ciccotti@roma1.infn.it

Abstract. In this Chapter we review the core ingredients of a class of mixed quantum-classical methods that can naturally account for quantum coherence effects. In general, quantum-classical schemes partition degrees of freedom between a quantum subsystem and an environment. The various approaches are based on different approximations to the full quantum dynamics, in particular in the way they treat the environment. Here we compare and contrast two such methods: the Quantum Classical Liouville (QCL) approach, and the Iterative Linearized Density Matrix (ILDM) propagation scheme. These methods are based on evolving ensembles of surface-hopping trajectories in which the ensemble members carry weights and phases and their contributions to time-dependent quantities must be added coherently to approximate interference effects. The side by side comparison we offer highlights similarities and differences between the two approaches and serves as a starting point to explore more fundamental connections between such methods. The methods are applied to compute the evolution of the density matrix of a challenging condensed phase model system in which coherent dynamics plays a critical role: the asymmetric spin-boson. Various implementation questions are addressed.

1 Introduction

The difficulty in simulating the full quantum dynamics of large many-body systems has stimulated the development of mixed quantum-classical dynamical schemes. In such approaches, the quantum system of interest is partitioned into two subsystems, which we term the quantum subsystem, and quantum bath. Approximations to the full quantum dynamics are then made such that

I. Burghardt et al. (eds.), *Theory of Charge Transfer Dynamics in Biomaterial Systems*, Springer Series in Chemical Physics 93, DOI 10.1007/978-3-642-02306-4_13,

the bath or environmental degrees of freedom are treated classically. The manner in which approximations are made to achieve this limit, and the resulting nature of the coupling between the quantum and classical subsystems distinguish the various quantum-classical schemes. While there are fundamental issues and difficulties that must be addressed when attempting to combine quantum and classical dynamics, quantum-classical schemes are, at present, the most useful and practical methods for treating realistic physical systems. A variety of such methods has been proposed [1, 2]. Some of the most popular quantum-classical methods are based on surface-hopping dynamics, where the system evolves classically on single adiabatic surfaces, with quantum transitions between these surfaces to account for nonadiabatic effects [3]. An important issue concerning the validity and implementation of surface-hopping schemes is the manner in which quantum coherence is treated.

In this chapter we describe two quantum-classical schemes that account for quantum coherence and involve simulations using ensembles of surface-hopping trajectories: the Quantum Classical Liouville (QCL) approach, and the iterative linearized density matrix (ILDM) propagation scheme. These methods are based on different approximations to the full quantum dynamics, in particular in the way they treat the environment. The QCL approach starts from an expansion of the quantum Liouville operator and develops approximate evolution equations for the density, while the ILDM approach employs a linearized path integral expression for the same quantity. Previous work has been done that begins to explore the relationship between these approaches [4] but more theoretical analysis is needed to understand the precise connection. In this chapter we present a side by side comparison of the two theoretical approaches, the algorithmic issues needed to implement them, and explore their performances on a common benchmark problem as a prelude for the analysis of this connection. Rather than give complete and detailed derivations of these two approaches, here we summarize the conceptual framework underlying the different methods and, where appropriate, point the reader to the original articles for complete details.

A complete and detailed analysis of the formal properties of the QCL approach [5] has revealed that while this scheme is internally consistent, inconsistencies arise in the formulation of a quantum-classical statistical mechanics within such a framework. In particular, the fact that time translation invariance and the Kubo identity are only valid to $\mathcal{O}(\hbar)$ have implications for the calculation of quantum-classical correlation functions. Such an analysis has not yet been conducted for the ILDM approach. In this chapter we adopt an alternative prescription [6, 7]. This alternative approach supposes that we start with the full quantum statistical mechanical structure of time correlation functions, average values, or, in general, the time dependent density, and develop independent approximations to both the quantum evolution, and to the equilibrium density. Such an approach has proven particularly useful in many applications [8, 9]. As was pointed out in the earlier publications [6, 7], the consistency between the quantum equilibrium structure and the approximate

dynamics is lost with such an approach, though we gain the ability explore different independent approximations to the evolution and the equilibrium structure.

The focus of this chapter is exploration of the ability of mixed quantum classical approaches to capture the effects of interference and coherence in the approximate dynamics used in these different mixed quantum classical methods. As outlined below, the expectation values of computed observables are fundamentally non-equilibrium properties that are not expressible as equilibrium time correlation functions. Thus, the chapter explores the relationship between the approximations to the quantum dynamics made in these different approaches that attempt to capture quantum coherence.

The main goal in the development of mixed quantum classical methods has as its focus the treatment of large, complex, many-body quantum systems. While applications to models with many realistic elements have been carried out [10,11], here we test the methods and algorithms on the spin-boson model, which is the standard test case in this field. In particular, we focus on the asymmetric spin-boson model and the calculation of off-diagonal density matrix elements, which present difficulties for some simulation schemes. We show that both of the methods discussed here are able to accurately and efficiently simulate this model.

The chapter is organized as follows: The quantum-classical Liouville dynamics scheme is first outlined and a rigorous surface hopping trajectory algorithm for its implementation is presented. The iterative linearized density matrix propagation approach is then described and an approach for its implementation is presented. In the Model Simulations section the comparable performance of the two methods is documented for the generalized spin-boson model and numerical convergence issues are mentioned. In the Conclusions we review the perspectives of this study.

2 Quantum-Classical Liouville Dynamics

In quantum-classical Liouville (QCL) dynamics the partition of the system into bath and subsystem is motivated by the observation that for many condensed phase processes it is essential to account for the quantum mechanical character of only a few light (characteristic mass m) degrees of freedom; the remaining heavy (characteristic mass M) degrees of freedom may be treated classically to a high degree of accuracy.

2.1 Evolution equation

In this scheme, for a system with hamiltonian $\hat{H}$, the starting point is the quantum Liouville equation for the density matrix, $\hat{\rho}(t)$,

$$\frac{\partial}{\partial t}\hat{\rho}(t) = -\frac{i}{\hbar}[\hat{H}, \hat{\rho}(t)]. \tag{1}$$

The quantum-classical Liouville equation is obtained from this equation by introducing scaled variables such that the characteristic momenta of the light and heavy degrees of freedom are comparable. This scaling introduces a small parameter $\mu = (m/M)^{1/2}$ in the equations of motion. Expansion of the quantum Liouville operator to $\mathcal{O}(\mu)$ yields the quantum-classical Liouville equation [2, 4, 12–20],

$$\begin{aligned}\frac{\partial \hat{\rho}_W(R,P,t)}{\partial t} &= -\frac{i}{\hbar}\left[\hat{H}_W(R,P), \hat{\rho}_W(R,P,t)\right] \\ &\quad +\frac{1}{2}(\{\hat{H}_W(R,P), \hat{\rho}_W(R,P,t)\} - \{\hat{\rho}_W(R,P,t), \hat{H}_W(R,P)\}) \\ &= -i\hat{\mathcal{L}}\hat{\rho}_W(R,P,t). \end{aligned} \tag{2}$$

The last line defines the mixed quantum-classical Liouville operator $\hat{\mathcal{L}}$. The W subscripts denote a partial Wigner transform of an operator or density matrix. The phase space variables of the bath are (R, P) and the partial Wigner transform of the total hamiltonian is given by,

$$\hat{H}_W(R,P) = \frac{P^2}{2M} + \frac{\hat{p}^2}{2m} + \hat{V}_W(\hat{q}, R), \tag{3}$$

where $\hat{p}$ is the set of momentum operators for the quantum subsystem with coordinate operators $\hat{q}$, and $\hat{V}_W(\hat{q}, R)$ is the partial Wigner transform of the total potential energy operator of the system. As usual, square brackets denote quantum commutators and curly brackets denote Poission brackets. Similarly, the quantum-classical Liouville equation of motion for an operator $\hat{B}$ is

$$\frac{d\hat{B}_W(R,P,t)}{dt} = i\hat{\mathcal{L}}\hat{B}_W(R,P,t). \tag{4}$$

One noteworthy feature of Eqs. (2) and (4) is that they provide an exact quantum description for an arbitrary quantum subsystem bilinearly coupled to a quantum harmonic bath. Other aspects of this equation have been discussed previously in the literature [2, 5].

2.2 Simulation of expectation values

The expectation value of an operator $\hat{B}$ is given by

$$\overline{B(t)} = \mathrm{Tr}\hat{B}\hat{\rho}(t) = \mathrm{Tr}\hat{B}(t)\hat{\rho}(0) = \mathrm{Tr}' \int dR dP\ \hat{B}_W(R,P,t)\hat{\rho}_W(R,P). \tag{5}$$

In the last equality here we have introduced the partial Wigner transforms of the density matrix and operator. The prime on the trace indicates a trace over the subsystem degrees of freedom. All information on the quantum initial distribution is contained in $\hat{\rho}_W(R,P,0)$. In the evaluation of this expression we assume that the time evolution of $\hat{B}_W(R,P,t)$ is given by Eq. (4). This

equation may be simulated in a variety of representations, using various algorithms [2, 21]. Here we focus on a representation in the adiabatic basis and a Trotter-based scheme which leads to a simulation algorithm involving an ensemble of surface-hopping trajectories [22].

Given that the total hamiltonian may be written as $\hat{H}_W = P^2/2M + \hat{h}_W(R)$, the adiabatic eigenfunctions $|\alpha; R\rangle$ are the solutions of the eigenvalue problem, $\hat{h}_W(R)|\alpha; R\rangle = E_\alpha(R)|\alpha; R\rangle$. In this adiabatic basis the quantum-classical Liouville operator has matrix elements [12],

$$\begin{aligned} i\mathcal{L}_{\alpha\alpha',\beta\beta'} &= (i\omega_{\alpha\alpha'} + iL_{\alpha\alpha'})\delta_{\alpha\beta}\delta_{\alpha'\beta'} - \mathcal{J}_{\alpha\alpha',\beta\beta'} \\ &\equiv i\mathcal{L}^0_{\alpha\alpha'}\delta_{\alpha\beta}\delta_{\alpha'\beta'} - \mathcal{J}_{\alpha\alpha',\beta\beta'} \ . \end{aligned} \tag{6}$$

Here $\omega_{\alpha\alpha'}(R) = (E_\alpha(R) - E_{\alpha'}(R))/\hbar$ and $iL_{\alpha\alpha'}$ is the Liouville operator that describes classical evolution determined by the mean of the Hellmann-Feynman forces corresponding to adiabatic states α and α',

$$iL_{\alpha\alpha'} = \frac{P}{M}\cdot\frac{\partial}{\partial R} + \frac{1}{2}\left(F^\alpha_W + F^{\alpha'}_W\right)\cdot\frac{\partial}{\partial P} \ , \tag{7}$$

where $F^\alpha_W = -\langle\alpha; R|\frac{\partial \hat{H}_W(\hat{q},R)}{\partial R}|\alpha; R\rangle$ is the Hellmann-Feynman force for state α. The operator $\mathcal{J}_{\alpha\alpha',\beta\beta'}$ is responsible for nonadiabatic transitions and associated changes in the bath momentum and can be written as the sum of two terms,

$$\mathcal{J}_{\alpha\alpha',\beta\beta'} = J_{1\,\alpha\alpha',\beta\beta'} + J_{2\,\alpha\alpha',\beta\beta'}, \tag{8}$$

where

$$J_{1\alpha\alpha',\beta\beta'} = -\left(d_{\alpha\beta}\delta_{\alpha'\beta'} + d^*{}_{\alpha'\beta'}\delta_{\alpha\beta}\right)\cdot\frac{P}{M} \ , \tag{9}$$

$$J_{2\alpha\alpha',\beta\beta'} = -\frac{1}{2}\Big((E_\alpha - E_\beta)d_{\alpha\beta}\delta_{\alpha'\beta'} + (E_{\alpha'} - E_{\beta'})d^*_{\alpha'\beta'}\delta_{\alpha\beta}\Big)\cdot\frac{\partial}{\partial P}, \tag{10}$$

and $d_{\alpha\beta}(R) =< \alpha; R|\frac{\partial}{\partial R}|\beta; R >$ is the nonadiabatic coupling matrix element. The matrix elements of the quantum-classical propagator in the adiabatic basis are $\left(\exp\left(i\mathcal{L}t\right)\right)_{\alpha\alpha',\beta\beta'}$. The superoperator notation involving pairs of quantum states can be eliminated by associating an index $s = \alpha\mathcal{N} + \alpha'$ with the pair $(\alpha\alpha')$, where $0 \le \alpha, \alpha' < \mathcal{N}$ for an $\mathcal{N}$-state quantum subsystem [22]. The quantum-classical propagator then takes the form $\left(\exp\left(i\mathcal{L}t\right)\right)_{ss'}$ where $i\mathcal{L}_{ss'} = i\mathcal{L}^0_s\delta_{ss'} - \mathcal{J}_{ss'}$.

Since the Liouville operator is time independent and commutes with itself we may write the propagator exactly as the product of N short time propagators as

$$\left(e^{i\mathcal{L}t}\right)_{s_0 s_N} = \sum_{s_1 s_2 \ldots s_{N-1}} \prod_{j=1}^{N} \left(e^{i\mathcal{L}(t_j - t_{j-1})}\right)_{s_{j-1}s_j} \ , \tag{11}$$

where $t_j = j\delta$ and $t = N\delta$. The propagator for each of the small time intervals $t_j - t_{j-1} = \delta$ may be computed by using a Trotter factorization as

$$\left(e^{\imath\mathcal{L}(t_j - t_{j-1})}\right)_{s_{j-1}s_j} \approx e^{\imath\mathcal{L}^0_{s_{j-1}}\delta/2}\left(e^{-\mathcal{J}\delta}\right)_{s_{j-1}s_j} e^{\imath\mathcal{L}^0_{s_j}\delta/2} + \mathcal{O}(\delta^3)\,, \tag{12}$$

where we have used the fact that $i\mathcal{L}^0$ is diagonal in the adiabatic basis. The propagator $e^{i\mathcal{L}^0_s(t_j - t_{j-1})}$ can be written as the product of a phase factor and a classical evolution operator as [12]

$$\begin{aligned} e^{i\mathcal{L}^0_s(t_j - t_{j-1})} &= e^{i\int_{t_{j-1}}^{t_j} d\tau\ \omega_s(R_{s,\tau})} e^{iL_s(t_j - t_{j-1})} \\ &\equiv \mathcal{W}_s(t_{j-1}, t_j) e^{iL_s(t_j - t_{j-1})}, \end{aligned} \tag{13}$$

where $R_{s,\tau}$ denotes the value of R at time τ obtained by classical evolution under the Hellmann-Feynman force with quantum state index s.

The propagator $\left(e^{-\mathcal{J}\delta}\right)_{ss'}$ is responsible for quantum transitions and bath momentum changes. In order to compute its action, we use the momentum-jump approximation [12, 23] that replaces the small continuous momentum changes with momentum jumps that accompany each quantum transition. In this approximation, the matrix elements of $e^{-\mathcal{J}\delta}$ can be written in terms of a matrix $\mathcal{M}$ to $\mathcal{O}(\delta^2)$,

$$\left(e^{-\mathcal{J}\delta}\right)_{ss'} \approx (Q_1)_{ss'} e^{C_{ss'}\cdot\frac{\partial}{\partial P}} + \mathcal{O}(\delta^2) = \mathcal{M}_{ss'}(\delta) + \mathcal{O}(\delta^2). \tag{14}$$

The explicit forms of the Q_1 and C matrices may be written for any $\mathcal{N}$-state quantum system. For a two-level system they have the forms,

$$Q_1 = \begin{pmatrix} \cos^2(a) & -\cos(a)\sin(a) & -\cos(a)\sin(a) & \sin^2(a) \\ \sin(a)\cos(a) & \cos^2(a) & -\sin^2(a) & -\sin(a)\cos(a) \\ \sin(a)\cos(a) & -\sin^2(a) & \cos^2(a) & -\sin(a)\cos(a) \\ \sin^2(a) & \sin(a)\cos(a) & \sin(a)\cos(a) & \cos^2(a) \end{pmatrix}, \tag{15}$$

where $a = \frac{P}{M}\cdot d_{10}(R)\delta$ and

$$C = \begin{pmatrix} 0 & S_{01} & S_{01} & 2S_{01} \\ S_{10} & 0 & 0 & S_{01} \\ S_{10} & 0 & 0 & S_{01} \\ 2S_{10} & S_{10} & S_{10} & 0 \end{pmatrix}, \tag{16}$$

where $S_{\alpha\beta} = \hbar\omega_{\alpha\beta} d_{\alpha\beta}/(2(P/M)\cdot d_{\alpha\beta})$. The momentum jump operators can be evaluated as

$$\begin{aligned} e^{S_{\alpha\beta}\cdot\partial/\partial P} f(P) &= e^{\hbar\omega_{\alpha\beta} M\partial/\partial(\hat{d}_{\alpha\beta}\cdot P)^2)} f\left(P_\perp + \hat{d}_{\alpha\beta}\mathrm{sgn}(\hat{\mathrm{d}}_{\alpha\beta}\cdot \mathrm{P})\sqrt{(\hat{\mathrm{d}}_{\alpha\beta}\cdot \mathrm{P})^2}\right) \\ &= f(P + \Delta P_{\alpha\beta}). \end{aligned}$$

where

$$\Delta P_{\alpha\beta} = \hat{d}_{\alpha\beta}\left(\mathrm{sgn}(\hat{d}_{\alpha\beta}\cdot P)\sqrt{(\hat{d}_{\alpha\beta}\cdot P)^2+\hbar\omega_{\alpha\beta}M}-(\hat{d}_{\alpha\beta}\cdot P)\right) \tag{17}$$

and P has been decomposed into its components along and normal to $\hat{d}_{\alpha\beta}$ as $P=(1-\hat{d}_{\alpha\beta}\hat{d}_{\alpha\beta})\cdot P+\hat{d}_{\alpha\beta}(\hat{d}_{\alpha\beta}\cdot P)\equiv P_\perp+\hat{d}_{\alpha\beta}(\hat{d}_{\alpha\beta}\cdot P)=P_\perp+\hat{d}_{\alpha\beta}\mathrm{sgn}(\hat{\mathrm{d}}_{\alpha\beta}\cdot \mathrm{P})\sqrt{(\hat{\mathrm{d}}_{\alpha\beta}\cdot \mathrm{P})^2}$.

Using these expressions in the Trotter expansion (12) we obtain

$$\begin{aligned}\left(e^{i\mathcal{L}(t_j-t_{j-1})}\right)_{s_{j-1}s_j} &\approx e^{i\mathcal{L}^0_{s_{j-1}}\delta/2}\mathcal{M}_{s_{j-1}s_j}(\delta)e^{i\mathcal{L}^0_{s_j}\delta/2} \\ &= \mathcal{W}_{s_{j-1}}(t_{j-1},t_j-\delta/2)e^{iL_{s_{j-1}}\delta/2}\mathcal{M}_{s_{j-1}s_j}(\delta)\mathcal{W}_{s_j}(t_j-\delta/2,t_j)e^{iL_{s_j}\delta/2}\,.\end{aligned} \tag{18}$$

From left to right, the short-time propagator describes classical propagation on the s_{j-1} surface through a time interval $\delta/2$, a transition $s_{j-1}\to s_j$ determined by the elements of $\mathcal{M}$ and classical propagation on the s_j surface for a time interval $\delta/2$.

Short time segments may be concatenated to obtain the time evolution for any time. Using Eq. (18), we may write the expression for $\overline{B(t)}$ more explicitly as

$$\begin{aligned}\overline{B(t)} &= \sum_{s_0}\int dRdP\; B_W^{s_0}(R,P,t)\rho_W^{s_0'}(R,P)dRdP \\ &= \sum_{s_0}\int \rho_W^{s_0'}(R,P)\sum_{s_1,\ldots,s_N}\Big[\prod_{j=1}^{N}\mathcal{W}_{s_{j-1}}(t_{j-1},t_j-\delta/2)e^{iL_{s_{j-1}}\delta/2} \\ &\times \mathcal{M}_{s_{j-1}s_j}(\delta)\mathcal{W}_{s_j}(t_j-\delta/2,t_j)e^{iL_{s_j}\delta/2}\Big]B_W^{s_N}(R,P),\end{aligned} \tag{19}$$

where $s_0'=(\alpha_0',\alpha_0)$ is obtained from $s_0=(\alpha_0,\alpha_0')$ by the interchange $\alpha_0\rightleftharpoons\alpha_0'$. The summations on quantum indices and phase space integrals can be performed through Monte Carlo sampling. The simulation algorithm consists of three steps based on the structure of Eq. (19). The total time of the simulation is divided into $t/\delta=N$ short time segments. Given the form of the short time propagator in Eq. (18) we can rearrange Eq. (19) into the form

$$\begin{aligned}\overline{B(t)} = \frac{\mathcal{N}^2}{K}\sum_{\kappa=1}^{K}\frac{\rho_W^{s_0'^\kappa}(R^\kappa,P^\kappa)}{|\rho_W^{s_0'^\kappa}(R^\kappa,P^\kappa)|}\Big[\prod_{j=1}^{N}\Big(&\mathcal{W}_{s^\kappa_{j-1}}(t_{j-1},t_j-\delta/2)e^{iL_{s^\kappa_{j-1}}\delta/2} \\ &\times\frac{\sum_{s_j^\kappa}|(Q_1)_{s^\kappa_{j-1}s^\kappa_j}(\delta)|}{|(Q_1)_{s^\kappa_{j-1}s^\kappa_j}(\delta)|}\mathcal{M}_{s^\kappa_{j-1}s^\kappa_j}(\delta)\mathcal{W}_{s^\kappa_j}(t_j-\delta/2,t_j)e^{iL_{s^\kappa_j}\delta/2}\Big)_{s^\kappa_{j-1}s^\kappa_j}\Big] \\ &\times B_W^{s^\kappa_N}(R^\kappa,P^\kappa),\end{aligned} \tag{20}$$

that can be evaluated by Monte Carlo sampling. Here the index κ refers to the Monte Carlo sampling of the elementary event $(R^\kappa,P^\kappa,s_0'^\kappa,s_1^\kappa,\ldots,s_N^\kappa)$,

and results are averaged over K such events. The $\mathcal{N}^2$ factor arises from the uniform sampling for the sum on the initial states s_0. Phase space is importance sampled according to $|\rho_W^{s_0'}(R,P)|$, which leaves in the sum the phase factor, $\sigma = \rho_W^{s_0'}(R,P)/|\rho_W^{s_0'}(R,P)|$.

Evaluation of Eq. (20) involves a combination of Monte Carlo sampling and propagation steps. For $(j = 1)$ the phase space point (R,P) is propagated classically to $e^{iL_{s_0}\delta/2}(R,P) = (R',P')$. The phase factor $\mathcal{W}_{s_0}$ and all of the matrix elements and operators, including the observable, at the value of this evolved phase point, are updated. The value of the index s_1 in the matrix $\mathcal{M}_{s_0 s_1}(\delta)$ is chosen by sampling with probability $|(Q_1)_{s_0^\kappa s_1^\kappa}(\delta)|/\sum_{s_1^\kappa}|(Q_1)_{s_0^\kappa s_1^\kappa}(\delta)|$. This introduces the factor $\sum_{s_1^\kappa=0}|(Q_1)_{s_0^\kappa s_1^\kappa}(\delta)|/|(Q_1)_{s_0^\kappa s_1^\kappa}(\delta)|$. Once the index s_1 is selected, the momentum jump (if any) specified by $\mathcal{M}_{s_0 s_1}(\delta)$ is applied to all functions and operators to its right so that the new bath phase space point is $(R',\bar{P}')$, where the overline denotes the momentum after the momentum-jump operation. The phase factor $\mathcal{W}_{s_1}$ is then computed and the evolution operator $e^{iL_{s_1}\delta/2}$ is used to propagate the bath phase space coordinates $(R',\bar{P}')$ to time t_1: $e^{iL_{s_1}\delta/2}(R',\bar{P}') = (R'',P'')$. The procedure is then repeated starting from the index $j = 2$ in the product in Eq. (20) with the updated value of the bath phase space point.

An important additional part of the algorithm is the use of a filter. Estimates of averages are dominated by large fluctuations which come from unusually large values of the summand of Eq. (20) and exacerbate the sign problem that comes from the phase factors in the evolution. The use of a filter can eliminate improperly large biasing fluctuations which should not contribute to the averaged quantity. A simple filter involves putting an upper bound, Z, on the magnitude of the factor in the square brackets appearing in the summand in Eq. (20). When, at step j in the calculation of the product in the summand, the running summand exceeds the bound, the factor in the updating of the running product is put to unity and the index s_j is set to s_{j-1}. The reader can find details of this approach in reference [10, 22].

3 Iterative Linearized Density Matrix Propagation

Rather than starting from the exact quantum Liouville equation for the density matrix and approximating it by the mixed quantum-classical Liouville equation as in the QCL scheme outlined above, the iterative linearized density matrix propagation approach, in contrast, starts from an exact expression for the evolution of the density operator and then uses the time composition property of the quantum propagators to write this evolution in terms of concatenated time segments. In much the same way as with the formal development of path integral expressions, a short time approximation for the propagating density matrix in each segment is developed. With in each individual time segment evolution occurs according to the prescriptions of the

linearized approximation as outlined in the literature [24–28]. The basic idea behind this alternative approximate scheme is that, for sufficiently short times, the forward and backward paths of the environmental degrees of freedom that are used to represent the evolving density matrix must remain close to one another. Truncating an expansion in the difference between forward and backward paths for these degrees of freedom at linear order should provide a good short time approximation. With this approach, contributions from forward and backward paths of the quantum subsystem degrees of freedom are included to all orders. The time segments in the iterative implementation of this short time approximation are joined by a stochastic mechanism that samples the relevant contributions to the evolving density matrix at any given time. Thus, linearization becomes a tool to obtain a satisfactory approximation for a sequence of propagators in the spirit of a "finite time" path integral expression for the density operator in which the length of the "time slices" is not necessarily infinitesimal. Since the approximations underlying the linearized expression for the propagators are more accurate for short times, the performance of the overall dynamics is expected to improve with the number of time slices. During each individual propagation leg, non adiabaticity is described through the evolution of quantum amplitudes represented in the mapping formulation [29–33]. At the end of each finite time slice, the quantum subsystem representation is refreshed by a Monte Carlo selection of the most important term in the density matrix at that particular time in a similar fashion to that outlined in the previous section. In the following we summarize the results needed to derive the approach and present an algorithm that combines evolution of classical trajectories and Monte Carlo sampling to implement the theory.

3.1 Theory

The time evolution of density operator $\hat{\rho}(t)$ in the Heisenberg picture is given by

$$\hat{\rho}(t = n\Delta) = e^{-\frac{i}{\hbar}\hat{H}\Delta} \ldots e^{-\frac{i}{\hbar}\hat{H}\Delta} \hat{\rho}(0) e^{\frac{i}{\hbar}\hat{H}\Delta} \ldots e^{\frac{i}{\hbar}\hat{H}\Delta} \tag{21}$$

where, to set the stage for the approach to be described, the total time propagation to t has been broken up into n time intervals of finite duration Δ.

Inserting resolutions of the identity written in terms of tensor product states $|R_{j\Delta}\alpha_{j\Delta}\rangle$ (with $0 \leq j \leq (n-1)$) in the coordinate and diabatic state representation, matrix elements of the time dependent density operator are conveniently written as

$$\langle R_{n\Delta}\alpha_{n\Delta}|\hat{\rho}(n\Delta)|R'_{n\Delta}\alpha'_{n\Delta}\rangle =$$
$$\sum_{\alpha_{(n-1)\Delta},\alpha'_{(n-1)\Delta}} \int dR_{(n-1)\Delta} dR'_{(n-1)\Delta} \cdots \sum_{\alpha_0,\alpha'_0} \int dR_0 dR'_0$$
$$\times \langle R_{n\Delta}\alpha_{n\Delta}|e^{-\frac{i}{\hbar}\hat{H}\Delta}|R_{(n-1)\Delta}\alpha_{(n-1)\Delta}\rangle \ldots \langle R_{\Delta}\alpha_{\Delta}|e^{-\frac{i}{\hbar}\hat{H}\Delta}|R_0\alpha_0\rangle$$
$$\times \langle R_0\alpha_0|\hat{\rho}(0)|R'_0\alpha'_0\rangle$$
$$\times \langle R'_0\alpha'_0|e^{\frac{i}{\hbar}\hat{H}\Delta}|R'_{\Delta}\alpha'_{\Delta}\rangle \ldots \langle R'_{(n-1)\Delta}\alpha'_{(n-1)\Delta}|e^{\frac{i}{\hbar}\hat{H}\Delta}|R'_{n\Delta}\alpha'_{n\Delta}\rangle \tag{22}$$

In this expression, each individual sum extends over all the $\mathcal{N}$ diabatic basis states.

A convenient expression for the incremental time evolution of the density matrix in the time interval $0 \leq \tau \leq \Delta$, for example, can be obtained as described in detail in references [34–36]. Briefly, a hybrid coordinate-momentum path integral representation of the forward and backward propagators for the environmental degrees of freedom is introduced, together with the mapping hamiltonian representation of the evolution of the quantum subsystem [29–33]. The latter can be evaluated explicitly and exactly as a parametric function of the paths of the bath variables by averaging the contributions of a set of auxiliary classical trajectories for the mapping variables $(p_{\tau,\lambda}, q_{\tau,\lambda})$ obtained by solving the following equations:

$$\dot{q}_{\tau,\lambda} = h_{\lambda,\lambda}(R_\tau)p_{\tau,\lambda} + \sum_{\mu\neq\lambda} h_{\lambda,\mu}(R_\tau)p_{\tau,\mu}$$
$$\dot{p}_{\tau,\lambda} = -h_{\lambda,\lambda}(R_\tau)q_{\tau,\lambda} - \sum_{\mu\neq\lambda} h_{\lambda,\mu}(R_\tau)q_{\tau,\mu} \tag{23}$$

Here $h_{\lambda,\mu}(R_\tau)$ is the matrix element of the quantum subsystem hamiltonian in the diabatic basis, including its interaction with the environment (see reference [37] for details). These manipulations transform the integrand in Eq. (22) into an explicit complex function of the bath and mapping variables. A change of variables is introduced that transforms the integration over forward, R_τ, and backward, R'_τ environmental paths into integration over the mean $\bar{R}_\tau = (R_\tau + R'_\tau)/2$ and difference paths $Z_\tau = (R_\tau - R'_\tau)$. The total phase of the new path integral expression is then expanded to linear order in the bath difference path. This approximation makes it possible to evaluate all difference integrals analytically to arrive at the following result for the reduced density matrix elements for the first time increment Δ which is divided into K discrete environmental path integral time steps of duration δ, *i.e.* $\Delta = K\delta$.

$$\langle \bar{R}_K + \frac{Z_K}{2}\alpha_\Delta|\hat{\rho}(\Delta)|\bar{R}_K - \frac{Z_K}{2}\alpha'_\Delta\rangle =$$
$$\sum_{\alpha_0,\alpha'_0}\int d\bar{R}_0 dq_0 dp_0 dq'_0 dp'_0 r'_{0,\alpha'_0} e^{-i\Theta'_{0,\alpha'_0}} G'_0 r_{0,\alpha_0} e^{i\Theta_{0,\alpha_0}} G_0$$
$$\times \int \prod_{k=1}^{K-1} d\bar{R}_k \frac{d\bar{P}_k}{2\pi}\frac{d\bar{P}_K}{2\pi}[\hat{\rho}]_W^{\alpha_0,\alpha'_0}(\bar{R}_0,\bar{P}_1)e^{i\bar{P}_K Z_K} \tag{24}$$
$$\times r_{\Delta,\alpha_\Delta}(\{\bar{R}_k\})r'_{\Delta,\alpha'_\Delta}(\{\bar{R}_k\})e^{-i\delta\sum_{k=1}^{K}(\theta_{\alpha_\Delta}(\bar{R}_k)-\theta_{\alpha'_\Delta}(\bar{R}_k))}$$
$$\times \prod_{k=1}^{K-1}\delta\left(\frac{\bar{P}_{k+1}-\bar{P}_k}{\delta} - F_k^{\alpha_\Delta,\alpha'_\Delta}\right)\prod_{k=1}^{K}\delta\left(\frac{\bar{P}_k}{M} - \frac{\bar{R}_k - \bar{R}_{k-1}}{\delta}\right)$$

here, the notation $\delta(\cdot)$ in the last line of Eq.(24) is the Dirac δ-function, $G_0 = e^{-\frac{1}{2}\sum_\lambda(q_{0,\lambda}^2+p_{0,\lambda}^2)}$, $r_{\Delta,\alpha_\Delta}(\{R_k\}) = \sqrt{q_{\Delta,\alpha_\Delta}^2(\{R_k\}) + p_{\Delta,\alpha_\Delta}^2(\{R_k\})}$, and

$$\Theta_{\Delta,\alpha_\Delta}(\{R_k\}) = \tan^{-1}\left(\frac{p_{0,\alpha_\Delta}}{q_{0,\alpha_\Delta}}\right) + \int_0^\Delta d\tau h_{\alpha_\Delta,\alpha_\Delta}(R_\tau)$$
$$+\int_0^\Delta d\tau \sum_{\lambda\neq\alpha_\Delta}\left[h_{\alpha_\Delta,\lambda}(R_\tau)\frac{(p_{\tau\alpha_\Delta}p_{\tau\lambda}+q_{\tau\alpha_\Delta}q_{\tau\lambda})}{(p_{\tau\alpha_\Delta}^2+q_{\tau\alpha_\Delta}^2)}\right]$$
$$= \tan^{-1}\left(\frac{p_{0,\alpha_\Delta}}{q_{0,\alpha_\Delta}}\right) + \int_0^\Delta \theta_{\alpha_\Delta}(R_\tau)d\tau \tag{25}$$

The partial Wigner transform of the initial density matrix element (2nd line of Eq.(24)) is

$$(\hat{\rho})_W^{\alpha_0,\alpha'_0}(\bar{R}_0,\bar{P}_1) = \int dZ_0\langle \bar{R}_0 + \frac{Z_0}{2}\alpha_0|\hat{\rho}|\bar{R}_0 - \frac{Z_0}{2}\alpha'_0\rangle e^{-\frac{i}{\hbar}\bar{P}_1 Z_0} \tag{26}$$

and the "force" is

$$F_k^{\alpha_\Delta,\alpha'_\Delta} = -\frac{1}{2}\left\{\nabla_{\bar{R}_k}h_{\alpha_\Delta,\alpha_\Delta}(\bar{R}_k) + \nabla_{\bar{R}_k}h_{\alpha'_\Delta,\alpha'_\Delta}(\bar{R}_k)\right\} \tag{27}$$
$$-\frac{1}{2}\sum_{\lambda\neq\alpha_\Delta}\nabla_{\bar{R}_k}h_{\alpha_\Delta,\lambda}(\bar{R}_k)\left\{\frac{(p_{\alpha_\Delta k}p_{\lambda k}+q_{\alpha_\Delta k}q_{\lambda k})}{(p_{\alpha_\Delta k}^2+q_{\alpha_\Delta k}^2)}\right\}$$
$$-\frac{1}{2}\sum_{\lambda\neq\alpha'_\Delta}\nabla_{\bar{R}_k}h_{\alpha'_\Delta,\lambda}(\bar{R}_k)\left\{\frac{(p'_{\alpha'_\Delta k}p'_{\lambda k}+q'_{\alpha'_\Delta k}q'_{\lambda k})}{(p'^2_{\alpha'_\Delta k}+q'^2_{\alpha'_\Delta k})}\right\}$$

A detailed description of the derivation of these results can be found in references [34, 36].

Using Eq.(24) in Eq.(22) gives the iterative scheme developed in reference [37].

3.2 Implementation

In the iterative scheme outlined above, the evolution of all degrees of freedom has been reduced to classical trajectory propagation that can be efficiently performed. However, the number of terms included in the multiple sums in Eq. (22) grows exponentially with the number of time segments. This exponential growth can be controlled using an importance sampled Monte Carlo approach (see step (3) below). This involves implementing a trajectory surface hopping -like technique similar to that adopted in Ref. [39] and outlined under Eq. (20) above. The Monte Carlo induces hops between density matrix elements, *i.e.* pairs of state labels, and generates dynamical information about both populations (diagonal elements of the density matrix) and coherences (off-diagonal density matrix elements).

To demonstrate the algorithm let us consider two segments. There are five relevant times or time intervals:

(1) $\tau = 0$: The sum over initial quantum states α_0, α_0' is performed explicitly. For each pair of initial quantum states selected, initial conditions for the bath variables are sampled from a probability density derived from the partial Wigner transform $[\hat{\rho}]_W^{\alpha_0,\alpha_0'}$ [25,38]. The initial conditions for the mapping variables are specified by focusing on the occupied states for the forward and backward propagation [33,37]. This initializes the occupied state mapping variables at the phase space point $(p^o_{\alpha_0}, q^o_{\alpha_0}) = (1/\sqrt{2}, 1/\sqrt{2})$, while the unoccupied state mapping variables originate from $(p^u_{\alpha_0}, q^u_{\alpha_0}) = (0,0)$ (a similar set of conditions, with reversed initial momentum, is used to propagate the mapping variables in the backward propagator).

(2) $\tau \in (0, \Delta)$: The forces that evolve the initial conditions specified in (1), $F^{\alpha_\Delta,\alpha'_\Delta}$, depend on the labels of the quantum states at the end of the first time segment. According to Eq. (22) we must sum over all these labels as the starting states for the second propagation leg. Our approach thus generates $\mathcal{N} \times \mathcal{N} = \mathcal{N}_\rho$ trajectories, each governed by a different force $F^{\alpha_\Delta,\alpha'_\Delta}$, for the first propagation leg. The characteristics of the individual trajectories depend on the pair of indexes selected as the final quantum states and on the coupling between the electronic states during the propagation. In particular, if $\alpha_\Delta = \alpha'_\Delta$, Eq. (27) induces evolution on a single diabatic surface (first term on the right hand side) modulated by the coupling matrix elements and the mapping variables (second and third terms). On the other hand, if $\alpha_\Delta \neq \alpha'_\Delta$, the first term in the definition of the force amounts to propagation on a mean surface, while the second and third terms include modulation from couplings and mapping evolution as in the previous situation. Along the trajectories, the polynomial phase weights $r_{\Delta,\alpha_\Delta} r'_{\Delta,\alpha'_\Delta} \exp[-i \int_0^\Delta d\tau(\theta_{\alpha_\Delta}(\tau) - \theta_{\alpha'_\Delta}(\tau))]$ estimate the contributions of the different evolutions to the various density matrix elements. Note that, due to the focusing, initially occupied states start with weight equal to one, while unoccupied states begin with zero weight. These weights change, in the presence of couplings between the electronic

states, due to the amplitude transfer described by the evolution of the mapping variables.

(3) $\tau = \Delta$: At the end of the first segment, the $\mathcal{N}_\rho$ trajectories have moved to different bath and mapping phase space points. In order to propagate the next leg we should, for each final point, propagate a new set of $\mathcal{N}_\rho$ trajectories that experience different forces $F^{\alpha_{2\Delta},\alpha'_{2\Delta}}$. If we were to propagate all these alternatives, the number of trajectories would grow as $\mathcal{N}_\rho^\sigma$ where there are σ trajectory segments. To tame the exponential growth of the number of trajectories we implement a Monte Carlo (MC) procedure that substitutes the brute force sum over the quantum states at the intermediate time points along the propagation with an importance sampling of the different terms contributing to the value of the density matrix at the given time. The approach exploits the observation that during a given trajectory segment many of the quantum amplitudes that start out at zero at the beginning of the segment, remain very small at the end of the segment and this results in small polynomial weights and therefore small contributions to the integrals in Eq. (22). An MC branching procedure, whose probability distribution is based on the change in the quantum amplitudes during the current segment, is then used to decide which term in the double sum over states at the intermediate time is the most important. Thus, at the end of the first segment we compute the magnitudes of the contribution of the particular initial phase space point $(R_0, P_1, \alpha_0, \alpha'_0)$ to the density matrix elements for the new time, Δ, when this point has evolved to the $\mathcal{N}_\rho$ final points $(R_K^{(\alpha_\Delta,\alpha'_\Delta)}, P_K^{(\alpha_\Delta,\alpha'_\Delta)}, \alpha_\Delta, \alpha'_\Delta)$ under the influence of the different forces $F^{\alpha_\Delta,\alpha'_\Delta}$. As described above, the magnitudes of these different contributions are $r_{\Delta,\alpha_\Delta} r'_{\Delta,\alpha'_\Delta}$, so we define the normalized probability distribution

$$M_{\alpha_\Delta,\alpha'_\Delta} = r_{\Delta,\alpha_\Delta} r'_{\Delta,\alpha'_\Delta}/\eta(\Delta) \tag{28}$$

with $\eta(\Delta) = \sum_{\alpha_\Delta,\alpha'_\Delta} r_{\Delta,\alpha_\Delta} r'_{\Delta,\alpha'_\Delta}$. We define the cumulative probabilities $C_{\beta_\Delta,\beta'_\Delta} = \sum_{\alpha_\Delta=1}^{\beta_\Delta} \sum_{\alpha'_\Delta=1}^{\beta'_\Delta} M_{\alpha_\Delta,\alpha'_\Delta}$. A uniform random number ξ on the interval $(0 < \xi < 1)$ is then selected. If the cumulative probability first becomes larger than ξ for indexes $\beta_\Delta = \alpha^*_\Delta$ and $\beta'_\Delta = \alpha'^*_\Delta$, the trajectory segment generated with forces $F^{\alpha^*_\Delta,\alpha'^*_\Delta}$ which evolves the density matrix from (α_0, α'_0) to $(\alpha^*_\Delta, \alpha'^*_\Delta)$ over the current segment is used as the MC sampled representative for the double sum $\sum_{\alpha_\Delta,\alpha'_\Delta}$ in Eq. (22). Since the Monte Carlo branching process is normalized by dividing by $\eta(\Delta)$ we must multiply out this time dependent normalization to preserve the true weight of the sampled trajectory segment. The sampled trajectory segment thus carries a weight and phase factor $\eta(\Delta)\exp[-i\int_0^\Delta d\tau(\theta_{\alpha_\Delta}(\tau) - \theta_{\alpha'_\Delta}(\tau))]$ which multiplies its contributions to the ensemble averages. Once the new pair of quantum state labels $(\alpha^*_\Delta, \alpha'^*_\Delta)$ is selected, the integrals over the corresponding mapping variables are again performed by focusing and this may introduce discontinuities in the polynomial weights and in the forces acting on the bath variables.

(4) $\tau \in (\Delta, 2\Delta)$: The new propagation segment evolves as in (2) with forces $F^{\alpha_{2\Delta},\alpha'_{2\Delta}}$.

(5) $\tau = 2\Delta$: At the final time of the propagation, the "measurement" time, the overall weight of each contribution to the Monte Carlo in the initial conditions and state labels is computed. In the case of two segments, this is given by $\eta(\Delta)\exp[-i\int_0^{\Delta} d\tau(\theta_{\alpha_\Delta}(\tau)-\theta_{\alpha'_\Delta}(\tau))]r_{2\Delta,\alpha_{2\Delta}}r'_{2\Delta,\alpha'_{2\Delta}}\exp[-i\int_{\Delta}^{2\Delta} d\tau(\theta_{\alpha_{2\Delta}}(\tau)-\theta_{\alpha'_{2\Delta}}(\tau))]$. The different elements of the evolved density matrix can be evaluated by averaging these contributions over a set of repetitions of the Monte Carlo (and molecular dynamics) procedure described in (1)-(4).

The approach outlined above can be immediately generalized to the case of n propagation segments simply by iterating points (3) and (4). In this case, the weight at the final time $n\Delta$ becomes

$$\Omega_n = \left\{\prod_{k=1}^{n-1}\eta(k\Delta)\exp[-i\int_{(k-1)\Delta}^{k\Delta} d\tau(\theta_{\alpha_{k\Delta}}(\tau)-\theta_{\alpha'_{k\Delta}}(\tau))]\right\} \times r_{n\Delta,\alpha_{n\Delta}}r'_{n\Delta,\alpha'_{n\Delta}}\exp[-i\int_{(n-1)\Delta}^{n\Delta} d\tau(\theta_{\alpha_{n\Delta}}(\tau)-\theta_{\alpha'_{n\Delta}}(\tau))] \quad (29)$$

The combination of these phase factors and the weights that come from renormalizing after implementing the Monte Carlo density matrix element sampling lead to the same sorts of statistical convergence problems observed with the QCL implementation. Filtering techniques have not been implemented in these ILDM calculations so far, however, an approach inspired by the method outlined at the end of section 2 could be used to mitigate these convergence difficulties that can be particularly serious at longer times.

4 Model Simulations

In this section we present results using the two approaches described in the previous sections: the Trotter factorized QCL (TQCL), and iterative linearized density matrix (ILDM) propagation schemes, to study the spin-boson model consisting of a two level system that is bi-linearly coupled to a bath with M_h harmonic modes. This popular model of a quantum system embedded in an environment is described by the following general hamiltonian:

$$\hat{H} = \frac{1}{2}\sum_{j=1}^{M_h}(\hat{P}_j^2+\omega_j^2\hat{R}_j^2)+\epsilon\hat{\sigma}_z+\hat{\sigma}_z\sum_{j=1}^{M_h}g_j\hat{R}_j-\Omega\hat{\sigma}_x \quad (30)$$

where mass scaled coordinates have been used for the bath. We choose the couplings, g_j, and mode frequencies, ω_j, to be consistent with the exponentially truncated ohmic spectral density model for which the spectral density is $J(\omega) = \xi\omega e^{-\omega/\omega_c}$ [34,39], where ξ is the friction or Kondo parameter and ω_c is the peak frequency in the spectral density. All the calculations outlined below

employ 20 bath modes coupled to the two level spin system. In this model hamiltonian Ω is the off-diagonal coupling strength between the two diabatic states of the quantum subsystem, and the parameter ϵ controls the asymmetry in energy between these states. This term acts like a "driving force" when the spin-boson model is applied to study charge transfer reactions in solution.

As noted earlier, the fundamental equations of the QCL dynamics approach are exact for this model, however, in order to implement these equations in the approach detailed in section 2 the momentum jump approximation of Eq.(14) is made in addition to the Trotter factorization of Eq.(12). Both approximations become more accurate as the size of the time step δ is reduced. Consequently, the results presented below primarily serve as tests of the validity and utility of the momentum-jump approximation. For a discussion of other simulation schemes for QCL dynamics see Ref. [21] in this volume. The linearized approximate propagator is not exact for the spin-boson model. However when used as a short time approximation for iteration as outlined in section 3 the approach can be made accurate with a sufficient number of iterations [37].

Figure 1 presents results for the time dependence of the diabatic state population difference, $\bar{B}(t) = \langle \sigma_z \rangle(t)$, for the symmetric spin-boson model ($\epsilon = 0$) for two interesting sets of conditions corresponding to low temperature-low friction, and intermediate temperature-high friction cases (see captions for details). Results from calculations employing the approximate methods outlined above are compared with exact benchmark results. Generally the agreement between results from the different approaches is quite reasonable though some systematic differences are apparent. The results obtained with the TQCL approach for the low temperature - low friction conditions show coherent population oscillations that have a slightly higher frequency and a slower decay than those obtained with the ILDM propagation scheme which generally show very good agreement with the exact results under these conditions. Much smaller differences between the various results are found at higher temperatures and frictions. The results presented here are converged with Trotter timestep (TQCL), number of attempted hops (ILDM), and ensemble size. Given that the QCL formulation should be exact for the spin-boson model the systematic differences observed in the low temperature-low friction results for TQCL approach can be attributed to the momentum-jump approximation that is made when implementing the formulation. This approximation seems to have the most noticeable effect under weak coupling conditions. If simulations of QCL dynamics for these system parameters are carried out using a mapping hamiltonian basis, the results are indistinguishable from exact quantum dynamics [40]. This again suggests that the small discrepancies are due to the use of the momentum-jump approximation.

The asymmetric spin boson model presents a significantly more challenging non-adiabatic condensed phase test problem due to the asymmetry in forces from the different surfaces. Approximate mean field methods, for example, will fail to reliably capture the effects of these different forces on the dynamics.

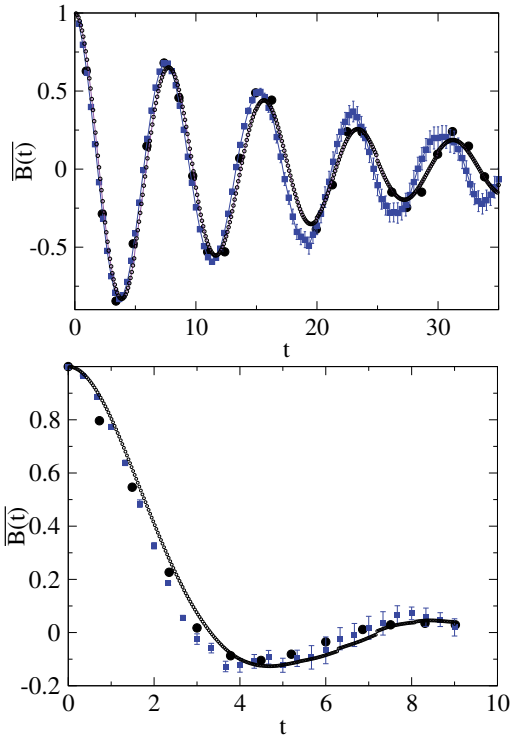

Fig. 1: Plots of $\bar{B}(t)$ = population difference = $\langle \sigma_z \rangle(t)$ for the symmetric spin-boson ($\epsilon = 0$) as functions of time: Exact quantum results from Ref. [41] (solid circles), TQCL algorithm (squares), ILDM propagation (open circles). Upper panel presents results for low temperature, weak system-bath coupling case: $\beta = 12.5$, $\xi = 0.09$ and $\Omega = 0.4$. Lower panel presents exact quantum results from Ref. [42] (solid circles), TQCL algorithm (squares), and ILDM propagation (open circles) for intermediate temperature and strong system-bath coupling: $\beta = 3$, $\xi = 0.5$ and $\Omega = 0.333$.

In Fig. 2 we compare results using $\epsilon = 0.4$ for the two mixed quantum-classical methods outlined in this chapter with exact results obtained from MCTDH wavepacket dynamics calculations. To make a reliable comparison the approximate finite temperature calculations were performed at very low temperatures ($\beta = 25$), though a product of ground state wave functions for the independent harmonic oscillator modes could have been used to make the initial conditions identical to those used in the MCTDH calculations.

From the upper panel in Fig. 2 we see that both the ILDM, and TQCL results reproduce those obtained from MCTDH wavepacket propagation. The ILDM calculations were run with 2 attempted hops per time unit and results

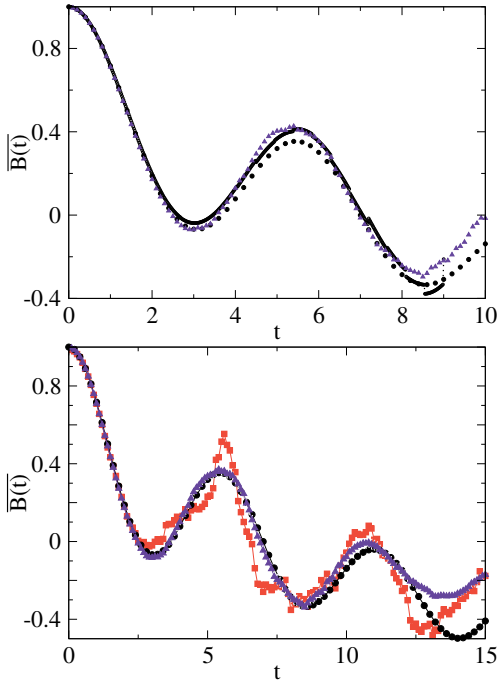

Fig. 2: $\bar{B}(t) = \langle \sigma_z \rangle(t)$ versus time for the asymmetric spin-boson model with $\beta = 25$, $\xi = 0.13$ and $\Omega = 0.4$, $\epsilon = 0.4$. (Top) Comparison of exact quantum results (filled circles), ILDM simulations (small open circles), and QCL dynamics (filled triangles). Both ILDM and QCL simulations were carried out for an ensemble of 2×10^6 trajectories and no filters are employed. (Bottom) Convergence of TQCL dynamics with ensemble size: 2×10^4 (filled squares) and 1×10^6 (filled triangles). Exact quantum results (filled circles). A filter parameter of $Z = 500$ is used for these calculations .

are presented for an ensemble of $\mathcal{N} = 2 \times 10^6$ trajectories. Beyond this time, without using a filtering approach the statistical noise in the ILDM calculations becomes overwhelming. Convergence with ensemble size for the TQCL approach using a small value of the filter cutoff (Z=500) is explored in the other curves presented in the lower panel.

The nature of the quantum coherent dynamics in the system can be investigated by computing the off-diagonal elements of the quantum subsystem density matrix obtained by tracing over the bath degrees of freedom, $\rho_{12}(t) = \int dRdP\rho_{12}(R, P, t)$. The time dependence of the real and imaginary parts of $\rho_{12}(t)$ are shown in Fig. 3. The off-diagonal elements of the reduced density matrix computed with the two different mixed quantum classical ap-

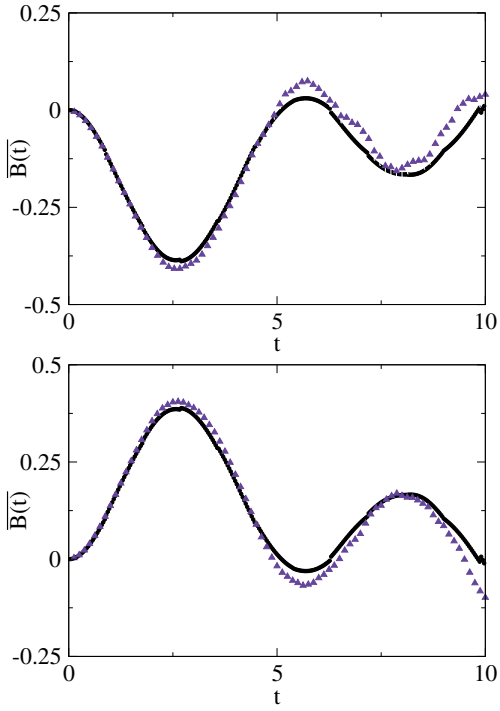

Fig. 3: Real (top) and imaginary (bottom) parts of $\rho_{12}(t)$ versus time for the same system parameters as in Fig. 2. Small circles, ILDM simulations; triangles, QCL dynamics. In both cases 10^6 trajectories were used to obtain the results.

proaches agree to within the statistical uncertainty of the calculations. One of the important properties of these methods that distinguishes them from many other mixed quantum classical approaches is their ability to treat these coherence terms with out making *ad hoc* approximations. Traditional surface hopping trajectory approaches [1, 3], for example, either completely neglect decoherence, or incorporate its effects by damping out off-diagonal elements of the reduced density matrix with some phenomenological exponential decoherence time. In contrast, both the QCL and ILDM propagation schemes include decoherence effects in a completely *ab initio* fashion by accumulating interfering contributions to the off-diagonal density matrix elements over the ensemble of phase factor weighted trajectories. In general the reliable computation of such interference effects is numerically intensive as large ensembles are required to accurately add the interfering contributions. The results in Fig. 3 for the asymmetric spin-boson system considered here show long lived coherent oscillation of the off-diagonal elements for these conditions, with

no evidence of exponential decay assumed in the phenomenological models of condensed phase decoherence processes. The dephasing is at least as long lived as the population relaxation dynamics for this model system.

5 Conclusion

The two quantum-classical dynamical schemes discussed in this Chapter provide ways to investigate the dynamics of large, many-body systems where quantum degrees of freedom are coupled to an environment. The results presented here have shown that both schemes yield good agreement with exact calculations for the symmetric and asymmetric spin-boson models for a wide range of system parameters. In particular coherences are accurately described. Our simulation results have documented the performances of the algorithms with respect to quantities such as the number of trajectories in the ensemble needed to obtain good results, the use of filters and the utility of the momentum-jump approximation. The QCL formulation can be shown to be exact for the spin-boson model so our comparison with numerically exact results for this model tests only the approximations in the implementation scheme. Calculations on models for which this formulation is not exact would offer more challenging tests and may provide a more stringent basis for comparing the different methods in future studies.

While the two methods are, at face value, quite different in the ways in which full quantum dynamics is reduced to quantum-classical dynamics, there are common elements in the manner in which they are simulated. The Trotter-based scheme for QCL dynamics makes use of the adiabatic basis and is based on surface-hopping trajectories where transitions are sampled by a Monte Carlo scheme that requires reweighting. Similarly, ILDM calculations make use of the mapping hamiltonian basis and also involve a similar Monte Carlo sampling with reweighting of trajectories in the ensemble used to obtain the expectation values of quantum operators.

As noted above, however, the theoretical frameworks of the two approaches appear quite different. This is a common situation in mixed quantum-classical simulations: many methods exist, and they may have very different ranges of applicability. A systematic assessment of differences and similarities, of the accuracy of various approximations, and in general of their relative merits presents a significant challenge. Investigating the relationships between different methods, however, can provide a better understanding of the nature, advantages and limitations of mixed quantum-classical methods in general, and may lead to a more firm theoretical foundation on which to base the development of new methods, as well as more efficient algorithms for implementation.

The two methods described in this Chapter are good candidates for such comparative investigation. They are both derived employing well-defined approximations to exact quantum expressions and they can be used to study

the same set of, general, observables. Furthermore, it has already been shown that, for some choices of the quantum sub-system basis set, QCL can be obtained via a linearization procedure that shares some similarities with the linerization used to derive the ILDM propagation [4]. Future work will investigate the theoretical connections between the methods that, as a first step, we have compared in their existing formulations in this Chapter.

Acknowledgements

The research of RK was supported in part by a grant from the Natural Sciences and Engineering Research Council of Canada. DFC acknowledges support for this research from the US National Science Foundation under grant number CHE-0616952, as well as his Stokes Professorship from Science Foundation Ireland, and funding from University College Dublin. A grant from Ministero dell'Ambiente e della Tutela del Territorio e del Mare is acknowledged by SB and GC.

References

1. Tully JC. Mixed quantum-classical dynamics: mean-field and surface-hopping. In *Classical and Quantum Dynamics in Condensed Phase Simulations*, ed. B.J. Berne, G. Ciccotti, D.F. Coker. Chapter 21. Singapore: World Scientific, 1998.
2. For a review with references to the literature on this topic, see, R. Kapral. Progress in the theory of mixed quantum-classical dynamics. *Annu. Rev. Phys. Chem.*, 57:129, 2006.
3. J. C. Tully. Molecular dynamics with electronic transitions. *J. Chem. Phys.*, 93(2):1061, 1990.
4. Q. Shi and E. Geva. A derivation of the mixed quantum-classical Liouville equation from the influence functional formalism. *J. Chem. Phys.*, 121(8):3393, 2004.
5. S. Nielsen, R. Kapral, and G. Ciccotti. Statistical mechanics of quantum-classical systems. *J. Chem. Phys.*, 115(13):5805, 2001.
6. H. Kim and R. Kapral. Transport properties of quantum-classical systems. *J. Chem. Phys.*, 122:214105, 2005.
7. G. Ciccotti, D.F. Coker, and R. Kapral, *Quantum statistical dynamics with trajectories*, in *Quantum dynamics of complex molecular systems*, David Micha and Irene Burghardt, Chemical Physics series vol. 83, (Springer, Berlin), p. 275, 2006.
8. H. Kim and R. Kapral. Nonadiabatic quantum-classical reaction rates with quantum equilibrium structure. *J. Chem. Phys.*, 123:194108, 2005.
9. R. Grunwald, H. Kim and R. Kapral. Surface hopping and decoherence with quantum equilibrium structure. *J. Chem. Phys.*, 128:164110, 2008.
10. G. Hanna and R. Kapral. Quantum-classical Liouville dynamics of nonadiabatic proton transfer. *J. Chem. Phys.*, 122(24):244505, 2005.

11. G. Hanna and R. Kapral. Quantum-classical Liouville dynamics of proton and deutron transfer rates in a hydrogen bonded complex. *J. Chem. Phys.*, 128:164520, 2008.
12. R. Kapral and G. Ciccotti. Mixed quantum-classical dynamics. *J. Chem. Phys.*, 110:8919, 1999.
13. I. V. Aleksandrov. The statistical dynamics of a system consisting of a classical and a quantum subsystem. *Z. Naturforsch.*, 36:902, 1981.
14. V. I. Gerasimenko. Correlation-less equations of motion of quantum-classical systems. *Repts. Acad. Sci. Ukr.SSR*, (10):64, 1981.
15. V. I. Gerasimenko. Dynamical equations of quantum-classical systems. *Theor. Math. Phys.*, 50:49, 1982.
16. W. Boucher and J. Traschen. Semiclassical physics and quantum fluctuations. *Phys. Rev. D*, 37(12):3522, 1988.
17. W.Y. Zhang and R. Balescu. Statistical mechanics of a spin polarized plasma. *J. Plasma Physics*, 40:199, 1988.
18. Y. Tanimura and S. Mukamel. Multistate quantum Fokker–Planck approach to nonadiabatic wave packet dynamics in pump–probe spectroscopy. *J. Chem. Phys.*, 101:3049, 1994.
19. C. C. Martens and J. Y. Fang. Semiclassical-limit molecular dynamics on multiple electronic surfaces. *J. Chem. Phys.*, 106(12):4918, 1997.
20. I. Horenko, C. Salzmann, B. Schmidt, and C. Schutte. Quantum-classical liouville approach to molecular dynamics: Surface hopping gaussian phase-space packets. *J. Chem. Phys.*, 117(24):11075, 2002.
21. R. Grunwald, A. Kelly and R. Kapral. Quantum dynamics in almost classical environments. *this volume* , 2009.
22. D. Mac Kernan, G. Ciccotti, and R. Kapral. Trotter-based simulation of quantum-classical dynamics. *J. Phys. Chem. B*, 112:424, 2008.
23. R. Kapral and G. Ciccotti, *A Statistical Mechanical Theory of Quantum Dynamics in Classical Environments*, in *Bridging Time Scales: Molecular Simulations for the Next Decade*, eds. P. Nielaba, M. Mareschal, G. Ciccotti, (Springer, Berlin), p. 445, 2002.
24. R. Hernandez and G. Voth. Quantum time correlation functions and classical coherence. *Chem. Phys.*, 223:243, 1998.
25. J.A. Poulsen and G. Nyman and P.J. Rossky. Practical evaluation of condensed phase quantum correlation functions: A Feynman-Kleinert variational linearized path integral method. *J. Chem. Phys.*, 119:12179, 2003.
26. Q. Shi and E. Geva. Vibrational energy relaxation in liquid oxygen from a semiclassical molecular dynamics simulation. *J. Phys. Chem. A*, 107:9070, 2003.
27. Q. Shi and E. Geva. Semiclassical theory of vibrational energy relaxation in the condensed Phase. *J. Phys. Chem. A*, 107:9059, 2003.
28. Q. Shi and E. Geva. Nonradiative electronic relaxation rate constants from approximations based on linearizing the path-integral forward-backward action. *J. Phys. Chem. A*, 108:6109, 2004.
29. X. Sun and W.H. Miller. Semiclassical initial value representation for electronically nonadiabatic molecular dynamics. *J. Chem. Phys.*, 106:6346, 1997.
30. G. Stock and M. Thoss. Semiclassical description of nonadiabatic quantum dynamics. *Phys. Rev. Lett.*, 78:578, 1997.
31. G. Stock and M. Thoss. Mapping approach to the semiclassical description of nonadiabatic quantum dynamics. *Phys. Rev. A*, 59:64, 1999.

32. S. Bonella and D.F. Coker. A semi-classical limit for the mapping Hamiltonian approach to electronically non-adiabatic dynamics. *J. Chem. Phys.*, 114:7778, 2001.
33. S. Bonella and D.F. Coker. Semi-classical implementation of the mapping Hamiltonian approach for non-adiabatic dynamics: Focused initial distribution sampling. *J. Chem. Phys.*, 118:4370, 2003.
34. S. Bonella and D.F. Coker. LAND-map, a linearized approach to nonadiabatic dynamics using the mapping formalism. *J. Chem. Phys.*, 122:194102, 2005.
35. S. Bonella, D. Montemayor, and D.F. Coker. Linearized path integral approach for calculating nonadiabatic time correlation functions. *Proc. Natl. Acad. Sci.*, 102:6715, 2005.
36. D.F. Coker and S. Bonella, *Linearized path integral methods for quantum time correlation functions*, in *Computer simulations in condensed matter: From materials to chemical biology*, eds. M. Ferrario and G. Ciccotti and K. Binder, Lecture Notes in Physics 703, (Springer-Verlag, Berlin), p. 553, 2006.
37. E. Dunkel, S. Bonella, and D.F. Coker. Iterative linearized approach to nonadiabatic dynamics. *J. Chem. Phys.*, 129:114106, 2008.
38. Z. Ma and D.F. Coker. Quantum initial condition sampling for linearized density matrix dynamics: Vibrational pure dephasing of iodine in krypton matrices. *J. Chem. Phys.*, 128:244108, 2008.
39. D. Mac Kernan, G. Ciccotti, and R. Kapral. Surface-hopping dynamics of a spin-boson system. *J. Chem. Phys.*, 116(6):2346, 2002.
40. H. Kim, A. Nassimi, and R. Kapral. Quantum-classical Liouville dynamics in the mapping basis. *J. Chem. Phys.*, 129:084102, 2008.
41. D. E. Makarov and N. Makri, *Chem. Phys. Lett.*, 221:482, 1994.
42. K. Thompson and N. Makri. Rigorous forward-backward semiclassical formulation of many-body dynamics. *Phys. Rev. E*, 59(5):R4729, 1999.

Do We Have a Consistent Non-Adiabatic Quantum-Classical Statistical Mechanics?

Giovanni Ciccotti, Sergio Caprara, and Federica Agostini

[1] CNISM Unità Roma 1 and Università degli Studi di Roma "La Sapienza", piazzale Aldo Moro 2, I-00185 Roma, Italy, giovanni.ciccotti@roma1.infn.it
[2] Università degli Studi di Roma "La Sapienza", piazzale Aldo Moro 2, I-00185 Roma, Italy, sergio.caprara@roma1.infn.it
[3] Università degli Studi di Roma "La Sapienza", piazzale Aldo Moro 2, I-00185 Roma, Italy, federica.agostini@roma1.infn.it

Abstract. A rigorous derivation of quantum-classical equations of motion is still lacking. The framework proposed so far to describe in a consistent way the dynamics of a mixed quantum-classical system using systematic approximations have failed. A recent attempt to solve the inconsistencies of quantum-classical *approximated* methods by introducing a group-theoretical approach is discussed in detail. The new formulation which should restore the consistency of the proposed quantum-classical dynamics and statistical mechanics will be shown to produce, instead, a purely classical description. In spite of that, the discussed approach remains interesting since it could produce non-trivial formulations.

1 Introduction

The formulation of a consistent scheme to derive mixed quantum-classical equations of motion is a relevant goal both from a purely theoretical point of view and for practical (e.g., computational) applications.

Although the constituents of matter are ultimately quantum objects, in many circumstances the behaviour of nuclei is satisfactorily described by the laws of classical mechanics. This is the reason why classical molecular dynamics is a formidable tool to derive the statistical properties of macroscopic bodies. However, there are situations in which the classical description is not suitable, because at least some degrees of freedom behave according to the laws of quantum mechanics. Examples are given by the motion of light particles in a system composed by heavier particles (e.g., an electron or a proton diffusing in a condensed phase system), or the interaction of spin variables with the surrounding environment. In this case, the alternative route of a full quantum dynamical approach is usually made arduous by the large number of degrees of freedom: the solution of the time-dependent Schrödinger equation

I. Burghardt et al. (eds.), *Energy Transfer Dynamics in Biomaterial Systems*, Springer Series in Chemical Physics 93, DOI 10.1007/978-3-642-02306-4_14,

for the full many-body wavefunction of a macroscpic body is not computationally achievable.

The question then arises if a convenient mixed quantum-classical description exists, which allows to treat as quantum objects only the (small number of) degrees of freedom whose dynamics cannot be described by classical equations of motion. Apart in the limit of adiabatic dynamics, the question is open and a coherent derivation of a consistent mixed quantum-classical dynamics is still lacking. All the methods proposed so far to derive a quantum-classical dynamics, such as the linearized path integral approach [2, 6, 7], the coupled Bohmian phase space variables dynamics [3, 4, 9] or the quantum-classical Liouville representation [11, 17–19], are based on approximations and typically fail to satisfy some properties that are expected to hold for a consistent mechanics [5, 19].

Let us briefly discuss, as an example of inconsistency, the case of the quantum-classical Liouville representation [19]. The starting point of such a derivation is the Liouville-von Neumann equation of motion for the evolution of the density matrix $\hat{\rho}$,

$$\frac{\partial \hat{\rho}}{\partial t} = -\frac{i}{\hbar}\left[\hat{\mathcal{H}}, \hat{\rho}\right] \tag{1}$$

where $\hbar$ is the reduced Planck constant, $\hat{\mathcal{H}}$ is the hamiltonian operator, and $[\,\cdot\,,\,\cdot\,]$ is the commutator. The hamiltonian $\hat{\mathcal{H}}$ can be generically written as

$$\hat{\mathcal{H}} = \frac{\hat{P}^2}{2M} + \frac{\hat{p}^2}{2m} + \hat{V}\left(\hat{r}, \hat{R}\right) = \frac{\hat{P}^2}{2M} + \hat{h}$$

where we assumed that the system can be divided into two interacting subsystems, respectively composed by n light particles of mass m, with phase-space coordinates $(r, p) = (r_1, \ldots, r_n, p_1, \ldots, p_n)$ and by N heavy particles of mass M ($M \gg m$) with phase-space coordinates $(R, P) = (R_1, \ldots, R_N, P_1, \ldots, P_N)$.

To exploit the classical nature of the heavier particles, it is convenient to introduce the partial Wigner transform [10] for the density matrix,

$$\hat{\rho}_w(R, P) = \left(\frac{1}{2\pi\hbar}\right)^{3N} \int dz\, e^{iPz/\hbar} \left\langle R - \frac{z}{2}\right| \hat{\rho} \left| R + \frac{z}{2}\right\rangle \tag{2}$$

and for a generic operator $\hat{A}$,

$$\hat{A}_w(R, P) = \int dz\, e^{-iPz/\hbar} \left\langle R + \frac{z}{2}\right| \hat{A} \left| R - \frac{z}{2}\right\rangle. \tag{3}$$

The last expression allows us to write the partial Wigner transform of the hamiltonian

$$\hat{\mathcal{H}}_w\,(R, P) = \frac{P^2}{2M} + \frac{\hat{p}^2}{2m} + \hat{V}\,(\hat{r}, R) = \frac{P^2}{2M} + \hat{h}_w(R)$$

which acts as an operator on the quantum degrees of freedom, through the dependence on $\hat{r}$ and $\hat{p}$, and is a function of the classical phase-space variables (R, P).

Performing the partial Wigner transform in eq.(1) and applying the rule for the partial Wigner transform of the product of two operators [10]

$$\left(\hat{A}\hat{B}\right)_w = \hat{A}_w\left(R,P\right) e^{\frac{\hbar\Lambda}{2i}} \hat{B}_w\left(R,P\right) \tag{4}$$

we obtain

$$\frac{\partial\hat{\rho}_w}{\partial t} = -\frac{i}{\hbar}\left[\hat{\mathcal{H}}_w(R,P)e^{\frac{\hbar\Lambda}{2i}}\hat{\rho}_w(R,P) - \hat{\rho}_w(R,P)e^{\frac{\hbar\Lambda}{2i}}\hat{\mathcal{H}}_w(R,P)\right]. \tag{5}$$

The operator Λ is given by $\Lambda \equiv \overleftarrow{\nabla}_P\overrightarrow{\nabla}_R - \overleftarrow{\nabla}_R\overrightarrow{\nabla}_P = -\{\cdot,\cdot\}$, where $\{\cdot,\cdot\}$ are the Poisson brackets with respect to the classical phase-space variables (R, P) [10].

A quantum-classical approximation for eq.(5) can be obtained by expanding the exponential operator in a power series of the reduced Planck constant $\hbar$ (or, equivalently, in a power series of $(m/M)^{1/2}$ [11])

$$e^{\frac{\hbar\Lambda}{2i}} \simeq 1 + \frac{\hbar\Lambda}{2i} + \mathcal{O}(\hbar^2). \tag{6}$$

Using this approximation, eq.(5) becomes [5, 11]

$$\frac{\partial\hat{\rho}_w}{\partial t} = -\frac{i}{\hbar}\left[\hat{\mathcal{H}}_w, \hat{\rho}_w\right] + \frac{1}{2}\left(\left\{\hat{\mathcal{H}}_w, \hat{\rho}_w\right\} - \left\{\hat{\rho}_w, \hat{\mathcal{H}}_w\right\}\right) \equiv -\left(\hat{\mathcal{H}}_w, \hat{\rho}_w\right). \tag{7}$$

However, the quantum-classical brackets $(\cdot,\cdot)$ introduced in eq.(7) are not Lie brackets [19], because they do not satisfy properties that are instead satisfied by the commutator and the Poisson brackets (respectively, quantum and classical Lie brackets), e.g., the Jacobi identity.

Indeed, the product $\left(\hat{A}\hat{B}\hat{C}\right)_w$ is associative but, if the exponential operator is linearized, we obtain

$$\left[\left(\hat{A}_w\left(1+\frac{\hbar\Lambda}{2i}\right)\hat{B}_w\right)\left(1+\frac{\hbar\Lambda}{2i}\right)\hat{C}_w\right] =$$
$$\left[\hat{A}_w\left(1+\frac{\hbar\Lambda}{2i}\right)\left(\hat{B}_w\left(1+\frac{\hbar\Lambda}{2i}\right)\hat{C}_w\right)\right] + \mathcal{O}(\hbar^2).$$

As a consequence, the Jacobi identity is no longer valid, and instead

$$\left(\left(\hat{A}_w, \hat{B}_w\right), \hat{C}_w\right) + \left(\left(\hat{C}_w, \hat{A}_w\right), \hat{B}_w\right) + \left(\left(\hat{B}_w, \hat{C}_w\right), \hat{A}_w\right) = \mathcal{O}(\hbar).$$

An immediate and undesirable consequence of the violation of the Jacobi identity is that the quantum-classical brackets between two constants of motion

are no longer a constant of motion, as it would instead be expected within a consistent formulation of quantum-classical dynamics.

Another important property which is missed by the approximate quantum-classical mechanics based on the Liouville representation is the time traslational invariance of the response functions at equilibrium, i.e., given any two operators $\hat{A}$ and $\hat{B}$,

$$\left\langle \left(\hat{B}_w^\dagger, \hat{A}_w(t) \right) \right\rangle_{\text{eq}} \neq \left\langle \left(\hat{B}_w^\dagger(\tau), \hat{A}_w(t+\tau) \right) \right\rangle_{\text{eq}}, \tag{8}$$

where the subscript eq indicates that the averages are calculated at equilibrium. As a consequence of non-associativity, the Kubo formula [16] holds only approximately, since

$$\left(\hat{\rho}_w, \hat{B}_w^\dagger \right) = \int_0^\beta d\lambda \, \hat{\rho}_w \left(1 + \frac{\hbar \Lambda}{2i} \right) \dot{\hat{B}}_w^\dagger(-i\hbar\lambda) + \mathcal{O}(\hbar).$$

The inconsistencies arising from the formulation of quantum-classical mechanics based on eq.(7) are at the origin of important complications within numerical implementations of the resulting quantum-classical molecular dynamics.

Recently, a formal derivation of a consistent quantum-classical mechanics has been proposed [12–14, 20], which is based on a group-theoretical formulation of quantum and classical mechanics. The quantum-classical brackets introduced thereby are easily shown to obey the Jacobi identity. Therefore, the resulting quantum-classical mechanics has attracted a great interest, and some effort was devoted to clarify the meaning of the quantum-classical brackets and of the coupling between the quantum and the classical subsystems. In the formal derivation, the two subsystems were equipped with two different values of the Planck constant, h_1 and h_2. The quantum-classical limit was then formally obtained as the limit $h_1 \to h$ and $h_2 \to 0$. However, a deeper glance at the formal derivation allowed us to put in evidence the purely classical nature of the assumedly quantum-classical equations of motion [1]. The present work is devoted to a pedagogical derivation of this result. This is not without interest, since the group-theoretical approach may provide the tools to introduce more successful schemes. We failed until now, but our failure is far from conclusive.

The plan of the paper is the following. In section 2 we introduce the elements at the basis of the Heisenberg group representation representation theory [12–14,20] that are needed to understand the alternative group-theoretical formulation of quantum mechanics. In section 3 the Heisenberg representation of quantum mechanics (with the time dependence transferred from the vectors of the Hilbert space to the operators) is used to introduce quantum observables and quantum Lie brackets within the group-theoretical formalism described in the previous section. In section 4 classical mechanics is obtained by taking the formal limit $h \to 0$ of quantum observables and brackets to obtain their classical counterparts. Section 5 is devoted to the derivation of

the mixed quantum-classical mechanics, as presented in Ref. [15], and to the proof that the proposed ansatz brings to a purely classical evolution [1]. A deeper discussion concerning this proof is contained in section 6. Throughout the paper we indicate with h the Planck constant and with $\hbar$ the reduced Planck constant, such that $h = 2\pi\hbar$.

2 Heisenberg group description

In this section, we provide a succinct survey of the definitions and results of group theory required for a group-theoretical formulation of quantum and classical mechanics, which are the objects of the following sections.

A group $\mathbb{G}$ is a set of elements g equipped with an application $\mathbb{G} \times \mathbb{G} \to \mathbb{G}$ (called *multiplication*) such that $\forall g_1, g_2 \in \mathbb{G}$ also $g_1 g_2 \in \mathbb{G}$, and for which the following properties hold:

associativity	$(g_1 g_2)\, g_3 = g_1\, (g_2 g_3) \;\; \forall\, g_1, g_2, g_3 \in \mathbb{G}$
existence of the identity	$\exists\, e \in \mathbb{G}$ such that $eg = ge = g, \;\forall\, g \in \mathbb{G}$
existence of the inverse	$\forall\, g \in \mathbb{G}\, \exists\, g^{-1} \in \mathbb{G}$ such that $g^{-1} g = g g^{-1} = e.$

The definition is very abstract. In general, the nature of a group $\mathbb{G}$ can be understood by studying its *representations*, $\rho(g)$, by linear operators acting on vector spaces V of various dimensions. The formulation of quantum mechanics we deal with requires that the elements of the group are associated with linear operators acting on a vector Hilbert space V, since we need a one to one correspondence between group elements and the linear operators of the chosen representation. The application $\rho(g)$ defines then an isomorphism of the group. In particular, $\rho(e) = \hat{I}$, where $\hat{I}$ is the identity operator acting on V.

The representation is called *unitary* if $\rho(g)$ is a unitary operator for all g. The representation $\rho(g)$ is called *irreducible* if a non-trivial invariant subspace V_1 does not exist[4]. We are now ready to introduce the Heisenberg group, which is the main object of this section.

The Heisenberg group $\mathbb{H}^n$ is defined by the nature of its elements g and by the law which defines the *multiplication* between group elements. Each element is a set of $2n + 1$ variables

$$g \equiv (s, x, y) \quad \text{where} \quad s \in \mathbb{R};\, x, y \in \mathbb{R}^n.$$

The variables carry physical units: s has units of the inverse of an action $\left[tm^{-1}l^{-2}\right]$, x has units of the inverse of a length $\left[l^{-1}\right]$; y has units of the inverse of a momentum $\left[tm^{-1}l^{-1}\right]$. The multiplication law is[5]

[4] An invariant subspace of the representation $\rho(g)$ is a subspace V_1 of the Hilbert space V such that for all $g \in \mathbb{G}$ and $\psi \in V_1$, $\rho(g)\psi \in V_1$.

[5] The products xy' and $x'y$ are understood as scalar products in $\mathbb{R}^n$. This convention for products involving the variables x and y will be maintained henceforth.

$$gg' = (s,x,y)(s',x',y') = \left(s+s'+\frac{1}{2}(xy'-x'y), x+x', y+y'\right). \quad (9)$$

It is therefore evident that $\mathbb{H}^n$ is a non-abelian group (i.e., $gg' \neq g'g$). The identity and inverse elements are $e = (0,0,0)$ and $g^{-1} = (-s,-x,-y)$, respectively, as it is easily proved using eq.(9).

The formulation of quantum mechanics requires a representation of the Heisenberg group on the Hilbert space $L_2(\mathbb{R}^n)$ spanned by the functions $\psi(\xi)$ where the variable ξ indicates a $n-$dimensional vector $\xi = (\xi_1 \ldots, \xi_n)$ whose elelments have physical units of a length $[l]$. Let us first introduce the set of operators, generators of the Lie group $\mathbb{H}^n$, $\hat{I}$, $\hat{X}_j$, and $h\hat{D}_j$ $(j = 1, \ldots, n)$ satisfying the commutation relation

$$2\pi\left[\hat{X}_j, h\hat{D}_k\right] = ih\delta_{jk}.$$

The operators $\hat{I}$, $\hat{X}_j$, and $h\hat{D}_j$ are identified with the identity, position and momentum operators on $L_2(\mathbb{R}^n)$, respectively. Their action is specified as follows

$$\begin{array}{rcl} \hat{I}\psi(\xi) & = & \psi(\xi) \\ \hat{X}_j\psi(\xi) & = & \xi_j\psi(\xi) \\ h\hat{D}_j\psi(\xi) & = & -i\hbar\dfrac{\partial}{\partial\xi_j}\psi(\xi). \end{array} \quad (10)$$

These operators are used to define the isomorphism $\rho(g)$ which characterizes the unitary irreducible and infinite-dimensional representation of $\mathbb{H}^n$, through the *exponential map*

$$\rho_h(g) = e^{2\pi i\left(-hs\hat{I}+yh\hat{D}+x\hat{X}\right)}, \quad (11)$$

where we made explicit that the representation of the Heisenberg group has a parametric dependence on the Planck constant. The set of operators $\rho_h(g)$ preserves the multiplication law in eq.(9), i.e.,

$$\rho_h(g)\rho_h(g') = \rho_h(gg'), \quad (12)$$

and $\rho_h(e) \equiv \rho_h(0,0,0) = \hat{I}$. The proof of eq.(12) will be left to the reader. It requires the use of the Weyl identity[6]

$$e^{\hat{A}+\hat{B}} = e^{\hat{A}}e^{\hat{B}}e^{-\frac{1}{2}[\hat{A},\hat{B}]} \quad (13)$$

[6] The proof of eq.(12) is obtained starting from Weyl identity, by showing that the r.h.s.,

$$e^{2\pi i\left(-hs\hat{I}+yh\hat{D}+x\hat{X}\right)}e^{2\pi i\left(-hs'\hat{I}+y'h\hat{D}+x'\hat{X}\right)} = e^{2\pi i\left[-h(s+s')\hat{I}+(y+y')h\hat{D}+(x+x')\hat{X}\right]} e^{-2\pi^2\sum_{j,k}\left[h\hat{D}_j,\hat{X}_k\right](x'_k y_j - x_k y'_j)},$$

is exactly $\rho_h(gg')$.

which holds whenever the commutator of two operators $\hat{A}$ and $\hat{B}$ commutes with both, as it is the case for $\hat{X}_j$ and $h\hat{D}_k$.

The Weyl identity is also used to derive the identity

$$e^{2\pi i\left(-hs\hat{I}+yh\hat{D}+x\hat{X}\right)} = e^{-2\pi ih\left(s+\frac{1}{2}xy\right)}e^{2\pi iyh\hat{D}}e^{2\pi ix\hat{X}}, \tag{14}$$

which is used to determine the action of the representation $\rho_h(g)$ on each element of the Hilbert space $\psi(\xi) \in L_2(\mathbb{R}^n)$:

$$\rho_h(s,x,y)\psi(\xi) = e^{-2\pi ihs+2\pi i\xi x+\pi ihxy}\psi(\xi+hy), \tag{15}$$

where we also used eqs.(10).

Although the representation of the Heisenberg group on $L_2\left(\mathbb{R}^{2n}\right)$ allows for a straightforward formulation of quantum mechanics, in the following we shall also discuss the classical limit. This is much more easily obtained by a different representation of the group, acting on a vector space $\mathcal{F}_h^2 \subset L_2\left(\mathbb{R}^{2n}\right)$, spanned by the functions $f(q,p)$, where both q and p are $n-$dimensional vectors, whose components carry physical units of a length and a momentum, respectively. As we shall see, these variables yield, in the classical limit, the values of the corresponding observables.

The vector space $\mathcal{F}_h^2$ is defined through the application w acting on $L_2(\mathbb{R}^n)$ such that

$$f(q,p) = w\left[\psi(\xi)\right](q,p) \equiv \left\langle \Phi_0(\xi), \rho_h\left(0, -\frac{2}{h}p, \frac{2}{h}q\right)\psi(\xi)\right\rangle_{L_2(\mathbb{R}^n)}, \tag{16}$$

which is called *Fourier-Wigner transform* [8]. The symbol $\langle\cdot,\cdot\rangle_{L_2(\mathbb{R}^n)}$ indicates the standard scalar product in $L_2(\mathbb{R}^n)$,

$$\langle\psi_1(\xi),\psi_2(\xi)\rangle_{L_2(\mathbb{R}^n)} \equiv \int_{\mathbb{R}^n} d\xi\psi_1^*(\xi)\psi_2(\xi)$$

and $\Phi_0(\xi)$ is a real normalized gaussian in $L_2(\mathbb{R}^n)$

$$\Phi_0(\xi) = \left(\frac{2}{h\Delta}\right)^{\frac{n}{4}} e^{-\frac{\pi}{h\Delta}\xi^2}.$$

As the value of the parameter Δ is immaterial, in the following we set $\Delta = 1$.

The map w from $L_2(\mathbb{R}^n)$ to $\mathcal{F}_h^2$ is a **one-to-one** mapping of $\psi(\xi)$, **onto** $f(q,p)$ (by definition), i.e.,

surjective (onto)	$\forall f \in \mathcal{F}_h^2,\ \exists\psi \in L_2(\mathbb{R}^n)$ such that $f = w[\psi]$
injective (one-to-one)	$\forall\,\psi_1,\psi_2 \in L_2(\mathbb{R}^n), f_1 = f_2$ if and only if $\psi_1 = \psi_2$, with $f_1, f_2 \in \mathcal{F}_h^2$.

If we define the norm of the function $f(q,p)$ as

$$||f||_{\mathcal{F}_h^2} \equiv \left(\frac{4}{h}\right)^n \int_{\mathbb{R}^{2n}} dqdp \left|f(q,p)\right|^2, \tag{17}$$

the Fourier-Wigner transform preserves the distances

$$d\left[\psi_1,\psi_2\right] \equiv ||\psi_1-\psi_2||_{L_2(\mathbb{R}^n)} = d\left[f_1,f_2\right] \equiv ||f_1-f_2||_{\mathcal{F}_h^2}.$$

To demonstrate this equality, we show that the Fourier-Wigner transform preserves the norm. The action of ρ_h on ψ can be determined by means of eq.(15), which yields

$$\rho_h\left(0,-\frac{2}{h}p,\frac{2}{h}q\right)\psi(\xi) = e^{-\frac{4\pi i}{h}pq}e^{-\frac{4\pi i}{h}p(\xi+2q)}\psi(\xi+2q). \tag{18}$$

The scalar product in $L_2(\mathbb{R}^n)$ brings then to the result

$$f(q,p) = \left(\frac{2}{h}\right)^{\frac{n}{4}} \int_{\mathbb{R}^n} d\xi e^{-\frac{4\pi i}{h}pq}e^{-\frac{4\pi i}{h}p(\xi+2q)}\psi(\xi+2q)e^{-\frac{\pi}{h}\xi^2}, \tag{19}$$

which gives the expression of the function $f(q,p)$ obtained from the function $\psi(\xi)$.

The proof of the equivalence of the two norms is straightforward, since we have only to calculate the integral

$$||f||_{\mathcal{F}_h^2} = 2^n\left(\frac{2}{h}\right)^{\frac{3}{2}n} \times$$
$$\int_{\mathbb{R}^{2n}} dqdp \int_{\mathbb{R}^{2n}} d\xi d\xi' e^{-\frac{8\pi}{h}q^2}e^{-\frac{\pi}{h}\left(\xi^2+\xi'^2\right)}e^{-\frac{4\pi}{h}q(\xi+\xi')}e^{-\frac{4\pi i}{h}p(\xi-\xi')}\psi(\xi)\psi^*(\xi').$$

The integration over the variable p gives as result $(h/2)^n\delta(\xi-\xi')$ and this makes trivial the integration over ξ',

$$||f||_{\mathcal{F}_h^2} = 2^n\left(\frac{2}{h}\right)^{\frac{n}{2}} \int_{\mathbb{R}^n} dq \int_{\mathbb{R}^n} d\xi e^{-\frac{2\pi}{h}(\xi+2q)^2}\left|\psi(\xi)\right|^2.$$

The integral over q is a gaussian integral that yields to the final result

$$||f||_{\mathcal{F}_h^2} = \int_{\mathbb{R}^n} d\xi \left|\psi(\xi)\right|^2 = ||\psi||_{L_2(\mathbb{R}^n)}.$$

Using the Fourier-Wigner transform, we can calculate the explicit expressions for position and momentum operators, corresponding to eqs.(10). The transformation is applied to the functions $\hat{X}_j\psi(\xi)$ and $h\hat{D}_j\psi(\xi)$ to obtain the results

$$w\left[\hat{X}_j\psi(\xi)\right](q,p) = w\left[\xi_j\psi(\xi)\right](q,p)$$

and

$$w\left[h\hat{D}_j\psi(\xi)\right](q,p) = w\left[\frac{h}{2\pi i}\frac{\partial}{\partial\xi_j}\psi(\xi)\right](q,p).$$

For instance, the expression of the position operator is calculated starting from the expression

$$w\left[\xi_j\psi(\xi)\right](q,p) = \left(\frac{2}{h}\right)^{\frac{n}{4}}\int_{\mathbb{R}^n} d\xi\, e^{-\frac{4\pi i}{h}p(\xi+q)}e^{-\frac{\pi}{h}(\xi+2q)^2}\xi\psi(\xi),$$

which is obtained from eq.(18). Due to the exponential dependence of the integrand on p, the multiplication by ξ inside the integral is equivalent to the action of the operator

$$-\frac{1}{2\pi i}\left(\frac{h}{2}\frac{\partial}{\partial p} - 2\pi i q\right)$$

where $\partial/\partial p$ acts on the function $e^{-\frac{4\pi i}{h}p(\xi+q)}$. The operator can be brought outside the integral and we find that it acts on the remaining expression, which is exactly $f(q,p)$, as given by eq.(19). The same procedure is performed to calculate te expression of $h\hat{D}$ on $f(q,p)$ and this yields the expressions we are looking for,

$$\begin{aligned}\hat{X}_j f(q,p) &= \left(q_j + \frac{ih}{4\pi}\frac{\partial}{\partial p_j}\right) f(q,p)\\ h\hat{D}_j f(q,p) &= \left(p_j - \frac{ih}{4\pi}\frac{\partial}{\partial q_j}\right) f(q,p)\end{aligned} \tag{20}$$

with $j = 1,\ldots,n$. These expressions are particularly suitable to obtain the classical limits, since the action of each operator is simply multiplicative in the corresponding classical variable, and the operatorial part vanishes when the formal limit $h \to 0$ is taken.

Eqs.(20) are also used to calculate the expression describing the action of the operator $\rho_h(g)$ on the vector space $\mathcal{F}_h^2$. We start introducing in eq.(14) the expressions given by eqs.(20) for position and momentum operators,

$$\rho_h(s,x,y) = e^{-2\pi i h\left(s+\frac{1}{2}xy\right)}e^{y\left(\frac{h}{2}\frac{\partial}{\partial q}+2\pi i p\right)}e^{-x\left(\frac{h}{2}\frac{\partial}{\partial p}-2\pi i q\right)}.$$

The application of this operator to $f(q,p)$ gives

$$\rho_h(s,x,y)f(q,p) = e^{2\pi i(-hs+qx+py)+\pi i h x y}f\left(q+\frac{h}{2}y, p-\frac{h}{2}x\right), \tag{21}$$

which is the expression corresponding to eq.(15).

We described so far the mathematical apparutus which will be used to obtain a group-theoretical formulation of quantum mechanics (section 3), by means of the Heisenberg group, and to obtain the connection between quantum and classical mechanics (section 4) within the group-theoretical formalism.

3 Quantum mechanics

In order to discuss the group-theoretical formulation of quantum mechanics, which is the object of this section, we need to show that the infinite-dimensional representation of the Heisenberg group $\rho_h(g)$ can be used as a basis for the vector space of hermitian operators [8].

In the formalism of quantum mechanics, observables are associated to hermitian operators that act on the Hilbert space of square integrable functions representing the state of the quantum system. In the following, for the sake of definiteness, we shall consider hermitian operators $\hat{B}$ which can be written as hermitain combinations of position and momentum operators,

$$\hat{B} \equiv \hat{B}\left(\hat{X}, h\hat{D}\right),$$

and cover the most familiar examples of observables (e.g., energy, angular momentum, virial, ...)

Interestingly, hermitian operators can be expressed as a Fourier-like expansion with the basis provided by the operators $\rho_h(g)$,

$$\begin{aligned}\hat{B}\left(\hat{X}, h\hat{D}\right) &= \int_{\mathbb{H}^n} dg\, \widetilde{B}(g)\rho_h(g) \\ &\equiv \int_{\mathbb{R}^{2n+1}} dsdxdy\, \widetilde{B}(s,x,y) e^{2\pi i\left(-hs\hat{I}+yh\hat{D}+x\hat{X}\right)}. \end{aligned} \tag{22}$$

Thus, a generic hermitian operator can be expressed in terms of the representation of the group $\mathbb{H}^n$. The existence of this expansion is demonstrated in Appendix 1. There, we also prove that the functions $\widetilde{B}(g)$ have to be obtained as the inverse Fourier transform of the functions $B_w(q,p)$ of the phase-space variables $(q,p) = (q_1,\ldots,q_n,p_1,\ldots,p_n)$, which are associated to the quantum operators, $\hat{B}$, via the Wigner transform [10]. Since we are considering hermitian operators of the form $\hat{B}\left(\hat{X}, h\hat{D}\right)$, the coefficients in eq.(22) are

$$\widetilde{B}(s,x,y) = \delta(s) \int_{\mathbb{R}^{2n}} dqdp\, B_w(q,p)\, e^{-2\pi i(qx+py)} \tag{23}$$

where the presence of $\delta(s)$ is the consequence of the assumed independence of $\hat{B}$ (or, equivalently of B_w) on $h\hat{I}$, that is the operator conjugated to s in the expansion (22). As shown in Appendix 1, the function $B_w(q,p)$ has to be obtained from eq.(3). This is a standard way to associate functions of the phase-space variables (q,p) to hermitian operators, like $\hat{B}$, that are hermitian combinations of position and momentum operators.

Since the commutator of two hermitian operators multiplied by the imaginary unit, $i[\hat{A},\hat{B}] \equiv i(\hat{A}\hat{B} - \hat{B}\hat{A})$, is still a hermitian operator, it can be represented by an expression similiar to eq.(22),

$$i\left[\hat{A},\hat{B}\right] = i\int_{\mathbb{H}^n} dg\, \left(\widetilde{\left[\hat{A},\hat{B}\right]}\right)(g)\rho_h(g), \tag{24}$$

where we have to determine explicitly the quantity in brackets. As we show hereafter, it can be expressed as a convolution integral on the group $\mathbb{H}^n$. The product $\hat{A}\hat{B}$ is

$$\hat{A}\hat{B} = \int_{\mathbb{H}^n} dg\, \widetilde{A}(g)\rho_h(g) \int_{\mathbb{H}^n} dg'\, \widetilde{B}(g')\rho_h(g'). \tag{25}$$

Here, we make use of the property of the representation $\rho_h(g)$ given in eq.(12) and we write

$$\hat{A}\hat{B} = \int_{\mathbb{H}^n} dg \int_{\mathbb{H}^n} dg'\, \widetilde{A}(g)\widetilde{B}(g')\rho_h(gg').$$

Performing the change of variable $g'' = gg'$ (i.e., $g' = g^{-1}g''$) we find

$$\hat{A}\hat{B} = \int_{\mathbb{H}^n} dg''\, \left[\int_{\mathbb{H}^n} dg\, \widetilde{A}(g)\widetilde{B}(g^{-1}g'')\right] \rho_h(g'').$$

The *convolution product* in square brackets is indicated as

$$\left(\widetilde{A} * \widetilde{B}\right)(g'') \equiv \int_{\mathbb{H}^n} dg\, \widetilde{A}(g)\widetilde{B}(g^{-1}g''). \tag{26}$$

This is used to write the commutator as

$$\left[\hat{A}, \hat{B}\right] = \int_{\mathbb{H}^n} dg''\, \left(\widetilde{A} * \widetilde{B} - \widetilde{B} * \widetilde{A}\right)(g'')\rho_h(g'').$$

Further manipulations can be performed on the convolution products in the integral

$$\left(\widetilde{A} * \widetilde{B} - \widetilde{B} * \widetilde{A}\right)(g'') = \int_{\mathbb{H}^n} dg\, \left[\widetilde{A}(g)\widetilde{B}(g^{-1}g'') - \widetilde{B}(g)\widetilde{A}(g^{-1}g'')\right].$$

The change of variable $g' = g^{-1}g''$ (i.e., $g = g''g'^{-1}$) in the second term on the r.h.s. yields

$$\left(\widetilde{A} * \widetilde{B} - \widetilde{B} * \widetilde{A}\right)(g'') = \int_{\mathbb{H}^n} dg\, \widetilde{A}(g)\widetilde{B}(g^{-1}g'') - \int_{\mathbb{H}^n} dg'\, \widetilde{B}(g''g'^{-1})\widetilde{A}(g').$$

Since g' is an dummy integration variable, it is possible to change $g' \to g$ and obtain the result

$$\begin{aligned}\left(\widetilde{A} * \widetilde{B} - \widetilde{B} * \widetilde{A}\right)(g'') &= \int_{\mathbb{H}^n} dg\, \widetilde{A}(g)\left[\widetilde{B}(g^{-1}g'') - \widetilde{B}(g''g^{-1})\right] \\ &\equiv \widetilde{\left[\hat{A}, \hat{B}\right]}(g''). \end{aligned} \tag{27}$$

This result can be inserted in eq.(24) to obtain an implicit expression for the commutator.

The group-theoretical formalism we have introduced so far is particularly suited to formulate quantum mechanics in the Heisenberg representation, where the time dependence is shifted from the wavefunctions to the operators. As we shall show in the next section, the formalism allows to show in a straightforward way that the Poisson brackets are obtained as a formal limit of the commutator when $h \to 0$.

In the following, we indicate the time derivative of a hermitian operator $\hat{B}$ with the symbol $\dot{\hat{B}}$. In the Heisenberg representation of quantum mechanics, it obeys the Heisenberg equation of motion

$$\dot{\hat{B}} = \frac{2\pi}{ih} \left[\hat{B}, \hat{\mathcal{H}}\right]. \tag{28}$$

This equation defines the quantum Lie brackets and consequently the operator $2\pi/(ih) \left[\cdot, \hat{\mathcal{H}}\right]$, which generates the dynamical evolution of $\hat{B}$.

To take full advantage of the group-theoretical formulation, it is desirable to write the pre-factor $2\pi/(ih)$ in eq.(28) as a group integral of a suitable operator. This is achieved introducing the *antiderivative operator* $\mathcal{A}$ [12], which acts on functions $f(s) \in L_1^v(\mathbb{R})$, $L_1^v(\mathbb{R})$ being the linear subspace of $L_1(\mathbb{R})$ such that

$$\lim_{s\to-\infty} s \int_{-\infty}^{s} ds'\, f(s') = 0 \qquad \lim_{s\to+\infty} s \int_{s}^{+\infty} ds'\, f(s') = 0.$$

The antiderivative operator acts as

$$[\mathcal{A}f](s) = 4\pi^2 \int_{-\infty}^{s} ds'\, f(s')$$

and it is easily proved that the equalities $(\partial/\partial s)\mathcal{A} = \mathcal{A}(\partial/\partial s) = 4\pi^2 \hat{I}$ hold in $L_1^v(\mathbb{R})$. The equality

$$\int_{\mathbb{R}} ds \left[\mathcal{A}\widetilde{B}\right](s)\, e^{-2\pi ihs} = \frac{2\pi}{ih} \int_{\mathbb{R}} ds\, \widetilde{B}(s)\, e^{-2\pi ihs} \tag{29}$$

can be derived as it is shown in [12] with an integration by parts.

Introducing the operator $\mathcal{A}$ to get the pre-factor in eq.(28) and representing the commutator by means of eq.(24) and eq.(27), we write the r.h.s. of the Heisenberg equation of motion in the form

$$\frac{2\pi}{ih} \left[\hat{B}, \hat{\mathcal{H}}\right] = \int_{\mathbb{H}^n} dg \left(\widetilde{\mathcal{A}\left[\hat{B}, \hat{\mathcal{H}}\right]}\right)(g) \rho_h(g). \tag{30}$$

This expression will be used in the next section to obtain the classical equation of motion as a straighforward formal limit of the quantum equation of motion.

We summarize the results of this section. We start expressing hermitian operators as a Fourier-like expansion, with the basis set being provided by

the representation of the Heisenberg group $\rho_h(g)$. The coefficients of such an expansion can be obtained by inverse Fourier transform of the Wigner transform of the initial operator. Then, we find a group-integral representation of the commutator of two hermitian operators. These results are then used to write the r.h.s. of the Heisenberg equation of motion as a group integral, after introducing the antiderivative operator $\mathcal{A}$. As we will discuss in section 4, the presence of the operator $\mathcal{A}$ removes the apparent singularity of the Heisenberg equation of motion (28) when $h \to 0$. Therefore, the formal limit $h \to 0$ (*classical limit*) can be taken and yields the classical equation of motion, giving a prescription on the connection between quantum and classical mechanics.

4 Classical mechanics

This section is devoted to the derivation of classical mechanics (observables and equations of motion) as a formal limit of quantum mechanics, within the group-theoretical formulation discussed in the previous sections. To this purpose, we need to recall here some properties of the Heisenberg group.

First of all, we want to emphasize once again the parametric dependence of the representatives of the group $\mathbb{H}^n$ on the Planck constant h,

$$\rho_h(g) = e^{2\pi i\left(-hs\hat{I}+yh\hat{D}+x\hat{X}\right)}.$$

Another crucial ingredient to derive classical mechanics, is the Fourier-Wigner transform, defined in eq.(16). Thereby, we introduced the vector space $\mathcal{F}_h^2 \subset L_2(\mathbb{R}^{2n})$ spanned by the functions $f(q,p)$, on which position $\hat{X}_j$ and momentum $h\hat{D}_j$ operators (as usual, $j = 1, \ldots, n$ is a vector index in $\mathbb{R}^n$) act as

$$\hat{X}_j f(q,p) = \left(q_j + \frac{ih}{4\pi}\frac{\partial}{\partial p_j}\right) f(q,p),$$
$$h\hat{D}_j f(q,p) = \left(p_j - \frac{ih}{4\pi}\frac{\partial}{\partial q_j}\right) f(q,p).$$

Finally, when these expressions are inserted into $\rho_h(g)$ to determine the action of the representatives of the Heisenberg group on $\mathcal{F}_h^2$, we obtain

$$\rho_h(s,x,y) = e^{-2\pi ih\left(s+\frac{1}{2}xy\right)} e^{y\left(\frac{h}{2}\frac{\partial}{\partial q}+2\pi ip\right)} e^{-x\left(\frac{h}{2}\frac{\partial}{\partial p}-2\pi iq\right)}.$$

When the formal limit $h \to 0$ is taken on $\hat{X}_j$ and $h\hat{D}_j$, we obtain

$$\lim_{h\to 0} \hat{X}_j f(q,p) = q_j\, f(q,p),$$
$$\lim_{h\to 0} h\hat{D}_j f(q,p) = p_j\, f(q,p),$$

i.e., the generators of the group act multiplicatively, and the corresponding eigenvalues are the classical counterparts of position and momentum operators. Thus, q and p are to be interpreted as the phase-space variables. The above expressions are used to take the limit $h \to 0$ on $\rho_h(g)$, which yields

$$\lim_{h\to 0} \rho_h(g) = \rho_{(q,p)}(g) = \rho_{(q,p)}(s,x,y) = e^{2\pi i(qx+py)}. \tag{31}$$

Hence, we see that the isomorphic representation of the group $\mathbb{H}^n$ becomes abelian. According to eq.(22), the classical observable B, that is a function of the phase-space variables (q,p), can be written as

$$B(q,p) = \int_{\mathbb{H}^n} dg\, \widetilde{B}(g)\rho_{(q,p)}(g) = \int_{\mathbb{R}^{2n+1}} dsdxdy\, \widetilde{B}(s,x,y)e^{2\pi i(qx+py)} \tag{32}$$

having replaced $\rho_h(g)$ with $\rho_{(q,p)}(g)$ after eq.(31). It is worth noting that the expansion coefficients $\widetilde{B}(g)$ are the same as in eq.(22), and we only changed the basis set elements on which the expansion is performed.

A similiar procedure is applied to obtain the time derivative $\dot{B}(q,p)$. As we did for eq.(22) to deduce eq.(32), we will calculate

$$\lim_{h\to 0} \int_{\mathbb{H}^n} dg \left(\mathcal{A}\widetilde{\left[\hat{B},\hat{\mathcal{H}}\right]}\right)(g)\rho_h(g) = \int_{\mathbb{H}^n} dg \left(\mathcal{A}\widetilde{\left[\hat{B},\hat{\mathcal{H}}\right]}\right)(g)\rho_{(q,p)}(g)$$

in which the limit is taken on $\rho_h(g)$ only, because it is the only element depending on h. The corresponding expression yields the time derivative of the function $B(q,p)$,

$$\dot{B}(q,p) = \int_{\mathbb{H}^n} dg \left(\mathcal{A}\widetilde{\left[\hat{B},\hat{\mathcal{H}}\right]}\right)(g)\rho_{(q,p)}(g) \tag{33}$$

represented as a Fourier-like expansion on the basis set $\rho_{(q,p)}(g)$. As before, the coefficients in this expansion are

$$\widetilde{\left[\hat{B},\hat{\mathcal{H}}\right]} = \widetilde{B} * \widetilde{\mathcal{H}} - \widetilde{\mathcal{H}} * \widetilde{B}.$$

To find the explicit expression of the r.h.s. in eq.(33) we have to show how the antiderivative operator acts. In this case we have

$$\int_{\mathbb{R}} ds\, \left[\mathcal{A}\widetilde{B}\right](s) = \int_{\mathbb{R}} ds\, \widetilde{B}(s)\,(-4\pi^2 s) \tag{34}$$

as it is easily obtained performing an integration by parts [12]. If the result in eq.(34) is inserted in eq.(33) we can write

$$\dot{B}(q,p) = \int_{\mathbb{R}^{2n+1}} dsdxdy\, \widetilde{\left[\hat{B},\hat{\mathcal{H}}\right]}(s,x,y)\left(-4\pi^2\, s\right)\, e^{2\pi i(qx+py)}.$$

Hence, by making the convolution product in $\widetilde{\left[\hat{B},\hat{\mathcal{H}}\right]}$ explicit and by algebraically manipulating the expression as shwon in Appendix 2, we obtain the Poisson brackets between the function $B(q,p)$ and the hamiltonian H.c.(q,p)

$$\begin{aligned}\dot{B}(q,p) &= \frac{\partial B(q,p)}{\partial q}\frac{\partial \text{H.c.}(q,p)}{\partial p} - \frac{\partial B(q,p)}{\partial p}\frac{\partial \text{H.c.}(q,p)}{\partial q} \\ &\equiv \{B(q,p), \text{H.c.}(q,p)\}_{(q,p)} \,. \end{aligned} \tag{35}$$

We have thus obtained the expected result: classically, the time derivative of a function of the phase-space (that does not depend explicitly on time) is given by the Poisson brackets between the function itself and the hamiltonian. This result has been obtained by taking the formal limit $h \to 0$ on the quantum expression in eq.(30), i.e.,

$$\lim_{h\to 0} \frac{2\pi}{ih}\left[\hat{B}\left(\hat{X}, h\hat{D}\right), \hat{\mathcal{H}}\left(\hat{X}, h\hat{D}\right)\right] = \{B(q,p), \text{H.c.}(q,p)\}_{(q,p)} \,. \tag{36}$$

The apparent singularity of the pre-factor $2\pi/(ih)$ in the l.h.s. for $h = 0$ is removed because of the presence of $\rho_h(g)$ in the Fourier-like expansion of the commutator. The limit for $h \to 0$ exists and indeed it corresponds to the Poisson brackets.

This result concludes the presentation of the Heisenberg group approach as the powerful tool that allows to derive classical mechanics as a formal limit of quantum mechanics, for $h \to 0$. The most important ingredients that have been introduced to obtain this result are the Fourier-like representation of observables and equations of motion and the definition of the antiderivative operator. These elements will be used in section 5 to derive a similiar procedure for a mixed quantum-classical mechanics. An ansatz on the quantum-classical equations of motion will be necessary, but the subsequent application of Heisenberg group formalism will be a straightforward generalization of what has been done so far.

5 Mixed quantum-classical dynamics

In the present and in the following section we discuss the application of the group-theoretical formalism to the formulation of quantum-classical mechanics. Our purpose is to determine evolution equations for two coupled subsystems, with two different *degrees of quantization*. We have shown in the previous sections that the classical behaviour of a system is formally obtained as a limiting case of the quantum behaviour, when the Planck constant h tends to zero. In this section we will associate two different values of the Planck constant, say h_1 and h_2, to the two subsystems and introduce suitable Lie brackets to determine the evolution of the two subsystems [15]. The consistency, e.g., with respect to Jacobi identity, is guaranteed by the very definition of the

quantum-classical brackets. The claim is that the formal limit $h_1 \to h, h_2 \to 0$ should allow for a quantum-classical description, obtained by a consistent and formally rigorous derivation. However, problems arise when we try to single out the starting assumptions. Quantum dynamics is described by the Heisenberg equation of motion: the group-theoretical formalism has been successfully applied to translate this equation by means of the irreducible representations of the Heisenberg group. Classical dynamics has been subsequently obtained as a formal limit of quantum dynamics, letting $h \to 0$ in the quantum equation of motion. The expression for the generator of the time evolution in the mixed quantum-classical case is instead unknown, i.e., we are not equipped with quantum-classical Lie brackets which take the place of the commutator or of the Poisson brackets. In Ref. [15], an ansatz for quantum-classical Lie brackets has been introduced. However, these assumedly quantum-classical brackets produce instead a purely classical evolution. In this section we will describe the derivation of the supposed quantum-classical equations of motion whereas in section 6 this derivation will be commented and corrected.

In Ref. [15] the group $\mathbb{D}^n$ has been introduced as the direct sum of two Heisenberg groups, $\mathbb{D}^n \equiv \mathbb{H}^n \oplus \mathbb{H}^n$. The elements of $\mathbb{D}^n$ are

$$g \equiv (g_1; g_2) \quad \text{where} \quad g_1 \in \mathbb{H}^n,\ g_2 \in \mathbb{H}^n.$$

The multiplicative law is

$$gg' = (g_1; g_2)(g_1'; g_2') = (g_1 g_1'; g_2 g_2')$$

where the products $g_i g_i'$, with $i = 1, 2$, are read off eq.(9),

$$g_i g_i' = \left(s_i + s_i' + \frac{1}{2}(x_i y_i' - x_i' y_i), x_i + x_i', y_i + y_i' \right).$$

As in section 2, we introduce the identity, position and momentum operators, labelling the two subsystems with $\alpha = 1, 2$, $\hat{I}_\alpha, \hat{X}_{j,\alpha}, h_\alpha \hat{D}_{j,\alpha}$ (as before, $j = 1, \ldots, n$ is a vector index in $\mathbb{R}^n$), whose commutation relations are

$$2\pi \left[\hat{X}_{j,\alpha}, h_\beta \hat{D}_{k,\beta} \right] = i h_\alpha \delta_{\alpha\beta} \delta_{jk}. \tag{37}$$

and we define the unitary irreducible infinite-dimensional representation $\rho_{h_1,h_2}(g_1; g_2)$ of the group $\mathbb{D}^n$ as

$$\rho_{h_1,h_2}(g_1; g_2) = e^{2\pi i(-h_1 s_1 \hat{I}_1 + y_1 h_1 \hat{D}_1 + x_1 \hat{X}_1)} e^{2\pi i(-h_2 s_2 \hat{I}_2 + y_2 h_2 \hat{D}_2 + x_2 \hat{X}_2)} \tag{38}$$

$$= \rho_{h_1}(g_1)\rho_{h_2}(g_2). \tag{39}$$

As in eq.(12), we have

$$\rho_{h_1,h_2}(g_1; g_2)\rho_{h_1,h_2}(g_1'; g_2') = \rho_{h_1,h_2}(g_1 g_1'; g_2 g_2') \tag{40}$$

using eq.(13) also for this proof.

On the Hilbert space $L_2\left(\mathbb{R}^{2n}\right)$ spanned by the functions $\psi\left(\xi_1;\xi_2\right)$, where[7] $(\xi_1,\xi_2)=(\xi_{1,1}\ldots,\xi_{1,n},\xi_{2,1}\ldots,\xi_{2,n})$, identity, position and momentum operators, introduced above, act as

$$\begin{array}{rcl}\hat{I}_\alpha\psi\left(\xi_1;\xi_2\right) & = & \psi\left(\xi_1;\xi_2\right)\\ \hat{X}_{j,\alpha}\psi\left(\xi_1;\xi_2\right) & = & \xi_{\alpha,j}\psi\left(\xi_1;\xi_2\right)\\ h\hat{D}_{j,\alpha}\psi\left(\xi_1;\xi_2\right) & = & -i\hbar_\alpha\dfrac{\partial}{\partial\xi_{\alpha,j}}\psi\left(\xi_1;\xi_2\right),\end{array} \tag{41}$$

having used the relations in eqs.(10). More useful expressions for these operators, that will be used later, are obtained after defining the Fourier-Wigner transform which yields the functions $f(q_1,p_1;q_2,p_2)\in\mathcal{F}^2_{h_1,h_2}\subset L_2(\mathbb{R}^{4n})$ of the phase-space variables[8] $(q_1,p_1;q_2,p_2)=(q_{1,1}\ldots,q_{1,n},p_{1,1}\ldots,p_{1,n};$ $q_{2,1}\ldots,q_{2,n},p_{2,1}\ldots,p_{2,n})$ from $\psi\left(\xi_1;\xi_2\right)\in L_2\left(\mathbb{R}^{2n}\right)$,

$$\begin{array}{l}f(q_1,p_1;q_2,p_2)=w\left[\psi(\xi_1,\xi_2)\right](q_1,p_1;q_2,p_2)\\ =\left\langle\Phi_0(\xi_1,\xi_2),\rho_{h_1,h_2}\left(0,-\dfrac{2}{h_1}p_1,\dfrac{2}{h_1}q_1;0,-\dfrac{2}{h_2}p_2,\dfrac{2}{h_2}q_2\right)\psi(\xi_1,\xi_2)\right\rangle_{L_2(\mathbb{R}^{2n})}\end{array} \tag{42}$$

having simply generalized its espression in eq.(16). The symbol $\langle\cdot,\cdot\rangle_{L_2(\mathbb{R}^{2n})}$ indicates the standard scalar product in $L_2(\mathbb{R}^{2n})$,

$$\left\langle\psi_1\left(\xi_1;\xi_2\right),\psi_2\left(\xi_1;\xi_2\right)\right\rangle_{L_2(\mathbb{R}^{2n})}=\int_{\mathbb{R}^{2n}}d\xi_1d\xi_2\psi_1^*\left(\xi_1;\xi_2\right)\psi_2\left(\xi_1;\xi_2\right),$$

and $\Phi_0\left(\xi_1;\xi_2\right)$ is a real normalized gaussian in $L_2(\mathbb{R}^{2n})$

$$\Phi_0\left(\xi_1;\xi_2\right)=\left(\frac{2}{h_1\Delta_1}\right)^{\frac{n}{4}}e^{-\frac{\pi}{h_1\Delta_1}\xi_1^2}\left(\frac{2}{h_2\Delta_2}\right)^{\frac{n}{4}}e^{-\frac{\pi}{h_2\Delta_2}\xi_2^2}.$$

As before, the values of the parameters Δ_1,Δ_2 are immaterial, so we set $\Delta_1=\Delta_2=1$.

We presented the formal elements that are necessary to discuss the mixed quantum-classical mechanics, but we still need to define the dynamical quantities characterizing the two coupled systems to which we associate h_1 and h_2 as the values of the Planck constant.

An observable B is represented by the expression

$$\hat{B}\left(\hat{X}_1,h_1\hat{D}_1;\hat{X}_2,h_2\hat{D}_2\right)=\int_{\mathbb{D}^n}dg_1dg_2\,\widetilde{B}\left(g_1;g_2\right)\rho_{h_1,h_2}(g_1;g_2) \tag{43}$$

and its time evolution is described by the equation of motion, first introduced in Ref. [15],

[7] The variables $\xi_{1,j};\xi_{2,j}$ have physical units of a length.

[8] The variables $q_{1,j};q_{2,j}$ have physical units of a length and $p_{1,j};p_{2,j}$ of a momentum.

$$\dot{\hat{B}}\left(\hat{X}_1, h_1\hat{D}_1; \hat{X}_2, h_2\hat{D}_2\right) = \frac{1}{2}\left(\frac{2\pi}{ih_1} + \frac{2\pi}{ih_2}\right)\left[\hat{B}, \hat{\mathcal{H}}\right]. \tag{44}$$

Some remarks about this equation of motion will be made later on, in section 6. Here, we only want to underline that we recover quantum and classical dynamics by performing the limits $h_1, h_2 \to h$ and $h_1, h_2 \to 0$, respectively. Using an integral representation of the form of eq.(43), eq.(44) becomes

$$\dot{\hat{B}}\left(\hat{X}_1, h_1\hat{D}_1; \hat{X}_2, h_2\hat{D}_2\right) = \int_{\mathbb{D}^n} dg_1 dg_2 \left(\frac{\mathcal{A}_1 + \mathcal{A}_2}{2}\widetilde{\left[\hat{B}, \hat{\mathcal{H}}\right]}\right)(g_1; g_2) \rho_{h_1,h_2}(g_1; g_2), \tag{45}$$

where the antiderivative operators $\mathcal{A}_1$ and $\mathcal{A}_2$ have been introduced. They are defined as in eq.(3), but they only act on s_1 or s_2, respectively.

The property of the new (Lie) brackets (44) of being correct in the known full quantum and full classical limits may reasonably convince ourselves that the intermediate situation, in which $h_1 \to h$ and $h_2 \to 0$, generates quantum-classical dynamics. If the assumedly quantum-classical limit is performed on $\rho_{h_1,h_2}(g_1; g_2)$, we obtain

$$\lim_{h_1 \to h, h_2 \to 0} \rho_{h_1,h_2}(g_1; g_2) = \rho_h(g_1)\, \rho_{(q,p)}(g_2) \tag{46}$$

$$= e^{2\pi i\left(-hs_1\hat{I} + y_1 h\hat{D} + x_1\hat{X}\right)} e^{2\pi i(qx_2 + py_2)} \tag{47}$$

for the quantum-classical expression of the representations of the group $\mathbb{D}^n$. The quantum-classical expression for an observable B is, using eq.(46),

$$\hat{B}^{qc} = \int_{\mathbb{D}^n} dg_1 dg_2\, \widetilde{B}\,(g_1; g_2)\, \rho_h(g_1)\, \rho_{(q,p)}(g_2) \tag{48}$$

and its time evolution is determined by the expression

$$\dot{\hat{B}}^{qc} = \int_{\mathbb{D}^n} dg_1 dg_2 \left(\frac{\mathcal{A}_1 + \mathcal{A}_2}{2}\widetilde{\left[\hat{B}, \hat{\mathcal{H}}\right]}\right)(g_1; g_2)\, \rho_h(g_1)\, \rho_{(q,p)}(g_2) \tag{49}$$

$$= \int_{\mathbb{D}^n} dg_1 dg_2 \left(\frac{\pi}{ih} - 2\pi^2 s_2\right)\widetilde{\left[\hat{B}, \hat{\mathcal{H}}\right]}(g_1; g_2)\, \rho_h(g_1)\rho_{(q,p)}(g_2). \tag{50}$$

The second line has been obtained by making the action of $\mathcal{A}_1$ and $\mathcal{A}_2$ in the first line explicit, as shown in eq.(29) and eq.(34). Eq.(49) defines the quantum-classical brackets as

$$\lim_{h_1 \to h, h_2 \to 0} \frac{1}{2}\left(\frac{2\pi}{ih_1} + \frac{2\pi}{ih_2}\right)\left[\hat{B}, \hat{\mathcal{H}}\right] = \left[\hat{B}^{qc}, \hat{\mathcal{H}}^{qc}\right]_{qc}, \tag{51}$$

and a more explicit expression can be obtained by algebraically manipulating eq.(50). We start by dividing eq.(50) in the two following terms

$$\left[\hat{B}^{qc},\hat{\mathcal{H}}^{qc}\right]_{qc} = \frac{\pi}{ih}\int_{\mathbb{D}^n} dg_1 dg_2 \widetilde{\left[\hat{B},\hat{\mathcal{H}}\right]}(g_1;g_2)\,\rho_h(g_1)\rho_{(q,p)}(g_2) + \tag{52}$$

$$\int_{\mathbb{D}^n} dg_1 dg_2 \left(-2\pi^2 s_2\right) \widetilde{\left[\hat{B},\hat{\mathcal{H}}\right]}(g_1;g_2)\,\rho_h(g_1)\rho_{(q,p)}(g_2). \tag{53}$$

We will now introduce the short-hand notation $g_1 g_2 = g$ and $\rho_h(g_1)\rho_{(q,p)}(g_2) = \rho^{qc}(g)$ to simplify the following equations.

The term in the r.h.s. of eq.(52) has a simple interpretation, as it gives to the standard commutator between the quantum-classical expression for the observables B and H.c., multiplied by the factor $\pi/(ih)$,

$$\frac{\pi}{ih}\int_{\mathbb{D}^n} dg \widetilde{\left[\hat{B},\hat{\mathcal{H}}\right]}(g)\,\rho^{qc}(g) = \frac{\pi}{ih}\left[\hat{B}^{qc},\hat{\mathcal{H}}^{qc}\right]. \tag{54}$$

This is easily shown if we remember that the function $\widetilde{\left[\hat{B},\hat{\mathcal{H}}\right]}$ is the coefficient used for the representation of the commutator as a Fourier-like expansion. Eq.(53) is more complicated but we will use the procedure adopted in Appendix 2 on a similar expression. We will use the equality

$$\widetilde{\left[\hat{B},\hat{\mathcal{H}}\right]}(g) = \int_{\mathbb{D}^n} dg' \left[\widetilde{B}(g')\,\mathrm{H.c.}\left(g'^{-1}g\right) - \widetilde{\mathrm{H.c.}}(g')\,\widetilde{B}\left(g'^{-1}g\right)\right]$$

which is obtained by a change of variables in the equation

$$\widetilde{\left[\hat{B},\hat{\mathcal{H}}\right]}(g) = \int_{\mathbb{D}^n} dg'\,\widetilde{B}(g')\left[\mathrm{H.c.}\left(g'^{-1}g\right) - \widetilde{\mathrm{H.c.}}\left(gg'^{-1}\right)\right],$$

used in Appendix 2. Indeed, after the change of variable $g'^{-1}g = g''$ in the second term, we have $g = g'g''$. Since g'' is a dummy integration variable, we set $g'' \to g$ and write eq.(53) as

$$\int_{\mathbb{D}^n} dg \left(-2\pi^2 s_2\right) \widetilde{\left[\hat{B},\hat{\mathcal{H}}\right]}(g)\,\rho^{qc}(g) = \int_{\mathbb{D}^n} dg \int_{\mathbb{D}^n} dg' \rho^{qc}(g'g)\left(-2\pi^2\right)$$
$$\left[\widetilde{B}(g')\widetilde{\mathrm{H.c.}}(g) - \widetilde{\mathrm{H.c.}}(g')\widetilde{B}(g)\right]\left[s_2 + s_2' + \frac{1}{2}\left(x_2' y_2 - x_2 y_2'\right)\right].$$

From the r.h.s. of this expression we obtain two terms: the first is

$$\mathrm{I}_1 = -2\pi^2 \int_{\mathbb{D}^n} dg \int_{\mathbb{D}^n} dg' \left[\widetilde{B}(g')\widetilde{\mathrm{H.c.}}(g) - \widetilde{\mathrm{H.c.}}(g')\widetilde{B}(g)\right](s_2 + s_2')\,\rho^{qc}(g'g) \tag{55}$$

and we will keep it unchanged; the second is the difference

$$\mathrm{I}_2 - \mathrm{I}_3 = \pi^2 \int_{\mathbb{D}^n} dg \int_{\mathbb{D}^n} dg' \left[\widetilde{\mathrm{H.c.}}(g')\widetilde{B}(g) - \widetilde{B}(g')\widetilde{\mathrm{H.c.}}(g)\right]$$
$$\times \left(x_2' y_2 - x_2 y_2'\right)\rho^{qc}(g'g)$$

that can still be manipulated. We use eqs.(81) to obtain[9]

$$\mathrm{I}_2 = \frac{1}{4}\left(\frac{\partial \hat{B}^{qc}}{\partial q}\frac{\partial \hat{\mathrm{H.c.}}^{qc}}{\partial p} - \frac{\partial \hat{B}^{qc}}{\partial p}\frac{\partial \hat{\mathrm{H.c.}}^{qc}}{\partial q}\right) \tag{56}$$

$$= \frac{1}{4}\left\{\hat{B}^{qc}, \hat{\mathrm{H.c.}}^{qc}\right\}_{(q,p)} \tag{57}$$

and[10]

$$\mathrm{I}_3 = \frac{1}{4}\left(\frac{\partial \hat{\mathrm{H.c.}}^{qc}}{\partial q}\frac{\partial \hat{B}^{qc}}{\partial p} - \frac{\partial \hat{\mathrm{H.c.}}^{qc}}{\partial p}\frac{\partial \hat{B}^{qc}}{\partial q}\right) \tag{58}$$

$$= \frac{1}{4}\left\{\hat{\mathrm{H.c.}}^{qc}, \hat{B}^{qc}\right\}_{(q,p)}. \tag{59}$$

The quantum-classical brackets, using eqs.(54), (55), (57) and (59), are finally written as

$$\left[\hat{B}^{qc}, \hat{\mathrm{H.c.}}^{qc}\right]_{qc} = \frac{\pi}{ih}\left[\hat{B}^{qc}, \hat{\mathrm{H.c.}}^{qc}\right] + \frac{1}{4}\left[\left\{\hat{B}^{qc}, \hat{\mathrm{H.c.}}^{qc}\right\} - \left\{\hat{\mathrm{H.c.}}^{qc}, \hat{B}^{qc}\right\}\right]$$
$$-2\pi^2 \int_{\mathbb{D}^n} dg \int_{\mathbb{D}^n} dg'(s_2 + s_2')\left[\widetilde{B}(g')\widetilde{\mathrm{H.c.}}(g) - \widetilde{\mathrm{H.c.}}(g')\widetilde{B}(g)\right]\rho^{qc}(g'g). \tag{60}$$

We have thus reconstructed the derivation and interpreted the results of Ref [15]. The first two terms, i.e., the commutator and the Poisson brackets, are already present in a theory based on the quantum-classical Liouville representation discussed in section 1. The new term, which appears within the Heisenberg group approach, needs to be explained. In the attempt to provide a physical interpretation to this term we have shown, in Ref. [1], that the new equation of motion is purely classical. This will be illustrated in the following section.

[9] The intermediate step is

$$\mathrm{I}_2 = \frac{1}{4}\left[\frac{\partial}{\partial q}\int_{\mathbb{D}^n} dg'\widetilde{B}(g')\rho^{qc}(g')\frac{\partial}{\partial p}\int_{\mathbb{D}^n} dg\widetilde{\mathrm{H.c.}}(g)\rho^{qc}(g) - \right.$$
$$\left.\frac{\partial}{\partial p}\int_{\mathbb{D}^n} dg'\widetilde{B}(g')\rho^{qc}(g')\frac{\partial}{\partial q}\int_{\mathbb{D}^n} dg\widetilde{\mathrm{H.c.}}(g)\rho^{qc}(g)\right].$$

[10] The intermediate step is, as before,

$$\mathrm{I}_3 = \frac{1}{4}\left[\frac{\partial}{\partial q}\int_{\mathbb{D}^n} dg'\widetilde{\mathrm{H.c.}}(g')\rho^{qc}(g')\frac{\partial}{\partial p}\int_{\mathbb{D}^n} dg\widetilde{B}(g)\rho^{qc}(g) - \right.$$
$$\left.\frac{\partial}{\partial p}\int_{\mathbb{D}^n} dg'\widetilde{\mathrm{H.c.}}(g')\rho^{qc}(g')\frac{\partial}{\partial q}\int_{\mathbb{D}^n} dg\widetilde{B}(g)\rho^{qc}(g)\right].$$

6 Comments

This section represents the conclusive part of our work on the quantum-classical equations of motion derived in section 5, following the prescriptions of Ref. [15]. We will show an alternative derivation of the quantum-classical equation of motion (60), obtained by taking the limit $h_1 \to h, h_2 \to 0$ in eq.(44), which is an ansatz on the mixed dynamical generator, after making some remarks on the equation of motion itself and on the operators used as generators in the representation of the group $\mathbb{D}^n$, i.e., the position $\hat{X}_{j,\alpha}$ and momentum $h_\alpha \hat{D}_{j,\alpha}$ operators.

As we anticipated in the previous section, we need to underline two aspects emerging from the analysis of eq.(44), which we recall here

$$\dot{\hat{B}} = \frac{1}{2}\left(\frac{2\pi}{ih_1} + \frac{2\pi}{ih_2}\right)\left[\hat{B}, \hat{\mathcal{H}}\right]. \tag{61}$$

First of all, we observe that this equation of motion couples the two systems even in the absence of an interaction potential in the hamiltonian $\hat{\mathcal{H}}$. Suppose that the two systems are not coupled by the hamiltonian, that is, the hamiltonian is the sum of two hamiltonians $\hat{\mathcal{H}}_1$ and $\hat{\mathcal{H}}_2$, each acting ont the corresponding subsystem only. The time evolution of an observable $\hat{B}_1$ representing a property of system 1 is

$$\dot{\hat{B}}_1 = \frac{1}{2}\left(\frac{2\pi}{ih_1} + \frac{2\pi}{ih_2}\right)\left[\hat{B}_1, \hat{\mathcal{H}}_1\right].$$

We used the property $\left[\hat{B}_1, \hat{\mathcal{H}}_2\right] = 0$, because the operators $\hat{B}_1$ and $\hat{\mathcal{H}}_2$ act on two different vector spaces, each representing the state of a different subsystem. The expression just written shows that the two systems influence each other even if they are not interacting, through the presence of the Planck constant of the subsystem whose degrees of freedom are not involved in the commutator (h_2, in this example). The peculiar form of the pre-factor $[2\pi/(ih_1) + 2\pi/(ih_2)]/2$ is the cause of this undesirable behaviour.

The second aspect is connected to the mathematical properties at the basis of the theory. The commutation relations holding for position and momentum operators, as illustrated in section 2, are

$$\frac{2\pi}{ih}\left[\hat{X}_j, h\hat{D}_k\right] = \delta_{jk} \tag{62}$$

and are strictly linked to the equation of motion

$$\dot{\hat{B}} = \frac{2\pi}{ih}\left[\hat{B}, \hat{\mathcal{H}}\right].$$

Indeed, in this context, position and momentum operators are canonically conjugated operators, through the relations (62). When eq.(61) is used as

dynamical generator, new commutation relations must be introduced to define conjugated operators, as it is correctly observed in Ref. [15]. Hence, position $\hat{X}_{j,\alpha}$ and momentum $h_\alpha \hat{D}_{j,\alpha}$ are no longer conjugated operators, since

$$\frac{1}{2}\left(\frac{2\pi}{ih_1}+\frac{2\pi}{ih_2}\right)\left[\hat{X}_{j,\alpha}, h_\beta \hat{D}_{k,\beta}\right] \neq \delta_{jk}\delta_{\alpha\beta},$$

and instead, according to eq.(62) and to the commutativity of operators referring to different subsystems, we have

$$\frac{2\pi}{ih_\alpha}\left[\hat{X}_{j,\alpha}, h_\beta \hat{D}_{k,\beta}\right] = \delta_{jk}\delta_{\alpha\beta}.$$

A new momentum operator $\hat{P}_{j,\alpha}$ must therefore be introduced, defined in such a way to be canonically conjugated to $\hat{X}_{j,\alpha}$ through the commutation relations

$$\frac{1}{2}\left(\frac{2\pi}{ih_1}+\frac{2\pi}{ih_2}\right)\left[\hat{X}_{j,\alpha}, \hat{P}_{k,\beta}\right] = \delta_{jk}\delta_{\alpha\beta}. \tag{63}$$

The operator $\hat{P}_{j,\alpha}$ is easily shown to be

$$\hat{P}_{j,\alpha} = \frac{2h_{3-\alpha}}{h_1+h_2} h_\alpha \hat{D}_{j,\alpha}, \tag{64}$$

so it is strictly connected to the old momentum operator. Its action on the functions $\psi(\xi_1;\xi_2) \in L_2(\mathbb{R}^{2n})$ is

$$\hat{P}_{j,\alpha}\psi(\xi_1;\xi_2) = \frac{2h_1h_2}{h_1+h_2}\frac{1}{2\pi i}\frac{\partial}{\partial \xi_{\alpha,j}}\psi(\xi_1;\xi_2)$$

and on the functions $f(q_1,p_1;q_2,p_2) \in \mathcal{F}^2_{h_1,h_2}$ is

$$\hat{P}_{j,\alpha}f(q_1,p_1;q_2,p_2) = \frac{1}{2\pi i}\frac{2h_{3-\alpha}}{h_1+h_2}\left(\frac{h_\alpha}{2}\frac{\partial}{\partial q_{j,\alpha}} + 2\pi i p_{j,\alpha}\right) f(q_1,p_1;q_2,p_2). \tag{65}$$

This expression has been obtained by the application of the Fourier-Wigner transform of eq.(42) to the function $\hat{P}_{j,\alpha}\psi(\xi_1;\xi_2)$,

$$\hat{P}_{j,\alpha}f(q_1,p_1;q_2,p_2) = w\left[\hat{P}_{j,\alpha}\psi(\xi_1,\xi_2)\right](q_1,p_1;q_2,p_2),$$

whereas the corresponding expression for the position operator is

$$\begin{aligned}\hat{X}_{j,\alpha}f(q_1,p_1;q_2,p_2) &= w\left[\hat{P}_{j,\alpha}\psi(\xi_1,\xi_2)\right](q_1,p_1;q_2,p_2)\\ &= -\frac{1}{2\pi i}\left(\frac{h_\alpha}{2}\frac{\partial}{\partial p_{j,\alpha}} - 2\pi i q_{j,\alpha}\right) f(q_1,p_1;q_2,p_2).\end{aligned} \tag{66}$$

We are now ready to deduce the consequences of the quantum-classical limit derived in section 5.

If the limit $h_1 \to h, h_2 \to 0$ is taken in eqs.(65) and (66), we obtain

$$\begin{array}{ll} \hat{X}_{j,1} = -\dfrac{1}{2\pi i}\left(\dfrac{h}{2}\dfrac{\partial}{\partial p_{j,1}} - 2\pi q_{j,1}\right) & \hat{X}_{j,2} = q_{j,2} \\ \hat{P}_{j,1} = 0 & \hat{P}_{j,2} = 2p_{j,2}, \end{array} \tag{67}$$

that are different from either the full quantum or the full classical expressions. This unusual behaviour of the position and momentum quantum-classical operators does not support the hypothesis that the limit $h_1 \to h, h_2 \to 0$ in the dynamics defined by eq.(61) gives a correct way to formulate a coherent quantum-classical dynamics. Indeed, already a first observation should raise doubts on such a construction. The pre-factor in eq.(61) can be rewritten introducing the *effective Planck constant*

$$h_{\text{eff}} = \frac{2h_1h_2}{h_1 + h_2} \longrightarrow \frac{1}{h_{\text{eff}}} = \frac{1}{2}\left(\frac{1}{h_1} + \frac{1}{h_2}\right), \tag{68}$$

which is the harmonic average of h_1 and h_2. In eq.(61) we thus have

$$\dot{\hat{B}} = \frac{2\pi}{ih_{\text{eff}}}\left[\hat{B}, \hat{\mathcal{H}}\right]. \tag{69}$$

Moreover, the definition (64) can be written as

$$\hat{P}_{j,\alpha} = h_{\text{eff}}\hat{D}_{j,\alpha},$$

and the canonical commutation relations in eq.(63) is recovered,

$$\frac{2\pi}{ih_{\text{eff}}}\left[\hat{X}_{j,\alpha}, \hat{P}_{k,\beta}\right] = \delta_{\alpha\beta}\delta_{jk}. \tag{70}$$

With that in mind, we have to suggest a second important correction which concerns the role of the momentum operators, $h_\alpha\hat{D}_{j,\alpha}$ and $\hat{P}_{j,\alpha}$. Once we realize that the momentum operator $\hat{P}_{j,\alpha}$ is the canonically conjugated partner of $\hat{X}_{j,\alpha}$, we understand that the use of $h_\alpha\hat{D}_{j,\alpha}$ in the representation $\rho_{h_1,h_2}(g_1; g_2)$, although legitimate, is improper and subtle. Moreover, since h_1 and h_2 are connected by the relation (68), it should be useful to introduce the new parameter h_{eff} in the formulation. Both these requirements can be fulfilled if we determine a new unitary irreducible and infinite-dimensional representation of the group $\mathbb{D}^n$

$$\rho_{h_1,h_2}(g_1; g_2) \longrightarrow \rho_{h_{\text{eff}}}(g_1; g_2)$$

where the rescaled variables

$$s'_\alpha = \frac{h_{\text{eff}}}{h_\alpha}s_\alpha;\ x'_\alpha = x_\alpha;\ y'_\alpha = \frac{h_{\text{eff}}}{h_\alpha}y_\alpha.$$

are used. We note that between $\rho_{h_1,h_2}(g_1; g_2)$ and $\rho_{h_{\text{eff}}}(g_1; g_2)$, whose expression is

$$\rho_{h_{\text{eff}}}(g_1;g_2) = \rho_{h_{\text{eff}}}(g_1)\rho_{h_{\text{eff}}}(g_2)$$
$$= e^{2\pi i\left(-h_{\text{eff}}s_1\hat{I}_1+y_1\hat{P}_1+x_1\hat{X}_1\right)}e^{2\pi i\left(-h_{\text{eff}}s_2\hat{I}_2+y_2\hat{P}_2+x_2\hat{X}_2\right)}, \quad (71)$$

there is a one-to-one correspondence. The new representation will be used to define a new Fourier-Wigner transform, because the latter is strictly related to the representation adopted. The suitable Fourier-Wigner transform is

$$f(q_1,p_1;q_2,p_2) = w\left[\psi(\xi_1,\xi_2)\right](q_1,p_1;q_2,p_2)$$
$$= \left\langle \Phi_0(\xi_1,\xi_2), \rho_{h_{\text{eff}}}\left(0,-\frac{2}{h_{\text{eff}}}p_1,\frac{2}{h_{\text{eff}}}q_1;0,-\frac{2}{h_{\text{eff}}}p_1,\frac{2}{h_{\text{eff}}}q_1\right)\psi(\xi_1,\xi_2)\right\rangle_{L_2(\mathbb{R}^{2n})},$$

which can be used to determine the action of position and momentum operators on $\mathcal{F}^2_{h_1,h_2}$,

$$\begin{aligned}\hat{X}_{j,\alpha} &= -\frac{1}{2\pi i}\left(\frac{h_{\text{eff}}}{2}\frac{\partial}{\partial p_{j,\alpha}} - 2\pi i q_{j,\alpha}\right)\\ \hat{P}_{j,\alpha} &= \frac{1}{2\pi i}\left(\frac{h_{\text{eff}}}{2}\frac{\partial}{\partial q_{j,\alpha}} + 2\pi i p_{j,\alpha}\right).\end{aligned} \quad (72)$$

The quantum-classical limit $h_1 \to h, h_2 \to 0$ can be replaced by the equivalent limit $h_{\text{eff}} \to 0$ in which the new effective Planck constant appears. The representation of the group becomes

$$\lim_{h_{\text{eff}}\to 0}\rho_{h_{\text{eff}}}(g_1;g_2) = \rho_{(q_1,p_1)}(g_1)\rho_{(q_2,p_2)}(g_2) = e^{2\pi i(q_1x_1+p_1y_1)}e^{2\pi i(q_2x_2+p_2y_2)}, \quad (73)$$

like the full classical representation determined in section 4, eq.(31); positions and momenta act multiplicatively, yielding the classical phase-space variables corresponding to the quantum operators

$$\lim_{h_{\text{eff}}\to 0}\hat{X}_{j,\alpha} = q_{j,\alpha} \qquad \text{and} \qquad \lim_{h_{\text{eff}}\to 0}\hat{P}_{j,\alpha} = p_{j,\alpha},$$

and the equation of motion becomes

$$\lim_{h_{\text{eff}}\to 0}\frac{2\pi}{ih_{\text{eff}}}\left[\hat{B},\hat{\mathcal{H}}\right] = \{B,\text{H.c.}\}_{(q_1,p_1;q_2,p_2)}. \quad (74)$$

as it shown in section 4.

We can summarize the procedure followed in the present section to achieve the result obtained above. In Ref. [15] the new momentum operator was correctly introduced, together with the new commutation relations of eq.(70), but $\hat{P}_{j,\alpha}$ was not used in the formal construction of the theory. The expressions for the quantum-classical variables (position and momentum) are those shown in eqs.(67), insted of eq.(72), because $\hat{X}_{j,\alpha}$ and $\hat{P}_{j,\alpha}$ are represented using $\rho_{h_1,h_2}(g_1;g_2)$ in which the operators $h_\alpha\hat{D}_{j,\alpha}$, no more generators of the corresponding Lie group, are present[11].

[11] The variable $p_{j,\alpha}$ used in eqs.(65) and (66) is the eigenvalue of the operator $h_\alpha\hat{D}_{j,\alpha}$ when it acts on the eigenfunctions $\psi_{hD}(\xi_1;\xi_2)$

The generalization of the Heisenberg group formalism to the group $\mathbb{D}^n$ is not consistent. The comparison between the approaches proposed in section 3 and in section 5 can be summarized in the following scheme:

1. commutation relations to single out the canonically conjugated position and momentum operators;
2. equation of motion directly derived from the commutation relations (or vice versa);
3. use of the right operators to create the representation of the group.

In the theory based on the group $\mathbb{D}^n$, as presented in section 5, the third point is missing. In the present section, we removed the inconsistency of the whole construction and showed the classical nature of the presumed quantum-classical limit, which was hidden when the inconsistent, although formally equivalent, representation of the group $\mathbb{D}^n$ where adopted.

A comment on eq.(61) is in order. The direct introduction of h_{eff} in eq.(61), as it was done to derive eq.(69), would have brought straightforwardly to eq.(74) because in section 4 we learnt how to treat the singularity for $h_{\text{eff}} \to 0$ ($h \to 0$ in eq.(36)).

$$\psi_{hD}(\xi_1;\xi_2) \propto e^{2\pi i\left(\frac{p_1}{h_1}\xi_1+\frac{p_2}{h_2}\xi_2\right)}$$

because

$$h_\alpha \hat{D}_{j,\alpha}\psi_{hD}\left(\xi_1,\xi_2\right) = p_{j,\alpha}\psi_{hD}\left(\xi_1,\xi_2\right).$$

The eigenfunctions of $\hat{P}_{j,\alpha}$ are plane waves of a different kind,

$$\psi_P\left(\xi_1,\xi_2\right) \propto e^{2\pi i\left(\frac{\widetilde{p}_1}{h_{\text{eff}}}\xi_1+\frac{\widetilde{p}_2}{h_{\text{eff}}}\xi_2\right)}.$$

Indeed,

$$\hat{P}_{j,\alpha}\psi_P\left(\xi_1,\xi_2\right) = h_{\text{eff}}\hat{D}_{j,\alpha}\psi_P\left(\xi_1,\xi_2\right) = \widetilde{p}_{j,\alpha}\psi_P\left(\xi_1,\xi_2\right).$$

The eigenfunctions $\psi_P\left(\xi_1,\xi_2\right)$ can be obtained from $\psi_{hD}\left(\xi_1,\xi_2\right)$ by making the substitution

$$\frac{p_\alpha}{h_\alpha} \longrightarrow \frac{\widetilde{p}_\alpha}{h_{\text{eff}}}$$

that can be performed as well on eqs.(65) and (66) to obtain

$$\hat{X}_{j,\alpha} = -\frac{1}{2\pi i}\left(\frac{h_{\text{eff}}}{2}\frac{\partial}{\partial \widetilde{p}_{j,\alpha}} - 2\pi i q_{j,\alpha}\right)$$

$$\hat{P}_{j,\alpha} = \frac{1}{2\pi i}\frac{2h_{3-\alpha}}{h_1+h_2}\left(\frac{h_\alpha}{2}\frac{\partial}{\partial q_{j,\alpha}} + 2\pi i\frac{h_\alpha}{h_{\text{eff}}}\widetilde{p}_{j,\alpha}\right)$$

in order to express $\hat{P}_{j,\alpha}$ using its eigenvalues. This expression for $\hat{P}_{j,\alpha}$ is the same as in the second line of eqs.(72).

7 Conclusion

In this piece of work we analyzed some open issues concerning the formulation and implementation of a mixed quantum-classical dynamics, beyond the adiabatic approximation. We discussed the reasons why, in many circumstances, a quantum treatment of the (statistical) mechanical properties of a physical system is necessary, at least for some degrees of freedom, and described some of the existing mixed quantum-classical approximations that allow to generate a computationally feasible dynamical evolution. We observed that such approximated approaches need to be overcome by a rigorous and consistent method based on a coherent derivation of quantum-classical mechanics, suitable for wide-range applications. This is not the state of the art, because the existing approximation schemes are generally appropriate for a resctricted class of systems, sometimes depending on the properties under investigation. Nonetheless, approximated methods are able to produce reliable results, especially in the field of numerical simulations.

An attempt to solve the difficulties and inconsistencies arising from an approximated derivation of quantum-classical equations of motion was made some time ago [15] to restore the properties that are expected to hold within a consistent formulation of dynamics and statistical mechanics, and are instead missed by the existing approximate methods. We refer not only to the properties that the Lie brackets, which generate the dynamics, satisfy in a full quantum and full classical formulation, e.g., the bi-linearity and anti-symmetry properties, the Jacobi identity and the Leibniz rule[12], but also to statistical mechanical properties, like the time translational invariance of equilibrium correlation functions [see eq.(8)].

The derivation of a consistent mixed quantum-classical dynamics discussed in this paper was first proposed in Ref. [15] and commented and clarified in Ref. [1]. This derivation is based on a group-theoretical formulation of quantum and classical mechanics, which introduces a very elegant and formally rigorous mathematical apparatus and allows to directly obtain classical mechanics as the limit for $h \to 0$ of quantum mechanics, in the Heisenberg representation of quantum dynamics.

However, the Heisenberg group formalism is a very useful tool to represent quantum and classical dynamical quantities, such as observables and equations of motion, only when a prescription on the generator of the time evolution exists. The comparison with the fully quantum or fully classical dynamics allows us to deduce only the formal properties that the mixed quantum-classical brackets have to satisfy in order to generate a consistent evolution, but does

[12] For generic operators $\hat{A}$, $\hat{B}$ and $\hat{C}$, the Leibniz rule states that the equality

$$\left(\hat{A}\hat{B}, \hat{C}\right) = \hat{A}\left(\hat{B}, \hat{C}\right) + \left(\hat{A}, \hat{C}\right)\hat{B}$$

holds, where the symbol $(\,\cdot\,,\,\cdot\,)$ represents some (quantum or classical) Lie brackets.

not produce a unique recipe for mixed quantum-classical Lie brackets (or dynamical generators). The need for an ansatz on the quantum-classical equations of motion leaves the question about the existence of a consistent way to generate a mixed quantum-classical dynamics still open. The ansatz proposed in Ref. [15] was proved to lead to a purely classical dynamics [1] and more work is certainly needed to find a conclusive solution to this problem.

Appendix 1

In this appendix we shall demonstrate the existence of the expansion in eq.(22),

$$\hat{B}\left(\hat{X}, h\hat{D}\right) = \int_{\mathbb{R}^{2n+1}} dsdxdy\, \widetilde{B}(s,x,y) e^{2\pi i\left(-hs\hat{I}+yh\hat{D}+x\hat{X}\right)}.$$

This is done by showing that the set of operators $e^{2\pi i\left(-hs\hat{I}+yh\hat{D}+x\hat{X}\right)}$ represents a basis set for the space of operators $\hat{B} \equiv \hat{B}\left(\hat{X}, h\hat{D}\right)$. We have to show that the operators $e^{2\pi i\left(-hs\hat{I}+yh\hat{D}+x\hat{X}\right)}$ are an orthogonal and complete set, for all the values of $g \equiv (s,x,y)$, defining a scalar product on the space of operators. Since we are restricting our analysis to hermitian operators of the form $\hat{B}\left(\hat{X}, h\hat{D}\right)$, the coefficient $\widetilde{B}(s,x,y)$ will depend on the variable s as $\delta(s)$. Therefore, we can limit ourselves to show that the expansion

$$\hat{B}\left(\hat{X}, h\hat{D}\right) = \int dxdy\, \widetilde{B}(x,y) e^{2\pi i(yh\hat{D}+x\hat{X})} \tag{75}$$

exists, with the function $\widetilde{B}(x,y)$ defined as the inverse Fourier transform of the Wigner transform of the operator $\hat{B}$, i.e.,

$$\widetilde{B}(x,y) = \int dqdp\, B_w(q,p)\, e^{-2\pi i(qx+py)} \tag{76}$$

where $B_w(q,p)$ is obtained from $\hat{B}$ according to eq.(3). We show that both sides of this equality have the same matrix elements on a basis set, and to this purpose we choose the position operators eigenstates $|q\rangle$. Thus, we need to prove that

$$\langle q''|\, \hat{B}\, |q'\rangle = \int dxdy\, \widetilde{B}(x,y)\, \langle q''|\, e^{2\pi i(yh\hat{D}+x\hat{X})}\, |q'\rangle\,. \tag{77}$$

Using Weyl identity (13), the matrix elements in the r.h.s. are

$$\langle q''|\, e^{2\pi i(yh\hat{D}+x\hat{X})}\, |q'\rangle = e^{2\pi i\left(q'+\frac{1}{2}hy\right)x} \delta\left(hy-(q''-q')\right)$$

and replacing the function $\widetilde{B}(x,y)$ with the expression (76) we obtain

$$\int dxdy \int dqdp\, B_w(q,p)\, e^{-2\pi i(qx+py)} e^{2\pi i\left(q'+\frac{1}{2}hy\right)x} \delta\left(hy-(q''-q')\right).$$

The integration over the variable y is straightforward, because of the presence of the $\delta-$function, and yields

$$\frac{1}{h}\int dqdp\, B_w(q,p) e^{-2\pi i\frac{p}{h}(q''-q')} \int dx\, e^{-2\pi i\left(q-\frac{1}{2}q''-\frac{1}{2}q'\right)x}.$$

The integrations over the variables x and q bring to the expression

$$\frac{1}{h}\int dp\, B_w\left(\frac{1}{2}\left(q'+q''\right),p\right) e^{-2\pi i\frac{p}{h}(q''-q')}.$$

The function B_w is now replaced by the explicit expression of the Wigner transform, yielding

$$\frac{1}{h}\int dp \int dz e^{-2\pi i\frac{p}{h}\left(z+q''-q'\right)} \left\langle \frac{1}{2}(q'+q'')+\frac{z}{2}\right| \hat{B} \left|\frac{1}{2}(q'+q'')-\frac{z}{2}\right\rangle.$$

The two integrations over p and z bring to the expected identity

$$\int dxdy\, \widetilde{B}(x,y) \left\langle q''\right| e^{2\pi i(yh\hat{D}+x\hat{X})} \left|q'\right\rangle = \left\langle q''\right| \hat{B} \left|q'\right\rangle.$$

Moreover, we can show that the operators $e^{2\pi i(yh\hat{D}+x\hat{X})}$ are orthogonal if the scalar product

$$\left\langle \hat{A},\hat{B}\right\rangle = \mathrm{Tr}\left(\hat{A}^\dagger \hat{B}\right)$$

is defined between two generic elements of the space of linear operators ($\hat{A}^\dagger$ being the adjoint of $\hat{A}$). We need to calculate

$$\left\langle e^{2\pi i(y'h\hat{D}+x'\hat{X})}, e^{2\pi i(yh\hat{D}+x\hat{X})}\right\rangle = \int dq \left\langle q\right| e^{-2\pi i(y'h\hat{D}+x'\hat{X})} e^{2\pi i(yh\hat{D}+x\hat{X})} \left|q\right\rangle$$

where in the r.h.s. the trace is explicitly calculated in the basis of the eigenstates $|q\rangle$.
As usual we rely on the Weyl identity and find

$$\left\langle e^{2\pi i(y'h\hat{D}+x'\hat{X})}, e^{2\pi i(yh\hat{D}+x\hat{X})}\right\rangle = \int dq\, e^{-\pi ih(xy+x'y')} \left\langle q\right| e^{-2\pi iy'h\hat{D}} e^{-2\pi ix'\hat{X}} e^{2\pi iyh\hat{D}} e^{2\pi ix\hat{X}} \left|q\right\rangle. \tag{78}$$

Hence, we get

$$\left\langle q\right| e^{-2\pi iy'h\hat{D}} e^{-2\pi ix'\hat{X}} e^{2\pi iyh\hat{D}} e^{2\pi ix\hat{X}} \left|q\right\rangle = \left\langle q\right| e^{2\pi i\left(x-x'\right)\left[q+h(y-y')\right]} \left|q+h\left(y-y'\right)\right\rangle.$$

When the integral over the variable q is performed, the result is

$$\left\langle e^{2\pi i(y'h\hat{D}+x'\hat{X})}, e^{2\pi i(yh\hat{D}+x\hat{X})} \right\rangle = \delta\left(h(y-y')\right)\delta(x-x')$$

that proves the orthogonality of the elements $e^{2\pi i(yh\hat{D}+x\hat{X})}$ which then provides a basis for the vector space of the hermitian operators $\hat{B}\left(\hat{X}, h\hat{D}\right)$.

Appendix 2

In this appendix we will show the calculations which have to be performed to obtain the Poisson brackets expression in eq.(35) starting from eqs.(33) and (34).

The starting point is

$$\dot{B}(q,p) = \int_{\mathbb{H}^n} dg \left(\mathcal{A}\widetilde{\left[\hat{B},\hat{\mathcal{H}}\right]} \right)(g)\rho_{(q,p)}(g)$$

that becomes

$$\dot{B}(q,p) = \int_{\mathbb{R}^{2n+1}} dsdxdy \widetilde{\left[\hat{B},\hat{\mathcal{H}}\right]}(s,x,y)\left(-4\pi^2 s\right) e^{2\pi i(qx+py)} \tag{79}$$

when the action of the antiderivative operator $\mathcal{A}$ on the s-variable functions is explicited. In the integral, we make the substitution

$$\widetilde{\left[\hat{B},\hat{\mathcal{H}}\right]}(g) = \int_{\mathbb{H}^n} dg' \widetilde{B}(g') \left[\widetilde{\text{H.c.}}\left(g'^{-1}g\right) - \widetilde{\text{H.c.}}\left(gg'^{-1}\right) \right]. \tag{80}$$

The products $g'^{-1}g$ and gg'^{-1} are

$$g'^{-1}g = \left(s - s' + \frac{1}{2}\left(xy' - x'y\right), x - x', y - y' \right)$$
$$gg'^{-1} = \left(s - s' + \frac{1}{2}\left(x'y - xy'\right), x - x', y - y' \right)$$

and we change variables $g'' = g'^{-1}g, g'' = gg'^{-1}$ in both expressions to write

$$(s,x,y) = \left(s'' + s' + \frac{1}{2}\left(x'y'' - x''y'\right), x'' + x', y'' + y' \right)$$
$$(s,x,y) = \left(s'' + s' + \frac{1}{2}\left(x''y' - x'y''\right), x'' + x', y'' + y' \right).$$

The integration variables in eq.(79), using eq.(80), are g' and $g'' \to g$, so we write

$$\dot{B}(q,p) = \int_{\mathbb{R}^{2n+1}} dsdxdy \int_{\mathbb{R}^{2n+1}} ds'dx'dy' \widetilde{B}(s',x',y') \widetilde{\text{H.c.}}(s,x,y) \left(-4\pi^2\right)$$
$$\left[\left(s+s'+\frac{1}{2}(x'y-xy')\right) - \left(s+s'+\frac{1}{2}(xy'-x'y)\right)\right] e^{2\pi i\left[q(x+x')+p(y+y')\right]},$$

that is

$$\dot{B}(q,p) = \int_{\mathbb{R}^{2n+1}} dsdxdy \int_{\mathbb{R}^{2n+1}} ds'dx'dy' \widetilde{B}(s',x',y') \widetilde{\text{H.c.}}(s,x,y)$$
$$\left[-4\pi^2\,(x'y-xy')\right] e^{2\pi i\left[q(x+x')+p(y+y')\right]}.$$

The r.h.s of this expression can be written in a suitable way

$$\begin{aligned}\dot{B}(q,p) = &\int_{\mathbb{R}^{2n+1}} ds'dx'dy' \widetilde{B}(s',x',y')(2\pi i x')\, e^{2\pi i(qx'+py')} \\ &\int_{\mathbb{R}^{2n+1}} dsdxdy \widetilde{\text{H.c.}}(s,x,y)(2\pi i y)\, e^{2\pi i(qx+py)} - \\ &\int_{\mathbb{R}^{2n+1}} ds'dx'dy' \widetilde{B}(s',x',y')(2\pi i y')\, e^{2\pi i(qx'+py')} \\ &\int_{\mathbb{R}^{2n+1}} dsdxdy \widetilde{\text{H.c.}}(s,x,y)(2\pi i x)\, e^{2\pi i(qx+py)}\end{aligned}$$

to recognize the Poisson brackets. In fact,

$$\begin{aligned}(2\pi i x) e^{2\pi i(qx+py)} &= \frac{\partial}{\partial q}\, e^{2\pi i(qx+py)} \\ (2\pi i y) e^{2\pi i(qx+py)} &= \frac{\partial}{\partial p}\, e^{2\pi i(qx+py)}\end{aligned} \tag{81}$$

and the same identities hold for the prime variables. Thus we write

$$\begin{aligned}\dot{B}(q,p) = &\frac{\partial}{\partial q} \int_{\mathbb{H}^n} dg'\, \widetilde{B}(g') \rho_{(q,p)}(g') \frac{\partial}{\partial p} \int_{\mathbb{H}^n} dg\, \widetilde{\text{H.c.}}(g) \rho_{(q,p)}(g) - \\ &\frac{\partial}{\partial p} \int_{\mathbb{H}^n} dg'\, \widetilde{B}(g') \rho_{(q,p)}(g') \frac{\partial}{\partial q} \int_{\mathbb{H}^n} dg\, \widetilde{\text{H.c.}}(g) \rho_{(q,p)}(g).\end{aligned}$$

But each integral represents the classical expression of the corresponding observable, so

$$\begin{aligned}\dot{B}(q,p) &= \frac{\partial}{\partial q} B(q,p) \frac{\partial}{\partial p} \text{H.c.}(q,p) - \frac{\partial}{\partial p} B(q,p) \frac{\partial}{\partial q} \text{H.c.}(q,p) \\ &= \left\{B(q,p), \text{H.c.}(q,p)\right\}_{(q,p)}.\end{aligned}$$

In the last line, the Poisson brackets have been obtained and the procedure just shown explains how to deduce eq.(35) from eq.(33).

References

1. Agostini, F., Caprara, S., Ciccotti, G.: Do we have a consistent non-adiabatic quantum-classical dynamics?. Europhys. Lett. **78** 30001 (2007).
2. Bonella, S., Coker, D.F. : LAND-map, a linearized approach to non-adiabatic dynamics using the mapping formalism. J. Chem. Phys. **122** 194102 (2005).
3. Burghardt, I.: Dynamics of coupled Bohmian and phase-space variables: a moment approach to mixed quantum-classical dynamics. J. Chem. Phys. **122** 94103 (2005).
4. Burghardt, I., Parlant, G.: On the dynamics of coupled Bohmian and phase-space variables: a new hybrid quantum-classical approach. J. Chem. Phys. **120** 3055 (2004).
5. Caro, J., Salcedo, L.L.: Impedimets to mixing classical and quantum dynamics. Phys. Rev. A **60** 842 (1999).
6. Causo, M.S., Ciccotti, G., Montemayor, D., Bonella, S., Coker, D.F.: An adiabatic linearized path integral approach for quantum time correlation functions: electronic transport in metal-molten salt solutions. J. Phys. Chem. B **109** 6855 (2005).
7. Causo, M.S., Ciccotti, G., Bonella, S., Vuilleumier, R.: An adiabatic linearized path integral approach for quantum time-correlation functions II: a cumulant expansion method for improving convergence. J. Phys. Chem. B **110** 16026 (2006).
8. Folland, G.B.: *Harmonic analysis in phase space*. Princeton University Press, Princeton, NJ (1989).
9. Hughes, K.H., Parry, S.M., Parlant, G., Burghardt, I.: A hybrid hydrodynamic-liouvillian approach to mixed quantum-classical dynamics: application to tunneling in a double well. J. Phys. Chem. A. **111** 10269 (2007).
10. Imre, K., Özimir, E., Rosenbaum, M., Zweifel, P.F.: Wigner method in quantum statistical mechanics. J. Math. Phys. **8** 1097 (1967).
11. Kapral, R., Ciccotti, G.: Mixed quantum-classical dynamics. J. Chem. Phys. **110** 8919 (1999).
12. Kisil, V.V.: Quantum-classical brackets. Internat. J. Theoret. Phys. **41** 63 (2002).
13. Kisil, V.V.: p-Mechanics as a physical theroy: an introduction. Internat. J. Phys. A **37** 183 (2004).
14. Kisil, V.V.: p-Mechanics and field theory. Rep. Math. Phys. **56** 161 (2005).
15. Kisil, V.V.: A quantum-classical bracket from p-Mechanics. Europhys. Lett. **72** 873 (2005).
16. Kubo, R., Toda, M., Hashitsume, N.: *Statistical physics II: non equilibrium statistical mechanics*. Ed. Springer-Verlag (1985).
17. Mac Kernan, D., Ciccotti, G., Kapral, R.: Surface-hopping dynamics of a spin-boson system. J. Chem. Phys. **116** 2346 (2002).
18. Nielsen, S., Kapral, R., Ciccotti, G.: Mixed quantum-classical surface hopping dynamics. J. Chem. Phys. **112** 6543 (2000).
19. Nielsen, S., Kapral, R., Ciccotti, G.: Statistical mechanics of quantum-classical systems. J. Chem. Phys. **115** 5805 (2001).
20. Prezhdo, O.V., Kisil, V.V.: Mixing quantum and classical mechanics. Phys. Rev. A **56** 162 (1997).

Index